CENTRAL LIBRARY

SCHOLARLY ARTICLES

A CURRENT AWARENESS BULLETIN OF ARTICLES BY FACULTY, STUDENTS AND ALUMNI

~ *JUNE 2013* ~

DELHI TECHNOLOGICAL UNIVERSITY
(FORMERLY *DELHI COLLEGE OF ENGINEERING)*
GOVT. OF N.C.T. OF DELHI
SHAHBAD DAULATPUR, MAIN BAWANA ROAD
DELHI 110042

PREFACE

This is the Sixth Issue of Current Awareness Bulletin for the year 2013, started by Delhi Technological University Library. The aim of the bulletin is to compile, preserve and disseminate information published by the Faculty, Students and Alumni for mutual benefits. The bulletin also aims to propagate the intellectual contribution of DTU as a whole to the academia. It contains information resources available in the internet in the form of articles, reports, presentation published in international journals, websites, etc. by the faculty and students of Delhi Technological University in the field of science and technology. The publication of Faculty and Students, which are not covered in this bulletin, may be because of the reason that the full text either was not accessible or could not be searched by the search engine used by the library for this purpose. To make the bulletin more comprehensive, the learned faculty and Students may provide their uncovered publication to the library either through email or in CD, etc.

This issue contains the information published during June 2013. The arrangement of the contents is alphabetical wise starting from A-Z. The Full text of the article, which is either subscribed by the University or available in the web, is provided in this Bulletin.

CONTENTS

1. A Two Layer Approach to Image Authentication and Encryption through ECC & Voice Features (MFCC, Pitch Value) *__Vikas Pardesi__ *and* __*N. S. Raghava__

2. An Efficient Biogeography based Face Recognition Algorithm *__Daya Gupta,*Lavika Goel__ and *__Abhishek__

3. Bio-Inspired Distributed Sensing Using a Self-Organizing Sensor Network __*Indu Sreedevi__ *and* __*Asok Bhattacharyya__

4. ChaMAILeon: Exploring the Usability of a Privacy Preserving Email Sharing System __$Mayank Gupta__

5. *Characterization of PV Cell- Environmental factors consideration** __Dr.Vishal Verma__

6. *Current mode full wave rectifier based on a single MZC-CDTA* __*Neeta Pande__ *and* __*Rajeshwari Pandey__

7. *Disturbance Immune DFIG based Wind Energy Conversion System* __*Vishal Verm__ *and* __*Swati Tanton__

8. Economic Analysis of Biodiesel Produced from Waste Cooking Oil __$Shashank Mohan__

9. Effect of holmium substitution on electrical properties of strontium bismuth tantalate ferroelectric ceramics __*A. K. Jha__

10. EFFECT OF MILLING TIME ON PHASE TRANSITION IN BaTi0.095W0.05O3 NANOCERAMICS SYNTHESIZED BY HIGH-ENERGY BALL MILLING __*A. K. JHA__

11. Band gap maps for Photonic Crystal with Honeycomb lattice for different shapes of scatterers *__Vinita__ *and* __*A. Kumar__

12. Enhancement Of Voltage Profile Of Transmission Line By Using Static VAR Compensator-An Overview __*Rishabh K. Gupta, *Rahul Kapoor__ *and* __*Rajesh Garai__

13. **Face Recognition Using Moments and Wavelets** ***Rajiv Kapoor***

14. From the Executive Editor __*Dr. Ruchika Malhotra__

15. Influence of Aggressive Chemical Environment on High Volume Fly Ash Concrete ***Verma, A.** and __*Sahu, A. K__

16. NATURAL PIGMENTS-A MEDICINAL PERSPECTIVE ***Anuja Agrawal***

17. On The Application Of Artificial Life Based Test Data Generation ***Harsh Bhasin***

18. Optical and electro-catalytic studies of nano structured thulium oxide for vitamin C detection ***Appan Roychoudhury*** and ***B. D. Malhotra***

19. Particle Swarm Optimization and Firefly Algorithm: Performance Analysis ***Bharat Bhushan*** and ***Sarath S. Pillai***

20. Performance of Fly Ash and Stone Dust Blended Concrete in Acidic Environment ***Verma, A***. and ***Sahu, A. K.***

21. Public Key Cryptography Using Genetic Algorithm ***Swati Mishra*** and ***Siddharth Bali***

22. SCOPE OF BETALAINS AS A FOOD COLORANT ***@Anuja Agrawal***

23. Selection of Optimal Mother Wavelet for Fault Detection Using Discrete Wavelet Transform ***@H. L. Yadav***

24. Single Input Four Output Current mode filter using Operational Floating Current Conveyor ***Neeta Pandey, *Deva Nand*** *and* ***Zubair Khan***

25. The Comparative Study of Software Maintenance Forecasting Analysis Based on Back propogation (NFTOOL and NTSTOOL) and Adaptive nuero fuzzy interference system ANFIS ***@Anuradha Chug***

26. Waste cooking oil: a promising feedstock for biodiesel production through power ultrasound and hydrodynamic cavitation **Amit Pal**

***** **Faculty**
# **Alumni**
$ **PG Scholar**
@ **Research Scholar**

A Two Layer Approach to Image Authentication and Encryption through ECC & Voice Features (MFCC, Pitch Value)

Vikas Pardesi, N. S. Raghava

Abstract- Speech Processing is an area in which we can find such unique features (Mel Frequency Cepstrum Coefficients, Pitch value, zero crossing rates etc.) in voice segment for recognition of any individual and pre-processing for further synthesis. In this paper we are presenting a simplified approach to image authentication with MFCC (Mel Frequency Cepstrum Coefficients) and Pitch Value and image Encryption through Elliptic Curve Cryptography. Because of ECC great advantages (small key size, no solution to discrete logarithmic problem, less time consuming encryption, infinite time taken for brute force attack) for handheld, portable devices. Applying MFCC and Pitch information with various methods on various encrypted images which is encrypted by Elliptic Curve Cryptography and at the receiver side we do reverse process of this approach for authentication and decryption of image .With this approach we can authenticate an image through voice segment which is advantageous because speech is a natural way to interact with people, Not required to sit and work with a keyboard and finally no specific training is required for end users.

***Index Terms*— Elliptic curve cryptography, MFCC, Pitch value, public key cryptography, Speech Processing**

I. INTRODUCTION

Today, in this information era we are just totally dependent on the computers, internet and such other information technology, here we are talking about security. Security is a very small term to understand but it is very difficult to implement a better security approach in transferring of the data. In area of information security [1] there are many algorithms and techniques which is using for secure transferring of the data as data encryption standard [1], elliptic curve cryptography [2] and RSA [1] technique. Apart from this if we are talking about speech processing [3] area then it should be no hyperbole that it is a very vast area for research. Speech is biometric for human being that is freely available to every individual.

Speech of any individual has many properties such as it is a unique feature of every individual, processing of speech is very easy, easy input given method (no need of computer keyboard for inserting data).

In this paper we are describing our two layer secure approach to image security through Elliptic curve cryptography and voice features (MFCC [4] & Pitch [4] value), first we will see how a voice can be helpful for processing of images in secure environment.

Manuscript received April, 2013

Vikas Pardesi, Dept. of Information Technology, Delhi Technology University, Delhi, India.

N. S. Raghava, Dept. of Information Technology, Delhi Technology University, Delhi, India.

Any human being speech or voice has many unique properties or we can say features such as Mel Frequency Cepstrum Coefficients [4], Pitch of voice [4], fundamental frequency [4], fundamental formants [4], linear predictive coefficients [4],
Cepstrum coefficients, line spectral Pairs, 2-D, 3-D-spectrogram etc. now our main motive is to find the Mel frequency Cepstrum coefficients and pitch value through best approach.

Mel frequency Cepstrum can be defined as the short time power spectrum [16] of a speech signal. It can be calculated as linear cosine transform of the log power spectrum on a nonlinear Mel scale of frequency. Mel frequency Cepstrum coefficients are the unique features that can be acquired from the voice segment.

$$MelFrequency = 2595 * \log(1 + \frac{F}{700})$$

Where F is the linear frequency. Procedure and method is given in separate section in detail to calculate Mel frequency Cepstrum coefficients.

Pitch of any human being's voice is also unique feature. Voice speech is generated when the excitation comes from a periodic pulse train generated by vocal cords [15]. These vocal cords vibrate with their natural frequency of vibration like a tuning fork and generate pulses at regular interval. A speech signal consists of different frequencies which are harmonically related to each other in the form of a series. The lowest frequency of this series is known as the fundamental frequency or pitch frequency. Pitch calculation can be done with four method (1) Autocorrelation method [6], Average Magnitude difference method [6], these methods were in time domain (2) Parallel processing approach [6], (3) pitch period using spectral domain [6] or frequency domain, (4) pitch period using Cepstrum domain. For example With Auto-correlation method

$$Rxx = \lim_{N \to w} \frac{\sum_{i=0}^{2N} a(i) * a(i+k)}{2N+1}$$

Where $a(i)$ is the sample number and k is the interval and N is the total number of samples, R_{xx} is the resultant.

Now we show a brief introduction to encryption and decryption of image. In encryption method we are taking those points which are satisfying the elliptic curve, from these points we take one point AF(x, y) which is affine point and a base point BP(x, y). Base point is the smallest (x, y) point i.e., satisfying the Elliptic curve $y^2=x^3+ax+b$ where $4a^3+27b^2 \neq 0$. Each value of 'a' and 'b' can give a different curve. We take one affine point and then we take each pixel value one by one onto image. We perform point multiplication operation with two entity i.e., pixel value and affine point $S=P_I*AF(x, y)$.

Where P_I is pixel value. In Elliptic Curve Cryptography point multiplication is the basic operation which consists of two operation point addition & point doubling. After multiplication operation we get a point cipher text as {N*BP(x, y)} where N is the random number and BP is the base point and (x, y) one point we get after multiplication. Ultimately we get our Cipher Text CT_T= {(x1, y1), (x2, y2)} Where (x1,y1) we got from N and BP multiplication and (x2, y2) is (S + N*PK_B) where S=P_I*AF and P_I is scalar value i.e. pixel value and AF is affine point. And N is a random number and PK_B is public key of user B so at last we got encrypted message in co-ordinate format, namely (N*BP, S + N*PK_B).

In Decryption of the encrypted Image we use the private key of the user B i.e. PRK_B on the first element i.e. N*BP. This will be subtracted from the other term (S+N*PK_B) to recover the S. In last we apply Discrete Logarithmic problem [7] to recover our pixel value i.e., P_I.

Due to using discrete logarithmic approach it is also advantageous that no solution till now found for breaking this. Biggest use of the ECC in security due to it's smallest key.

Structure of this paper follows these points-

- Section 2 describes the concept of finding the MFCC coefficients from a voice segment.
- Section 3 describes that how we can find the pitch information through a voice and different-2 techniques for finding pitch information.
- Section 4 describes two layer approach i.e., main concern of this paper, states that how encryption is done through Elliptic Curve Cryptography and results of implementation.
- Section 5 describes that how image authentication works through MFCC coefficients and pitch information.
- Section 6 states its application and future work.
- Section 7 is separated for conclusion and discussion.

II. CONCEPT OF EXTRACTING THE MFCC FEATURE THROUGH VOICE SEGMENT

In Auditory System as a filter bank gives a clear indication that critical band filters must be formed but the shape and the structure of the filter is not clear. Two commonly used frequency scales they are bark scale [13] and Mel scale [13], here we describes about Mel frequency and Mel scale. Basis of the Mel scale is pitch perception and filter is used in this i.e., triangular filter. The scale is linear below 1000 Hz and non-linear (logarithmic) above 1000 Hz. We can convert normal frequency to Mel frequency with formula Mel frequency=2595*log (1+linear frequency/700).

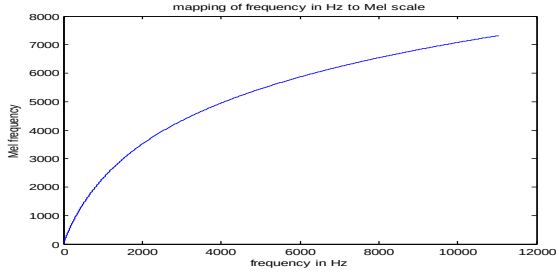

Fig-1.1 Mapping of frequency in Mel Scale

Now Mel frequency Cepstrum can be described as the short time power spectrum of a speech segment, which can be computed as linear cosine transform of the log power spectrum on a non-linear Mel scale of frequency. MFCC are the coefficients we got in the MFC representation. Now consider about the difference about Cepstrum [9] and MFC, in MFC frequency band are equally spaced on the Mel scale. Mel scale approximates the human auditory response very much closed to than the linearly-spaced frequency bands used in the case of spectrum. Mel scale wrap up the frequency and allows better representation similar to the human auditory system.

A. Procedure for calculating the Mel frequency Cepstrum coefficients:

- Take the FFT [14] (fast Fourier transform of a windowed signal).calculate its squared magnitude i.e., power spectrum.
- Pre analysis the spectrum to approximate the unequal sensitivity of human hearing at different frequencies.
- Combined the power spectrum within the overlapping critical band filter response. This integration is being done through triangular overlapping windows called Mel filters. This reduces the frequency sensitivity over the original spectral estimate; basically on higher frequencies are analyzed because of the wider band.
- Compress the spectral amplitude by taking log. Optionally the combination of log power spectrum [8] may be done.
- Take the IDFT (inverse discreet cosine transforms). This gives the cepstral coefficients.
- Perform spectral smoothing this is achieved by the truncating the spectrum, lower 12 or 14 coefficients are used out of 20 or more coefficients.

B. On the basis of these steps flow chart for better understanding of extraction method-

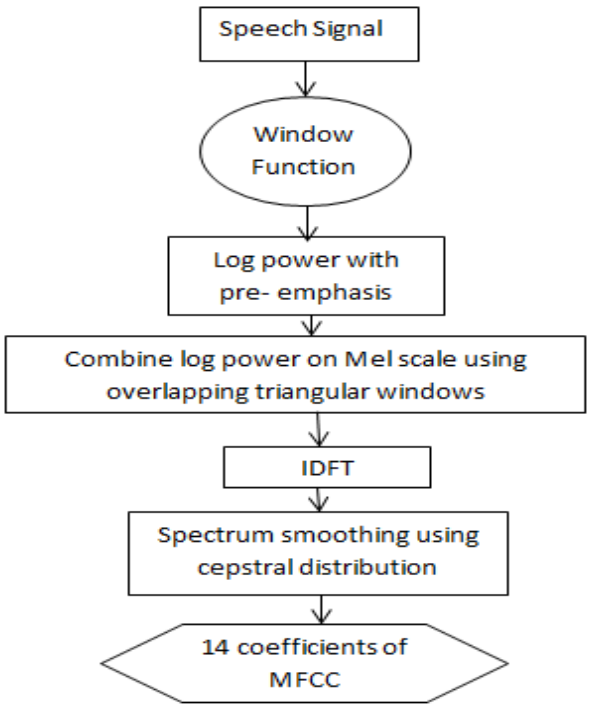

Fig-1.2 Flow Chart For Extracting MFCC

C. Algorithm-

Step-1 open the audio voice segment with FOpen()command;

Step-2 Read this voice segment with Fread ();

Step-3 fix the number of samples as you required and find FFT of this segment of voice.

Step-4 Find the log of the previous step output.

Step-5 for 1 to sample number Convert linear frequency to Mel frequency

Step-6 using function melcepst() for finding the Mel frequency Cepstrum coefficients.

Generally our speech does not follow linear way so this natural frequency we have to convert into Mel frequency or in any kind of frequency on which we can do analysis or synthesis of our speech signal. Above we discussed how can we convert our normal frequency to Mel frequency and also that how can we find the Mel frequency Cepstrum coefficients.

III. FIND PITCH VALUE FROM VOICE SEGMENT

There are different frequencies in the speech signal which are periodically related to each other in a manner. The lowest frequency of this series is known as the pitch frequency or fundamental frequency. Basic frequency of the vibrations of the vocal cords is called pitch frequency. vocal cords generate this frequency in the form of periodic excitation passes via the vocal tract filter and become convolved with the impulse response of the filter to produce a voice or speech signal because speech is a convolved signal. The number of samples after which the waveform repeats itself will reveal the pitch period in terms of number of samples. We can also find the time corresponding to these samples and calculate the inverse of time period then we get frequency in Hz.in time domain main theory is used for pitch detection i.e., find the similarity between the original speech and it's shifted speech. There are many methods for finding the pitch they are as follows.

1. Time Domain Approach

A. Autocorrelation Method for finding pitch Frequency:

Autocorrelation is the correlation of a signal with itself. We can say that this is a measure of the similarity between samples as a function of the time separation between them. It can be considered as a mathematical tool to find repeating patterns and their periods. Autocorrelation methods need at least two pitch periods to detect pitch.

$$R_{xx} = \lim_{N \to w} \frac{\sum_{i=0}^{2N} a(i) * a(i+k)}{2N+1}$$

Where *a(i)* is the i^{th} sample number and *N* is total number of samples and *K* is the interval and R_{xx} is the result.

B. Average Magnitude Difference Function:

We make the difference signal D by delaying the input speech by various amounts, subtracting the delayed waveform from the original, and summation of the magnitude of the difference between sample values. Finally we take the average of the difference function over the number of samples. Difference signal is always zero at delay zero.

$$AMDF\ (k) = \frac{\sum_{i=1}^{N} abs[a(i) - a(i+k)]}{N}$$

Where *a(i)* is the current sample and *N* is the total number of samples and *k* is the interval.

2. Frequency Domain Approach

A. FFT (fast Fourier transform) based method in Spectral domain:

First we have to know about spectral domain so we studied in above approach that are time domain approach and now we discuss about Frequency domain approach, in frequency domain we work with speech spectrum so it is called spectral domain. Generally there are four method for finding pitch in frequency domain they are as follows (a) FFT based Method, (b) Harmonic peak detection method, (c) spectrum similarity method, (d) spectral autocorrelation method. Here we discuss only one i.e., FFT based method. In this FFT is a very fast algorithm for computing the discrete Fourier transform. When we say take K=130 point DFT, we will get 130 DFT coefficients. The n^{th} DFT coefficients X (n) of any sampled signal x (k) is given by

$$X(n) = \sum_{n=0}^{K-1} x(k)(W)^{nk} \quad \text{Where W is } W = e^{-j4\frac{\pi}{2}/N}$$

Algorithm-

Step-1 Take the voiced Segment of speech containing N samples.

Step-2 Take a N-samples point FFT and plot it.

Step-3 Track First Frequency as fundamental frequency.// resolution of the fundamental frequency measurement is achieved by the number of points in the FFT. Say a N point FFT, the frequency resolution will improve to (basic frequency)/N. Using FFT is not sure that it gives exact pitch , it depends on the DFT domain resolution.

Step-4 fundamental frequency is the FFT point number (first peak) multiplied by the frequency resolution.

Step-5 Note the position of the first peak and multiply with step (4).

Step-6 END.

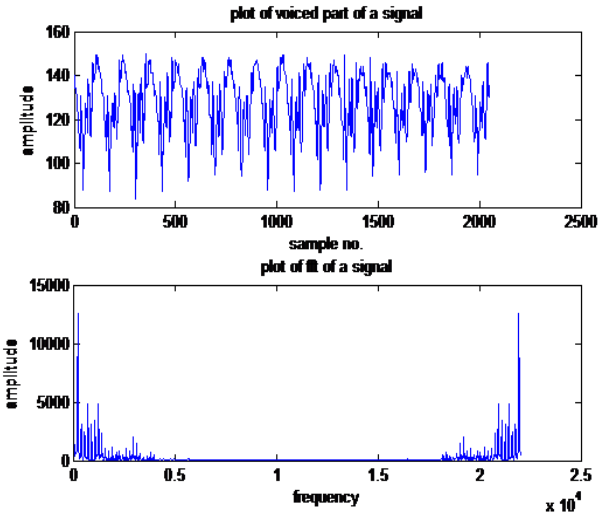

Fig-1.3 Plot of voiced part of a signal and FFT of that signal

For example we took a speech segment and first we separate the voiced part and unvoiced part of the signal then we find th pitch value through Fast Fourier Transform. Above given graph is showing plot of voiced part of the signal and plot of FFT of the voiced part of the signal. From our example we find our first peak occurs at 16^{th} position and has a value of 12560. Resolution frequency is 10.80 Hz so fundamental frequency is 10.8*16 i.e., 172.26 Hz. It is a valid pitch frequency and further we will use in our implementations.

IV. TWO LAYER APPROACH AND IMPLEMENTATION RESULTS

The main area of interest of this paper is here because here we have two layer approach and applied this on an image in secure transferring over network. We have to find Mel frequency Cepstrum coefficients with the above given formulas. So here we take one speech segment

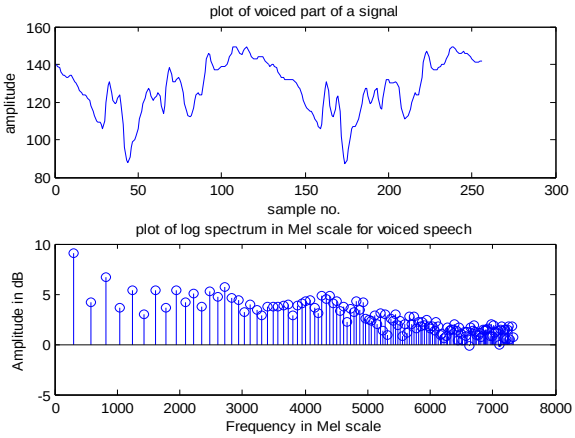

Fig-1.4 Plot of Voiced part of signal

We took one speech segment and find its voiced part first and then we find the log spectrum in Mel scale frequency. We got above given plot of that result. Now we have to find the MFCC for voiced speech [25] then below given graph is showing that 14 coefficients we are getting and they are plotted s follows.

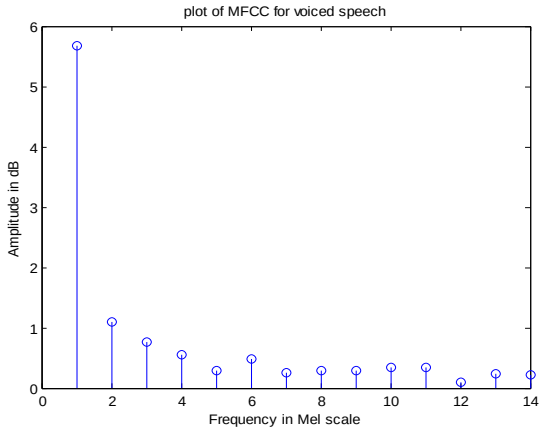

Fig-1.5 Plot of MFCC for voiced part of Speech

We got array of 14 coefficients they are as follows 5.6999, 1.0993, 0.7545, 0.5487, 0.2899, 0.4800, 0.2525, 0.2825, 0.2831, 0.3480, 0.3459, 0.1003, 0.2398 and 0.2271. if we plot a graph for this then the graph will show actual flow of the data in voiced part.

We can also find these coefficients from MATLAB command 'melcepst' for voice box, but you have to first install that tool box into your MATLAB software. Now we have to perform operation and apply these coefficients and pitch value to an image with this approach-

$$R = \sum_{i=1}^{14} \left(\frac{Xi}{14}\right) * \mathrm{P}$$

Where X_i is the coefficients and P is the pitch value and R is the resultant. Apply this resultant in a 2D image given below.

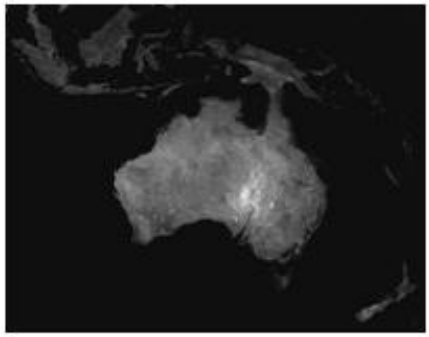

Fig-1.6 Original Image

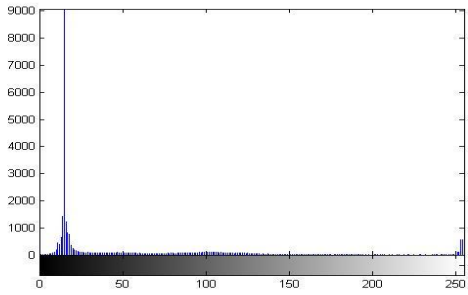

Fig-1.7 Histogram of Original Image

For applying on each pixel of the image we call a function

MFCConIMAGE (A[N][M], R)

```
Step-1 for (i=0 to N-1)
      {
        For (j=0 to M-1)
          {
            A[i] [j] =A [i] [j]*R;
          }
    }
```

Step-2 Traverse on each pixel value of the image to locate the pixel value.

Step-3 End;

After apply this approach we get below shown result.

Where i and j is the pixel values at x axis and y axis respectively. R we got from above mentioned formula. After applying MFCC value and pitch value our image get distracted and will be noisy that is also good for secure transferring over network. Here result of image is purely black and no one can identify any thing in the resultant image. Further we will find it's histogram for see the changes after performing operation.

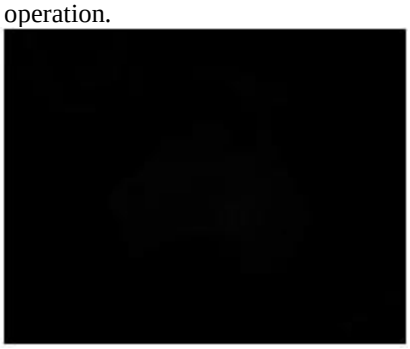

Fig-1.8 MFCC coefficients and pitch value applied on Image

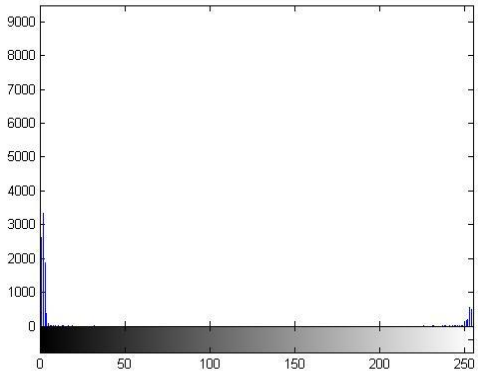

Fig-1.9. Histogram of above image after applied MFCC and pitch value to image

Now we have to apply ECC (Elliptic Curve Cryptography) on this output image and then we transfer over network, so now task is how to encrypt the image with ECC Encryption so we have to understand some points about ECC Encryption they are as follows-

- ECC is a public key algorithm which works on private key and public key.
- ECC designed and mainly used for handheld devices and small devices which are low in memory and resources.
- ECC successfully implemented first by Koblitz and miller [10].
- ECC encryption uses elliptic graph, onto this graph which points are generated that are taken for encryption.
- Main use of ECC is for those devices which can work only in constrained environment.

There is two operations involved in ECC which are (1) Point Multiplication [11] which internally consists two operation i.e., point addition and point doubling, in point doubling it doubles the point which is of same kind with point doubling formula i.e., say one point is $T(X_T, Y_T)$

$L(X_L, Y_l)=2T(X_T, Y_T)$

$X_L=S^2-2X_T \bmod p$

$Y_L=-Y_T+S(X_T-X_L) \bmod p$

$S=(3X_T^2+a)/(2Y_T) \bmod p$

Where S is the tagent at point T and a is one of the parameter chosen with the elliptic curve and p is a prime number.

Now in point addition it is used for addition of two points with point addition formula i.e., say two points $P(X_P, Y_P)$ and

$Q(X_Q, Y_Q)$ then $I(X_I, Y_I)$

$X_I= S^2-X_P-X_Q \bmod p$

$Y_I= -Y_P+S(X_P-X_I) \bmod p$

$S=(Y_P-Y_Q)/(X_P-X_Q) \bmod p$

Where S is the tagent passing through P and Q and p is a prime number.

ECC point generation

According to elliptic curve $y^2=(x^3+ax+b) \bmod p$ where $4a^3+27b^2\neq0$ we have to generate points that lies on elliptic curve. Let p=39, a=-1, b=1 on which 'a' and 'b' value satisfying above equation. We do encrypt so first of all we generate all points that satisfies the elliptical curve follow this function **GeneratePoints (a, b, p)**

Step 1 take x=0 or any other positive integer

Step 2 loop until x<p

I. $Y^2=(x^3+ax+b) \bmod p$

II. If y^2 is perfect square

Print(x, square root (y))

Else

x=x+1;

Step 3 End

where p is a prime number, x and y are co-ordinates.

ECC Encryption

Step 1-For all P_I (pixel value)

Find $S=P_I *AF_M$ //*P_I is constant, AF_M is random Affine-point in elliptic curve. *//

Step 2- Find $PK_B=PRK_B*BP$ //*B_P is the base point Of Elliptic curve, PRK_B is the private key. *//

Step 3- End;

Encrypted data= $(N*BP, S+N*PK_P)$

ECC decryption

Follow this method for decryption,

Let N*BP be the first point and $(S+N*PK_B)$ be the second point PRK_B *N*BP=PRK_B *first point

Calculate $S=S+N*PK_B-PRK_B*N*BP$

Calculate the scalar value of 'P_I' from S_M using discrete logarithmic problem [7]. Where PK_A, PRK_A and PK_B, PRK_B is the public key and private key of user A and B respectively.

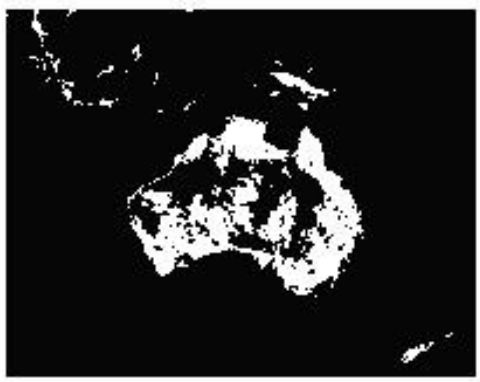

Fig-1.10 After ECC decryption of Image

In decryption of the ECC we will use the Discrete logarithmic Problem, after applying on each pixel we get all the decrypted 2D-matrix i.e., image. Below histogram is shown of above image and we can analyze this histogram with original image's histogram. It is approximately same.

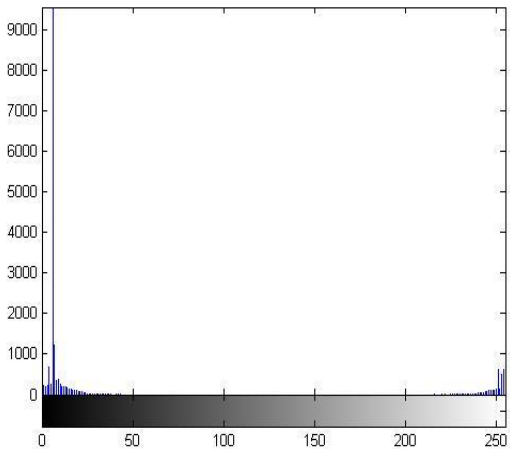

Fig-1.11 Histogram of Decrypted mage

Above shown image is the decrypted image after Discrete Logarithmic problem [7]. Now this image we got at the

receiver side but we have to follow one operation also i.e., remove the MFCC coefficients from encrypted image then we got our real image.

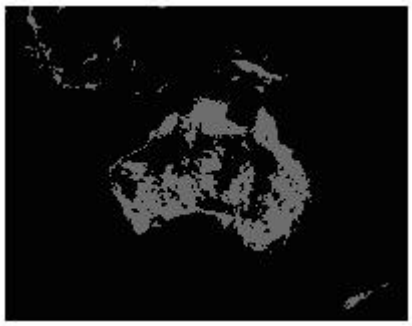

Fig-1.12 Remove MFCC and Pitch from Original Image

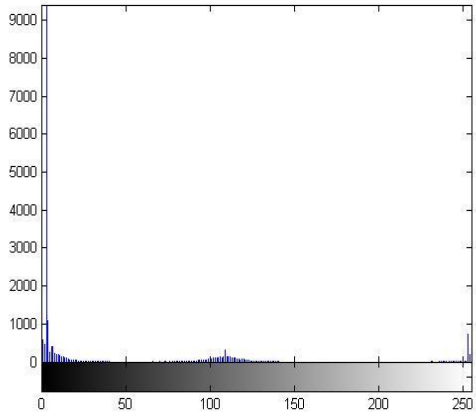

Fig-1.13 Histogram of Received Image after removing MFCC and Pitch.

We just apply reverse operation for removing the MFCC and pitch value. Now we can analyze our result image maximum feature of the image can be identified and this method is better working for satellite image further more operation can be performed on the resultant image if we want to enhance the image.

V. IMAGE AUTHENTICATION THROUGH MFCC

As we know very well use of images in now days is very much, in area of cryptography, in area of forensic science, in daily life and images is the best option to hide the data and transfer over network. Main concern in today's life is to secure the images and authentication of genuine images is very much. We have to protect our image from hackers and authenticate the sender is genuine or not and also we have to maintain the integrity of the data. In information security there are many algorithms which are used for authentication such as digital signature, digital certificate etc. in this paper our new idea is we are protecting the image from MFCC coefficients.

According to the paper we are using one sample voice segment and we find the MFCC coefficients and apply on image and then we are encrypting the image through MFCC and we all know very well that each human's voice is unique and MFCC also used for speaker verification so at the receiver side when we find same MFCC coefficients from same voice then we will remove MFCC feature from the image and then we can verify our image is that it is coming from genuine user or not. If anyone alters the message in between the network then real image will not recover. Some malfunctioned image we will get and then that image will not be accepted so with this we can also maintain the message integrity. So with MFCC coefficients we can do image authentication and message integration.

VI. APPLICATIONS & FUTURE WORK

Cryptography has a very great advantage in information security area that except of the expert no one can do harm to the information and securely we can transfer our confidential data to other party. Elliptic Curve Cryptography is a new technology which came in existence since 1965 by Koblitz [10] and miller. A large number of researches is going on ECC but ECC great advantage is its smaller key size compare to other algorithms such as DES (Data Encryption Standard) and RSA (Rivest- Shamir- Adelman). ECC works on small device in a better way compare to huge machines, ECC works on those device which are in constrained environment or use resources in a limit. We can make use of MFCC in making Elliptic curve digital signature through MFCC coefficients and we also can make Elliptic Curve Cryptography Digital certificate Through MFCC. These certificates can also be used further by the third party and also used by many users in different-2 encryption algorithm.

Future work related to decrypted image and image recovered after removing the MFCC coefficients from image, we can further perform image enhancement techniques such as histogram equalization and contrast stretching and noise removal from an image. Further this image can be recovered in a better way by applying the digital image processing [12]. Further if we analyze the histogram of the each image then one by one histogram of the original image and decrypted image is approximately same. Drawback is exactly we are not getting original image but further we can also do many operation with received image for improvement.

VII. CONCLUSION

Proposed approach in this paper works better for satellite images and can better work for text data and further we can also us MFCC coefficients in other encryption algorithm because it is the unique feature from human characteristics and freely available from every user. Here we mean to say each individual can use their voice for authentication of the data and this is more secure in public network. Generally in biometrics speech is available easily and also can detect and synthesized in any condition and in any environment but there is a drawback i.e., noise. If your recording of voice is in noisy environment then it will be a little bit more complex to detect easily the data. With use of speech user need not required keyboard but recording device quality must be better in recording manner. Furthermore work is going on speech processing. We are also just improving our implementation in better way.

REFERENCES

[1] William Stallings,"Cryptography & Network Security", Printce Hall, 5th Edition.

[2] Alessandro Cilardo, Luigi coppolino, Nicola Mazocca, and Luigi Roman, "Elliptical Curve Cryptography Engineering", Proceedings of the IEEE, vol. 94, no 9, pp. 395-406, Feb. 2006 .

[3]"SpeechProcessing",dea.brunel.ac.uk/cmsp/home…/chapter13-speech%20processing.pdf.

[4] en.wikipedia.org/wiki/Speech_processing.

[5] G. Khare, M. Kulkarni, "Generation of excitation signal in voice excited linear predictive coding using discrete cosine transform", TENCON 2005, IEEE region 10, page 1-4.

[6] S.S. Upadhyay , "Pitch detection in time and frequency domain", ICCICT 2012,IEEE, page 1-5.
[7] Adam J. Albirt, "Understanding & Applied Cryptography and Data Security" CRC press, Pearson
[8] G. Malherpe, O. Mesde and H. Riz, "Acoustic synthesis and methodology for improving cochlear implant speech processing techniques", Proc. Of the 25th annual international conference of IEEE *EMBS*, 2003
[9] H.Nagahama, Y.Miyanaga and N.Ohtsuki, "An adaptive speech analysis for speech recognition system", Proc. Of IEEE ISPACS 1999, pp.745-748, Dec. 1999.
[10] N. Kolbitz, Elliptic Curve Cryptosystems, Mathematics of Computation, vol.48, 1987, pp.203-209.
[11] Certicom website http://www.certicom.com/index.php? action =ecc_tutorial, home.
[12] Rafael C. Gonzalez, "Digital Image Processing", Third Edition.
[13] http://en.wikipedia.org/wiki/Mel_scale
[14] http://en.wikipedia.org/wiki/FFT
[15] H. Teffahi, "Relationship between control parameters and outputs in the two massmodel of vocal cords", ICMCS , 2011 IEEE page 1-5.
[16] H.Hoge "A parametric representation of short time power spectrum based on the acoustic properties of the ear", ICASSP 1984, speech and signal processing page 49-51.

Mr. Vikas pardesi, completed his B.Tech from AJAY KUMAR GARG ENGINEERING COLLEGE, Ghaziabad (U.P), INDIA. He currently pursuing M.Tech from DELHI TECHNOLOGICAL UNIVERSITY, DELHI, INDIA. His area of interests are Digital Image Processing, Speech Processing, Graph Theory, Data Structure.

Mr. N. S. Raghava Currently serving DELHI TECHNOLOGICAL UNIVERSITY, DELHI as ASSOCIATE PROFESSOR in Department of Information Technology since 1998. He has a very vast experience in ANTENNA theory. His area of interests are Signal Processing, Wavelet theory, Antenna theory, Speech processing.

An Efficient Biogeography based Face Recognition Algorithm

Daya Gupta
Delhi Technological University
Computer Engineering Department
Delhi, India
e-mail: dgupta@dce.ac.in

Lavika Goel
Delhi Technological University
Computer Engineering Department
Delhi, India
e-mail: goel_lavika@yahoo.co.in

Abhishek
Delhi Technological University
Computer Engineering Department
Delhi, India
e-mail: abhi_umb@yahoo.com

***Abstract*—Extracting the optimal features from images is always required in face recognition algorithm to achieve high accuracy. In this paper we have presented an efficient face recognition algorithm based on Biogeography Based Optimization (BBO). First we extract the features using the principal Component Analysis (PCA) after applying gabor filters and then we apply BBO to get the most desirable features. The proposed biogeography based face recognition algorithm is applied to search the most desirable features based on well defined fitness function. Performance analysis is performed using Olivetti Research Laboratory (ORL) face database. Performance results show that biogeography based face recognition algorithm generates better results than the original PCA technique with gabor filters.**

Keywords-Face Recognition, Biogeography Based Optimization, PCA, Gabor Filter

I. INTRODUCTION

There is a lot of research avenues in the field of face recognition due to challenges present in the field. The goal of face recognition is to match a given image against a large database of images to check its presence. The face recognition has been applied to two most important applications i.e verification (one to one matching) and identification (one to many matching) [9]. Researchers have presented a lot of techniques for face recognition [1]. These techniques can be categorized as holistic matching method for e.g Principal Component Analysis (PCA) and local feature matching method [2]. In this paper we will focus on PCA. One of the biggest challenges in PCA is that we cannot use it on raw images directly. They need to be properly aligned and uniformly illuminated. This challenge can be solved using gabor filters which takes a raw image, generates gabor filter response and convert the raw image into properly aligned and constantly illuminated image. We have explored the research that showed that Gabor PCA based method for face recognition outperforms PCA based Eigenface method [3]. To improve further this hybrid technique we applied BBO to further optimize the desirable features from the image and go on to illustrate that in our results.

A. Principal Component Analysis

Extraction of features from the images is the foremost step in face recognition. PCA is a standard technique used for feature extraction. The image in the form of A x A matrix can be expressed as a point in the space A x A dimensions. The goal of PCA is to find the required vectors that can represent the image information and form another space. PCA steps are as follows:

1. Let the training set of face images be $\Gamma_1, \Gamma_2, \Gamma_3, \dots\dots\dots, \Gamma_p$.
2. We calculate the average face of the set by $\psi = \frac{1}{p}\sum_{r=1}^{p}\Gamma_r$.
3. We calculate the difference of each face from the average by vectors $\phi = \Gamma_i - \psi$.
4. We calculate eigenvalues and eigen vectors from covariance matrix as shown (1) and a new face image is transformed into its face components by this operation [2].
$$c = \frac{1}{p}\left[\sum_{R=1}^{p}\emptyset_R{\emptyset_R}^T\right] \quad (1)$$
5. We calculate weights using (2) and from them we form a vector $\Omega = \omega_1, \omega_2, \dots.\omega_p$ that represents the contribution of each eigenvector in representation of input face image.
$$\omega_k = \mu_K^T(\Gamma - \psi), \text{ k = 1,2,……P} \quad (2)$$
where μ_k is eigen vector.

These weights may be used in a face classification algorithm to find which of predefined face classes that describe the face [12].

B. Gabor Filters

Gabor filters generally called as Gabor wavelets or kernels are complex band pass filters. They have shape similar to the shape of the cells of the visual cortex of mammalian brains. These are used in many applications such as extraction of multiresolutional, spatially local features of a confined frequency band [5]. Another important feature of the =Gabor filters is that they act as an efficient tool for facial feature extraction and robust face recognition [3]. In general the family of 2D Gabor filters can be defined in the spatial domain in the following manner. [4, 6, 7, 8, 9]:

$$\psi_{u,v}(a,b) = \frac{f_u^2}{\pi K\eta}e^{-\left((f_u^2/k^2)a'^2+(f_u^2/\eta^2)b'^2\right)}e^{j2\pi f_u a'} \quad (3)$$

Where $a' = acos\theta_v + bsin\theta_v$, $b' = -asin\theta_v + bcos\theta_v$, $f_u = f_{max}/2^{(u/2)}$ and $\theta_v = v\pi/8$.

Each gabor filter represents a gaussian kernel function modulated by complex plane wave whose center frequency and orientation are given by *fu* and *θv*, respectively. The parameter κ and η determine the ratio between center frequency and size of Gaussian envelope. Though we can have different values for above mentioned parameters determining characteristics of the filters, the most common

© 2013. The authors - Published by Atlantis Press

parameters used for face recognition are $\kappa = \eta = \sqrt{2}$ and $f$max = 0.25 [6,7,8,9]. When using gabor filters for facial feature extraction, researchers typically construct a filter bank featuring filter of five scale and eight orientation (comprised of 40 filters as shown in Fig. 1),that is u = 0,1…...p-1 and v = 0,1…,r-1,where p = 5 and r = 8[4].

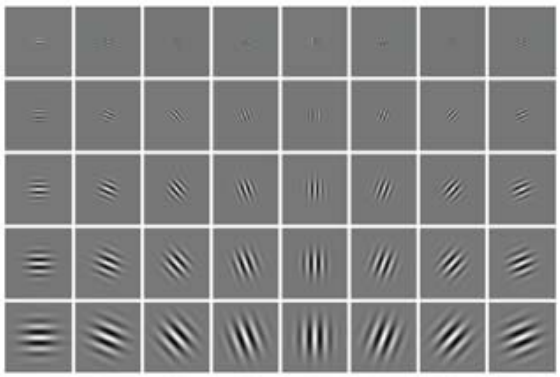

Figure 1. The real parts of the Gabor filter bank commonly used for feature extraction in the field of face recognition [4].

C. *Pricipal Component Analysis of gabor filters*

First we need to apply gabor filter to the raw images to generate gabor filter response and then these gabor filter response act as input to the PCA. The whole process till now is shown in the Fig. 2. Gabor filter provides robustness against varying contrast and brightness. It can also represent characteristic of local face area.

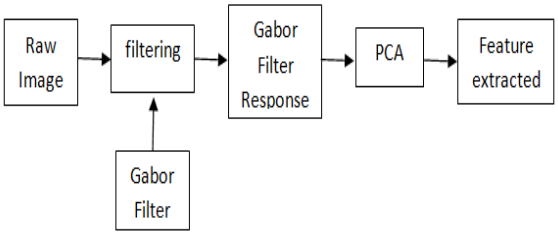

Figure2. Features extraction

Let D(a, b) be a grey scale image of size m x n pixels and let $\psi_{u,v}(a,b)$ denote a gabor filter given by its center frequency fu and orientation θv. The filtering operation of the given face image D(a, b) can be defined as [4, 6, 7, 8, 9]

$$M_{u,v}(a,b) = D(a,b) * \Psi_{u,v}(a,b) \quad (4)$$

Where$M_{u,v}(a,b)$denote the gabor filter response which can be decomposed into real ($E_{u,v}(a,b)$) and imaginary part ($O_{u,v}(a,b)$).

$$E_{u,v}(a,b) = \text{R}\varepsilon[M_{u,v}(a,b)] \quad (5)$$

$$O_{u,v}(a,b) = \text{Im}[M_{u,v}(a,b)]$$

D. *Selecting Optimal features using BBO*

We extract the features using the principal component analysis of gabor filter. But further we need to find the most optimal set of features without compromising accuracy.In the proposed algorithm we are using an evolutionary algorithm based on swarm intelligence known as BBO [14]. BBO is explained in the next section [10].

E. *Biogeography based optimization*

Biogeography is the study of geographical distribution of biological organisms. It aims to learn how species migrate from one island to another. Biogeography is expressed in terms of various factors such as habitat area, immigration rate, emigration rate, habitat suitability index (HSI) and suitability index variables (SIV). Each individual is considered as a "habitat" with a habitat suitability index to measure individual. Suitability index variables (SIV) are those variables of an individual by which we can characterize habitability. A good solution always has a high HSI and a poor solution has low HSI. A good solution shares its features with the poor ones using migration [11, 13, 15, 16].

II. PROPOSED APPROACH FOR USING BBO

After features are extracted using gabor filter and PCA. The extracted features are further minimized using BBO. The final feature subset consists of the most optimal features. Table 1 shows some information about the BBO.

A. *Suitability Index Variable*

In the proposed approach the habitat represents a possible solution (optimal features). The habitat comprises of several Suitability Index Variable (SIVs). Features extracted from every single image represent a SIV.

B. *Habitat Suitability Index and Fitness Function*

Each habitat is evaluated on the basis of habitat suitability index (HSI). Habitat Suitability Index can be considered as a value return by the fitness function. A habitat is considered rich in features if its HSI value is closer to the ideal habitat's HSI value and if its value is far from the ideal HSI value then the habitat is considered as a poor habitat containing less features. Based on the HSI value we can always distinguish between good solution and the bad ones. In order to improve the bad solutions we can migrate certain set of selected features from the ideal solution to bad ones. We have used standard mean as the fitness function for the approach. After developing the training model we use Euclidean distance to calculate the matching score between the features of test image and that of training model.

C. *Distance Calculation*

After the development of train model from the training set images, we calculate the similarity matrix using the matrix which contains the features extracted from test set of images. The distance used to compute the similarity matrix is 'Euclidean'. Euclidean distance is the straight line

distance between two points present in a N-dimensional space. For example, the Euclidean distance between any two points x_i and y_i present in N-dimensional space is given by [10]:

$$D = \sqrt{\sum_{i=1}^{N}(x_i - y_i)^2} \quad (6)$$

TABLE 1. BBO PARAMETERS

Number of iterations of BBO algorithm	120
SIV value	Real
Number of SIVs in a Habitat	120

Extract the features from the training set and test set in matrices as shown in Fig. 2 using Gabor filter and PCA.Lets say 'train_data' is a matrix contains feature extracted from training set and 'test_data' contains features extracted from test set.

1. Calculate the hsi value for the whole train data using fitness function.It will be treated as ideal HSI.
2. Apply BBO for 120 (number of SIVs) iterations and in each iteration do the following :
    a. Calculate HSI value for the SIV (or column) of the image present in test_data matrix.
    b. Compare the calcultaed HSI value with ideal HSI.
    c. If calculated HSI value is close to ideal HSI do nothing.Go to next iteration.
    d. If calculated HSI is not close to ideal HSI then perform migration to improve test_data.
3. Calculate similarity matrix from train_data and test_data using euclidean distance and plot the required curve.

Figure 3: Proposed BBO Algorithm for face recognition.

III. DATABASE AND EXPERIMENTAL SETUPS

For our biogeography based face recognition algorithm we use standard ORL database acquired at the Olivetti Research Laboratory in Cambridge, U.K. The database consists of 400 distinct images that correspond to 40 distinct subjects. Therefore, each subject has 10 facial images each image has got different illumination, pose and facial expression. The size of each image is 92 x 112 pixels and has 8-bit grey levels [9]. Some of the images from the ORL database are shown below in Fig. 4.

Figure 4: Representative set of ORL face database

For our experiment we have used 360 images that is six images per subject. We have divided the images of every subject into two sets. First set (training set) contains the first three images of every subject. Second set (test set) contains the next three images of every subject. So, both training set and test set consists of 120 images each. Training set trains the system and build the train model. Test set is used for assessment and calculation of certain parameters. We develop the train model from the training set by applying gabor filter and PCA and use the same techniques to extract features from test set. Both training set and features extracted from test set images are matrices of size 119 x 120. Each column represents an image or a SIV of length equal to 119. Now, we apply BBO to the features extracted from the test set and use train model as ideal habitat.

IV. PERFORMANCE ANALYSIS

For performance analysis of our biogeography based face recognition algorithm we calculate the similarity matrices, in which each of the image vector is compared with each image vector present in the train model and client and imposter matching scores are calculated. A client is an entity who is making a genuine identity claim whereas imposter is the one making a false identity claim. We calculate performance metrics from the similarity matrix like false acceptance rate (FAR), false rejection rate (FRR), half total error rate (HTER), verification rate at 1%, .1% and 1, etc [4].

$$FRR = (a/b) \times 100\% \quad (6)$$

Where a = number of rejected genuine identity claims and b = total number of genuine claims made.

$$FAR = (c/d) \times 100\% \quad (7)$$

Where c = number of accepted false identity claims and

d = number of false identity claims made.

And HTER is given by

$$HTER = 0.5(FAR + FRR) \quad (8)$$

And verification rate is equal to 1-FRR.

Now, in order to show the efficiency of the proposed biogeography based algorithm we have plotted the receiver operating characteristic (ROC) curve having verification rate on the Y- axis and False Acceptance rate at X-axis. We have plotted two ROC curves in Fig. 5. In Fig. 5 the lower dashed line shows the ROC curve for simple gabor filter and PCA technique without applying BBO and the upper solid line shows the ROC curve for the proposed BBO

based algorithm. Clearly, the proposed biogeography based algorithm shows better verification rate

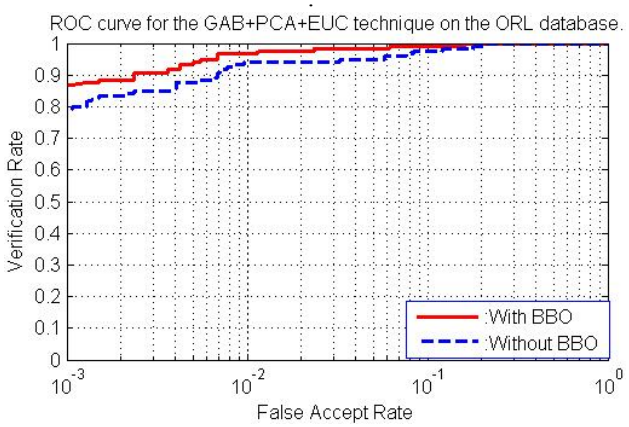

Figure 5. ROC curve for gabor and PCA technique.

V. CONCLUSION

In this paper, we propose an efficient biogeography based face recognition algorithm. We apply Biogeography Based Optimization (BBO) to the features extracted from test set of images after applying gabor filters and PCA as shown in Fig. 2. The proposed algorithm tries to find the most optimal set of features from the images. The performance is evaluated using the standard ORL face database. The results obtained in Fig. 5 shows that the proposed biogeography based algorithm shows better verification rate than the normal face recognition algorithm.

REFERENCES

[1] Rabia Jafri and Hamid R. Arabnia"A survey of face recognition techniques," Journal of Information Processing Systems, Vol.5, No.2, June 2009 .

[2] M. Turk and A. Pentland, "Eigenfaces for recognition. Journal of cognitive neuroscience",3:72-86,1991.

[3] D Murugan, Dr. S Arumugam, K Rajalakshmi and Manish T I "Performance Evaluation of face recognition using Gabor filter, log Gabor filter and discrete wavelet transform", International jouranal of computer science & information Technology(IJCSIT), Vol.2,No.1,February 2010

[4] Vitomir truc and Nikola Pave ic, "The complete Gabor-Fisher classifier for robust face recognition," EURASIP journal on Advances in Signal Processing volume 2010.

[5] V. truc, B. Vesnicer, N. Pave ic, "The phase-based Gabor Fisher classifier and its application to face recognition under varying illumination conditions," in Proceedings of the 2nd International Conference on Signal Processing and Communication Systems (ICSPCS '08), pp, 1-6, Gold Coast, Australia, December 2008.

[6] C. Liu and H. Wechsler, "Gabor feature based classification using the enhanced Fisher linear discriminant model for face recognition", IEEE Transactions on image Processing, vol. 11, no. 4, pp. 467-476,2002.

[7] L. Shen and L. Bai, "A review of Gabor wavelets for face recognition", Pattern Analysis and Applications, vol. 9, no. 2,pp.273-292,2006.

[8] L. Shen,L.Bai, and M. fairhurst, "Gabor wavelets and general discriminant analysis for face identification and verification", Image and Vision Computing,vol. 25, no. 5, pp. 553-563, 2007.

[9] Vitomir truc and Nikola Pave ic, "Gabor-based kernel partial-least squares discriminantion features for face recognition", Informatica, vol.20,no.1,pp.115-138,2009.

[10] Er. Navdeep Kaur Johal, Er. Poonam Gupta and Er. Amanpreet kaur, "Face recognition using biogeography based optimization", International Journal of Computer Science and Information Security, Vol.9,No.5,May2011.

[11] D. Simon, "Biogeography –based optimization", IEEE Transactions on Evolutionary Computation, vol. 12, no. 6, pp. 702-713,2008.

[12] Ki-Chung Chung, Seok Cheol Kee and Sang Ryong Kim, " Face recognition using principal component analysis of Gabor filter responses".

[13] Lavika Goel, Daya Gupta and V. K Panchal, "Hybrid bio-inspired techniques for land cover feature extraction: a remote sensing perpective", Applied soft computing. Elsevier publications, pp. 832-849, vol. 12(2),2011.

[14] Lavika Goel, Daya Gupta and V.K Panchal, "Information sharing in swarm intelligence techniques: a perspective application for natural terrain feature elicitation" International Journal of Computer Applications (IJCA), vol. 32,2011.

[15] Lavika Goel, Daya Gupta and V. K Panchal, " Embedding expert knowledge to Hybrid Bio-Inspired Techniques :an adaptive strategy towards focused land cover feature extraction", International Journal of Computer Science and Information Security (IJCSIS), 1(2),pp. 244-253, 2010.

[16] Lavika Goel, Daya Gupta and V. K Panchal, "Performance governing factors of BBO for land cover feature extraction : An Analytical Study, World Congress on Information and Communication Technologies (WICT) IEEE Publications, pp. 165-170, 2011.

Hindawi Publishing Corporation
Journal of Engineering
Volume 2013, Article ID 959430, 16 pages
http://dx.doi.org/10.1155/2013/959430

Research Article

Bio-Inspired Distributed Sensing Using a Self-Organizing Sensor Network

Indu Sreedevi,[1] Shubham Mankhand,[2] Santanu Chaudhury,[2] and Asok Bhattacharyya[1]

[1] *Electronics and Communication Engineering Department, Delhi College of Engineering, India*
[2] *Electrical Engineering Department, IIT Delhi, India*

Correspondence should be addressed to Indu Sreedevi; s.indu@rediffmail.com

Received 22 August 2012; Revised 22 March 2013; Accepted 14 April 2013

Academic Editor: Piero Castoldi

Copyright © 2013 Indu Sreedevi et al. This is an open access article distributed under the Creative Commons Attribution License, which permits unrestricted use, distribution, and reproduction in any medium, provided the original work is properly cited.

Nature offers several examples of self-organizing systems that automatically adjust to changing conditions without adversely affecting the system goals. We propose a self-organizing sensor network that is inspired from real-life systems for sampling a region in an energy-efficient manner. Mobile nodes in our network execute certain rules by processing local information. These rules enable the nodes to divide the sampling task in a manner such that the nodes self-organize themselves to reduce the total power consumed and improve the accuracy with which the phenomena are sampled. The digital hormone-based model that encapsulates these rules, provides a theoretical framework for examining this class of systems. This model has been simulated and implemented on cricket motes. Our results indicate that the model is more effective than a conventional model with a fixed rate sampling.

1. Introduction

Self-organizing mobile sensor network is built with sensor nodes that may spontaneously create an ad hoc network, assemble the network themselves, dynamically adapt to degradation or device failure, manage movement of sensor nodes, and react to changes in task and network requirement. Such networks can be deployed for environmental monitoring, surveillance application, disaster management, and so forth.

Sensor networks are event-based systems that rely on the collective effort of densely deployed sensor nodes which continuously observe physical phenomenon. The main objective of a sensor network is to reliably detect/estimate event features from the collective information provided by sensor nodes [1]. Therefore, the energy and hence processing constraints of small wireless sensor nodes overcome by this collective sensing notion which is realized via their networked deployment. While the collaborative nature of sensor nodes brings significant advantages over traditional sensing including greater accuracy, larger coverage area, and extraction of localized features, the spatiotemporal correlation among the sensor observations is another significant and unique characteristic of the sensor networks which can be exploited to drastically enhance the overall network performance.

In addition to the collaborative nature of sensor networks, the existence of spatial and temporal correlations [2] bring significant potential advantages for the development of efficient communication protocols [3] well suited for the sensor networks paradigm. For example, intuitively, due to the spatial correlation, data from spatially separated sensors is more useful to the base station than highly correlated data from nodes in proximity. Therefore, it may not be necessary for every sensor node to transmit its data to the base station; instead, a smaller number of sensor measurements might be adequate to report the event features within a certain error level. Similarly, for a certain event tracking application, the measurement reporting frequency, at which the sensor nodes transmit their observations, can be adjusted such that temporally correlated signal is captured at the fusion center within a certain distortion level and with a minimum energy expenditure.

In this paper, we propose a scheme for building an autonomous system, for spatio-temporal reconstruction of environmental phenomena using mobile nodes. A key feature of our approach will be the focus on energy efficiency,

by employing adaptive sampling in both space and time. In the process, we optimize the number of message transmissions needed for collaboration among nodes, since the transmission contributes significantly to the total power consumption. The most important point, however, is to make the system self organizing and is achieved using simple, local rules. The main advantage of such systems is that it reduces the dependence of critical nodes for their proper functioning. For example, in case of multisensor detection, if a fusion center fails, most likely a new one will be elected, but it will waste resources in doing nonproductive work. Also, readings need to be collated at fusion centers, before a result is produced. Clearly, this produces accurate results, but again, at increased resource/energy costs. We envisage that using a self-organizing system shall maintain the balance between fidelity of results and energy consumed, while retaining scalability and fault tolerance.

The remaining part of the paper is organized as follows. In Section 2, some previous works in the field of self-organizing sensor network are discussed. In Section 3, a detailed discussion of the problem is presented. In Section 4, the proposed EDHM is described in detail. In Section 5, the EDHM-based spatio-temporal signal reconstruction is presented. In Section 6, results of both simulation and hardware implementation are discussed. Finally, Section 7 concludes the paper.

2. Related Work

A novel computational model for self-organization was first proposed by Turing as Turing's reaction-diffusion model [4]. This model was mathematically supported by [5] and experimentally by [6]. Later, cellular automata-(CA-) based model for self-organization was developed by Gutowitz [7]. The CA-based model was further modified by Leach and Taffoli for incorporating nonlinearity.

In fact, the DHM [8] for self-organization has been proposed as a potential mechanism for development and differentiation in artificial life systems [9]. Swarm robotics [10] is a very active research area and has proposed many approaches. References [11, 12] showed that a set of autonomous agents can use pheromone to form interesting and complex global behaviors and exhibit swarming behaviors [13].

The concept of biological hormones proposed by [14] was one of the earliest attempt to build systems that are robust, flexible, and have the capability to self-organize. The ADS (autonomous decentralized systems) technology has been applied to industrial problems [15] and has the properties of on-line expansion, on-line maintenance, and fault tolerance. This attracted researchers to build ADS [16, 17].

Hormone-inspired DHM (digital hormone model) [8] extends Turning's reaction-diffusion model by considering not only the interplay between reactions and diffusions, but also the network topological structure around each robot, the local sensory and actuator states, and the movements of individual robots. Ant colony, schooling fish, and nectar source selection by honey bees are examples of biological self-organization systems. A simulation of task allocation in the multirobot system using DHM for optimizing the cost of robot system is proposed by Li et al. [18]. Conservation and effective prolong lifetime of WSN are established by hormone-based distributed clustering algorithm [19]. Inspired from bioendocrine systems, a tracking strategy is devised in [20]. Hormone messages are used in sensor networks to coordinate sensor nodes for mobile target tracking in a self-adaptive way.

Reference [21] defines a sensor network architecture which allows sensor nodes to autonomously adapt their duty cycles for power efficiency and responsiveness of data transmission, to collectively self-heal (i.e., detect and eliminate) false positives in their sensor readings, and to be lightweight. This method assumes a regular grid deployment structure which is not always possible in remote areas. Authors of [22] address node localization using particle swarm optimization (PSO) and bacterial foraging algorithm (BFA). This method is computationally expensive due to its iterative nature. Authors of [23] report a design of a distributed sampling scheme referred to as the virtual sampling scheme with a fixed sampling period.

The proposed work is an example of a self-organizing wireless sensor network which is partially inspired from the foraging in bees and has been theoretically described using a digital hormone model [8]. The existing extensions of DHM [18–20] are modeling spatial behavior of static robots, whereas the proposed extended DHM is used for modeling a self-configuring system of static and mobile robots based on spatio-temporal environment and tasks. Unlike DHM proposed by Shen et al. [8], EDHM uses lazy cascading to avoid message flooding. The rules are so defined that different nodes will do different actions with the same hormone message as it depends on the current state of the node. This avoids multiplexing of communication, sampling, and locomotion and makes the node simple. The novelty of the proposed method is its autonomous behavior with adaptive spatiotemporal sampling feature.

The proposed model (extended DHM) behaves like natural systems, executes various rules, based on the local information obtained through sensors. The individual nodes communicate with each other through hormone exchanges. The model shows analogies that can be applied to spatiotemporal sensing and form the basis for the theoretical framework. Due to the judicial combination of self-organization based on natural systems and DHM, EDHM maintains a neat balance between the amount of local and distributed processing, taking into account the task deadlines and available computation and communication resources.

3. Problem Description

The aim of the proposed work is to design and implement a sensor network that uses mobile nodes to sample a region for reconstructing the spatiotemporal signal.

A Digital hormone model (DHM) [8] encapsulates dynamic networks of mobile nodes or robots that use hormone-like messages to communicate, collaborate, and

achieve their goals. The hormones received by a node influence but do not determine their local behaviors, as it is the function of both the type of hormone and local state of the node. Thus, different nodes react differently to the hormones despite the fact that all are running the same protocol. The DHM consists of three components: a dynamic network of mobile nodes, a Probabilistic Function for individual node behavior, and a set of rules and equations for hormone reaction and propagation.

3.1. Dynamic Network of Mobile Nodes. Distributed control of mobile nodes is a difficult task as the global behavior of the network should emerge as a result of local actions. Therefore, we propose the bio-inspired digital hormone model for spatiotemporal sampling of sensing space. In this model, the nodes are considered as biological cells that communicate and collaborate via hormones and execute local actions via receptors. The model can be visualized as a system having 3 basic components which makes it dynamic, probabilistic, and fault tolerant as in the case of a biological hormone. This model is used for implementing event-based relocation of sensors in a distributed manner.

(i) Each node has a set of "connectors" through which it can connect to other nodes. In a wireless network, "connectors" mean connecting link (1). These connectors or connecting links dynamically change with the movement of nodes.

(ii) A set of probabilistic "receptors" or functions allows individual nodes to take actions based on the current state of the node and received hormone (2).

(iii) The nodes interact within a cell of radius "R" directly through relayed "messages".

A dynamic network of mobile nodes is a formal representation of the traditional wireless sensor network that has been deployed for spatiotemporal sensing. The term dynamic emphasizes the impromptu links that form as mobile nodes move or nodes fail or come up at a time instance t. Each node has a set of connectors through which nodes dynamically connect with each other.

In this model, connectors simply denote a radio link that comes up whenever a probing node transmits a hormone and a listening node receives that hormone. Note that the links are formed only between a transmitting node and a listening node within its transmitting range. Let N_t denote the set of active nodes at time t and L_t the set of links, then DN can be defined as

$$DN \equiv (N_t, L_t). \tag{1}$$

Through the DN nodes can exchange hormones. In our model, a hormone generated at a node is propagated on all the links of that node and it is not propagated further.

3.2. Function for Node Behavior. Each node runs a protocol that identifies its behavior based on the current state of events. A mobile node selects its actions B, based on a probability function P, that is, trained on three local factors: the state information S, the sensor data D, and the hormone level H:

$$P(B \mid S, D, H). \tag{2}$$

The actions include commands to transmit a hormone, move to another location, or switch sensors on/off. The function P simulates the hormone receptors found in various biological organisms. Although P is local, yet it greatly influences the global behavior. P, in fact, is the key to achieving self-organization in the network. The rules for self-organization of mobile sensor nodes for implementing reconstruction of a spatio-temporal signal are proposed in the next section using an extended digital hormone model frame work.

4. Extended Digital Hormone Model (EDHM)

Sensor networks have been used for a variety of applications one such being spatio-temporal sampling of an environment. It has been previously brought out that such kind of sampling is analogous to foraging activities of bees. Taking that analogy further, we present a tailored, extended digital hormone model (EDHM) that succinctly captures the rules required for spatio-temporal sampling, in a theoretical framework. This model defines the rules for collaboration among mobile nodes for sampling a region in space and time, in an energy efficient manner. We further look at the conditions under which our model will serve its purpose of being energy efficient and also see how can a spatio-temporal signal be reconstructed using this method.

4.1. Foraging Activities of Honey Bee. honey bees have been found to focus their foraging activities around more profitable nectar sources. A collaborative effort of several bees maintains a steady flow of food supply in the bee hive. It has been verified that the foraging activities emergent at the colony level occur without any central leadership or a global rule. The overall nectar source election process can be understood with respect to the behavior of individual bees [24].

The following steps are used for the collaboration of honey bees.

(1) Honey bees are divided into employed and unemployed forager.

(2) The employed forager will communicate by performing a waggle dance to share the knowledge (quality, distance, and route) about the food source with other bees.

(3) Unemployed forager observing the dance has an opportunity to become well informed about the various food sources exploited by their colony.

(4) Based on the observed dance, the unemployed forager decides whether to start foraging that particular source or to wait for other dances. It has been deduced that the decision to forage is based on the information

received during a small time frame and as such does not involve an accumulation of knowledge over successive dances by different bees.

To implement the above steps in mobile robots, for sensing signal in a collaborative fashion, we considered the following assumptions and framed rules based on these assumptions.

4.2. Assumptions

(A1) The state of mobile robots is classified as Probe, Listen, and Move. The state information of nodes is represented by a variable S. In the probe state the node takes samples of environmental data through its sensors and conditionally transmits hormones. In the Listen state, a node turns off its sensors and listens to its neighbors for possible hormone transmissions. The Move state captures the locomotion of the node from an initial coordinate to a final one.

(A2) D refers to both the set of sensor readings $r_i(t_x)$, from sensor i of node at sampling instance t_x and the remaining battery batt, where

$$\text{batt} \leq 1. \tag{3}$$

(A3) All robots have short range wireless communication facility (either RF or infrared) and can talk to robots that are in proximity.

(A4) H denotes the hormone that is transmitted from a probing node to a listening node. Each H is a three tuple containing the (x, y) coordinates of the transmitting node as well as the sensor reading $r_i(t_x)$.

(A5) We assume that a node remains in the Probe or Listen states for a time T, before executing P. The node can be in the Move state as long as it does not reach its target location.

(A6) It is also assumed that each node knows its location in a global co-ordinate system, and that this information is transmitted along with the sensor reading whenever a hormone H is propagated. The model does not require any global node identifiers.

(A7) The value of r_i can fall in three regions as shown in Figure 1. r_i falls in the region L if $r_i \leq LTH_i$, M if r_i in between HTH_i, and LTH_i and H if $r_i \geq HTH_i$, where LTH_i and HTH_i are lower threshold and upper threshold values set for r_i. Let MAX_I be the maximum possible value of sensor reading r_i.

4.3. Actions

(B0) (State change rule)

If S = Probe AND $r_i(t_x) < LTH_i$ for entire T, then S = Listen

OR

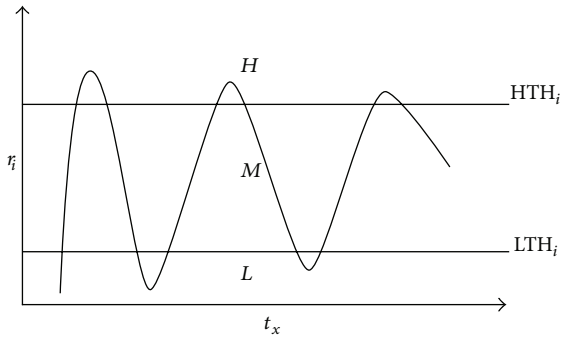

Figure 1: Sensor-reading regions.

If S = Listen AND $H = 0$ for entire T, then S = Probe

where LTH_i is a threshold parameter for sensor i.

(B1) (Random Move rule) if (B0) has been executed continuously for more than a number of times, then a random vector $\mathbf{R}$ is calculated that determines the direction and distance to move. The target point (x_t, y_t) is such that distance $d_{i,t}$ between the initial and final coordinates is proportional to batt^{α}, that is,

$$|\mathbf{R}| \propto d_{i,t} \propto \text{batt}^{\alpha}, \tag{4}$$

where, $\alpha \geq 1$. We took $\alpha = 1$ for all calculations. The direction to Move is, though, randomly determined. The node finally sets S = Move.

(B2) (Hormone transmission rule) A node with S = Probe transmits a hormone $H(x_i, y_i, r_i(t_x))$ if there is zero-crossing between $r_i(t_{x-1})$ and $r_i(t_x)$

or

$$r_i(t_x) > HTH_i. \tag{5}$$

Using this rule, we are doing a differential sampling. If there is a change in reading (positive or negative), a hormone message is generated and transmitted. This reduces redundancy.

(B3) (Gradient Move rule) This rule is particularly important as it significantly contributes to macroscopic self-organization through microscopic actions.

A node in S = Listen accumulates all the hormones H_k it receives for the duration T.

After that, the node calculates gradient g_k, towards each of the nodes in its vicinity that transmitted the hormone,

where

$$g_k = \frac{(r_k(t_x) - r_i(t_x))}{d_{i,k}}. \tag{6}$$

Based on the g_k, $g_k^{\max}$ is determined for all nodes within the communication range of kth node at time t_x, and a locomotion vector $\mathbf{L}$ is calculated. Like $\mathbf{R}$,

$$|\mathbf{L}| \propto \text{batt}^{\alpha}. \tag{7}$$

The direction is, however, towards the node with a maximum gradient. The node then sets S = Move. This rule helps in adaptive sampling.

(B4) (Destination arrival rule)

If S = Move, then {S = Probe if $(x_i, y_i) = (x_t, y_t)$ else S = Move}.

(B5) (Adaptive sampling rule) This rule is the key to saving energy while taking sensor readings. It defines how often to take samples during the sampling period T when S = Probe. A node predicts when to take the next sample based on the past values of sensor readings. The next sampling instance t_{x+1} is given by

$$t_{x+1} = t_x + \left(\mathrm{MAX}_i - r_i\left(t_x\right)\right) \frac{\left(t_x - t_{x-1}\right)}{\left(r_i\left(t_x\right) - r_i\left(t_{x-1}\right)\right)}. \quad (8)$$

Here, $0 < t_i \leq T$. The value of sampling interval is directly proportional to the ratio of time interval and difference in sensor reading between two consecutive samples and also to variation with MAX_i. Hence, the sampling interval is decided adaptively which further optimizes energy consumption.

The sensor will be moving in a direction where the

4.3.1. Action Execution Probabilities. We define the following probabilities for classifying $r_i(t_x)$ into three regions formed between LTH_i and HTH_i, assuming a uniform distribution of values. MAX_i denotes the maximum value returned by sensor s_i:

$$P_L = \frac{LTH_i}{\mathrm{MAX}_i},$$
$$P_M = \frac{HTH_i - LTH_i}{\mathrm{MAX}_i}, \quad (9)$$
$$P_H = \frac{\mathrm{MAX}_i - HTH_i}{\mathrm{MAX}_i}.$$

P_L, P_M, and P_H denote the probability that $r_i(t_x)$ falls in the region L, M, and H, respectively, defined in Figure 1, also,

$$P_L + P_M + P_H = 1. \quad (10)$$

We next define a probability function $P(H_{Tx})$ for a node to transmit a hormone, based on the rule (B2):

$$P\left(H_{Tx}\right) = P\left(S = \text{Probe}\right)\left[2P_L P_M + P_H\right]. \quad (11)$$

The probability of a node being in Probe, Listen, or Move states is defined in the following equations:

$$P\left(S = \text{Probe}\right) = \left[1 - P\left(S = \text{Move}\right)\right]\left[1 - P\left(H_{Tx}\right)\right]^m, \quad (12)$$

where m is equal to the number of neighbors, that is, nodes within its communication range:

$$P\left(S = \text{Listen}\right) = \left[1 - P\left(S = \text{Move}\right)\right]\left[1 - P\left(S = \text{Probe}\right)\right],$$
$$P\left(S = \text{Move}\right) = P\left(B1\right) + P\left(B3\right). \quad (13)$$

Also,

$$P\left(S = \text{Probe}\right) + P\left(S = \text{Listen}\right) + P\left(S = \text{Move}\right) = 1. \quad (14)$$

This means that a node can be exactly in one state at any given time.

Assuming $P(S$ = Move$) > 0$, and considering $P(S$ = Probe$)$ and $P(S$ = Listen$)$ to be equally likely implies that

$$P\left(S = \text{Probe}\right) \approx P\left(S = \text{Listen}\right) < 0.5. \quad (15)$$

Based on the above equations, we define the probability of each action, (B0)–(B5), being executed:

$$P\left(B0\right) = \left[1 - P\left(S = \text{Move}\right)\right]\left[P_L + \left(1 - P\left(H_{Tx}\right)\right)^m\right],$$
$$P\left(B1\right) = P(B0)^{\delta}. \quad (16)$$

δ is an implementation-specific constant for specifying how long should a node wait at a point before moving to a new, random, location in case of low sensor activity and no received hormones:

$$P\left(B2\right) = P\left(H_{Tx}\right),$$
$$P\left(B3\right) = mP\left(H_{Tx}\right)\left[1 - P\left(S = \text{Move}\right)\right], \quad (17)$$
$$P\left(B4\right) = P\left(S = \text{Move}\right),$$
$$P\left(B5\right) = \beta P_H P\left(S = \text{Probe}\right),$$

where β is an adaptive value depending on the frequency of events.

In (B5), the samples are taken more frequently as $r_i(t_x)$ approaches HTH_i, therefore, we assume that the average number of times (B5) is executed and is directly proportional to P_H.

The rule (B0) ensures that a node alternatively probes or listens. (B1) prevents a node from being stationed at a point in case the sensors denote low activity for too long. (B2) propagates the information from a node to another and is the basis for internode communication. (B3) is generally a consequence of another node executing (B2), and it helps in accumulating more nodes towards regions with high sensor activity.

Since our objective is to probe with reference to the threshold, that is, for sensor values above a threshold, (B2) and (B3) together form an effective way for reconstructing the spatiotemporal signal at a global level through simple, local interactions. (B4) simply ensures that a node does not respond to D or H as long as it is moving. (B5) is another important rule that makes energy-efficient sampling possible by varying the sampling rate based on the stream of samples collected so far. Specifically, rules (B2)-(B3) guide sampling in space, whereas (B5) guides sampling in time. It should be noted that the above rules are designed so as not to do multiplexing of tasks such as sampling, communication, or locomotion. The objective behind this is to reduce

Table 1: Probability of execution.

Action/state	S = Probe	S = Listen	S = Move
B0	P_L	$[1 - P(H_{Tx})]^m$	0
B1	P_L^δ	$[1 - P(H_{Tx})]^{m\delta}$	0
B2	$P(H_{Tx})$	0	0
B3	0	$mP(H_{Tx})$	0
B4	0	0	1
B5	βP_H	0	0

the instantaneous power consumption and also to simplify the model. It should be noted that what action is selected at a time is mainly dependent on the current state of node and environmental factors such as received hormones and sensor readings. A summary of action execution probabilities for each action/state pair is listed in Table 1. When a node is in the Listen state, $P(H_{Tx})$ represents the probability of a neighbor to transmit a hormone.

4.4. Rules for Hormone Reaction and Propagation. The propagation of hormone occurs in a two-dimensional space and is governed by standard laws for radio signal propagation. Although in biological organisms, hormones diffuse through a cellular interaction; in case of mobile sensor nodes, the radio transmission reception helps in the hormone diffusion. The gradient calculated towards each hormone transmitting node aptly represents the concentration C of hormone and therefore C is a function of both relative difference in sensor readings and distance between the nodes, that is, $C(\Delta r_i, d_{i,k})$. The DHM proposed by Shen et al. [8] establishes C as a function of time, but, in our case, we simply assume that a hormone H is of merit to a node only up to the next decision-making step.

Our approach, though a bit discreet, still serves the purpose of guiding nodes towards regions of high sensor activity; as hormones are transmitted every time, conditions for rule B2 are met. Thus, if a node missed a transmission, it might receive it the next time it enters the Listen state. The hormone H in our model is analogous to the activator hormone A, though the inhibitor hormone I is implicit and can be assumed, for the sake of completeness, to be virtually generated on timeouts. We shall like to mention here that classical hormone-based models generally retransmit a received hormone to generate a cascading motion with immediate effect. Our approach, however, allows only fresh hormone transmissions (i.e., no forwarding of hormone messages) based entirely on local sensor readings, since we are dealing with a time-varying signal and it may be possible that by the time a node reaches towards a target point the signal has died out. This effect will be more pronounced as more and more nodes, situated multiple hops away, move towards the target region. Hence, our model results in lazy cascading wherein the propagation of hormones is deferred until the receiving node starts probing at the new target point. This method also helps to reduce the overall energy consumption of the network.

4.5. The DN-EDHM Control Loop. Each of the nodes can be assumed to occupy a location in a 2-D grid space, where each grid box is equal to the resolution of the localization system deployed. At powerup, the nodes initialize their states S, to either Probe or Listen, and execute the following loop.

(1) Select actions by executing $P(B \mid S, D, H)$.

(2) Execute the selected action. This includes sampling, hormone transmission/reception, and locomotion.

(3) Go to Step (1).

DN-EDHM control loop has fewer steps than DHM because we have coupled hormone generation, propagation, and reaction with action steps. Another major difference with DHM is that it is not guaranteed that all the nodes will be executing the same step in the control loop, since B1 and B3 may take different times to execute in different nodes based on **R** and **L**.

5. Reconstructing the Spatiotemporal Signal

Sensor networks are characterized by the dense deployment of sensor nodes that continuously observe physical phenomena. Due to high density in the network topology, sensor observations are highly correlated in the space domain. Furthermore, the nature of the physical phenomena constitutes the temporal correlation between each consecutive observation of a sensor node. These spatial and temporal correlations along with the collaborative nature of the sensor networks make it suitable for spatio-temporal sampling of physical fields. The dense deployment of sensors increases redundancy which makes the system energy craving. Accurate temporal reconstruction of signals depends on frequency of temporal sampling. EDHM reduces redundancy through rule (B_2) and (B_3) and optimizes temporal sampling frequency through rule (B_5). Rule (B_3) decides the direction of motion of nodes towards maximum signal level.

The model proposed above demonstrates how self-organization and distributed actuation can be achieved using simple rules that process only local information. Even though the nodes carry out the sensing task without any intervention, yet the readings taken by the network as a whole need to be collated for further analysis. This shall require the nodes to periodically (or in response to a query) transmit the sensor readings to a base station.

Watching the data sent by geographically spread nodes is like watching a "sensor movie" [25], since the readings of a sensor correspond to pixel values of varying intensity in an *environment image*, and watching a sequence of such images (or frames) gives the impression of a video of sampled values.

(1) *PREMON Model.* Reporting the values to a base station is, nevertheless, a costly task and therefore should be minimized. Reference [25] proposes a *prediction-based monitoring (PREMON)* model, where the base station computes a "prediction model" for a sensor, and the sensor transmits a value if it significantly differs from the value computed

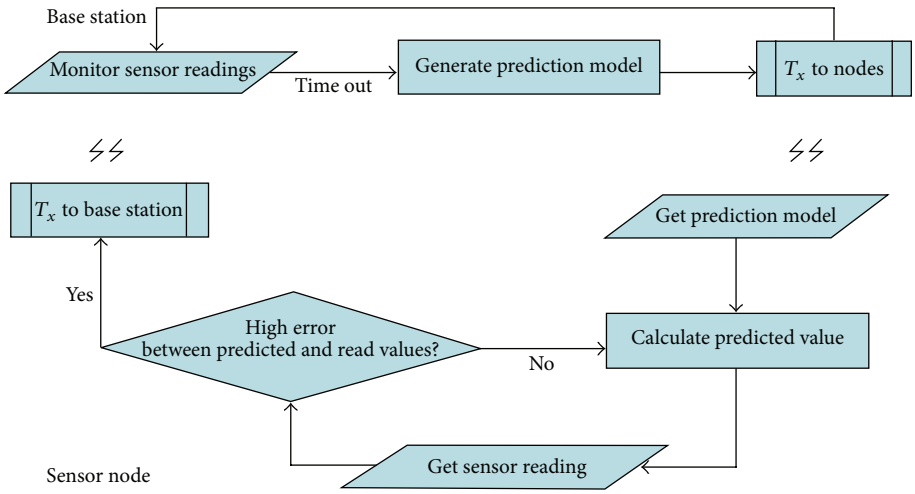

Figure 2: PREMON loop.

using the prediction model (see Figure 2). The prediction model is valid only for a limited time interval, after which it should be recomputed. In the proposed model, the hormone messages are sent only if there is a significant difference in the consecutive readings. The sampling frequency is also adaptively varied according to the difference in the sensor readings. Hence, the prediction model can be easily applied in this model.

In view of our case, the prediction model can be classified as follows.

(i) *Spatial.* When the reading at sensor s_i is a function of the reading at sensor s_k during the time slot t_x.

(ii) *Temporal.* When the reading at sensor s_i at a time t_x is a function of its reading at a previous time slot t_{x-j}.

(iii) *Spatiotemporal.* When the reading at sensor s_i at a time t_x is a function of reading at s_k in a previous time slot t_{x-j}.

The *PREMON* model can be suitably applied in our case also, the only difference being that [25] uses a setup of static nodes, as compared to mobile nodes in our approach. Figure 3 illustrates that by superimposing snapshots taken at different time intervals, we can construct the environment image at a base station. The coloured grids specify the information collected from that grid. Clearly, the mobile nodes provide a dynamic coverage of the spatial region (the number of coloured grid is more), whereas static nodes cannot provide dynamic coverage. Thus, by combining *PREMON* with mobile nodes and *EDHM,* we can obtain a far more accurate spatio-temporal reconstruction at reduced energy costs.

5.1. Energy Savings through EDHM. In a conventional, fixed rate, sampling model, sensor readings are categorised as those above or below a certain threshold TH_i. Let us assume that the sampling rate in this case is proportional to P_T, the probability of a value being above TH_i:

$$P_T = \frac{\mathrm{MAX}_i - TH_i}{\mathrm{MAX}_i}, \tag{18}$$

where, $LTH_i \approx HTH_i < TH_i \approx MTH_i < MAX_i$. MTH_i is the *maximum threshold value.*

A simple hormone or message transmission rule in this case can be to transmit whenever $r_i(t_x) > TH_i$, where the probability of transmitting a hormone is defined by

$$P\left(H'_{Tx}\right) = P(1)\, P_T, \tag{19}$$

thus, the hormone transmission rule for the conventional model becomes

$$P\left(B2'\right) = P\left(H'_{Tx}\right) \tag{20}$$

and that for the sampling is

$$P\left(B5'\right) = \beta P_T P(1). \tag{21}$$

Here, $P(1) = 1$ denotes that a node is always probing.

The energy savings at a node can then be calculated by comparing the relative execution probabilities of actions B2 and B5 in EDHM with $B2'$ and $B5'$ in a conventional model. The value of RP_i, defined below is an indication of how often these actions are executed *vis'-a-vis'* the conventional model, thus, giving an indication, how often the transmission and sampling costs are incurred. A value less than 1 shall denote

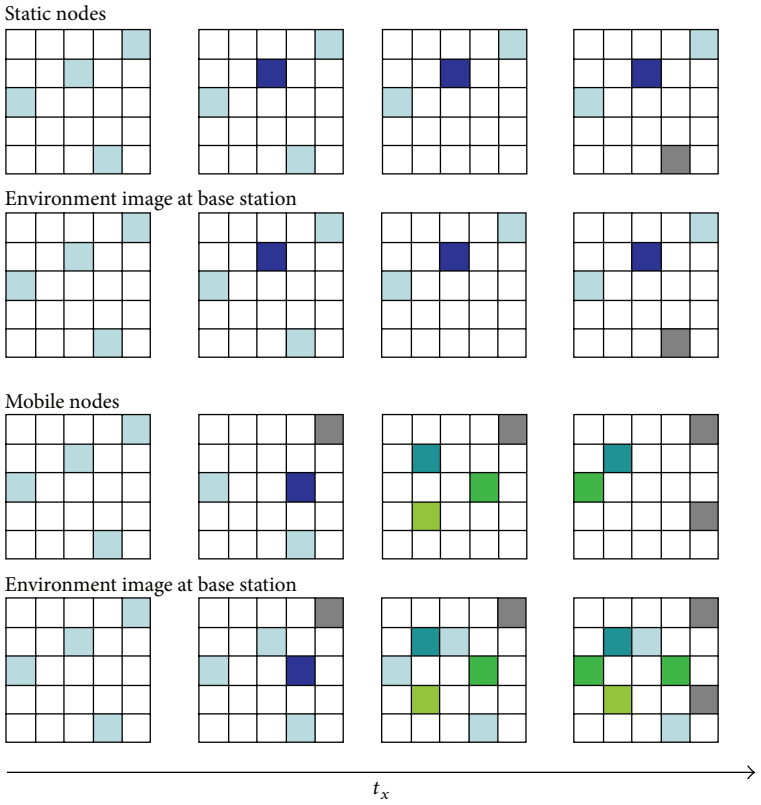

Figure 3: PREMON using static and mobile nodes.

energy savings in our approach, whereas a value greater than 1 means that our model is not energy efficient. Consider

$$\begin{aligned} RP_i &= \frac{P(B2)}{P(B2')} + \frac{P(B5)}{P(B5')} \\ &= \frac{P(H_{Tx})}{P(H'_{Tx})} + \frac{P_H P(S = \text{Probe})}{P_T P(1)} \\ &= \frac{P(S = \text{Probe})[2P_L P_M + P_H]}{P(1) P_T} + \frac{P_H P(S = \text{Probe})}{P_T} \\ &= \frac{P(S = \text{Probe})[2P_L P_M + P_H]}{P_T} + \frac{P_H P(S = \text{Probe})}{P_T} \\ &= 2P(S = \text{Probe}) \frac{[P_L P_M + P_H]}{P_T} \\ &\approx 2P(S = \text{Probe}) \frac{[P_L(P_M + 1)]}{P_T}. \end{aligned} \tag{22}$$

We know that, $P(S = \text{Probe}) < 0.5$, that is, $2P(S = \text{Probe}) < 1$. This means that for RP_i to be less than 1, $[P_L(P_M + 1)]/P_T$ should be less than 1. By suitably choosing the threshold parameters LTH_i and HTH_i based on TH_i, we can guarantee RP_i to be less than 1, that is, saving energy. In this case if we assume $P_L \approx P_M$ we get

$$RP_i \leq P_L + \frac{P_L}{P_T}. \tag{23}$$

The condition for RP_i to be less than 1, in terms of P_L and P_T, then becomes

$$P_L < \frac{P_T}{P_T + 1}. \tag{24}$$

The above discussion only provides a theoretical insight of the savings possible with a hormone-based model while transmitting messages or sampling at a point in space. More savings are possible if we also consider the fact that a mobile node in this model will move less often than where nodes randomly move about to sample the region. Our experiments show a significant saving in such a case, albeit at the cost of less accurate signal reconstruction, the results of which are discussed in Section 4.

6. Results

6.1. Simulation. In order to carry out experiments on the power consumption and accuracy in signal reconstruction using the hormone-based model, a simulator called *Shimla*, was designed. Shimla compares the power consumption of nodes, as they move around, by simultaneously executing

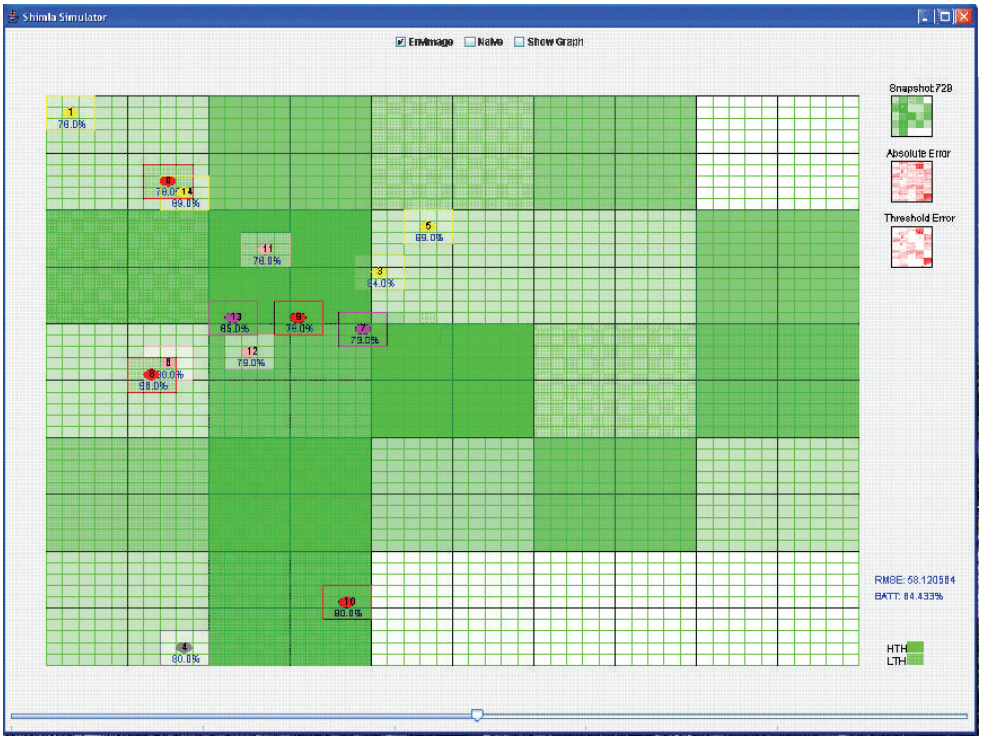

Figure 4: Shimla simulator.

a simple probabilistic model and our digital hormone-based model. Shimla is a discreet time simulator. The entire simulation period is divided into a number of epochs, where each epoch represents a fraction of the time T for which a node is in Probe or Listen state. It also calculates the error in reconstruction of a static and time-varying spatio-temporal signal. Simulations can be made by varying many parameters such as number of nodes, number of epochs, their initial position, and signal. The results are written to a file, that can be accumulated for a number of runs and viewed in a companion utility called RView. The results of simulation under Mirchi and Shimla are discussed in the next section.

We carried out simulations using Shimla simulator as (Figure 4) to find out how does our approach fare in terms of power consumption and how well can it reconstruct a spatiotemporal signal. Experiments were carried out to measure the performance in terms of average battery remaining and root-mean-squared error. Simultaneously, a naive protocol was also executed which served as a benchmark for our model. Due to the inherent randomness in self-organizing systems, for better accuracy, each experiment was repeated 50 times as (Figure 5) for the same signal and the same set of parameters, though at each run the initial location and state of the node were randomly chosen. Based on the compiled data from these experiments, the effectiveness of our model was calculated as a ratio between relative battery savings and relative root-mean-squared error (*RMSE*).

This process was repeated again by increasing the nodes to 2, 3, . . . up to a total of 25 nodes, without changing the signal.

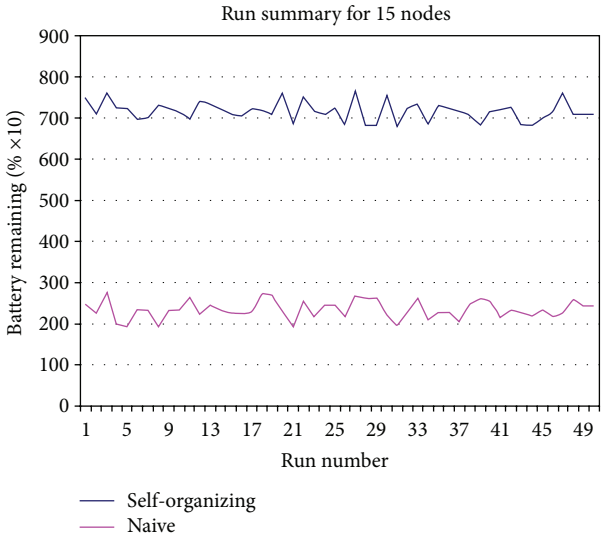

Figure 5: Simulation summary for 15 nodes.

Thus, a total of 1250 executions each, of Shimla, were carried out for static and time-varying signal. The environment consisted of a grid of 50 × 50, with a communication range set to 25 units, and sensor range set to cover an area of 9 grid squares. It should be noted that Shimla primarily calculates the energy expanded in locomotion and radio communication, since these two costs are much higher than the cost of probing (see Table 2).

Table 2: Power model for mica mots.

Mode cpu	Current	Mode radio	Current
Active	17 mA	R_X	7 mA
Idle	3.2 mA	T_X (−20 dBm)	3.7 mA
Power down	103 μA	T_X (−15 dBm)	5.4 mA
Power save	110 μA	T_X (−8 dBm)	6.5 mA
Standby	216 μA	T_X (−5 dBm)	7.1 mA
Extended standby	223 μA	T_X (0 dBm)	8.5 mA
Internal oscillator	930 μA	T_X (+4 dBm)	11.6 mA
LEDs	2.2 mA	T_X (+6 dBm)	13.8 mA
Sensor board	0.7 mA	T_X (+8 dBm)	17.4 mA
Ower save	103 μA	T_X (−15 dBm)	5.4 mA

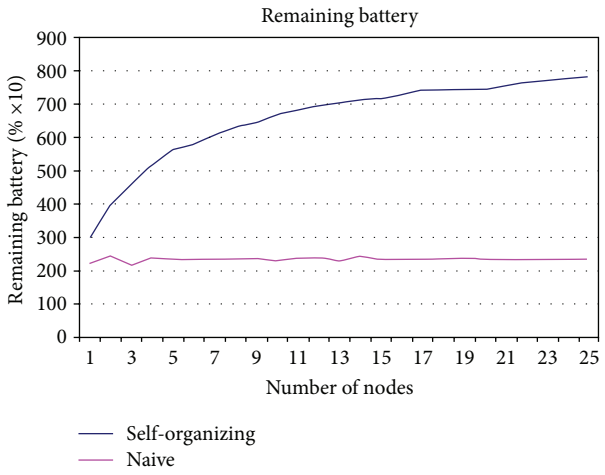

Figure 6: Battery consumption while sampling a spatiotemporal signal.

6.2. Execution of EDHM for Spatiotemporal Reconstruction. Executing the hormone-based model in parallel to a naive algorithm (where nodes probabilistically move to sample a region) helped us compare the performance of the model in terms of power consumed and error in a signal reconstruction. The results (shown below) demonstrate that the nodes self-organize themselves to decrease the per node power consumption and reduce the error in a signal reconstruction.

6.2.1. Energy Consumption. Figure 6 compares the average battery remaining after 1500 epochs (over 50 runs) the against number of nodes with a naive algorithm, for both static and time-varying signal. In both cases, as the number of nodes is increased the average battery remaining increases implying a *decrease* in the power consumed per node, for EDHM. If we look at the power remaining in the naive case (conventional fixed rate sampling), we find that it remains close to 20% *irrespective* of the number of nodes, even though the naive case does not expend any energy in radio communication. The increase in battery remaining, as the number of nodes increases, establishes the fact that nodes do collaborate

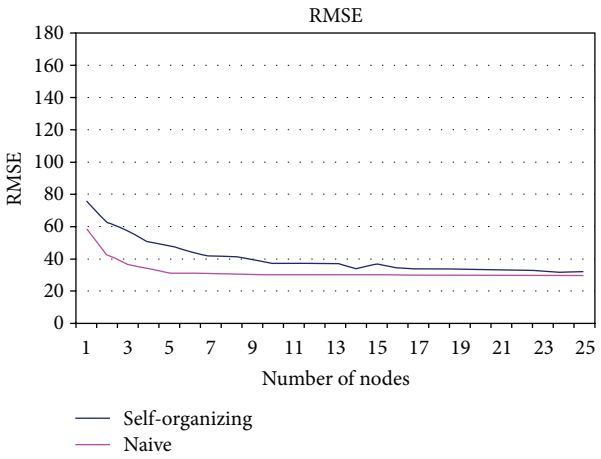

Figure 7: RMSE in spatiotemporal signal.

among themselves by sharing the task. This collaboration, therefore, achieves our goal of energy efficiency.

6.2.2. Error in Reconstruction. Besides saving energy, the collaboration among nodes also decreases the error in signal reconstruction, as visible in Figure 7. Again, compared to EDHM model, in the random sampling approach the *RMSE* remains roughly the same even as the number of nodes increases. The self-organizing nature of the proposed model helps us to achieve both our goals of improving energy efficiency and reducing RMSE error. It should also be noted that even though the random approach produces less error in reconstructing the signal, the difference from our model decreases, as the number of nodes increases. This is mainly because the random strategy results in oversampling of the region, whereas the nodes in our case coordinate their activities by dividing the sampling task.

6.3. Effectiveness of the Model. It is clear from the above results that the proposed model offers a tradeoff between energy efficiency and error in a signal reconstruction. The model can be compared (naive protocol whose characteristics are explained in Section 5.1) on the basis of how much energy it saves and how much error does it produce. The aim of the proposed work is to maximize energy savings while reducing the error. To gauge the model on these two metrics, we define the utility U of the model as the ratio of relative battery savings (between our model and the naive algorithm) to relative root-mean-squared error, for a given set of parameters:

$$U = \frac{R_{\text{batt}}}{R_{\text{rmse}}}. \tag{25}$$

Our aim, now, is to find those set of parameters that maximize the utility. In the proposed model, the behavior of a node is mostly affected by the sensor readings and the hormone receptions, both of which are dependent on external factors. Figure 8 shows how the utility of model increases as the number of nodes are increased.

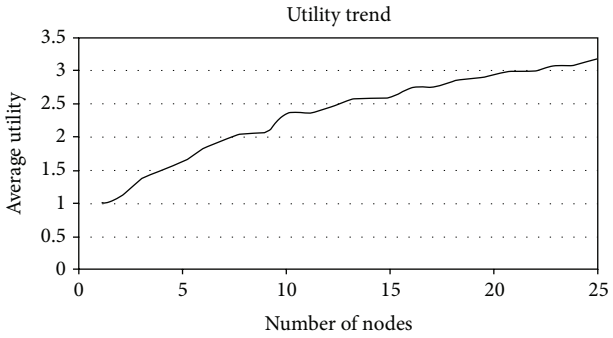

Figure 8: Utility of hormone-based model.

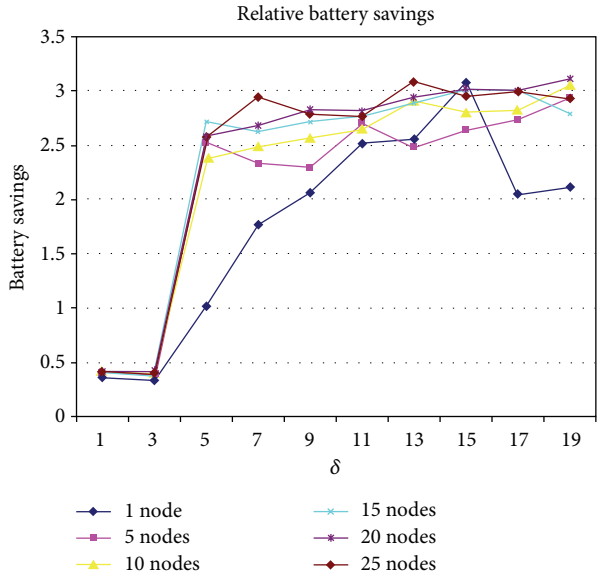

Figure 9: Relative battery savings.

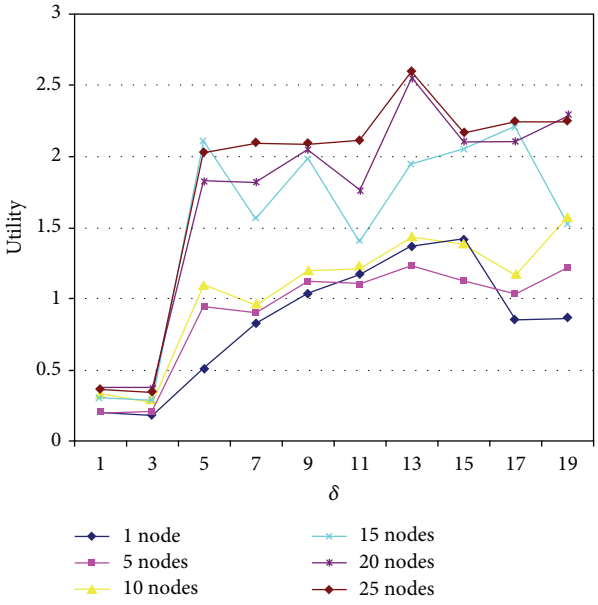

Figure 10: Correlation between delta and utility.

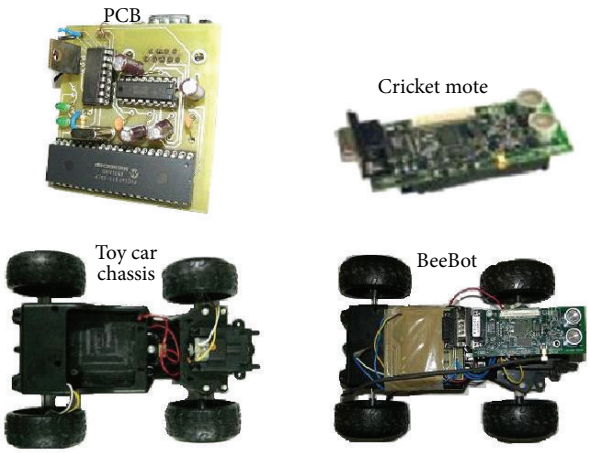

Figure 11: From a toy car to a mobility platform.

For a given node, the only parameter that can be controlled is δ, that affects the execution of rule (B1). The parameter δ is important because it determines how often a node should do random sampling in case of no sensor or hormonal activity. A low value of δ will result in frequent wandering of a node which improves spatial sampling but also costs heavily on the battery (Figure 9). Another parameter that can be controlled, at the network level though, is the number of nodes deployed. We have seen from the results that a larger number of nodes reduce average battery consumption and root-mean-squared error. We used Shimla to calculate the utility U for a given number of nodes at a particular value of δ (Figure 10) and also averaged it over 50 runs. The value pairs where the utility is more than 1 indicate that the model performs better than the naive model, if battery savings are considered as equally important as reducing the error in signal reconstruction. For a grid size of 50×50, the maximum utility is obtained at a deployment of 20 to 25 nodes with δ between 13 and 17. It should be noted that the value of δ is expressed in terms of number of epochs.

At a given number of nodes, for lower values of δ, rule (B1) executes too frequently resulting in decreases in relative battery saving and hence decreasing the utility. On the other hand, at higher values the execution of (B1) is differed too late, causing it to idle and consequently miss events, hence, increasing the error in signal reconstruction and therefore decreasing the utility. It can also bee seen in Figure 9.

Thus, it can be concluded that an effective deployment requires higher number of nodes with combined sensor coverage of around 10% of the total area and an idling time (δ) of the order of lower tens of the probing epoch.

6.4. Hardware Implementation. In order to verify the feasibility of an extended hormone-based model for spatiotemporal sensing, we implemented the project in 3 phases. In phase 1, we simulated a basic hormone-based model using

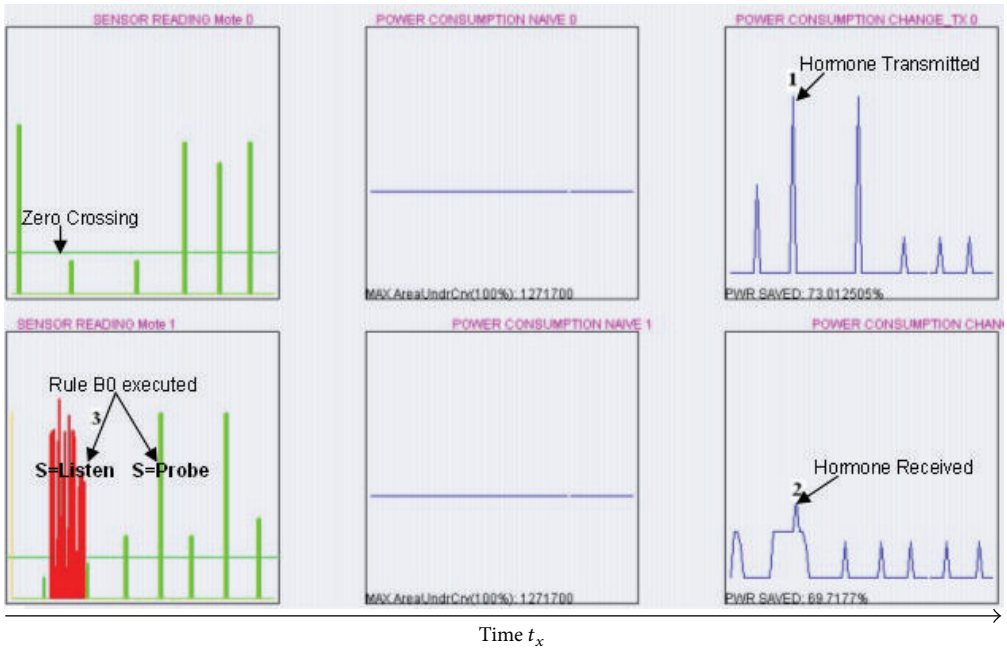

Figure 12: Execution of rule (B0).

static nodes for studying the self-organization among nodes, through hormone exchanges. Phase 2 involved implementing the basic model on Mica2-cricket motes. In the last phase, we implemented the complete model with mobile nodes and a localization system. We used Crossbrow cricket motes as sensor nodes. We placed these nodes over a toy car chassis and used PIC microcontroller for driving the car. The whole system works as a mobile sensor node (Figure 11). Experimental set up is as shown in Figure 16.

6.4.1. Mirchi. Before the cricket motes were procured, we made a plugin for TinyViz called Mirchi as (Figure 13). It is a Java-based plugin made by extending the simulation environment provided in TinyViz. We designed Mirchi for estimating the energy saved through the use of adaptive sampling, along with bistate operation of a node, where in one state only the sensor was on (with occasional transmissions) and the other only for receiving messages. The plugin demonstrates the execution of rules (B0) and (B5) as (Figure 12) for a pair of two nodes in each others neighborhood. The power model used in Mirchi was that of Mica2 (see Table 2). Based on the feedback from Mirchi, we went ahead with the implementation of the model on cricket motes.

6.4.2. MirchiBLUE. MirchiBLUE was built in Java for displaying, in real time, the on-going network activity. Besides, the network's traffic, it displays the tessellation of the region sampled by the nodes. MirchiBLUE supports the light, temperature, pressure, and humidity sensing modalities alog with the remaining power level in a node. MirchiBLUE receives data from the network through a cricket mote attached to it through the serial port. MirchiBLUE can also be extended to give commands to the motes in real time.

6.4.3. Embedded Code. Three separate softwares were used to implement the system. Firstly, the firmware supplied with the motes was uploaded on three motes which served as *beacons*. This firmware was modified slightly for use as a *Listener*, that ran the hormone model. Finally, a single node was programmed to act as a packet forwarder for the MirchiBLUE application.

6.4.4. Navigation. Rules (B1) and (B3) require the node to move to a new target location. Since (B1) makes a random movement, we implemented it by having the node choose a random direction (among forward, back, forward left, forward right, backward left and backward right) and executing it for a time proportional to the remaining battery power. (B3), however, requires an accurate displacement of the node from the initial to the target co-ordinate.

This requires the bot to know its orientation and that of the target relative to it for it to choose the appropriate locomotion command (Figures 14 and 15). The navigation logic is incorporated as rule (B4), and the algorithm for that can be stated as shown in Algorithm 1.

Algorithm 1 iteratively navigates the bot to the target by deciding what direction to move to, from a given point, by calculating the bots orientation.

The implementation of the hormone model has been largely successful, except for the time it takes for a bot to settle down at the target point. In order to implement the model, for deployment in a real world scenario, it would be advisable to use a digital compass and a separate hardware for localization. We developed a coverage panel in Java for displaying, in real time, the actual location of sensor nodes as shown in Figure 17. Three cricket beacons were used for localization of nodes which are represented as black dots

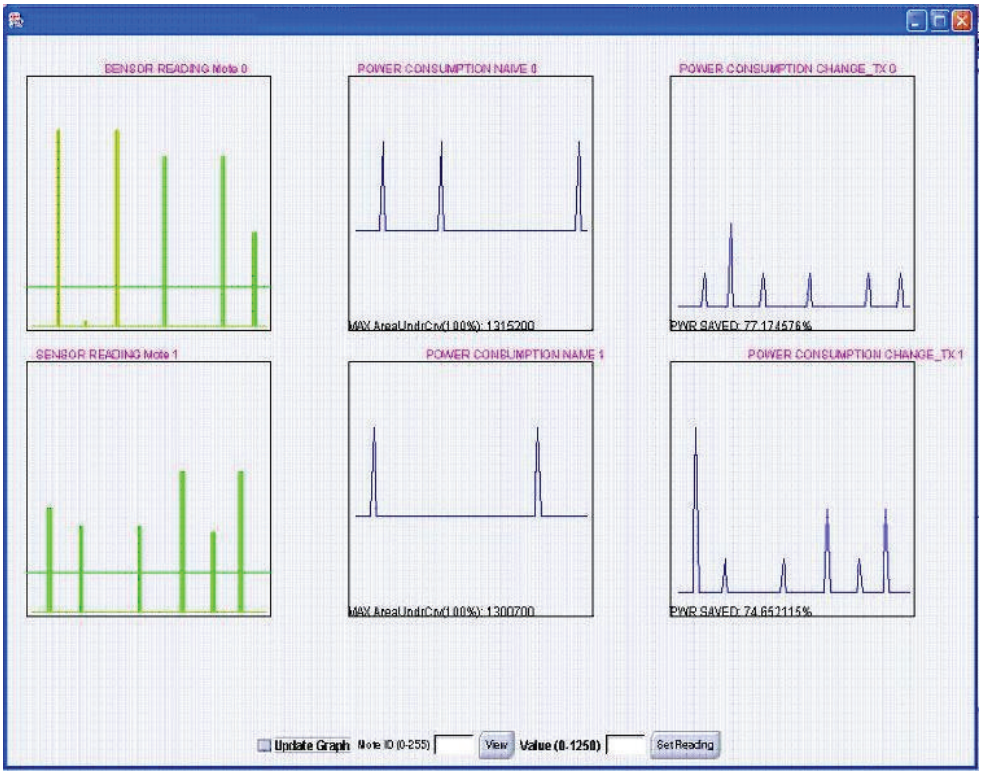

Figure 13: Mirchi plugin for TinyViz.

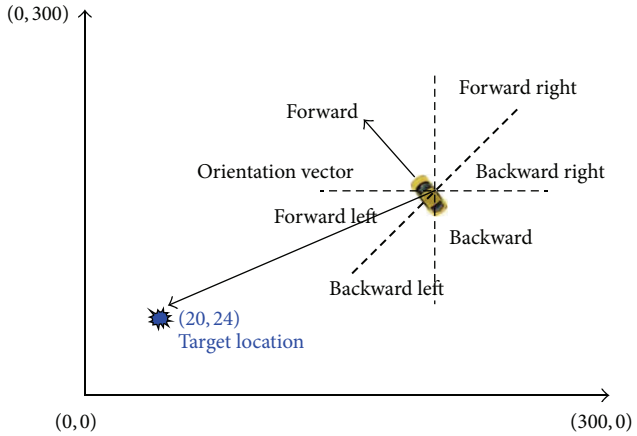

Figure 14: Relative orientation of target.

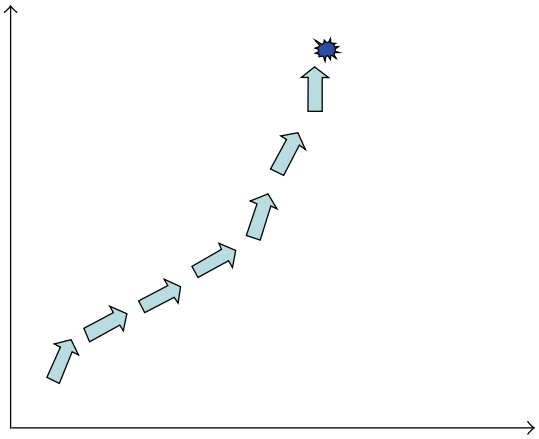

Figure 15: Navigation to the target.

and the distribution of nodes after deployment algorithm is shown in Figure 17. We used nesC to embody the structuring concepts of TinyOS operating system. Three separate softwares were used to implement the system. Firstly the firmware supplied was uploaded on 3 motes which served as beacons. This firmware was slightly modified to use as a node which ran our model. Finally, a single node was programmed as a packet forwarder and connected to the serial port to display details in the coverage panel. This packet forwarder acts as an interface between sensor nodes and serial port of computer. We programmed the nodes to handle self deployment, localization, event detection, and relocation themselves [26].

Figures 18 and 19 give the intermediate location and final positions of mobile nodes after implementation of DHM-based self-organizing algorithm. Figure 20 shows the final location of mobile node after doing the experiment.

6.4.5. Practical Issues. While implementing the model, we faced several issues that need to be understood for improving the performance of the model in an actual deployment. These are summarized below.

(1) Get Target Location.
(2) Get Current location.
(3) If current location is within a distance d_n of target then STOP.
(4) Get orientation of the bot.
(5) Calculate the orientation ort of target, relative to the bot.
(6) Select locomotion action act, based on the following:
  (6a) If ort < 30 AND ort > −30 then act = FWD
  (6b) If ort < −150 AND ort > 150 then act = BACK
  (6c) If ort < −30 AND ort > −90 then act = FWD_RIGHT
  (6d) If ort > 30 AND ort < 90 then act = FWD_LEFT
  (6e) If ort > 90 AND ort < 150 then act = BACK_LEFT
  (6f) If ort < −90 AND ort > −150 then act = BACK_RIGHT
(7) Execute action act
(8) Go to step 1.

Algorithm 1: Navigation algorithm.

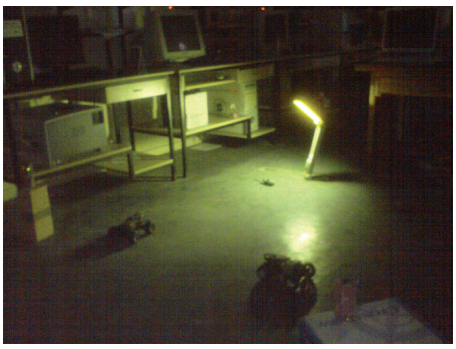

Figure 16: Experimental set up.

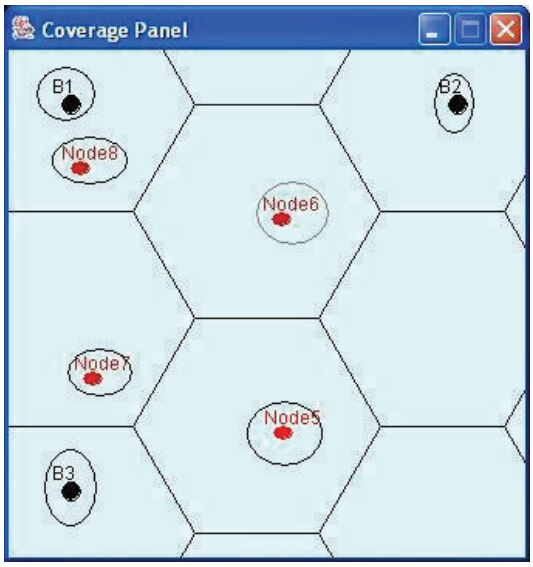

Figure 17: Coverage pannel.

(i) *Radio Conflict*. As has been previously bought out, localization uses RF (along with ultrasound) which is also required for transmitting and receiving hormones. This not only leads to a time duration where no useful work is being done (model execution is paused) which can cause missed events and hormones resulting in loss of performance, but also increases channel contention. Having a second radio for communication is feasible if the cost of hardware is not of concern. Another solution can be to synchronize the transmission schedules using protocols such as S-MAC [27].

(ii) *Localization Time*. Since the localization code is multiplexed with the model on the same processor, the model is paused from executing. Only the possible approach is to either have a separate node running the localization code (on a different frequency) or use another localization system such as GPS (which dose not work indoors).

(iii) *Braking*. Since the BeeBot does not have an instantaneous brake and due to the time required for knowing the coordinates, often the bot overshoots the target region leading to oscillatory behavior. This leads to an increase in the converging time for the navigation algorithm. The problem can be solved by making the localization hardware separate and also by providing an effective braking mechanism.

(iv) *Orientation*. Knowing the orientation is another challenging task. The methods discussed in the last chapter are only partly successful as they are either susceptible to errors or require more number of nodes. The best way to get the orientation shall be to use a digital compass as it will provide instantaneous readings with comparatively less hardware cost and power consumption.

(v) *Beacon Coverage*. Since we have only used three beacons, accurate localization can only be done where the ultrasound pulses from all three beacons reach (Figure 21). More accuracy and wider coverage are possible by using a greater number of beacons.

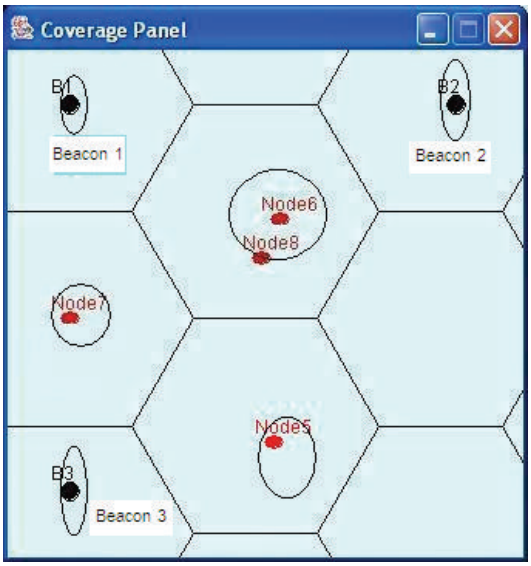

Figure 18: Intermediate location of mobile nodes.

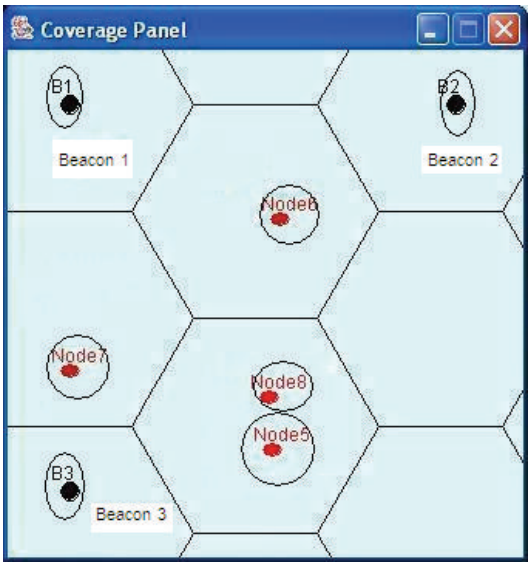

Figure 19: Final location of nodes.

Figure 20: Final location of mobile node.

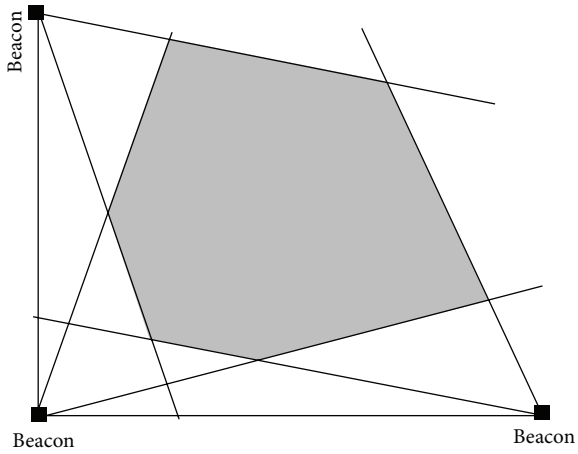

Figure 21: Effective localization area.

7. Conclusion

We have seen that EDHM helps to attain balance between the extent to which battery saving is required and the tolerance in reconstruction error. The simulation results exhibit how larger the number of nodes share the task, improving on both the fronts of efficiency and sampling. We shall, however, like to comment that our model is slightly biased towards saving energy than accurately sampling the region. Nevertheless, the utility U is above one for most of the cases, except when the number of nodes is too less to effectively collaborate. Our experiments also reinforce the view that for a self-organizing system to succeed, the number of individual units should be considerably large.

It can be also seen from the above discussion that simulations are a good instrument for verifying the validity of theoretical proposal, but the actual implementation might require tackling issues that are totally unrepresented (in the theoretical model). Such issues, nevertheless, *must* be resolved for the implementation to perform as expected.

References

[1] M. C. Vuran, Ö. B. Akan, and I. F. Akyildiz, "Spatio-temporal correlation: theory and applications for wireless sensor networks," *Computer Networks*, vol. 45, no. 3, pp. 245–259, 2004.

[2] Q. Huang, C. Lu, and G. Catalin, "Spatio-temporal multicast in sensor networks," in *Proceedings of the ACM Conference on Embedded Networked Sensor Systems (SenSys '03)*, pp. 38–45, 2003.

[3] M. A. Batalin, "Spatio-temporal multicast in sensor networks," in *Proceedings of the 2nd ACM International Conference on Embedded Networked Sensor Systems (SenSys '04)*, pp. 25–38, Baltimore, Md, USA, November 2004.

[4] A. M. Turing, "The chemical basis of morphogenesis," *The Philosophical Transactions of the Royal Society B*, vol. 237, no. 641, pp. 37–72, 1952.

[5] J. D. Murray, *Mathematical Biology*, Springer, Berlin, Germany, 1989.

[6] Q. Ouyang and H. L. Swinney, "Transition from a uniform state to hexagonal and striped turing patterns," *Nature*, vol. 352, no. 6336, pp. 610–612, 1991.

[7] H. Gutowitz, *Cellular Automata: Theory and Experiment*, The MIT Press, Cambridge, Mass, USA, 1991.

[8] W. M. Shen, P. Will, A. Galstyan, and C. M. Chuong, "Hormone-inspired self-organization and distributed control of robotic swarms," *Autonomous Robots*, vol. 17, no. 1, pp. 93–105, 2004.

[9] W. M. Shen, B. Salemi, and P. Will, "Hormone-inspired adaptive communication and distributed control for CONRO self-reconfigurable robots," *IEEE Transactions on Robotics and Automation*, vol. 18, no. 5, pp. 700–712, 2002.

[10] E. Bonabeau, M. Dorigo, and G. Theraulaz, *Swarm Intelligence from Natural to Artificial Systems*, Oxford University Press, New York, NY, USA, 1999.

[11] H. van Dyke Parunak and S. Brueckner, "Entropy and self-organization in multi-agent systems," in *Proceedings of the 5th International Conference on Autonomous Agents*, pp. 124–130, Montreal, Canada, June 2001.

[12] D. Payton, R. Estkowski, and M. Howard, "Entropy and selforganization in multiagent systems," in *Proceedings of the International Conference on Autonomous Agents*, pp. 23–28, Montreal, Canada, 2002.

[13] H. van Dyke Parunak, "Making swarming happen," in *Proceedings of the Swarming Network Enabled C4ISR Conference*, pp. 170–179, Tysons Corner, Va, USA, 2003.

[14] E. A. Kravitz, "Hormonal control of behavior: amines and the biasing of behavioral output in lobsters," *Science*, vol. 241, no. 4874, pp. 1775–1781, 1988.

[15] K. Mori, "Autonomous decentralized system technologies and their application to train transport operation system," in *Proceedings of the High Integrity Software Conference*, pp. 75–81, Albuquerque, NM, USA, 1999.

[16] H. Ihara and K. Mori, "Autonomous decentralized computer control systems," *Computer*, vol. 17, no. 8, pp. 57–66, 1984.

[17] K. Mori, S. Miyamoto, and H. Ihara, "Autonomous decentralized computer system and software structure," *Computer Systems Science and Engineering*, vol. 1, no. 1, pp. 17–22, 1985.

[18] X. Li, X. Wang, Y. Lei, and H. You, "A self-organized algorithm based on digital hormone," in *Proceedings of the 3rd International Conference on Advanced Computer Theory and Engineering (ICACTE '10)*, pp. 398–402, August 2010.

[19] D. Dong, H. You, Y. Zhang, and X. Wang, "A hormone-based clustering algorithm in wireless sensor networks," in *Proceedings of the 2nd International Conference on Computer Engineering and Technology*, pp. 555–559, 2010.

[20] Y. Zhang, H. You, and X. Wang, "A hormone based tracking strategy for wireless sensor network," in *Proceedings of the IEEE International Conference on Intelligent Computing and Intelligent Systems*, pp. 104–108, 2009.

[21] P. Boonma, P. Champrasert, and J. Suzuki, "Bisnet a biologicallyinspired architecture forwireless sensor networks," in *Proceedings of the 21st International Annual Joint Conference of the IEEE Computer and Communications Societies (INFOCOM '07)*, pp. 17–22, 2007.

[22] R. V. Kulkarni, G. K. Venayagamoorthy, and M. X. Cheng, "Bio-inspired node localization in wireless sensor networks," in *Proceedings of the IEEE International Conference on Systems, Man and Cybernetics (SMC '09)*, pp. 205–210, 2009.

[23] L. Xun, T. Shiqi, G. V. Merrett, and N. M. White, "Energy-efficient data acquisition in wireless sensor networks through spatial correlation," in *Proceedings of the International Conference on Mechatronics and Automation (ICMA '11)*, pp. 210–215, 2011.

[24] S. Camazine, *Self-Organization in Biological Systems*, Princeton Studies in Complexity, Princeton University Press, 2001.

[25] S. Goel and T. Imielinski, "Prediction-based monitoring in sensor networks," Tech. Rep. DCS-TR-438, 2001.

[26] Manohar, *Configuring mobile sensors for maximizing even coverage [M.S. thesis]*, IIT Delhi, Delhi, India, 2008.

[27] D. E. Y. Wei and J. Heidmann, "An energy-efficient mac protocol for wireless sensor networks," in *Proceedings of the 21st International Annual Joint Conference of the IEEE Computer and Communications Societies (INFOCOM '02)*, pp. 17–22, 2002.

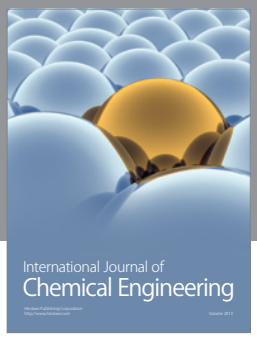

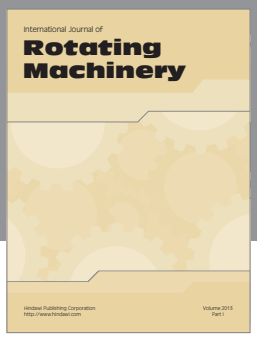

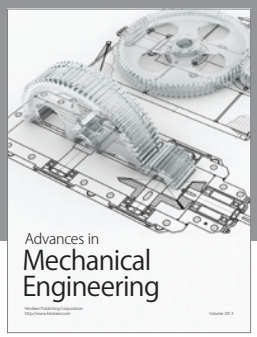

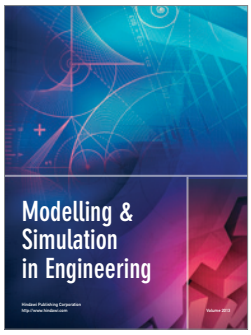

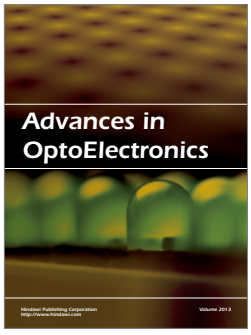

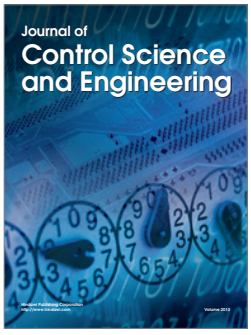

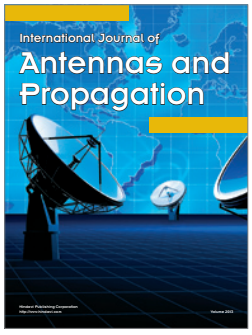

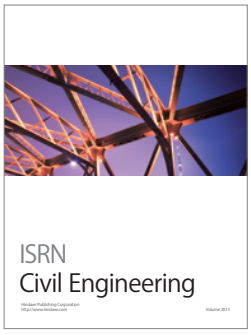

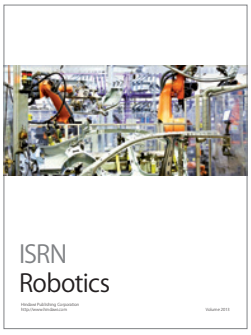

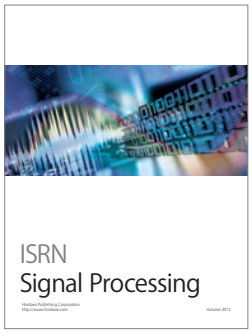

Hindawi
Submit your manuscripts at
http://www.hindawi.com

arXiv:1306.0195v1 [cs.CY] 2 Jun 2013

ChaMAILeon: Exploring the Usability of a Privacy Preserving Email Sharing System.

†Prateek Dewan, †Niharika Sachdeva, *Mayank Gupta, †Ponnurangam Kumaraguru
†Indraprastha Institute of Information Technology - Delhi, *Delhi Technological University
†{prateekd,niharikas,pk}@iiitd.ac.in, *mayank.gupta@dce.edu

ABSTRACT

While passwords, by definition, are meant to be secret, recent trends have witnessed an increasing number of people sharing their email passwords with friends, colleagues, and significant others. However, leading websites like Google advise their users not to share their passwords with anyone, to avoid security and privacy breaches. To understand users' general password sharing behavior and practices, we conducted an online survey with 209 Indian participants and found that 64.35% of the participants felt a need to share their email passwords. Further, about 77% of the participants said that they would want to use a system which could provide them access control features, to maintain their privacy while sharing emails. To address the privacy concerns of users who need to share emails, we propose ChaMAILeon, a system which enables users to share their email passwords while maintaining their privacy. ChaMAILeon allows users to create multiple passwords for their email account. Each such password corresponds to a different set of access control rules, and gives a different view of the same email account. We conducted a controlled experiment with 30 participants to evaluate the usability of the system. Each participant was required to perform 5 tasks. Each task corresponded to different access control rules, which the participant was required to *set*, for a dummy email account. We found that, with a reasonable number of multiple attempts, all 30 participants were able to perform all 5 tasks given to them. The system usability score was found out to be 75.42. Moreover, 56.6% of the participants said that they would like to use ChaMAILeon *frequently*.

Categories and Subject Descriptors

H.1.2 [**User / Machine Systems**]: Human factors; H.4.3 [**Communications Applications**]: Electronic mail

General Terms

Human Factors, Design

Keywords

Email, usable security, password

Copyright is held by the author/owner. Permission to make digital or hard copies of all or part of this work for personal or classroom use is granted without fee.

1. INTRODUCTION

A password is a *secret* word or string of characters that is widely used by humans to authenticate themselves against computer systems. Most computer systems rely on passwords to verify an individual's identity, and grant access to the system. It has been well studied that, shared or compromised passwords can lead to serious security implications like identity theft, undue infringement of privacy, security breaches, and misuse of administrative privileges [8, 30]. Not surprisingly, the main aspect associated with a password is its secrecy. In the modern world, keeping a password safe, and not sharing it with anyone, features as the top advice in every organization's security policy. Companies like Google, and Yahoo, highly recommend that their users do not share their passwords with anyone. [1] [2]

Even though the repercussions of password sharing are well and widely known, it has been observed and studied that, users come across a variety of scenarios in their day-to-day lives, where they share their password with other users. Patrick [24] used the Enron email corpus to identify instances of password sharing. A study of banking and security in Australia also unveiled the practice of sharing passwords [28]. In order to be more productive, leading executives expressed that they need to share their email accounts with their assistants [19]. Sharing passwords amongst teenagers has also become a trend in the recent times (Figure 1).

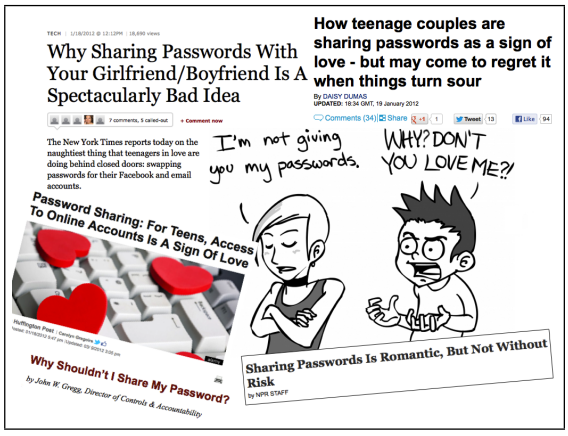

Figure 1: News clips from various international newspapers reporting password sharing among teens as a universal phenomenon.

[1] https://accounts.google.com/PasswordHelp
[2] http://help.yahoo.com/kb/index?page=content&y=PROD_ACCT&locale=en_US&id=SLN3012&impressions=true

In a recent study, the Pew Internet Research Center found that 1 in 3 teenagers share passwords with their friend, boyfriend or girlfriend [21]. As reported by The New York Times, some of the implications of sharing passwords include, obsessive monitoring of a significant other's account for signs of infidelity, and using the access for sabotage when a relationship goes sour [15]. These examples clearly indicate that exposing private information while sharing emails is an evident breach of an individual's privacy, which can lead to serious security implications. Users should be able to control which emails they wish to share, and which emails they wish to keep private, when they need to share their email account with their parents, friends, spouse, assistant, or anyone else. Moreover, users should be able to control operations like deletion, and sending of / replying to emails, while they share emails with another user. To the best of our knowledge, there has been some work done to propose methods for sharing emails [4], [14], [16], and [18], but there exists very little work which caters to the users' privacy needs.

To cater to the users' need for maintaining privacy while sharing emails and email passwords, we introduce ChaMAILeon, a system which allows users to share their email while maintaining their privacy. We present a novel approach of sharing emails, by allowing users to create multiple passwords for a single email address. An email account is thus accessible using more than one password. The user can control which emails and features (reading / sending / deleting) are visible / available if a particular password is used to access her email account. For instance, a supervisor can create 2 passwords, and grant access of her account to her assistant, and her spouse. To maintain privacy, personal emails can be hidden from the assistant, while professional emails can be hidden from the spouse. Our main contributions here are as follows:

- An online survey with 209 Indian participants to understand users' general password sharing behavior in the Indian context.
- A web application which allows users to share their emails without compromising their privacy. ChaMAILeon is a proof of concept for our approach of associating multiple passwords with a single email account, where each password corresponds to a different, restricted view of the email account.
- A comprehensive evaluation to comprehend the usability, and scope of ChaMAILeon. We conducted a controlled experiment with 30 participants to evaluate the usability of ChaMAILeon.
- We propose general guidelines for building usable email sharing applications, which provide mechanisms to share emails while maintaining privacy.

The rest of the paper is organized as follows. Section 2 discusses the existing work in the area of password practices and email sharing. Section 3 describes the methodology we followed for our online survey and controlled experiment. The system design, and definition of ChaMAILeon are covered in section 4. Section 5 discusses the results of the online survey and controlled experiments. Section 6 summarizes and discusses this work, and explores future scope. The last section contains some general guidelines, which we propose, for building usable and privacy preserving email sharing applications.

2. RELATED WORK

The practice of sharing passwords, and it's implications have been widely explored in the computer security community. Patrick [24] used the Enron email corpus to identify instances of password sharing, and found a total of 642 instances of password sharing involving 500 different email addresses. In another work by Alarifi et al., a survey conducted in Saudi Arabia brought out that 35.8% of 363 respondents shared their access passwords with their family members [2]. A study of banking and security in Australia unveiled the practice of sharing passwords [28]. According to Singh et al., password sharing was seen as a practical way of managing money and a demonstration of trust for married and de facto couples. Sharing Personal Identification Numbers (PINs) is a common practice among remote indigenous communities in Australia. Stanton et al.'s U.S. survey of non-malicious, low technical knowledge behaviors related to password creation and sharing showed that password "hygiene" was generally poor but varied substantially across different organization types (e.g., military organizations versus telecommunications companies) [29]. Their results indicated that 23% of respondents sometimes reveal their passwords to members of their work groups, 7% share their passwords with someone in their company but outside their work group, and 4.1% share their passwords with someone outside their company. Boyd et al.'s work suggests that teens feel safer, and closer to each other by sharing their passwords [5].

Apart from the research community, the implications related to password sharing have also caught attention in the news media. Sharing passwords amongst teenagers, has become a trend in the recent times. A recent survey known as 'Revenge of the Ex: Love, Relationships & Technology,' conducted across 10 countries (including USA, Canada, UK, France, Germany, Italy, Mexico, Brazil, Australia and India) revealed that India has the highest percentage of respondents at 43%, who have shared passwords with past partners. [3] However, apart from this study, most of the work in this space focuses on users from the U.S., Europe, and other developed nations. To the best of our knowledge, there exists very little, or no work to capture users' password sharing behavior and practices in the Indian context.

There has also been some work in the industry to cater to the need of sharing passwords, in particular, email passwords. The most recent patent describes a method for generating and managing a user account using a multi-password [18]. This invention specifically targets people in close relationships sharing passwords with each other. Multi-password indicates having multiple active passwords for one account, and therefore users are processed as if the users are logged into different accounts, depending on which password has been inputted. In another patent titled "Auto-forwarding and auto-delegating email folder control" [16], inventors describe a software controlled method for auto-forwarding emails to selected recipients, "enabling a busy executive to speed up forwarding of email messages, delegate their processing and obtain notification of the message processing." More patented works include a solution for delegating email messages for human summaries [4]. Here, unread emails can

[3] http://articles.timesofindia.indiatimes.com/2013-02-13/pune/37078553_1_passwords-partners-smartphone-users

be delegated to another email account (belonging to the delegatee), from where, the delegatee can prepare a summary of one or more emails, and send it back to the owner.

Considering the amount of work done in the research community and industry, real-world solutions for email sharing have been minuscule. Google's mail delegation feature [14] allows a user to delegate access to her Gmail account to another user / delegatee, so that the delegatee can read, send, and delete messages on behalf of the delegator. When a delegatee sends emails on behalf of the delegator, Google adds an additional "sent by" field in the email header. This explicitly shows the receiver of these emails, that the email has been sent by the delegatee on behalf of the delegator. However, the delegatee does not get permissions to change her account password or account settings, or chat on her behalf. He also gets full control of her email content. ChaMAILeon, in addition, allows users to control which emails is the delegatee able to read; and to whom is the delegatee able to send emails. This largely increases the application domain of such a system.

Mifrenz [4] is another application, which allows parents to control the email accounts of their children. This application gives parents the ability to let their children safely use email, with the minimum of intervention [17]. Although, Mifrenz does not directly relate to the problem of password sharing, it overlaps with ChaMAILeon's objective of allowing partial / controlled access to an individual's emails.

Most of the work mentioned above, provides mechanisms to share emails, but does not address any privacy concerns related to email sharing. To the best of our knowledge, ChaMAILeon is the first email application which provides access control in emails. ChaMAILeon specifically targets and caters to users' privacy concerns while sharing emails. Now, we discuss the methodology we followed for conducting the online survey and controlled experiment.

3. METHODOLOGY

To explore users' password sharing behavior and practices, we conducted an online survey with 209 Indian participants. Based on the insights from the survey, we developed ChaMAILeon. We built a prototype to incorporate features from the users' requirements and concerns, as found in the survey. Even though the data was collected only from India, we believe, the solution we propose is applicable worldwide, for anybody who wants to share their emails without compromising their privacy. Finally, to better explore the system and usage behavior of the participants with the system, we designed and conducted a controlled experiment.

3.1 Online Survey

We first conducted an online survey to study users' general password sharing trends and practices (See Appendix A). The motivation behind conducting this survey was to discover users' intent towards sharing their email passwords, and to see how comfortable they were in sharing passwords. In addition, we also captured if users were willing to use a system which provided them with various access control features on their emails. The online survey was filled by 209 participants from India. The survey was open to everyone, and was publicized on Facebook and through word of mouth. We also sent the survey link to student mailing list of different schools in India. On average, the survey took 15 minutes to complete. Participants were also given the option to participate in a lucky draw by submitting their contact information (email ID or mobile number).

3.2 Controlled experiment

We designed a controlled experiment to capture the users' interaction with ChaMAILeon. As depicted in Figure 2, the complete experiment consisted of 3 phases; a pre-study questionnaire, an activity involving the user's interaction with ChaMAILeon, and a post-study questionnaire. All the 3 phases were run in the presence of a moderator in a lab at IIIT - Delhi, India. Before starting the activity, all participants were asked to fill the pre-study questionnaire containing 10 questions, along with a consent form, privacy statement, and some general instructions as shown in Appendix B. The activity consisted of a think-aloud session in which participants were asked to play the role of "Bob Smith", the CEO of Bob Construction Company. As part of learning, participants were shown 2 videos, a 5 minute long tutorial video [5] about how ChaMAILeon works and another 2 minute long video titled "Setting up Gmail Delegation". [6] We developed counterbalancing schedule to avoid influence of the natural responses of the participants while interacting with the two systems (Gmail and ChaMAILeon); this also helped in reducing the learning effect on the participants. The participants were divided randomly and equally in two groups of 15. Each participant in the group was assigned tasks on Gmail and ChaMAILeon using Latin squares of 2 X 2 [6]. We designed five simple tasks, and asked each participant to perform them on ChaMAILeon, as well as on Google's Gmail to get a comparison between existing techniques and our proposed technique. Figure 3 depicts the setup of a study session. We provided the participants with a printout that included some general instructions, details about the role, and details and email IDs of people, Bob would be required to interact with, to perform the tasks (as shown in Appendix 2). Participants were free to refer back to both the tutorial videos at any point during the activity.

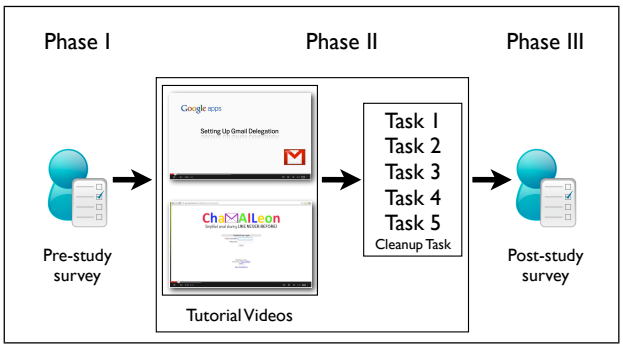

Figure 2: The controlled experiment consisted of 3 phases. Phase I: Pre-study survey, which collected participants' background and demographics, Phase II: Tutorial videos and activity, and Phase III: Post-study survey, which captured participants' experience and feedback for the system.

[4] http://mifrenz.com/

[5] http://www.youtube.com/watch?v=R4gN_GFylzY

[6] http://www.youtube.com/watch?v=1I5Xq69E0M8

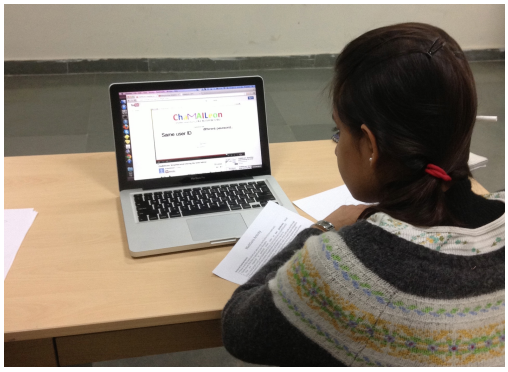

Figure 3: Control experiment sessions were conducted inside a lab, one participant at a time.

After the pre-study and the tutorial videos, we asked participants to perform 5 tasks in the activity. These tasks touched upon various aspects of everyday life, where a need for such a system was felt. We gave users the following scenario for performing the tasks: "Imagine yourself to be Bob Smith, the CEO of Bob Construction Company. You visit your office at 9 am in the morning, and you have 5 tasks to perform in the day, related to your emails. You may perform these tasks in any order, according to your priority." We created a dummy account in the name of Bob, and specified Bob's account credentials with the participants. We further created dummy accounts for various entities which were part of the tasks, and sent some emails from these accounts to Bob's account. The following tasks were required to be performed by the participants:

- *There are some legal cases currently going on, which you are part of. You (Bob Smith) need to give access to your email to your lawyer Amy. You want Amy to be able to read all your emails, but do not want her to be able to send or delete any emails from your account.*
- *You (Bob Smith) want your personal assistant, Penny, to keep a track of emails from a certain set of your foreign collaborators. You thus need to share your email account with her, but wish that Penny reads emails from ONLY collaborator1.mailguru@gmail.com, collaborator2.mailguru@gmail.com, and collaborator3.mailguru@gmail.com.*
- *You (Bob Smith) would not be able to access your emails for a few hours during the day, and so, you want your colleague Howard to access your emails during these hours. However, you wish that Howard does not get to read emails from your wife (wife.mailguru@gmail.com) and son (son.mailguru@gmail.com).*
- *There are some financial emails that you want your accountant Stuart to handle. You (Bob Smith) thus need to give access to your email to Stuart, but you wish that he should be able to see only those emails which contain the word "accounts" in the subject line.*
- *You (Bob Smith) learn that all your appointments for the day have been cancelled, and you realize that you no longer need Howard to access your emails. You want to revoke Howard's access to your account.*

To perform a task, participants were required to log into the account as Bob, configure the settings for the sub-user (discussed in the next section), and log out. To verify if the settings made were correct, participants were required to log into Bob's account as the sub-user. This process was repeated for each task, until the participants were satisfied, or gave up. After completion, we asked the participants if they were satisfied with the settings and how different / similar the results were from their expectations. We were not required to go through an IRB-type approval process before conducting the experiment in India. However, authors of this paper have previously been involved in studies with the U.S. Institutional Review Board (IRB) approvals, and have applied similar practices in this study. Prior to the study, participants were shown a consent form, which they had to read and accept, if they were comfortable with it. The form stated that an audio recording and a screencast would be taken during the activity, and that the collected data would be anonymized and used only for the purpose of this research. Furthermore, participants were informed that they could withdraw from the study at any point and request the deletion of the audio recording and screencast.

The controlled experiment was followed by a post-study feedback questionnaire with 11 questions. This comprised of 10 standard SUS questions [7] and 1 optional open feedback field.

3.3 Participants

Online Survey: Participants were recruited through Facebook posts, student mailing lists, and word of mouth. In all, 209 participants from various ethnic backgrounds participated in the survey. Table 1 discusses the demographics of the participants from the online survey. The participants used various email services. 97.60% were Gmail users, 49.76% were using Yahoo Mail, 26.31% were Hotmail users and 9.56% were Rediffmail users. The male population comprised of 66.5% of the participants, whereas 33.5% were females. Authors of this paper recently conducted a large-scale privacy study across all states in India, with over 10,000 participants, and reflected very similar male : female ratio; which helps us to safely conclude that our sample is representative of a bigger population [20].

Controlled study: We recruited participants through advertisements on mailing lists, and word of mouth. Each participant was offered a monetary reward of 100 Indian Rupees (approx. USD 2) for participating in the study. Most of the participants in the controlled experiment were graduate and undergraduate students and were heavily using emails as a medium of communication. Participants in the control experiment had a decent computer science and technology exposure. Majority of the participants belonged to 18-25 age group as this group constitutes the majority of users who would need an application like ChaMAILeon. Table 2 summarizes the demographics of the participants from the control experiment.

4. SYSTEM DESIGN

In response to the results of the online survey (discussed in section 5.1), we developed ChaMAILeon, an email application which provides users with the features described in the survey scenarios. ChaMAILeon is a modified version of SquirrelMail [7], which is an open source email package built

[7] `http://squirrelmail.org`

Table 1: Demographics of online survey participants; (N = 209).

Gender	(In %)
Female	33.50
Male	66.50
Age (in years)	(In %)
13 to 18	18.66
19 to 25	73.68
26 to 32	5.27
33 to 40	0.48
41 to 50	1.43
Above 50	0.48
Education Completed	(In %)
High school	45.94
Under graduation	35.89
Post graduation	15.79
Ph. D.	1.43
Other	0.95
Occupation / Profession	(In %)
Computer Science	44.98
Engineering	37.80
Business	2.87
Finance	2.39
Other	11.96

Table 2: Demographics of controlled experiment participants; (N = 30).

Gender	(In %)
Female	53.33
Male	46.67
Age (in years)	(In %)
18 to 25	96.67
26 to 32	3.33
Education Completed	(In %)
School / High school	43.33
Undergraduation	36.67
Post Graduation	20.00
Doctorate	0.00

using PHP. SquirrelMail was altered to support a "Configure Account" option to enable users to set access control over their email accounts. ChaMAILeon can be configured to work with any of the existing email services, like Gmail, Yahoo! Mail, Hotmail etc., or an organization's own proprietary mail service. In our case, we configured ChaMAILeon to work with Gmail. Since ChaMAILeon makes use of Simple Mail Transfer Protocol (SMTP) and Internet Message Access Protocol (IMAP), it is fairly simple to configure the system to work with any email service which makes use of these protocols. Apparently, configuring ChaMAILeon is very similar to configuring email clients like Microsoft Outlook, Mozilla Thunderbird, Apple Mail etc., and supports all email services which these clients can support. Figure 4 represents how ChaMAILeon communicates between a user and Gmail.

Technically, ChaMAILeon adds two new features to the existing web mail technology, which alters the way the conventional email works. First, it allows the owner of the email account to create "sub-users" for their email account. A "sub-user" essentially corresponds to a new password P_i,

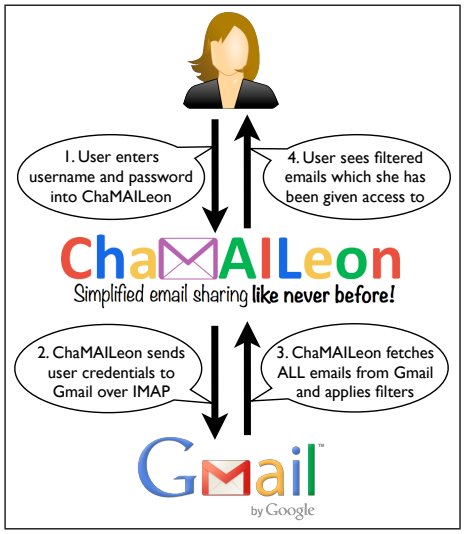

Figure 4: Flow diagram depicting how ChaMAILeon works as a middleware between a user and Gmail's mail server.

which can be used to access this email account (Figure 5). ChaMAILeon thus allows to log into one email account using one email ID E, and multiple passwords P_1, P_2, P_3... Each password (or sub-user) P_i can be configured by the "owner" of the email account, to provide different views V_i of the email account and grant different permissions. This can be viewed similar to roles in Role Based Access Control in databases [12, 27, 31]. In contrast to databases, however, ChaMAILeon identified the access controls using passwords instead of user-names. Each "sub-user" can be thought of as a role, and gets a different level of access to an email account. The various rules that can be configured are:

1. Allow reading emails from IDs present in Contacts (optional keyword filter for these emails)
2. Allow sending / replying emails to IDs present in Contacts
3. Allow reading emails from IDs not present in Contacts (optional keyword filter for these emails)
4. Allow sending / replying emails to IDs not present in Contacts
5. Enable deletion of emails
6. Allow marking emails as "unread"
7. Let mailbox "appear" as owner's mailbox
8. List specific permissions (read, send, keyword filtering)

Secondly, ChaMAILeon provides the owner of the account, with an option to create "lists". Each list is simply a collection of email addresses clubbed together under one name; the name of the list. The advantages of creating such lists are realized through configuring the sub-users. Each list can act as a blacklist or a whitelist for a sub-user, i.e. a sub-user can be allowed / restricted to "send to" and "read emails" from a "list" of email addresses specified in the list.

A combination of sub-users and lists form a powerful and robust mechanism to generate and implement fine-grained access control rules on emails. For instance, consider a scenario where Alice, a company supervisor, wants to share her email with her personal assistant Bob. Alice wants that Bob should log into her email account, and read / respond

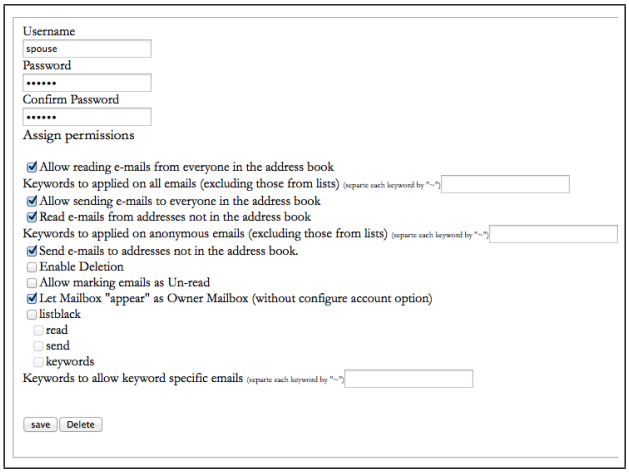

Figure 5: ChaMAILeon's "Create sub-user" page. It can be used by the owner of an email account to create another password and allow partial access of her account to someone.

to only those emails which contain the word "office" in their subject line. However, Alice wants that Bob should not be able to see any of her personal emails sent to her from her husband (husband@somemail.com), and her daughter (daughter@anemail.com). Also, Alice does not want that the receivers of emails sent by Bob on her behalf, should come to know that the emails have not been sent by Alice herself, but by Bob. Alice does not want Bob to be able to delete any of her emails either.

To the best of our knowledge, none of the existing web mail services provide mechanisms to do this. However, this can be easily set up using ChaMAILeon. Alice can simply add her husband's and daughter's email addresses in a list, and create a sub-user for Bob, which does not have access to this list. Alice can also specify the keyword "office" in the keyword filter that may be applied to all other emails. Other options like allowing to send emails, and disabling deletion can be applied by simply checking a check-box.

ChaMAILeon was set up on an IBM server with Intel Xeon processor, and 32 Gigabytes of RAM. [8] The system uses a MySQL database to store users' Gmail passwords in an encrypted form, their imported contacts, sub-user details, lists, and usage logs. Access control rules on emails are enforced by parsing the entire set of the user's emails fetched from the Gmail server. Restricted emails are identified based on the sender's address and keywords, as defined by the user. Once these emails are identified, they are removed from the set of emails which are presented to the user on the mailbox interface page. Features like restriction on deletion of emails, composing new emails, replying to emails, etc. are implemented by removing the "buttons" responsible for these actions. Implementing all of the aforementioned features only requires basic knowledge of PHP programming language, and MySQL.

4.1 System definition

A user logging into ChaMAILeon can have 2 different roles, viz. *the owner*, and *the sub-user*. When a user logs in as the owner, she gets full control of the email account, and the user interface includes features like *Import contacts*, *Configure account*, *See account activity*, and *Report a bug*. We call this interface as the *"owner's interface"*. However, except for *Report a bug*, all other features are not present in the user interface when a user logs in as a sub-user (Figure 6). In the *add / edit sub-user* page (Figure 5), we also give an option to the owner, to *"let mailbox look like the owner's mailbox"*. Enabling this option adds dummy buttons for "Compose", and "Addresses" to the sub-user's interface. These buttons are non-functional. Clicking either of them points back to the user's inbox. This is done to avoid a sub-user from getting a non-familiar feeling by not finding these essential features in a mailbox user interface.

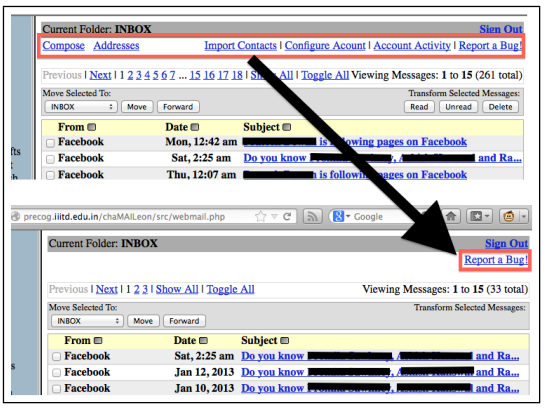

Figure 6: The sub-user does not get to see all features, which are otherwise present in the owner's inbox. The highlighted area in the top image is different from that in the bottom image.

We now formally define the parameters associated with each instance of a sub-user S as a 10-tuple vector, where each vector represents a specific permission.

$$S = \text{param}<R_c,\ R_c^k,\ S_c,\ R_{nc},\ R_{nc}^k,\ S_{nc},\ D,\ U,\ Z,\ L>$$

where:

R_c = Read emails from contacts
R_c^{kc} = Read email from contacts, containing *keywords kc* in the subject line
S_c = Send / reply emails to contacts
R_{nc} = Read emails from non-contacts
R_{nc}^{knc} = Read email from non-contacts, containing *keywords knc* in the subject line
S_{nc} = Send / reply emails to non-contacts
D = Delete emails
U = Mark emails as unread
Z = Spoofing (Making interface "look" like the owner's interface)
L = *name1*$<R, S, K>$, *name2*$<R, S, K>$, ...

All vectors except L are binary vectors and take only two possible values, i.e. *1 - enabled*, or *0 - disabled*. List permissions L are an array of 3-tuple vectors, where R, and S respectively represent *read-from* permissions, *send / reply to* permissions, and K is a *set* of keywords. R_i and S_i are binary vectors.

5. RESULTS

In this section, we will discuss the results of the online survey and controlled experiment.

[8] Live at `http://precog.iiitd.edu.in/chaMAILeon`

5.1 Online survey

Our online survey was taken by 209 Indian participants. To the best of our knowledge, this is the first work on studying password sharing perceptions and practices in India.

5.1.1 Current user behavior and expectations

Participants showed contradictory behavior to what was recommended by popular email services (Gmail, and Yahoo). We asked participants, if they share or feel the need for sharing passwords of their email accounts, and found that 64.35% of the participants felt a need for sharing email passwords. We observed that 97.60% of all participants were using Gmail, and 49.76% were using Yahoo Mail. To support our findings, we visited the security policies of these two email services, and found that both of them highly recommended their users not to share passwords.

We asked participants how comfortable they were in sharing their passwords with one or more people, and found that majority of the participants (74.64%) were not comfortable sharing passwords. Further, 38.75% were *very uncomfortable* with sharing passwords. This indicated a need for systems which allow privacy preserving email password sharing facilities to the users.

5.1.2 Fears, worries and actions

Password sharing leads to various apprehensions and worries for the security of the email account in users. We wanted to investigate the post effects of password sharing in the context of Indian users. To understand this, we asked if participants thought password sharing might lead to unwanted consequences. We found that 88.51% of the participants thought password sharing may lead to unwanted consequences. In fact, 11.48% of these participants mentioned that they had to face unwanted consequences as a result of sharing their password with someone.

To understand the user apprehensions, we asked participants, if they would consider changing their password after sharing it. We found that 96.65% of the participants felt the need to change their passwords after sharing. Among these, 45.93% mentioned that they would definitely change the password immediately, and 35.40% felt that they would probably change it whenever convenient. 15.31% of the participants mentioned that they may consider changing it some time. These results indicated user worries and uneasiness when they share their passwords, and reasonably signify the need for systems which could provide users with easy and fearless email sharing.

5.1.3 Need for a system

To better understand the exact system utilities, features and requirements, we gave participants a scenario, in which a system allows them to control the accessibility of their emails, settings, and features, when they share their email password. We then gave participants 3 scenarios as mentioned in Appendix A.

Share emails with spouse: We asked participants to consider a situation, where they wanted to share their email with their spouse, but did not want him / her to see emails from a particular friend, or did not want him / her to be able to reply to any emails. We then asked them if they were willing to use a system which could provide them with this functionality. We found that 65.55% of the participants were willing to use such a system. Moreover, 26.31% opted for *definitely* using such a system (See Figure 7).

Share emails with assistant: In the next scenario, we touched upon the need of such a system in a professional environment. We asked participants to consider a scenario where they were an official at a high post in a company, and received many emails every day. They wished to allow their assistant to be able to log into their account and reply to emails on their behalf. However, they would want the assistant to be able to see emails sent from only specific people, and not all of them. We found that participants felt the need for such a system more in a professional environment, as compared to the previous scenario (See Figure 7), with 85.64% agreeing to use of such a system in the current scenario.

Accessing emails in an insecure environment: In the last scenario, participants were enquired about the need for such a system in not so secure environments or untrusted networks. We asked, if participants were in a cyber cafe where they were not sure if the network was secure, and they needed to check their email. In such a setting, users would be afraid that their password and email content might get compromised over the insecure network. Under such a scenario, they were given an option to log into their account with a different password, such that, logging in with this password would give them very limited / restricted access to their account. In addition, their important emails would be filtered, and would not be transmitted to them over this insecure / untrusted network. 81.82% of the participants mentioned that they would use such a system (See Figure 7).

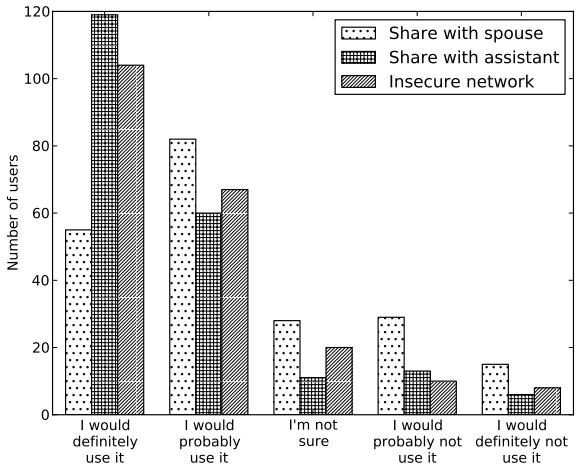

Figure 7: The need for a system like ChaMAILeon was felt the most in professional environments. A big fraction of participants (85.64%) said that they would want to use such a system while sharing their emails with their assistant.

5.2 Controlled experiment

We conducted a controlled experiment with 30 participants. Including the pre-study questionnaire, screening of two videos (5 minutes + 2 minutes), 5 tasks, and a post-study questionnaire, the experiment took about 45 minutes for each participant to complete. All participants were asked to perform all 5 tasks on both Gmail, and ChaMAILeon. Apparently, 20 out of 30 participants had never heard of Gmail's delegation feature before. Further, only 12 out of

the 30 participants attempted at least one task on Gmail. The other 18 participants stated that none of the 5 tasks (mentioned in section 3.2) could be performed on Gmail. Also, none of the 12 participants who attempted one or more tasks on Gmail, could achieve success in any of the tasks they attempted. On the contrary, all 30 participants were able to complete all 5 tasks on ChaMAILeon, with an average of 1.33 attempts per task per user.

5.2.1 Password sharing practices and trust

From the pre-study questionnaire, we found that 40% of the participants in the control study shared their passwords with others, and 80% maintained different email accounts for personal and professional needs. To analyze the level of comfort and trust participants experienced while sharing their passwords with different people, we asked participants how comfortable they felt in sharing passwords with parents, siblings, spouse, relatives, friends and colleagues. We found that participants were most uncomfortable sharing passwords with colleagues (86.67%). This supports our results from the online survey which suggested that a majority of users wanted to use systems like ChaMAILeon to share their emails with their assistants, or in professional environments. We also found that participants felt very uncomfortable sharing passwords with friends (53.34%) and parents (33.34%) as shown in the Figure 8. These results indicate towards a need for a system which enables role based password sharing and access to emails.

5.2.2 Participants' Experience and Interface Feedback

After the experiment, we asked participants a set of 10 questions to evaluate the usability of ChaMAILeon [7]. The System Usability Score (SUS) came out to be 75.42. It can be interpreted as a grade of a B-. A score of above 80.3 is required to get an A. This is also the point where users are more likely to be recommending the product to a friend. [9] We conclude with this score, that ChaMAILeon is fairly usable. The evaluation process and user feedback helped us to identify the various issues with the interface, and possible scope of improvement.

We also asked participants an open ended question about their comments and feedback for the system. Despite pointing out some interface issues, 83.3% of the participants seemed to be happy with their experience with the system, and stated that they would like to use such a system regularly. Participants also stated that such a system was really needed. One participant quoted, "Nice and very well needed system since almost everyone has a Gmail account these days and need to share their password at times." Participants seemed to like the idea very much, and said, "Apart from minor interface issues, the system is user friendly and the idea is amazing, and very practical, as well as easy to get used to. Thumbs up!" ChaMAILeon's use in the professional environment was also pointed out by one of the participants when they said, "The system is an excellent initiative which can prove to be very useful for corporate organizations." Some overwhelming responses included a participant saying, "After using this system I am thinking why this system is not so popularized. It is very easy to use, all functionalities are well defined, so why should I use any other mail system instead of ChaMAILeon? After some time I can say surely that it will be the 1st popular mail system. I enjoyed by playing with this system." A quote from another participant was, "Great feature of hiding your personal mails and still getting your work done!!! Would love to use this system."

[9] `http://www.measuringusability.com/sus.php`

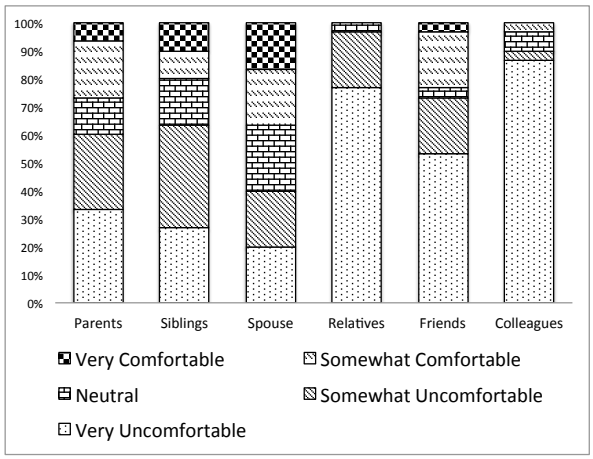

Figure 8: Comfort levels of participants in sharing email passwords with various entities. Users were found to be least comfortable in sharing email passwords with their colleagues.

There were 5 participants (16.6%) who found the interface non-intuitive and hard to use, and stated that, "User interface could be better." Another such participant said, "Very useful, but higher learning curve than expected / desired. Can be easy to use with better UI and more clear options. Definitely an edge over Google's delegate function." One participant was more specific with the issues she faced with the interface, and stated, "Checkboxes and a delete button around the place where the users and lists are given, would be of great help." We will now discuss the most common experiences and interface feedback by the participants in detail.

Common experiences.

We found that, on multiple occasions, participants forgot the passwords of the sub-user accounts they created. This phenomenon of users forgetting passwords is well established where users have multiple accounts, and are required to remember multiple passwords [23]. As a solution for this problem, in ChaMAILeon, a password generation and management system can be provided to the user, which can generate and store secure passwords for various sub-users. These passwords would be visible only to the owner, and she would not have to remember all passwords. Few participants were found to be using the same passwords for two different sub-user accounts. This lead to two different permission tuples being mapped to a single password, which eventually confused the system, and resulted in a failed attempt. Participants suggested that the system should prompt if a user tries to keep the passwords for two different sub-user accounts. Participants were also found to use interesting names for the lists and sub-users they created. While most participants named the sub-user accounts as "Amy", "Penny", "Howard", and "Stuart", some participants used names according to tasks, (like "Task 1", "Task 2" etc.), and roles (like "Accountant", "Lawyer" etc.). Similarly, participants used various conventions for naming

lists. Most participants named the two lists as "collaborators", and "family", while others named lists according to the sub-users. For instance, a few participants named the list of collaborators as "Penny", since Penny was supposed to be given access to this list. Other names included "foreign_collab", "personal", "secret", "relatives" etc. Observing the arbitrary conventions, we infer that automatic email labeling and classification techniques can be used to generate lists automatically [3, 11, 25]. Almost all participants referred to the tutorial video during the tasks. Since this was the first interaction of the participants with ChaMAILeon, we expected participants to seek help. It was interesting to find that using only the tutorial video as helping material, all participants were able to successfully complete all tasks.

Interface feedback.

Most participants found the interface reasonably usable, but suggested various changes to make the system more intuitive. For Task 5, which required the deletion of a sub-user account in order to revoke access, most participants found it surprisingly hard to locate the "Delete" button on the sub-user page. This button was placed right next to the "Save" button on the sub-user page, and all participants used the "Save" button multiple times while performing the tasks. Surprisingly, it seems like most participants never noticed the "Delete" button placed right next to the "Save" button. As a result, participants consumed a lot of time trying to find how to delete a sub-user, which lead to an increase in the average completion time for this task. The most common suggestion to fix this issue was to have an "Edit", and a "Delete" button next to each sub-user and list visible on the "Configure Account" page (as shown in Figure 9), instead of having to go to each sub-user and list, and delete it.

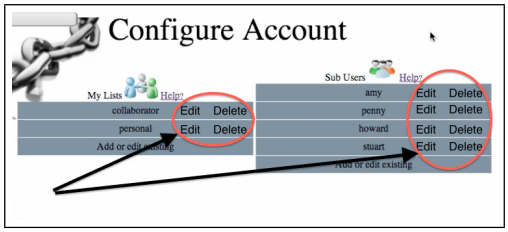

Figure 9: A snapshot of the "Configure Account" page after completion of Task 4. Participants proposed to have "Edit" and "Delete" buttons for lists and sub-users at the areas marked and pointed in this image.

Setting permissions for lists required participants to check / uncheck the checkboxes corresponding to "Read", "Send", and "Keywords" permissions under each list created by the participant. All checkboxes were unchecked by default. During Task 3, participants found it clumsy to check all permissions corresponding to each list separately, and stated that it would be a tedious process if the number of lists were large. Participants suggested to have all list permissions checked by default, and preferred to uncheck the lists which needed to be blacklisted. A better suggestion was to have separate "pools" for black lists and white lists, with all lists in the whitelist pool by default. Participants then proposed a "drag-and-drop" approach to "move" lists from the pool of whitelists to the pool of blacklists, as required.

Further, in order to ensure that the settings made for each task were satisfactory; participants had to log out after making the settings, and log back in as the sub-user that they wanted to verify the settings for. Participants complained that this process was tedious, and suggested to have a "preview" pane within the sub-user settings page, which would contain the dynamic view of each sub-user's view of the email inbox.

5.2.3 Task Completion Time

On an average, a participant took 17 minutes and 53 seconds to perform all 5 tasks (min. 10:17, max. 37:17). However, the complete experiment session (excluding pre-study and post-study), from first sign in to the last sign out, took 32 minutes and 35 seconds on average, for each participant. The difference between the two time values can be attributed to the time spent on the cleanup task, verification of each task, attempts made on Gmail, and reading the tasks from the handouts. The time taken for each task was calculated on the basis of the session duration i.e. time between a participant logging in as Bob, and logging out. Session durations for all such sessions, which were required to successfully complete one task, were aggregated to get the final duration of time that was taken for the completion of a task. We performed a two-tailed Student's T-Test, and did not find any statistically significant difference in the total time taken between the group of participants who viewed the Gmail delegation video first, and the group of participants who viewed the ChaMAILeon tutorial video first (2 sample t test, p-value > 0.1).

Task 1, on average, took 2 minutes and 48 seconds to complete (std = 2:02)(See Figure 10). This task required the participants to create a sub-user, and assign it only read permissions. Since this task was the very first interaction of the participants with the system, it would be safe to infer that the time taken to perform this task was higher than the actual time that is required to perform this task. The average completion time for Task 2 was 5 minutes and 9 seconds (std = 2:35). This time was considerably higher than the time taken to perform Task 1 (paired t test: $\mu 1$ = 2:48, $\mu 2$ = 5:09, p-value = 0.0001), since Task 2 required the participants to create a list ($collaborators < 1, 0, 0 >$) containing 3 email IDs, as well as a sub-user. Task 3 took an average of 5 minutes and 27 seconds to complete (std = 2:54), and was the most time consuming of all the 5 tasks. This task also needed the participants to create a list ($family < 0, 0, 0 >$, with 2 email IDs) and a sub-user, the time taken for Task 3 was only slightly higher the time taken for Task 2 (t test, t = -0.423, p-value > 0.3). This happened because a majority of participants made mistakes in this task, and had to re-perform it. We discuss the mistakes in the next subsection.

Task 4, like Task 1, also required the participants to create one sub-user, and the time taken was similar to Task 1 (t test, t = 0.613, p-value = 0.2904). In addition to Task 1, this task also required participants to add a keyword filter. Time taken to complete this task was 2 minutes and 32 seconds (std = 1:09); which is about 16 seconds lesser than the time taken to perform Task 1. This verifies our conclusion, that the first interaction of the participants with the system took more time than actually required. Further, it depicts the learning that users achieved in 4 or more interactions (depending upon the number of attempts in earlier tasks) with the system [22]. Task 5 was the least time consuming, and took 1 minute and 56 seconds to complete, on

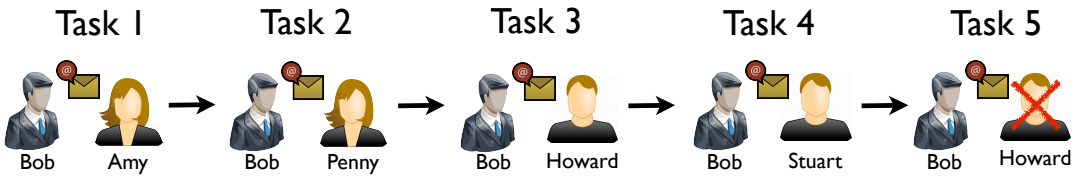

	Task 1	Task 2	Task 3	Task 4	Task 5
Time in seconds	168.43 (122.64)	309.10 (155.93)	327.20 (174.75)	152.63 (69.86)	115.83 (74.56)
Attempts	1.10 (0.30)	1.50 (0.68)	1.90 (0.96)	1.13 (0.43)	1.03 (0.18)

Figure 10: Average completion time and average number of attempts per task. The values within braces represent the standard deviation. (i) Amy (lawyer) is allowed to read all emails; (ii) Penny (assistant) is allowed to read emails from collaborators only; (iii) Howard (colleague) is not allowed to read personal emails; (iv) Stuart (accountant) is allowed to read emails related to accounts only; and (v) Bob revokes Howard's access.

average. This task required the participants to delete the sub-user created in Task 3. There was no statistically significant difference between the two groups (Gmail video first and ChaMAILeon video first) in the time taken to perform a particular task. To verify, the lowest p-value given by t test among all 5 tasks was p-value > 0.15 (p-value $= 0.1603$, for Task 2).

5.2.4 *Attempts to success*

The number of attempts taken to perform a task were also calculated based on sessions. Each session was counted as one attempt. All 5 tasks were successfully performed on ChaMAILeon in 1.33 attempts per task, per participant. Considering that all users were completely new to the system, and that there exist no other systems similar in functionality to ChaMAILeon, we consider this value to be very reasonable. However, during the entire process, each participant was required to log into ChaMAILeon 2.98 times per task, on average. This was because after each attempt, participants had to log in as sub-users to verify the settings they made. As discussed in the *Interface feedback* section, this number could be reduced by the introduction of a "preview" pane, which shows the participants a dynamic view of each sub-user's view of the email inbox.

Participants completed Task 1 in 1.10 attempts (std = 0.30) on an average (Figure 10). Only 3 out of the 30 participants (10%) failed in the first attempt. Out of the 3 failed attempts, there was only one participant whose attempt failed due to incorrect settings made while configuring the sub-user for this task. This participant set the value of $R_{nc} = 0$, while it was supposed to be 1 for success (Table 3). The other two failed attempts included a participant forgetting the sub-user's password, and a participant who wanted to verify the settings twice.

Task 2, on average, took 1.50 attempts (std = 0.68) to complete successfully. This task was completed successfully on the first attempt by 18 out of the 30 participants. Common errors made during this task included R_c and R_{nc} being set to 1 by the participants, and participants creating the list and leaving the permissions to $collaborator < 0, 0, 0 >$ (the default value) instead of setting it to $collaborator < 1, 0, 0 >$ (Table 3). A few participants also made the error of using the same passwords for sub-users created in Task 1 and Task 2, which lead to a clash, and the permissions were reset.

The most error-prone task was Task 3, where only 12 out of the 30 participants were able to successfully complete the task in the first attempt. The most common error made by the participants in this task was to miss out on setting $collaborator < 1, 0, 0 >$ (Table 3). More than half of the participants were found to simply ignore the permissions for the *collaborator* list, and only verify that the $family$ list was set to $family < 0, 0, 0 >$, which was its default value. A small percentage of participants were also found to be confused between the use of $keyword\ filters$ and $lists$. These participants tried to set the permissions by adding the email addresses of *wife* and *son* in the *keyword filter* field.

Task 4 turned out to be one of the easier tasks. 27 out of the 30 participants completed it successfully in the first attempt. Two out of the 3 failed attempts were caused due to the participants setting the permissions as $R_{nc}^{knc} = 1$ (k=NULL) instead of $R_{nc}^{knc} = 1$ (k=accounts) (Table 3). We did not consider list permissions i.e. collaborator <1,0,1(k=accounts)>, and family <1,0,1(k=accounts)> for this task, since these were not a mandate for achieving success in the example we considered. The easiest of all the tasks was Task 5, which was failed by only 1 participant in the first attempt. This participant, in his first attempt, tried to remove all permissions for the sub-user created in Task 3, instead of deleting the sub-user account, which was the actual success definition for this task.

There were some common errors that the participants made across all 5 tasks, which hampered the overall number of attempts. Participants kept same passwords for different sub-users, and forgot the passwords for their sub-user accounts. These are problems which can be addressed at the system level, and can further reduce the average number of attempts for achieving success.

5.2.5 *Success Scenarios*

Upon analyzing different tasks, we found that participants made different settings to suit their needs apart from the basic settings required for the assigned tasks. Some participants preferred to remove the compose, and send / reply options to explicitly convey to the sub-user that they had restricted access. Others preferred to avoid letting their sub-users know about the restricted access, and made their system look exactly the same, with functions disabled. Participants made use of the Z permissions to achieve this, and 46.6% of the participants set this binary variable to 1, at least once during the 5 tasks. The value of this variable did not have any effect on the success or failure of any task. Different participants interpreted the settings required for Task 3 differently. This task stated that Bob needs to give access to his emails to Howard. While some participants (43.3%)

Task/Permissions	R_c	R_c^{kc}	S_c	R_{nc}	R_{nc}^{knc}	S_{nc}	D	U	Z	L
Task 1	1	0	0	1	0	0	0	0	X	-
Task 2	0	0	0	0	0	0	0	0	X	collaborator<1,0,0>
Task 3	1	0	X	1	0	X	X	X	X	collaborator<1,0,0>, family<0,0,0>
Task 4	0	1 (k=accounts)	0	0	1 (k=accounts)	0	0	0	X	collaborator <1,0,1(k=accounts)>, family <1,0,1(k=accounts)>

Table 3: Table describing success scenarios for Tasks 1 - 4. 1 **represents** ***enabled*****,** 0 **represents** ***disabled*****,** *X* **represents** ***don't care condition*****, and '-' represents** ***not applicable.***

interpreted *access* as both sending and reading emails, others (56.7%) interpreted the meaning of *access* as only read. Only 6.6% of the participants set the *D* variable to 1, and granted "Delete" permissions to Howard in this task. Table 3 describes the various success scenarios as set by the participants for Task 1 through Task 4. Success of Task 5 was defined by deletion of the sub-user account created during Task 3. We use the terminology from section 4.1 to represent the state (permissions) of the four sub-users corresponding to the first four tasks.

In Figure 11, we present the different views of Bob's inbox, as configured for various sub-users. Bob's inbox is depicted in Figure 11(a), where Bob can see all emails, and has access to all functionalities like "Compose email", "Configure account", "View account activity", "Delete email" etc. Figure 11(b) represents Amy's view of the inbox, corresponding to Task 1. Note that Amy has only read access to the account, and so, all other features are missing. Penny's view of the same account is represented in Figure 11(c). Penny only gets to read Collaborators' emails. Figure 11(d) depicts Howard's view, who gets access to all except 4 emails viz. 2 from *wife*, and 2 from *son*. Stuart gets to see only one email, which contains the word *accounts* in the subject line, as shown in Figure 11(e).

6. DISCUSSION

In this paper, we presented and evaluated ChaMAILeon, a system which allows users to share their emails while maintaining their privacy. Our results show that apart from certain user interface issues, ChaMAILeon is fairly useful and usable. In particular, ChaMAILeon can be useful for: (1) users whose emails need to be managed by their assistants, and (2) users who wish to maintain their privacy while sharing their passwords with their partners. ChaMAILeon can also be used in scenarios where one is forced to access her email over an insecure network, like a cyber cafe. A sub-user can be created for one's own self, and confidential emails (for example, related to health, finance, etc.) can be refrained from being transmitted over insecure, or possibly compromised networks, by getting them filtered at the server-end itself. We conducted an online survey to gather users' password sharing trends and practices, and found that a large percentage of participants (74.64%) were uncomfortable with sharing their passwords.

To the best of our knowledge, ChaMAILeon is the first attempt to provide access control over emails. In the future, we intend to improve ChaMAILeon's user interface, fix the various bugs discovered during the controlled experiment, and conduct a more comprehensive evaluation of its usability in the real world. We also intend to study and investigate the various downsides of using ChaMAILeon. Especially under professional environments, ChaMAILeon can be exploited when a user grants access to her email account to a sub-user and asks the sub-user to impersonate her in her absence. We thus plan to conduct a comprehensive analysis of the potential pros and cons of such a system, before recommending its use in the professional environment.

Under the current settings, an implicit assumption is that the user trusts the server on which ChaMAILeon is hosted. The existing implementation of the system requires to store users' actual passwords (in encrypted form) on the ChaMAILeon server. Whenever a genuine sub-user logs into an account through ChaMAILeon, the system, in turn, requires to fetch emails from the Gmail server. This can only be done using the owner's actual password. We are in the process of exploring alternate ways like OAuth to avoid storing passwords. Although the concern regarding trust would not exist for organizations which run their own email servers, we envision ChaMAILeon's features to be an integral part of existing email services like Gmail, Yahoo Mail, Hotmail etc. This would completely eliminate the need for a middleware. Also, creating a large number of sub-users and passwords would, theoretically, lead to a reduction in the attack space for brute-force attacks. Associating x number of passwords with one email account directly increases the chances of a successful attack by x times. We would therefore suggest ChaMAILeon's users to create longer and non-trivial passwords to keep their accounts protected.

7. GUIDELINES

Based on our evaluation of ChaMAILeon, and feedback from our controlled experiment, we propose some generic guidelines that could be kept in mind while designing email management systems providing role based access control mechanisms in general.

Provide visualization mechanisms for verification of settings made by the users. Users were required to log out, and log in again as sub-users themselves to verify if the settings they had made were satisfactory. This process is time consuming, and can largely hamper the chances of users adopting this feature. It is therefore advisable to give users a visual preview of the settings they have made, without them having to verify the settings manually. A quick-preview window on the sub-user settings page, containing the sub-user's view of the mailbox, can be utilized for providing this.

Build intuitive interfaces where excessive information from the user is required. It is important to create interfaces which are comforting and intuitive to users, and do not overload users with too much information [9]. Participants from the controlled study were found to be over-

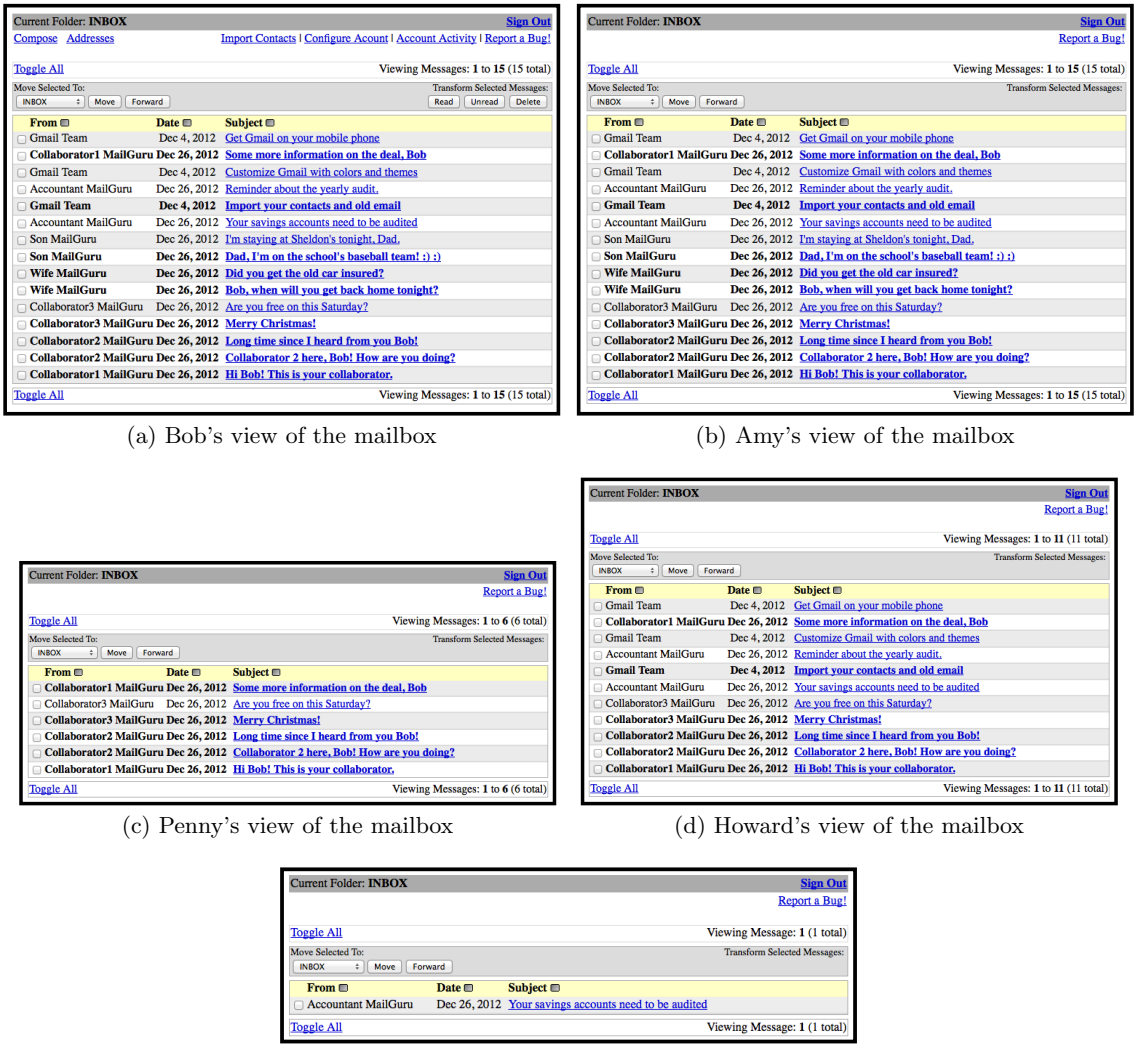

(a) Bob's view of the mailbox

(b) Amy's view of the mailbox

(c) Penny's view of the mailbox

(d) Howard's view of the mailbox

(e) Stuart's view of the mailbox

Figure 11: Different views of the same mailbox for different sub-users. Note that only Bob (subfigure 11(a)), the owner of the account gets access to the "Configure Account", "Account Activity", "Import Contacts", "Compose", and "Addresses" features.

whelmed at times, while setting permissions for sub-users due to the wide range of settings available. We advise developers to have a step-by-step interface for setting permissions, where each step contains settings for only one permission. This would reduce the amount of information presented to users at any point during the process, and would enable them to make better decisions.

Include comprehensive system walk-throughs and screen-casts as learning material for the users. Exposing users to new technology and features requires well thought out learning material to accompany the technology, in order to enable users to use it effectively. This can be achieved by building step-by-step system screen-casts, which walk users through comprehensive examples [10]. Care should be taken to make sure that walk-through videos or animations cover the most basic and important features of the technology, and at the same time, are short enough for users to view. Users tend to skip longer and too comprehensive walk-throughs.

Provide users with additional tools to assist them with newly introduced features. Extra features (like list and sub-user features) added to email management systems introduce extra work and more things to remember (like sub-user passwords) for the users. The overhead of remembering multiple passwords becomes too much for handling email accounts securely by the users [13]. We advise developers to provide users with software or hardware based password manager tools [1, 26]. Further, automatic email filtering and labeling techniques [3, 25] can be tuned and utilized to pre-generate common lists, like "Family", "Friends", "Colleagues" etc. This can help reduce users' overhead further.

8. ACKNOWLEDGEMENTS

We would like to thank all members of our research group, PreCog@IIITD. We would also like to thank Sheethal Shreedhar for helping us with the implementation of some of the

earlier versions of ChaMAILeon.

9. REFERENCES

[1] H. Al-Sinani and C. Mitchell. Using cardspace as a password manager. *Policies and Research in Identity Management*, pages 18–30, 2010.

[2] A. Alarifi, H. Tootell, and P. Hyland. A study of information security awareness and practices in saudi arabia. In *Communications and Information Technology (ICCIT), 2012 International Conference on*, pages 6 –12, june 2012.

[3] R. Bekkerman. Automatic categorization of email into folders: Benchmark experiments on enron and sri corpora. *Computer Science Department Faculty Publication Series*, page 218, 2004.

[4] S. Best, J. Girouard, and T. Snow. Handling email communications having human delegate prepared summaries, Nov. 9 2010. US Patent App. 12/942,216.

[5] D. Boyd and A. Marwick. Social privacy in networked publics: Teens' attitudes, practices, and strategies. *A Decade in Internet Time: Symposium on the Dynamics of the Internet and Society, September 2011*, 2011.

[6] J. Bradley. Complete counterbalancing of immediate sequential effects in a latin square design. *Journal of the American Statistical Association*, 53(282):525–528, 1958.

[7] J. Brooke. SUS-a quick and dirty usability scale. *Usability evaluation in industry*, 189:194, 1996.

[8] J. M. Butler. Privileged password sharing: "root" of all evil. *SANS Whitepaper*, 2012.

[9] W. Buxton. *Sketching user experiences: getting the design right and the right design*. Morgan Kaufmann, 2007.

[10] R. Clark and R. Mayer. *E-learning and the science of instruction: Proven guidelines for consumers and designers of multimedia learning*. Pfeiffer, 2011.

[11] E. Crawford, J. Kay, and E. McCreath. Automatic induction of rules for e-mail classification. 2001.

[12] D. Ferraiolo, J. Cugini, and D. Kuhn. Role-based access control (RBAC): Features and motivations. In *Proceedings of 11th Annual Computer Security Application Conference*, pages 241–48. sn, 1995.

[13] D. Florencio and C. Herley. A large-scale study of web password habits. In *Proceedings of the 16th international conference on World Wide Web*, pages 657–666. ACM, 2007.

[14] Google. Set up mail delegation. *http://support.google.com/mail/bin/answer.py?hl=en&answer=138350*, 2012.

[15] K. Hill. Why sharing passwords with your girlfriend/boyfriend is a spectacularly bad idea. *Forbes*, 2012.

[16] M. Hudecek. Auto-forwarding and auto-delegating email folder control, Jan. 7 2005. US Patent App. 11/030,818.

[17] T. Hunt. Mifrenz: Safe email for children. *New Zealand Journal of Applied Computing and Information Technology. Volume*, 12(1), 2008.

[18] J. HWANG and G. YANG. Method for generating and managing a user account using a multi-password, Nov. 2 2012. WO Patent 2,012,148,145.

[19] M. Hyatt. Managing email with an assistant. *Michael Hyatt Intentional Leadership*, 2010.

[20] P. Kumaraguru and N. Sachdeva. Privacy in India: Attitudes and Awareness V 2.0. Technical report, PreCog-TR-12-001, PreCog@IIIT-Delhi, 2012. http://precog.iiitd.edu.in/research/privacyindia/.

[21] A. Lenhart, M. Madden, A. Smith, K. Purcell, K. Zickuhr, and L. Rainie. Teens, kindness and cruelty on social network sites. *Washington, DC, Pew Research Center*, 2011.

[22] J. Nielsen and J. Hackos. *Usability engineering*, volume 125184069. Academic press San Diego, 1993.

[23] G. Notoatmodjo and C. Thomborson. Passwords and perceptions. In *Proceedings of the Seventh Australasian Conference on Information Security-Volume 98*, pages 71–78. Australian Computer Society, Inc., 2009.

[24] A. S. Patrick. Monitoring corporate password sharing using social network analysis. In *In International Sunbelt Social Network Conference, St. Pete Beach*, 2008.

[25] J. Provost. Naıve-bayes vs. rule-learning in classification of email. *University of Texas at Austin*, 1999.

[26] M. Safriel. Portable password manager, Mar. 26 2004. US Patent App. 10/811,278.

[27] R. Sandhu, E. Coyne, H. Feinstein, and C. Youman. Role-based access control models. *Computer*, 29(2):38–47, 1996.

[28] S. Singh, A. Cabraal, C. Demosthenous, G. Astbrink, and M. Furlong. Password sharing: implications for security design based on social practice. In *Proceedings of the SIGCHI Conference on Human Factors in Computing Systems*, CHI '07, pages 895–904, New York, NY, USA, 2007. ACM.

[29] J. Stanton, K. Stam, P. Mastrangelo, and J. Jolton. Analysis of end user security behaviors. *Computers & Security*, 24(2):124–133, 2005.

[30] S. Wilson. Combating the lazy user: An examination of various password policies and guidelines. 2002.

[31] X. Zhang, S. Oh, and R. Sandhu. Pbdm: a flexible delegation model in RBAC. In *Proceedings of the eighth ACM symposium on Access control models and technologies*, pages 149–157. ACM, 2003.

APPENDIX

A. ONLINE SURVEY QUESTIONNAIRE

Except Question 2, all questions in this survey were mandatory.

1. Do you share your email password with one or more people?
   - Yes [Go to question 3]
   - No [Go to question 2]
2. If no, do you think such a need may arise in future?
   - Yes
   - No
3. On a scale of 1 to 5, how comfortable are you with sharing your password?
   - 1 (very comfortable)

- 2 (somewhat comfortable)
- 3 (neutral)
- 4 (somewhat uncomfortable)
- 5 (very uncomfortable)

4. Do you think sharing passwords may lead to unwanted consequences?
   - Yes. It has happened to me.
   - Yes, but it has never happened to me.
   - No
   - May be
5. How would you consider changing your password after sharing it?
   - I would definitely change my password immediately.
   - I would probably change it whenever convenient.
   - I may consider changing it some time.
   - I would probably not change it.
   - I would definitely not change it.
6. Imagine, a system which allows you to control the accessibility of your emails / settings / features, when you share your password. Read the three example scenarios below, and state how you would consider using such a system. Assume that the system is capable of providing all functionality required for the scenarios mentioned below.

   Example scenario 1: You want to share your email with your spouse, but do not want him/her to see emails from a particular friend, or do not want him/her to be able to reply to any emails. How would you consider using such a system?
   - I would definitely use it.
   - I would probably use it.
   - I'm not sure.
   - I would probably not use it.
   - I would definitely not use it.

   Example scenario 2: You are an official at a big post in a company, and receive a lot of emails every day. You wish to allow your assistant to be able to log into your account and reply to emails on your behalf. However, you want your assistant to be able to see emails sent from only specific people, and not all of them. How would you consider using such a system?
   - I would definitely use it.
   - I would probably use it.
   - I'm not sure.
   - I would probably not use it.
   - I would definitely not use it.

   Example scenario 3: You are in a cyber cafe where you are not sure if the network is secure. You need to check your email, but you are afraid your password and email content might get compromised over the insecure network. You have an option to log into your account with a different password, such that, logging in with this password gives you very limited / restricted access to your account. How would you consider using such a system?
   - I would definitely use it.
   - I would probably use it.
   - I'm not sure.
   - I would probably not use it.
   - I would definitely not use it.
7. Have you ever come across any such system, which gives you some kind of access control over emails?
   - Yes. I use it.
   - Yes, I have heard of it. But I don't use it.
   - No, I have never heard of it.

   Demographic information
8. What age group do you belong to?
   - 13 - 18 years
   - 19 - 25 years
   - 26 - 32 years
   - 33 - 40 years
   - 41 - 50 years
   - Above 50 years
9. Highest educational qualification completed.
   - School / High School
   - Under graduation
   - Post graduation
   - Ph.D.
   - Other:
10. Occupation / Profession
    - Computer Science
    - Engineering
    - Medicine
    - Science, Pharmaceuticals
    - Law
    - Journalism
    - Finance
    - Business
    - Home maker
    - Social sciences
    - Other:
11. Gender
    - Male
    - Female
12. Which email services do you use? Tick all that you use
    - Google (Gmail)
    - Yahoo! Mail
    - Rediffmail
    - AOL mail
    - Hotmail
    - Other:
13. Country of residence

    If you want to take part in the lucky draw, please specify an email address or phone number where we could contact you, if you are a winner. All data collected during this survey will be anonymized and aggregated for dissemination of the results. Your answers are treated confidentially and used for research purposes only. We will not use your contact information for any other purposes but to contact you to collect your prize.

    Email ID / Phone number (This is optional.)

B. PRE-STUDY

B.1 Privacy Statement

Q: What data do we collect?
A: During the study we will ask you several questions related to your use of emails, and will give you a set of tasks to perform. We will take an audio-visual recording of your answers using a laptop. We will also record the screen activity during the experiment. The collected data will be anonymized and treated confidentially. This data will serve as answers to research questions and will be used solely for the purpose of this study.

Q: Who has access to this data?
A: Access to collected data is restricted to researchers involved in the study. Your personal information will never be transferred to another party. Aggregated statistics and anonymized quotes / clips from the audio-visual recordings will be published in an academic article.

Q: What are my rights?
A: You can interrupt or withdraw form the study at any time. You may ask to see the collected data. You have the right to demand the deletion of parts or all it.

B.2 Questionnaire

All questions in this questionnaire were mandatory.

1. How many email accounts do you have?
   - 1
   - 2 or 3
   - 4 or 5
   - More than 5
2. Which email services do you use?
   Tick all that you use.
   - Google (Gmail)
   - Yahoo! Mail
   - Rediffmail
   - AOL Mail
   - Hotmail
   - Other:
3. Do you maintain separate email accounts for personal and official purposes?
   - Yes
   - No
4. Do you share your email password with one or more people?
   - Yes
   - No
5. How comfortable are you with sharing your password with the following:
   - Parents
     - Very uncomfortable
     - Somewhat uncomfortable
     - Neutral
     - Somewhat comfortable
     - Very comfortable
   - Siblings
     - Very uncomfortable
     - Somewhat uncomfortable
     - Neutral
     - Somewhat comfortable
     - Very comfortable
   - Spouse
     - Very uncomfortable
     - Somewhat uncomfortable
     - Neutral
     - Somewhat comfortable
     - Very comfortable
   - Relatives
     - Very uncomfortable
     - Somewhat uncomfortable
     - Neutral
     - Somewhat comfortable
     - Very comfortable
   - Friends
     - Very uncomfortable
     - Somewhat uncomfortable
     - Neutral
     - Somewhat comfortable
     - Very comfortable
   - Colleagues
     - Very uncomfortable
     - Somewhat uncomfortable
     - Neutral
     - Somewhat comfortable
     - Very comfortable
6. Highest educational qualification completed.
   - School / High School
   - Under graduation
   - Post graduation
   - Ph.D.
7. What age group do you belong to?
   - 18 - 25 years
   - 26 - 32 years
   - 33 - 40 years
   - 41 - 50 years
   - Above 50 years
8. Occupation / Profession
   - Computer Science
   - Engineering
   - Medicine
   - Science, Pharmaceuticals
   - Law
   - Journalism
   - Finance
   - Business
   - Home maker
   - Social sciences
   - Other:
9. Gender *

- Male
- Female

10. Have you heard of Gmail's mail delegation feature?
    - Yes, I have used it.
    - Yes, but I have never used it.
    - No.

C. CONTROLLED EXPERIMENT

C.1 Instructions

1. Please read the tasks aloud and ask for any clarification (if you need any).
2. Think aloud. Feel free to speak out your thoughts.
3. You are required to perform these tasks on two platforms; Gmail (`http://gmail.com`), and ChaMAILeon (`http://precog.iiitd.edu.in/chaMAILeon`).
4. Please be patient with the system; it might take some time to log you in.
5. We will now play two videos; a tutorial video of Gmail's Email Delegation feature, and a tutorial video of ChaMAILeon, which will walk you through the system with some example scenarios. Please watch the videos carefully to understand how both these systems works.
6. For any help during the activity, feel free to refer back to these videos at any point of time.

C.2 Scenario and tasks

Imagine yourself to be Bob Smith, the CEO of Bob Construction Company. You visit your office at 9 am in the morning, and you have five tasks (plus one clean-up task) to perform in the day, related to your emails. The tasks are as follows: You may perform these tasks in any order, according to your priority.

Your (Bob's) email address: bob.mailguru@gmail.com
Your (Bob's) password: <password>

Task 1: There are some legal cases currently going on, which you are part of. You need to give access of your email to your lawyer Amy. You want Amy to be able to read all your emails, but do not want her to be able to send or delete any emails from your account.

- *Once you have configured this, log into your account as Amy to check if you are satisfied with the settings you have made. (How different / similar is the result from your expectations?)*

Task 2: You want your personal assistant, Penny, to keep a track of emails from a certain set of your foreign collaborators. You thus need to share your email account with her, but wish that Penny reads emails from ONLY collaborator1.mailguru@gmail.com, collaborator2.mailguru@gmail.com and collaborator3.mailguru@gmail.com

- *Once you have configured this, log into your account as Penny to check if you are satisfied with the settings you have made. (How different / similar is the result from your expectations?)*

Task 3: You would not be able to access your emails for a few hours during the day, and so, you want your colleague Howard to access your emails during these hours. However, you wish that Howard does not get to read emails from your wife (wife.mailguru@gmail.com) and son (son.mailguru@gmail.com)

- *Once you have configured this, log into your account as Howard to check if you are satisfied with the settings you have made. (How different / similar is the result from your expectations?)*

Task 4: There are some financial emails that you want your accountant Stuart to handle. You thus need to give access to your email to Stuart, but you wish that he should be able to see only those emails which contain the word "accounts" in the subject line.

- *Once you have configured this, log into your account as Stuart to check if you are satisfied with the settings you have made. (How different / similar is the result from your expectations?)*

Task 5: You learn that all your appointments for the day have been cancelled, and you realize that you no longer need Howard to access your emails. You want to revoke Howard's access to your account.

- *Once you have configured this, try to log into your account as Howard to check if you are satisfied with the settings you have made. (How different / similar is the result from your expectations?)*

Cleanup task: Delete all lists and sub-users you have created during the activity.

Email IDs for the various people to whom you (participant) will give (not give) access to:

- Bob's wife: wife.mailguru@gmail.com
- Bob's Son: son.mailguru@gmail.com
- Bob's Foreign Collaborators:
  - collaborator1.mailguru@gmail.com
  - collaborator2.mailguru@gmail.com
  - collaborator3.mailguru@gmail.com
- Accountant: acc0untant.mailguru@gmail.com

Characterization of PV Cell- Environmental factors consideration

Aarti Kane *, Dr.Vishal Verma **

* Bharati Vidyapeeth College of Engineering, Delhi, India

** Delhi Technological University, Delhi, India

sanikakane@rediffmail.com, vishalverma@dce.ac.in

Abstract- **The objective of this paper is to develop mathematical model of Photovoltaic (PV) module and study effects of environmental factors on its performance. Output of PV module strongly depends on environmental conditions like solar irradiance, ambient temperature and wind speed etc. Mathematical model is developed in Matlab/Simulink environment by considering effect of above conditions. Maximum power point voltage and PV module temperature relationship is determined utilizing simulated results. An attempt has been done to develop Maximum power point tracking (MPPT) algorithm based on cell temperature and solar irradiance to improve the efficiency of PV power generation system.**

Keywords: **Solar PV modeling, Solar cell characterization, maximum power point tracking, temperature and insolation effect, Matlab Simulink**

I. INTRODUCTION

The electricity requirements of the world including India are increasing at alarming rate and we are facing critical problem of energy deficit. Solution to our energy problems is transition from traditional energy sources to renewable energy sources thereby reducing greenhouse gas emission, detoriation of environment and energy sources. Solar energy is clean and abundant renewable source of energy. Solar system is noiseless and free of moving parts and its maintenance and operation costs are less. It is a relatively expensive means of producing electricity due to its high fabrication cost and less conversion efficiency. Solar energy can be converted into direct current electricity by PV effect. Output power of PV system depends on solar irradiance, temperature of solar cell and wind speed and operating voltage. This paper focuses on developing PV model with consideration of electrical and thermal relationship. Electrical energy is one of the components of solar energy conversion process. A typical PV module has ideal conversion efficiency in the range of 15%. The remaining energy is converted into heat and this heat increases operating temperature of PV system which affects electrical power production of PV modules. This paper focuses on effect of temperature on electrical characteristic of PV module. Temperature of the module can rise to 70^0C, this can cause structural damage of PV modules shorting its life span and lowering conversion efficiency. Output power of PV module drops by 0.45% per ^{0}C rise in temperature if heat is not removed [5]. The PV models developed so far describe output characteristics with solar insolation and cell temperature as input parameters whereas in this paper cell temperature is determined by taking into account ambient temperature, solar insolation and wind speed [3-4].

In order to use PV panel effectively maximum power point tracking (MPPT) methods are used. Generally MPPT methods use DC-DC converter as an interface between PV array and the load and it is controlled using tracking algorithm. Selection of converter and control algorithm are main tasks of MPPT methods. Commonly used algorithms are Perturb and Observe, Incremental Conductance, constant voltage. These algorithms require measurement of PV output voltage and current or both [6-12]. This paper proposes a new MPPT method based on temperature and solar insolation of PV module. This method doesn't require any sensor connected with PV cell, as temperature of PV module is determined by considering solar insolation, wind speed and ambient temperature.

Section II deals with the basic equations of PV module. These equations are implemented for simulation purpose. Model development stages are described in section III. In Section IV simulation results and development of MPPT algorithm is discussed. Section V gives the conclusion.

II. SOLAR SYSTEM

Solar cell converts electromagnetic radiation into electricity by PV effect. When cells are exposed to appropriate wavelengths, electrons in p-type region will be excited from valence band to conduction band and they contribute to a current. The equivalent circuit of solar cell is represented by connecting current source in parallel with a diode. The current source represents the current generated by PV cell. In ideal solar cell series and parallel resistance are not

978-1-4673-6030-2/13/$31.00 ©2013 IEEE

present but in practical case these resistance are included due to ohmic resistances and leakage current.

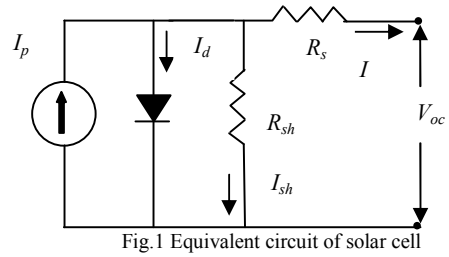

Fig.1 Equivalent circuit of solar cell

If solar cell is not exposed to solar irradiation, it behaves as p-n junction diode and if connected to external supply it generates a current I_d, i.e. diode current [1]-[2].

$$I_d = I_0\left[\exp\left(\frac{qv_d}{nkT}\right)-1\right] \quad (1)$$

where

v_d - Voltage across diode

I_0 - Reverse saturation current of a diode

K - Boltzmann's constant ($1.38\text{x}10^{-23}$J/K)

n - Diode ideality factor (typically between 1 and 2)

The output current from the PV cell can be found using the equation

$$I = I_L - I_d \quad (2)$$

where I_L is light generated current and is given as

$$I_L = G\left(I_{sc}\left(1 + a*\left(T - T_{ref}\right)\right)\right) \quad (3)$$

where

I_{sc} – short circuit current of the PV cell

a- Short circuit current temperature coefficient (%/C)

G- Solar irradiance (W/m^2)

I_{sc} is maximum current at zero voltage and it is directly proportional to solar irradiance.

Characteristic equation of solar cell is given as

$$I = I_{L-I_0}\left[\exp\left(\frac{q(v+IR_s}{nkT}\right)-1\right]-\frac{v+IR_s}{R_{sh}} \quad (4)$$

R_s-series resistance

R_{sh}-parallel resistance

T- absolute temperature

q-Electric charge ($1.69\text{x}10^{-19}$C)

Major contributors to the series resistance are the bulk resistance of semiconductor material, the metallic contacts, and interconnections. Series resistance has significant effect on the PV power output. The shunt resistance is due to p-n junction non-idealities and impurities near the junction. PV efficiency is insensitive to variation in R_{sh} and it is considered as infinity and therefore current through parallel resistance I_{sh} is very less and therefore neglected in this paper.

The open circuit voltage V_{oc} is maximum voltage at zero current. Value of V_{oc} increases logarithmically with increased sunlight and is given as

$$V_{oc} = \frac{kT}{q}\ln\left[\frac{I_L}{I_o}+1\right] \cong \frac{kT}{q}\ln\frac{I_L}{I_o} \quad (5)$$

Solar PV cells with similar characteristics are connected and encapsulated to form modules which are building blocks of solar array. Maximum voltage from single silicon cell is about 600mV and maximum current delivered by cell is approximately 30mA [2]. Cells are connected in series and parallel combination in order to get desired voltage and current respectively.

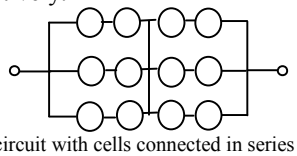

Fig.2 Module circuit with cells connected in series and parallel connection (3 parallel, 2 series and 2 cells per substring connection)

III. MODELLING OF SOLAR CELL

Mathematical model of PV cell is developed with consideration of the influence of ambient radiation G and cell temperature T on the cell characteristics as shown in Fig.3. The two key parameters are most often used to characterize solar cell are its short circuit current and open circuit voltage. These values are taken from manufacturer's data sheet. Here MAX60 solar cell is used for simulation purpose and specifications are shown in Table 1.

Parameter	Value
Open circuit voltage(V_{oc})	21.1V
Short circuit current(I_{sc})	3.8A
Maximum power	59.85≅60W
Voltage at max power	17.1A
Current at max power	3.5A
No of cell in series (N_s)	36

Table1. Solar array datasheet parameters of MAX60

As shown in Fig.3b 'Photovoltaic' S-function is developed to simulate PV panel. Inputs to this function are output voltage, ambient temperature and solar irradiation while output is I_L; light generated current. This simulated photocurrent is used for modeling PV panel by considering practical condition of series resistance, R_s and output power of PV panel is calculated as shown in Fig. 3.

Study of thermal behaviour of solar cell is necessary to determine temperature of solar cell. Modeling of PV panel temperature can be done by evaluating energy inputs and outputs through radiation, convection and conduction and power generated. Convection heat transfer from back and front surfaces of the module are significant while heat conducted from PV panel to structural

framework is considered negligible as the area of contact point is very small.

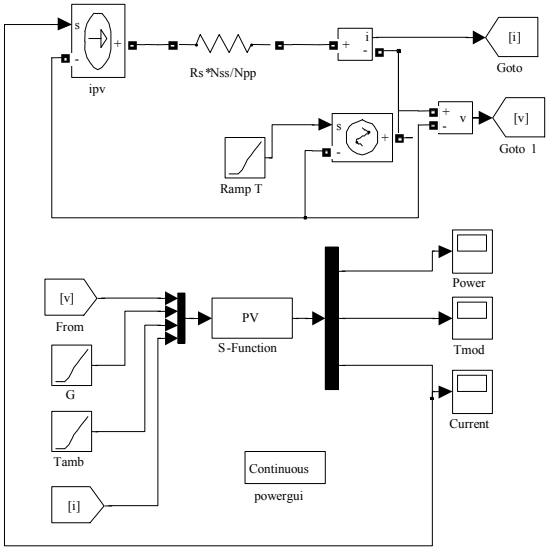

Fig.3 Model development stages

Radiation heat transfer is also very negligible and not considered for simulation. Temperature of solar panel is given by applying energy balance equation of solar panel as follows,

$$C_{\mathrm{mod}} \frac{dT}{dt} = q_{conv} - P_{out} \qquad (6)$$

C_{mod} is heat capacity of module expressed in J/kg K and q_{conv} is convected heat expressed in W.

Temperature of solar panel varies with variation in solar radiation, ambient temperature and wind speed.

$$T = 0.943T_{amb} + 0.028G*1000 - 1.521*ws + 4.3 \qquad (7)$$

here ws wind speed is considered as 1m/s.

IV. SIMULATION RESULTS

V.

Fig 4-7 shows the simulation results of above developed model. Model is simulated by applying different cases of temperature and insolation levels. When temperature increases amount of saturation current will increase more than amount of photocurrent and therefore makes V_{oc} decreased rapidly. Fig. 4 and Fig. 6 shows effect of PV module temperature on the output power and short circuit current. With increase in temperature the short circuit current of the PV cell increases whereas maximum power output decreases. Increase in output current is much less than decrease in voltage so net power decreases at high temperature as shown in Fig.4.

Fig.6 shows effect of solar insolation on short circuit current and output power. From the graph it can be concluded that with increase in solar insolation, the short circuit current and maximum power output increases. Temperature and insolation curve is plotted in Fig.4 and Fig. 6 respectively to show variation of maximum power point voltage.

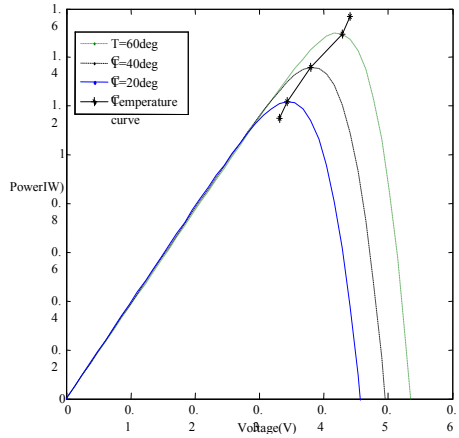

Fig.4 P-V characteristic of PV cell at various temperature with constant solar irradiation (G=1kW/m^2)

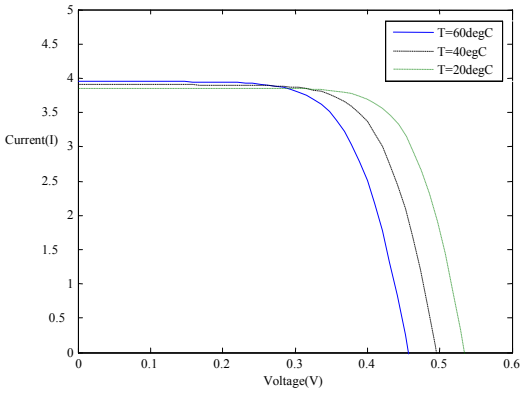

Fig.5 V-I characteristics of PV cell at various temperatures with constant solar irradiation G=1kW/m^2

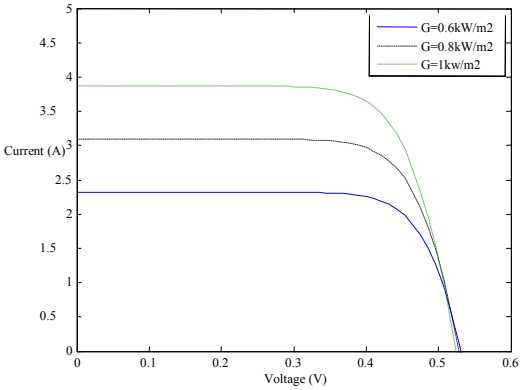

Fig.6 V-I characteristic of PV cell at various solar irradiation with constant temperature (25^{0}C)

Maximum power point voltage (Vmpp) varies with temperature and solar insolation but variation with temperature is more significant as compared to variation with solar insolation. Both conditions are

considered in this paper while developing MPPT algorithm.

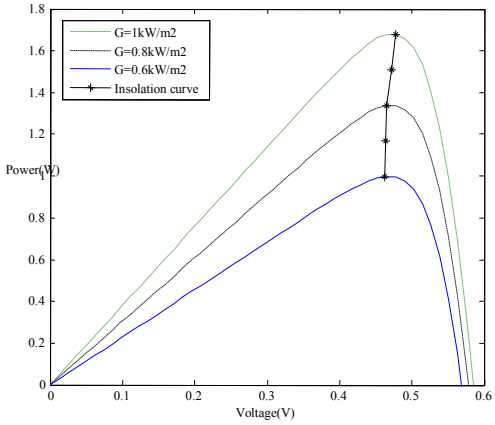

Fig.7 P-V characteristics of PV cell at various solar irradiation at constant ambient temperature (25^0C)

Ambient temperature doesn't change significantly during day time but solar insolation level changes depending upon solar insolation and cloud conditions. A change in solar insolation causes a change in cell temperature which will affect output voltage of cell and in turn maximum power point voltage. Operating voltage is varied to find maximum power point voltage and current. For known temperature and solar insolation maximum power point voltage is obtained as shown in Fig4&6. Cubical approximate curve fitting method is used to find equations for above curves. Finally mathematical equations are formed to obtain maximum power point voltage as a function of temperature and insolation. This model can be used to characterize and obtain maximum power point voltage at any temperature and solar insolation levels.

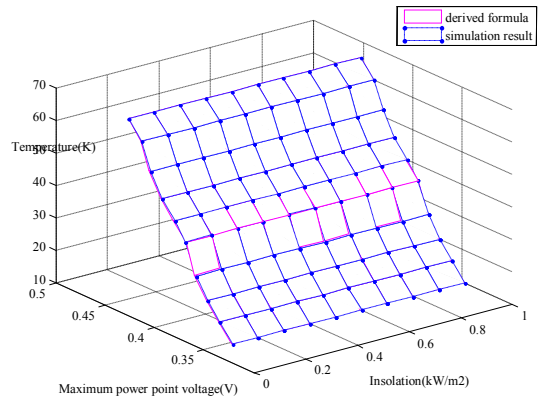

Fig.8 Comparison of maximum power point voltage obtained by derived formula and simulated results at various values of ambient temperature and solar insolation.

As shown in Fig.8 maximum power point voltages obtained by derived formula and actual simulation shows similarity for normal operating range of PV module.

VI. CONCLUSION

This paper is a representation of an attempt to study the Performance of photovoltaic cell considering effects of environmental factors. MPPT algorithm has been developed and shown comparatively better and accurate results. Tracking method in proposed algorithm is oscillation-free unlike in conventional algorithms like perturb and observe, incremental inductance and common voltage method etc. Detailed study of the PV Module with respect to comparative study of simulated results with theoretical calculations for various factors like temperature, solar irradiation and wind speed has been done to establish correctness of Algorithm. Proposed Algorithm will be an effective tool for optimizing performance of PV System banking on its direct output capability.

REFERENCES

[1] Duffie, J.A. & Beckman, W.A. (1991), Solar Engineering of Thermal Processes, 2nd Edition, Wiley-Interscience, New York

[2] Stuart R. Wenham, Martin A. Green, "Applied photovoltaics", ISBN:1844074013, Feb 2007

[3] R J. A. Gow, C. D. Manning **"**Development of a photovoltaic array model for use in power electronics simulation studies," IEE Proceedings on Electric Power Applications, vol. 146, no. 2, pp. 193-200, March 1999.

[4] Salam, Z.; Ishaque, K.; Taheri, H., "An Improved Two Diode Photovoltaic (PV) model for PV System", Joint International Conference on Power Electronics, Drives and Energy Systems (PEDES) & 2010 Power India, 2010, pp.1-5

[5] Min-Jung Wu; Timpson, E.J.; Watkins, S.E., "Temperature Considerations in Solar Arrays", Region 5 Conference: Annual Technical and Leadership Workshop, 2004 , pp. 1-9

[6] Walker G., "Evaluating MPPT converter topologies using a MATLAB PV model," Journal of Electrical & Electronics Engineering, Australia, IEAust, vol.21, No. 1, 2001, pp.49-56.

[7] I. H. Altas and A.M. Sharaf: A Novel On-Line MPP Search Algorithm for PV Arrays, IEEE Transactions on Energy Conversion, Vol. 11, No. 4, December 1996, pp. 748-754.

[8] M. Veerachary, T. Senjyu, and K. Uezato, "Voltage-based maximum power point tracking control of PV system," IEEE Transactions on Aerospace and Electronic Systems, vol. 38, no. 1, 2002, pp. 262-270.

[9] K. H. Hussein, I. Muta, T. Hoshino, and M. Osakada, "Maximum photovoltaic power tracking: an algorithm for rapidly changing atmospheric conditions," IEE Proceedings of Generation, Transmission and Distribution, vol. 142, no. 1, 2005, pp. 953-959

[10] Kourtoulis E, Kalaitzakis K, Voulgaris NC. "Development of a microcontroller-based, photovoltaic maximum power point tracking control system." IEEE Transactions on Power Electronics 2001; 16(1): 46–54.

[11] Y-C. Kuo, T-J. Liang, and J-F. Chen: Novel Maximum-Power-Point-Tracking Controller for Photovoltaic Energy Conversion System, IEEE Transactions On Industrial Electronics, Vol. 48, No. 3, June 2001, pp.594-601.

[12] Enslin JHR,Wolf M, SwiegersW., "Integrated photovoltaic maximum power point tracking converter.", IEEE Transactions on Industrial Electronics 1997; 44(6): 769–773.

`

Current mode full wave rectifier based on a single MZC-CDTA

Neeta Pandey, Rajeshwari Pandey

Department of Electronics and Communications Engineering,
Delhi Technological University, Delhi, India,
Email: n66pandey@rediffmail.com, rajeshwaripandey@gmail.com

Abstract - This paper presents a current mode full wave rectifier based on single modified Z copy current difference transconductance amplifier (MZC-CDTA) and two switches. The circuit is simple and is suitable for IC implementation. The functionality of the circuit is verified with SPICE simulation using 0.35 μm TSMC CMOS technology parameters.

Keywords: CDTA, full wave rectifier

I. Introduction.

The full wave rectifiers are used in varied applications [1–4] such as signal-polarity detectors, averaging circuits, peak value detectors, clipper circuits, amplitude-modulated signal detectors etc. Conventionally full wave rectifier is implemented using operational amplifiers which are not capable of operating at higher frequencies because of slew rate and fixed gain-bandwidth product limitations [5]. Current mode approach due to its inherent wide bandwidth which is virtually independent of closed loop gain, greater linearity, and large dynamic range [5] has generated lots of interest and significant research efforts have been directed towards developing new active blocks based on this approach. Among these blocks CDTA [6, 7, 8] has received considerable attention as the external resistors may be implemented by TA block of CDTA, thereby reducing/ avoiding external resistors usage in the applications based on CDTA [8] and making these suitable for on-chip implementation Additionally due to low input impedance terminals, CDTA is free from parasitic capacitances and hence is appropriate for high frequency operation. This has resulted in development of a wide range of CDTA based applications [7 – 17].

A variety of FWR circuits using CDTA [14-17] have been reoprted in literature. The CDTA based FWR circuits presented in [14 – 16] use single CDTA whereas configuration reported in [17] employs two CDTAs and a multiple output current follower. The structures [14, 15, 17] use four pn junction diodes whereas two schottky diodes are used in [16]. Additionally auxiliary bias is employed in [14] and a grounded resistor is employed in [17]. In this paper a new approach for designing a single CDTA based current mode full wave rectifier (FWR) configuration is presented The proposed current mode FWR configuration uses a single CDTA called MZC-CDTA (modified Z copy CDTA) and two MOS switches. The features of the CDTA based FWR circuits are summarized in Table 1new. It may be noted that the proposed FWR uses similar number of active elements as given in [16], however, the use of MOS switches makes it more suitable from integration viewpoint. The functionality of the circuit is verified with SPICE simulations using 0.35 μm TSMC CMOS technology parameters.

Table 1 Summary of available CDTA based FWR

Ref. No.	Number of CDTAs	Additional active block	Number/ Type of passive elements	Auxiliary Bias Current sources
[14]	1	4 pn junction diodes	-	Yes
[15]	1	4 pn junction diodes	-	No
[16]	1	2 schottky diodes	-	No
[17]	2	multiple output current follower, 4 pn junction diodes	1 grounded resistor	Yes
Proposed	1	2 MOS transistors	-	No

II. Circuit Description

The circuit symbol of MZC-CDTA is shown in Fig. 1. It is similar to ZC-CDTA except an extra zc- port. The port relationship of the MZC-CDTA is characterized by the following matrix:

$$\begin{bmatrix} V_p \\ V_n \\ I_z \\ I_{zc} \\ I_{zc-} \\ I_{x+} \\ I_{x-} \end{bmatrix} = \begin{bmatrix} 0 & 0 & 0 & 0 & 0 & 0 \\ 0 & 0 & 0 & 0 & 0 & 0 \\ 1 & -1 & 0 & 0 & 0 & 0 \\ 1 & -1 & 0 & 0 & 0 & 0 \\ 1 & -1 & 0 & 0 & 0 & 0 \\ 0 & 0 & g_m & 0 & 0 & 0 \\ 0 & 0 & -g_m & 0 & 0 & 0 \end{bmatrix} \begin{bmatrix} I_p \\ I_n \\ V_z \\ V_{zc} \\ V_{zc-} \\ V_{x+} \\ V_{x-} \end{bmatrix} \quad (1)$$

where g_m is transconductance of the MZC-CDTA. The CMOS based internal circuit of MZC-CDTA is depicted in Fig. 2 and is based on the CDTA schematic given in Ref. 14. The value of transconductance (g_m) is expressed as

$$g_m = \sqrt{2\mu C_{ox}(W/L)_{21,23} I_0} \quad (2)$$

which can be adjusted by bias current I_0 of MZC-CDTA.

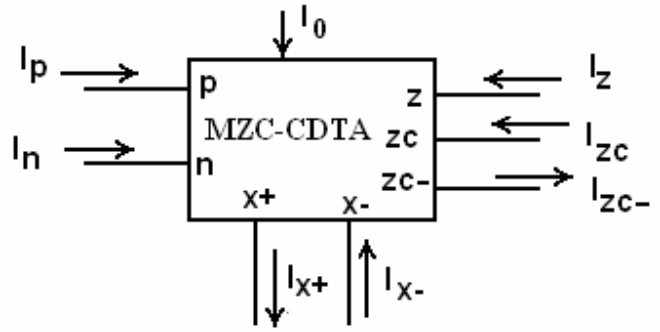

Fig. 1. Circuit symbol of MZC-CDTA

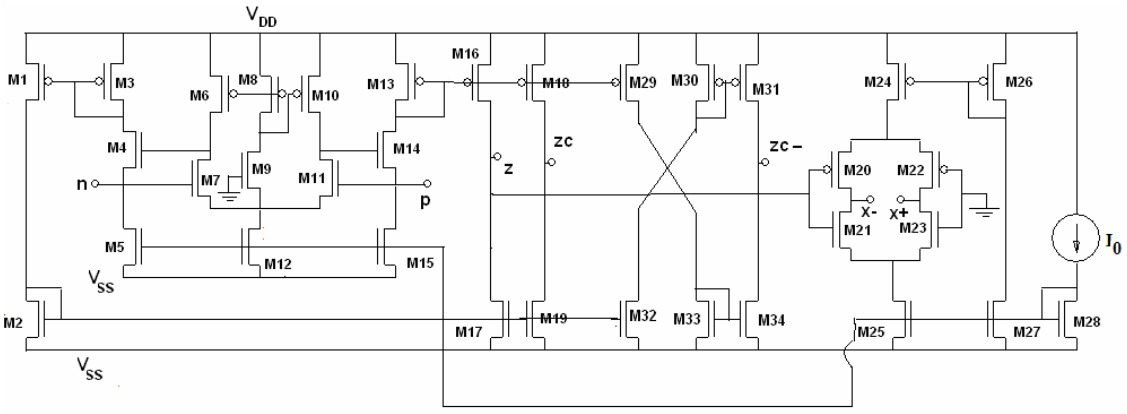

Fig. 2.MZC-CDTA implementation

The proposed MZC-CDTA based full wave rectifier is shown in Fig. 3. It uses a single MZC-CDTA, and two MOS switches (M_{p1} and M_{n1}) connected at zc and zc- ports respectively. The z port being open, its voltage would approach to V_{DD} or V_{SS} depending upon the current flowing into p terminal. Further as x- terminal of the circuit is also not drawing any current so for small current inputs, it would be saturating to supply voltage, resulting in

$$\begin{aligned} V_{x-} &= V_{DD} \qquad for\, I_{in} \le 0 \\ V_{x-} &= V_{SS} \qquad for\, I_{in} \ge 0 \end{aligned} \tag{3}$$

At any instant, either of the two transistors M_{p1} and M_{n1} will be in ON condition as the current through zc and zc- ports are out of phase. The transistor M_{p1} will be ON for positive input currents whereas the negative input current will bring transistor M_{n1} in ON condition thereby making I_{out} a unidirectional current.

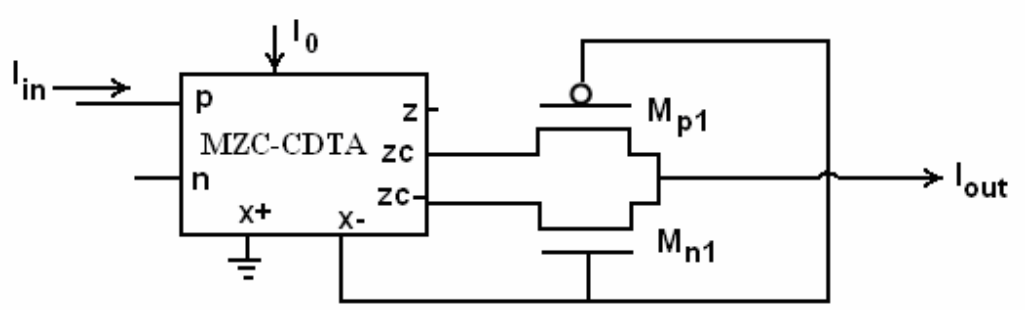

Fig. 3 Proposed current mode rectifier.

III. Non-ideal Analysis

The actual behavior of the circuit may deviate from the ideal one due to error in current transfer from p and n terminals to z, zc and zc- terminals; and also current at x+ and x- terminals. The current transfer from p and n ports to z, zc and zc- port may differ from unity value and these tracking errors are represented by α_p and α_n. The inaccuracy in transconductance transfer from z to x+ and x- ports is modeled by $\beta g_m V_z$. Considering the inaccuracies outlined above, the output current I_{out} becomes unidirectional current of value $\alpha_p|I_{in}|$. Depending upon the internal structure and technology used, the tracking errors α_p, α_n and β also have first order low pass roll off which affects the performance at high frequencies.

Apart from error in current transfer, there are parasitic impedances at p and n ports (resistances R_p and R_n) and shunt output impedances (R//C) at ports z, zc, zc- x+ and x-. The input current is applied at p port in the proposed circuit and n port is left open so resistances at p and n ports do not put restriction in the behavior of the circuit. The impedances at z, zc, zc-, x+ and x- ports will have impact at higher operating frequencies.

IV. Simulation results

The functionality of the proposed current mode rectifier is validated using MZC-CDTA schematic of Fig. 2. The model parameters of TSMC 0.35µm CMOS process and supply voltages of $V_{DD} = -V_{SS} = 1.8V$ are used. The aspect ratios of various transistors are taken from [12] and the bias current of 60 µA is used. The circuit of Fig. 3 is excited by a 10 KHz, 20 µA sinusoidal current signal. The time domain behaviour of voltage developed at x- port due to input current is shown in Fig. 4. For positive half cycle of the input current, a negative voltage is developed at x- port which in turn makes the transistor Mp1 ON whereas transistor Mn1 remains OFF. , thus output current I_{out} is equal to input current for positive half cycle. The negative half cycle of the input current makes x- port voltage positive and turns transistor Mn1 ON. The current through transistor Mn1 is out of phase with input current therefore the output current would be positive. The input and output currents for the proposed circuit under sinusoidal excitation are shown in Fig. 5 and conform to the theoretical predictions. The simulated ripple factor curve is plotted in Fig. 6 and its value is approximately 0.5. Figure 7 shows the response of the circuit under sinusoidal excitation. The simulated total power consumption of the circuit is 14 mW.

The DC response of the proposed circuit is also studied and the transfer characteristics are shown in Fig. 6. It may be noted that the proposed circuit behavior is linear for input currents ranging between -300 µA to +300 µA. The positive and negative slopes of 0.967 and 0.993 respectively are observed. The deviation of slope from unity value may be attributes to CDTA non-idealities.

The proposed circuit is also tested to judge the level of harmonic distortion at the output of the signal. The %THD result is shown in Fig. 9 which shows that the output distortion is around 22% for input currents up to 300 µA.

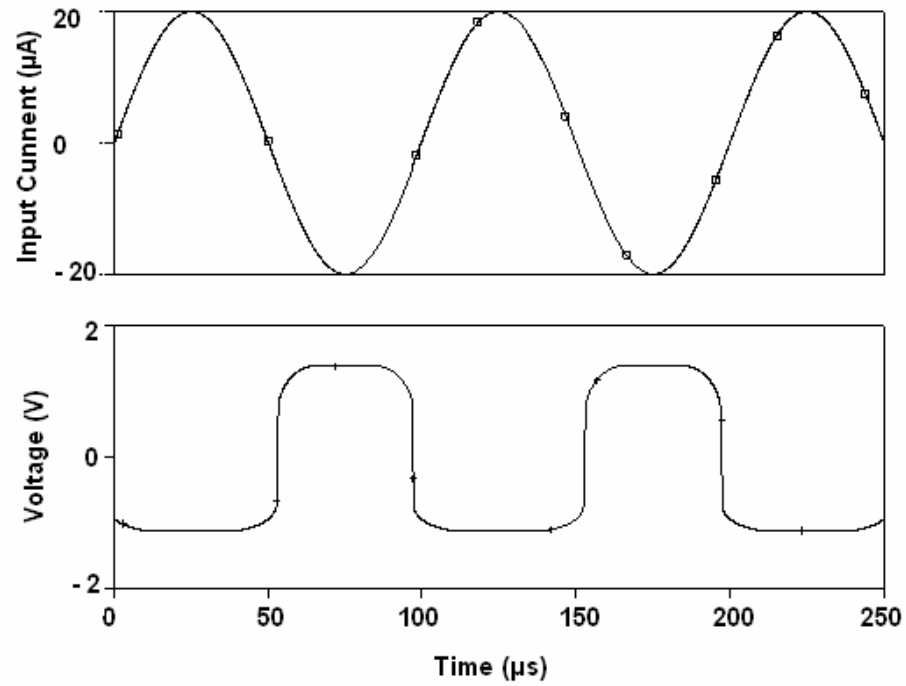

`Fig 4 Time domain response of input current and x- port voltage

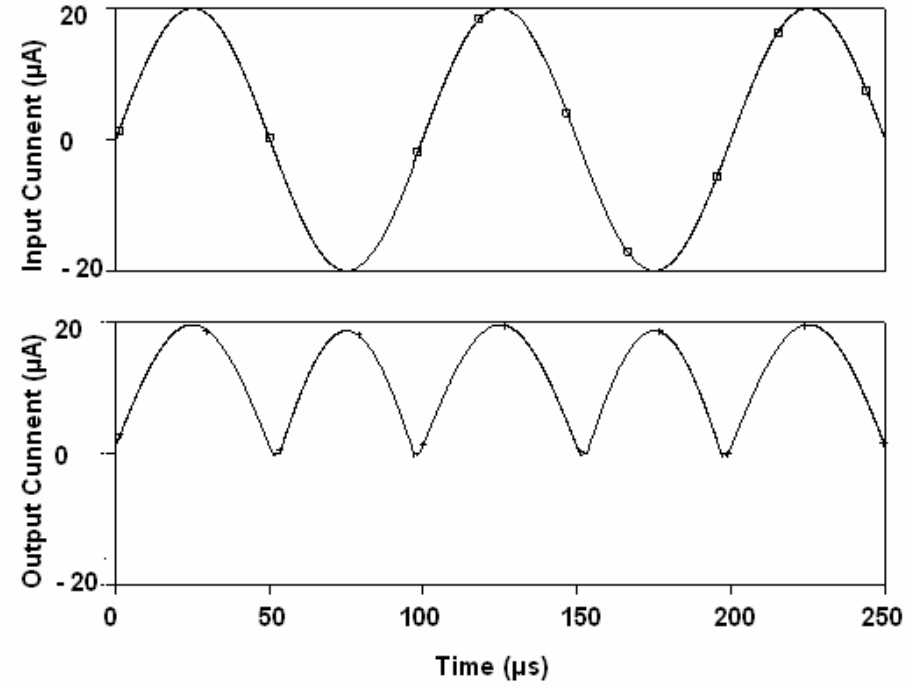

Fig. 5 Input and output waveforms for sinusoidal excitation

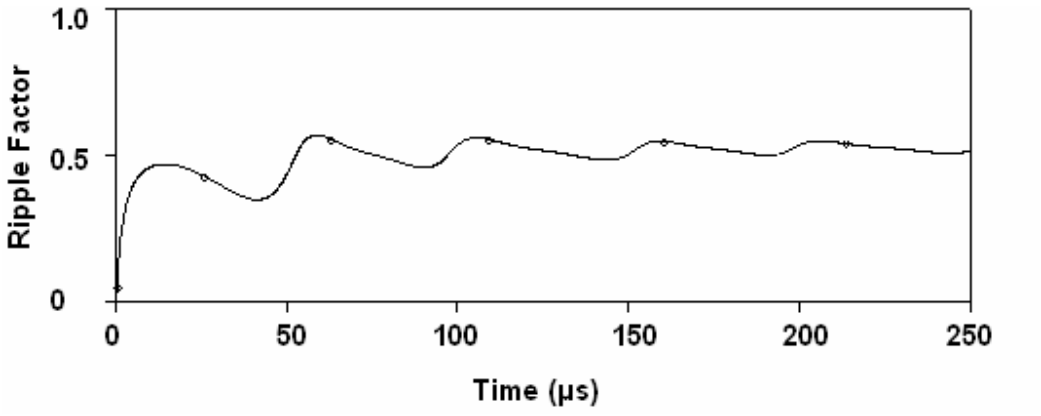

Fig. 6 Simulated curve for ripple factor

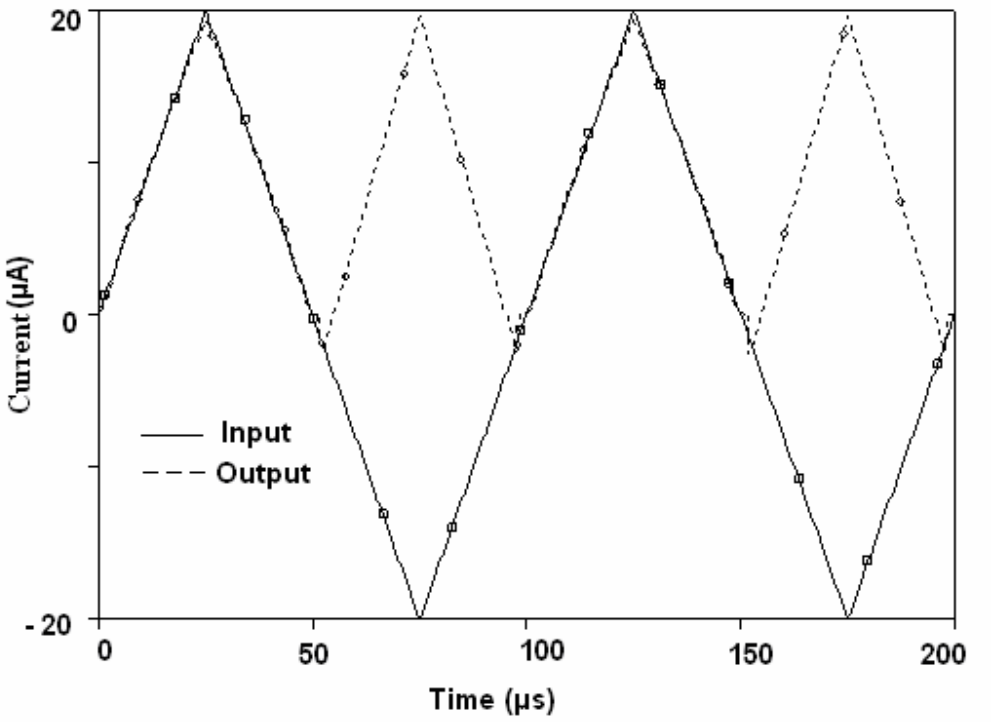

Fig. 7 Input and output waveforms for triangular excitation

V. Conclusion

A single MZC-CDTA based current mode full wave rectifier is presented in this paper. It uses two switches. As the circuit uses only MOS transistors, it is suitable for IC implementation. SPICE simulation results using 0.35 µm TSMC CMOS technology parameters are given in support of theory.

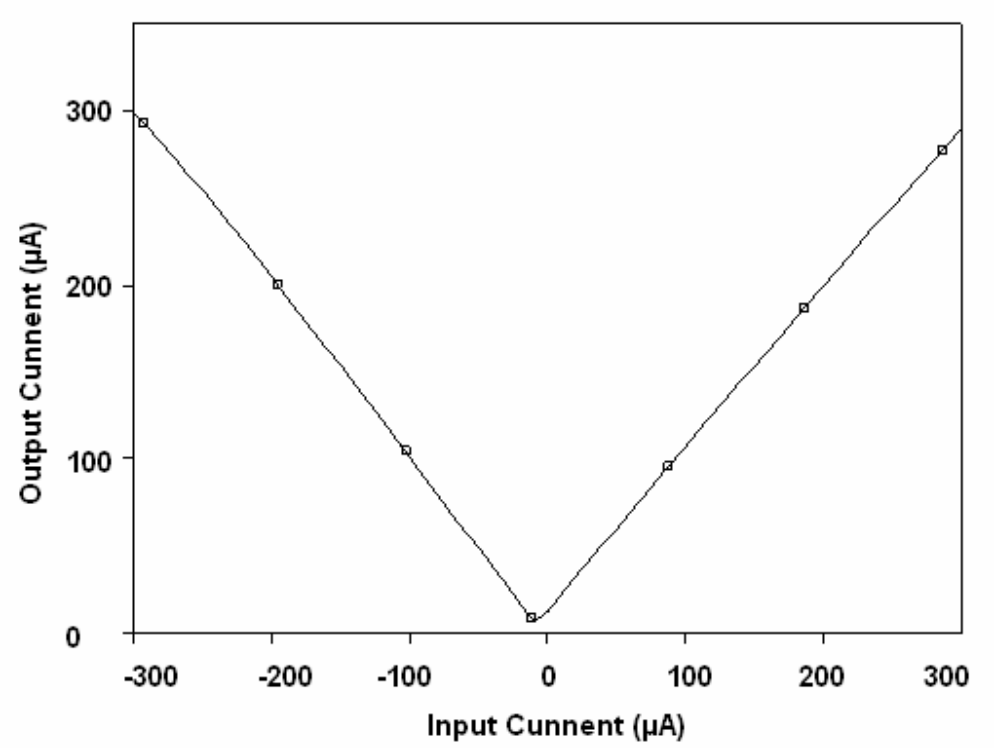

Fig.8 DC response of the proposed circuit

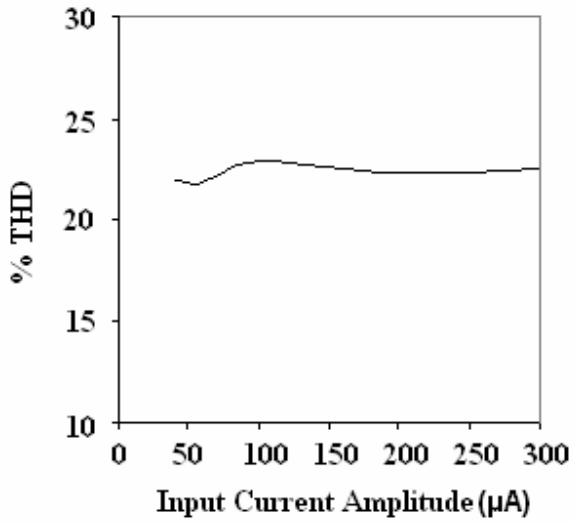

Fig. 9 Percentage THD versus input bias current

References

1. S.J.G. Gift, A high performance full-wave rectifier circuit, International Journal of Electronics, 87, pp. 925–930, 2000.

2. S.J.G. Gift,, B. Maundy, Versatile precision full-wave rectifiers for instrumentation and measurement, IEEE Transaction on Instrumentation and Measurement, 56, pp. 1703–1710, 2007.

3. S. R. Djukic, Full-wave current conveyor precision rectifier, Serbian Journal of Electrical Engineering, 5, pp. 263–271, 2008.

4. K. Hayatley, S. Porta, F. Lidgey, Temperature independent circuit conveyor precision rectifier, Electronics Letters, 30, pp. 2091-2093, 1994.

5. C. Toumazou, F. J. Lidgey, and D. G. Haigh, Analogue IC Design: the Current Mode Approach, Chapter 1, Peregrinus, Stevenage, UK, 1990.

6. D.Biolek, R. Senani, V. Biolkova, Z. Kolka, Active Elements for Analog Signal Processing: Classification, Review, and New Proposals, Radioengineering, Vol. 17, pp. 15 – 32, 2008

7. D. Biolek, CDTA-building block for current-mode analog signal processing, In: Proceedings of the ECCTD'03, vol. III, Krakow, Poland, 2003. p. 397–400.

8. A.U. Keskin,, D. Biolek, Current mode quadrature oscillator using current differencing transconductance amplifiers (CDTA), IEE Proceedings - Circuits Devices Systems, 153, 3, pp. 214-218, 2006.

9. W. Tangsrirat, W. Tanjaroen, T. Pukkalanun, Current-mode multiphase sinusoidal oscillator using CDTA-based all pass sections, International Journal of Electronics and Communication (AEU), 63, pp. 616 – 622, 2009.

10. A. Lahiri, A. Chowdhury, Novel First-Order Current-Mode All-Pass Filter Using CDTA, Radioengineering, 18, pp. 300 – 306, 2009.

11. W. Tangsrirat, T. Pukkalanun, W. Surakampontorn, Resistorless realization of current-mode first-order all pass filter using current differencing transconductance amplifiers, Microelectronics Journal, 41, pp. 178–183, 2010.

12. A. Lahiri, Novel voltage/current-mode quadrature oscillator using current differencing transconductance amplifier, Analog Integrated Circuit and Signal Processing, 61, pp. 199–203, 2009.

13. D. Prasad, , D.R. Bhaskar, A.K. Singh, Universal current-mode biquad filter using dual output current differencing transconductance amplifier, International Journal of Electronics Communication.(AEÜ), 63, pp. 497 – 501, 2009.

14. D. Biolek, E. Hancioglu, A. Ü. Keskin, High-performance current differencing transconductance amplifier and its application in precision current-mode rectification, International Journal of Electronics Communication (AEÜ), 62, pp. 92 – 96, 2008.

15. J. Koton, N. Herencsar, K. Vrba , S. Minaei, Precision Full-Wave Current-Mode Rectifier using Current Differencing Transconductance Amplifier, Proc. of IEEE International conference on communication software and network, pp. 460-463, 2011.

16. F. Khateb , J. Vávra, D. Biolek, A Novel Current-Mode Full-Wave Rectifier Based on One CDTA and Two Diodes, Radioengineering, 19, pp. 437-445, 2010.

17. W. Tangsrirat, T. Pukkalanun, W. Surakampontorn, Synthesis of current differencing transconductance amplifier-based current limiters and its applications, Journal of Circuits, Systems and Computers, vol.20, no.2, pp.185-206, 2011.

2013 International Conference on Power, Energy and Control (ICPEC)

Disturbance Immune DFIG based Wind Energy Conversion System

Vishal Verma, Swati Tanton
Delhi Technological University, Delhi, India

***Abstract*—Power generation capacity in general is now-a-days augmented in terms of wind energy farms. The stable operation of the Wind Energy Conversion System (WECS) amidst variety of disturbance on the microgrid is seen as a challenging task. Unbalanced magnetization of the Doubly Fed Induction Generator (DFIG) largely affect the generation profile and could cause cascading effect eventually led to shut down of the farm. Moreover, Induction Generators (IG) in order to generate real power consumes reactive power from the mains making the operation with relatively lower power factor (pf). In order to provide requisite immunity to the DFIG based WECS, each system should be controlled in way that only balanced currents are transacted by the WECS at unity pf. Synchronous reference frame (SRF) method both in positive and negative sequence is used for current estimation of the reference currents to be supplied by the stator side Voltage Source Converter (VSC). MATLAB based simulation results shows the efficient working of WECS amidst distorted conditions at Point of Common Coupling (PCC).**

***Index Terms*—Induction Generator, Back-to-Back Converters, Wind Energy Conversion, DFIG, Voltage Source Converter.**

I. INTRODUCTION

Wind energy being non polluting and freely available energy source has witnessed tremendous growth in past two decades. Wind turbines now are not only required to remain connected by riding through over grid faults, but they are also required to inject reactive current to assist the grid in recovering to rated voltage levels. In order to extract maximum power from available wind energy, DFIG supported wind turbine systems (WTS) are largely recommended [2].

Turbines using DFIG are dominant due to their eligibility for variable speed operation, durability, simple structure, and ability to adjust reactive power. It has the capability to provide independent active and reactive power control in a cost-effective way amidst varying input power. Such asynchronous generators utilizes voltage source converter (VSC) on the rotor to adjust the rotor currents to regulate the active power drawl from the stator side, whereas, the other VSC connected on stator terminals handles the reactive power and other power quality problems experienced by DFIG[6][3]. The DFIG can advantageously operate in a higher wind speed range and produce or consume reactive power through a low rated stator-side VSC. DFIG wind turbines (WTs) also offer other advantages, such as low converter and inverter cost, reduced cost of the inverter, filters and improved WTs efficiency.

Most system design codes and standards have so far not strategized wind farms support to the power system from disturbance arising during unbalanced conditions in the feeder or sudden drop in frequency [10]. In majority cases prevailing norms the WTs are required to be taken off from the power system for their own protection. But with the increased penetration of wind energy, wind farms are now required to continue their operation during system disturbances. For unbalanced conditions on the feeder it is required to and compensates for the negative sequence currents to keep the magnetic circuit balanced and steady. Under the influence of unbalanced voltages/currents at stator terminal, the most DFIG may witness large power due to large voltage ripple in the dc link of back-to-back VSC, which may decrease the lifetime of the dc capacitor also. Further any unbalance in the stator circuit distorts the magnetization of the DFIG and affect operation of generation with distorted generated voltages [12]. So it is vital to ensure balanced transaction of currents, by proper control over currents at PCC by stator side converter. Moreover the VSC is required to manage its own reactive power demand.

This paper aims at providing solutions to major problems associated with DFIG supported wind farm under unbalance condition on the feeder. A control strategy is proposed to prevent the system from cascade tripping due to unbalance in a single generating unit or occurrence of fault. The control scheme is based on the computation of reactive component of positive sequence fundamental component and negative sequence component in the current for realizing direct control of stator side converter (SSC) and controlling the rotor side converter (RSC) under current control for fast stabilizing the power fluctuations arising from fluctuation in wind power input[7],[13]. The proposed scheme is simulated under MATLAB/PSB block set and the effectiveness of scheme is demonstrated by simulation results under varying and unbalanced power demanding by the load.

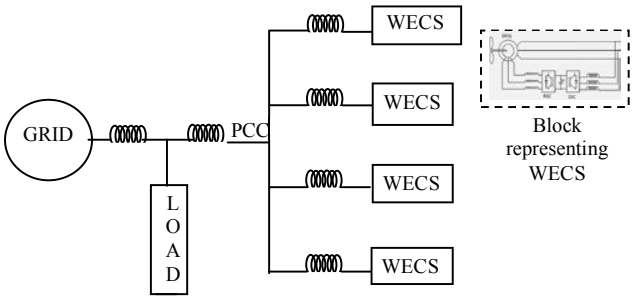

Fig. 1 Block diagram for DFIG supported Wind farm

978-1-4673-6030-2/13/$31.00 ©2013 IEEE

The paper is organized as follows: Section II introduces the system configuration; Section III elaborates the control topology for negative sequence and reactive power compensation; Section IV describes the result through verification by MATLAB simulation, followed by the conclusion in the last section.

II. System Configuration

The system configuration of proposed grid connected DFIG wind energy system is shown in Fig.1. The system includes number of wind turbines (WECS) connected in parallel forming a micro grid which in turn supply a common load from the feeder. WRIG controlled by low rating back-to-back converters, one of which is connected to the rotor of the

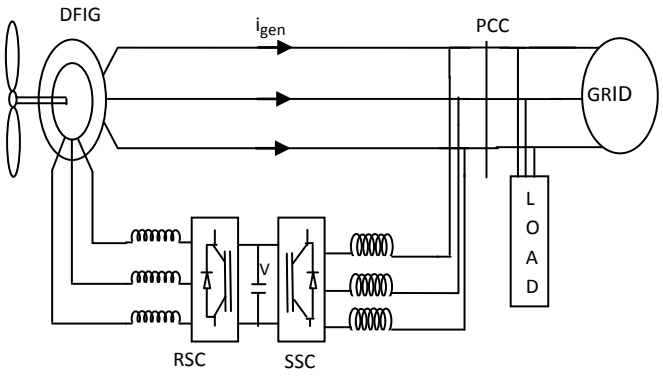

Fig. 2. Block diagram for proposed DFIG system

DFIG while other converter is coupled to the stator terminal. VSC supported DFIG system is connected in a manner such that the SSC (stator side converter) is connected in shunt with the line through coupling transformers to compensate for reactive power demand of generator [4]. A transformer of suitable rating must be used in accordance with the bus voltages. The compensation through DFIG allows use of converters, with lower power rating as they deals only with fraction of total power delivered to the system As the stator is connected directly to the PCC, any unbalance in feeder current will cause voltage distortion at PCC, which in turn will distort stator flux affecting the generation if not compensated by SSC. Each WECS is independently controlled to transact only balanced upf current with the PCC [6],[11].

III. Modelling of WECS

The modelling of the wind turbine is presented in two parts; DFIG and the wind turbine (WT).

A. DFIG System

A DFIG wind turbine primarily consists of two major parts: a wind turbine, an induction generator, and two power electronic VSC [6]. The induction generator is a standard, wound rotor induction machine with its stator windings directly connected to the load and its rotor windings connected to the load through a back-to-back VSC, namely the RSC and the SSC. The RSC controller regulates the DFIG to curb the wind power fluctuation due to varying wind speed and the SSC controller injects/absorb desired reactive current maintains the DC bus and compensate the unbalanced currents being transacted by DFIG due to corruption of voltage at PCC.

Following equations represents the dynamic modelling of DFIG system in synchronous reference frame [16].

Stator & Rotor voltage equations-

$$V_{sd} = R_s i_{sd} + p\psi_{sd} - \omega_s \psi_{sq} \quad \ldots.(1)$$
$$V_{sq} = R_s i_{sq} + p\psi_{sq} + \omega_s \psi_{sd} \quad \ldots.(2)$$
$$V_{rd} = R_r i_{rd} + p\psi_{rd} - \omega_s \psi_{rq} \quad \ldots.(3)$$
$$V_{rq} = R_r i_{rq} + p\psi_{rq} + \psi_{rd} \quad \ldots.(4)$$

Stator & Rotor flux equations-

$$\psi_{sd} = L_s i_{sd} + L_m i_{rd} \quad \ldots.(5)$$
$$\psi_{sq} = L_s i_{sq} + L_m i_{rq} \quad \ldots.(6)$$
$$\psi_{rd} = L_m i_{sd} + L_r i_{rd} \quad \ldots.(7)$$
$$\psi_{rq} = L_m i_{sq} + L_r i_{rq} \quad \ldots.(8)$$

B. Wind Tubine Modelling

The energy produced by different types of wind turbine in different conditions depends on its rated wind speed. The wind turbine is coupled to the rotor of the DFIG. The mechanical power extracted from the wind marks the rotor speed. The characteristic curve of the turbine determines the speed at which the power extracted from the wind is maximum [13]. This is the minimum wind speed at which a wind turbine produces its rated power.

$$P_m = \frac{1}{2}\rho C_p A V^3$$

Where ρ is the air density, Cp is the power coefficient, A is the area swept by the rotor and V is the wind velocity. For radius R, mechanical power output will be-

$$P_m = \frac{1}{2}\rho C_p \pi R^2 V^3$$

The maximum mechanical power for rotor speed ω will be-

$$P_{max} = \frac{1}{2} C_p \pi \left(\frac{R^5}{\lambda^3}\right) \omega^3$$

where λ= tip speed ratio and C_p= optimal value at given λ.

IV. Control Scheme

The situation becomes more demanding when a WECS is required to produce constant voltage and constant frequency power in a weak grid or with unbalanced operations on the feeder at PCC. The control in grid connected mode is relatively much simpler in comparison with offgrid mode. LC filters are connected to both the stator and rotor side converter to absorb the generated switching harmonics [9],[7].

The main aim of the proposed control scheme is to provide compensation for negative sequence and variable reactive power demand during unbalanced conditions on the feeder as well as during normal operating conditions. A direct current control scheme employed to SSC for compensation of requisite problems [5],[12]. The control technique for SSC and RSC are described in Fig.3 for grid connected operations. It involves synchronous reference frame approach for estimation of various parameters. The proposed scheme operates such that RSC maintains requisite frequency at the stator terminals by levelling the power at rotor while SSC injects the desired current on the stator side to have purely balanced and

undistorted currents transacted by the stator of the DFIG from the feeder, which ascertains the unity power factor operation at the connection point of DFIG with the PCC [11].

A. A. Stator Side Converter control (SSC)

This scheme is designed to to compensate for negative sequence component of current due to unbalance in current/voltage at PCC on feeder and provides either voltage regulation at PCC by requisite reactive power insertion at PCC or to have upf operation. It involves computation of reference converter currents to be injected into the system at fundamental frequency using Synchronous Reference Frame (SRF) theory. In the Fig 3 q-axis component of CT2 provide the estimate of desired reactive power compensation to be

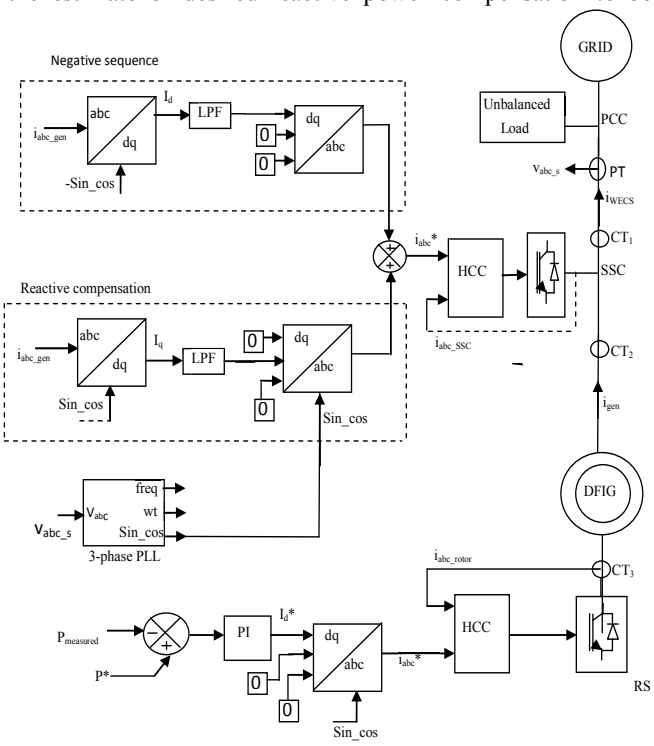

Fig. 3 Block diagram of proposed control strategy for a grid connected DFIG based WECS

provided to have upf operation of WECS at PCC. Whereas, the reference negative sequence component of current can be extracted by rotating synchronous reference frame in opposite direction upon the current sensed by CT2. The compensation of such negative sequence currents prohibit any ill effect of unbalance at PCC entering into the generator terminal. The current control is achieved through hysteresis controller which in turn generates pulses to shape the current close to reference value. The injected current through coupling transformer provides adequate reactive power and negative sequence compensation.

B. Rotor Side converter Control (RSC)

RSC is employed to provide power leveling at rotor side to invoke grid frequency at stator terminals even under fluctuating wind condition avoiding stress on the magnetic circuits [5]. This can be achieved by injecting/absorbing real power into/out from the rotor circuit through RSC. The control philosophy of proposed scheme also utilizes SRF theory for extraction of real power component of current from rotor side at slip frequency [7],[12]. Here the rated power is compared with the measured instantaneous power at stator terminals. The generated error is then fed to PI Controller which estimates the reference rotor current as d-axis component responsible for power leveling at stator terminals.

The reference current generated and the sensed value of instantaneous current are fed to hysteresis controller (HCC) to reduce the requisite current control.

V. MATLAB SIMULATION

The grid source, three phase load, LC filter, DFIG Model and control unit are modelled in MATLAB using Power System Block set. Fig 3 depicts the MATLAB model of the DFIG based WECS for evaluating the performance of proposed scheme under different operational conditions on the feeder: Balanced and unbalanced condition of voltage and currents.

The AC grid is presented as three-phase voltage source with line impedance of 1Ω and 5mH per phase and connected to the DFIG system and balanced/unbalanced static R-L load. The loads considered are star connected 15.8kW and 31.7kW resistive load. A PLL block is used to generate sine and cosine synchronizing signals. Assuming constant balanced source, DFIG operates under variable load condition by a variable resistor whereas; the unbalance is introduced by single phasing the resistive load at 0.3sec. The rated capacity of DFIG under consideration is 37kW at 400V/50Hz with the variable wind speed of 10m/sec with ±10% variations. DFIG based WECS incorporates SSC and RSC of 7kW rating, the switching signals with frequency of 10kHz are generated by hysteresis current controller (HCC) and depending on the switching frequency of VSC, LC filter is modelled with 4.2mH inductor and 1μF capacitor to filter the switching harmonics. The PI controller in the proposed scheme is tuned by Ziggler Nicholas method and as the system is highly non-linear, fine tuning is done by hit and trial method. Also, three CTs are designed to estimate instantaneous values of currents at rotor and stator ends and a PT is designed to estimate voltage at PCC. Table I depicts parameters of the considered system.

TABLE I PARAMETERS OF DFIG CONSIDERED

Rated Power	37kw/50HP
Stator Voltage/frequency	400V/50Hz
No. Of poles	4 pole
Rated speed	1480 rpm
Stator and Rotor resistance (pu)	0.1904 & 0.01163 pu
Stator and rotor reactance (pu)	0.0526 pu
Inertia Constant (J)	0.1234 pu
K_P and K_I	0.00985 & 0.0759

VI. PERFORMANCE EVALUATION

The performance of 37kW grid connected DFIG system is studied under normal operation and unbalanced operation at PCC due to unbalanced loading condition for balanced current

transaction of DFIG with feeder at PCC and upf operation of WECS under fluctuating wind conditions.

The performance of the proposed scheme is evaluated under two sets of loading conditions: Balanced loading condition to evaluate upf operation of WECS under varying load levels and with unbalanced loading to create voltage unbalance at PCC to verify balanced current transaction by DFIG with PCC.

A. Under balanced load

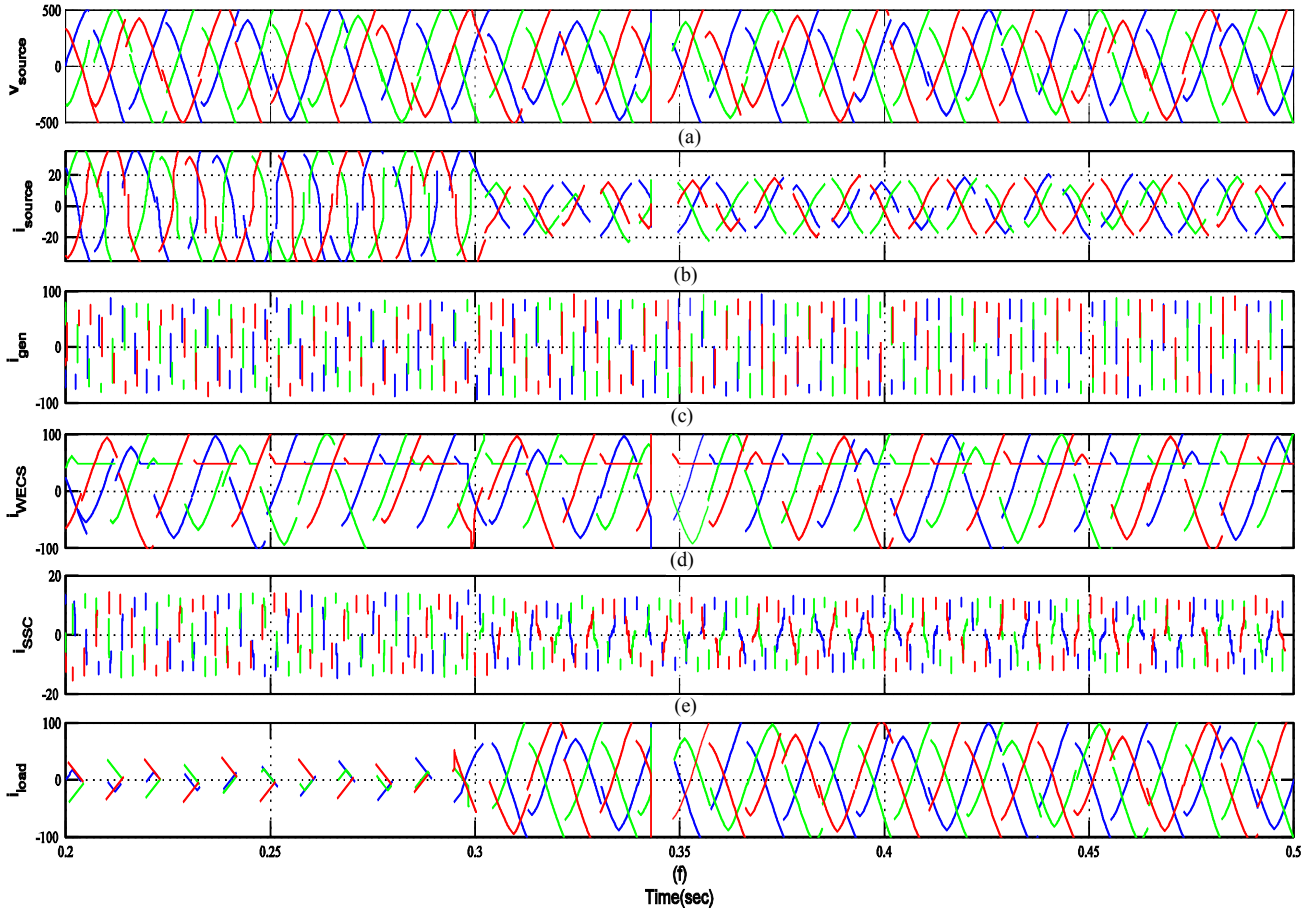

Fig. 4. Dynamic response of WECS transacting power at unity pf for balanced conditions on the feeder with varying loading condition when load is changed from 15.87kw to 31.74kw

Initially system is tested under balanced load for validating DFIG system supplying constant active power of 37kW, where19KVAr demand of DFIG is met by SSC such that WECS supply balance power to the grid. Fig.4 shows simulation results of DFIG system under step load change with transient response of three-phase voltages (v_{source}), generator current (i_{gen}), load currents and converter currents. To test the effectiveness and capability of WECS, load is considered lesser than the generation capacity (31.75kW), so that part of power is pushed into the grid. The result in Fig 4 clearly demonstrates that scheme is able to keep upf operation of DFIG based WECS even with varying loading conditions under balanced operating conditions. Since the direction of voltage/current measurement is taken positive from grid source to load/WECS (Refer fig.2), the i_{WECS} which depicts the actual current emanating from the generator is shown negative (Refer Fig 4(d)). Similar conditions exist for i_{source} (Fig 4(b)) which is also negative since the power is being pushed into the mains. It may also be observed from Fig 4(c) that i_{gen} is slightly leading representing consumption of equivalent reactive VAr by DFIG in order to keep the i_{WECS} in phase with the phase voltages at PCC. Whereas, in Fig 4(e) it is clear that current supplied by the SSC is in quadrature with the phase voltages at PCC representing supply of requisite reactive VAr into the system. As the load is changed from 15.87kw to 31.74kw at 0.3 s*ec depicted in Fig 4(f), almost* instantaneously current going to grid (i_{source}) is reduced from 24.75A to 14.14 A, and the transients is subsided within 1/10th of a cycle, and upf operation is sustained.

To ensure the stabilized performance of DFIG based WECS under fluctuating wind conditions. The considered system is tested under varying wind condition. Fig 5 shows simulation result of the rotor circuit of DFIG system under variable wind condition. The transient response to per unit power from wind (P_{wind}), rotor speed (wr), power transacted by RSC (PRSC), total power generated (P_{gen}) and RSC current is observed to evaluate the performance of RSC for levelling of power generated by WECS. The simulated result

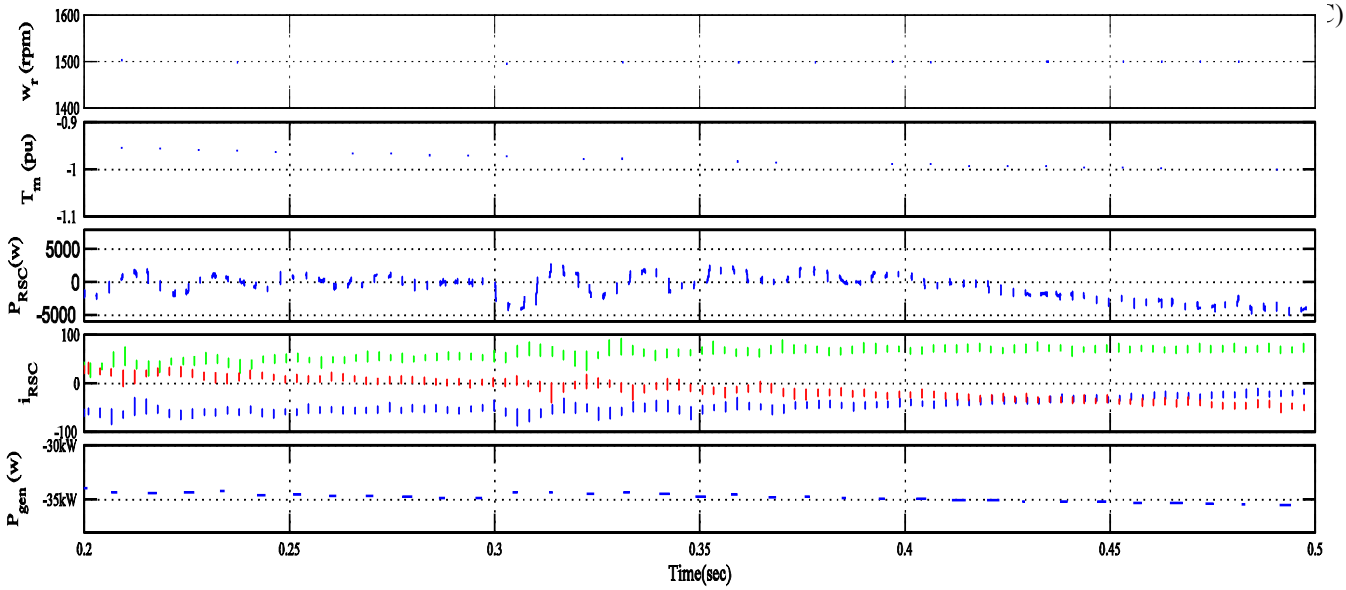

Fig.5 Dynamic response of WECS on rotor side under varying wind conditions

demonstrates that control scheme is capable of balancing the power under fluctuating wind speed input. In Fig 5(a), it is clear that rotor is maintaining a constant speed of 1500rpm (Refer Fig 5(b)) even with variable shaft power shown in fig 5(b). Fig 5(c) depicts the variable power which is being transacted by RSC in order to maintain constant power output of 37kw at generator terminal (Refer fig 5(e)).

B. Under Unbalanced load

Initially DFIG system is operating under balanced loading

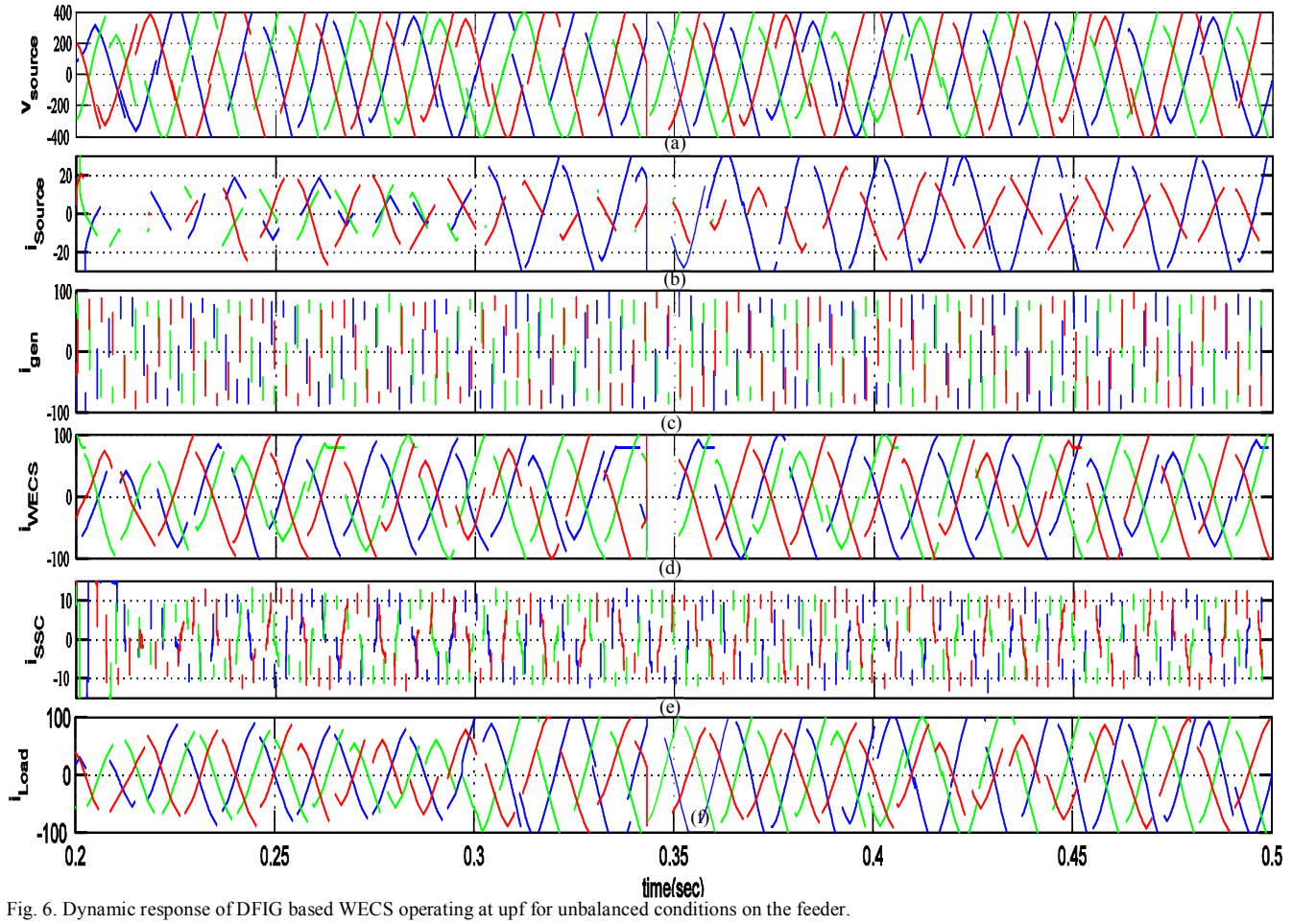

Fig. 6. Dynamic response of DFIG based WECS operating at upf for unbalanced conditions on the feeder.

condition supplying a constant load of 15.87kw. To evaluate the performance of DFIG based WECS, the underlying system is subjected to highest degree of unbalance by opening one phase going to the load, at t=0.3sec, which causes immediate distortion in voltages at PCC (Refer Fig 6(a)) and these unbalanced voltages tries to induce negative sequence current in the WECS and source connected (refer Fig 6(b)). The simulation result shown in Fig 6 demonstrates the effectiveness of control scheme to keep the balanced operation of DFIG system under the influence of unbalanced load. The unbalance if allowed to pass through the DFIG would have distorted the magnetising flux and in turn have produced more serious distortion at PCC and damage to the machine. The transient response of three-phase voltages (v_{source}), generator current (i_{gen}), loads current (i_{load}) and converter currents is presented in Fig 6 to evaluate the performance of the proposed scheme with DFIG based WECS. The result in Fig 6 demonstrates that proposed scheme is capable of providing immunity to the DFIG by sustaining balanced unity pf operation of WECS system even under unbalanced loading condition. It may be clearly seen from Fig 6(c) that i_{gen} is purely sinusoidal and generator is drawing requisite reactive VAr required by the DFIG, thus maintaining i_{WECS} at upf which is in phase with the phase voltages at PCC (Fig 6(d)). It is observed from the Fig 6(e) that the current supplied by SSC is having negative sequence component and it is in quadrature with the phase voltages allowing reactive and negative sequence compensation at generator terminal. The unbalanced load when introduced at t = 0.3sec, the load demand changes from 15.87kw to 31.74kw (Fig 6(f)).

VII. CONCLUSION

A direct current control of back-to-back connected VSCs has been investigated for leveling of real power in rotor circuit and compensation of reactive power and unbalanced in current in stator circuit of DFIG based WECS. The observed performance of back-to-back VSCs has demonstrated the capability of proposed control scheme to transact balanced current even amidst unbalanced condition at PCC, upf operation and supply of rated power by WECS from disturbances in power system and varying wind condition. It has also been observed that the proposed scheme has a fast response. The simulated result has been successfully validated the effectiveness of the proposed scheme for ensuring the sustenance of WECS against odd conditions on PCC and protect it from cascade tripping. The scheme is simple and easily implementable.

References

[1] V. V. Phan, S. kwak, H. H. Lee, "An improved control method for DFIG-based wind system supplying unbalanced stand-alone loads", in Proc. of IEEE, ISIE, pp. 1081- 1086, 2009.

[2] M. Chomat, L. Schreier, J. Bendl, "Control method for doubly fed machine supplying unbalanced load," in Proc. IEEE EPE , France,2003.

[3] S. Muller, M. Deicke, R. W. De Doncker, "Doubly fed induction generator systems for wind turbines," IEEE Ind. Appl. Mag., vol. 8, no. 3, pp. 26–33, May/Jun.

[4] M. Kayikci, J.V. Milanovic, " Assessing Transient Response of DFIG-Based Wind Plants—The Influence of Model Simplifications and Parameters", IEEE Trans, vol. 23,pp. 545-554.

[5] X. Lie, "Coordinated Control of DFIG's Rotor and Grid Side Converters During Network Unbalance", IEEE Trans. Power Electronics, vol. 23, pp. 1041-1049, May 2008.

[6] R. Teodorescu, F. Blaabjerg, "Flexible control of small wind turbines with grid failure detection operating in stand-alone and grid-connected mode," IEEE Trans. Power Electron., vol. 19, no. 5, pp. 1323–1332, Sep.2004.

[7] M.I Martinez, G. Tapia, A. Susperregui, "DFIG Power Generation Capability and Feasibility Regions Under Unbalanced Grid Voltage Conditions", IEEE Trans. Energy Conversion, vol. 26, pp. 1051-1062, Dec 2011.

[8] G. Iwanski, W. Koczara, "DFIG-Based Power Generation System with UPS Function for Variable-Speed Applications", IEEE Trans. Industrial Electronics, vol. 55, pp. 3047-3054, Aug. 2008.

[9] H. H Lee, "Improved predictive current control for unbalanced stand-alone doubly-fed induction generator-based wind power systems", in Proc. of IET, vol. 5, pp. 275-287, March 2011

[10] T. Brekken, N. Mohan, T. Undeland, "Control of a doubly fed induction wind generator under unbalanced grid voltage conditions", IEEE Trans. Energy Conversion, vol. 22, pp. 129–135,2007.

[11] L. Xu, D. Zhi, B. Williams, "Predictive current control of doubly fed induction generators," IEEE Trans. Ind. Electron., vol. 56, no. 10, pp. 4143–4153, Oct. 2009.

[12] V.T Phan, H.H Lee, "Performance Enhancement of Stand-Alone DFIG Systems with Control of Rotor and Load Side Converters Using Resonant Controllers", IEEE Trans. Industry Applications, vol.48, pp. 199-210, Jan.-Feb. 2012.

[13] V. Verma, B. Singh, P. Pant, "Decoupled indirect current control of DFIG for wind energy applications", in Proc. of IEEE IICPE, pp. 1-6, Jan. 2011.

[14] A. Petersson, L. Harnefors, T. Thiringer, "Evaluation of current control methods for wind turbines using doubly-fed induction machines," IEEE Trans. on Power Electronics, vol. 20, pp. 227-35, Jan. 2005.

[15] E. Tremblay, A Chandra, P. J. Lagace, " Study of Grid-side Converter control for Grid-connected DFIG Wind turbines under unbalanced load condition", in Proc. of IEEE, ISIE ,vol.2, pp. 1619-1624 , July 2006.

[16] L. Xu and Y. Wang, "Dynamic modelling and control of DFIG based wind turbines under unbalanced network conditions", IEEE Trans. Power System, vol. 22, no. 1, pp. 314–323, Feb. 2007.

[17] Y. He, J. Hu, "Reinforced control and operation of DFIG based wind power generation system under Unbalanced Grid voltage conditions", IEEE Trans. on Energy Conversion, vol. 24, no. 4, pp. 905-915, Dec. 2009.

Research Paper Engineering

Economic Analysis of Biodiesel Produced from Waste Cooking Oil

* Shashank Mohan ** Amit Pal

* PG Scholar, Mechanical Department, Delhi Technological University, Bawana Road, Delhi-110042, India

** Asst. Prof. Mechanical Department, Delhi Technological University, Bawana Road, Delhi-110042, India

ABSTRACT

Present work is focused on comparing the economic feasibility of biodiesel with conventional petroleum diesel. It includes estimates of various resources used in the production of biodiesel from waste cooking oil starting from waste cooking oil to various reactants, energy and labor cost. Estimates are prepared using some existing data and other suitable assumptions. It is found that the biodiesel conversion cost comes about 11 rupees per kg. With waste cooking oil net biodiesel cost comes at 35 rupees per kg. Hence waste cooking oil proves to be a greener as well as economically viable feedstock for biodiesel production.

Keywords : Economic feasibility, Biodiesel production, waste cooking oil.

INTRODUCTION

The world is presently confronted with the twin crises of fossil fuel depletion and environment degradation. Indiscrimination extraction and lavish consumption of fossil fuels have led to reduction in underground based carbon resources. According to an estimate, the reserves will last 218 yrs for coal, 41 yrs for oil and 63 yrs for natural gas. Depleting reserves of crude petroleum, uncertainty in availability, environmental degradation and rapid hike in petroleum prices have led to search of alternate fuels (Lin et al., 2011). Many researchers around the world have explored several alternative energy resources, like biogas, biomass, alcohol, hydrogen, vegetable oil, which have the potential to quench the ever-increasing energy thirst of today's population (Denis et al., 2009).

Biodiesel, a clean renewable fuel, has recently been considered as the best substitute for a diesel fuel because it can be used in any compression ignition (CI) engine without the need for modification. The feed stocks used for biodiesel production currently are mainly high quality food grade vegetable oils, such as soya bean oil in U.S.A, rapeseed oil in Europe, palm oil in Malaysia (Azam et al., 2005). Lower cost feed stocks, such as waste cooking oil, grease, soap stocks are preferred because of their economic viability, since feedstock costs are about more than 85% of the total cost of biodiesel production (Hass et al., 2006; Zhang et al., 2003).Some of the properties, such as the high cetane value or good lubricity and lower sulphur content, are obvious advantages of bio-diesel while others, including the lower heating value, high freezing point (and inferior flow properties at low temperature), or corrosion properties are its drawbacks.

MATERIAL

Many vegetable oils like Soybean, Groundnut, Rapeseed, Palm, Olive etc. are wildly used for frying a number of food items. But after heating above a critical temperature for deep frying, they become unfit for further cooking, as their further use may lead to cholesterol formation in human beings. Presently, the WCOs are still lower cost feedstock making biodiesel production more competitive to the production of petroleum based diesel fuel. Waste cooking oil can be used as a biodiesel feedstock, as it is available in vast quantities and in its present form if it is used in engines, it will be big threat to the environment (Buasri et al., 2008; Cigizoglu et al., 1997; Kerschbaum and rinke, 2004). Some researchers (Pugazhvadivu and Jeyachandran, 2005) suggested to pre-heating the WCO before using it in diesel engines which reduces the viscosity of the WCO and lowers the exhaust emissions as compared to the diesel.

WCO BIODIESEL PREPARATION

In this work the WCO was first properly filtered to separate any kind of suspended impurities present. Then WCO is heated up to 120^{0}C for about 10 minutes in order to remove water content in the oil to avoid soap formation. This oil is then allowed to cool up to 65^{0}C temperature before mixing with KOH and methanol to prevent methanol evaporation. Simultaneously methyl alcohol (CH_3OH) is taken in molar ratio of 1:6 and Catalyst (KOH) is taken as 1% by weight of oil. The mixture of methyl alcohol and KOH is stirred until whole KOH dissolves in methyl alcohol. This mixture is poured in WCO. Since methanol is immiscible with the oil, the mixture is stirred continuously for about 30 minutes. During the reaction the temperature of mixture is kept about 55-60^{0}C. The mixture is left for 2-3 hours for gravity separation of methyl esters and glycerol. The heavier glycerin settled at the bottom was removed and then remaining sample was washed in warm water (about 80^{0}C) by stirring with about 30% warm water for one minute and then again this water is allowed to settle in a separating chamber for 2-3 hours to remove the catalyst and other impurities which are dissolved in water. Finally, the remaining sample is heated up to 110^{0}C ~120^{0}C for 8-10 minutes for removing any water content.

ECONOMICS OF BIO-DIESEL

The term ''Life Cycle Assessment'' is used to assess the total environmental performance of a product all along its lifetime, often referred as from 'cradle to grave'. Other terms, such as life cycle analysis and eco-balance, are also used. When talking about fuels, the proper term in use is ''Well-to-Wheel (WTW) Analysis''. Similarly in case of minerals, ''Mine-to-Mill Analysis'' is carried out. In order to be able to examine the

complete cycle of a transport fuel, the analysis is often divided into following five stages:

- Feedstock production.
- Feedstock transportation.
- Fuel production.
- Fuel distribution.
- Vehicle use.

These stages can be divided even further into a Well-to-Tank (WTT) and Tank-to-Wheel (TTW) portions of the WTW analysis. The WTT analysis considers the fuel from resource recovery to the delivery to the vehicle tank, i.e., the feedstock production, transportation, fuel production and fuel distribution. The TTW analysis considers the fuel economy, i.e., the vehicular use of the fuel. This way, the WTW analysis integrates WTT and TTW into a complete fuel history.

COST ESTIMATION OF BIODIESEL PRODUCTION
COST OF RAW MATERIALS
Cost of Waste Cooking Oil
Assuming the market Price of WCO = Approx. 20 / Kg

Requirement of WCO per day = 800 Kg

Requirement of WCO for a month = 800 * 25 = 20000 Kg

Cost of WCO for a month = Rs. 20 * 25 * 800 = 400,000 Rs

Cost of Methanol
Price of 1Kg of Methanol is Rs. 40

Daily requirement of Methanol = 176 Kg

Cost of Methanol for a month = 176 * 25 * 40 = 176,000 Rs

Cost of KOH
Price of 1Kg of KOH = Rs. 300 / Kg

Daily requirement of KOH = 8 Kg

Cost of KOH for a month = 8 * 25 * 300 = 60,000 Rs

Cost of Water
Monthly requirement of water for water washing = 0.3 * 20000 = 6000 Kg

Cost of water for a month = 6000 * 0.25 = 1500 Rs

Total raw material cost for a month = 637,500 Rs

ELECTRICITY COST
Assumptions:
- 1KWh of electricity = Rs. 7/-(for industrial uses)
- Specific heat of WCO is 1.97 KJ/Kg K
- Specific heat of water is 4.2 KJ/Kg K
- Heat loss due to radiation, convection = 10%
- Power of heater is 40 KW.
- 25 Working day in a month.

1) Electricity cost for heating oil from 20 ^{o}C to about 120 ^{o}C.

$Q = m*C_p*\Delta T$ / efficiency

= 100 kg * 1.97 * (120-20) / 0.9

= 21888.89 KJ

Heating duration = 21888.89 / 40 = 547.22 sec or 10 min (approx.) is required to reach 120 ^{o}C.

Electricity cost = 1/6 h* 40 KW * 7

= 46.67 Rs / batch of 100 Kg oil

= 46.67 * 8 * 25 per month

= 9334 Rs / month

2) Electricity cost for stirring alcohol and catalyst Assumptions
- Power of motor is 7.2 KW
- We stir the solution for 10 minutes in 7 batches of 25 Kg each

Electricity cost per batch = 7.2 KW * 1/6 hr * 7 = 8.4 Rs
Electricity cost per month = 8.4 * 7 * 25 = 1470 Rs

3) Electricity cost for stirring alcohol and catalyst mixture with WCO for 30 minutes Assumption
- Power of motor is 10 KW
- We stir the solution for 30 minutes

Electricity cost per batch of (100+22+1=123) Kg of mixture

= 10 KW * ½ hr * 7 = 35Rs

Electricity cost per month = 35 * 8 * 25= 7000 Rs

4) Maintenance of temperature during mechanical stirring
Tank in which mechanical stirring is taking place is insulated but still radiation losses takes place and even convection losses cannot be neglected. Cost of maintaining temperature of about 60 ^{0}C is assumed to be 900 Rs per month.

5) Electricity cost for heating water 200C to 800C for water washing
Q (for 30 Kg batch) = $m*C_p*\Delta T$ / efficiency

= 30 * 4.2 * 60 / 0.9 = 8400 KJ

Power of heater is 10 KW

Heating duration = 8400 / 10 = 840 sec or 0.233 hr

Electricity Cost per batch = Rs. 0.233 * 10 * 7 = Rs. 16.33

Electricity Cost per month = 16.33 * 8 *25

= 3267 Rs

6) Electricity cost for final heating of sample to 1200C for removing water if present
Assume this cost to be 9000 Rs.

Total electricity cost involved is

= Rs. (9334 + 1470 + 7000 + 900 + 3267 + 9000) = Rs. 30,971

APPARATUS COST
Total cost of apparatus and equipments is about 200000 Rs
Assuming these equipments works for 10 yrs and taking 6% interest rate

Equipment cost for a month Rs. 2670 (approx.)
MISCELLANEOUS COST
Miscellaneous cost is as shown in Table 1.

Purpose	Cost per month (Rs.)
Transportation Cost	8,000
Labour Cost	20,000
Rent Cost	2,000
Maintenance Cost	1,000
Manufacturing Unit Establishment Cost	2,500

Table 1
Net Miscellaneous Cost = Rs. 33,500 for a month.

CONCLUSION
On the basis of present work it can be concluded that the bio-

diesel conversion cost comes about 11 rupees per kg, hence with waste cooking oil net biodiesel cost comes at 35 rupees per kg where as diesel cost without subsidies. Hence waste cooking oil biodiesel found to be a better alternative to petro diesel and in future help to acquire the energy security for coming generations and provide a safe passage for waste cooking oil disposal.

REFERENCES

Buasri, A., Chaiyut, N., Phongprasit, K. (2008). Production of Biodiesel from Waste Cooking Oil Using Mixed Alcohol System. KMITL Science Journal, 8(2), 59-63. Cigizoglu, K. B., Ozaktas, T., Karaosmanoglu, F., (1997). Used sunflower oil as an alternative fuel for diesel engines. Energy Sources, 19 (6), 559–. 566. Denis, Y.C., Wu, L.X., Leung, M.K.H., (2009). "A review on biodiesel production using catalyzed transesterification" Appl Energy, 87,1083-1095. Kerschbaum, S., Rinke, G., (2004). Measurement of the temperature dependent viscosity of biodiesel fuels. Fuel, 83, 287–291. Lin, L., Cunshan, Z., Vittayapadung, S., Xiangqian, S., Minutesgdong, D., (2011). Opportunities and challenges for biodiesel fuel, Appl Energy, 88,1020–1031. Haas, M.J., McAloon, A.J., Yee, W.C.,Foglia, T.A., (2006). A process model to estimate biodiesel production cost, Bioresource Technol., 97, 671-678. Azam, N.M., Waris, A., Nahar, N.M. (2005). Prospects and potential of fatty acid methyl esters of some non traditional seed oils for use as biodiesel in India, Biomass Bioenergy, 29, 293-302. Pugazhvadivu, M., Jeyachandran, K., (2005). Investigations on the performance and exhaust emissions of a diesel engine using preheated waste frying oil as fuel. Renewable Energy, 30(14), 2189-2202. Zhang, Y., Dubé, M.A., McLean, D.D., Kates, M. (2003). Biodiesel production from waste cooking oil: 2. Economic assessment and sensitivity analysis, Bioresource Technol., 90, 229-240.

Author's Accepted Manuscript

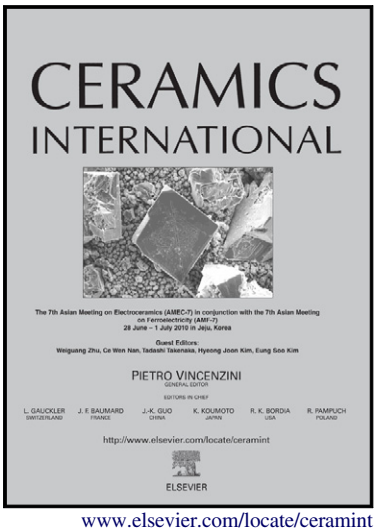

www.elsevier.com/locate/ceramint

Effect of holmium substitution on electrical properties of strontium bismuth tantalate ferroelectric ceramics

Sugandha Miglani, A.K. Jha

PII: S0272-8842(13)00571-3
DOI: http://dx.doi.org/10.1016/j.ceramint.2013.05.056
Reference: CERI6788

To appear in: *Ceramics International*

Received date: 28 February 2013
Revised date: 5 May 2013
Accepted date: 11 May 2013

Cite this article as: Sugandha Miglani, A.K. Jha, Effect of holmium substitution on electrical properties of strontium bismuth tantalate ferroelectric ceramics, *Ceramics International,* http://dx.doi.org/10.1016/j.ceramint.2013.05.056

This is a PDF file of an unedited manuscript that has been accepted for publication. As a service to our customers we are providing this early version of the manuscript. The manuscript will undergo copyediting, typesetting, and review of the resulting galley proof before it is published in its final citable form. Please note that during the production process errors may be discovered which could affect the content, and all legal disclaimers that apply to the journal pertain.

ACCEPTED MANUSCRIPT

Effect of holmium substitution on electrical properties of strontium bismuth tantalate ferroelectric ceramics

Sugandha[1] and A. K. Jha[1, 2]

[1]Thin Film and Material Science Laboratory, Department of Applied Physics,
Delhi Technological University (Formerly Delhi College of Engineering),
Delhi-110042, India.
[2]Department of Applied Sciences, A.I.A.C.T.R.
Geeta Colony, Delhi 110031, India.
[2]Corresponding author email: prof.akjha@gmail.com

Abstract:
The holmium substituted $SrBi_{2-x}Ho_xTa_2O_9$ (x= 0.00-2.0) compositions were synthesized by the solid state reaction method. The synthesized specimens were characterized for their structural and electrical properties. X-ray diffractograms reveal single phase layered perovskite structure formation for holmium content up to $x \leq 0.1$. The variation of dielectric constant with temperature shows that the Curie temperature (T_c) decreases on increasing the holmium content. The specimen with x=2.0 i.e. the bismuth free specimen, has very low dielectric constant and does not show any appreciable variation with temperature. The dielectric loss reduces significantly with holmium substitution. The ferroelectric property has been observed to improve with Ho substitution. The specimen with x=0.01 exhibits highest remnant polarization (P_r= 9.22 μC/cm^2) while the bismuth free specimen shows the lowest value of remnant polarization. It is expected that the above ferroelectric materials can be used to replace static (SRAM) and dynamic (DRAM) random access memories with ferroelectric random access memories (FeRAMS).

Keywords: A. Solid state reaction, B. Electron microscopy, C. Feroelectric properties, D. Perovskites.

Accepted manuscript

ACCEPTED MANUSCRIPT

Introduction

A large number of ferroelectric materials have been intensely investigated for applications in non-volatile ferroelectric random access memories (FeRAMs), piezoelectric transducers, actuators, pyroelectric sensors, high dielectric constant capacitors, etc. [1-5]. Among various ferroelectric materials, lead zirconate titanate (PZT) has been regarded as the best potential material for memory device applications because of its superior ferroelectric properties [6, 7]. However, PZT has limitations such as environmentally hazardous lead content, high leakage current and poor fatigue endurance [8]. The bismuth layered ferroelectric materials such as Strontium Bismuth Tantalate (SBT) has attracted a lot of attention of the researchers as an alternative ferroelectric material to PZT. In addition to being lead free, it has various other advantages such as low leakage current and high fatigue endurance up to 10^{12} switching cycles [9-12]. Therefore, it is important to find alternative lead free ferroelectric material exhibiting superior ferroelectricity comparable to PZT.

SBT is a member of bismuth layer structured ferroelectric material with a general formula of $(Bi_2O_2)^{2+}$ $(A_{n-1}B_nO_{3n+1})^{2-}$, where A = Ca^{2+}, Ba^{2+}, Sr^{2+}, Bi^{3+}, La^{3+}, Sm^{3+}, etc. and B = Fe^{3+}, Ti^{4+}, Nb^{5+}, Ta^{5+},W^{6+},Mo^{6+}, etc; and n indicates the number of corner sharing octahedra forming the perovskite like slabs [13, 14]. The crystal structure of $SrBi_2Ta_2O_9$ comprises of pseudo-perovskite blocks $(SrTa_2O_7)^{2-}$ that are sandwiched between $(Bi_2O_2)^{2+}$ layers. Sr atom occupies the A-site of the perovskite blocks and Ta atoms occupy the B-site. However, pure SBT suffers from various major limitations such as high dielectric loss, low remnant polarization values, high processing temperature, bismuth volatilization, etc [15-17]. Significant efforts have been made to improve the dielectric and ferroelectric properties of this compound. It has been reported that

Accepted manuscript

ACCEPTED MANUSCRIPT

substitution by various cations at A-site or B- site or Bi_2O_2 layer can effectively enhance the physical and chemical properties of parent SBT structure for various device applications [18-22]. **Several investigations have indicated that the defects such as oxygen vacancies accumulate near the grain boundaries leading to strong domain pinning. This results in decrease in remnant polarization [23, 24]. Therefore it is essential to control the defects in perovskite blocks and Bi_2O_2 layer to obtain improved ferroelectric properties. Many investigations on $Bi_4Ti_3O_{12}$ (BIT) indicated that the substitution of rare earth ions for volatile bismuth ion was effective in suppressing the concentration of oxygen vacancies. For instance, it has been reported that La doped BIT exhibited enhanced Pr value [25]. In addition, Chon et al. reported that the Sm doped BIT thin films show excellent fatigue free characteristics and very large $2P_r$ value of 49C/μcm^2 [26]. Similarly, Srinivas et al. reported that substitution of Sm, Gd and Dy rare earth ions in Bi_2O_2 layer of SBT lattice resulted in enhanced dielectric and ferroelectric properties [27].**

Detailed literature survey revealed that even though a lot of work has been done on pristine SBT compound, hardly any systematic work dealing with the characterization of rare earth Ho substituted SBT as a function of composition has been reported. This prompted the authors to synthesize the holmium containing $SrBi_{2-x}Ho_xTa_2O_9$ (x=0.0-2.0) compounds and investigate their structural and electrical properties.

Accepted manuscript

ACCEPTED MANUSCRIPT

Experimental Technique

$SrBi_{2-x}Ho_xTa_2O_9$ compositions with x = 0.0, 0.01, 0.025, 0.05, 0.075, 0.1, 0.5 and 2.0 were synthesized by the solid-state reaction method taking SrCO3, Bi2O3, Ta2O5 and Ho_2O_3 (all from Aldrich purity 99.9%) in their stoichiometric proportions. The powder mixtures were thoroughly grounded and passed through a sieve of appropriate size and then calcined at 900°C in air for 2 h. The calcined mixtures were grounded and admixed with 1.5 wt% polyvinyl alcohol (Aldrich) as a binder and then pressed at 300 MPa into disk shaped pellets. The pellets were sintered at 1200°C for 2 h in air.

X-ray diffractograms of the sintered pellets were recorded using a Bruker diffractometer (model D8 Advance) in the range $20^o \leq 2\theta \leq 70^o$ with Cu Kα radiation(λ= 1.5405 Å) at a scanning rate of 1°/min. The granular morphology was investigated using scanning electron microscope (Hitachi, S-3700 N). The sintered pellets were polished and silver paste was applied on both sides and cured at 500°C for 1 h. The dielectric measurements were carried out using a precision LCR meter (Agilent 4284A) operating at oscillation amplitude of 1V. The polarization–electric field (P–E) hysteresis loops were recorded using a P–E loop tracer based on Sawyer–Tower circuit.

Results and Discussions

Fig. 1 shows the XRD patterns of the sintered samples. The XRD peaks are similar to those in the standard diffraction pattern of SrBi2Ta2O9 on the JCPDS card (JCPDS file no- 072-7073) for the samples upto x≤ 0.1. Further, the specimens remain single phase up to x≤ 0.1 suggesting the incorporation of Ho atoms at Bi site in the SBT lattice. However, for x>0.1, additional peaks are also observed indicating the formation of secondary phase. A comparison of the additional peaks with standard XRD patterns of

Accepted manuscript

ACCEPTED MANUSCRIPT

JCPDS file no- 024-0478 shows the formation of HoTaO4 as the secondary phase. Lattice parameters were calculated from the XRD patterns using a powder-X software package [28] and are listed in Table 1. A decrease in lattice parameters with increasing Ho substitution is observed which can be understood as the ionic radius of Ho3+ (0.91Å) is smaller than that of Bi3+ (0.96Å) [29].

It is known that the composition and sintering temperature influences the microstructure such as grain growth and densification of the specimen, which in turn control other properties of the material [30-32]. The effect of Ho substitution on the microstructure has been examined using SEM and the obtained micrographs are shown in Fig. 2. It is clearly observed that Ho substitution has pronounced effect on the average grain size, density and homogeneity of the grains. Table 1 lists the average grain size for all the synthesized specimens. The sample with x=0.01 has higher grain size compared to Ho free SBT. However, beyond x>0.01 the average grain size decreases gradually with increasing Ho content. Further, sample with x=0.01 exhibits homogeneous microstructure with well defined grains and grain boundaries compared to other specimens with higher holmium content. **The above observed behavior can be explained as follows. It is well known that the diffusion coefficient is directly proportional to the sintering temperature and inversely proportional to the radius of the diffusing ion [33, 34]. Therefore, in the present study, it is expected that for x>0.01 lower sintering temperature might have been required for the diffusion of small sized Ho^{+3} ions (I.R.-0.91Å) into Bi^{3+} (I. R. -0.96Å) site. However, in all the specimens the sintering temperature was the same (1200^{o}C). Therefore, it is possible that at this sintering temperature in the higher holmium containing specimens, Ho^{3+} atoms segregate at the grain boundaries progressively inhibiting grain growth [35, 36].**

Accepted manuscript

ACCEPTED MANUSCRIPT

Dielectric studies

Fig. 3 illustrates the variation of the dielectric constant (Fig. 3(a)) and dielectric loss (Fig. 3(b)) with temperature at a frequency of 100 kHz. The following observations can be made from Fig. 3(a). Firstly, the compound with x=0.0–0.5 undergo ferroelectric–paraelectric phase transition of diffuse type at the Curie temperature (Tc), whereas the specimen with x =2.0 i.e. the bismuth free composition does not show any dielectric anomaly in the studied temperature range. Secondly, the Curie temperature (Tc) is observed to decrease with increase in holmium concentration upto x=0.5. However, specimen with x=2.0 does not exhibit transition temperature values. Thirdly, the specimen with x=0.01 exhibits higher value of dielectric constant (ε_{max}=279.53) as compared to Ho free SBT (ε_{max}=212.74) and thereafter dielectric constant decreases continuously. The observed behavior can be explained as follows.

The broad dielectric peak in Fig. 3(a), indicate that the transition in the compositions within $0.0 \leq x \leq 0.5$ is of the diffuse type, an important characteristic of a disordered perovskite structure [37]. The diffuseness of the peak can be calculated by diffusivity constant (γ) using the empirical relation [38].

$$\ln(1/\varepsilon - 1/\varepsilon max) = \gamma \ln (T-Tc) + \text{constant}$$

where εmax is the maximum value ε at T = Tc. The values of γ at 100 kHz for all the samples are obtained from the slope of $\ln[(1/\varepsilon) - (1/\varepsilon max)]$ versus $\ln[T-Tc]$ curve and are listed in Table 1. For all the studied composition, γ is found to be between 1 (obeying Curie–Weiss law) and 2 (for completely disordered system) confirming the diffuse phase transition nature in the specimen. The value of γ is observed to decrease from Ho free

Accepted manuscript

ACCEPTED MANUSCRIPT

(x=0.0) to x =0.01 composition however it increases as the concentration of holmium is further increased. This suggests that sample with x = 0.01 is more ordered than other compositions and disorderness increases as holmium content is increased in the specimens.

The observed higher dielectric constant for x=0.01 can be understood on the basis of the variation of grain size of the synthesized specimens [39]. It is well known that in most cases the dielectric constant of the ferroelectric materials depends upon the composition, grain size, secondary phases etc. [40-42]. As observed in the SEM micrographs (Fig. 2(a and b)), the specimen with x=0.01 exhibits enhanced microstructure with higher grain size as compared to the holmium free SBT specimen. Higher grain size facilitates easier domain wall motion resulting into higher dielectric constant values [43-45]. However, beyond x>0.01, dielectric constant decreases with increase in holmium content. This is possibly due to comparatively smaller grains as observed in Table 1 [46-49]. Also, the decrease in dielectric constant values can also be attributed to the porous microstructure and presence of secondary phases, which is indeed observed in Figs. 1 and 2(c-h) [50, 51]. **Further, it is observed that sample with x=0.025 and 0.05 exhibit higher grain size and lower dielectric constant values as compared to holmium free sample. It is known that higher grain size facilitates higher dielectric constant values; however grain size and porosity are not the only factors which determine the net dielectric constant of the specimen. Therefore the observed variation is possibly due to the decrease in the net polarization in the holmium containing compounds as the ionic polarizabilty of Ho^{3+} (3.97Å^3) is lower than that of Bi^{3+}(6.12 Å^3) [52, 53]. This results in lowering of dielectric permittivity in the specimen as indeed observed.** It is also important to note that in the specimen with x=2.0, there is almost no variation in the

Accepted manuscript

ACCEPTED MANUSCRIPT

dielectric constant with temperature signifying the importance of Bi_2O_2 layer in these perovskite structures. It is expected that the above behavior will have implications on ferroelectric property as discussed later.

The decrease in Curie temperature (Tc) in Ho substituted samples can be explained on the basis of decrease in structural distortion [54, 47]. This is due to the fact that in SBT structure there exist strong hybridization between Bi 6s and O 2p orbit. In Bi2O2 layer, Bi3+ ions with lone pair 6s electron bonds covalently with O2- ions resulting into drastic distortion of the pseudo perovskite blocks [55, 56]. When holmium ion without 6s electron occupies the Bi site, the structural distortion relives resulting into decrease in Tc [47]. The observed dielectric behavior is the cumulative effect of all the above discussed causes.

Fig. 3(b) shows the dielectric loss (at 100 kHz) as a function of temperature for the studied specimens. It is observed that dielectric loss reduces significantly on holmium substitution. Further, sample with x=0.01 exhibit minimum loss values as compared to other compositions. The source of dielectric loss in these ceramics is space charge polarization/domain wall relaxation [57]. The presence of defects like oxygen vacancies, V••, act as space charge and contribute to the dielectric loss in these materials [58]. It is known that the pristine $SrBi_2Ta_2O_9$ is not perfectly stoichiometric, but contains a certain amount of inherent defects (e.g. oxygen vacancies) resulting from the volatilization of Bi2O3 at high temperatures [59]. When Bi_2O_3 is lost, bismuth and oxygen vacancy complexes are formed in the $(Bi_2O_2)^{2+}$ layers. It has been established through X-ray photoemission spectroscopy studies that the oxygen ions in $(Bi_2O_2)^{2+}$ layers are less stable than the $O2^-$ ions in $(SrTa_2O_7)^{2-}$ perovskite slabs [59, 60]. Many investigations of Pb(Zr,Ti)O3 have indicated that the defects such as oxygen vacancies, V••, act as space

Accepted manuscript

ACCEPTED MANUSCRIPT

charge which plays an important role in increase of dielectric loss in the perovskite materials [61]. Therefore, substitution of Ho atoms into Bi_2O2 layer reduces the number of oxygen vacancies resulting into lower loss values.

Ferroelectric properties

To confirm the ferroelectric nature of the studied compounds, hysteresis loops were recorded at room temperature at a frequency of 100 Hz. Fig. 4 shows the variation of polarization as a function of applied electric field for all the studied samples. Table 1 lists the values of remnant polarization (Pr) for all the samples. It is observed that the Pr value increases with holmium substitution. Further, the sample with x=0.01 exhibit well saturated P-E loop with highest remnant polarization value (9.22μC/cm2) and thereafter Pr values decreases at higher holmium concentrations. The observed behavior can be explained as follows.

It is well known that the polarization switching behavior of ferroelectric materials is strongly influenced by defects like oxygen vacancies [62]. These oxygen vacancies assemble near domain walls and thus the polarization reversal of these domains is suppressed due to "pinning" by these defects near the domain boundaries resulting in smaller remnant polarization values [63]. There is sufficient experimental evidence to indicate that the defects accumulated at electrode-ferroelectric interfaces (or grain and domain boundaries) are mainly oxygen vacancies which have a direct effect on the ferroelectric properties [64-66]. In the present case, the observed ferroelectric behavior can be understood in terms of the reduction in the number of oxygen vacancies. As discussed earlier, the pure SBT sample has inherent oxygen vacancies resulting from the volatilization of Bi_2O_3, whereas partial substitution of holmium atoms into Bi_2O_2 layer

Accepted manuscript

ACCEPTED MANUSCRIPT

effectively reduces the number of oxygen vacancies. This is consistent with the observation of enhanced ferroelectric properties in holmium substituted samples. Further, the decrease in remnant polarization values for samples beyond x>0.01 can be attributed to the decrease in grain size and comparatively porous microstructure [67, 68]. Also, it is important to note that the specimen with x=2.0, exhibit negligible remnant polarization value (Pr=0.36 μC/cm2). This reveals the importance of Bi_2O_2 layer in these perovskite compounds. While there is a significant reduction in the Pr value nevertheless this bismuth free specimen have a finite low value of Pr.

Conclusion

A single phase layered perovskite structure is maintained in SrBi2-xHoxTa2O9 (SBHT) samples up to x=0.1 and secondary phases appear for higher holmium content. Higher dielectric constant value is observed for the specimen with x=0.01 and thereafter dielectric constant decreases. The Curie temperature decreases with increase in holmium content and the dielectric loss reduces significantly. The ferroelectric property enhances on Ho substitution. The maximum Pr value of ~9.22 μC/cm2 is obtained for x = 0.01. Also, degraded dielectric and ferroelectric behavior is observed in the bismuth free specimen with x=2.0.

Accepted manuscript

ACCEPTED MANUSCRIPT

References

[1] S.B. Desu, D.P.Vijay, Novel fatigue-free layered structure ferroelectric thin films, Mater. Sc. & Eng. B, 32 (1995) 75.

[2] J. F. Scott, F. M. Ross, C. A. Araujo, M. C. Scott and M. Huffman, Ferroelectric thin films: Review of materials, properties, and applications, Mater. Res. Soc. Bull. 21 (1996).

[3] K. Takemura, T. Noguchi and M. Miyasaka, Dielectric anomaly in strontium bismuth tantalate thin films, Appl. Phys. Lett. 73 [12] (1998) 1649-51.

[4] R.R. Neurgaonkar, W. F. Hall, J. R. Oliver, W. W. Ho, W. K. Cory, Ferroelectric properties of tetragonal tungsten bronze single crystals, Ferroelectrics 56 (1984) 31-36.

[5] Sugandha and A. K. Jha , Nanocrystalline non-stoichiometric SBT: Effect of milling duration on structural and electrical characteristics, Mater. Charact. 65 (2012) 126-132.

[6] B. H. park, B. S. Kang, S. D. Bu, T. W. Noh, W. Jo, Lanthanum-substituted bismuth titanate for use in non-volatile memories, Nature 401 (1992) 682.

[7] D. Wu, A. Li, T. Zhu, Z. Liu, N. Ming, Ferroelectric properties of Bi3.25La0.75Ti3O12 thin films prepared by chemical solution deposition J. Appl. Phys. 88 (2000) 5941.

[8] H. Watanabe, T. Mihara, H. Yoshimori, C. A. P. De. Araujo, Preparation of Ferroelectric Thin Films of Bismuth Layer Structured Compounds, Jpn. J. Appl. Phys. 34 (1995) 5240.

[9] C. A. P. de Araujo, J. D. Cuchlaro, L. D. Mcmillan, M. C. Scott, J. F. Scott, Fatigue-free ferroelectric capacitors with platinum electrodes, Nature 374 (1995) 627.

[10] R. Jain, V. Gupta, K. Sreenivas, Sintering characteristics and properties of sol gel derived Sr0.8Bi2.4Ta2.0O9 ceramics, Mater. Sci. Eng. B78 (2000) 63.

[11] L. S. Zheludev, Physics of Crystalline Dielectrics, Electrical properties, vol 2, Plennum, New york, (1971) 474.

[12] V. Shrivatava, A. K. Jha and R. G. Mehdiratta, Structural distortion and phase transition studies of Aurivillius type Sr1-xPbxBi2Nb2O9 ferroelectric ceramics, Solid St. Commu. 133 (2004) 125.

[13] B. Aurivillius, Dielectric relaxation in layered oxides of the Aurivillius phase family. Ark. Kemi. 1 (1949) 463.

[14] E. C. Subbaro, J. Phys. Chem.. solids, A family of ferroelectric bismuth compounds 23 (1962) 665.

[15] J. F. Scott, High Dielectric Constant Thin Films for Dynamic Random Access memories (DRAM) Annu. Rev. Mater. Sci. 28 (1998) 79.

Accepted manuscript

ACCEPTED MANUSCRIPT

[16]F. Kulcsar, Electromechanical Properties of Lead Titanate Zirconate Ceramics Modified with Certain Three-or Five-Valent Additions J. Am. Carem. Soc. 42 (1959) 343.

[17] A. Li, D. Wu, H. Ling, T. Yu, X. Yin, N. Ming, Thin Solid Films, Effect of excess bismuth on the microstructures and electrical properties of strontium bismuth tantalate (SBT) thin films 375 (2000) 215

[18] R. B. Atkin, R. L. Holman and R. M. Fulrath, Substitution of Bi and Nb Ions in Lead Zirconate-Titanate, J. Amer. Ceram. Soc. 54 (1971) 113.

[19] P. Duran Martin, A. Catro, P. Millan R. Jimnez, Influence of Bi-site Substitution on the Ferroelectricity of the Aurivillius Compound Bi2SrNb2O9 J. Mater. Res. 13 (1998) 2565.

[20] R. R. Das, P. Bhattacharya, W. Perez, R. S. Katiyar, S. B. Desu, Ferroelectric properties of laser-ablated$Sr_{1-x}A_xBi_2Ta_2O_9$ thin films (where A = Ba, Ca) Appl. Phys. Lett. 80 (2002) 637.

[21] T. J. Boyle, P. G. Clem, B. A. Juttle, T. D. Dunbarb, W. F. Hammetter, Structural and electrical properties of $SrBi_2V_xNb_{2-x}O_9$ ferroelectric ceramics: Effect of temperature and frequency, J. Mater. Res. 17 (2002) 4.

[22] S. Sahoo, R. N. P. Choudhary, B. K. mathur Structural, ferroelectric and impedance spectroscopy properties of Y3+ modified Pb(Fe0.5Nb0.5)O3 ceramics : Physica B 406 (2011) 1660-64.
[23] Y. Noguchi, I. Miwa and M. Miyayama, Jpn. J. Appl. Phys. 39 (2000) L125.

[24]H. Watanabe, T. Mihara and C. A. P. Araujo, Jpn. J. Appl. Phys. 34 (1995) 5240.

[25] J. C Bae, S. S. Kim, E.K. Choi, T. K. Song and Y. Lee, Ferroelectric properties of lanthanum-doped bismuth titanate thin films grown by a sol–gel method:Thin Solid Films 472 (2005) 90-95

[26] U. Chon, K. B. Kim, H. M. Jang and G. C. Yi, Appl. Phys. Lett. 79 (2001) 3137.

[27] A. Srinivas, F. Y. C Boey, T. J. Sritharan, Synthesis of a new electroceramic by replacement of Bi in strontium bismuth niobate, Electroceram, 16 (2006) 321

[28] C. Dong, windows-95-based program for powder X-ray diffraction data processing.J. Appl. Cryst. 32 (1999) 838.

[29] R.D. Shannon, C.T. Prewitt, Effective Ionic Radii in Oxides and Fluorides, Acta Crystallogr. B25 (1965) 925.

[30] T. Atsuki, N. Soyama, T. Yonezawa, K. Ogi, Preparation of Bi-Based Ferroelectric Thin Films by Sol-Gel Method, Jpn. J. Appl. Phys. 34 (1995) 5096.

Accepted manuscript

ACCEPTED MANUSCRIPT

[31] M. Noda, Y. Matsumuro, H. Sugiyama, M. Okuyama, A Fatigue-Tolerant Metal-Ferroelectric-Oxide-Semiconductor Structure with Large Memory Window Using Sr-deficient and Bi-excess Sr0.7Bi2+yTa2O9 Ferroelectric Films Prepared on SiO2/Si at Low Temperature by Pulsed Laser Deposition, Jpn. J. Appl. Phys. 38 (1999) 2275.

[32] Sugandha and A. K. Jha, Synthesis and characterization of nanocrystalline ferroelectric $Sr_{0.8}Bi_{2.2}Ta_2O_9$ by conventional and microwave sintering: A comparative study, Mater Res. Bull. 48 (2013) 1553-1559.

[33] K. Huang, Statistical Mechanics (Wiley, New York, 1987).

[34] P. A. Jha and A. K. Jha, Effect of sintering temperature on the grain growth and electrical properties of barium zirconate titanate ferroelectric ceramics, J. Mater. Sci: Mater. Electron, 24 (2103) 1511.

[35] K. Raman, K. Chandramouli, Effect of rare earth donor Ce^{3+} doping at A-site of PLSZNT on dielectric and piezoelectric properties, Curr. Appl. Phys. 9 (2009) 907-912.

[36] J. C Bae, S. S. Kim, E.K. Choi, T. K. Song and Y. Lee, Ferroelectric properties of lanthanum-doped bismuth titanate thin films grown by a sol–gel method, Thin Solid Films, 472 (2005) 90-95.

[37] R. Rai, S. Sharma, R.N.P. Choudhary, Structural and dielectric properties of Bi modified PLZT ceramics, Solid State Commun. 133 (2005) 635.

[38] S.M. Pilgrim, A.E. Sutherland, S.R. Winzer, Dffuseness as a Useful Parameter for Relaxor Ceramics, J. Am. Ceram. Soc. 73 (1990) 3122.

[39] C. Yichan, S. Yuming, L. Chiping, Enhanced a-axis-oriented crystal growth of Nd-substituted bismuth titanate thin films with layer-by-layer crystallization, J. Cryst. Growth 268 (2004) 210.

[40] R.R. Das, P. Bhattacharya, W. Perez, R.S. Katiyar, Effect of electrolyte additives on sol-precipitated nano silica particles, Ceram. Int. 30 (7) (2004) 1175.

[41] E.C. Subbarao, Systematics of bismuth layer compounds, Integr. Ferr. 12 (1996) 33.

[42] I. Coondoo, N. Panwar and A. K.Jha, Effect of sintering temperature on the structural, dielectric and ferroelectric properties of tungsten substituted SBT ceramics, Physica B, 406 (2011) 374.

[43] H.T. Martirena, J.C. Burfoot, Grain-size effects on properties of some ferroelectric ceramics. J. Phys. C: Solid State Phys 7, 3162 (1976)

[44] I. Coondoo and A. K. Jha, Investigations of structural, dielectric and ferroelectric behavior of europium substituted $SrBi_2Ta_2O_9$ ferroelectric ceramics, Solid State. Commun., 142 (2007) 561

Accepted manuscript

ACCEPTED MANUSCRIPT

[45] A. K. Jha and Sugandha, Structural and Dielectric Investigations of Bismuth Excess Strontium Bismuth Tantalate Ferroelectric Ceramics Ferroelectrics, 421 (2011) 1-8.

[46] Z. H. Bao, Y. Y. Yao, J. S. Zhu, Y. N. Wang, Study on ferroelectric and dielectric properties of niobium doped $Bi_4Ti_3O_{12}$ ceramics and thin films prepared by PLD method , Mater lett. 56 (2002) 861.

[47] F. Qiang, J. H. He, J. Zhu, X. B. Chen, Ferroelectric and dielectric properties of bismuth-layered structural $Sr_2Bi_{4-x}Ln_xTi_5O_{18}$ (Ln=La, Nd, Sm and Dy) ceramics, J. Solid St. Chem, 179 (2006) 1768.

[48] H. Huang, C. Q. Sun, Z. S. Tian, Grain-size effect on ferroelectric Pb(Zr1-xTix)O3 solid solutions induced by surface bond contraction Phys. Rev. B, 63 (2001) 184112.

[49] F. Suhua, C. Wen, H. Guangda, Effects of Excess Bismuth on Structure and Properties of SrBi4 Ti4 O15 Ceramics, J. Rare Earths, 25 (2007) 317.

[50] P. Ganguly and A. K. Jha, Structural and electrical properties of $Ba_{5-x}Ca_xSmTi_3Nb_7O_{30}$ (x=0–5) ferroelectric ceramics. J. Alloys Compd. 495 (2010) 7-12.

[51] K. K. Tae and K. Chang, Effect of bismuth excess on the crystallization of Bi3.25La0.75Ti3O12 thin films on Pt/Ti/SiO2/Si substrates, Microelect. Engg. 71 (2004) 266.

[52]R. D. Shannon, Dielectric polarizabilties of ions in oxides and florides, J. Appl. Phys. 73 (1993) 348-366.

[53]P. Ganguly and A. K. Jha, Investigations of structural, dielectric and electrical behavior of calcium substituted $Ba_5NdTi_3Nb_7O_{30}$ ferroelectric ceramics, Int. Ferroelectrics, 113 (2010) 149-56

[54] Y. Shimakawa, Y. Kubo, Y. Nakagawa, S. Goto, Crystal structure and ferroelectric properties of ABi2Ta2O9(A=Ca, Sr, and Ba), Phys. Rev. B. 61 (2000) 6559.

[55] Y. Noguchi, M. Miyayama, T. Kudo, Effect of Bi substitution at the Sr site on the ferroelectric properties of dense strontium bismuth tantalate ceramics J. Appl. Phys. 88 (2000) 2146.

[56] Y. Noguchi, M. Miyayama, T. Kudo, Direct evidence of A-site-deficient strontium bismuth tantalate and its enhanced ferroelectric properties Phys. Rev. B 63 (2001) 214102.

[57] I.S. Zheludev, Physics of Crystalline Dielectrics, Electrical Properties, vol. 2, Plenum, New York, 1971, p. 474.

Accepted manuscript

ACCEPTED MANUSCRIPT

[58] Y. Noguchi, M. Miyayama, Large remanent polarization of vanadium doped $Bi_4Ti_3O_{12}$ Appl. Phys. Lett. 78 (2001) 1903.

[59] B. H. Park, S. J. Hyun, S. D. Bu, T. W. Noh, J. Lee, H. D. Kim,T. H. Kim, and W. Jo,Differences in nature of defects between $SrBi_2Ta_2O_9$and $Bi_4Ti_3O_{12}$ Appl. Phys. Lett. 74 (1999) 1907–1909.

[60] I. Coondoo, A. K. Jha and S. K. Aggarwal, Enhancement of dielectric characteristics in donor doped Aurivillius $SrBi_2Ta_2O_9$ ferroelectric ceramics J. Europ. Ceram. Soc. 27 (2007) 253.

[61] A. Chen, Y. Zhi, and L. E. Cross, Oxygen-vacancy-related low-frequency dielectric relaxation and electrical conduction in Bi:$SrTiO_3$ Phys. Rev. B, 62 (2000) 228–236.

[62] Y. Noguchi, M. Miyayama, K. Oikawa, T. Kamiyama, M. Osada, M. Kakihana, Defect Engineering for Control of Polarization Properties in $SrBi_2Ta_2O_9$, Jpn. J. Appl. Phys., Part 1 41 (2002) 7062.

[63]W.L. Warren, D. Dimos, B.A. Tuttle, Electronic and Ionic Trapping at Domain Walls in BaTiO3, J. Am. Ceram. Soc. 77 (1994) 2753.

[64] Q.Y. Jiang, L.E. Cross, Effects of porosity on electric fatigue behaviour in PLZT and PZT ferroelectric ceramics J. Mater. Sci. 28 (1993) 4536.

[65] J.F. Scott, C.A. Araujo, B.M. Melnik, L.D. McMillan, R. Zuleeg, Quantitative measurement of space charge effects in lead zirconate titanate memories, J. Appl. Phys. 70 (1991) 382.

[66] Sugandha and A. K. Jha, Investigations of Dielectric and Ferroelectric properties of yttrium substituted $SrBi_2Ta_2O_9$ ferroelectric ceramics, proceedings of IEEE (2012) ISBN: 978-1-4673-2668-1.

[67] Sugandha and A. K. Jha, Effect of sintering temperature on the microstructural and electrical properties of non stoichiometric strontium bismuth tantalate ferroelectric ceramics, Ind. J. Phys.87[4] (2013) 325-31..

[68] M. Yamaguchi, T. Nagamoto, and O. Omoto, Preparation of highly c-axis-oriented $Bi_4Ti_3O_{12}$ thin films and their crystallographic, dielectric and optical properties, Thin Solid Films 300 (1997) 299.

Accepted manuscript

ACCEPTED MANUSCRIPT

Figure Captions

Figure 1: X-ray diffraction patterns of $SrBi_{2-x}Ho_xTa_2O_9$(x=0.0-2.0) compounds

Figure 2: SEM micrographs of SrBi2-xHoxTa2O9 [(a) x=0.0, (b) x=0.01, (c) x=0.025, (d) x=0.05, (e) x=0.075, (f) x=0.1, (g) x=0.5, (h) x=2.0]

Figure 3: (a) Variation of dielectric constant and (b) dielectric loss with temperature of $SrBi_{2-x}Ho_xTa_2O_9$(x=0.0-2.0) compounds

Figure 4: P–E hysteresis loops of $SrBi_{2-x}Ho_xTa_2O_9$(x=0.0-2.0) compounds at room temperature.

Accepted manuscript

ACCEPTED MANUSCRIPT

Table 1: Variation of different parameters of $SrBi_{2-x}Ho_xTa_2O_9$ (x=0.0-2.0) Compounds.

x	a (Å)	b (Å)	c(Å)	ε_{max} (100 KHz)	Grain size (μm)	P_r (μC/cm^2)	Diffusivity (γ)	T_c (^{o}C)
0.0	5.4983	5.5131	24.9688	212.374	2.33	2.55	1.326	335
0.01	5.4963	5.5126	24.8352	279.530	5.62	9.22	1.304	250
0.025	5.4928	5.5121	24.7894	157.717	4.13	6.39	1.367	185
0.05	5.4878	5.5111	24.6201	126.246	3.53	4.99	1.518	175
0.075	5.4848	5.4984	24.2928	104.735	3.13	2.47	1.794	155
0.1	5.4812	5.4968	24.0114	94.501	2.47	2.02	1.797	150
0.5	5.4809	5.4962	23.9728	82.761	2.15	1.86	1.797	142
2.0	5.4809	5.4959	23.9691	-	1.67	0.36	-	-

Accepted manuscript

ACCEPTED MANUSCRIPT

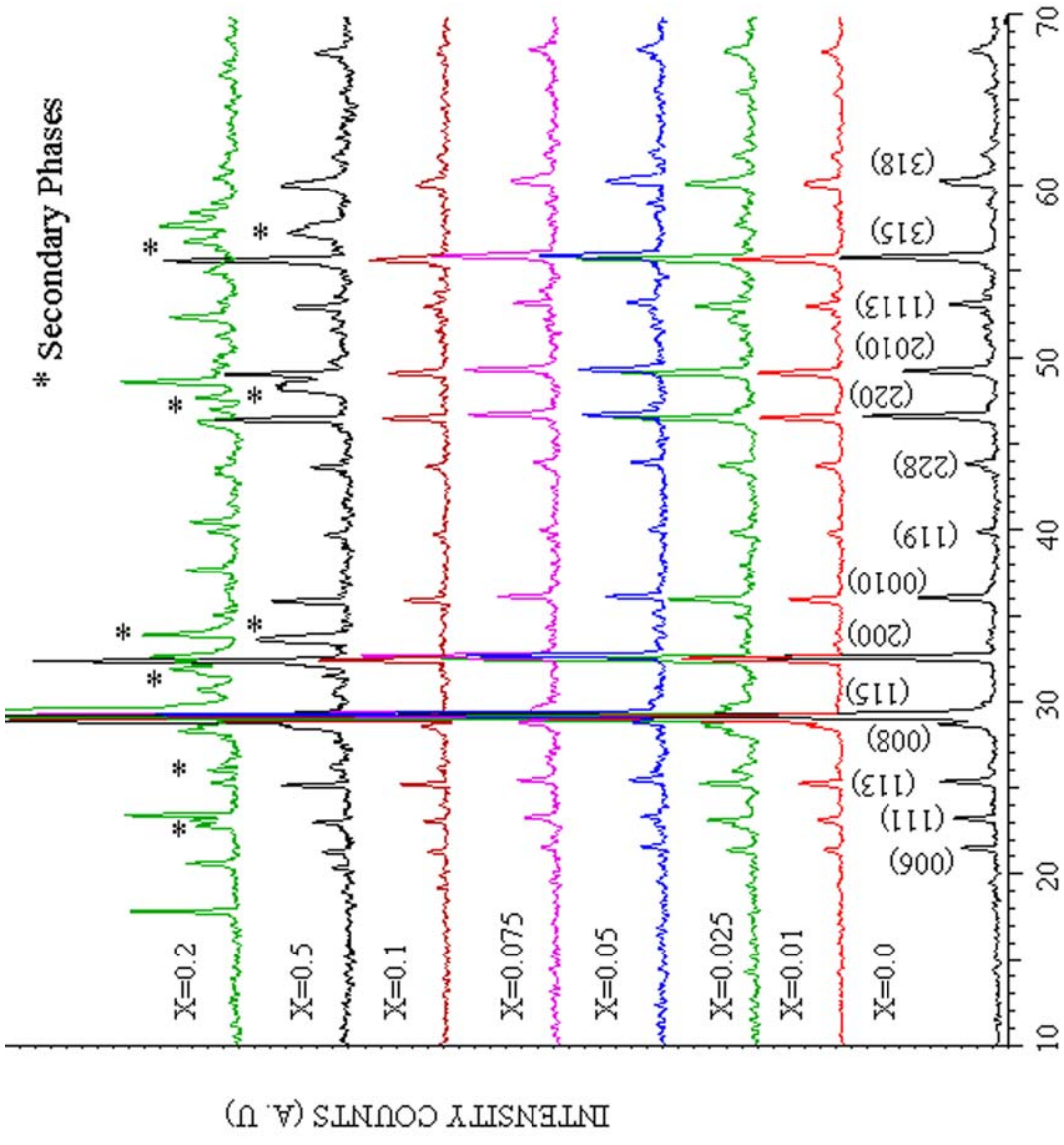

ACCEPTED MANUSCRIPT

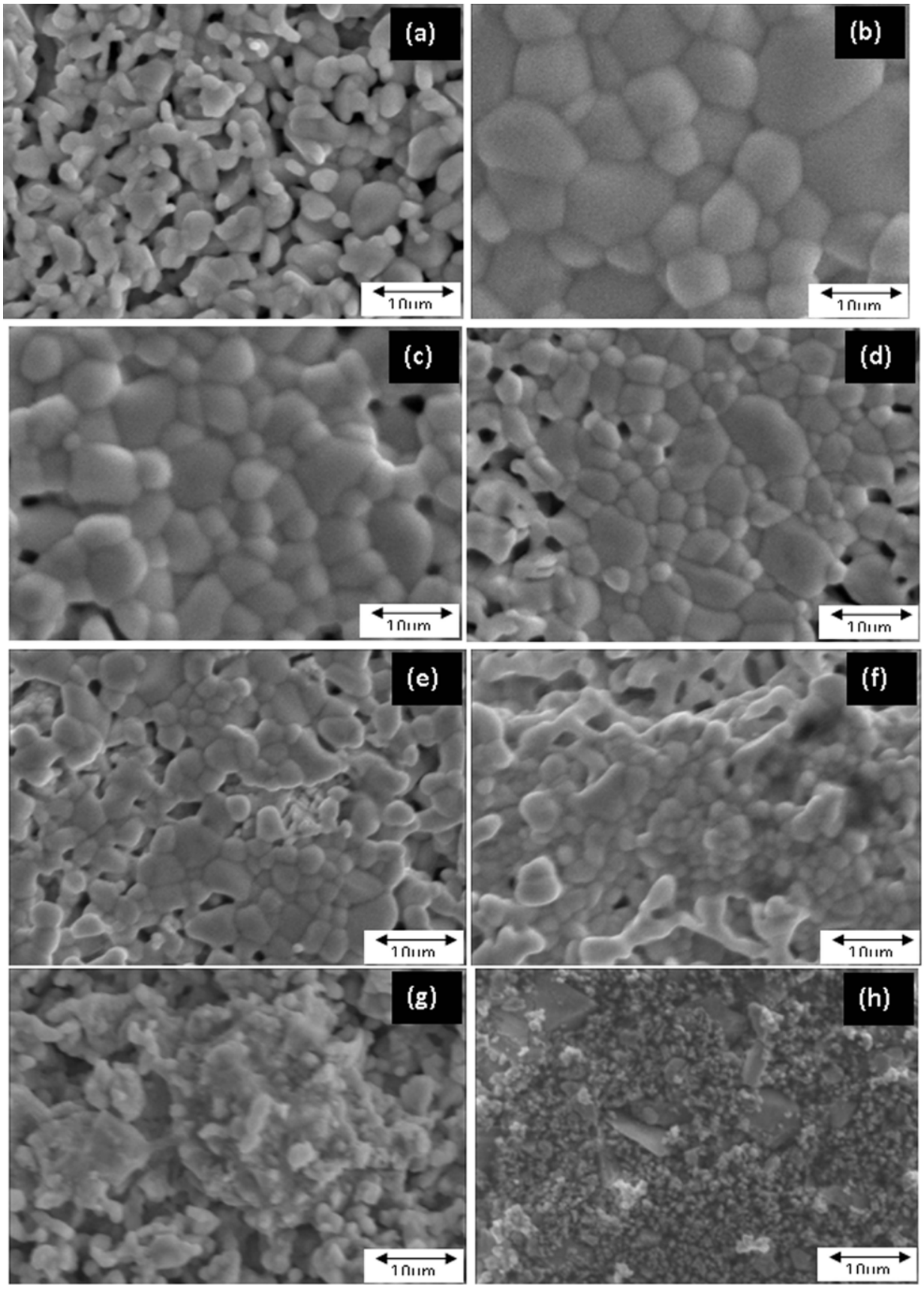

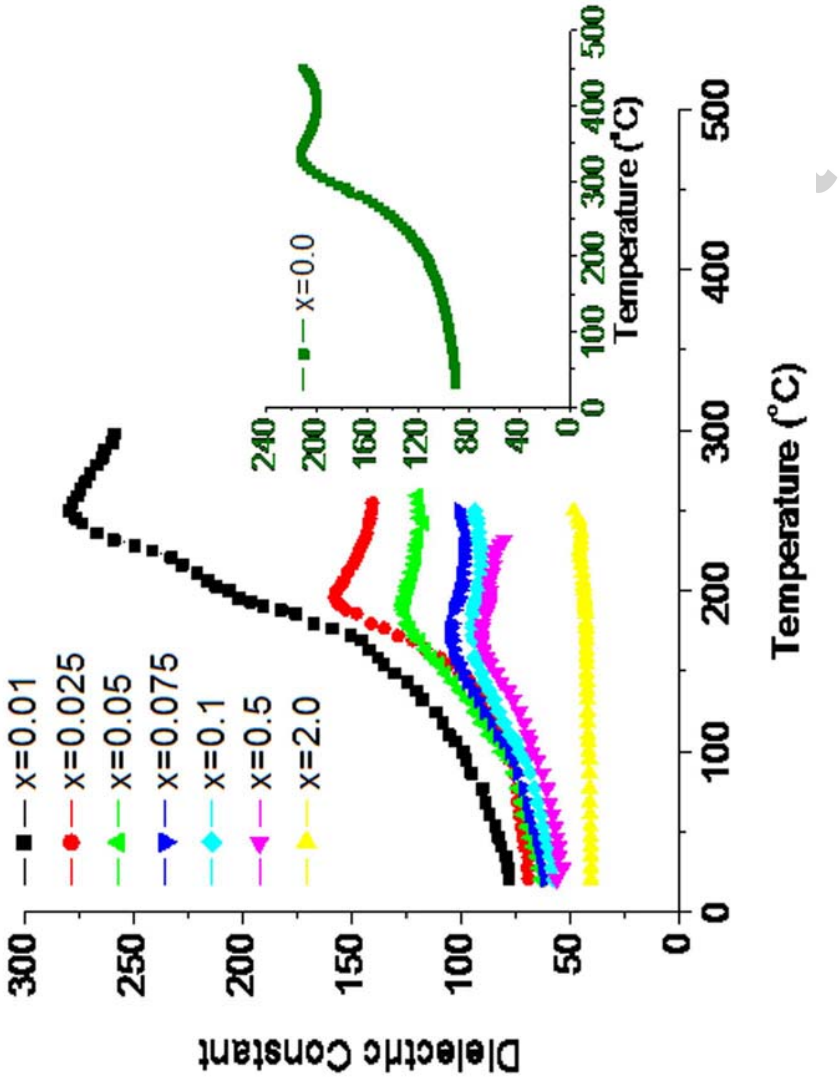
Dielectric Constant
Temperature (°C)
x=0.01
x=0.025
x=0.05
x=0.075
x=0.1
x=0.5
x=2.0
x=0.0
Temperature (°C)

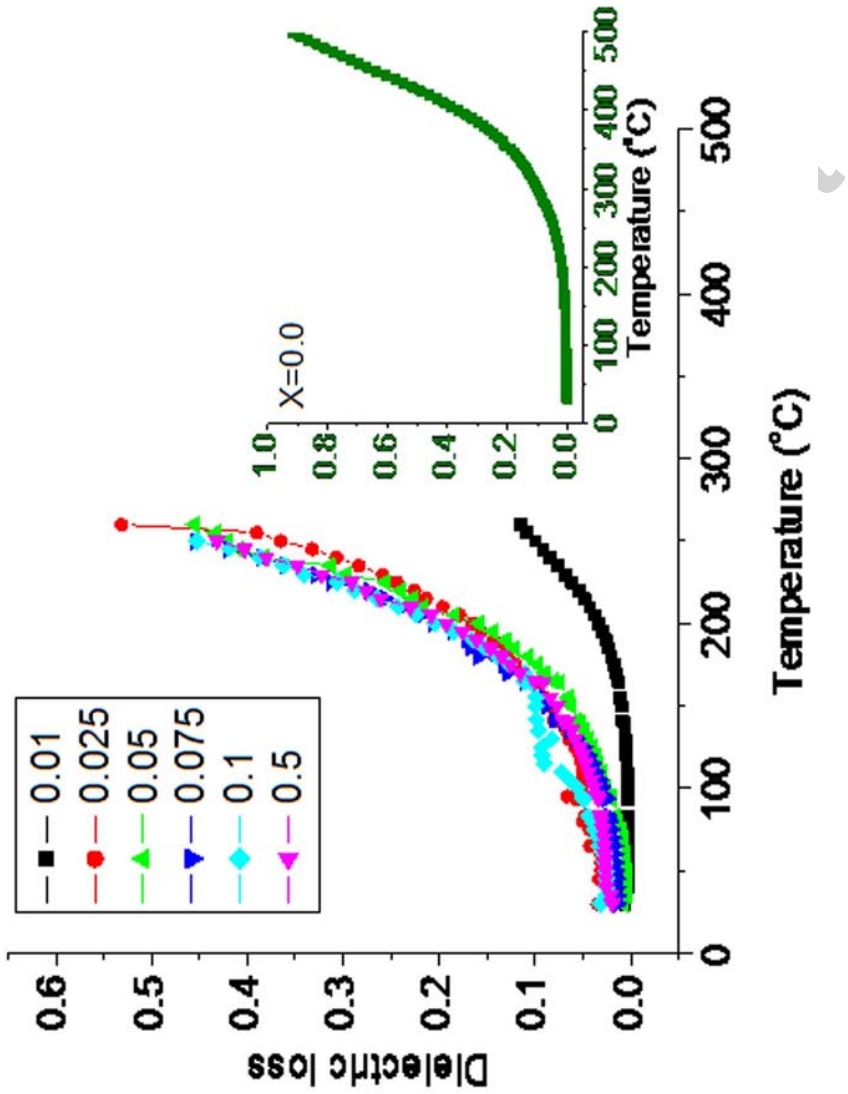
Dielectric loss
Temperature (°C)
0.01
0.025
0.05
0.075
0.1
0.5
X=0.0
Temperature (°C)

ACCEPTED MANUSCRIPT

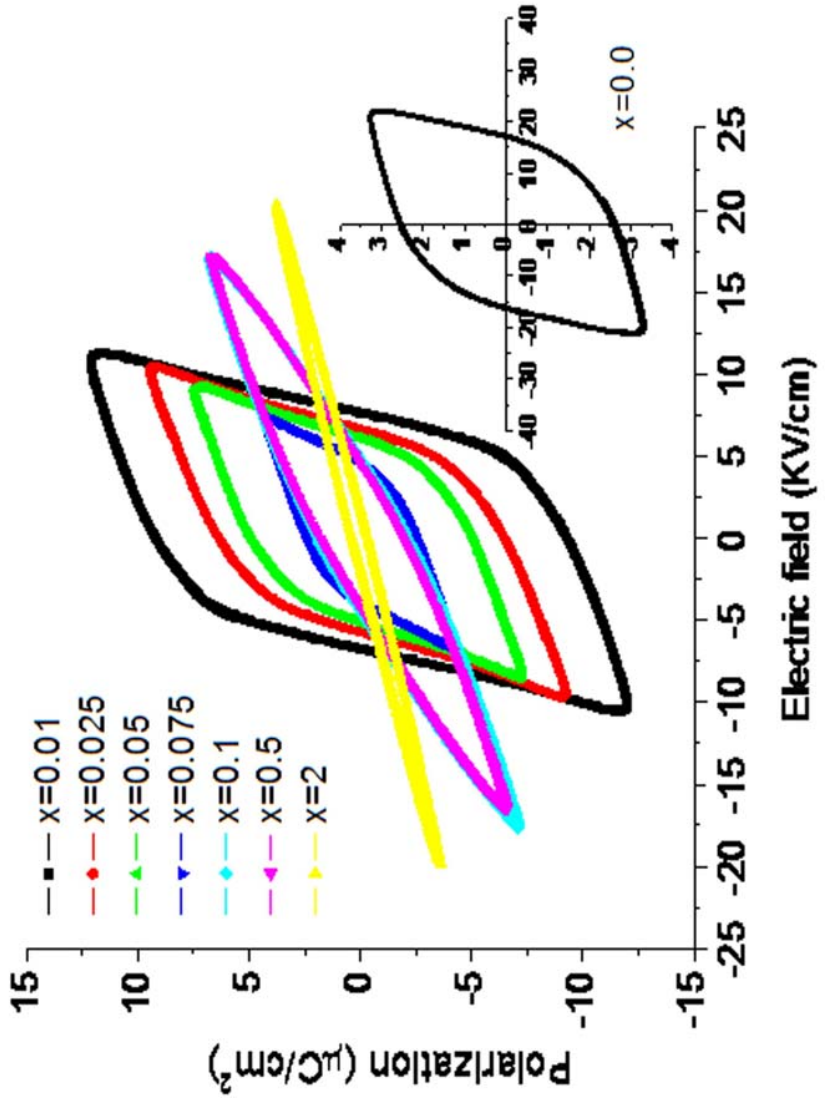

International Conference on Ceramics, Bikaner, India
International Journal of Modern Physics: Conference Series
Vol. 22 (2013) 140–147
© World Scientific Publishing Company
DOI: 10.1142/S2010194513010027

World Scientific
www.worldscientific.com

EFFECT OF MILLING TIME ON PHASE TRANSITION IN $BaTi_{0.095}W_{0.05}O_3$ NANOCERAMICS SYNTHESIZED BY HIGH-ENERGY BALL MILLING

SHEELA DEVI

Maharaja Surajmal Institute of Technology, Department of Applied physics
C-4 Janakpuri, New Delhi-110058, India, Email: physics_sheela@yahoo.co.in

A. K. JHA

Thin Film & Materials Science Laboratory, Deptt. of Applied physics
Delhi Technological University (Formerly Delhi College of Engineering)
Delhi – 110042, INDIA, Email: dr_jha_ak@yahoo.co.in

Nanocrystalline $BaTi_{0.095}W_{0.05}O_3$ has been synthesized by mechanical activation process using high-energy ball milling. The powders milled for (10 hours, 20 hours, 30 hours respectively) were characterized by X-ray diffraction (XRD) and Scanning electron microscopy (SEM). Transmission electron microscopy images showed that in W- substituted barium titanate nanoparticles are formed in the range of 20-50 nm. Crystallite size decreases with increasing milling time in the samples. Detailed Dielectric and ferroelectric properties with different milling times are discussed in detail. Diffusivity of the samples increases with milling time. Piezoelectric properties increase with increase in milling time in the samples.

Keywords: Mechanochemical synthesis; dielectric properties; ferroelectric properties.

1. Introduction

Barium titanate is one of the best known and widely used materials for electrocermics due to its excellent dielectric[1], ferroelectric[2] and piezoelectric properties[3, 4]. Nanocrystalline materials are of great importance both from fundamental and commercial point of view [5]. $BaTiO_3$ nanocrystals have been synthesized by various techniques like hydrothermal method[6, 7], sol-gel processing[8] oxalate route[9] and polymeric precursor methods[10]. Although $BaTiO_3$ nanoparticles produced by these methods are smaller than 100 nm, they contain residual hydroxide ions[11, 12]. It has been reported that hydroxide ions in $BaTiO_3$ nanoparticles result in the formation of intergranular pores in MLCCs during annealing[13]. The mechanochemical route has several advantages over both conventional solid state reaction and liquid phase processes, including the use of low cost raw materials, simplicity of process and the ability to obtain fine particles[14]. The properties of nanocrystalline materials are found superior those of polycrystalline coarse grained materials. Though literature survey shows that this novel technique has been used to synthesize several ferroelectric ceramics[15, 16], no reports were found on tungsten substitute barium titanate nanoceramics synthesized by mechanical activation method. This prompted the authors to synthesize the compound $BaTi_{0.95}W_{0.05}O_3$ by mechanical

activation process and investigate their structural, dielectric, ferroelectric and piezoelectric properties.

2. Experimental Method

High purity $BaCO_3$, TiO_2 and WO_3 (all from M/s Aldrich, USA) were taken in stoichiometric proportions. This stoichiometric mixture of powders was milled in a high energy planetary ball mill (Retsch-PM 100) for 10 hours, 20 hours and 30 hours at a milling speed of 400 rpm. Milling was carried out in toluene medium with 10 mm zirconium oxide balls in a zirconium oxide vial with a ball-to-powder weight ratio of 8:1. The mixture was then added with appropriate quantity of polyvinyl alcohol (M/s Aldrich, USA) as a binder and then pressed at 300 MPa into disk shaped pellets. These pellets were then sintered at 1250 ºC for 2 hours. Phase development in the mechanically activated powders was monitored using an X-ray diffractometer (Bruker D8 Advance). Transmission electron microscopy (Technia G^2 F 30S TWIN) and scanning electron microscopy (Hitachi-S3700) were used to study their particle size and granular morphology. For dielectric measurement the pellets were polished and silver pasted on both sides and cured at 300 ºC for 15 minutes. The dielectric measurements were carried out using a precision LCR meter (Agilent 4284A) operating at oscillation amplitude of 1 V. The polarization-electric field (*P-E*) hysteresis loop was recorded using a *P–E* loop tracer based on Sawyer–Tower circuit. The sample was poled at 17 kV/cm at an elevated temperature for 8 hours in silicon oil. Piezoelectric co-efficient, (d_{33}) was measured using a piezometer system (PiezoTest PM300).

3. Results and Discussion

3.1. *Structural analysis*

Fig. 1 (a) shows the XRD patterns of the studied samples milled for different durations i.e. 10 hours, 20 hours and 30 hours respectively. It is observed that an increasing milling time, XRD pattern changes and peaks slightly shift towards higher angles. The peaks become increasingly broader with increasing milling time. These changes indicate size reduction and lattice distortion in the samples. However, the reaction appears to be incomplete even after 30 hours of milling and hence subsequent thermal treatment is required to complete the reaction. The intensity of the TiO_2 peaks decreases when the milling duration increases. Fig. 1 (b) shows XRD patterns of the sintered samples. The formation of single phase compounds at higher milling time is observed. In addition to pervoskite phase, additional peaks have also been observed in the XRD patterns of the sintered sample. The lattice parameters were calculated using the observed interplanar spacing, *d*-values, obtained from the diffractograms and refined using the least square refinement method by computer program package Powder-X [17] are given in Table 1. It is found that the compound prepared by mechanical activation process has a tetragonal perovskite structure. The tetragonal strain (c/a) of the compounds

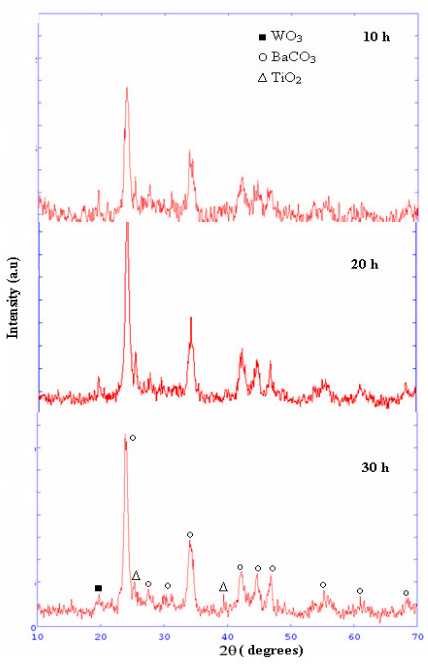

Fig. 1(a)

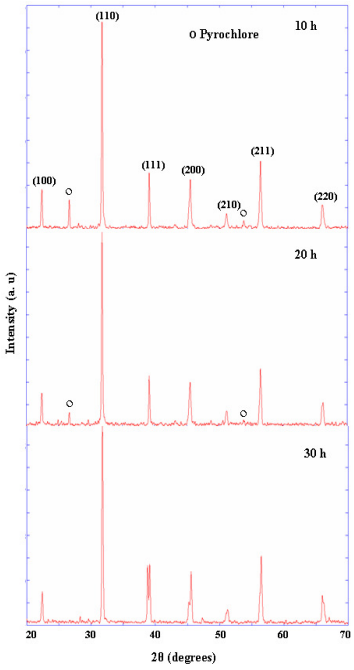

Fig. 1(b)

Fig. 1 XRD patterns of the studied samples

It is also revealed from X-ray diffractograms [Fig. 1(b)], that the intense peak (relative intensity Ip =100) of the diffractogram shifts towards higher 2θ value with decrease in crystallite size. This is inferred from the change in lattice parameters or lattice volume $V_o = a^2c$.

Table 1. Comparison of lattice parameters, unit cell volume, tetragonal strain, crystallite size, diffusivity and piezoelectric coefficient for different milling times

Milling time (hours)	a (A^0)	c (A^0)	Volume $(A^0)^3$	T_c (°C)	ε_{max} (1kHz)	c/a	Crystallite size (nm)	d_{33} (pC/N)	Diffusivity (γ)
10	3.9945	4.0246	64.216	80	2380.6663	1.0075	26.52	220	1.6407
20	3.9918	4.0213	64.077	75	2964.6095	1.0073	22.12	237	1.5247
30	3.9915	4.0197	64.042	70	3618.8421	1.0070	18.09	257	1.6263

The average crystallite size was calculated using the Debye- Scherrer method from the broadening of the diffraction line using the expression

$$d = 0.9\,\lambda / \beta\cos\theta \qquad (1)$$

where λ is the wavelength of the CuK_α radiation, β is the FWHM of the diffraction peak and θ is the Bragg diffraction angle. It is observed that the average particle size decreases with increasing milling time.

Fig. 2 (a) and (b) show SEM micrographs of tungsten substituted barium titanate milled for different milling durations before and after sintering. It is observed that agglogrametes are formed at the higher milling time which indicates reduction in particle size.

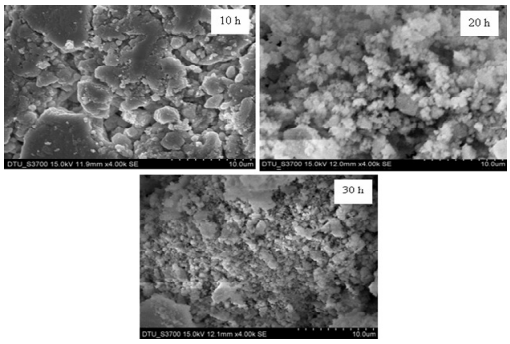

Fig. 2 (a)

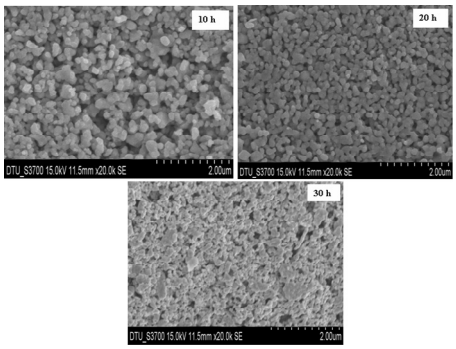

Fig. 2 (b)

Fig. 2 SEM Micrograph of the studied samples

The grains are uniformerly distributed and particles are more or less spherical in their morphology and grain size decreases with milling time. The average grain size is determined by linear intercept method. After sintering grain size is observed to be in the range of ~0.3-0.2 μm. Transmission electron microscopy (TEM) and electron diffraction (ED) of the studied specimen milled for 30 hours are shown in Fig. 3

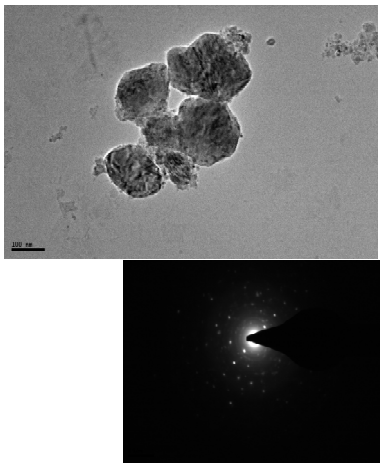

Fig. 3 Transmission electron microscopy and electron diffraction) of the studied specimen milled for 30 hours

It is seen that the particles are of varying shape and morphology and connect with each other to form a large network system with irregular sizes and shapes. The particle size is found in the range 20-50 nm. The formation of particles of nanodimension is also confirmed by diffraction rings consisting of discrete diffraction spots. The observed crystallite size is comparable with the crystallite size measured using XRD patterns.

3.2. *Dielectric studies*

Fig. 4 and 5 show the variation of dielectric constant and loss at different milling durations at frequency 1 kHz. It is observed in Fig. 4 that dielectric constant increases with increase in milling time and is maximum in the sample milled for 30 hours (Table 1). As it is known that the dielectric constant increases with decreasing crystallite size because of the increasing residual internal stress and domain-wall contribution[18-21].

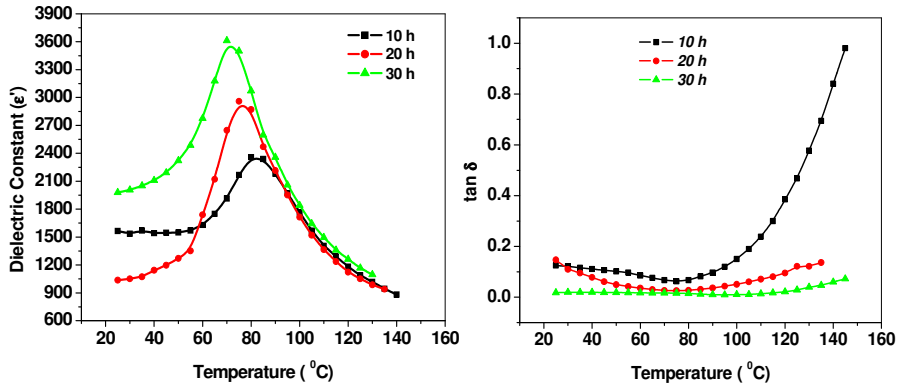

Fig. 4 and 5 show the variation of dielectric constant and loss with temperature for different milling durations

It is observed that in all milling time the dielectric constant increases with rise in temperature and reaches a maximum value at transition temperature (T_c) and then decreases with further increase in temperature. This large dielectric constant of mechanically alloyed and sintered samples could be due to nanocrystalline nature of studied compound. The increase in dielectric constant with milling time can be understood by finer grain structure as follows. As the grain boundary is the structural discontinuity, coupling between adjacent grains in the samples with fine grain structure becomes weak and hence, it is comparatively easy for the electric dipoles to align when an external electric field is applied. This implies a higher net electrical polarization and thus the high dielectric constants in the samples with fine grain structrure [22, 23]. The small observed reduction of unit cell volume (Table 1) with increase in milling time may additionally be increasing the observed dielectric constant. It follows from Clausius-Mossotti relation,

$$\alpha_D = (3/4\pi)\, V_m\, (\varepsilon_r\text{-}1)/(\varepsilon_r + 2) \qquad (2)$$

where V_m = molar volume (= $V_{unit\ cell}/Z$) and ε_r is the relative dielectric constant and α_D is the net dielectic polarizability, However, the Curie temperature (T_c) is found to decrease with increase in the milling time (Table 1). Smaller value of tetragonal strain (c/a) on increasing milling duration indicates that a smaller amount of thermal energy is required for the phase transition resulting in decrease of T_c. Another possible reason for decrease in Curie temperature is more interfacial or grain boundary energy as it contains larger number of grain boundaries (Fig. 2). In all the samples, the dielectric loss has smaller values at lower temperatures but at higher temperatures it increases sharply (Fig. 5). This sharp increase of dielectric loss in high temperature region may be attributed to the increased mobility of space charges arising from the defects or vacancies (like oxygen vacancies) in the samples[26]. The dielectric peak in all the samples is found to be broadened indicating the existence of diffuse phase transition. The diffusivity constant (γ) have been calculated using the empirical relation[25],

$$\ln\left(\frac{1}{\varepsilon}-\frac{1}{\varepsilon_{max}}\right) = \gamma \ln (T\text{-}T_c) + \text{constant} \qquad (3)$$

where ε_{max} is the maximum ε value at $T = T_c$. The values of γ for all the samples are obtained from the slope of ln ($1/\varepsilon$ - $1/\varepsilon_{max}$) versus ln (T-T_c) curve and are listed in Table 1. γ is found to be between 1 (obeying Curie-Weiss law) and 2 (for completely disordered system) confirming the diffuse phase transition in all the samples as shown in Fig. 6

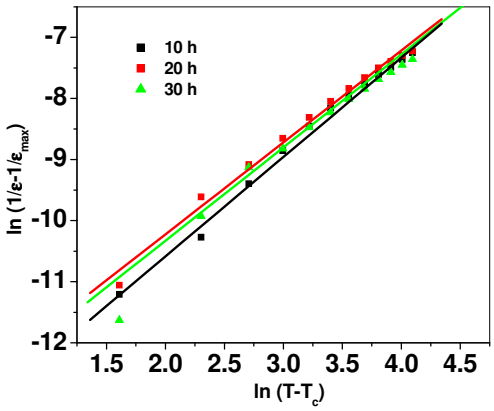

Fig. 6 Variation of ln ($1/\varepsilon' - 1/\varepsilon'_{max}$) with ln ($T$-$T_c$)

3.3. *Ferroelectric and Piezoelectric studies*

P-E hysteresis loops were recorded for different milling times at room temperature at a frequency of 100 Hz and are shown in Fig. 7. The existence of well-defined hysteresis loop confirms the ferroelectric nature of the compound prepared by mechanical activation technique. The maximum remnant polarization (P_r) for 30 h milling time value is found

to be 7.41 μC/cm^2. The value of remnant polarization is increased with increasing milling duration. The value of remnant polarization is much higher as compared to that obtained from solid –state reaction method`[27]. Piezoelectric coefficients of the studied samples is shown in Table 1. It is observed that 30 h milling shows maximum d_{33} value of 257 pC/N.

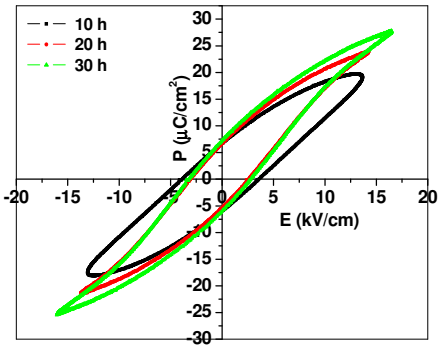

Fig. 7 P-E hysteresis loops were recorded for different milling times at room temperature

4. Conclusion

Nanocrystalline tungsten substituted barium titanate compound has been successfully synthesized by mechanical activation process. The synthesized compound is in single-phase having tetragonal pervoskite crystal structure. SEM and TEM micrographs reveal that the particles size milled for 30 hours reduces to nano-range. BTW sample prepared by this technique for 30 hours milling shows highest dielectric constant and lowest dielectric loss as compared to other lower milling time samples. The room temperature *P-E* hysteresis loop with P_r value of 7.41 μC/cm^2 confirms the ferroelectric nature of the compound prepared by this novel technique.

References

1. G. B. Li, S.X.Liu, F. H. Liao, S.J. Tian, X. P. Jing, J. H. Lin, Y. Uesu, K. Kohn, K. Saitoh, M. terauchi, N. L. Di, Z. H. Cheng, *J. Solid State Chem.*, **177**, 1695 (2004).
2. S.Sen, R.N. P. choudhary, P. Pramanik, *Mater. Lett*. **58,** 3486 (2004).
3. Q.Xu, S. T. Chen, W. Chen, S. J. Wu, J. Lee, J. Zhou, H. J. Sun, Y. M. Li, *J. Alloys and compound* **381,** 221 (2004).
4. C. Ang, Z. Yu, Z. Jing, R. Guo, A. S. Bhalla, L.E. Cross, *Appl. Phys. Lett*. **80**, 3424 (2002).
5. R. Andrievski and A. M. Glazer. *Scr. Mater*., **44**, 1621 (2001).
6. E. B. Slamovich, I. A. Aksay, *J. Am. Ceram. Soc*. **79**, 239 (1996).
7. T. Noma, S. Wada, M. Yano, T. Suzuki, *J. Appl. Phys*, **80**, 5223 (1996).
8. M. H. Frey, D. A. Payne, *Phys. Rev. B* **54**, 3158 (1996).
9. H. I. Hsiang, F.S. Yen*, J. Am. Ceram. Soc*. **79**, 1053 (1996).
10. W.S. Cho, *J. Phys. Chem. Solid* **59**, 659 (1998).
11. S. W. Lu, B. I. Lee, Z. L. Wang, W. D.*, J. Cryst. Growth* **219**, 269 (2000).
12. I. J. Clark, T. Takeuchi, N. Ohtori, D.C. Sinclair, *J. Mater. Chem*. **9**, 83 (1999).

13. D. F. K. Hennings, C. Metzmacher, B. S. Schreinemacher, *J. Am. Ceram. Soc*. **84**, 179 (2001).
14. B. D. Stojanovic, *J. Mater. Process. Technol*. **143**, 78 (2003).
15. L.B. Kong, W. Zhu and O. K. Tan, *Ferroelectrics*, **230**, 281 (1999).
16. B.D. Stojanovic, A. Z. Simoes, C. O. Paiva-Santos, C. Jovalekic, V.V. Mitic and J. varela, *J. Eur. Ceram. Soc*. **25**, 1985 (2005).
17. C. Dong, *J. Appl Cryst*., **32**, 838 (1999).
18. W. R. Buessem, L. E. Cross, and A. K. Goswami, *J. Am. Ceram. Soc.*, **49**, 33 (1966).
19. G. Arlt, D. Hennings and G. de With, *J. Appl. Phys.*, **58**, 1619 (1985).
20. K. Uchino, E. Sadanaga and T. Hirose, *J. Am. Ceram. Soc.* **72** 1555-1558 (1989).
21. W. Kanzig, *Phys. Rev*. **98**, 549 (1955).
22. Y. Park, Y. H. Kim and H. G. Kim, *Mater. Lett.* **28**, 101 (1996).
23. K.L. Ying and T. E. Hsieh, *J. Appl.. Polym. Sci*, **106**, 1550 (2007).
24. W. D. Callister, *Materials Science and Engineering*, Wiley, India, 2006.
25. S. M. Pilgrim, A.E. Sutherland and S.R.Winzer, *J. Amer. Ceram. Soc.* **73**, 3122 (1990).
26. T. Friessnegg, S. Aggarwal, R. Ramesh, B. Nielsen, E. H. Poindexter and D. J. Keeble *Appl. Phys. Lett.* **77** 127-129 (2000).
27. Sheela Devi and A. K. Jha, *Asian Journal of Chemistry*, **21**, 10, 117-124 (2009).

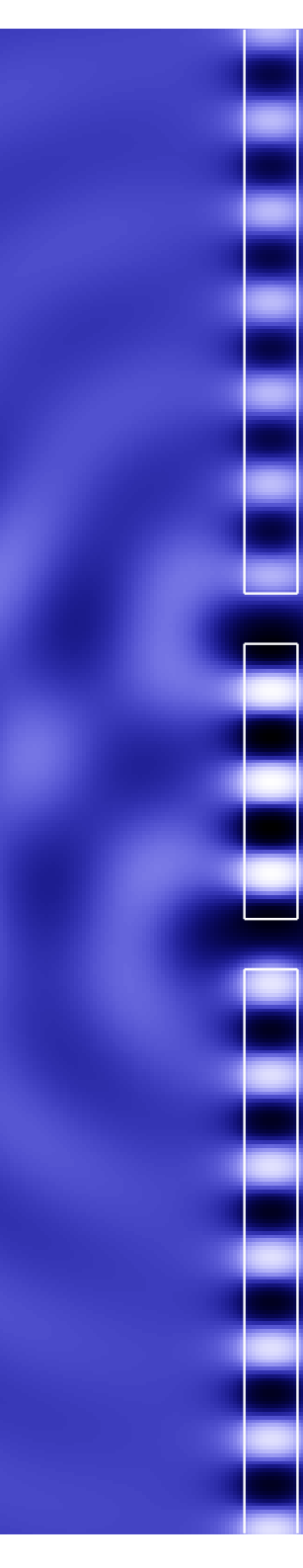

owtnm13.ewi.utwente.nl

OWTNM 2013 Enschede, The Netherlands Proceedings

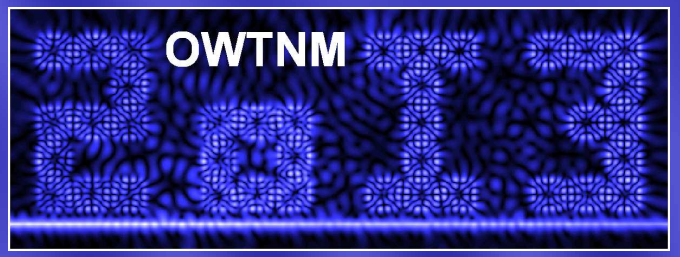

XXI International Workshop on Optical Wave & Waveguide Theory and Numerical Modelling

Enschede, The Netherlands
April 19 & 20, 2013

Proceedings

Contact information:
Dr. Manfred Hammer
University of Twente,
Faculty EEMCS,
P.O. Box 217,
7500 AE, Enschede,
The Netherlands;
Phone: +31 (0)53 489 3448, +31 (0)53 489 4768
Fax: +31 (0)53 489 3996
E-mail: owtnm13@ewi.utwente.nl
Web: http://owtnm13.ewi.utwente.nl/

2013 University of Twente
Printed in Enschede, The Netherlands
ISBN: 978-90-365-3538-0

OWTNM 2013

XXI International Workshop on Optical
Wave & Waveguide Theory and Numerical Modelling

19-20 April 2013, Enschede, The Netherlands

Proceedings

UNIVERSITY OF TWENTE.

Acknowledgments

The organizers thank the following companies and institutes for their interest and support:

PhoeniX Software, Software for micro- and nano technologies,
P.O. Box 545, 7500 AM Enschede, The Netherlands

MESA+ Institute for Nanotechnology, University of Twente,
P.O. Box 217, 7500 AE Enschede, The Netherlands

JCMwave GmbH
Bolivarallee 22, D-14050 Berlin, Germany

Optiwave, Design software for Photonics
7 Capella Court, Ottawa, ON K2E 7X1, Canada

IEEE Photonics Society
http://www.photonics-benelux.org/

Lumerical Solutions, illuminating the way
Suite 300 – 535 Thurlow Street, Vancouver, BC V6E 3L2, Canada

Focal Machine Vision and Optical Systems
Zutphenstraat 10-28, 7575 EJ Oldenzaal, The Netherlands

LioniX
PO Box 456, 7500 AL Enschede, The Netherlands

Preface

The 21st edition of the *International Workshop on Optical Wave & Waveguide Theory and Numerical Modelling (OWTNM)* will be held in Enschede, the Netherlands, on April 19 & 20, 2013. Since 1992, the annual workshop has been a forum for enthusiastic scientists in the field of integrated optics to exchange ideas, and to discuss problems, related to optical theory, computational modelling, and novel device concepts. The organizers hope and expect that the 21st OWTNM will be just as successful as the previous meetings.

Integrated optics must nowadays be seen in an evolutionary context of related fields such as photonic nanostructures, metamaterials, and plasmonics, not to speak of the established areas of optical micro-resonators or photonic crystals. With the continuously increasing available computing power, the emphasis of simulation techniques shifts towards the modelling of larger or more complex systems, towards higher dimensionality, or towards more rigorous simulations. The field has thus seen quite some broadening, when compared to its origins. Respective suggestions from the 2012 meeting of the OWTNM technical committee led to a slight modification of the title of the workshop, where the traditional term *waveguide* gave way to the broader *wave*. Some emphasis on the traditional problems of integrated optics remains with the *waveguide*-subscript. This change might be continued or reversed for future editions of the OWTNM; the slight shift of emphasis, however, is well perceptible in the technical program on the following pages.

The OWTNM 2013 encompasses 55 scientific contributions, including 9 invited talks, distributed over 8 oral and one poster session. The organization could benefit from the financial support of 8 companies and institutions, which will have posters on display in a separate section of the poster area. Adhering to a tradition of the OWTNM series, a special journal issue of *Optical and Quantum Electronics* will be organized on the occasion of the workshop.

We are looking forward to an enjoyable, scientifically inspiring OWTNM 2013.

Enschede, March 2013
The local organizing committee

Organizers

Local Organizing Committee OWTNM 2013

- Manfred Hammer, University of Twente, Netherlands
- Hugo J.W.M. Hoekstra, University of Twente, Netherlands
- Remco Stoffer, PhoeniX Software, Enschede, Netherlands
- Sonia Garcia-Blanco, University of Twente, Netherlands
- Milan Maksimovic, Focal Optical Systems, Netherlands
- Liantian Chang, University of Twente, Netherlands
- Mustafa Akin Sefunc, University of Twente, Netherlands

OWTNM Technical Committee

- Trevor Benson, University of Nottingham, UK
- Jiří Čtyroký, Institute of Electronics and Photonics, Czech Republic
- Manfred Hammer, University of Twente, Netherlands
- Andrei V. Lavrinenko, COM-DTU, Lyngby Kgs., Denmark
- Xavier Letartre, LEOM, Ecole Centrale de Lyon, France
- John Love, Australian National University, Australia
- Andrea Melloni, DEI-Politecnico di Milano, Italy
- Olivier Parriaux, University of Saint Etienne, France
- Reinhold Pregla, FernUniversität Hagen, Germany
- Ivan Richter, Chech Technical University, Chech Republic
- Christoph Wächter, Fraunhofer IOF, Jena, Germany

Programme

Workshop schedule

Friday, April 19, 2013

08:55	Welcome address
09:00 – 10:15	O-1: Methods & algorithms I
	Coffee break
10:45 – 12:00	O-2: Active structures
	Lunch
13:00 – 14:15	O-3: Functional devices
	Coffee break
14:45 – 16:00	O-4: Nanophotonics
	Drinks
16:00 – 18:00	P: Poster session
19:00	*Workshop dinner*

Saturday, April 20, 2013

09:00 – 10:15	O-5: Methods & algorithms II
	Coffee break
10:45 – 12:00	O-6: Metamaterials & nanostructures
	Lunch
13:00 – 14:15	O-7: Physical phenomena
	Coffee break
14:45 – 16:00	O-8: Plasmonics
16:00	Closing remarks

Friday, 09:00 – 10:15: *Methods & algorithms I*

09:00 O-1.1 P.A. Postigo (invited),
Three-dimensional finite-difference time-domain (3D-FDTD) methods for photonic crystal lasers, solar cells and quantum nanophotonics

09:30 O-1.2 M. Maksimovic,
Resonances in high-contrast gratings with complex unit cell topology

09:45 O-1.3 D.D. El-Mosalmy, M. Farhat, O. Hameed, N.F.F. Areed, S.S.A. Obayya,
Radial basis function neural network based optimization approach for photonic devices

10:00 O-1.4 C. Kluge, L.T. Neustock, J. Adam, M. Gerken,
Calculation of leaky-wave radiation from compound binary grating waveguides

Friday, 10:45 – 12:00: *Active structures*

10:45 O-2.1 M. Pollnau, M. Eichhorn (invited),
Theory of lasing resonators: Quality factor and line width

11:15 O-2.2 A. Liu, J. Pond,
Nonlinear and gain simulation in waveguide systems: methods and applications

11:30 O-2.3 S. Malaguti, G. Bellanca, A. Bazin, F. Raineri, R. Raj, S. Trillo,
Hybrid III-V semiconductor/silicon three-port Filter on 1D-PhC wire

11:45 O-2.4 J. Ctyroky,
Full-vector analysis of photonic structures with a balance of loss and gain

Friday, 13:00 – 14:15: *Functional devices*

13:00 O-3.1 T. Mizumoto, Y. Shoji (invited),
Magneto-optical nonreciprocal devices on silicon

13:30 O-3.2 M. Farhat, O. Hameed, A.M. Heikal, S.S.A. Obayya,
Passive polarization rotator based on spiral photonic crystal fiber

13:45 O-3.3 B.B. Oner, M. Turduev, I.H. Giden, H. Kurt,
Enhancing light manipulation by graded index photonic crystal media

14:00 O-3.4 A.-L. Fehrembach, K. Chan Shin Yu, A. Monmayrant, O. Gauthier-Lafaye, P. Arguel, A. Sentenac,
1D crossed guided mode resonant gratings for tunable filtering

Friday, 14:45 – 16:00: *Nanophotonics*

14:45 O-4.1 J. Knoester (invited),
Collective optical excitations in self-assembled molecular nanotubes for light-harvesting

15:15 O-4.2 V. Grigoriev, A. Tahri, S. Varault, B. Rolly, B. Stout, J. Wenger, N. Bonod,
Decomposition of Mie scattering coefficients and polarizabilities of nanoshell structures into Lorentzian resonances

15:35 O-4.3 S. She, Y.Y. Lu,
Extraordinary optical transmission through circular metallic cylinder arrays

15:45 O-4.4 D. Ketzaki, O. Tsilipakos, T.V. Yioultsis, E.E. Kriezis,
Electromagnetically induced transparency with hybrid silicon-plasmonic traveling-wave resonators

Friday, 16:00 – 18:00: Poster session

P-01 D.K. Sharma, A. Sharma,
Low-loss splicing of microstructured optical fibers and single-mode fibers: an analytical study

P-02 K. Gehlot, A. Sharma,
Simple analytical approach to optimize structure parameters of photonic crystal waveguide coupler

P-03 A. Parini, G. Calo, G. Bellanca, V. Petruzzelli,
Vertical links for multilayer optical-networks-on-chip topologies

P-04 Q. Cao, S. Li, D. Teng, H. Gao,
A terahertz waveguide coupler with a tapered dual elliptical metal structure

P-05 P. Kwieicen, V. Kuzmiak, I. Richter, J. Ctyroky,
Nonreciprocal waveguiding EM surfaces and structures for THz region

P-06 A.M. Heikal, M. Farhat, O. Hameed, S.S.A. Obayya,
Coupling characteristic for novel hybrid long-range plasmonic waveguide including bends

P-07 S.I.H. Ibrahim, S.S.A. Obayya,
Novel mixed finite element method analysis of leaky photonic nanowires

P-08 S.I.H. Ibrahim, S.S.A. Obayya, R. Letizia,
Efficient bidirectional beam propagation method for multiple longitudinal optical waveguide discontinuities

P-09 R. Stoffer,
Mode Polishing for 3D Finite Element BPM

P-10 M.G. Can, B.B. Oner, H. Kurt,
Numerical modeling of human eye with electromagnetic approach

P-11 A.-L. Fehrembach, A. Sentenac,
A vectorial simplified model for Fano resonances of guided-mode resonant gratings

P-12 A.-L. Fehrembach, D. Shu, E. Popov,
Electro-optic effect in guided mode resonance gratings for tunable narrow-band filtering

Friday, 16:00 – 18:00: Poster session

P-13 A. Auditore, M. Conforti, C. De Angelis, A.B. Aceves,
Solitons in binary waveguide arrays

P-14 Vinita, A. Kumar, V. Rastogi,
Bandgap maps for photonic crystal with honeycomb lattice for different shapes of scatterers

P-15 Z. Hu, Y.Y. Lu,
Standing waves on periodic arrays of circular dielectric cylinders

P-16 Babita, V. Rastogi,
Design and analysis of a low cost highly sensitive refractive index sensor

P-17 H.J.W.M. Hoekstra,
Integrated optics refractometry: sensitivity in relation to spectral shifts

P-18 F. Civitci, M. Hammer, H.J.W.M. Hoekstra,
Reflection of semi-guided plane waves at angled thin-film transitions

P-19 S.F. Helfert,
Time domain method of lines

P-20 M.A. Botchev,
Matrix exponential and Krylov subspaces for fast time domain computations: recent advances

P-21 J.P. Epping, M. Kues, P.J.M. van der Slot, C.J. Lee, C. Fallnich, K.-J. Boller,
Numerical modeling of seeded FWM in silicon nitride waveguides for CARS

P-22 E.K. Sharma, J. Anand,
Propagation of a periodic sequence of Gaussian pulses in a coaxial optical fiber: occurrence of "Talbot Effect" in the time domain

P-23 S.G. Moiseev, V.A. Ostatochnikov, D.I. Sementsov,
The peculiarities of optical spectra of photonic crystal with plasmonic defect

P-24 G. Boudarham, B. Rolly, B. Stout, R. Abdeddaim, J.M. Geffrin, N. Bonod,
Manipulating light matter interaction with Mie resonators

Saturday, 09:00 – 10:15: *Methods & algorithms II*

09:00 O-5.1 K. Busch (invited),
Discontinuous Galerkin methods in nano-photonics
09:30 O-5.2 A.A. Shcherbakov, A.V. Tishchenko,
Generalized source method in curvilinear coordinates
09:45 O-5.3 K. Gehlot, A. Sharma,
Modified optimal variational method to study modal characteristics of Si photonic wire waveguides
10:00 O-5.4 M. Blome, K. McPeak, S. Burger, F. Schmidt,
Back-reflector optimization in thin-film silicon solar cells by rigorous FEM light propagation modeling

Saturday, 10:45 – 12:00: *Metamaterials & nanostructures*

10:45 O-6.1 F. Lederer, S. Muhlig, C. Rockstuhl, R. Alaee, C. Menzel (invited),
Tailoring meta-atoms for specific metamaterial applications
11:15 O-6.2 J. Benedicto, E. Centeno, A. Moreau,
Lens equation for flat lenses made with hyperbolic metamaterials
11:30 O-6.3 S. Bin Hasan, C. Etrich, R. Filter, C. Rockstuhl, F. Lederer,
Tailoring the quadratic response of nanoantennas: use of a waveguide model
11:45 O-6.4 P.J. Compaijen, V.A. Malyshev, J. Knoester,
Transmission of optical excitations through a linear chain of metal nanoparticles in the presence of a reflector

Saturday, 13:00 – 14:15: *Physical phenomena*

13:00 O-7.1 J.L. O'Brien & collaborators (invited),
Integrated quantum photonics
13:30 O-7.2 W.L. Vos (invited),
Looking in and through opaque material
14:00 O-7.3 A.V. Tishchenko, O. Parriaux,
Intriguing relations between "pseudo-Brewster incidence" and the plasmon mode at a metal surface

Saturday, 14:45 – 16:00: *Plasmonics*

14:45 O-8.1 Z. Han, S.I. Bozhevolnyi (invited),
Modelling of plasmonic waveguides
15:15 O-8.2 W. Walasik, Y. Kartashov, G. Renversez,
Plasmon-soliton waves: towards realistic modelling
15:30 O-8.3 P. Kwiecien, J. Ctyroky, I. Richter,
Hybrid dielectric plasmonic slot guiding nanostructures — analysis with Fourier modal methods
15:45 O-8.4 A. Alparslan, Ch. Hafner,
Analysis of layered media plasmonic waveguides by Multiple Multipole Program

Abstracts

Three-dimensional finite-difference time-domain (3D-FDTD) methods for photonic crystal lasers, solar cells and quantum nanophotonics

Pablo A. Postigo

[1]*IMM-Instituto de Microelectrónica de Madrid (CNM-CSIC), Isaac Newton 8, PTM, E-28760 Tres Cantos, Madrid, Spain.*

* pabloaitor.postigo@imm.cnm.csic.es

We have used the three-dimensional finite-difference time-domain (3D-FDTD) method to design new optoelectronic devices based in two-dimensional photonic crystals. Two–dimensional photonic crystals have the big advantage of being highly compatible with many optoelectronic devices, allowing for a high control of the light in the nanoscale. Here we will present the 3D-FDTD method for 1) the design of photonic crystal lasers with low threshold and high quality factor [1], 2) simulations of the strong coupling regime in a photonic crystal cavity for quantum photonics [2] and 3) the design of photonic crystals for efficient light trapping in solar cells [3].

References

[1] I. Prieto, L. E. Munioz-Camuniez, J. Canet-Ferrer, A. Gonzalez-Taboada, J.M. Ripalda, G. Muñoz-Matutano, J. Martinez-Pastor and P. A. Postigo, *Room temperature lasing at 1.3 microns in GaAs-based photonic crystal cavities with a single layer of InAsSb quantum dots*, 31st ICPS 2012, Zurich, Switzerland, 2012.

[2] J. M. Llorens, I. Prieto, L. E. Muñoz, and P. A. Postigo, *FDTD description of strong coupling regime in InP photonic crystal microcavity*, Optics of Excitons in Confined Systems (OECS12), Paris, 2011

[3] J. Buencuerpo, L. E. Munioz-Camuniez, M. L. Dotor, and Pablo A. Postigo, *Optical absorption enhancement in a hybrid system photonic crystal – thin substrate for photovoltaic applications*, Optics Express 20, A452-A464 (2012)

Resonances in high-contrast gratings with complex unit cell topology

Milan Maksimovic
Focal Vision and Optics, Oldenzaal, The Netherlands
milan.maksimovic@focal.nl

We analyze origin and properties of the spectral resonances in sub-wavelength high-contrast gratings with complex unit cell topology. We show examples of novel resonances absent from the spectrum of simple periodic structures. Our results can be used as an initialization step in the grating topology optimization.

Summary

High-contrast gratings (HCGs) are the ultra-thin elements with the period smaller than the wavelength and with the high-index grating material fully surrounded by low-index material. Recently a plethora of novel applications emerged utilizing HCGs e.g.: ultra-broadband high reflectivity mirrors, high-quality-factor resonators, wavefront phase control for planar focusing reflectors and lenses [1]. We specialize to analysis of the high-quality factor resonances in the transmission or reflection spectrum using standard rigorous coupled wave analysis (RCWA) for numerical simulations. First, we investigate spectral response of systematically perturbed periodic HCGs with otherwise simple periodic topology. We show that the spectral response of HCGs is robust to the symmetric perturbations (e.g. periodic defects in the topology), while asymmetric perturbations introduce significant changes to the spectral response. Second, we analyze origin and properties of the spectral resonances in HCGs with the complex unit cell topology fixed as a particular generation of a deterministic aperiodic sequence (e.g. Thue-Morse, see [2]). We choose the global period to be smaller than the wavelength to preserve sub-wavelength nature of HCGs. Spectral response reveals a highly fragmented resonance features displaying hierarchical structure with some of the spectral resonances not present in the case of HCGs with simple unit cell topology (see Figure below). These topics are scarcely explored in the literature on HCGs. Our analysis points to a systematic way to utilize new degrees of freedom in tailoring spectral response of HCGs similar to approaches used in the field of photonic quasi-crystals [2]. Moreover, our methodology and analysis can be used for selection of the efficient initial topology for the design and the topology optimization of the finite aperiodic HCGs.

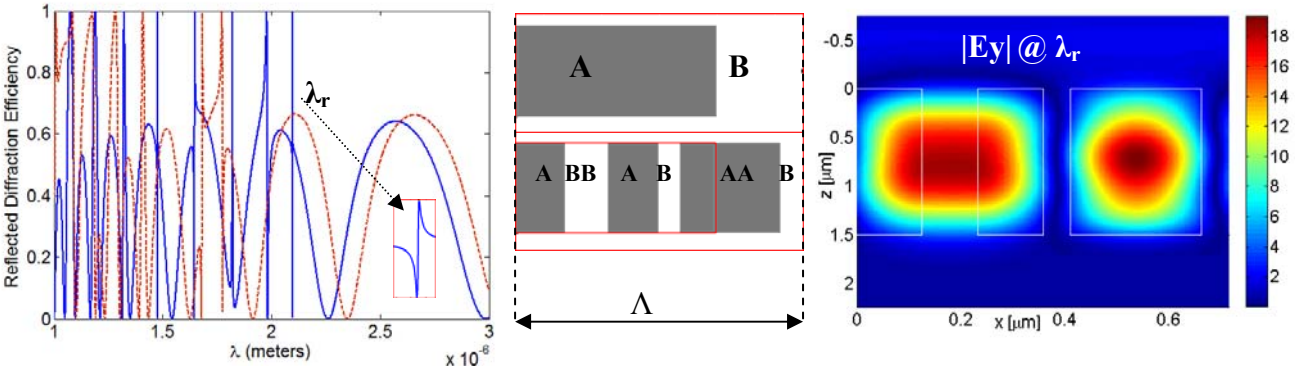

Spectral reflection response for TE –polarization (left) of HCG with the simple (dashed) and complex (solid)unit cell topology. Grating topology (center) for simple (center: top) and complex (center: bottom) unit cell with the high index bars of refractive index 3.48 (labeled A) embedded in air with refractive index 1 (labeled B). Parameter of gratings: height=1.494μm, period Λ=0.716 μm and duty cycle of 0.7 for simple unit cell (parameters chosen from [1] to enable comparison). Complex unit cell topology follows the 3rd generation Thue–Morse sequence (ABBABAAB) with the same global period and preserves volumetric content of the high and low index material as in the case of the simple unit cell Modulus of the electric field (right) in the complex unit cell at the resonance wavelength λ_r=2.0968 μm with nearly perfect reflection (boundaries show region with the high index material).

References

[1] C. J. Chang-Hasnain and W. Yang, *Advances in Optics and Photonics,* (4) 379, 2012
[2] E. Macia**,** *Reports on Progress in Physics*, (75) 036502, 2012

Radial Basis Function Neural Network Based Optimization Approach for Photonic Devices

Dalia D. El-Mosalmy[2], Mohamed Farhat O. Hameed[1], Nihal F. F. Areed[1], S. S. A. Obayya[1*]

[1]*Centre for Photonics and Smart Materials, Zewail City of Science and Technology, Sheikh Zayed District, 6th of October City, Giza, Egypt. * sobayya@zewailcity.edu.eg*
[2] *Faculty of Engineering, Mansoura University, Egypt*

A novel optimization technique based on radial basis function artificial neural network is proposed for designing photonic devices. The robustness of the suggested approach is demonstrated through the numerical precision and fast convergence of the design cycle performed on a slanted rib waveguide polarization rotator.

Analysis and Simulation Results

Our aim is to find an accurate method to optimize and design photonic devices with high accuracy and short computational time. The suggested approach relies on the use of radial bases function based artificial neural network (RBF-ANN) which shows excellent performance, and rapid convergence in comparison with conventional artificial neural network (ANN) technique. The RBF-ANN as shown in Fig. 1 consists of three layers, input, hidden and output layers. The RBF-ANN uses Gaussian transfer function as radial basis function in the hidden layer. The suggested approach is used for design and analysis of photonic devices such as passive polarization rotator (PR) based on slanted rib waveguide as shown in Fig.2 to obtain high conversion ratio with small device length. Therefore, it is required to maximize the ratio between the conversion ratio and the device length. In the RBF-ANN approach, the full vectorial finite difference method (FVFDM) and full vectorial finite difference beam propagation method (FVFD-BPM) to obtain the conversion lengths L_C and maximum conversion powers P_{max}, simultaneously of the studied PR with different rib refractive indices and with different slant angles θ within a certain range of wavelengths. The calculated values of the ratio $R= P_{max}/ L_C$ are used in the training process of the RBF-ANN. Therefore, the input layer of the RBF-ANN has three neurons in order to define the input parameters λ, rib refractive index n_g, and slant angle θ. The three input parameters and interconnection weights are processed by a summation function and passed first to the transfer function in the hidden layer and then to the output layer. The output layer contains only one neuron in order to define the required parameter, R. The trained RBF-ANN can then be used to evaluate the ratio R accurately for a given rib refractive index at a specific wavelength and slant angle θ within the trained data range. Consequently, PR structure can be obtained at the desired wavelength λ with maximum ratio R at which maximum power conversion and minimum conversion length occur. The radial basis function provides a rapid and an accurate learning process. This approach overcomes the meshing problems and time consuming of other numerical modelling methods. In addition, the numerical results of the proposed approach are in excellent agreement with that of the FVFDM and FVFD-BPM which proves the robustness of the suggested approach. More results will be presented in the conference.

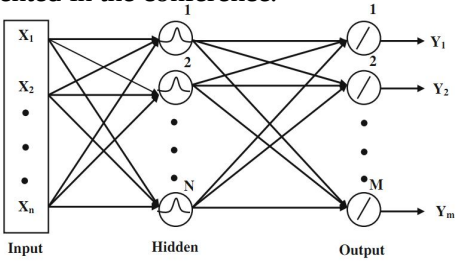

Fig.1 Schematic diagram of the RBF-ANN

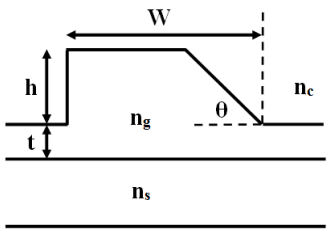

Fig.2 Schematic representation of a single-section PR

Calculation of leaky-wave radiation from compound binary grating waveguides

C. Kluge [1], L.T. Neustock [1], J. Adam [1,2], M. Gerken [1]

[1] *Institute of Electrical and Information Engineering, Christian-Albrechts-Universität zu Kiel, Kiel, Germany*
[2] *Electrical Engineering Department, University of California, Los Angeles, USA*
ckl@tf.uni-kiel.de

We present and validate rigorous coupled-wave calculations of waveguide binary gratings with multiple space-frequencies generated by superposition of different grating pitches. In the leaky-wave radiation pattern, the grating components produce pronounced directions.

Summary

In organic light-emitting diodes (OLEDs), high-index layer structuring is used to increase guided light outcoupling efficiency. Waveguide corrugation design is important to control the radiation pattern [1]. A single-pitch grating leads to sparse angle-dependent outcoupling peaks, which is potentially undesirable, e.g., in lighting applications. We investigate compound binary gratings combining two or more binary gratings with different pitches by logical disjunction [2]. We implemented a rigorous coupled-wave analysis (RCWA) [3] to find the leaky modes' complex propagation constants in a corrugated waveguide geometry (inset Fig. 1) and calculate the leaky-wave radiation without external excitation. The results are validated by finite-difference time-domain (FDTD) simulations (Fig. 1).

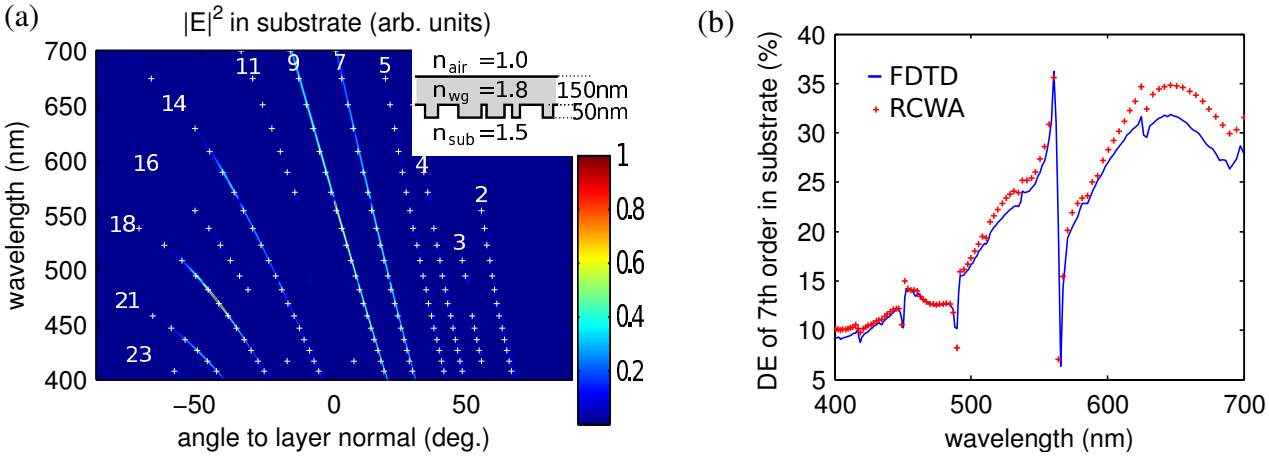

Fig. 1. The waveguide-to-substrate TE0 leaky-wave radiation, with a 350nm and 450nm pitch compound binary grating (total pitch 3150nm), shows good agreement between FDTD (background; solid line) and RCWA (crosses) calculations. (a) FDTD electric field intensity simulation, superimposed with RCWA diffraction angles. Numbers indicate the diffraction order. The 7th and 9th order correspond directly to the 450nm and 350nm grating component diffraction angles, respectively, and show the highest intensity over a wide wavelength range. (b) Exemplarily shown 7th order diffraction efficiency (DE).

References

[1] U. Geyer, J. Hauss, B. Riedel, S. Gleiss, U. Lemmer, and M. Gerken. *J. Appl. Phys.*, 104(9):093111, 2008.
[2] C. Kluge, M. Rädler, A. Pradana, M. Bremer, P.-J. Jakobs, N. Barié, M. Guttmann, and M. Gerken. *Opt. Lett.*, 37(13):2646, 2012.
[3] M. Moharam, E. Grann, D. Pommet, and T. Gaylord. *J. Opt. Soc. Am. A*, 12(5):1068, 1995.

Theory of Lasing Resonators: Quality Factor and Line Width

M. Pollnau[1,*], M. Eichhorn[2]
[1] *MESA+ Institute for Nanotechnology, University of Twente, Enschede, The Netherlands*
[2] *Institut Franco-Allemand de Recherches de Saint-Louis, Saint-Louis, France*
* m.pollnau@utwente.nl

This paper defines the quality factor of a continuous-wave laser and relates it to the laser line width.

The contradiction

The *Q*-factor of a passive resonator is defined as the energy stored in the resonator, E_{stored}, over the energy lost per oscillation cycle, E_{lost},

$$Q_c = 2\pi \frac{E_{stored}(t)}{E_{lost}(t)} = 2\pi \frac{\phi(t)}{-\frac{1}{\nu}\frac{d}{dt}\phi(t)} = 2\pi\nu\tau_c .$$

Here, the energy $E = h\nu V_{mode}\phi$ relates to the density ϕ of photons in the resonator via the single-photon energy $h\nu$ at frequency ν and the resonator mode volume V_{mode}. A Fourier transformation, resulting in

$$\tau_c = \frac{1}{2\pi\Delta\nu_c} ,$$

relates the photon decay time τ_c to the resonator line width $\Delta\nu_c$.

Current laser theories start from the assumption that in the resonator the gain equals the losses, i.e., the resonator losses quantified by the photon decay time τ_c are fully compensated by the generation of identical copies of photons in the resonator via stimulated emission. Consequently, there is no energy lost, $E_{lost} = 0$, and the *Q*-factor Q_L of a lasing resonator becomes infinitely high or is considered to be undefined. On the other hand, according to the derivation by Gordon, Zeiger, and Townes [1] for the microwave regime and its adaption to the optical regime by Schawlow and Townes [2] the laser line width is finite, thus resulting in a finite *Q*-factor,

$$Q_L = \frac{\nu}{\Delta\nu_L} .$$

The solution

By systematically including spontaneous emission into the calculation, we show that the *Q*-factor of a lasing resonator is finite, because the gain becomes smaller than the losses and, consequently, any coherent state inside the laser resonator decays with half the coherence time of the emitted laser light. The Schawlow-Townes line width of a laser is then straight-forwardly derived.

References

[1] J. P. Gordon, H. J. Zeiger, C. H. Townes, *The maser−New type of microwave amplifier, frequency standard, and spectrometer*, Phys. Rev. **99**, 1264–1274 (1955)

[2] A. L. Schawlow, C. H. Townes, *Infrared and optical masers*, Phys. Rev. **112**, 1940–1949 (1958)

Nonlinear and gain simulation in waveguide systems: methods and applications

A. Liu[1*], J. Pond[1]
[1] Lumerical Solutions, Inc, *Vancouver, BC, Canada*
* aliu@lumerical.com

We demonstrate how Lumerical's nonlinear material models, in combination with linear dispersion models, enable accurate modeling of nonlinear and gain phenomena in SOI waveguides and other systems. Examples include soliton propagation in waveguides, four-wave mixing, and lasing.

Simulation methodologies, the material plugin framework and anisotropy

As more complex nonlinear functionality is considered in waveguide systems [1], it is important to develop methods for omnidirectional propagation with arbitrary scattering. We show how a combination of eigenmode analysis and FDTD simulations can be used to model nonlinear effects in bidirectional and omnidirectional guided wave components by including an arbitrary polarization (or magnetization) update which can be added to any existing linear dispersive material. This polarization update is introduced using an open plugin framework. Nonlinear $\chi^{(2)}$, Raman and Kerr $\chi^{(3)}$, and four-level two-electron models with customizable source code have been created, and other models can be easily added and modified. Anisotropic nonlinear terms can be handled by performing a local unitary transformation to update the polarization in a reference frame where the nonlinearity is isotropic, such as one aligned with the crystalline axes [2].

Soliton propagation in SOI systems, four-wave mixing (FWM), gain models and lasing

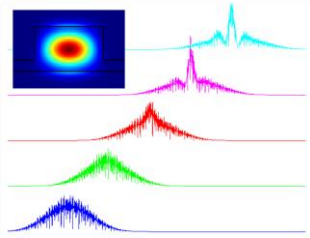

Soliton formation for the waveguide shown in the inset [3].

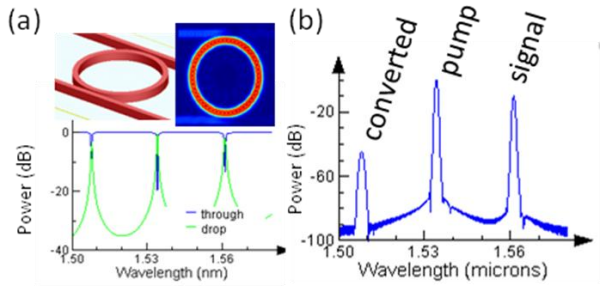

FWM in an SOI ring similar to a design in InP [4]. (a) Linear through and drop power. (b) Spectrum showing the pump, signal and converted light.

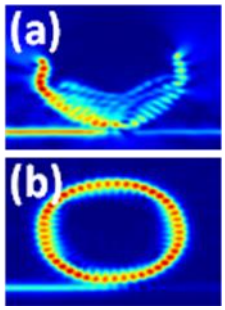

The field at 18ps (a) and 45ps (b) in a micro-disk laser as the mode is established

References

[1] Q. Lin, O.J. Painter, G. Agrawal, *Nonlinear optical phenomena in silicon waveguides: Modeling and Applications*, Opt. Express **15**, 16604-16644, 2007

[2] U.S. Patent Application No. 61/650,774, Unpublished (filing date May 23, 2012) (James Pond, applicant)

[3] V.M.N. Passaro, F. De Leonardis, *Solitons in SOI Optical Waveguides*, Adv. Studies Theor. Phys., **2**, 769-785, 2008

[4] C. Koos, M. Fujii, C.G. Poulton, R. Steingrueber, J. Leuthold, W. Freude, *FDTD-Modelling of Dispersive Nonlinear Ring Resonators: Accuracy Studies and Experiments*, IEEE J. of Quantum Electronics, **42**, 1215–1223, 2006

Hybrid III-V Semiconductor/Silicon Three-Port Filter on 1D-PhC Wire

S. Malaguti[1*], G. Bellanca[1], A. Bazin[2], F. Raineri[2], R. Raj[2], S. Trillo[1]
[1]*Department of Engineering, University of Ferrara, Via Saragat 1, 44122 Ferrara, Italy*
[2]*Laboratoire de Photonique et de Nanostructures, CNRS, Marcoussis, France*
*stefania.malaguti@unife.it

In this work we report on the design of a three port channel drop filter at 1550 nm on InP embedded on SOI substrate. The structure is built with two cavities realized on a 1D-PhC wire and properly coupled to exploit the resonant-tunneling reflection-feedback effect. A suitable mirror on the drop photonic wire waveguide has also been used to maximize the drop efficiency. The structure is fed through a silicon wire, vertically coupled with the 1D-PhC double-cavity structure. Simulation results will be compared with measurements.

Introduction

Heterogeneous integration of III-V semiconductors on Silicon is one the key technology for next-generation on-chip optical interconnects. This technology, in fact, enables the realization of sources [1], detectors [2] and control circuits [3] on the same chip by combining the superior silicon waveguiding capabilities with the efficient stimulated emission properties of direct band-gap of III-V materials.

Results

A sketch of the proposed Si/III-V semiconductor three-port filter is represented on the left side of Fig. 1. The bus is realized with a Si waveguide on a silica substrate embedded in BCB. InP photonic wires embedded in silica, on the contrary, are used for the double cavity and bus waveguide. Preliminary results illustrated on the right side of Fig. 1 report good drop efficiency (78%) and extinction ratio (-21dB). The 3dB linewidth of the proposed filter is of about 2.2 nm.

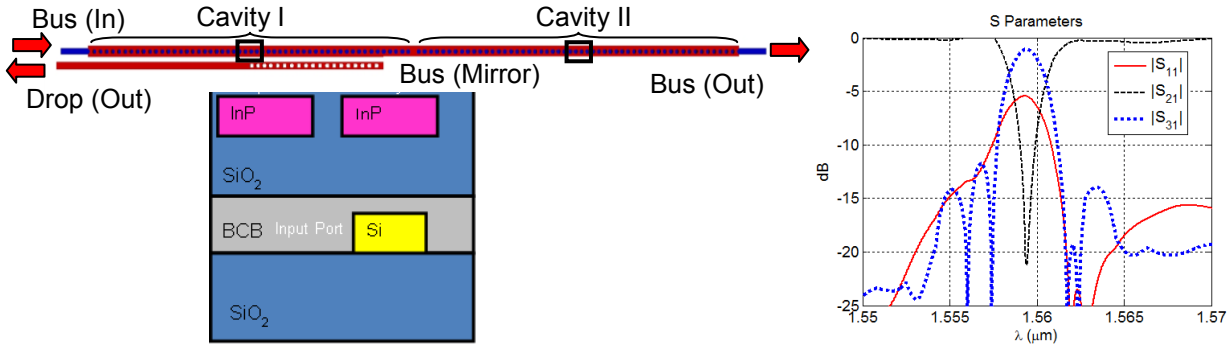

Fig. 1 On the left: sketch of the proposed device. Top view of the double cavity structure coupled with the bus waveguide and lateral view of the layered structure in vertical direction. On the right: S parameters computed by 3D-FDTD of the filter as a function of the wavelength. S_{11}: reflection coefficient at the input port; S_{21} transmission trough the bus; S_{31} transmission through the drop port.

References

[1] Y. Alioua et al., *Hybrid III-V semiconductor/silicon nanolaser*, Optics Express, Vol. 19, No. 10, 2011.

[2] L. Ottaviano et al., *High-speed photodetectors in a photonic crystal platform*, CLEO (CM1A), San Jose, California, May 6 (2012).

[3] S. Combrié et al., *Demonstration of Optically Controlled re-Routing in a Photonic Crystal Three-Port Switch*, IPRSN, Colorado Springs, CO, USA, 17th June 2012.

Full-vector analysis of photonic structures with a balance of loss and gain

J. Čtyroký
Institute of Photonics and Electronics AS CR, v.v.i., Prague, Czech Republic
ctyroky@ufe.cz

Waveguide structures with a balance of loss and gain are still more frequently discussed in the photonic community not only as photonic analogues of quantum-mechanical systems with parity-time symmetry (breaking), but also as components with potentially interesting technical applications. In this contribution we study the properties of gain/loss structures in full-vector approach, and consider also some more general cases of permittivity distribution exhibiting the behaviour analogous to *PT*-symmetry breaking.

Waveguide structures with a balance of loss and gain

Peculiar features of optical wavegide structures with a balance of loss and gain have been analyzed already more than 15 years ago [1]. Only comparatively recently these structures become rather popular as photonic analogues of quantum-mechanical systems with parity-time (*PT*) symmetry [2-4]. Since then, a number of other studies, mostly theoretical, have been published. In our first paper [1] we showed the existence of the critical (branching) point on the dispersion curves of the two-mode structure with permittivity distribution satisfying the relation $\varepsilon(-x) = \varepsilon^*(x)$ in the 2D, i.e., essentially scalar approximation. In this contribution we show that the basic character of gain/loss structures – the existence of a critical gain/loss value at which the behaviour of the structures is dramatically changed – is fully retained also in the 3D full-vector case, and to some extent also in a more general case of 2D permittivity distribution retaining the symmetry of the type $\varepsilon(-x, y) = \varepsilon(x, -y) = \varepsilon^*(x, y)$.

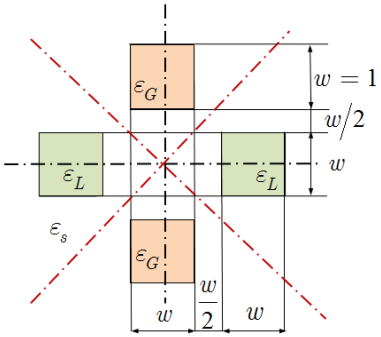

Figure 1. The cross section of the waveguide structure

Just as an example of the latter structure we briefly discuss results of the full-vector numerical analysis [5] of a 4-channel waveguide structure shown in Fig. 1. If each individual channel supports propagation of 2 (degenerate) modes of different polarizations, four from the total of 8 modes propagate without any singularity on the dispersion curves and exhibit either loss or gain, while the other four modes create two pairs of modes that exhibit the behaviour analogous to the "*PT* symmetry breaking". Weak perturbation of the gain/loss balance results in a rather smooth modification of the dispersion curves similar to the 2D case. Other cases will be discussed, too.

References

[1] H.-P. Nolting, G. Sztefka, M. Grawert, and J. Čtyroký, "Wave Propagation in a Waveguide with a Balance of Gain and Loss," in *Integrated Photonics Research '96*, Boston, USA, 1996, pp. 76-79.

[2] R. El-Ganainy, K. G. Makris, D. N. Chrisodoulides, and Z. H. Musslimani, "Theory of coupled optical PT-symmetric structures," *Optics Letters*, vol. 32, pp. 2632-2634, 2007.

[3] K. G. Makris, R. El-Ganainy, and D. N. Chrisodoulides, "Beam Dynamics in PT Symmetric Optical Lattices," *Physical Review Letters*, vol. 100, pp. 103904(1)-103904(4), 2008.

[4] C. E. Ruter, K. G. Makris, R. El-Ganainy, D. N. Christodoulides, M. Segev, and D. Kip, "Observation of parity-time symmetry in optics," *Nature Physics*, vol. 6, pp. 192-195, 2010.

[5] J. Čtyroký, "3-D Bidirectional Propagation Algorithm Based on Fourier Series," *J. Lightwave Technol.*, vol. 30, pp. 3699-3708, 2012.

Magneto-optical Nonreciprocal Devices on Silicon

T. Mizumoto* and Y. Shoji
Department of Electrical and Electronic Engineering, Tokyo Institute of Technology, Japan
** tmizumot@pe.titech.ac.jp*

Optical nonreciprocal devices such as isolators and circulators play unique roles in photonic circuits. The magneto-optic effect is important to realize the optical nonreciprocal function. In this article, magneto-optical nonreciprocal devices are discussed that are based on silicon waveguide platforms.

Introduction

The optical isolator provides one-way transmittance of light waves, which is used to prevent unwanted lightwave from launching into optically active devices. The optical circulator is important for constructing a highly functional photonic circuit. For example, it is used to build an optical add drop multiplexer together with a Bragg reflector. In an optical waveguide, it is hard to take TE-TM mode phase matching inevitable in a mode conversion isolator, which is similar to a bulk Faraday isolator. In order to overcome the difficulty, use of nonreciprocal phase shift given by a magneto-optical effect is effective especially in building nonreciprocal devices on a silicon waveguide platform.

Optical nonreciprocal devices based on magneto-optical phase shift

A magneto-optical phase shifter provides $-\pi/2$ phase difference between two interferometer arms in the rightward propagation direction and $\pi/2$ in the leftward direction, where the phase difference is measured in the upper arm with respect to the lower arm. A built-in phase bias provides a phase difference of $\pi/2$ independent of the light propagation direction. Constructive and destructive interferences occur in in the rightward and leftward directions, respectively, by combining the magneto-optical phase shift and the phase bias. An isolation of 28 dB was reported in a Mach-Zehnder interferometer (MZI) isolator, where a magneto-optical garnet Ce:YIG was directly bonded to a silicon waveguide [1].

A ring resonator equipped with a magneto-optical phase shift exhibits different resonant wavelengths depending on the propagation direction. Therefore, the transmittance in a bus line coupled with the resonator is dependent on the propagation direction at resonant wavelengths. An isolation of 20 dB was reported in a device fabricated by depositing a polycrystalline Ce:YIG on a silicon ring resonator [2].

By replacing the optical branching devices of MZI isolator with 3 dB directional couplers, a 4-port optical circulator was fabricated in a silicon nanowire waveguide with a maximum isolation of 15.3 dB at 1531 nm [3].

References

[1] Y. Shirato, Y. Shoji, T. Mizumoto, *High isolation in silicon waveguide optical isolator employing nonreciprocal phase shift*, OFC 2013, Anaheim, USA, OTu2C.5, 2013

[2] L. Bi, J. Hu, P. Jiang, D.-H. Kim, G. F. Dionne, L. C. Kimerling, and C. A. Ross, *On-chip optical isolation in monolithically integrated non-reciprocal optical resonators*, Nature Photon., 758-762, 2011

[3] K. Mitsuya, Y. Shoji, T. Mizumoto, *The first demonstration of silicon waveguide optical circulator*, OFC 2013, Anaheim, USA, JTh2A.25, 2013

Passive Polarization Rotator Based on Spiral Photonic Crystal Fiber

Mohamed Farhat O. Hameed, A. M. Heikal, S. S. A. Obayya*

*Centre for Photonics and Smart Materials, Zewail City of Science and Technology, Sheikh Zayed District, 6th of October City, Giza, Egypt. * sobayya@zewailcity.edu.eg*

A novel design of passive ultra-compact polarization rotator (PR) based on spiral tellurite photonic crystal fiber is proposed and analyzed using full vectorial finite difference approaches. The reported PR offers 97% polarization conversion ratio with ultra compact device length of 98 μm.

Simulation Results

Figure 1 shows cross section of the suggested polarization rotator (PR). The proposed design relies on using tellurite spiral PCF (TS-PCF) with eight arms and a central air hole. The central air hole of radius r_{h2} can be shifted equally in x and y directions to achieve complete polarization rotation. The first hole in each spiral arm is considered at a distance, $r_0 = r_c + r_h$ from the center where r_c and r_h are the radius of the core and cladding air holes, respectively. The distance of the second air hole of each arm from the center is taken as $r_1 = r_0 + 0.8(2r_h)$ with an angular displacement of $\theta_1 = 360^o/(2N)$, where N is the number of arms. Therefore, the n'th air hole in each arm is at a distance of $r_n = r_{n-1} + 0.8\times(2r_h)$ with an angular displacement of $\theta_n = (n\times 360^o)/(2\times N)$ from the first one. Therefore, the first, second, and third hole of each arm constitute the first, second, and third ring, respectively. In this study, r_c, r_h are taken as 0.7 μm, 0.3μm, respectively. In addition, the central hole of radius 0.25 μm is shifted equally in x and y directions by 0.36 μm. Moreover, the tellurite refractive index is fixed to 2.0278 at the operating wavelength 1.55 μm. The suggested TS-PCF PR offers polarization conversion ratio of almost 97% with a ultra compact device length of 98 μm as shown in Fig.2. The reported structure does not require a complex fabrication process like the semiconductor waveguide with slanted sidewalls. Therefore, the spiral TS-PCF PR is much shorter than single and multiple sectioned passive PRs with L-shaped core region [1] of device lengths of 1743 μm and 1265 μm, respectively. Moreover, the suggested PR is shorter than the triangular lattice silica PCF PR with device length of 206 μm [2]. More results will be presented in the conference.

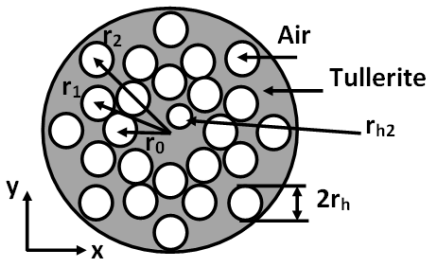

Cross section of the suggested spiral PCF PR

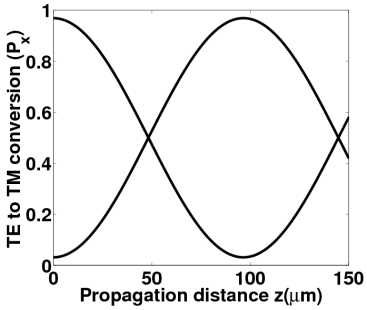

Evolution of the TM powers for the TE excitation along the propagation direction

References

[1] M. F. O. Hameed, S. S. A. Obayya, H. A. El-Mikati, and H. A. El-Mikati," Passive Polarization Converters Based on Photonic Crystal Fiber With L-Shaped Core Region " *J. of Lightwave Technol.*, vol. 30, pp. 283-289, 2012

[2] M.F.O. Hameed, Maher Abdelrazzak, S.S.A. Obayya, "Novel Design of Ultra-Compact Triangular Lattice Silica Photonic Crystal Polarization Converter", *IEEE J. Lightwave Technology*, vol. 31, no. 1, page 81-86, January 1, 2013

Enhancing Light Manipulation by Graded Index Photonic Crystal Media

B. B. Oner[1]*, M. Turduev[1], I. H. Giden[1], H. Kurt[1]
[1] *Nanophotonics Research Laboratory, Department of Electrical and Electronics Engineering TOBB University of Economics and Technology, 06560, Ankara, Turkey*

* bilgehan.oner@gmail.com

Various light manipulation scenarios including self-collimation, mode conversion, beam bending, and coupling properties of graded index (GRIN) media are explored. Specifically designed GRIN media yields impressive results with broad bandwidths that cover both lower and higher frequency regimes.

Photonic crystals (PCs) are periodic dielectric media that enable extraordinary manipulation of electromagnetic waves. Although the concept of GRIN media comprises different elemental parts from the basic PCs, combining GRIN and PC concepts enlarges the range of the photonic devices' area of usage. Refractive index profile of a GRIN medium gradually varies from point to point. Adjusting the gradient profile of the media enables one to design various integrated optical devices, such as couplers, spatial mode converters and waveguide bends [1-3]. In order to obtain the GRIN profiles, lattice spacing in the transverse direction of each cell is chosen as a variable while lattice spacing in the longitudinal directions is fixed at unit distance.

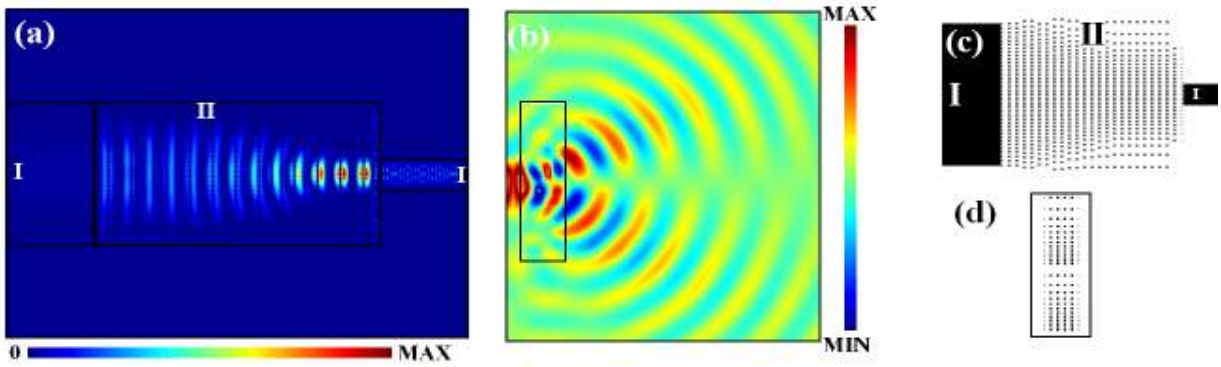

Figure 1 (a) *Intensity distribution of the GRIN PC coupler and (b) electric field distribution of GRIN PC spatial mode converter. Schematic representations of (c) GRIN PC coupler and (d) GRIN PC spatial mode converter.*

To date numerous studies about GRIN media and its' applications are reported. Nevertheless, many of them suffered from narrow bandwidth or being able to realize only for lower frequency regime. Our GRIN PC design method provides high transmission efficiency over broad bandwidth. Besides, we also realize superior property of being polarization insensitive. Fig. 1(a) demonstrates a compact optical waveguide coupler whose schematic forms is indicated in Fig. 1(c). Mode conversion process is shown in Fig. 1(b) and the corresponding schematic view is presented in Fig. 1(d). The details of the designs and optical characteristics of the inhomogeneous media will be presented in the conference.

References

[1] H. Kurt, B. Oner, M. Turduev, and I. Giden, *Modified Maxwell fish-eye approach for efficient coupler design by graded photonic crystals*, Opt. Express **20**, 22018-22033 (2012).

[2] B. Oner, M. Turduev, I. H. Giden, and H. Kurt, *Efficient mode converter design using asymmetric graded index photonic structures*, Opt. Lett. **38**, 220-222 (2013).

[3] H. Kurt and D. S. Citrin, *Graded index photonic crystals*, Opt. Express **15**, 1240-1253 (2007).

1D crossed guided mode resonant gratings for tunable filtering

A.-L. Fehrembach [1], K. Chan Shin Yu [2,3], A. Monmayrant [2,3], O. Gauthier-Lafaye [2,3], P. Arguel [2,3] and A. Sentenac [1]

[1] *Aix Marseille Université, CNRS, Ecole Centrale Marseille, Institut Fresnel, 13013 Marseille, France*
[2] *CNRS; LAAS; 7 avenue du Colonel Roche, F-31077 Toulouse, France*
[3] *Université de Toulouse, UPS, INSA, INP, ISAE; LAAS; F-31077 Toulouse, France*
anne-laure.fehrembach@fresnel.fr

We propose a narrow band, polarization independent filter tunable with respect to the angle of incidence over a 100 nm range. We explain its physical principles and show that its performances are reachable experimentally.

Guided mode resonance filters (GMRF) are composed with a planar waveguide structured with a subwavelength periodic pattern. The excitation of an eigenmode via a diffraction order leads to a resonance peak in the reflectivity spectrum of the structure. The peak can be very narrow (Q factor greater than 15000 in practice) and its centering wavelength is linearly tunable with respect to the angle of incidence. These properties are very interesting for example for imaging spectroscopy. But the peak depends strongly on the polarization of the incident wave in basic configurations.

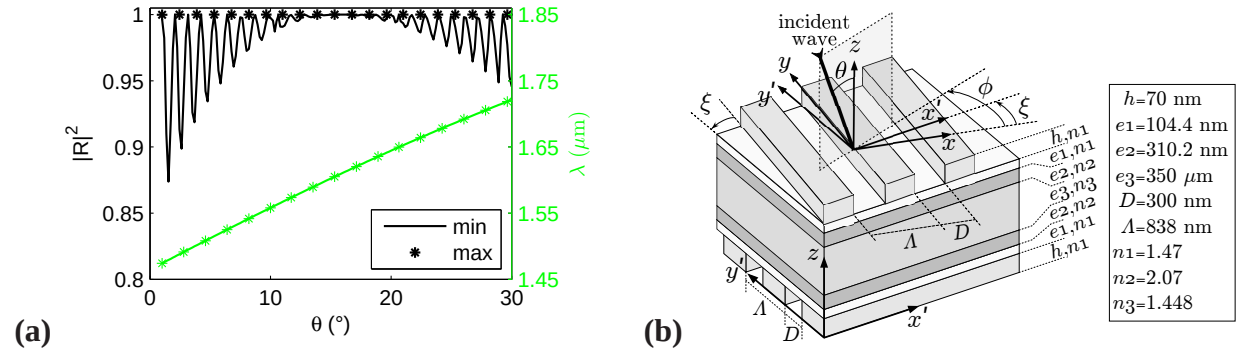

Fig. 1. (a) configuration, (b) minimum and maximum of reflectivity when the incident polarization varies, and resonance wavelength versus the polar angle of incidence.

We present a simple, yet promising configuration [1] able to generate a 0.1nm width (at 1550nm) polarization independent peak, angularly tunable over a wide range (100 nm) (see Figure (a)). The structure is composed with two identical multilayer stacks deposited on each side of a substrate, on top of which two identical 1D gratings are engraved, but with different directions of periodicity (see Figure (b)). This configuration differs from the reported configurations [2] in its basic principle, and being composed with 1D gratings, it is easier to fabricate. A prototype is into characterization process.

ACKNOWLEDGEMENT: The financial support of the CNES in this work is gratefully acknowledged.

References

[1] A. Monmayrant, O. Gauthier-Lafaye, A.-L. Fehrembach, K. Chan Shin Yu, A. Sentenac, P. Arguel, and J. Loesel. Filtre optique a reseaux resonnants insensible a la polarisation accordable en fonction de langle dincidence, 2011.

[2] A.-L. Fehrembach and A. Sentenac. Study of waveguide grating eigenmodes for unpolarized filtering applications. *J. Opt. Soc. A.*, 20:481–488, 2003.

COLLECTIVE OPTICAL EXCITATIONS IN SELF-ASSEMBLED MOLECULAR NANOTUBES FOR LIGHT-HARVESTING

Jasper Knoester[1]

[1] *Zernike Institute for Advanced Materials, University of Groningen, Nijenborgh 4, 9747 AG Groningen The Netherlands*
E-mail: j.knoester@rug.nl

Self-assembly is a promising route towards designing new nanoscale functional materials. In this talk, I will address self-assembled systems consisting of thousands of dye molecules with optical functionality. The collective optical excitations in such systems are Frenkel excitons. Their static and dynamic properties are responsible for the optical response of the aggregate. The excitons are governed by a complex interplay between intermolecular resonance interactions that delocalize the excitations and interactions with slow and fast degrees of freedom in the environment that lead to static and dynamic disorder, which counteract exciton delocalization and cause decoherence. Optical properties of special interest are motional narrowing, exciton superradiance, strong optical nonlinearities, and ultrafast energy transport. While these properties are interesting in their own right, they also may be used for applications, for instance in artificial light-harvesting systems and all-optical switches.
In this talk, I will focus in particular on tubular aggregates [1], which currently attract much attention. These systems, consisting, for instance, of cyanine molecules [2] or porphyrin derivatives [3], have recently attracted strong attention. They closely resemble in size (diameter approx 10 nm, length up to microns) and properties antenna systems that occur in bacterial light-harvesting systems. I will report on joint experimental-theoretical studies of the exciton dynamics and the resulting optical response of such aggregates [1-4]. Near-field optical experiments as well as various ensemble measurements can be well explained using phenomenological modeling and yield a model for the microscopic structure of the aggregate. Current research aiming at a first-principles modeling of the structure and optics of molecular aggregates will be introduced.

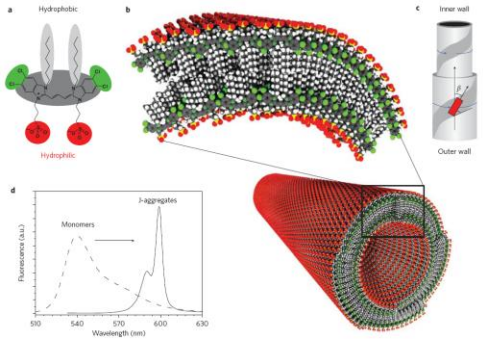

Figure: Double-walled aggregate of the amphiphilic cyanine dye C8S3, with fluorescence spectrum [2].

[1] C. Didraga, J.A. Klugkist, and J. Knoester, J. Phys. Chem. B **106**, 11474 (2002).
[2] D.M. Eisele, J. Knoester, S. Kirstein, J.P. Rabe, and D. Vanden Bout, Nature Nano **4**, 658 (2009).
[3] S.M. Vlaming, R. Augulis, M.C.A. Stuart, J. Knoester, and P.H.M. van Loosdrecht, J. Phys. Chem. B **113**, 2273 (2009); A. Stradomska and J. Knoester, J. Chem. Phys. **133**, 094701 (2010).
[4] D.M. Eisele, …, J. Knoester, J.P. Rabe, and D.A. Vandenbout, Nature Chemistry **4**, 655 (2012).

Decomposition of Mie scattering coefficients and polarizabilities of nanoshell structures into Lorentzian resonances

V. Grigoriev*, A. Tahri, S. Varault, B. Rolly, B. Stout, J. Wenger, N. Bonod
Institut Fresnel, CNRS, Aix Marseille Université, Ecole Centrale Marseille, Marseille, France
* victor.grigoriev@fresnel.fr

The analytical properties of the scattering matrix are applied to explain the frequency response of nanoshell structures. Their polarizabilities are decomposed exactly into resonances of Lorentzian shape regardless of material dispersion and nonlocal effects, if the size of particles becomes comparable to wavelength of light.

Coupled oscillator models for nanostructures

The ability to engineer the resonant properties of nanoparticles helps to strengthen their interaction with light, which is of utter importance for a number of practical applications. Such engineering is usually achieved by hybridization of plasmonic modes in nanoshell structures [1]. Nevertheless, the models based on coupled oscillators do not establish a firm link between the resonant properties of the structures and their actual frequency response. In particular, they do not treat consistently the excitation of multiple resonances and ignore nonlocal effects caused by the retardation of the signals.

Perfectly emitting and absorbing modes as a uniform basis for decomposition

We show that the frequency response of nanoshell structures can be completely restored from the analytical properties of the scattering matrix $S(\omega) = a_{\text{out}} / a_{\text{in}}$, which relates the amplitudes of outgoing a_{out} and incoming a_{in} spherical waves. The resonances reveal themselves as poles ω_r^- and zeros ω_r^+ of the *S*-matrix, so that the application of the Weierstrass factorization theorem gives

$$S(\omega) = A\exp(iB\omega)\prod_{r=-\infty}^{+\infty}\frac{\omega-\omega_r^+}{\omega-\omega_r^-} = A\exp(iB\omega)\left[1+\sum_{r=-\infty}^{+\infty}\frac{\sigma_r}{\omega-\omega_r^-}\right],$$

where the constants A and B are responsible for the external retardation effects, and the residues σ_r describe the strength of the Lorentzian resonances. All other spectra can be expressed in terms of the *S*-matrix, including the Mie coefficients $M = (S-1)/2$ and polarizabilities $\alpha \sim M$. An example of such decomposition is shown in the figure below. This approach offers new opportunities for the design of metamaterials, coherent absorbers, superscatterers and nanoantennas.

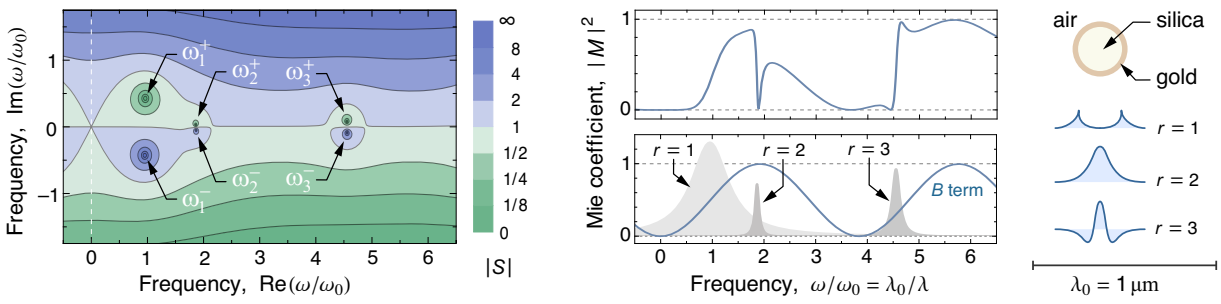

A contour plot of S-matrix (electric dipole) in the complex frequency plane. Spectrum of the Mie coefficient and its decomposition. A schematic picture of the nanoshell structure and its modes.

References

[1] E. Prodan, C. Radloff, N. J. Halas, and P. Nordlander, Science **302**, 419 (2003).

Extraordinary Optical Transmission Through Circular Metallic Cylinder Arrays

Shichang She, Ya Yan Lu

Department of Mathematics, City University of Hong Kong, Kowloon, Hong Kong
shichashe2@student.cityu.edu.hk

Light transmission through arrays of circular metallic cylinders with subwavelength gaps is analyzed theoretically. Features of the the transmission spectra are explained using band structures, a single Bloch mode model and complex-frequency resonant modes.

Introduction

The phenomenon of extraordinary optical transmission (EOT) through subwavelength apertures in metal films has been intensively investigated by many authors. We consider periodic arrays of circular metallic cylinders, and theoretically analyze light transmission through the metallic cylinder arrays. Numerical results indicate that high transmission is possible even when the gaps between nearby cylinders are much smaller than the wavelength. In particular, the transmitted light may carry much more power than the fraction of incident light illuminated directly on the gaps. Moreover, high transmission is concentrated on two wavelength intervals.

Results

We consider N one-dimensional arrays of circular silver cylinders (radius $r = 225$nm) arranged on a square lattice (lattice constant $a = 500$nm) and surrounded by air, where each array is infinite and periodic in the x direction. The gap between two nearby cylinders is $d = 50$nm. The case for $N = 3$ is shown in the figure below (left panel). For a normal incident plane wave in the H polarization, the

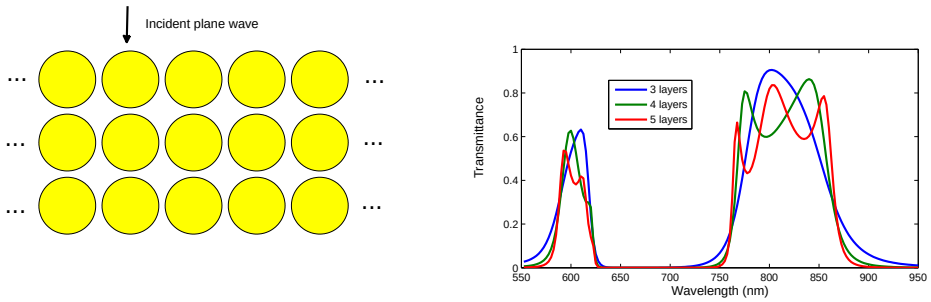

transmission spectra for a few values of N are given in the right panel of the figure. Notice that high transmission is only possible in two wavelength intervals. For some wavelengths the transmittance is more than 80% while the gap-period ratio d/a is only 0.1.

To understand the unusual light transmission behavior through the metallic cylinder arrays, we perform additional computations concerning band structures, Bloch modes, and complex frequency resonant modes. These results allow us to explain the location of two high transmission intervals, to develop a single mode theory based on the leading Bloch mode, and to explain a transmission peak as a resonant-tunneling effect.

Electromagnetically Induced Transparency with Hybrid Silicon-Plasmonic Traveling-Wave Resonators

Dimitra A. Ketzaki*, Odysseas Tsilipakos, Traianos V. Yioultsis, Emmanouil E. Kriezis
Department of Electrical and Computer Engineering, Aristotle University of Thessaloniki, Greece
* dketzaki@auth.gr

Spectral filtering and electromagnetically induced transparency (EIT) with hybrid silicon-plasmonic traveling-wave resonators are theoretically investigated. The rigorous three-dimensional vector finite element method (3D-VFEM) simulations are complemented with temporal coupled mode theory (CMT).

Introduction

Hybrid plasmonic waveguides have recently drawn considerable attention due to the favorable compromise between mode confinement and propagation loss they offer [1]. The recently-proposed conductor-gap-silicon (CGS) waveguide [Fig. 1(a)] can be bent with sub-micron radii and is moreover compatible with standard silicon-on-insulator waveguides [2]. As a result, it is a prime candidate for building integrated nanoscale structures comprising traveling wave resonators.

Results

The filtering capabilities of CGS-based microring resonator filters are investigated by means of 3D-VFEM modeling [3]. We show that resonators with sub-micron radii can efficiently filter the lightwave with minimal insertion loss (IL < 0.2 dB) and high quality factors (Q > 120), Fig. 1(b). By cascading two slightly-detuned resonators and providing an additional route for resonator interaction, a response reminiscent of EIT is observed [Fig. 1(c)]. The transmission peak can be shaped by means of resonator detuning ($\Delta\lambda_{res}$) and resonator separation (s). For example, a resonator detuning of 15 nm, corresponding to a radius variation of approx. ±5 nm, introduces an EIT peak with a quality factor of ~250 and an IL of -3 dB (resonator separation is $s = 3\lambda_g \sim 2.5R_0$).

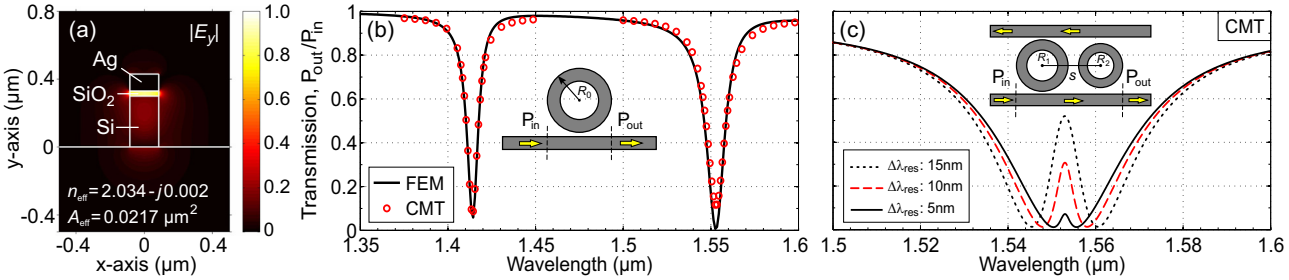

Fig. 1. (a) CGS waveguide (w = 170 nm, h = 300(Si) + 30(SiO_2) + 100(Ag) nm) and corresponding mode profile ($|E_y|$). (b) Transmission vs. wavelength for a 930-nm-radius microring resonator filter. CMT is fed with intrinsic and loaded quality factors determined from 3D-VFEM eigenvalue simulations of the coupled and uncoupled resonator, respectively. (c) EIT with two slightly detuned resonators for three detuning scenarios. Note the fundamental trade-off between peak transmission maximum and quality factor.

This work has been supported in part by the THALES Project ANEMOS, co-financed by the European Union (European Social Fund) and Greek National Funds through the Operational Program "Education and Lifelong Learning" of the National Strategic Reference Framework.

References

[1] R. F. Oulton, V. J. Sorger, D. A. Genov, D. F. P. Pile, X. Zhang, *Nat. Photon.*, **2**, 496, 2008

[2] M. Wu, Z. Han, V. Van, *Opt. Express*, **18**, 11728, 2010

[3] O. Tsilipakos, *et al.*, *Opt. Quant. Electron.*, **42**, 541, 2011

Low-Loss Splicing of Microstructured Optical Fibers and Single-Mode Fibers: An Analytical Study

Dinesh Kumar Sharma, Anurag Sharma
Physics Department, Indian Institute of Technology, New Delhi-110016, India
dk81.dineshkumar@gmail.com, *asharma@physics.iitd.ac.in*

Low-loss splicing of microstructured optical fibers (MOFs) and standard single-mode fibers (SMFs) can be achieved by enlarging the mode field diameter (MFD) of MOFs using, e.g., the controlled all air-hole collapse method. This leads to an optimum mode field match at the interface. We study analytically the splicing between such an MOF and an SMF using our analytical field model.

Introduction

The study of low-loss fusion splicing of MOFs with other types of optical fibers is essential for the practical realization of MOF based devices and sensors [1,2]. Conventional fusion splicing technologies are not usable for MOFs, as the characteristic air-holes pattern often collapses during the splicing process, which significantly increases the loss by distorting the light guiding structure of MOF near the joint interface. To overcome this problem, controlled air-hole collapse method has been used [2]. Here, we have analytically simulated interfacing of MOFs to SMFs using our earlier developed analytical field model [3].

Results and Discussion

On heating the MOF, air-holes are collapsed due to surface tension of the material and it is assumed that the total area of the MOF material remains constant, which yields the following relation [1,2];

$$\Lambda = \Lambda_0 \sqrt{\left(\sqrt{3}/2 - \pi/4\left(d_0/\Lambda_0\right)^2\right) \Big/ \left(\sqrt{3}/2 - \pi/4\left(d/\Lambda\right)^2\right)}$$

where d and Λ are the hole size and pitch of collapsed MOF, d_0 and Λ_0 are the parameters of initial MOF. Our field model based on variational method provides the optimized value of the propagation constant and the field parameters [3], which can be analytically expressed by fitting the polynomial of the 8th degree. We evaluated the splicing loss between an MOF having $d_0/\Lambda_0 = 0.612$ and $\Lambda_0 = 3.35\mu m$ and an SMF with core diameter 6.0μm, NA = 0.08 and $\Delta = 0.0154$, for $\lambda = 0.80\mu m$, using mode overlap integral. The splicing loss is 2.6dB without any air-hole collapse of MOF and with the increases of collapse ratio, we obtained the lowest loss of 0.08dB (see Fig.1). For high degree of collapse ratio the results deteriorate and the model based on three rings structure and one ring field is not adequate; one must add more number of rings in the field. Further work is in progress.

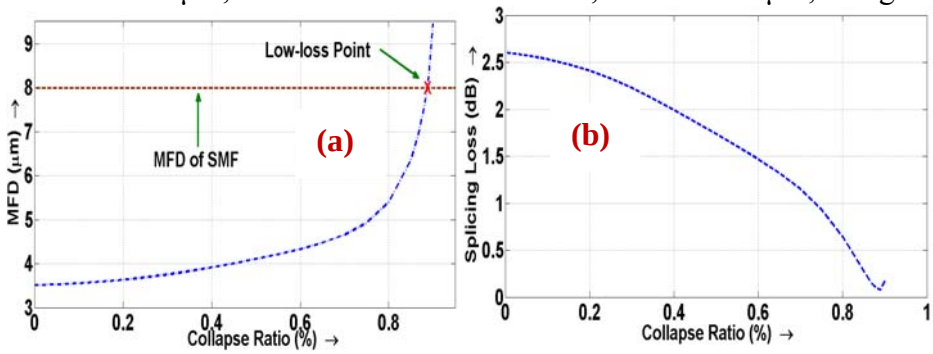

Fig.1 (a) MFD Vs collapse ratio. (b) Splicing loss Vs collapse ratio.

This work was supported by grant from the Council of Scientific and Industrial Research (CSIR), Govt. of India.

References

[1] J. Laegsgaard and A. Bjarklev, *Opt. Commun.*, **237**, 431 (2004).
[2] X. Xi, Z. Chen, G. Sun, and J. Hou, *Appl. Opt.*, **50**, E50 (2011).
[3] D.K. Sharma and A. Sharma, *OQE*, **44**, 415, (2012); also *OWTNM 2009* and *OWTNM 2012*.

Simple Analytical Approach to Optimize Structure Parameters of Photonic Crystal Waveguide Coupler

Kanchan Gehlot, Anurag Sharma

Department of Physics, Indian Institute of Technology Delhi, New Delhi 110 016, India
gehlot.kanchan@gmail.com, asharma@physics.iitd.ac.in

Simple analytical approach of optimal variational method (VOPT) is used to optimize structure parameters of a photonic crystal waveguide coupler to obtain desired power coupling ratio. In analysis of photonic crystal waveguides by VOPT, separate set of parameters are identified that control the guiding mechanism and Bragg reflections. This helps in optimizing the structure for desired application.

Summary

Optimal variational method (VOPT) [1] is based on variational principle and assumes field to be separable in two orthogonal directions. In [2], it is shown that VOPT approximates a two dimensional photonic crystal waveguide to a 1-D Bragg reflector and a multilayer slab waveguide. Reflection/transmission spectra of the structure are obtained from the Bragg reflector and modal field profile is obtained from the modes of multilayer waveguide. Analytical results obtained by VOPT are further used to optimize a photonic crystal waveguide coupler of configuration shown in Fig.1. The structure is excited asymmetrically from the input end and we find power distribution between two cores of coupler at the output. Optical field profile and the power coupling ratio predicted by VOPT method and FDTD analysis are very close.

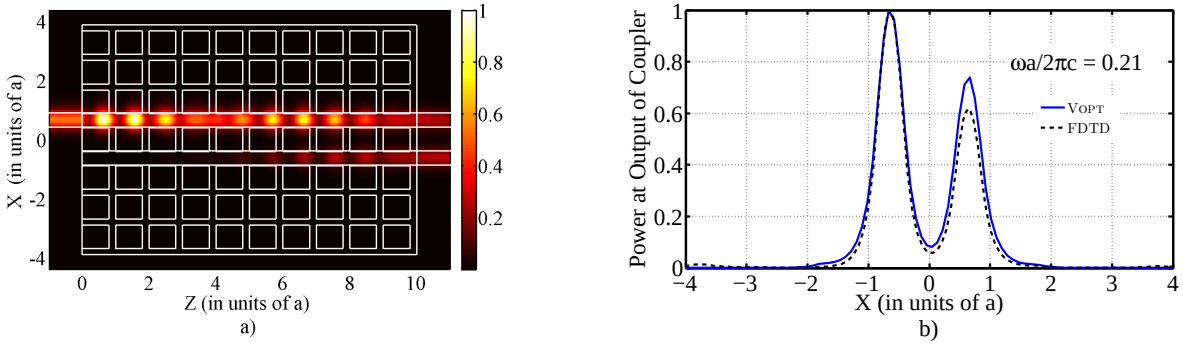

Fig. 1. a) Optical intensity profile of 2D photonic crystal waveguide coupler at normalized frequency, $\omega a/2\pi c = 0.21$, where a is the period of photonic crystal. The schematic of coupler is shown with white lines. Width of two cores of GaAs ($\epsilon = 12.96$) is $d = 0.375a$ and area of square air hole is $\pi(0.45a)^2$ b) Comparison of output intensity profile with FDTD results.

This analysis provides a simple model to understand properties of photonic crystal waveguides and devices. The analytical process reduces the computational time considerably and simplifies optimization of the structure.

This work was supported by grant from Council of Scientific and Industrial Research (CSIR), Govt. of India.

References

[1] A. Sharma, *Opt. Quant. Electron.*, **21**, 517–520 (1989)
[2] K. Gehlot, A. Sharma, *OWTNM-2012*, Barcelona, Spain, (2012)

Vertical Links for Multilayer Optical-Networks-on-Chip Topologies

A. Parini[1,3*], G. Calò[2], G. Bellanca[3], V. Petruzzelli[2]
[1]*Laboratory for Micro and Submicro Enabling Technologies of the Emilia-Romagna Region (MIST E-R), Via P. Gobetti 101, 40129 Bologna, Italy*
[2]*Dipartimento di Ingegneria Elettrica e dell'Informazione, Politecnico di Bari, Via Re David 200, 70125 Bari, Italy*
[3]*Department of Engineering, University of Ferrara, Via Saragat 1, 44122 Ferrara, Italy*
* alberto.parini@unife.it

In this work we propose two possible technological solutions that may allow the connection in the vertical direction between different layers of an Optical-Network-on-Chip (ONoC). The first solution relies on Multi-Mode Interference devices (MMI), while the second exploits a cascading between vertically stacked parallel waveguides. Comparisons in terms of efficiency, bandwidth and footprint will be reported.

Introduction

Networks-on-Chip (NoCs) can take advantage of the fully compatible CMOS silicon photonic integration to realize optical based interconnection links. In fact, optical (instead of electrical) interconnections among the different computational cores can provide a huge communication bandwidth with a favorable power budget [1]. At present, planar topologies are mainly proposed in the literature [2]. However, the inherent complexity of the optical circuitry and the constraints on the footprint lead toward the realization of vertically stacked layers, in order to avoid crossings, allow an efficient placing and routing of the different optical devices, and increase the integration density of the functional elements. In this work we design and compare two different techniques that can be used to implement vertical connections between two superposed optical layers.

Results

An MMI based solution to connect two waveguides, vertically separated by a gap of 820nm, is reported on the left panel of Fig. 1. The 3D-FDTD simulation shows an average efficiency of 90% on a 60nm band. The right panel of the figure presents an alternative strategy for the same connection, which exploits a cascaded coupling among three vertically stacked waveguides. In this second case, the Coupled Modes Theory provides an average efficiency of 97%. The existing trade-off between footprint, vertical distance and transmission efficiency must be carefully assessed.

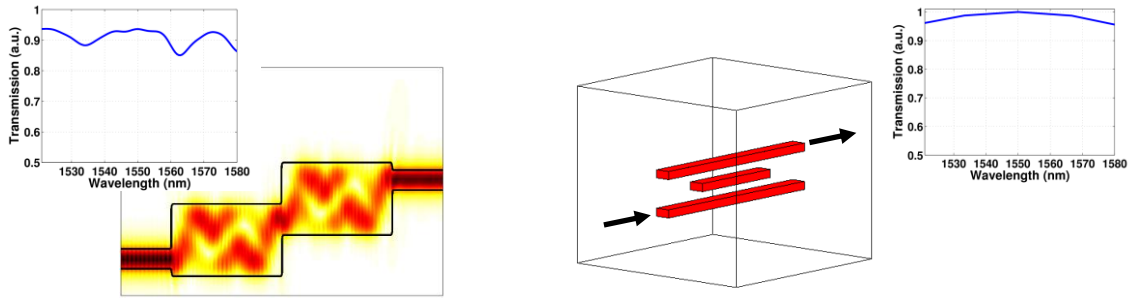

Figure 1: (Left panel) Vertical cross-section of the electrical field in the MMI based structure; the inset shows the transmission in the band 1520nm-1580nm. (Right panel) Coupled waveguides based solution: 3D sketch of the coupler and relative transmission curve.

References

[1] C. Batten et al., *Designing Chip-Level Nanophotonic Interconnection Networks*, IEEE Journal on Emerging and Selected Topics in Circuits and Systems, Vol. 2, No. 2, 2012.

[2] L. Chen et al., *Integrated GHz silicon photonic interconnect with micrometer-scale modulators and detectors*, Optics Express, Vol. 17, No. 17, 2009.

A Terahertz Waveguide Coupler with a Tapered Dual Elliptical Metal Structure

Qing Cao*, Shuang Li, Da Teng, and Hua Gao
Department of Physics, Shanghai University, 99 Shangda Road, Baoshan District, Shanghai 200444, China
***qcao@shu.edu.cn**

Abstract: A high efficient plasmon coupler is suggested for the coupling of terahertz wave from an approximate plate waveguide to a two-wire waveguide. We numerically show that the coupling efficiency of this kind of coupler can be as high as about 94%.

It was reported that the two-wire THz waveguide has the advantages of low bending loss and low attenuation [1-2]. Here, we present a new coupling structure for the highly efficient coupling from an approximate plate waveguide to a two-wire waveguide. This new coupler is composed of two tapered elliptical metal structures. As shown in Fig.1, through putting the long axis b decreases slowly, the two-ellipse structure gradually degenerates into two metal wires. As a result, the reflection can be eliminated and thus a high coupling efficiency can be obtained.

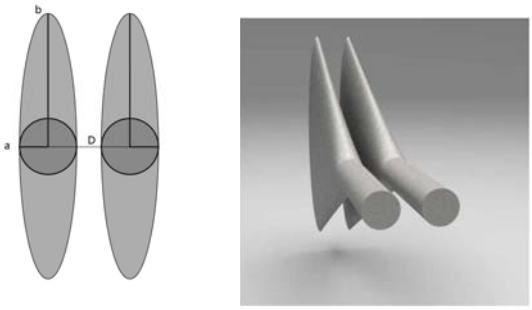

Fig.1. A tapered dual elliptical plasmon waveguide

We numerically test the coupling efficiency of the tapered dual elliptical plasmon waveguide coupler by use of the commercial software of COMSOL Multiphysics. At the output plane, each of the wires has a radius of 0.5 mm and the two wires are separated by a 2 mm distance. At the input plane, the long axes b and the short axes a are 5 mm and 0.5 mm, respectively. The coupling length l is 0.1 m. We first calculate the effective index n_{eff} of each 2-D cross-section of the tapered dual elliptical plasmon waveguide by use of the COMSOL software. We find that the mode coupling process meets the WKB approximation [3] very well. According to the WKB approximation, the coupling efficiency η can be calculated by the following formula. Through numerical calculations, we find that the coupling efficiency can be as high as about 94%.

$$\eta = \exp\left[-2k_0 \int_0^l \mathrm{Im}(n_{eff})dz\right]$$

References

[1] M. Mbonye, R. Mendis, and D. M. Mittleman, *A terahertz two-wire waveguide with low bending loss*, Appl. Phys. Lett. **95**, 233506, 2009

[2] H. Pahlevaninezhad, T. E. Darcie, and B. Heshmat, *Two-wire waveguide for terahertz*, Opt. Express **18**, 7415–7420, 2010

[3] A. Rusina, M. Durach, K. A. Nelson, and M. I. Stockman, *Nanoconcentration of terahertz radiation in plasmonic waveguides*, Opt. Express **16**, 18576–18589, 2008

Nonreciprocal waveguiding EM surfaces and structures for THz region

P. Kwieicen[1], V. Kuzmiak[2], I. Richter[1*], J. Čtyroký[2]

[1] *Czech Technical University in Prague, Faculty of Nuclear Sciences and Physical Engineering, Department of Physical Electronics, Břehová 7, 11519 Prague 1, Czech Republic*

[2] *Institute of Photonics and Electronics AS CR, v.v.i., Chaberská 57, 182 51 Praha 8, Czech Republic*

* ivan.richter@fjfi.cvut.cz

Based on combination of magnetooptic Fourier modal method (MOaRCWA) simulations and (quasi)analytical dispersion relation predictions, we have studied the magnetoplasmons in plasmonic nanostructures composed of highly-dispersive polaritonic InSb material, within the THz spectral region.

Introduction

Recently, among possible stable EM waves propagating within photonic nanostructures, surface waves constrained to the media interfaces have found an increasing scientific interest (and even application potential) in such areas as sensing, metamaterials, and nonreciprocal systems. Among these, surface plasmons polaritons (SPP) have become established in many practical areas, especially in surface plasmon resonance biosensing, waveguiding, and others [1]. One of only few possibilities how to impose nonreciprocity in these structures is to apply an external magnetic field [2] (mainly in the transverse, or Voigt configuration). In such a case, one-way (nonreciprocal) propagation of SP is not only possible but may bring many interesting phenomena in connection with magnetoplasmons (MSP) [3]. However, in order to properly simulate such MSP propagation, an appropriate numerical tools is necessary.

Results

Based on our previous studies [4], we have developed an efficient 2D numerical technique based on MO aperiodic rigorous coupled wave analysis (MOaRCWA). In our in-house tool, the artificial periodicity is imposed within a periodic 1D RCWA method, in the form of the complex transformation and / or uniaxial perfectly matched layers. Our approach, in which several key improvements have been implemented, is able to properly cope not only with SPP propagation in nanostructures, but also with a general form of permittivity / permeability anisotropy, and hence also with the Voigt MO effect. Next, we have combined the MOaRCWA simulations with (quasi)analytical predictions in order to study MSP performance of plasmonic nanostructures with highly-dispersive polaritonic InSb material, in the presence of external magnetic field. Here, Voigt MO effect can be used to impose nonreciprocity (one-way propagation) bringing new interesting phenomena in connection with MSP. As an example, Fig. 1 shows one of these structures studied [5], together with the InSb permittivity tensor dispersions, and corresponding nonreciprical dispersion diagram. In particular, we have explored nonreciprocal behavior of the MSP which reflects variety of interesting features associated with both surface and bulk polaritonic modes within the THz frequency range. The results of our studies will be shown and discussed in a detail.

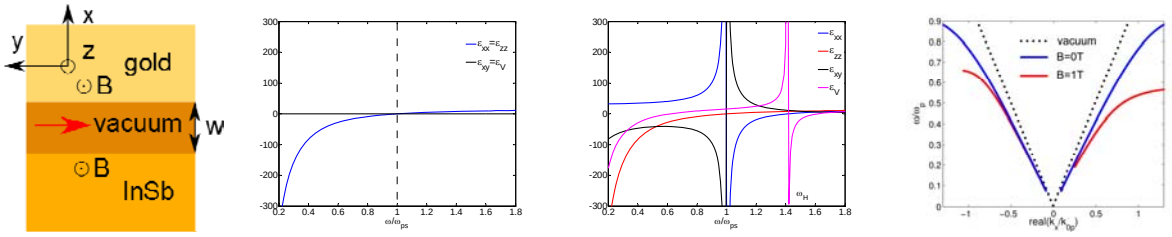

(a) (b) (c) (d)

Fig. 1: (a) Schematic picture of the one-way plasmonic waveguide operating at the THz range; the frequency dependence of the permittivity tensor (ε_{XX}, ε_{YY}, ε_{ZZ}, ε_{XY}) and the corresponding Voigt dielectric constant ε_V of InSb material: (b) case with no magnetic field, $\omega_b/\omega_p = 0$, (c) case with magnetic field, $\omega_b/\omega_p = 1$, ω_b is the cyclotron frequency, (d) THz magnetoplasmon dispersion relations for the structure w/o external magnetic field.

Acknowledgements: This work was financially supported by the Czech Science Foundation (projects P205/10/0046 and P205/12/G118).

References

[1] S.A. Maier, *Plasmonics: Fundamentals and Applications*, Springer, 1. ed. (2007).
[2] A. Figotin, I. Vitebsky, Phys. Rev. E **63**, 066609 (2001).
[3] A. Boardman, N. King, Y. Rapoport, L. Velasco, New J. Phys. **7**, 191 (2006).
[4] S. Eyderman, V. Kuzmiak, M. Vanwolleghem, in Proc. SPIE **7713**, 77130P-1 (2010).
[5] B. Hu, Q.J. Wang,Y. Zhang, Optics Letters **37**, 1895 (2012).

Coupling Characteristic for Novel Hybrid Long-Range Plasmonic Waveguide Including Bends

A. M. Heikal, Mohamed Farhat O. Hameed S. S. A. Obayya*

*Centre for Photonics and Smart Materials, Zewail City of Science and Technology, Sheikh Zayed District, 6th of October City, Giza, Egypt. * sobayya@zewailcity.edu.eg*

A novel design of hybrid long-range plasmonic waveguide is introduced and analyzed using full-vectorial finite difference method. The suggested design has high index material as a cap to reduce the propagation loss and optimum bending radius as well. The bending and coupling analysis of the reported design has been introduced.

Simulation Results

Figure 1 shows the suggested novel hybrid long-range plasmonic waveguide structure. The reported waveguide consists of a gold strip of thickness t_m = 20 nm, width W_m and has a permittivity ε_m= -131.95+j12.65. The metal strip is embedded in a rib waveguide with high index dielectric thin cap. In this study, Benzocyclobutene (BCB) of permittivity, ε_2 = 2.356225 is used as a rib core with total width W_r = 6.5 µm and total height h_r = 1.6 µm. In addition, SiO_2 is used as a substrate with permittivity ε_1 = 2.0736. The very thin dielectric cap has a thickness t_{Si} = 0.3 µm and a permittivity of ε_3 = 144.98327281. Figure 2 and 3 illustrate the variation of the effective index n_{eff} and propagation loss of the suggested structure with the bending radius, respectively with Si cap, with BCB cap and without cap at two different widths W_m, 0.5 µm and 3.0 µm. It is evident from Fig. 3 that the high index cap decreases the propagation loss. In addition, the propagation loss is decreased by increasing the refractive index of the cap. Therefore, the propagation loss without cap is higher than that with BCB cap and Si cap. It is also revealed from these figures that the effective index of the suggested structure with Si cap is greater than that with BCB cap. However, the propagation loss L_{pro} and optimum bending radius r_{opt} with Si cap with minimum propagation length, is smaller than that with BCB cap. At W_m = 3 µm, L_{pro} = 0.91 dB/mm and r_{opt} = 90 µm are obtained with BCB cap while L_{pro} = 0.77 dB/mm and, r_{opt} = 80 µm are achieved with Si cap. The numerical results also reveal that the effective index and propagation loss at W_m=3.0 µm are greater than those of W_m=0.5 µm as shown in Fig 2 and Fig.3. It is also shown from Fig. 2 that the effective index n_{eff} decreases by increasing the bending radius from r =70 µm to 1000 µm. If the bending radius is further increased, n_{eff} starts to be constant. The simulation results are obtained using full vectorial finite difference method [1]. More results will be presented in the conference.

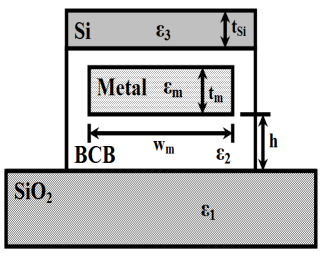

Figure 1 Schematic diagram of hybrid long-range plasmonic waveguide

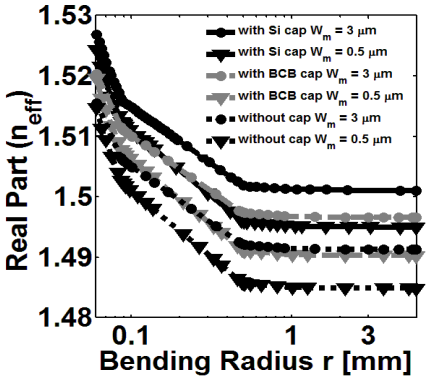

Figure 2 Variation of real part (n_{eff}) with the bending radius r

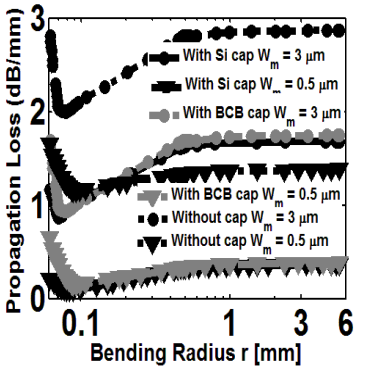

Figure 3 Variation of propagation loss (L_{prop}) with the bending radius r

References

[1] A. B. Fallahkhair, K. S. Li, and T. E. Murphy, "Vector Finite Difference Modesolver for Anisotropic Dielectric Waveguides," J.Lightwave Technol., vol.26 (11), pp. 1423-1431, 2008

P-07

Novel Mixed Finite Element Method Analysis of Leaky Photonic Nanowires

Shaymaa I.H.Ibrahim, S.S.A.Obayya*
Centre for Photonics and Smart Materials, Zewail City of Science and Technology, Sheikh Zayed District, 6th of October City, Giza, Egypt. *sobayya@zewailcity.edu.eg

A modified symmetric mixed finite element method is introduced and validated. Besides the benefits of conventional curl conforming mixed elements, the symmetric element has the advantage of being independent on the selection of facet related basis functions.

Summary and Results

Mixed finite elements are widely used for their ability to accurately apply boundary conditions to prohibit spurious modes and to eliminate unnecessary degrees of freedom. Figure 1 shows a second order vector element. The element has six tangential unknowns along with two facet unknowns. The facet related basis is hence asymmetric. This asymmetry may cause some problems: the choice of any two of possible three facet functions may influence the numerical accuracy of results. Special attention must be paid to numerical implementation of the asymmetric elements. Peterson introduced an efficient second order element that satisfies the Nedelec's constraints, however, it suffer from the asymmetry [1]. Modifying the facet related functions in [1] to get a set of dependent functions, we obtain a symmetric element. The developed finite elements technique is used analyze leaky photonic nanowire shown in Fig. 2 [2]. Photonic silicon nanowires are now a very important component in integrated photonics research as well as sensing applications.. Silicon nanowires enjoy a very good field confinement due to its high index contrast. However, this index contrast causes the field to be highly discontinuous at the interfaces which needs to be modeled correctly. A precise modal characterization of a silicon nanowire is extremely important as it forms the building block for almost all other circuitry components. Figure 2(b) shows the field discontinuities at the silicon-air interface and at oxide-silicon interfaces of the nanowire. The mode effective index calculated using the developed method shows an excellent agreement with other well-established mode solvers in [2]. In addition different choices of facet basis functions in our modified element almost give the same result unlike those calculated using facet function in [1] which gives different results for different selections, especially, on the imaginary part of the mode effective index which is the most sensitive parameter in sensing applications.

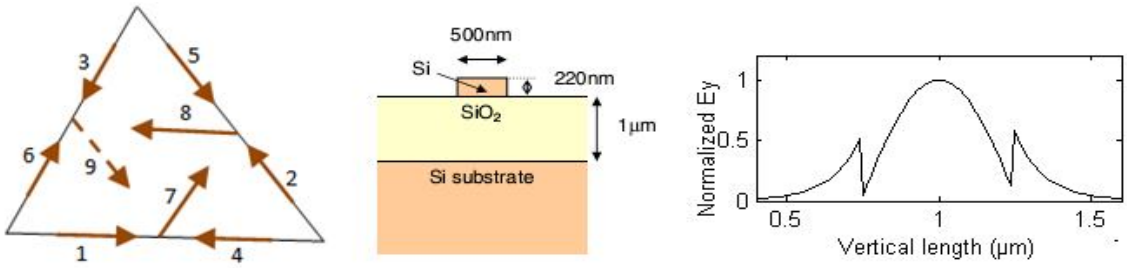

Figure 1 Second order mixed finite element. Figure 2(a) Leaky silicon nanowire, (b) Field discontinuities at the interfaces.

References

[1] Peterson, A.F.; , "Vector finite element formulation for scattering from two-dimensional heterogeneous bodies," *Antennas and Propagation, IEEE Transactions on* , no.3, pp.357-365, 1994.

[2] Bienstman, P. and Selleri, S. and Rosa, L. and Uranus, H.P. and Hopman, W.C.L. and Costa, R. and Melloni, A. and Andreani, L.C. and Hugonin, J.P. and Lalanne, P. and Pinto, D. and Obayya, S.S.A. and Dems, M. and Panajotov, K. (2006). Optical and Quantum Electronics, 38 (9-11). pp. 731-759. ISSN 0306-8919

Efficient Bidirectional Beam Propagation Method for Multiple Longitudinal Optical Waveguide Discontinuities

Shaymaa I.H.Ibrahim[1], S.S.A.Obayya[1]*, R. Letizia[2]

[1]*Centre for Photonics and Smart Materials, Zewail City of Science and Technology, Sheikh Zayed District, 6th of October City, Giza, Egypt.* *sobayya@zewailcity.edu.eg

[2]*Department of Engineering, Lancaster University, Lancaster, UK*

A new finite-element bidirectional beam-propagation method (FE-Bi-BPM) for the analysis of multiple longitudinal optical waveguide discontinuities is introduced. The method is very accurate with a very limited computational cost. Results show its agreement with well-established methods in the literature.

Summary and Results

Multiple longitudinal discontinuities are often encountered in optical devices. The analysis of such structures requires a bidirectional wave propagation technique to account for transmission and multiple reflections at the discontinuities. In the developed method, the square root of the characteristic matrix of both discontinuity sides is efficiently approximated using the Taylor's series expansion. By the enforcement of the boundary conditions at the discontinuity interface, both the reflected and the transmitted fields can be calculated while totally avoiding any matrix inversion and modal solutions. For multiple discontinuities, reflected and transmitted fields are solved at each interface and stored for each propagation trip until convergence is achieved.

To validate the proposed FE-Bi-BPM, a waveguide-loaded semiconductor laser [1], shown in Fig. 1, is simulated. Consider two symmetrical and single-mode waveguides connected by an air gap with 1μm height, where the TE_0 mode is injected as source at the operating wavelength, λ, is 1.55 μm. In Fig. 2, the variation of reflected, transmitted, and radiated power with the total number of propagation trips are shown. It may be noted that convergence of the numerical solution is achieved after only 4 propagation trips. Next, in Fig. 3, the reflected, transmitted, and radiated power are reported against the real-valued fundamental mode phase shift constant β_0. It is clear that the suggested technique has a low sensitivity to the variation of β_0. The results excellently agree with those obtained through FSRM technique [1].

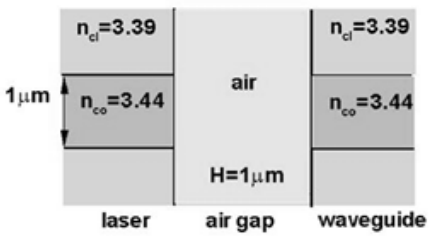

Figure 1 Schematic diagram of a waveguide-loaded semiconductor laser

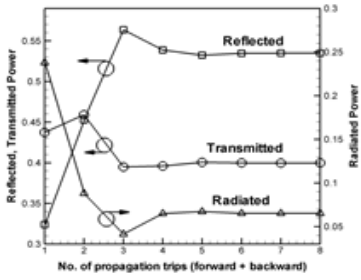

Figure 2 Convergence with the number of propagation trips

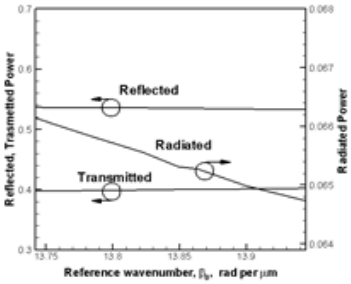

Figure 3 Variation with the reference wavenumber β0

References

[1] Smartt C. J., Benson T. M., Kendall P. C.: 'Free space radiation mode method for the anaysis of p ropagation in optical waveguide devices', IEE Proc.-Optoelectron., 1993, 140, (1), pp. 56-61

Mode Polishing for 3D Finite Element BPM

Remco Stoffer

PhoeniX Software, Enschede, The Netherlands
remco.stoffer@phoenixbv.com

A method to polish the modes to launch and analyze in a 3D Finite Element BPM is presented. It ensures that the modes that are used are eigenmodes of the numerical scheme.

Introduction

In the fixed-grid finite element vectorial 3D Beam Propagation Method (BPM), as presented in [1] and implemented in PhoeniX Software's Optodesigner, a relatively coarse grid can be used, since interfaces between materials are taken into account inside each element.

A numerical waveguide mode of the BPM will never be exactly equal to the analytical mode of a guide. If the analytical mode is simply used directly in the BPM for both launching and overlapping modal fields, unexpected bahaviour may occur, such as perceived gain in simple straight waveguides. Therefore, we developed a routine that polishes the analytical mode into the numerical BPM mode.

Implementation

We use a shift–and–invert method to obtain the modal field. The BPM algorithm (approximately) solves the equation $(\mathbf{A}\partial_{zz} + \mathbf{M})\mathbf{u} = 0$, where $\mathbf{A}$ and $\mathbf{M}$ are matrices describing the refractive index profile and the spatial derivatives, and $\mathbf{u}$ is a vector of discretized field components. Thus for a mode with propagation constant β_i, $(-\mathbf{A}\beta_i^2 + \mathbf{M})\mathbf{u_i} = 0$. If we then take trial β_t and (normalized) $\mathbf{u_t}$, which are close to β_i resp. $\mathbf{u_i}$, and calculate the expression $(-\mathbf{A}\beta_t^2 + \mathbf{M})^{-1}\mathbf{A}\mathbf{u_t}$, the component $\mathbf{u_i}$ in $\mathbf{u_t}$ will blow up: $(-\mathbf{A}\beta_t^2 + \mathbf{M})^{-1}\mathbf{A}\mathbf{u_t} \approx (\beta_i^2 - \beta_t^2)^{-1}\mathbf{u_i}$. This final expression can be used to obtain a better estimate for the numerical β_i. We find that two iterations of this procedure suffice to obtain a modal profile that propagates without noticeable distortion through the waveguide. An overlap of the field after some distance of propagation with another polished mode yields, as expected, a value of 1.

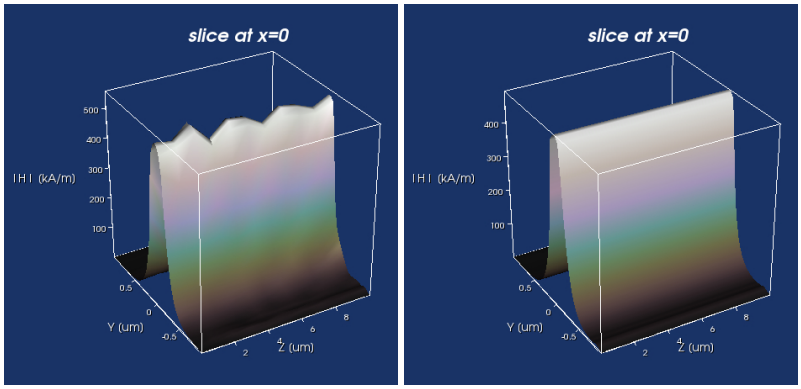

Slice of the field through a coarse grid BPM of a Silicon on Insulator waveguide. Left: Analytical mode launched into the structure. Right: Polished mode launched into the structure.

References

[1] R. Stoffer and J. Bos *Fixed-grid Finite Element Beam Propagation Method,* Proceedings of the OWTNM 2008, Eindhoven, The Netherlands, 2008, page 2

Numerical Modeling of Human Eye with Electromagnetic Approach

M. G. Can[1]*, B. B. Oner[1], H. Kurt[1]
[1] Nanophotonics Research Laboratory, Department of Electrical and Electronics Engineering
TOBB University of Economics and Technology, 06560, Ankara, Turkey
* m.can@etu.edu.tr

In this work we aimed to perform wave analysis of light propagation through the human eye implementing finite-difference time-domain (FDTD) method. Due to many orders of magnitude difference between the size of the human eye and operating wavelength in visible spectrum, we utilize additional asymptotic approach.

To the best of our knowledge, the electromagnetic wave approach is carried out for the first time to analyze the optical properties of the human eye. Wave theory of light has ability to explain interference, diffraction and aberrations contrary to ray optics approach that fails to take into consideration. Additionally, ray theory gives infinitesimal spot size at the focal point while wave theory analysis provides an exact full-width at half-maximum value of the focused light at the proximity of the retina.

The numerical computations are performed by means of the FDTD. The ratio between human eye size (~12 mm in diameter) and the visible light wavelength (400-750 nm) gives rise to numerical stability problem [1]. In order to overcome this issue, a proper description of the geometrical and dispersive properties of the eye is modelled by implementing asymptotic and numerical methods.

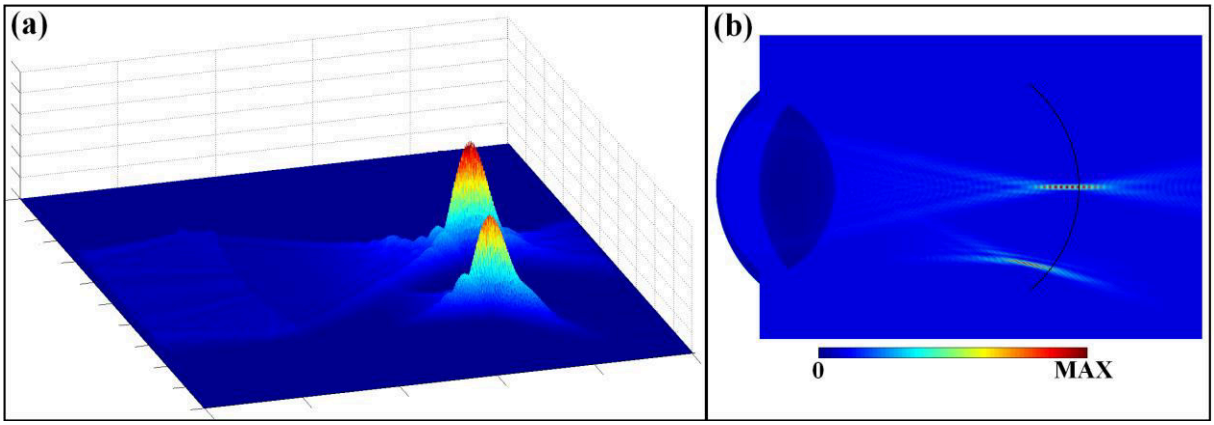

Figure 1 (a) Intensity distribution of the two focused beams with different incident angles. (b) A snapshot of the beams focused at the proximety of the retina (dark plotted arc represent retina).

Fig. 1(a) shows a snapshot of two different focused beams. The color bar represents the intensity variation for both Figs. 1(a) and 1(b). Beams have different incident angles (perpendicular and 20^0). While the perpendicular case gets focused on the retina, the tilted case focuses in front of the retina. The figure also indicates that the maximum intensity of the focused beam is getting low as we increase the incidence angle. Coma aberration and its properties are observed from the figure, not only coma but also other optical properties of our eye model are compatible with the literature. The details of the electromagnetic wave analysis of human eye will be presented in the conference.

References

[1] A. Taflove and S. C. Hagness, Computational Electrodynamics: The Finite-Difference Time-Domain Method, Artech House Publisher, 2005.

A vectorial simplified model for Fano resonances of guided-mode resonant gratings

A.-L. Fehrembach and A. Sentenac

Aix Marseille Université, CNRS, Ecole Centrale Marseille, Institut Fresnel, 13013 Marseille, France
anne-laure.fehrembach@fresnel.fr

We present a vectorial, semi-analytical model developed to understand the physics of guided mode resonant gratings and to express their properties with respect to the parameters of the structure.

Guided mode resonant gratings are simple structures, composed with a planar waveguide structured with a subwavelength periodic pattern. Their basic principle is simple: a leaky guided-mode can be excited by an incident wave via a diffraction order, which generates a resonance peak in the diffraction spectrum of the structure. Despite this outward simplicity, they are however very interesting for applications such as narrow band filtering, sensoring .... Yet, to obtain advanced properties (polarization independence, angular tolerance...) it is necessary to work with complex configurations (conical incidence, excitation of several modes...). Knowing the link between the parameters of the structure and its properties, or at least having some physical understanding in theses configurations is a crucial help in the design. Here, we present a semi-analytical model in the vectorial case, e.g. whatever the plane of incidence and the incident polarization. This is a further development of the scalar model which led us to propose configurations with enhanced angular tolerance [1, 2].

We start from Maxwell equations, and consider the grating as a perturbation over a reference, planar structure. We show that for an incident wave with wavelength λ and in-plane wavector $\vec{\kappa}$, the electric field diffracted at an abscissa z above or below the grating is solution of the equation

$$[\vec{F}(\lambda,\vec{\kappa},z)] = [\vec{E}_{ref}(\lambda,\vec{\kappa},z)] + h\mathbf{M}(\lambda,\vec{\kappa},z,0)[\vec{F}(\lambda,\vec{\kappa},0)] + o(h^2), \tag{1}$$

where $[\vec{F}(\lambda,\vec{\kappa},z)]$ is a vector containing the components of the electric field in the grating orders, $[\vec{E}_{ref}(\lambda,\vec{\kappa},z)]$ contains the incident field and the field reflected and transmitted by the reference structure, h is the grating depth, and $\mathbf{M}$ a matrix which depends on the reflection and transmission matrix $\mathbf{R}_{ref}$ and $\mathbf{T}_{ref}$ of the reference structure and of the gratings parameters.

Solving successively the homogeneous and the diffraction problems, we are able to express the reflection and transmission matrix of the structure with respect to the incident wavelength λ as

$$\mathbf{R} = \mathbf{R}_{ref} + h^2\frac{\mathbf{R}_{pert}}{\lambda-\lambda_{pole}} + o(h^2) \quad \text{et} \quad \mathbf{T} = \mathbf{T}_{ref} + h^2\frac{\mathbf{T}_{pert}}{\lambda-\lambda_{pole}} + o(h^2), \tag{2}$$

where $\mathbf{R}_{pert}$ and $\mathbf{T}_{pert}$ are matrix that express the coupling-in and out of the mode via the grating, and λ_{pole} is the eigen wavelength of the excited mode. We draw some physical interpretations out of these expressions and provide a numerical validation of the model.

ACKNOWLEDGEMENT: The financial support of the CNES in this work is gratefully acknowledged.

References

[1] A.-L. Fehrembach, F. Lemarchand, A. Talneau, and A. Sentenac. High q polarization independent guided-mode resonance filter with doubly periodic etched ta2o5 bidimensional grating. *I.E.E.E. J. Light. Tech.*, 28:2037–2044, 2010.

[2] A. Sentenac and A.-L. Fehrembach. Angular tolerant resonant grating filters under oblique incidence. *J. Opt. Soc. Am. A.*, 22:475–480, 2005.

Electro-optic effect in guided mode resonance gratings for tunable narrow-band filtering

A.-L. Fehrembach, D. Shu and E. Popov

Aix Marseille Université, CNRS, Ecole Centrale Marseille, Institut Fresnel, 13013 Marseille, France
anne-laure.fehrembach@fresnel.fr

We present a numerical study of guided mode resonant gratings including a layer of electro-optic material. The effect of the anisotropy of the electro-optic layer on the tunability and polarization dependence of the peak is taken into account.

A guided mode resonance filter is a simple structure composed of a stack of a few dielectric layers on which a sub-wavelength grating is engraved. Their main interest is the narrow spectral FWHM they can achieve: in practice, quality factors greater than 7000 have already been obtained. The potential application fields are: optical telecommunications, spectroscopy, lasers, sensoring, etc. We aim to develop the potential of resonant grating filters by studying the tunability of their center wavelength by electro-optic effect. Here, we present a numerical study of the properties of guided mode resonance filters including an electro-optic material [1]. We have used a numerical tool based on the Fourier Modal Method including anisotropic materials [2]. This is indispensable to analysis the effects related to the incident polarization.

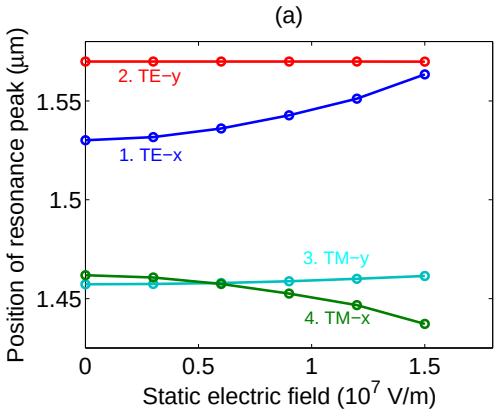

Fig. 1. Tunability of a guided mode resonance filter including a Barium Titanate layer

We work with two materials, Lithium Niobate and Barium Titanate, because of their large electrooptic coefficients. We compare several configurations, allowing either a strong (up to 90nm) or a weak tunability, toward greater or smaller wavelengths (see Fig. 1). For each case, a physical interpretation is given for the facts that are observed. We also study the behavior of the peak in the different configurations with respect to the incident polarization.

References

[1] D. Shu, E. Popov, and A.-L. Fehrembach. Electro-optic effect in batio3 for spectral tuning of narrow-band resonances. *J. Opt. Soc. Am. B*, 30, 2013.

[2] L. Li. Fourier modal method for crossed anisotropic gratings with arbitrary permittivity and permeability tensors. *J. Opt. A: Pure Appl. Opt.*, 5:345–355, 2003.

Solitons in binary waveguide arrays

Aldo Auditore[1], Matteo Conforti[1], Costantino De Angelis[1], Alejandro B. Aceves[2]

[1] *Dipartimento di Ingegneria dell'Informazione, Università degli Studi di Brescia, Brescia 25123, Italy.*
[2] *Department of Mathematics, Southern Methodist University, Dallas, Texas 75275, USA*
aldo.auditore@ing.unibs.it

We suggest a model describing light propagation in binary (linearly and nonlinearly) waveguide arrays. Performing a suitable continuum expansion, we find solitons for focusing, defocusing, and even for alternating focusing-defocusing nonlinearity. We also analyze modulational stability in the continuum limit and in the discrete system.

Model and results

We consider here a model that can be applied in different physical settings such as plasmonic, Bragg and photonic crystal waveguides [1, 2, 3, 4, 5]. The simplest form consists of a binary array designed in such a way that the coupling between successive waveguides switches periodically from C to $-C(1+\epsilon)$. For this case a gap centered at zero Bloch momentum in the linear dispersion relation opens, allowing the existence of bright solitons. Whereas, if the coupling coefficient have equal modulus, the gap closes, and a Dirac point emerges in the band structure at zero transverse momentum. Despite the absence of a gap in the linear spectrum, preventing the existence of bright gap solitons, a binary Kerr nonlinearity can open a gap, allowing for the existence of gap solitons sitting on a non-vanishing constant background. Our study has started considering coupled mode theory and taking into account third-order nonlinearities in the form of a pure Kerr effect, in order to obtain a system of equations describing the physical system. Performing a suitable Taylor expansion, we get two sets of coupled equations with constant coefficients describing beam propagation along the array. It is straightforward to write these equations in an Hamiltonian form; from the analysis of the associated dynamical system we obtain solitary-wave solutions corresponding to homoclinic or heteroclinic orbits in the phase plane. In this way, we describe in a simple and accurate fashion the entire spectrum of the soliton states of this system: bright-bright [3], bright-dark [4] and dark-antidark [5]. We also discuss the stability of plane wave solutions in both the discrete case and in the continuous long wavelength limit, finding that the discrete system can support stable plane wave propagation when the corresponding continuum approximation has no stable solutions.

References

[1] S. H. Nam, A. J. Taylor, and A. Efimov, *Diabolical point and conical-like diffraction in periodic plasmonic nanostructures*, Opt. Exp 18, 10120 (2010).
[2] N. K. Efremidis, P. Zhang, Z. Chen, D. N. Christodoulides, C. E. Rüter, and Detlef Kip, *Wave propagation in waveguide arrays with alternating positive and negative couplings*, Phys. Rev. A 81, 053817 (2010).
[3] M. Conforti, C. De Angelis and T. R. Akylas, *Energy localization and transport in binary waveguide arrays*, Physical Review A **83**, 043822 (2011).
[4] M. Conforti, C. De Angelis, T. R. Akylas and A. B. Aceves, *Modulational stability and gap solitons of gapless systems: continuous vs. discrete*, Physical Review A **85**, 063836 (2012).
[5] A. Auditore, M. Conforti, C. De Angelis, and A. B. Aceves, *Dark-antidark solitons in waveguide arrays with alternating positive-negative couplings*, Optics Communications, in press.

Bandgap maps for Photonic Crystal with Honeycomb lattice for different shapes of scatterers

Vinita[1], A. Kumar[1*], V. Rastogi[2]
[1] *Department of Applied Physics, Delhi Technological University, Delhi, India*
[2] *Department of Physics,Indian Institute of Technology Roorkee, Roorkee , India*
* ajeetdph@gmail.com

In this paper, two dimensional (2D) photonic crystal (PhC) with honeycomb lattice for non circular (square and hexagonal) shapes of rods has been investigated using plane wave expansion method. Photonic bandgap maps for different shapes of scatterers have been presented and their characteristics have been discussed.

Brief Summary

Photonic crystals (PhCs) are most valuable when they possess complete photonic bandgap (CPBG) where, propagating modes are forbidden regardless of polarization [1]. PhCs with triangular lattice have larger CPBG than square lattice but are difficult to fabricate. Previous work on honeycomb lattice for circular rods show CPBG at smaller filling fraction [2]. In this paper, CPBG and PBG maps for honeycomb lattice with non-circular shapes of dielectric rods in air column have been investigated. Results have been calculated for dielectric rods with GaAs material having relative dielectric constant, ε =11.4, since this is an important material for variety of PhC devices [1]. The gap maps for two shapes of rods (square and hexagonal) are presented in Fig. 1. For square rods, maximum CPBG has been found for l/a =0.38, where l is the length of the side of the square and a is lattice constant with maximum gap midgap ratio, ω_R = 5.8%. In case of hexagonal rods, two CPBG have been obtained. For first CPBG region, maximum CPBG has been found for d/a = 0.26, where d the length of side of the hexagon with maximum gap midgap ratio, ω_R = 10.5% while for second region, maximum CPBG has been found at d/a = 0.42 with maximum gap midgap ratio, ω_R = 5.4%. Hexagonal rods have the largest CPBG than square and circular rods at relatively smaller filling fraction. So, it is easy to fabricate devices for honeycomb structure with hexagonal rods than triangular lattice. As maximum gap midgap ratio is greater than 10% so it can be used as PhC mirrors with 100% reflection [2].

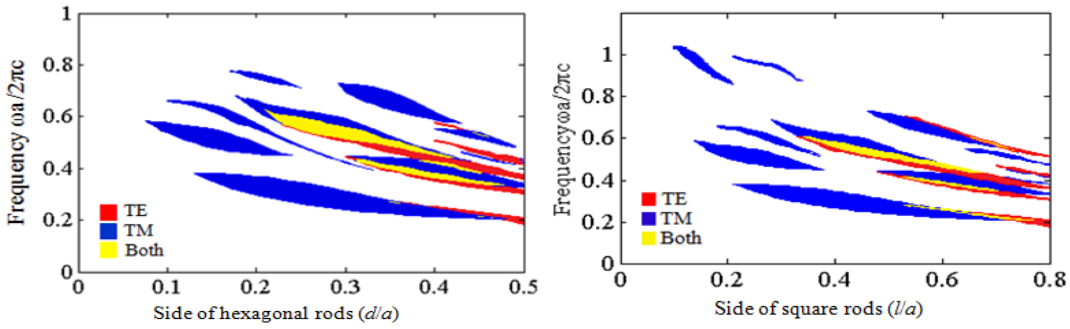

Fig.1 Gapmaps for (a) hexagonal rods, (b) square rods in honeycomb lattice

References

[1] A. V. Dyogtyev, I. A. Sukhoivanov, and R. M. De La Rue, *Photonic band-gap maps for different two dimensionally periodic crystal structures*, Journal of Applied Physics, 107, 013108, 2010

[2] J. D. Joannopoulos, R.D. Meade, and J. N. Winn, *Photonic Crystals*: *Molding the Flow of Light*, Princeton University Press, Chichester, West Sussex, 1995

Standing Waves on Periodic Arrays of Circular Dielectric Cylinders

Zhen Hu[1], Ya Yan Lu[2]

[1]*Department of Mathematics, Hohai University, Nanjing, Jiangsu, China*
[2]*Department of Mathematics, City University of Hong Kong, Kowloon, Hong Kong*
huzhen1230@gmail.com

Standing waves are known to exist on infinite arrays of dielectric circular cylinders. The frequencies of standing waves are calculated for different values of the dielectric constant and radius. The standing waves have real frequencies, and they correspond to resonances with infinite quality factor.

Introduction

Consider a periodic array (period a) of infinitely long and parallel (parallel to z axis) circular dielectric cylinders (radius r, dielectric constant ε) placed on the y-axis and surrounded by air. A standing wave on the array is periodic in y, and decays exponentially as $|x| \to \infty$.

Results

In Fig. 1, we show the lowest frequencies of the standing waves in the E polarization for different

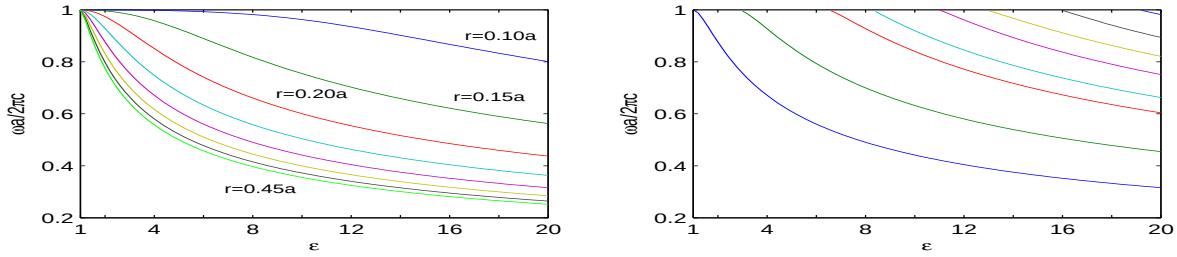

Fig. 1. Left: lowest frequencies for different r. Right: all frequencies for $r = 0.3a$.

values of r and ε, and the frequencies of all standing waves for $r = 0.3a$. For $\varepsilon = 11.56$, there are five standing waves whose frequencies are $\omega a/2\pi c = 0.4112$, 0.5897, 0.7841, 0.8590, and 0.9766, respectively. The electric field patterns of these standing waves are shown in Fig. 2.

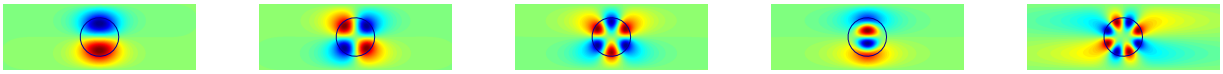

Fig. 2. Electric field patterns of the five standing waves for $r = 0.30a$ and $\varepsilon = 11.56$.

Acknowledgments

The work is partially supported by the National Science Foundation of China (project 11101122).

References

[1] S. Shipman and D. Volkov, SIAM J. Appl. Math. **67**, 687–713 (2007).

Design and Analysis of a Low Cost Highly Sensitive Refractive Index Sensor

Babita[1*], V. Rastogi[1]
[1] *Department of Physics, Indian Institute of Technology Roorkee, Roorkee-247667, India*
* babitaphy@gmail.com

A simple, compact, low cost and highly sensitive sensor for sensing refractive index of various biological and chemical samples has been presented. The maximum resolution of the sensor is of the order of 10^{-5} corresponding to 1% change in transmitted power.

Introduction

In biomedical applications, such as photodynamic therapy [1], functional imaging and optical biopsy light or laser beams are transported and distributed in biological tissues. When light enters in the biological tissue or in any chemical liquid, the optical properties of tissues like absorption coefficients, reflection, irradiance levels, and the scattering phase functions determine the light transmission and distribution. These phenomena are dependent on the refractive indices of tissues or liquids and reflect their structural organization, which can be used as an intrinsic marker for disease. Therefore, to understand the light behavior in biological tissues and chemical liquids, it has become imperative to have accurate data regarding refractive indices of the tissues or liquids. Here we present the design of a leaky planar optical waveguide based refractive index sensor. In the proposed design the test sample forms the leaky layer of the structure. Any change the refractive index of the leaky layer changes the leakage loss and hence transmittance of the structure and this forms the working principle of the sensor.

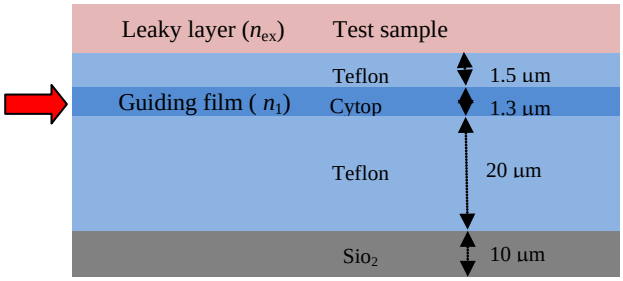

Fig. 1 (a) Schematic representation of sensor

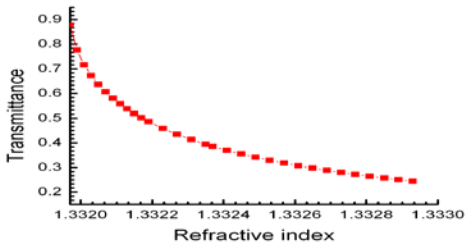

Fig. 1(b) Variation in transmittance with n_{ex}

Results and discussion

Schematic of the sensor design is shown in Fig. 1(a). Transmittance through guiding film has been modeled by using the transfer matrix method TMM [2]. Fig.1 (b) clearly shows that within the range 1.33197 to 1.33293 resolution of sensor is 1.5×10^{-5} for 1% change in output power at 633 nm wavelength. This range can be used to sense refractive index of proteins, glucose solution, sucrose solution, salt solution and for testing water adulteration.

References

[1] T. J. Dougherty, C. J. Gomer, B. W. Henderson, G. Jori, D. Kessel, M. Korbelik, J. Moan, and Q. Peng, *Photodynamic therapy*, J. Nat. Cancer Inst., 90 (12), 889-905, 1998.

[2] A. K. Ghatak, K. Thyagarajan, and M. R. Shenoy, *Numerical analysis of planar optical waveguides using matrix approach*, J. Lightwave Technol., 5 (5), 660-667 (1987).

Integrated Optics refractometry: Sensitivity in relation to spectral shifts

H.J.W.M. Hoekstra*, *MESA*$^{+}$ *Institute for Nanotechnology, University of Twente, Enschede, NL*
**h.j.w.m.hoekstra@ewi.utwente.nl*

A new variant of the Vernier-effect based sensor reported in ref. 1 is introduced. Both sensor types may show a huge index induced spectral shift. It will be shown in a poster presentation that with such sensors, as well as with surface plasmon based sensors, the constraints on the spectral resolution of the read out are strongly relaxed, but the sensitivity is not increased (unlike what is often reported in the literature).

Considered sensing devices

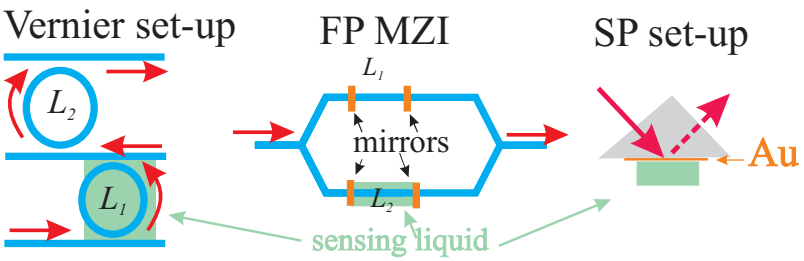

Figure 1. Schematics of the considered devices with potentially huge index-induced spectral shift enhancement.

The considered three sensing devices are depicted in fig. 1. Here we will discuss in some detail only the one based on the Vernier effect [1]. The lengths of the two cascaded ring resonators differ only slightly ($L_1 / L_2 = \eta / (\eta + 1)$; η integer) so that the transmission combs of the resonators have a slightly different free spectral range (FSR, $\Delta\lambda$) and their transmission peaks coincide periodically according to a FSR of $\Delta\lambda_V = \eta\Delta\lambda$ (see fig 2a), corresponding to the spectral spacing of the transmittance maxima of the cascaded cavities (see fig. 2b). For a relatively small spectral shift of the transmission comb of one of the cavities, $\delta\lambda$, the broadened total transmittance shows an enhanced shift of $\delta\lambda_V \approx \eta\delta\lambda$.

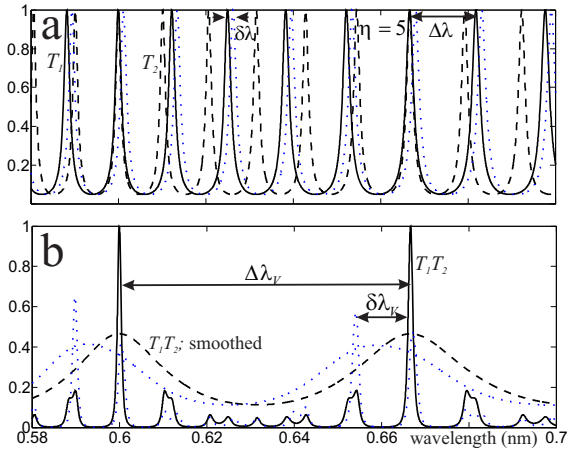

Figure 2. Graphs illustrating the Vernier effect based sensor, with (a) transmittances of the two separate cavities, T_1 (solid) and T_2 (dashed) and T_1 after a spectral shift $\delta\lambda$ (dotted, blue), and with (b) corresponding total transmittance T of the set-up (solid), T spectrally broadened (dashed) and both after the spectral shift (dotted, blue)

About sensitivity and spectral shift

The sensitivity of a device, *S*, can be defined by the maximum value of $|\partial \ln T / \partial n|$ and can be rewritten according to

$$S = |\partial \ln T / \partial n|_\lambda = |\partial \ln T / \partial \lambda|_n \, |\partial \lambda / \partial n|_T .$$

It is seen from the equation that the sensitivity of the Vernier set-up, with say only T_1 sensitive to index changes, is equal to that of the separate cavity with transmittance T_1. The huge spectral shift of the former is exactly neutralized by the smaller slope, i.e., generally $|\partial T / \partial \lambda| \ll |\partial T_1 / \partial \lambda|$. The key point for the sensitivity seems to be only the magnitude of the interaction between light and sensed matter; a point further elaborated during the poster presentation.

References

[1] T. Claes et al., *Experimental characterization of a Si photonic biosensor consisting of two cascaded ring resonators based on the Vernier effect etc.*, Opt. Expr. 18, 2010.

Reflection of semi-guided plane waves at angled thin-film transitions

Fehmi Çivitci, Manfred Hammer*, Hugo J.W.M. Hoekstra

MESA+ Institute for Nanotechnology, University of Twente, Enschede, The Netherlands
*m.hammer@utwente.nl

The propagation of thin-film guided, in-plane unguided plane optical waves, and their partial or total reflection at transitions between regions with different film thickness, is considered. The properties of reflected and refracted waves can be predicted reasonably by readily available Helmholtz- and/or eigenmode-solvers.

2-D optics

Classical concepts [1] for integrated optical components like mirrors, lenses, prisms, polarizers, but also for entire spectrometers [2], rely on the effects that a — tapered or step-like — transition between regions with different layering, specifically different core thickness, has on thin-film guided, in-plane unguided light. Results for the reflection and refraction of 1-D guided plane waves at such a discontinuity may form the basis for a description of the in-plane propagation by geometrical optics [1, 2]. Part (a) of the figure below shows a typical configuration. As a step beyond the classical effective index picture, we will discuss and compare two approaches on how this problem can be tackled — at least partly — by standard tools for integrated optics design.

(I) Accepting the scalar approximation, using an ansatz of a uniform harmonic field dependence on the interface coordinate y, the 3-D problem reduces to a 2-D Helmholtz problem, for guided wave input and transparent boundaries, where the permittivity depends on the incidence angle.

(II) By complementing the x-z-view with a mirrored interface at some faraway negative z-position, one obtains the 2-D cross section of a wide multimode rib channel. Constraints for transverse resonance permit to translate the propagation constants of its polarized modes into discrete samples of the phase factors experienced by an in-plane guided wave upon total internal reflection at the sidewalls.

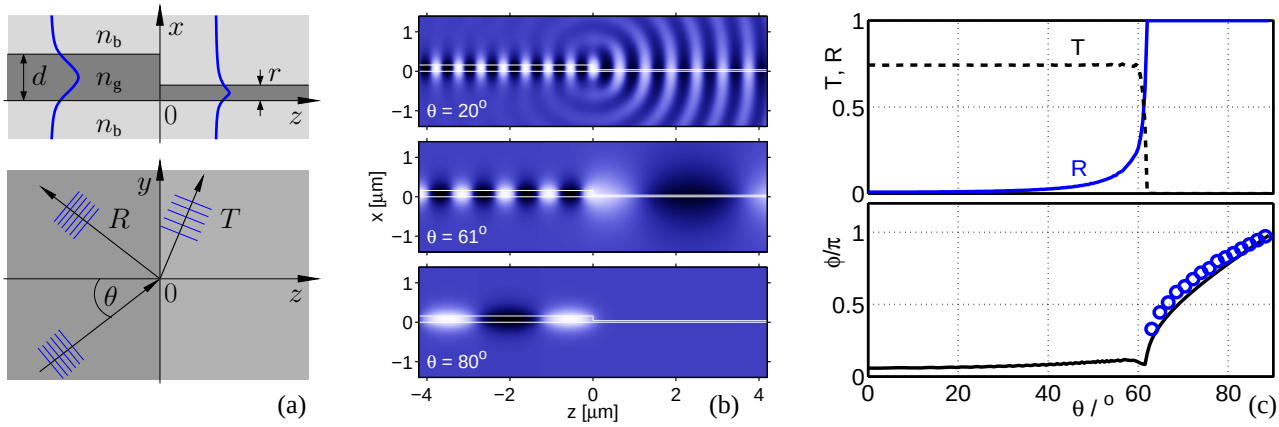

(a): Reflection of semi-guided plane waves at a thin film step discontinuity. (b): Snapshots for wave incidence at different angles θ. (c): Transmittance T, reflectance R, and phase shift ϕ upon reflection vs. incidence angle θ, predicted by a 2-D Helmholtz solver (I), and by mode analysis (II, markers) of an $8\,\mu$m wide rib. Parameters, cf. (a): $n_b = 1.4524$, $n_g = 2.0081$, $d = 160$ nm, $r = 40$ nm, TE-fields, vacuum wavelength $\lambda = 850$ nm.

References

[1] P. K. Tien. *Rev. Mod. Phys.*, 49(2):361, 1977; R. Ulrich, R. J. Martin, *Appl. Opt.*, 10(9):2077, 1971.
[2] F. Çivitci, H. J. W. M. Hoekstra. Europ. Conf. Integr. Optics (ECIO), Barcelona, Spain, paper 151, 2012.

Acknowledgement: This research is supported by the Dutch Technology Foundation STW (project 10051).

Time domain Method of Lines

S. F. Helfert

FernUniversität in Hagen, Chair of Optical Information Technology, Universitätsstr. 27
58084 Hagen, Germany
stefan.helfert@fernuni-hagen.de

In this presentation will be shown how the Method of Lines can be used to solve initial value problems in time domain. 1D numerical results are presented for standard dispersion free materials but also for dispersive media.

Introduction

The Method of Lines is a numerical algorithm that permits the solution of waveguide problems. Usually it is used in the frequency domain; the algorithm is described in detail e.g. in [1]. However, also time domain computations were performed in the past. In [2] the time dependency was treated with finite differences. A time dependency according to $\sin \omega_0 t$, $\cos \omega_0 t$ was applied in [3] and frequency solutions were combined with the discrete Fourier transform in [4]). In contrast to those papers, initial value problems with analytic time dependency will be treated here.

Numerical algorithm

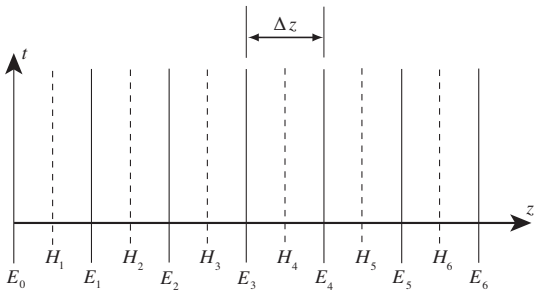

Fig. 1: Discretization in z-direction

To develop the algorithm we start with Maxwell's equations that are discretized in spatial directions. The 1D-case is shown in Fig. 1. Analytic expressions are used for the time-dependency, resulting in "time-lines". Different from frequency domain computations $E_0(t)$ will be given as initial value, here. Then, the discretized Maxwell' equations may be written as:

$$\frac{\partial \mathbf{F}}{\partial t} + \mathbf{Q}_1 \mathbf{F} = -\mathbf{Q}_0 E_0(t)$$

where $\mathbf{F}$ contains the discretized fields and the $\mathbf{Q}$-matrices contain finite difference approximations of the derivatives. Particularly, an inhomogeneous differential equation system is obtained. In the presentation will be shown how its solution is constructed from the inhomogeneous and the homogeneous differential equation. Numerical results will be shown for standard dispersion free materials, and for structures where a left handed material (LHM, see e.g. [5]) is sandwiched between two standard right handed materials. Since LHMs are dispersive it is also shown how such dispersive material may be incorporated into the algorithm.

References

[1] R. Pregla, *Analysis of Electromagnetic Fields and Waves - The Method of Lines*, Wiley & Sons, UK, 2008.
[2] W. E. Schiesser, *The Numerical Method of Lines Integration of Partial Differential Equations*, Academic Press, San Diego , USA, 1991.
[3] S. Nam, S. El–Ghazaly, H. Ling, and T. Itoh, *Electron. Lett.*, vol. 24, no. 2, pp. 128–129, 1988.
[4] J. Gerdes, in *ICTON Conf.*, Rome, Italy, 2007, vol. 4, pp. 324–327.
[5] G. V. Eleftheriades and Keith G. Balmain, (Eds.), *Negative-Refraction Metamaterials*, Wiley-Interscience, Hoboken, NJ, USA, 2005.

Matrix exponential and Krylov subspaces for fast time domain computations: recent advances

M.A. Botchev [1]

[1] *MESA$^+$ Institute for Nanotechnology, MaCS/EEMCS, University of Twente, Enschede, The Netherlands*
www.math.utwente.nl/ botchevma/, m.a.botchev@utwente.nl

We show how finite difference (or finite element) time domain computations can be accelerated by employing recent advances in the matrix exponential time integration and Krylov subspace techniques.

Matrix exponential time integration: no time stepping!

The finite difference time domain (FDTD) method is an efficient tool to model photonic nanostructures numerically. The standard FDTD method can be seen an application of the staggered leap frog time integration to the system of ordinary differential equations

$$y'(t) = -Ay(t), \quad y(0) = v, \qquad A \approx \begin{bmatrix} 0 & \mu^{-1}\nabla\times \\ \varepsilon^{-1}\nabla\times & \sigma\cdot \end{bmatrix} \in \mathbb{R}^{n\times n}.$$

Here A is the discrete Maxwell operator discretized in space by the standard staggered Yee method. μ, ε and σ are (relative) permeability, permittivity and conductivity, respectively. The vector function $y(t)$ contains unknown components of the magnetic and electric fields.

By using the matrix exponential operator, solution of the system can be written as $y(t) = \exp(-tA)v$. Numerical algorithms, which are based on this approach, are called exponential time integration methods. The essential point is that not the matrix exponential itself but rather *its action* on the vector v is computed. An attractive feature of the formula $y(t) = \exp(-tA)v$ is that it provides solution for virtually any time moment, without time stepping. Often, this leads to a significantly faster time solution than with the standard time integration, such as the classical FDTD method.

Rational shift-and-invert Krylov subspace techniques

An efficient way to compute the actions of $\exp(-tA)$ is by employing the so-called Krylov subspace methods. In this approach a projection of A onto the Krylov subspace $\mathrm{span}\{v, Av, A^2v, \ldots, A^{k-1}v\}$ is used and the approach is efficient as soon as $k \ll n$. Recently, an improvement has been proposed to the Krylov subspace methods for computing the actions of the matrix exponential, namely, the shift-and-invert Krylov subspace method. This method belongs to the class of the rational Krylov subspace methods. It provides a very fast and often grid independent convergence for the price of solving linear systems. We discuss its implementation issues.

Block Krylov subspaces to accommodate source terms

Source terms are often dealt with incorporating an inhomogeneous term $g(t)$ into the discretized Maxwell equations, e.g.,

$$y'(t) = -Ay(t) + g(t), \quad y(0) = v.$$

The presence of the source term renders the formula $y(t) = \exp(-tA)v$ invalid and usually one applies a time stepping where the matrix exponential approach can used at each time step. We propose another, often more efficient, approach. It is based on a low rank approximation of the source term $g(t)$ and a special block Krylov subspace method.

Numerical Modeling of Seeded FWM in Silicon Nitride Waveguides for CARS

J.P. Epping[1*], M. Kues[2], P.J.M. van der Slot[1], C.J. Lee[1,3], C. Fallnich[2], K.-J. Boller[1]
[1] *MESA+ Institute for Nanotechnology, University of Twente, Enschede, The Netherlands*
[2] *Institute of Applied Physics, Westfälische Wilhelms-Universität Münster, Germany*
[3] *FOM Institute DIFFER, Nieuwegein, The Netherlands*
* j.p.epping@utwente.nl

We propose and theoretically investigate a light source for CARS based on seeded four-wave mixing in silicon nitride waveguides. A tuning range (1290-2750 cm^{-1}) is expected via pumping at a wavelength of 1058 nm and the pump power is calculated to be one order of magnitude lower than what was previously reported.

Coherent anti-Stokes Raman scattering (CARS) offers label-free detection with chemical selectivity. In order to achieve spectral and therefore chemical resolution two synchronized narrowband pulses have to be provided by an appropriate light source. Here, we present theoretical investigations of a CARS light source based on seeded four-wave mixing (FWM) [1] in silicon nitride waveguides, which is of great interest for analyzing CARS spectra in a lab-on-a-chip setup.

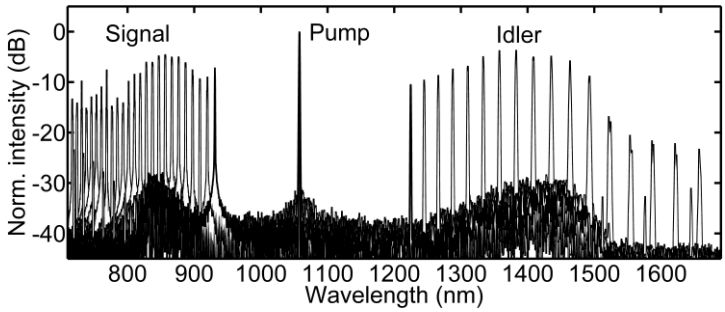

Fig. 1: *Superimposed spectra of cw seeded FWM for different seed wavelengths. The pump pulse has a center wavelength of 1058 nm and a pulse duration of 10 ps. The cw seed has a power of 100 mW and is tuned from 715 nm to 935 nm in 10 nm steps.*

We consider a silicon nitride waveguide and pump pulses with a pulse width of 10 ps and a peak power of 100 W. The center wavelength of 1058 nm is selected to lie in the normal dispersion regime. The waveguide dispersion is calculated using COMSOL Multiphysics. We calculate the seeded FWM by numerically integrating the generalized nonlinear Schrodinger equation [2]. For obtaining a spectral narrow idler wave a cw narrowband seed at the signal wavelength is also injected and tuned from 715 nm to 935 nm in order to generate synchronized idler pulses suitable for CARS. As can be seen in Figure 1 the idler pulses can be tuned from 1225 nm to 1492 nm (at -10 dB) corresponding to CARS signals from 1290 cm^{-1} to 2750 cm^{-1}. The pulse length of the idler wave is 6.4 ps and a maximum conversion efficiency of 46 % was calculated, while the pump power is one order of magnitude lower than in [1].

References

[1] M. Baumgartl, M. Chemnitz, C. Jauregui, T. Meyer, B. Dietzek, J. Popp, J. Limpert and A. Tünnermann, Widely tunable fiber optical parametric amplifier for coherent anti-Stokes Raman scattering microscopy, Opt. Exp. 20, 26583 (2012).

[2] M. Kues, N. Brauckmann, T. Walbaum, P. Groß, C. Fallnich, Nonlinear dynamics of femtosecond supercontinuum generation with feedback, Opt. Express 17, 15827 (2009)

Propagation of a Periodic Sequence of Gaussian Pulses in a Coaxial Optical Fiber: occurrence of "Talbot Effect" in the time domain

Enakshi K Sharma[1*] and Jyoti Anand[2]
[1] *Department of Electronic Science, University of Delhi South Campus, Delhi-110021, India*
[2] *Keshav Mahavidyalaya, University of Delhi, Delhi 110034, India*
* enakshi54@yahoo.co.in

We show that when a periodic sequence of Gaussian temporal light pulses propagates through a coaxial fiber each Gaussian pulse in the sequence splits into a series of narrow pulses within the broadened Gaussian envelope. However for a chosen repetition rate, the original Gaussian pulse sequence reappears.

Summary

Coaxial optical fibers [1] (Fig.1) support two symmetric modes (LP_{01} and LP_{02}) which at a certain wavelength (λ_o) have the same group velocity (v_o) and almost equal and opposite group velocity dispersion ($\pm\alpha_o$).When the coaxial fiber is excited by a periodic sequence of Gaussian temporal pulses (period T) of the form $f(t) = e^{j\omega_0 t}\left[E_0 e^{\frac{-t^2}{\tau_0^2}} * \frac{1}{T} Comb\left(\frac{t}{T}\right)\right]$ with $\omega_o = \frac{2\pi c}{\lambda_o}$ and $\tau_o = 1ps$, from a single mode fiber identical to the rod waveguide, both modes are excited [2] and due to same group delay, arrive at a distance, *z*, at the same time. If an output single mode fiber (identical to the input fiber) is spliced at any z, power from both the modes is coupled out and due to temporal interference between the spectral components, each Gaussian pulse splits into a series of narrow pulses within the broadened Gaussian envelope (Fig. 2). However if $T = \sqrt{2\alpha_o \pi z}$, defined as a " Talbot Revival Period" (TRP), the input sequence of pulses is reproduced, in general with a reduced amplitude. Further, in addition, if $z = \frac{2m\pi}{(\beta_1 - \beta_2)}$, (where $\beta_{1,2}$ are the propagation constants of the two modes, *m* is an integer) the amplitude of the pulses is also recovered. Fig. 3 shows the result at z=398m for which TRP is 25ps. The sequence of pulses with T=25ps is reproduced while at T=25$\pm$ 5ps, the pulses are distorted due to splitting and broadening (Fig. 3).

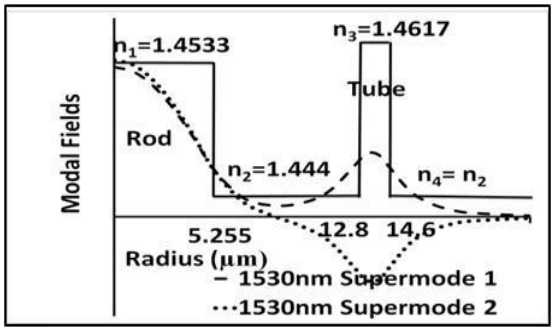

Fig. 1 Coaxial optical fiber and its modes

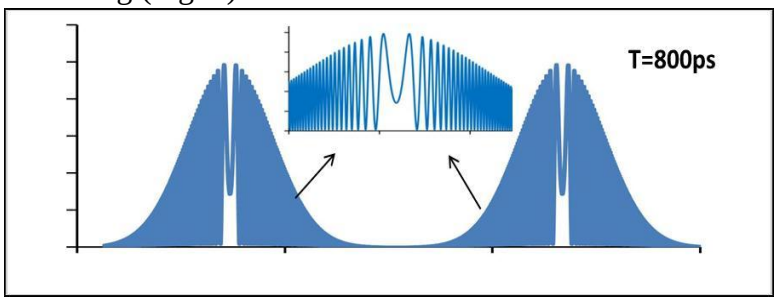

Fig. 2 Intensity of output pulse

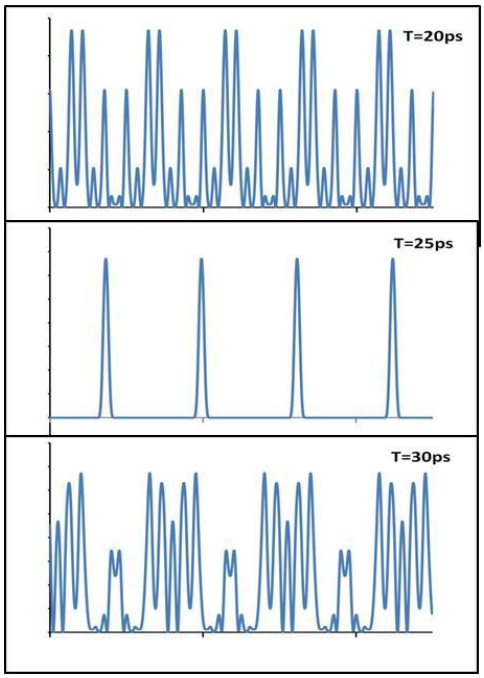

Fig. 3 Sequence of pulses at z=398m

References

[1] A C Boucouvalas, *J. Lightwave Technol.*, LT3, 1151-1158, 1985.
[2] Jyoti Anand, et al., *Optics & Laser Tech.*, 45, 688-695, 2012.

The Peculiarities of Optical Spectra of Photonic Crystal with Plasmonic Defect

S. G. Moiseev[1,2,3*], V. A. Ostatochnikov[1], D. I. Sementsov[1]
[1] *Ulyanovsk State University, Russia*
[2] *Ulyanovsk State Technical University, Russia*
[3] *Kotel'nikov Institute of Radio Engineering and Electronics of RAS, Ulyanovsk Branch, Russia*
* serg-moiseev@yandex.ru

Optical spectra of an artificial layered periodic structure with a finite number of periods and a plasmonic defect is analyzed. The case is considered when two orthogonal polarizations of an incident wave correspond to different plasmon resonance frequencies of the nanocomposite. If one of the plasmon frequencies coincides with the defect mode frequency in one of the photonic bandgaps, complete suppression of the defect mode in the transmission spectrum is possible, which makes the spectra of such structures polarization-sensitive.

In this work the possibility of using plasmonic nanocomposite with nonspherical inclusions as a tuning defect in a photonic crystal (PC) is considered and the features of the behavior of electromagnetic eigenmodes in an artificial layered periodic structure with a finite number of periods and a plasmonic defect are analyzed.

We consider a symmetric microcavity photonic crystal structure in which a nanocomposite layer is sandwiched between two dielectric photonic crystal mirrors inverted relative to one another. The structure has a double defect: inversion and inserted layer. The inversion is due to the change in the stacking sequence of the layers in going from one part of the structure to the other. The transfer matrix of the PC under consideration, with an inserted defect layer and two PC mirrors, has the form $\hat{G} = \hat{N}^a \hat{D} \hat{\bar{N}}^a$, where $\hat{N}^a = \left(\hat{N}_1 \hat{N}_2\right)^a$ and $\hat{\bar{N}}^a = \left(\hat{N}_2 \hat{N}_1\right)^a$ are the transfer matrices of defect-free PC mirrors having a periods. The PC mirrors have a finite number of structural periods, each consisting of two layers of isotropic dielectrics having permittivity ε_j and thickness L_j (j=1,2). We neglect absorption in the frequency range of interest, so ε_j is real-valued.

The defect layer in the PC structure under consideration consists of a nanocomposite, which has the form of a dielectric material containing evenly distributed metallic nanoparticles in the shape of ellipsoids of revolution. The nanoparticles are aligned with their polar axis parallel to the x axis. The nanocomposite has properties of a uniaxial crystal, and its effective permittivity is represented in the major axes by a diagonal tensor. The dependence of optical properties of the plasmonic defect on the geometric (shape and concentration of inclusions) and material (permittivities of the matrix and metal nanoparticles) parameters of composite are calculated within the Maxwell−Garnett effective-medium approximation.

It is shown, that reflection and transmission spectra of such defective periodic structure exhibit high polarization contrast. For radiation of the region near the spectral line of the defect mode, this PC absorbs the light polarized parallel to the long axis of spheroids, and for the light polarized parallel to the short axis of spheroids the structure is almost transparent. The performed analysis and the revealed features of wave characteristics of the PC with plasmonic defect can be used in the development of devices for the control of optical radiation on the basis of such structures.

This work was supported by the Russian Foundation for Basic Research and the Ministry of Education of the Russian Federation through project contracts within the framework of the Federal Target Program 'Science, Academic and Teaching Staff of Innovative Russia for 2009-2013'.

Manipulating light matter interaction with Mie resonators

G. Boudarham[1*], B. Rolly[1], B. Stout[1], R. Abdeddaim[1], J.M. Geffrin[1], N. Bonod[1]
[1]*Institut Fresnel, CNRS UMR 7249, Campus Universitaire de Saint-Jérôme, 13397 Marseille cedex 20, France*

* guillaume.boudarham@fresnel.fr

We explore the possibility to enhance and confine the magnetic near-field by using a dimer of dielectric resonators illuminated by a plane wave.

Electric and magnetic dipolar and quadrupolar Mie resonances in high-index dielectric particles exhibit high quality factor that compensates their low field confinement compared to the plasmon resonances of metallic particles [1]. In a host matrix of refractive index n=1.45, and when a dipolar electric or magnetic emitter is placed at the center of a dimer of Si spheres, we obtain enhancement factors of the magnetic versus electric decay rates of 4 around λ=1.54 µm [2], that could be interesting for manipulating decay rates of trivalent erbium ions (see Fig. 1 left). We derived the analytical expressions of the decay rates of an electric/magnetic dipole transition when coupled to an electric or magnetic dipolar or quadrupolar mode. We show that in parallel coupling, an electric mode (resp. magnetic) can increase the decay rates of both magnetic and electric dipoles. Motived by the results obtained by B. Rolly *et al* [2-3], we investigate in this contribution the reciprocal problem by studying the magnetic field enhancement within the nanogap of a dimer of dielectric resonators with moderate permittivity when illuminated by a plane wave [4].

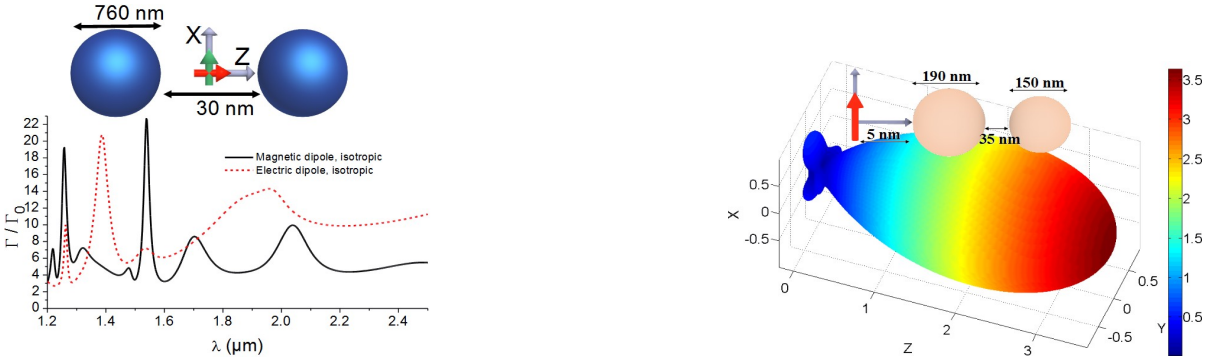

Fig 1: *left: isotropic averaged decay rates when an electric dipole (dashed red line) or magnetic dipole (solid black line) is placed in the centre of a Si dimer. right: radiation diagram at 570 nm of an electric dipole transversely coupled to two GaP spheres. Emission directivity is over 9 dBi.*

References

[1] A. García-Etxarri *et al*., "*Strong magnetic response of submicron Silicon particles in the infrared*," Optics Express 19, 4815-4826, 2011.
[2] B. Rolly *et al*., "*Promoting magnetic dipolar transition in trivalent lanthanide ions with lossless Mie resonances*", Physical Review B **85**, 245432, 2012.
[3] B. Rolly *et al*., "*Metallic dimers: When bonding transverse modes shine light*", Physical Review B **84**, 125420, 2011.
[4] G. Boudarham *et al*., submitted.

Discontinuous Galerkin Methods in Nano-Photonics

Kurt Busch
Humboldt-Universität zu Berlin, Institut für Physik, AG Theoretische Optik & Photonik, Newtonstr. 15, 12489 Berlin, and Max-Born-Institut, Max-Born-Str. 2A, 12489 Berlin, Germany
kurt.busch@physik.hu-berlin.de

The Discontinuous Galerkin Time-Domain Finite-Element approach and its applications to nano-photonic systems is reviewed. This includes technical aspects (curvilinear elements, graphic processors) as well as conceptual developments (electron energy loss spectroscopy, advanced material models).

Introduction

The past years have witnessed exciting developments in the area of time-domain computations of Maxwell's equations. In particular, the nodal Discontinuous Galerkin Time-Domain (DGTD) Finite-Element approach [1] has emerged as serious rival for the well-tested Finite-Difference Time-Domain (FDTD) approach. DGTD approaches are applied to a large variety of electromagnetic and optical problems including ordinary and ground penetrating radar, wireless communication, electro-physiology, plasma physics, and nano-photonics.

In particular, the DGTD method inherits the adaptive spatial resolution via unstructured grids and high-order spatial discretization of ordinary Finite Element techniques and combines them with explicit and high-order time-stepping schemes. As a result, DGTD allows one to effectively deal with some of the fundamental challenges associated with many nano-photonic problems: Complex geometries and multiple time and length scales [2].

Discussion

For instance, the essentially exact numerics provided by the DGTD approach may be utilized for assessing approximate coupled mode schemes for complex geometries [3]. Further, DGTD facilitates the modeling of advanced spectroscopic settings such as electron energy loss spectroscopy [4] and this significantly contributes in the interpretation of experimental data [5].

These encouraging results suggest to extent further DGTD's range of applicability through the development of advanced material models that can be efficiently integrated into a DGTD framework. This includes certain plasmonic systems where magneto-optical effects provide effective means of tuning their optical response [6]. By the same token, certain plasmonic systems exhibit (potentially) strong nonlocal and/or nonlinear optical properties where the standard description of metals as isotropic dispersive linear materials fails.

References

[1] J. Hesthaven and T. Warburton, J. Comput. Phys. **181**, 186 (2002)

[2] K. Busch, M. König, and J. Niegemann, Laser Photonics Rev. **5**, 773 (2011)

[3] K.R. Hiremath, J. Niegemann, and K. Busch, Opt. Express **19**, 8641 (2011)

[4] C. Matyssek, J. Niegemann, W. Hergert, and K. Busch, Photon. Nanostruct. **9**, 367 (2011)

[5] F. von Cube et al., Opt. Mater. Express **1**, 1009 (2011); F. von Cube et al., Nano Lett., in press (2013)

[6] C. Wolff, R. Rodriguez-Oliveros, and K. Busch, submitted (2013)

Generalized Source Method in Curvilinear Coordinates

A.A. Shcherbakov [1], A.V. Tishchenko [2]

[1] *Laboratory NFE, Moscow Institute of Physics and Technology, Dolgoprudny, Russia*
[2] *Laboratory Hubert Curien, University of Lyon, Saint-Etienne, France*
alex.shcherbakov@phystech.edu

This paper presents an extension of the generalized source method to curvilinear coordinates for modeling grating diffraction on 1D gratings. The method demonstrates linear time and memory complexity relative to the mesh node number.

The generalized source method (GSM) was recently developed for the light diffraction calculation on 2D periodic arbitrary shaped dielectric structures [1]. The method demonstrated $O(N \log N)$ of both time and memory consumption overwhelming widely used modal methods that have $O(N^3)$ complexity (N is a mesh node number). It is well-known that the Maxwell's equations can be written in the affine-invariant form when all the metric information is hidden in the constitutive relations. This fact was extensively used in computational electrodynamics for describing perfectly matched layers [2], and for introduction of adaptive spatial resolution in the Fourier Modal Method (FMM) [3]. In the last case curvilinear coordinates allowed for better adaptation to spatial field distributions and consequent reliable modeling of metallic gratings. Aiming at adapting the GSM to metallic gratings simulation we reformulate the method in a curvilinear coordinate system which contains a coordinate surface either coinciding with the corrugation profile if the latter is smooth or close to the profile if it contains sharp edges. The figure demonstrates an example of curvilinear coordinates introduced in a bounded region containing the grating.

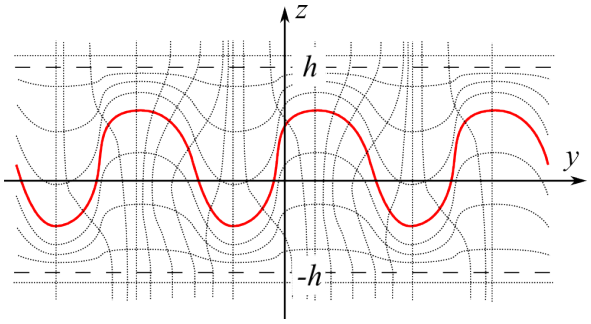

Illustrative example of curvilinear coordinates introduced inside a plane layer containing a 1D diffraction grating. One of coordinate surfaces coincides with the grating corrugation profile.

Acknowledgements

This work was supported in part by the Russian Ministry of Education and Science (agreement No. 14.A18.21.1946).

References

[1] A.A. Shcherbakov, A.V. Tishchenko, *New fast and memory-sparing method for rigorous electromagnetic analysis of 2D periodic dielectric structures,* JQSRT, 113, 158, 2012.
[2] W.C. Chew, W.H. Weedon, *A 3D perfectly matched medium from modified Maxwells equations with stretched coordinates,* Microwave Opt. Technol. Lett. 7, 599, 1994.
[3] G. Granet, *Reformulation of the lamellar grating problem through the concept of adaptive spatial resolution,* J. Opt. Soc. Am. A, 16, 2510, 1998.

Modified Optimal Variational Method to Study Modal Characteristics of Si Photonic Wire Waveguides

Kanchan Gehlot, Anurag Sharma

Department of Physics, Indian Institute of Technology Delhi, New Delhi 110 016, India
gehlot.kanchan@gmail.com, asharma@physics.iitd.ac.in

Earlier developed scalar VOPT method [1] is modified and a semi-vector approach is developed to study vector modes of high index contrast Si photonic wire waveguides. This iterative method is simple, fast and gives very accurate results.

Summary

In development of Si nanophotonics, Si photonic wire waveguide has emerged as a building block of various optical devices and interconnects for optoelectronic integrated circuits. High-index contrast and structural asymmetry of Si photonic wire waveguides give rise to large modal birefringence and it becomes essential to carry out vector mode analysis for the waveguide. Modified VOPT method is presented to provide an accurate semi-vector analysis of vector modes. This method uses a procedure similar to scalar VOPT to arrive at an iterative scheme for semi-vector wave equation. Accuracy of this method is tested by comparing present analysis with FEM results [2]. The waveguide considered in this paper consists of rectangular Si core surrounded by air cladding. At the operating wavelength of 1.55 μm, Si refractive index is taken as 3.50. For core height of 260 nm, fundamental E^x and E^y modes are calculated for wide range of waveguide width. In Fig. 1, variation of effective mode index, $n_{eff} = \beta/k$ for E^x_{11}, E^y_{11} mode and modal birefringence with waveguide width are plotted. Modal birefringence is defined as difference in n_{eff} of E^x_{11} and E^y_{11} mode. The comparison with FEM results shows that present method gives accurate results even for modes close to cut-off.

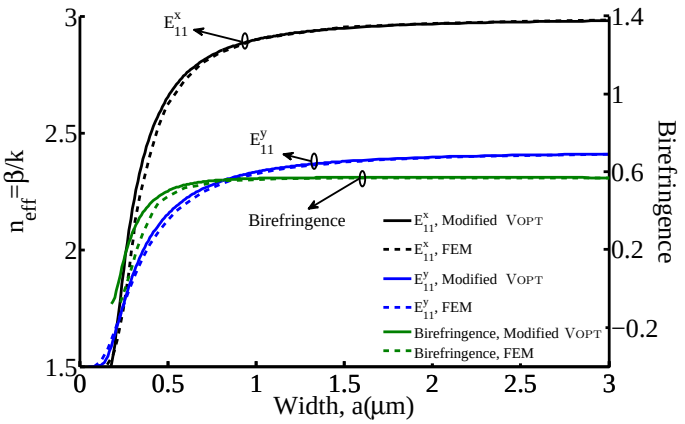

Fig. 1. Variation of n_{eff} for E^x_{11} and E^y_{11} modes (left scale) and modal birefringence (right scale) with width of waveguide core, a

This work was supported by grant from Council of Scientific and Industrial Research (CSIR), Govt. of India.

References

[1] A. Sharma, *Opt. Quant. Electron* **21**, 517–520 (1989)
[2] D. M. H. Leung et al. *Opt. Exp.*, **18**, 8528–8539 (2010)

Back-reflector optimization in thin-film silicon solar cells by rigorous FEM light propagation modeling

M. Blome [1], K. McPeak [2], S. Burger [1], F. Schmidt [1]

[1] *Computational Nano-Optics, Zuse Institute Berlin, Germany*
[2] *Optical Materials Engineering Laboratory, ETH Zürich, Switzerland*
blome@zib.de

We numerically optimize the light trapping efficiency of a periodic, pyramid structured back metal contact in thin-film amorphous silicon solar cells by rigorously solving Maxwell's equations. Identified optimal back contact geometries display a significant increase in short circuit current density over flat solar cells.

Introduction

Thin-film amorphous silicon based solar cells are an attractive design for providing cost-effective and efficient solar energy. Amorphous hydrogenated silicon (a-Si:H) can be deposited in thin layers on cheap substrate materials such as glass or plastic offering low fabrication costs suitable for mass production. Considering the large absorption length of amorphous silicon near its bandgap, the low absorber layer thicknesses typically employed necessitate light-trapping concepts for realizing efficient thin-film silicon solar cells.

Methodologies

Within this work we optimize geometry parameters of a periodic, pyramid structured back metal contact in a model (p-i-n type) thin-film solar cell. Our goal is to find optimal model parameters that considerably increase the solar cells light trapping efficiency compared to flat designs. We model the light propagation inside the investigated solar cell model using a frequency domain finite element Maxwell solver employing high order edge elements and adaptive perfectly matched layers for realizing transparent boundary conditions. To judge the efficiency of different solar cell models we compare computed short circuit current densities and reflection spectra.

For accurately predicting the material layer interfaces within the investigated solar cell model we employ a topology simulation method. The method simulates the chemical vapor deposition process that is typically used to fabricate thin-film solar cells by combining a ballistic transport and reaction model with a level-set method in an iterative approach.

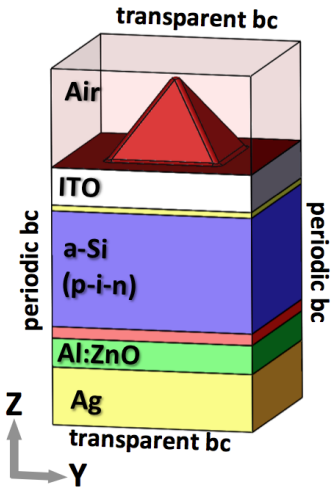

Sample CAD representation of the model (p-i-n type) solar cell considered.

Conclusions

In using our optimization approach we have identified nanostructured back reflector geometries that display a significant increase in short circuit current density over flat back reflectors. The employed topology simulation approach yield solar cell models that represent a far more realistic approximation to a real solar cell stack compared to solar cell models created by the frequently used conformal material layer growth assumption.

Tailoring meta-atoms for specific metamaterial applications

F. Lederer, S. Mühlig, C. Rockstuhl, R. Alaee, and C. Menzel
Institute of Condensed Matter Theory and Solid State Optics, Abbe Center of Photonics, Friedrich-Schiller-Universität Jena, Germany
falk.lederer@uni-jena.de

A strategic aim in contemporary optics is the desired control of light. Potentially this goal can be met by using metamaterials. We show how meta-atoms can be tailored to achieve various optical functionalities by a suitable multipole analysis of the scattered field.

Metamaterials are made of periodically or randomly arranged meta-atoms. Their optical properties are determined both by the arrangement and the shape of the respective meta-atoms. Sometimes a single meta-atom or an ensemble of a few of them provides also exciting functionalities, as e.g. optical nanoantennas. Thus there is an urgent requirement to develop tools that permit the control of the light field by tailoring the meta-atoms.
We describe here how to analyze the scattering response of individual meta-atoms in terms of multipole contributions. As a consequence the meta-atom can be modified such that particular multipole contributions are present or disappear depending on the envisaged functionality.
The scattered field of a selected meta-atom, calculated by rigorous means as FDTD, FEM, or FMM, is expanded into multipole contributions in spherical coordinates. These multipole moments are then transformed into their Cartesian counterparts. Thus the scattered field can be ultimately decomposed into contributions from arbitrary electric and magnetic multipole moments [1,2].

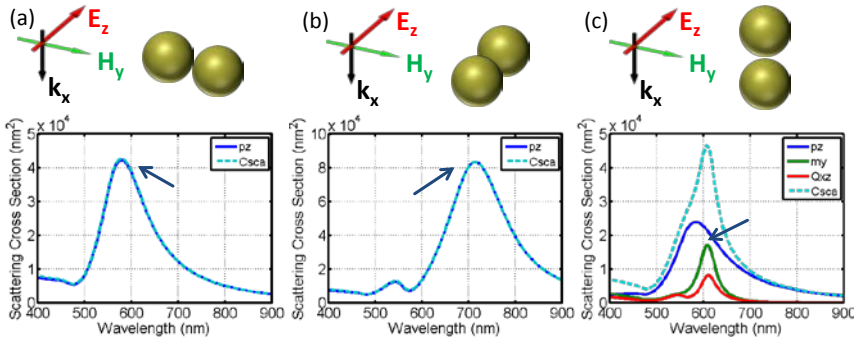

Contributing multipole moments to the scattered field of a gold dimer structure (radius = 40 nm, center-to-center distance = 83 nm) embedded into a dielectric host material (ε = 2.25) for three distinct illumination scenarios with a plane wave (a)-(c).

We use this powerful and versatile technique to design isotropic metamaterials consisting of both periodically (top down) and randomly (bottom up) arranged metaatoms. We show further that these metamaterials may be characterized by assigning genuine material parameters (permittivity and permeability) which do not depend on the wave vector of the exciting field (spatial dispersion) as it is usually the case. This can be achieved by tailoring the meta-atoms such that they exhibit only electric and magnetic dipole moments. A deep-subwavelength periodic or a random arrangement is further required to suppress spatial dispersion. It is also shown how nanoantennas can be designed the near-field of which contains a dominant quadrupole contribution thus fostering the excitation of dipole forbidden transitions in atomic systems.

References

[1] S. Mühlig, C. Menzel, C. Rockstuhl, and F. Lederer, *Multipole Analysis of Meta-Atoms*, Metamaterials 5, 64 (2011).
[2] C. Rockstuhl et al., *Scattering Properties of Meta-Atoms*, Phys. Rev. B83, 245119 (2011).

Lens equation for flat lenses made with hyperbolic metamaterials

J. Benedicto [1,2], E. Centeno [1,2], A. Moreau [1,2],

[1] *Université Blaise Pascal, Institut Pascal, BP 10448, F-63000 Clermont-Ferrand, France*
[2] *CNRS UMR 6602, F-63171 Aubière, France*
jessica.benedicto1@univ-bpclermont.fr

We give a general theory that enables the design of flat lenses based on hyperbolic metamaterials. The focal length can be finely controlled, and the losses are minimized by reducing drastically the amount of metal used. Super-resolution is obtained with a transmittance around 20 %.

Metamaterials are artificial medium with electric and magnetic effectif response that can be finely tuned. Pendry 's pioneer work, showing that a slab of such a material could be considered a perfect flat lens [1], is the best example of what can be achieved using such materials. Some metamaterials actually present a hyperbolic dispersion relation that allows for a self-collimation effect studied by P. Belov [2]. Near-field subwavelength images can be formed using hyperbolic metamaterials, which can be achieved by stacking dielectric and metallic layers. However, the flat lenses studied so far present a zero focal distance: the object and the image are formed at the very edge of the flat lens. Another way to stack the layers is to organize them in concentric circles. This forms an hyperlens, able to provide far-field images with subwavelength resolution [3].

In this study, a Fourier optics model is developed, providing a lens equation for flat lenses made of hyperbolic metamaterials. We demonstrate that, using a source on the edge of the lens, the focus can be arbitrarily chosen in a range extending from the very edge of the lens to one wavelength [4]. The numerical results show that the subwavelength resolution is preserved for a focal length below $\frac{\lambda}{2}$. Our approach even leads to an overall improvement of the transmission efficiency (the transmittance can be as high as 20%) of such lenses despite the optical losses induced by the metallic layers.

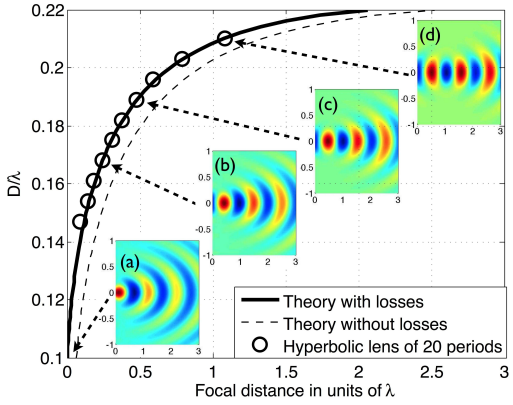

Variation of the focal distance as a function of the reduced frequency for a hyperbolic lens (20 periods). Theoretical calculations (solid line and circles) and full numerical simulations. (a-d) Field plot of the magnetic field. The focus is at a distance of 0, $\frac{\lambda}{4}$, $\frac{\lambda}{2}$ and λ of the edge.

References

[1] J.B. Pendry, *Negative Refraction Makes a Perfect Lens,* Physical Review Letters **85**, (18), 3966,2000.
[2] P.A. Belov, Y. Hao, *Subwavelength imaging at optical frequencies using a transmission device formed by periodic layered metal-dielectric structure operating in the canalization regime,* Physical Review B **73**, 113110,2006.
[3] Z. Liu, H.Lee, Y. Xiong, C. Sun, X. Zhang, *Far-field optical hyperlens magnifying sub-diffraction limited objects,* Science **315**, (5819), 1686, 2007.
[4] J. Benedicto, E. Centeno and A. Moreau, *Lens equation for flat lenses made with hyperbolic metametrials,* Optics Letters **37**, (22), 2012.

Tailoring the quadratic response of nanoantennas: use of a waveguide model

Shakeeb Bin Hasan*, Christoph Etrich, Robert Filter, Carsten Rockstuhl, and Falk Lederer
Institute of Condensed Matter Theory and Solid State Optics, Abbe Center of Photonics, Max-Wien-Platz 1, 07745 Jena, Germany. Tel. +49 3641 947179, Fax. +49 3641 947177
* shakeeb-bin.hasan@uni-jena.de

We employ a phenomenological model based on guided modes to access the localized resonances of plasmonic nanoantennas. It provides a systematic means to tune the resonance frequencies of antennas. In terms of quadratic nonlinearity, it is successfully exploited to achieve double resonant nanoantennas at both the fundamental and the second harmonic frequency to significantly boost the nonlinear interaction.

Unlike Kerr optical effect, which involves single frequencies, the majority of nonlinear processes involve multi-frequency interaction. These processes are significantly enhanced in plasmonic antennas, promoted by a subwavelength field confinement when the system sustains a resonance at one of the frequencies involved. The overall efficiency, however, could be further enhanced by achieving resonance at all involved frequencies. To this end, we consider the degenerate second harmonic generation in the presence of a dielectric medium exhibiting a strong $\chi^{(2)}$ nonlinearity ($LiNbO_3$). Without any loss of generality, we choose cylindrical metal wires as the geometry for the nanoantenna due to its amenability to both analytical and experimental studies. While more complicated antenna designs have been recently suggested for multiple resonances, we exploit the additional degree of freedom provided in terms of antenna termination for this purpose [Fig. 1(a)].

We view the localized resonances as standing-waves generated by the oscillations of guided modes supported by the cylindrical metal wire. Therefore, computing the modal dispersion and reflection coefficient of the guided mode provides us with all the data to locate the resonances supported by the structure. Allowing for resonances of different orders at fundamental harmonic (FH) and second harmonic (SH), we are able to identify frequency bands where these resonances appear at the FH and its corresponding SH. Figures 1(b-c) present one example in which double resonance is achieved for both FH (1st order) and SH (3rd order) to the betterment of the nonlinear interaction.

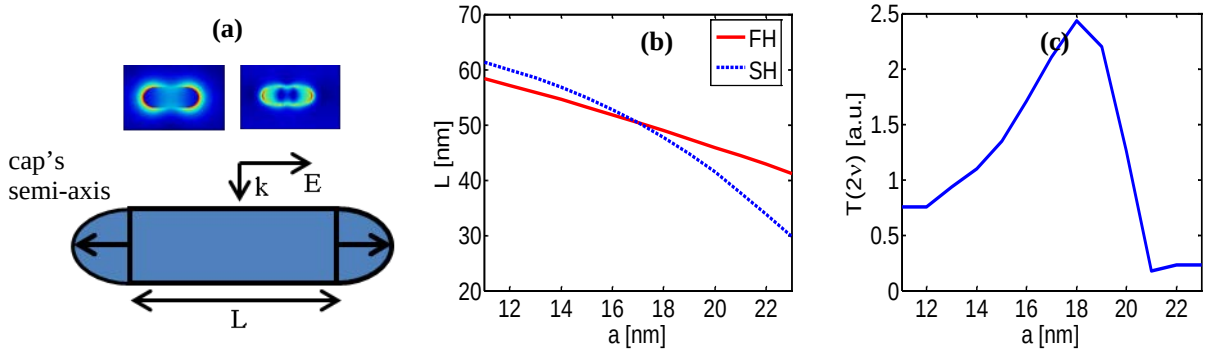

Figure 1: (a) Antenna geometry highlighting relevant geometrical features. Also shown is the amplitude distribution of the first and third order Fabry-Perot resonances FH and SH. (b) Antenna length and cap radius at which FH has 1st order (red) and SH has 3rd order (blue) resonances for the incident frequency ν_{FH} = 276THz. (c) SH transmission computed with the nonlinear FDTD at ν_{FH} = 276THz. FH is always kept resonant according to (b) but SH is resonant only when a = 17nm.

References:

[1] M. Ren, E. Plum, J. Xu, N. I. Zheludev, Nature Communications **3**, 833 (2012).
[2] M. Hentschel, T. Utikal, H. Giessen, M. Lippitz, Nano Lett. **12**, 3778 (2012).

Transmission of optical excitations through a linear chain of metal nanoparticles in the presence of a reflector

P.J. Compaijen, V.A. Malyshev, J. Knoester.

Zernike Institute for Advanced Materials, University of Groningen, Groningen, The Netherlands
p.j.compaijen@rug.nl

We study the transmission efficiency of optical signals in a linear chain of silver nanospheres in close proximity to a silver substrate and show that the coupling between surface plasmon polariton modes in the chain and on the interface enhances this efficiency. Studying the influence of the chain-interface spacing and polarization of the excitation, reveals a complicated interplay between several transmission channels.

Linear chains of Metal NanoParticles (MNPs) have been suggested for applications in nano-circuitry and nano-antennas (see, e.g., Ref. [1]). It has been shown that for such systems, the collective modes are Surface Plasmon Polaritons (SPPs) [2, 3]. The presence of a reflecting object in the proximity of the array may have a large influence on the collective modes of the chain and, therefore, on its ability to transmit optical signals. To explore this effect, we performed calculations of the dispersion relations and the Transmission Efficiency (TE), i.e. the ratio of the modulus squared of dipole moments of the last to the first MNP, assuming CW excitation of only the first particle.

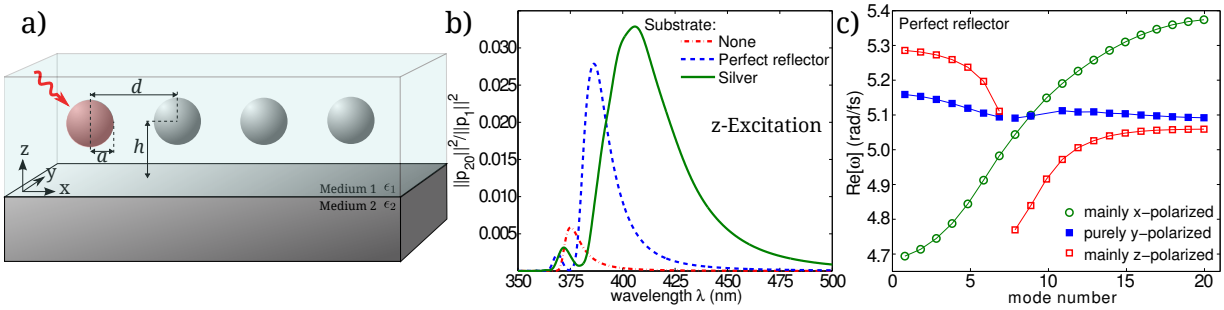

Fig. 1. a) Schematics of the system under consideration. b) TE for a chain of 20 MNPs with $a = 25$ nm, $d = 75$ nm and $h = 50$ nm for a chain over no substrate, a perfect reflector and a silver substrate. c) Dispersion relations for this chain over a perfect reflector.

Figure 1 shows that the presence of a reflector gives rise to an enhancement and an extra peak in the TE spectrum and that the main peak is red-shifted with respect to that of the isolated chain. The maximum transmission will occur for the mode with the highest group velocity (i.e. steepness of the dispersion curve) and the longest lifetime (not shown). This makes the calculation of dispersion relations a valuable tool for optimizing and understanding the TE. Interestingly, the silver substrate appears to give a stronger enhancement than a perfectly reflecting substrate, due to the possibility to decay into SPP modes of the silver substrate, which is manifested in both a broadening and an increase of the maximum transmission. Understanding the coupling between the SPP modes of the chain and the substrate, will allow to carefully manipulate the guiding properties of the MNPs.

References

[1] L. Novotny, B. Hecht, *Principles of Nano-Optics,* Cambridge University Press (2006).
[2] W.H. Weber, G.W. Ford, Physical Review B, **70**, 125429 (2004).
[3] A.F. Koenderink, A. Polman, Physical Review B, **74**, 033402 (2006).

Integrated Quantum Photonics

K. Aungskunsiri, D. Bonneau, J. Carolan, D. Fry, J. Hadden, S. Ho, J. Kennard, S. Knauer, E. Martin-Lopez, J. Meinecke, G. Mendoza, J. Munns, M. Piekarek, K. Poulios, X. Qiang, N. Russell, R. Santagati, A. Santamato, P. Shadbolt, P. Sibson, J. Silverstone, O. Snowdon, N. Tyler, J. Wang, C. Wilkes, S.R. Whittaker, J. Barreto, D. Beggs, X. Cai, P. Jiang, A. Laing, J.C.F. Matthews, G.D. Marshall, A. Peruzzo, X.-Q. Zhou, J.G. Rarity, M.G. Thompson, J.L. O'Brien and collaborators

Centre for Quantum Photonics, H.H. Wills Physics Laboratory
& Department of Electrical and Electronic Engineering, University of Bristol
www.phy.bris.ac.uk/groups/cqp

Quantum information science aims to harness uniquely quantum mechanical properties to enhance measurement, information and communication technologies, as well as to explore fundamental aspects of quantum physics. Of the various approaches to quantum computing [1], photons are particularly appealing for their low-noise properties and ease of manipulation at the single qubit level [2]. Encoding quantum information in photons is also an appealing approach to other quantum technologies [3], including quantum communication, metrology [4] and measurement [5]. We have developed an integrated waveguide approach to photonic quantum circuits for high performance, miniaturization and scalability [6–10]. We have begun to address the challenges of scaling up quantum circuits using new insights into how controlled operations can be efficiently realised [11], and demonstrated Shor's algorithm with consecutive CNOT gates [12] and the iterative phase estimation algorithm [13]. We have shown how quantum circuits can be reconfigured, using thermo-optic phase shifters to realise a highly reconfigurable quantum circuit able to perform almost any function on two photonic qubits [14], and electro-optic phase shifters in lithium niobate to rapidly manipulate the path and polarisation of telecomm wavelength single photons [15]. We have addressed miniaturisation using multimode interference coupler architectures to directly implement NxN Hadamard operations and the 'Boson sampling problem' [16], and by using high refractive index contrast materials such as SiO_x N_y , in which we have implemented quantum walks of correlated photons [17], and Si [18], in which we have demonstrated generation of orbital angular momentum states of light [19]. We have incorporated microfluidic channels for the delivery of samples to measure the concentration of a blood protein with entangled states of light [20]. We have begun to address the integration of superconducting single photon detectors [21] and diamond [22,23] and non-linear [24–6] single photon sources. Finally, we give an overview of recent work on fundamental aspects of quantum measurement, including a quantum version of Wheeler's delayed choice experiment [27].

References

[1] T. D. Ladd, F. Jelezko, R. Laflamme, Y. Nakamura, C. Monroe, and J. L. OBrien, ***Nature* 464**, 45 (2010).
[2] J. L. O'Brien, ***Science* 318**, 1567 (2007).
[3] J. L. O'Brien, A. Furusawa, and J.Vuckovic, ***Nature Photon.* 3**, 687 (2009).
[4] T. Nagata, R. Okamoto, J. L. O'Brien, K. Sasaki, and S. Takeuchi, ***Science* 316**, 726 (2007).
[5] R. Okamoto, J. L. O'Brien, H. F. Hofmann, T. Nagata, K. Sasaki, S. Takeuchi, ***Science* 323**, 483 (2009).
[6] A. Politi, M. J. Cryan, J. G. Rarity, S. Yu, and J. L. O'Brien, ***Science* 320**, 646 (2008).
[7] A Laing, A Peruzzo, A Politi, MR Verde, M Halder, TC Ralph, MG Thompson, JL O'Brien, ***Appl. Phys. Lett.* 97**, 211109 (2010)
[8] J. C. F. Matthews, A. Politi, A. Stefanov, and J. L. O'Brien, ***Nature Photon.* 3**, 346 (2009).
[9] A. Politi, J. C. F. Matthews, and J. L. O'Brien, ***Science* 325**, 1221 (2009).
[10] J. C. F. Matthews, A. Peruzzo, D. Bonneau, and J. L. O'Brien, ***Phys. Rev. Lett.* 107**, 163602 (2011)

[11] X-Q Zhou, TC Ralph, P Kalasuwan, M Zhang, A Peruzzo, BP Lanyon, and JL O'Brien, ***Nature Comm.*** **2** 413 2011

[12] E Martín-López, A Laing, T Lawson, R Alvarez, X-Q Zhou, JL O'Brien ***Nature Photon.*** doi:10.1038/nphoton.2012.259

[13] X.-Q. Zhou, P. Kalasuwan, T. C. Ralph, J. L. O'Brien, ***Nature Photon.*** in press; arXiv:1110.4276

[14] PJ Shadbolt, MR Verde, A Peruzzo, A Politi, A Laing, M Lobino, JCF Matthews, MG Thompson, JL O'Brien, ***Nature Photon.*** **6**, 45 (2012).

[15] D. Bonneau, *et al.* ***Phys. Rev. Lett.***, 108, 053601 (2012)

[16] A. Peruzzo, A. Laing, A. Politi, T. Rudolph, and J. L. O'Brien, ***Nature Comm.*** **2,** 224 (2011)

[17] A. Peruzzo, M. Lobino, J. C. F. Matthews, N. Matsuda, A. Politi, K. Poulios, X.-Q. Zhou, Y. Lahini, N. Ismail, K. Worhoff, Y. Bromberg, Y. Silberberg, M. G. Thompson, and J. L. O'Brien, ***Science*** **329**, 1500 (2010)

[18] D Bonneau, E Engin, K Ohira, N Suzuki, H Yoshida, N Iizuka, M Ezaki, CM Natarajan, MG Tanner, RH Hadfield, SN Dorenbos, V Zwiller, JL O'Brien, MG Thompson, ***New J. Phys.*** **14** 045003 (2012)

[19] X Cai, J Wang, MJ Strain, B Johnson-Morris, J Zhu, M Sorel, JL O'Brien, MG Thompson, S Yu ***Science*** **338**, 363 (2012)

[20] A. Crespi, M. Lobino, J. C. F. Matthews, A. Politi, C. R. Neal, R. Ramponi, R. Osellame, J. L. O'Brien, ***Appl. Phys. Lett.*** **100**, 233704 (2012).

[21] C. M. Natarajan, A. Peruzzo, S. Miki, M. Sasaki, Z. Wang, B. Baek, S. Nam, R. H. Hadfield, and J. L. O'Brien, ***Appl. Phys. Lett.*** **96**, 211101 (2010).

[22] J. P. Hadden, J. P. Harrison, A. C. Stanley-Clarke, L. Marseglia, Y.-L. D. Ho, B. R. Patton, J. L. OBrien, and J. G. Rarity, ***Appl. Phys. Lett.*** **97**, 241901 (2010)

[23] L. Marseglia, J. P. Hadden, A. C. Stanley-Clarke, J. P. Harrison, B. Patton, Y.-L. D. Ho, B. Naydenov, F. Jelezko, J. Meijer, P. R. Dolan, J. M. Smith, J. G. Rarity, J. L. O'Brien, ***Appl. Phys. Lett.*** **98**, 133107 (2011)

[24] C. Xiong, *et al.* ***Appl. Phys. Lett.*** **98**, 051101 (2011)

[25] M. Lobino, *et al*, ***Appl. Phys. Lett.*** **99**, 081110 (2011)

[26] E. Engin, *et al.* arXiv:1204.4922

[27] A. Peruzzo, P. Shadbolt, N. Brunner, S. Popescu J. L. O'Brien ***Science*** **338**, 634 (2012)

Looking in and through opaque material

Willem L. Vos

Complex Photonic Systems (COPS), MESA+ Institute for Nanotechnology, University of Twente, P.O. Box 217, 7500 AE Enschede, The Netherlands

Random multiple scattering of light is of fundamental physical interest and of great relevance for applications, as is apparent from the fact that it is readily observed in paper, paint, and biological tissue. From a theoretical perspective [1], light scattering allows the study of interference effects such as Anderson localization [2], the study of open transport channels in opaque media [3], and study of speckle correlations [4]. The importance of scattering to applications is obvious as scattering forms an obstacle to conventional high-resolution imaging and focusing.

Recently, the realization has arisen in Twente that the propagation of laser light in opaque scattering media can be controlled by shaping the incident wave front [5]. Such control is based on the realization that scattering by stationary media corresponds to a random linear transformation of incident light modes. Wave front shaping effectively inverts this transform. These advances have given rise to a surge of fundamental studies of light propagation and new modalities of imaging and focusing through and inside random photonic media [6-9]. These methods usually require some kind of calibration, such as the measurement of a transmission matrix [10], to characterize the scattering medium before imaging is possible [11].

We have demonstrated the use of speckle correlations to image objects through strongly scattering opaque layers without any invasive calibration [12]. This is the first ever high-resolution imaging method that uses only scattered light. We scan the angle of incidence of the light on the scattering layer, and record the resulting diffuse fluorescence from the object. Due to fluctuations in the overlap between the scattered speckle and the object the fluorescent signal fluctuates. These fluctuations contain sufficient information to allow us to obtain a high-resolution image of a small object with a typical size comparable to a cell. We will discuss the rapid progress in the development of imaging methods.

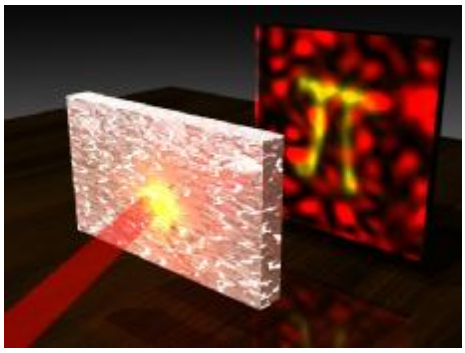

Figure 1*. Laser light that is incident on a strongly scattering screen is transmitted as a random speckle pattern. Speckle correlations can be used to focus light and retrieve image information, see Reference 12.*

References

[1] C. W. J. Beenakker, "*Random-matrix theory of quantum transport*," Rev. Mod. Phys. **69,** 731-808 (1997)
[2] A. Lagendijk, B. van Tiggelen, and D. S. Wiersma, "*Fifty years of Anderson localization*," Phys. Today **62**, 24 (2009).
[3] I. M. Vellekoop and A. P. Mosk, "*Universal Optimal Transmission of Light Through Disordered Materials*," Phys. Rev. Lett. **101,** 120601 (2008).
[4] E. Akkermans and G. Montambaux, "*Mesoscopic Physics of Electrons and Photons*," Cambridge University Press, 2007.
[5] I. M. Vellekoop and A.P. Mosk, "*Focusing coherent light through opaque strongly scattering media*," Opt. Lett. **32** 2309-2311 (2007).
[6] A. P. Mosk, A. Lagendijk, G. Lerosey, and M. Fink, "*Controlling waves in space and time for imaging and focusing in complex media*," Nature Photon. **6,** 283-292 (2012).
[7] O. Katz, E. Small and Y. Silberberg, "*Looking around corners and through thin turbid layers in real time with scattered incoherent light*," Nature Photonics **6**, 549-553 (2012).
[8] C. Hsieh, Y. Pu, R. Grange, G. Laporte, and D. Psaltis, "*Imaging through turbid layers by scanning the phase conjugated second harmonic radiation from a nanoparticle*," Opt. Express **18**, 20723-20731 (2010).
[9] T. Cizmár, M. Mazilu, and K. Dholakia, "*In situ wavefront correction and its application to micromanipulation*," Nat. Photon. **4**, 388 (2010).
[10] S. M. Popoff, G. Lerosey, R. Carminati, M. Fink, A. C. Boccara, and S. Gigan, "*Measuring the Transmission Matrix in Optics: An Approach to the Study and Control of Light Propagation in Disordered Media*," Phys. Rev. Lett. **104,** 100601 (2010).
[11] I. Freund, "*Looking through walls and around corners*," Physica A **168**, 49 (1990).
[12] J. Bertolotti, E. G. van Putten, C. Blum, A. Lagendijk, W. L. Vos, and A. P. Mosk, "*Non-invasive imaging through opaque scattering layers*," Nature **491**, 232–234 (2012).

Intriguing relations between "pseudo-Brewster incidence" and the plasmon mode at a metal surface.

A.V. Tishchenko, O. Parriaux
Laboratoire Hubert Curien UMR CNRS 5516, Université de Lyon à St-Etienne, F-42000 Saint-Etienne
* parriaux@univ-st-etienne.fr

There is nothing common between the "pseudo-Brewster condition" and the plasmon at a metal surface. Yet two puzzling features suggest that there is. What does it mean ?

Nothing common…

The so-called "pseudo-Brewster" incidence condition shows as a reflection minimum of a TM plane wave from a metal surface at a definite incidence angle θ_M [1]. The plasmon mode is a slow wave guided at the metal surface with a field which is purely evanescent in both adjacent media. One wave is above the light line, the other one below.

… yet two intriguing features

The ***first intriguing feature*** (Fig. 1) is the fact that the product of the effective index n_e of the plasmon mode by the horizontal projection of the incident wave k/k_0-vector $\sin\theta$ in air is always very close to *1* at $\theta=\theta_M$ whatever the metal. By using the expression of the plasmon effective index n_e and finding out the incidence angle of minimum Fresnel reflection θ_M , this product is given by the following expression which is close to 1 for most metals since $\mathrm{Re}(\varepsilon_m)$ is negative:

$$n_e^2 \sin^2\theta_M = 1 - (\mathrm{Re}(\varepsilon_m) + |\varepsilon_m| + 4)/|\varepsilon_m|^2 \qquad (1)$$

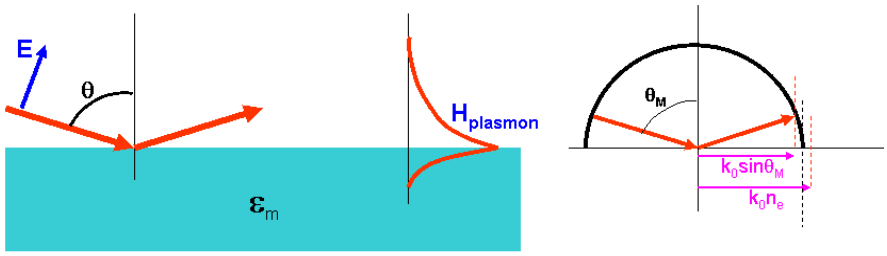

Fig. 1 Incident plane wave and plasmon fields. Right: the spatial frequencies whose product is k_0.

A ***second intriguing feature*** is that at the condition of minimum reflection, $\theta=\theta_M$, the reflection coefficient is purely imaginary, i.e., there is perfect matching between the line characteristic impedance (incident wave) and the load impedance. Pushing further and expressing the impedances as the normal components of the k-vector of the plane wave $k_0\cos\theta$ and of that, imaginary, of the plasmon, $k_0(1- n_e^2)^{1/2}$, and equating their modulus, leads to the simple analytical expression for θ_M:

$$\cos\theta_M = 1/(|1 + \varepsilon_m|)^{1/2} \qquad (2)$$

This expression fits with the numerical reflection minimum within much better than 1 degree with gold, silver, aluminium, nickel and even chromium in the visible and also with copper at 10.6 μm. Why two phase-mismatched waves of different nature show somehow related characteristics is still an interrogation for the authors who wish to submit the case to the attendance.

References

[1] A. Alsamman and R. M. A. Azzam, J. Opt. Soc. Am. A, Vol. 27, p. 1156 (2010)

Modelling of plasmonic waveguides

Z. Han and S. I. Bozhevolnyi*

Department of Technology and Innovation, University of Southern Denmark, Odense, Denmark

** seib@iti.sdu.dk*

Modelling of plasmonic waveguides is overviewed, considering different approaches for the description of strongly confined surface plasmon-polariton modes in various guiding configurations and paying special attention to accurate calculation of bending loss and optimization of the bending radius.

Recent years have seen an explosion of research into plasmonics instigated by a great promise of enabling energy-effective and highly-integrated optical interconnects that would exploit a special type of electromagnetic waves called surface plasmon-polaritons (SPP) propagating along and being controlled by metal circuitry, while also being strongly confined (beyond the diffraction limit) in the lateral cross section [1,2]. Modelling of SPP waveguides is an essential part of the development of SPP-based circuitry that allows one to properly choose the waveguide parameters in order to minimize the footprints of plasmonic components while keeping inevitable insertion losses associated with the radiation absorption by metals at an acceptable level. In this talk we overview different approaches to modelling of SPP waveguides paying special attention to the issue of bending loss. The latter determines not only the footprint but also the properties (e.g. quality factor is a ring resonator) of optical devices. For plasmonic waveguides, the bending loss comes from both propagation loss and radiation loss, which result in general an optimal bending radius in terms of transmission through the bends. The numerical calculation of bending loss can be achieved using the traditional method of conformal mapping of the refractive index in the bending area or using numerical simulations in the cylindrical coordinates. Here, we present the numerical results on the bending loss of some representative plasmonic waveguides [3] using the recently proposed transformation optics method [4]. A 90-degree bend of plasmonic waveguides in one Cartesian coordinates is conformably transformed to a straight waveguide in another Cartesian coordinates. The transmission through the 90-degree bends in different plasmonic waveguides can be calculated in the second coordinates, allowing us to determine the optimal bending radius.

References

[1] D. K. Gramotnev and S. I. Bozhevolnyi, *Plasmonics beyond the diffraction limit*, Nature Photonics **4**, 83 (2010).

[2] *Plasmonic Nanoguides and Circuits*, S. I. Bozhevolnyi, ed. (Pan Stanford, 2009).

[3] Z. Han and Sergey I. Bozhevolnyi, *Radiation guiding with surface plasmon polaritons*, Reports on Progress in Physics **76**, 016402 (2013).

[4] J. B. Pendry, D. Schurig, and D. R. Smith, *Controlling Electromagnetic Fields*, Science **312**, 1780 (2006).

Plasmon–soliton waves: towards realistic modelling

W. Walasik [1,2], Y. Kartashov [2], G. Renversez [1],

[1] *Institut Fresnel, CNRS, Université d'Aix-Marseille, Campus de St. Jérôme, 13013 Marseille, France*
[2] *ICFO, Universitat Politècnica de Catalunya, 08860 Castelldefels (Barcelona), Spain*
gilles.renversez@fresnel.fr

We study plasmon–soliton waves in multilayer nonlinear dielectric-metal planar structures using several improved vector models. We present, for the first time, low power plasmon–solitons in structures compatible with fabrication technology of chalcogenide waveguides.

Motivation

Nonlinear plasmon–soliton waves were predicted theoretically more than thirty years ago [1] and still attract a lot of attention [2]. Nevertheless, no experimental demonstration has been published so far due to the non-physically high power required. Our study is aimed to bring better understanding of the nature of plasmon–solitons and therefore facilitate the experimental observation of plasmon–solitons in realistic structures made of Kerr nonlinear dielectric, linear dielectric and metal.

Modelling plasmon–solitons

We use two complementary vector models based on Maxwell's equations to compute the nonlinear dispersion relation, the field profiles in structures shown below. The first one is a generalization of the model of Ref. [1] to 4-layers, and with an improved nonlinearity treatment. The nonlinearity is still treated in an approximate way, but it allows us to obtain the analytical formulas for the field shapes. The second model is an extension to 4 layers of a more recent model developed by Yin [3]. This model gives the dispersion relations with an exact nonlinearity treatment but the field shapes must be computed numerically. Moreover, we use a home made finite-element method adapted for Kerr nonlinear waveguides to verify our semi-analytical results. Thanks to these models we determined the types and the number of nonlinear solutions as a function of the structure parameters. We use the 1D nonlinear solution of the 4-layer structure to obtain a crude approximation of the 2D solutions.

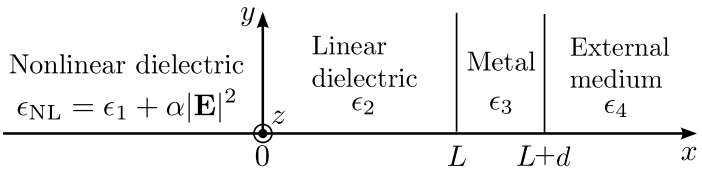

Geometry of the 4-layer configuration.

Using realistic material parameters, we were also able to design structures supporting plasmon–soliton coupling at significantly decreased light intensity ($\approx$1 GW/cm^2 that is 2 orders of magnitude less than in previous works) [4].

References

[1] V. M. Agranovich, V. S. Babichenko, and V. Y. Chernyak, *Nonlinear surface polaritons*, JETP. Lett. **32**, 512–515, 1980. J. Ariyasu, C. T. Seaton, G. I. Stegeman, A. A. Maradudin, and R. F. Wallis, *Nonlinear surface polaritons guided by metal films*, J. Appl. Phys. **58**, 2460–2466, 1985.

[2] E. Feigenbaum and M. Orenstein, *Plasmon–soliton*, Opt. Lett. **32**, 674–676, 2007. C. Miliàn, D. E. Ceballos-Herrera, D. V. Skryabin, and A. Ferrando, *Soliton-plasmon resonances as Maxwell nonlinear bound states*, Opt. Lett. **37**, 4221–4223, 2012.

[3] H. Yin, C. Xu, and P. M. Hui, *Exact surface plasmon dispersion relations in linear-metal-nonlinear dielectric structure of arbitrary nonlinearity*, Appl. Phys. Lett. **94**, 221102, 2009.

[4] W. Walasik, V. Nazabal, M. Chauvet, Y. Kartashov, and G. Renversez, *Low-power plasmon–soliton in realistic nonlinear planar structures*, Opt. Lett. **38**, 4579–4581, 2012.

Hybrid dielectric plasmonic slot guiding nanostructures – analysis with Fourier modal methods

P. Kwiecien[1], J. Čtyroký[2], I. Richter[1*]

[1] *Czech Technical University in Prague, Faculty of Nuclear Sciences and Physical Engineering, Department of Physical Electronics, Břehová 7, 11519 Prague 1, Czech Republic*

[2]*Institute of Photonics and Electronics AS CR, v.v.i., Chaberská 57, 182 51 Praha 8, Czech Republic*

* ivan.richter@fjfi.cvut.cz

Several different types of plasmonic guiding nanostructures, based on the hybrid plasmonic slot waveguide concept, has been recently proposed, simulated, and theoretically analyzed, based on our in-house 3D frequency-domain Fourier modal methods (BEX3, aRCWA).

Introduction

Plasmonic waveguides are finding their important place among other subwavelength-structured photonic and/or plasmonic nanostructures, especially as promising and versatile basic building blocks for the construction of extremely compact devices, targeted at various applications, i.e. for devices such as filters, switches, modulators, sensors, or lasers, in both passive and active regimes. Clearly, in parallel to experimental activities, there is also need for new theoretical exploitations of numerical methods and modeling activities in connection towards their direct application to realistic 3D geometries and problems within these plasmonic waveguides. A number of different types of plasmonic waveguide structures have been recently proposed, theoretically analyzed, and their properties experimentally verified [1]. Among them, one specific type, the hybrid dielectric-loaded plasmonic waveguide [2,3], have found particular interest. Our subtle modification, the hybrid dielectric-plasmonic slot waveguide (HDPSW) [4,5], exhibits very strong field confinement combined with tolerable losses which allows many applications in some integrated plasmonic devices.

Results

Recently, we have developed two independent 3D Fourier modal methods (aperiodic rigorous coupled wave analysis – aRCWA, bi-directional mode expansion propagation method – BX3) [6], based on the 2D approach developed earlier. We have applied our in-house methods to a number of challenging simulation problems, connected with HDPSW. Based on the optimization in terms of the mode effective area [4], and figures of merit [7], we have analyzed and discussed both simple HDPSW as well as more advanced devices such as directional couplers or multimode interference couplers.

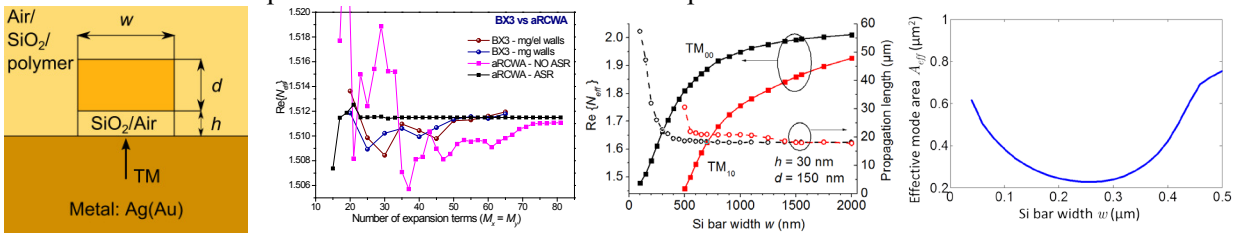

(a) (b) (c) (d)

Fig. 1: (a) Schematic cross-sectional view of HDPSW, (b) convergence of the real part of effective refractive indices - BEX3 × aRCWA, (c) the dependence of the effective refractive indices (solid) and the propagation length (dashed) of the HDPSW modes on the guide width w, (d) effective mode area of the HDPSW with respect to w of the high-index bar (d = 120 nm, gap size h = 30 nm, λ = 1500 nm).

Acknowledgements: This work was financially supported by the Czech Science Foundation (projects P205/10/0046 and P205/12/G118).

References

[1] P. Berini, I. De Leon, Nature Photonics **6**, 16 (2011).
[2] R. F. Oulton, et al., Nature Photonics **2**, 496 (2008).
[3] H.-S. Chu, Y. A. Akimov, P. Bai, E.-P. Li, JOSA B **28**, 2895 (2011).
[4] J. Čtyroký, P. Kwiecien, I. Richter, *submitted to* JEOS:RP (2013).
[5] P. Kwiecien, I. Richter, J. Čtyroký, Proceedings SPIE **8697**, 86971Y (2012).
[6] J. Čtyroký, J. Lightwave Technol. **30**, 3699 (2012).
[7] P. Berini, Optics Express **14**, 13030 (2006).

Analysis of layered media plasmonic waveguides by Multiple Multipole Program

A. Alparslan Ch. Hafner

Laboratory for Electromagnetic Fields and Microwave Electronics, ETH Zurich, 8092, Zurich, Switzerland
aytaca@ifh.ee.ethz.ch

The eigenvalue analysis of plasmonic waveguides is performed by Multiple Multipole Program (MMP) combined with modified layered media Green's functions (LMGF). By this new approach, the exact locations of the physical eigenvalues are determined, which is a troublesome task for all of the well known numerical methods.

Layered media are one of the mostly used building blocks of electromagnetical systems. In microwave regime, devices including microstrip antennas, transmission lines and waveguides were built by using the salient features of layered media for decades. Recent improvements in the fabrication process of materials made it possible to build structures with dimensions comparable with the wavelength range of the visible spectrum. Following these improvements, numerous nano-structures built in a general layered geometry, such as optical antennas and waveguides became popular research subjects in the electromagnetics society [1]. As a result of this interest, numerical tools that can perform the efficient and robust numerical analysis of nano-structures in layered geometries became very important. A candidate for such a tool is introduced by combining MMP [2], an efficient boundary discretization method for the solution of Maxwell's equations in general geometries, with LMGF [3], which are the fields generated by a point source in a layered geometry. The new tool can efficiently compute the scattering and the eigenvalue problems of nanostructures and it is implemented in the opensource environment OpenMAX [4]. In this talk, the eigenvalue analysis of plasmonic waveguides by the new tool is introduced. Since no truncation is needed for the layered geometries, problems originating from artificial truncation boundaries (such as absorbing boundary conditions and perfectly matched layers as in FDTD and FEM) are not present.

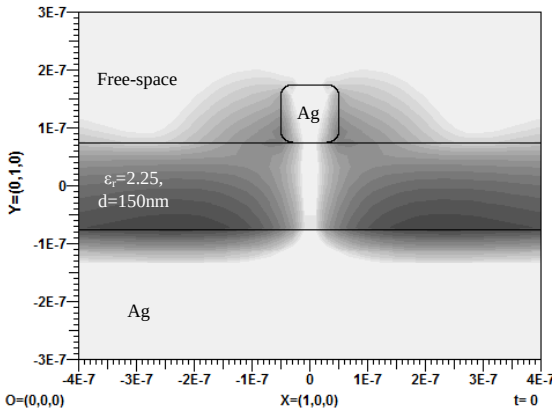

The eigenfield (magnitude of H field, z component in logarithmic scale) at $\lambda_0 = 600nm$ with the eigenvalue (out-of-paper wavenumber) $k_\gamma = (1.24+0.01i)k_0$. The waveguide is a rectangular single wire placed in a three layered geometry with the given material properties. The length of one of the sides of the wire is $100nm$ and the corners are rounded with $r = 20nm$.

References

[1] L. Novotny, *Effective wavelength scaling for optical antennas,* Phys. Rev. Lett. 98, 266802, 2007.
[2] Ch. Hafner, Generalized multipole technique for computational electromagnetics, Artech House Antenna library, Artech House, Boston, MA, 1990.
[3] A. Alparslan, M. I. Aksun, K. A. Michalski, *Closed-form greens functions in planar layered media for all ranges and materials,* IEEE Transactions on Microwave Theory and Techniques, 58, 2010.
[4] Ch. Hafner, A. Alparslan, *OpenMaX: OpenSource Maxwell solver package,* http://openmax.ethz.ch.

PhoeniX Software
Solutions for Micro and Nano Technologies

MESA+
INSTITUTE FOR NANOTECHNOLOGY

JCMwave

Optiwave

IEEE
photonics
SOCIETY

lumerical
illuminating the way

focal
vision & optics

LIONIX

Enhancement Of Voltage Profile Of Transmission Line By Using Static VAR Compensator-An Overview

J. N. Rai, Naimul Hasan*, Rishabh K. Gupta, Rahul Kapoor, Rajesh Garai
Dept. of Electrical Engineering
Delhi Technological University
Dept. of Electrical Engineering
Jamia Millia Islamia, New Delhi, India*

Abstract

One of the main prerequisite of the modern power system is the enhancement and control of voltage from varying from its desired value. For this we used many compensation techniques. In this paper a case study for a particular transmission line has been carried out to enhance and control the voltage profile using compensation. This paper presents the basic aspect of voltage profile enhancement and control without contingency by simple and efficient use of capacitor bank. The effectiveness of proposed experimental result demonstrated on model of 750 kV ,250 km,1000MW EHV lines.

Index terms--compensation, line compensation, series, shunt, static VAR compensation, contingency.

1. Introduction

In a power system, given the insignificant electrical storage, the power generation and load must balance at all times. To some extent, the electrical system is self-regulating. If generation is less than the load, voltage and frequency drop, and thereby reducing the load. However, there is only a few percent margins for such regulation. If voltage is propped up with reactive power support, then the load increase with consequent drop in frequency may result in system collapse. Alternatively, if there is inadequate reactive power, the system may have voltage collapse.

Electrical loads both generate and absorb reactive power. Since the transmitted load varies considerably from one hour to another, the reactive power balance in a grid varies as well. The result can be unacceptable voltage amplitude variations, a voltage depression, or even a voltage collapse. Therefore, transmission line require compensation for this varying reactive power.[4],[6]

2. Load Compensation

Load compensation is the management of the reactive power to improve the power quality i.e. V profile and p.f. Here the reactive power flow is controlled by installing shunt compensation devices (capacitor/reactors) at the load end bringing about power balance between generated and consumed reactive power. This is most effective in improving the power transfer capability of the system and its voltage stability. It is desirable both economically and technically to operate the system near unity power factor. This is why some utilities impose a penalty on low pf loads. Yet another way of improving the system performance is to operate it under near balanced conditions so as to reduce the flow of negative sequence currents thereby increasing the system's load capability and reducing power loss.

A transmission line has three critical loadings (1) natural loading (2) steady state stability limit and (3) thermal limit loading. For a compensated line the natural loading is the lowest and before the thermal loading limit is reached, steady state stability is arrived.[4]

The three main objectives of load compensation are:

a) Better voltage profile
b) p.f. correction
c) load balancing.[5]

3. Line Compensation

Line compensation can be defined as the use of electrical circuits to modify the electrical characteristics of the line so that the compensated electrical lines can achieved following objectives.

a) Ferranti effect is minimized so that a flat voltage profile is observed on the line during all load conditions.

b) Under excited as well as overexcited operation of line will be avoided and an economical means of reactive power management will be achieved.

c) The power transfer capability of the system will be enhanced and system stability margins increase.

In order to assess the effectiveness a compensated system a performance index in terms of length of line and the power to be transmitted is evaluated. It is very much necessary to fix this criteria as it is not possible to load the longer length line even to their natural loadings without compensation.[5]

IJERT

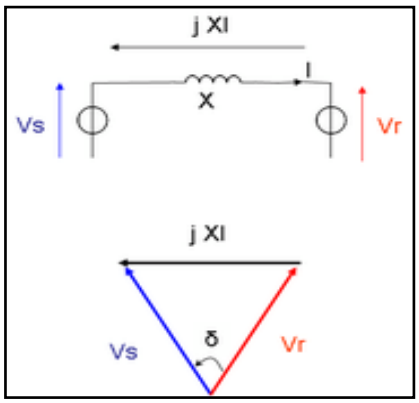

Figure1: Transmission on a no loss line

A. SERIES COMPENSATION

In series compensation, the FACTS is connected in series with the power system. It works as a controllable voltage source. Series inductance occurs in long transmission lines, and when a large current flow causes a large voltage drop. To compensate, series capacitors are connected. Series compensation increases transmission capacity, improve system stability, control voltage regulation and ensure proper load division among parallel feeders.[2],[7],[8]

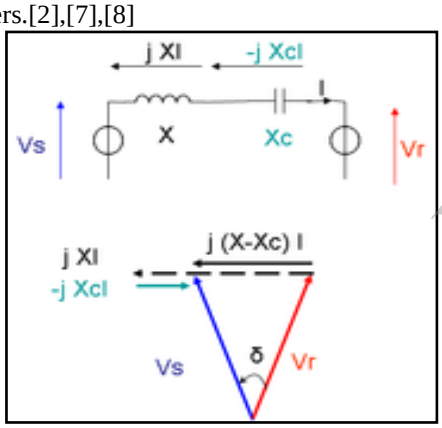

Figure 2: Series Compensation

B. *SHUNT COMPENSATION*

In shunt compensation, power system is connected in shunt (parallel) with the FACTS. It works as a controllable current source. Shunt compensation is used to influence the natural electrical characteristics of the transmission line to increase the steady state transmittable power and to control the voltage profile of the line. [2],[7],[8]

Shunt compensation is of two types:

i) Shunt capacitive compensation

This method is used improve the power factor. Whenever an inductive load is connected to the transmission line, power factor lags because of lagging load current. To compensate, a shunt capacitor is connected which draws current leading the source voltage. The net result is improvement in power factor.

ii) Shunt inductive compensation

This method is used either when charging the transmission line, or, when there is very low load at the receiving end. Due to very low, or no load - very low current flows through the transmission line. Shunt capacitance in the transmission line causes voltage amplification (Ferranti Effect). The receiving end voltage may become double the sending end voltage (generally in case of very long transmission lines). To compensate, shunt inductors are connected across the transmission line.[2],[7],[8]

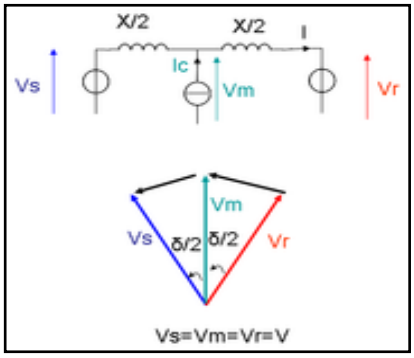

Fig.3: Shunt Compensation [10]

C. STATIC VAR COMPENSATOR (SVC)

A static VAR compensator is an electrical device for providing fast active, reactive power compensation on high voltage electricity transmission network. These comprise of three phase static capacitor bank fixed or switched (controlled) or fixed capacitor bank and switched reactor bank in parallel. The term 'static' refers to the fact that SVC has no moving parts. [4],[6]

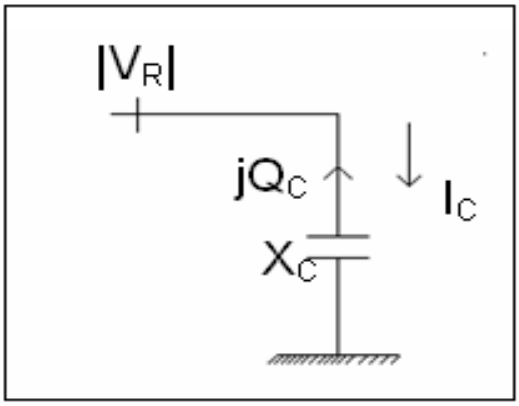

Fig.4: Static Capacitor Bank

A rapidly operating static VAR compensator (SVC) can continuously provide reactive power to control dynamic voltage swings under various system conditions and thereby improve the power system performance. Thus, these compensators draw reactive (leading or lagging) power† from the line there by regulating voltage, improve stability (steady state and dynamic), control over voltage and reduce voltage flicker. These also reduce voltage and current imbalances. In HVDC application these compensators provide the

IJERT

required reactive power and damp out sub harmonic oscillations. Since static VAR compensator use switching for VAR control. These are also called static VAR switches or systems. It means that terminology wise

SVC= SVS

and we can use these interchangeably.[4]

†A reactance connected in shunt to line at voltage V draws reactive power V^2/X. It is negative (leading) if reactance is capacitive and positive (lagging) if reactance is inductive.

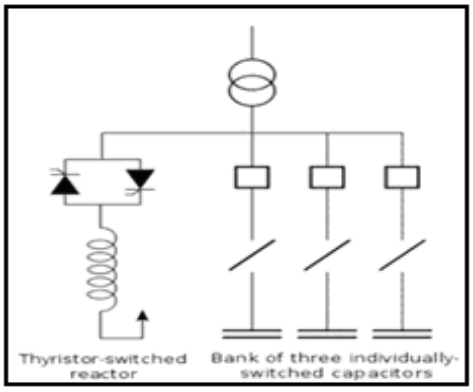

Fig.5: Typical one line diagram of a SVC

PRINCIPAL OF OPERATION

In the case of a no-loss line, voltage magnitude at receiving end is the same as voltage magnitude at sending end: $V_s = V_r = V$. Transmission results in a phase lag δ that depends on line reactance X.

$$\underline{V_s} = V\cos(\frac{\delta}{2}) + jV\sin(\frac{\delta}{2})$$

$$\underline{V_r} = V\cos(\frac{\delta}{2}) - jV\sin(\frac{\delta}{2})$$

$$\underline{I} = \frac{\underline{V_s} - \underline{V_r}}{jX} = \frac{2V\sin\frac{\delta}{2}}{X}$$

As it is a no-loss line, active power P is the same at any point of the line.

$$P_s = P_r = P = V\cos\left(\frac{\delta}{2}\right)\cdot\frac{2V\sin\frac{\delta}{2}}{X} = \frac{V^2}{X}\sin(\delta)$$

Reactive power at sending end is the opposite of reactive power at receiving end:

$$Q_s = -Q_r = Q = V\sin\left(\frac{\delta}{2}\right)\cdot\frac{2V\sin\frac{\delta}{2}}{X} = \frac{V^2}{X}(1-\cos\delta)$$

As δ is very small, active power mainly depends on δ whereas reactive power mainly depends on voltage magnitude.[10]

A. SERIES COMPENSATION

FACTS for series compensation modify line impedance: X is decreased so as to increase the transmittable active power. However, more reactive power must be provided.[10]

$$P = \frac{V^2}{X - Xc}\sin(\delta)$$

$$Q = \frac{V^2}{X - Xc}(1-\cos\delta)$$

B. SHUNT COMPENSATION

Reactive current is injected into the line to maintain voltage magnitude. Transmittable active power is increased but more reactive power is to be provided.[10]

$$P = \frac{2V^2}{X}\sin\left(\frac{\delta}{2}\right)$$

$$Q = \frac{2V^2}{X}\left[1-\cos\left(\frac{\delta}{2}\right)\right]$$

C. SVC TECHNOLOGY

If $|V_R|$ is in line KV and X_C is the per phase capacitive reactance of the capacitor bank on an equivalent star basis, the expression for the VARs fed into the line can be derived as under:-

$$\boldsymbol{I_C = j\frac{|V_R|}{\sqrt{3}X_C}\ \text{KA}}$$

$$\boldsymbol{jQ_C\ (3\text{-phase}) = 3\frac{|V_R|}{\sqrt{3}}(-I_C^*)}$$

$$\boldsymbol{= 3\frac{|V_R|}{\sqrt{3}}\times\frac{|V_R|}{\sqrt{3}}\ \text{MVA}}$$

$$\boldsymbol{Q_C\ (3\text{-phase}) = \frac{|V_R|^2}{X_C}\ \text{MVAr}}$$

If inductors are employed instead, VARs fed into the line are:

$$\boldsymbol{Q_C\ (3\text{-phase}) = -\frac{|V_R|^2}{X_L}\ \text{MVAr}}$$

Under heavy load conditions, when positive VARs are needed, capacitors are employed; while under light load conditions, negative VARs are needed, inductor banks are needed.[4]

IJERT

II.EXPERIMENTAL SET UP‡

We can experimentally check the influence of capacitor bank on the voltage profile by making the given set up.

a) Make connection as shown in figure (6).
b) Switch on the power supply, keeping switch 2 and 3 in open position. Adjust sending end voltage V_S and hence V_R at about 100V by adjusting variac across supply. I_{Line} is almost zero , the switch S_2 is closed because of high impedance of voltmeter V_R.
c) Switch on load by closing S_3. I_{Load} should not exceed rated wattmeter current which may otherwise get damaged. Note down V_R,V_S, I_L.
d) Close switch 3. Observe the V_R rises. Adjust capacitance values (by making parallel or series compensation) so that $V_R = V_S$ (full 100% compensation). Note V_S,V_R, I_{Line}, I_{Load} , I_C, W_S.
e) Repeat step 2 and 3 for different load voltages.

The following observations have been made as according to the table(s):

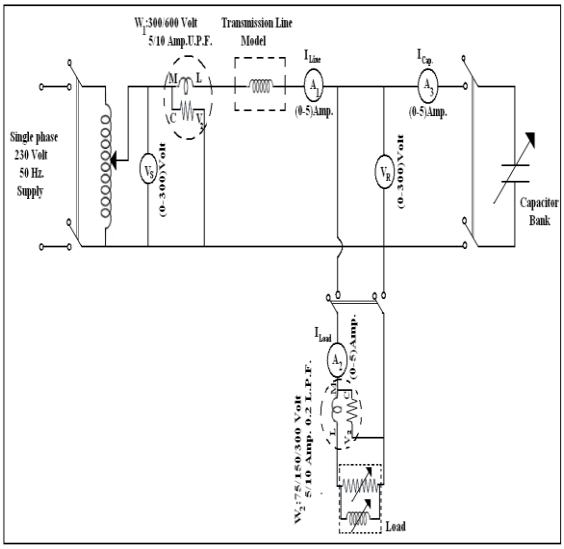

Figure 6. Model of a Transmission line with compensation

Table 1 Without Compensation

S.No.	V_S (Volt)	V_R (Volt)	I_S (Ampere)	I_L (Ampere)	W_S (Watt)	W_L
1	140	86	0. 32	0. 32	25	20
2	140	98	0.26	0.26	35	10
3	160	108	0.32	0.32	50	32

Table II: With Compensation

S.No.	V_S (Volt)	V_R (Volt)	I_S (Amp.)	I_L (Amp.)	I_C (Amp.)	W_S (Watt)	W_L (Watt)	KVARby Cap.	VARsby C*
1.	**140**	**138**	**1.58**	**0.54**	**1.54**	**120**	**70**	**1/3**	**137.16**
2.	**140**	**140**	**1.22**	**0.74**	**1.44**	**100**	**56**	**1/3**	**134.99**
3.	**160**	**164**	**1.74**	**0.52**	**1.78**	**135**	**79**	**1/3**	**185.22**

*written after calculations.

Calculations

Set 1:

Sending end VAR = $\sqrt{(V_S * I_S)^2 + (W_S)^2}$

$= \sqrt{(140*1.58)^2 + (120)^2}$

=185.82 VAR

VAR supplied by Capacitor = $1/3*1000(V_R/V_C)^2$

$= 1/3*1000(138/220)^2$

=131.16 VAR

Load VAR $= \sqrt{(V_R * I_L)^2 + (W_L)^2}$

$= \sqrt{(138*0.54)^2 + (70)^2}$ = 25.56 VAR

Set 2:

Sending end VAR = $\sqrt{(140*1.22)^2 + (100)^2}$

=138.46 VAR

VAR supplied by Capacitor = $1/3*1000(140/220)^2$

= 134.16 VAR

Load VAR = $\sqrt{(140*0.74)^2 + (56)^2}$

= 87.16 VAR

Set 3:

Sending end VAR = $\sqrt{(160*1.74)^2 + (135)^2}$

= 243.40 VAR

VAR supplied by Capacitor = $1/3*1000(164/220)^2$

= 185.24 VAR

Load VAR = $\sqrt{(164*0.52)^2 + (79)^2}$

= 32.20 VAR

4. CONCLUSION & DISCUSSION

This paper described an efficient and practical method to enhance the voltage profile and control for the particular rating of transmission line. Thus we see within experimental limitations reactive power consumed by the load is equal to the reactive VAR supplied by the capacitor for 100% compensation. Since Q_C is proportional to the square of terminal voltage, for a given capacitor bank, their effectiveness tends to decrease as the voltage sags under full load conditions. Capacitor acts as short circuit when switched on. We should also take the precautions of a possibility of series resonance with the line inductance particularly at harmonic frequencies. Step less (smooth) VAR can be achieved using SCR (silicon controlled rectifier circuitry) as with them we can switch capacitor and inductor in steps.

5. REFERENCE

[1] Narain G. Hingorani, Laszlo Gyugyi *Understanding FACTS: Concepts and Technology of Flexible AC Transmission Systems*, Wiley-IEEE Press, December 1999. ISBN 978-0-7803-3455-7

[2] Xiao-Ping Zhang, Christian Rehtanz, Bikash Pal, *Flexible AC Transmission Systems: Modelling and Control*, Springer, March 2006. ISBN 978-3-540-30606-1. http://www.springer.com/3-540-30606-4

[3] A. Edris, R. Adapa, M.H. Baker, L. Bohmann, K. Clark, K. Habashi, L. Gyugyi, J. Lemay, A. Mehraban, A.K. Myers, J. Reeve, F. Sener, D.R. Torgerson, R.R. Wood, *Proposed Terms and Definitions for Flexible AC Transmission System (FACTS)*, IEEE Transactions on Power Delivery, Vol. 12, No. 4, October 1997.

[4] Nagrath, I.J.,Kothari D.P. "Modern Power System Analysis" Third Edition TMH Publication.

[5] Wadhwa C.L. " Electrical Power System" Fourth Edition, New Age Publishers .

[6] K. R Padiyar , FACTS Controllers in Power Transmission & Distribution. New Age International (P) ltd., 2007.

[7] Giuseppe, Fusco / Mario, Russo, 2006, Adaptive Voltage Control in Power Systems: Modelling, Design and Applications (Advances in Industrial Control) Springer ISBN 184628564X November 13, 2006.

[8] P. Kundur. Power system stability and control. McGraw-Hill, New York, 1994.

[9] LEE S Y, Wu C Combined compensation of a static VAR compensator and an active filter for unbalanced three-phase distribution feeders with harmonic distortion. Electric Power System Research, 1998.

WEB Reference

[10] www.ieeeexplore.ieee.org
[11] www.wikipedia.org

IJERT

Rajiv Kapoor, Pallavi Mathur / International Journal of Engineering Research and Applications (IJERA) ISSN: 2248-9622 www.ijera.com
Vol. 3, Issue 4, Jul-Aug 2013, pp. 82-95

Face Recognition Using Moments and Wavelets

Rajiv Kapoor, Pallavi Mathur
(HOD, Department of Electronics and Communication, Delhi Technological University, Delhi-42
(Department of Electronics and Communication, University of Pune, Pune

ABSTRACT

The field of face recognition has been explored a lot and the work is still going on. In this paper we have proposed a novel approach for face recognition using moments. Four feature extraction methods have been used: Hu moments, Zernike moments, Legendre moments and Cumulants. Hu moments include a set of seven moments which are derived from the conventional geometric moments. These moments are invariant against rotation, scaling and translation. Legendre and Zernike moments have an orthogonal basis set and can be used to represent an image with minimum amount of information redundancy. These are based on the theory of orthogonal polynomials and can be used to recover an image from moment invariants. Cumulants are sensitive to image details and therefore are suitable for representing the image features. For feature extraction, moments of different orders are calculated which form the feature vectors. The feature vectors obtained are stored in the database and are compared using three different classifiers. In case of cumulants, we have calculated the bispectrum of images and compressed it using wavelets.

Keywords – Bispectrum, Biwavelant, Face Recognition, Moments, Wavelets,

I. INTRODUCTION

A face recognition system can be defined as a computer application for automatically identifying or verifying a person from a digital image or a video frame from a video source. The most convenient way to do this is by comparing selected facial features from the image and a facial database. The face recognition approaches can be classified as: Holistic approach, Region based approach and Hybrid and multimodal approach. Holistic approach involves matching of faces on the basis of entire face. This makes it sensitive to face alignment. Region based approaches work on the principle of applying different processing methods to distinct face regions. They filter out those regions that are mostly affected by expression changes or spurious elements.

Hybrid and multimodal approaches involve greater architectural complexity and hence provide highest accuracy. In hybrid approaches, different approaches like holistic or region based are combined or are used to perform matching separately and then their results are fused.

There are many variations in the facial images that need to be considered for face recognition. These are due to changes in illumination, direction of viewing, facial expression and aging etc. Also, the face images have similar geometrical features which make discriminating one face from the other in the database a challenging task. All these factors make it difficult to represent face images with distinct feature vectors that are invariant to transformation.

In this paper, feature extraction techniques using moments are considered. In image processing, computer vision and related fields, an image moment is a particular weighted average (moment) of the image pixels' intensities, or a function of such moments, generally chosen to have some attractive property or interpretation. These are useful to describe objects after segmentation. Simple properties of the image which can be found via image moments include area (or total intensity), its centroid and information about its orientation. Moments and their functions have been utilized as pattern features in a number of applications. These features can provide global information about the image. Cumulants and wavelets (wavelants) could result in easy distinction among the various faces.

Section 2 mentions the literature review, Section 3 discusses about the databases and the normalization of images, section 4 discusses about the features extraction and section 5 gives the classification. Section 6 is for results and section 7 is for conclusion and future scope.

II. LITERATURE SURVEY

A lot of work has been done in the field of face recognition using Linear Discriminant Analysis. In [1], the author has proposed a novel Bayesian logistic discriminant (BLD) model which addresses normality and heteroscedasticity (problem in which the LDA algorithm assumes the sample vectors of each class which are generated from underlying multivariate normal distributions of common covariance matrix with different means). Chao-Kuei Hsieh, Shang-Hong Lai and Yung-Chang Chen [2], proposed face recognition using an optical flow based approach. A single 2-D face image with facial expression is used. Information from the computed intrapersonal optical flow and

the synthesized face image are combined in a probabilistic framework for face recognition. However, the proposed integrated system is more computationally costly. Color Space Normalization to enhance the Discriminating Power of Color Spaces for Face Recognition was used in [3]. Here the authors explain the concept of color space normalization (CSN) and two CSN techniques for enhancing the discriminating power of color spaces for face recognition.

In [4], the author has combined Gabor features within the scope of diffusion-distance calculation. This strategy starts from the Gabor filtering that consists of three scales and six orientations. It is followed by the calculation of diffusion distance based on a Bayesian model. The recognition rate of the proposed algorithm reduces while handling the occlusions due to dramatical pose changes. Zhen Lei, Shengcai Liao, Matti Pietikäinen and Stan Z. Li [5], proposed a face representation and recognition approach by exploring information jointly in image space, scale and orientation domains.

In [6], Zhiming Liu and Chengjun Liu present a novel face recognition method by means of fusing color, local spatial and global frequency information. Specifically, the proposed method fuses the multiple features derived from a hybrid color space, the Gabor image representation, the local binary patterns (LBP) and the discrete cosine transform (DCT) of the input image.

Weiwen Zou and Pong C. Yuen [7], proposed multi-image face recognition, instead of using a single still-image-based approach in order to handle complex face image variations in face recognition.

Xiaoyang Tan and Bill Triggs [8] focused mainly on robustness to lighting variations. For this purpose, the author has combined robust illumination normalization, local texture-based face representations, distance transform based matching, kernel based feature extraction and multiple feature fusion. Richard M. Jiang, Danny Crookes and Nie Luo [9], concentrated on feature selection process. In the proposed scheme, global harmonic features instead of disconnected pixels are used, which represent information about 2-D spatial structures. Baochang Zhang, Yongsheng Gao, Sanqiang Zhao and Jianzhuang Liu in [10] worked on high-order local pattern descriptor, local derivative pattern (LDP), for face recognition.

Gui-Fu Lu, Zhong Lin and Zhong Jin [11], proposed a discriminant locality preserving projections based on maximum margin criterion (DLPP/MMC). DLPP/MMC seeks to maximize the difference, rather than the ratio, between the locality preserving between class scatter and locality preserving within class scatter. This method is a little rough and can be improved. In [12], Saeed Dabbaghchian, Masoumeh P. Ghaemmaghami and Aliaghagolzadeh proposed a new category of coefficient selection approach in the Discrete Cosine Transform domain for face recognition. The approach called Discrimination power analysis (DPA) is a statistical analysis based on the DCT coefficients properties and discrimination concept. In [13], Miao Cheng, Bin Fang, Yuan Yan Tang, Taiping Zhang and Jing Wen devised a supervised learning method, called local discriminant subspace embedding (LDSE), to extract discriminative features for face recognition. Imran Naseem, Roberto Togneri and Mohammed Bennamoun [14], in their research, proposed a linear Regression based classification (LRC) for the problem of face identification. Wen-Chung Kao, Ming-Chaihsu and Yueh-Yiing Yang [15] concentrated on recognizing human faces in various lighting conditions.

Shuicheng Yan, Huan Wang, Jianzhuang Liu, Xiaoou Tang and Thomas S. Huang [16], in their paper worked on providing solution to the face recognition problem under the scenarios with spatial misalignments and/or image occlusions. A comprehensive system was presented by Ritwik Kumar, Angelos Barmpoutis, Arunava Banerjee and Baba C. Vemuri [17], for capturing the reflectance properties and shape of the human faces using Tensor Splines. But the method requires at least nine input images with known illumination directions. Also, accurate recovery of Apparent Bidirectional Reflectance Distribution functions ABRDF field from a single image with cast shadows and specularities with no lighting information remains a challenge. In [18], Tae-Kyun Kim, Josef Kittler and Roberto Cipolla have addressed the problem of face recognition by matching image sets. Each set of face images is represented by a subspace (or linear manifold) and recognition is carried out by subspace to subspace matching.

Jiwen Lu and Yap-Peng Tan propose in their paper [19] a parametric regularized locality preserving projections (LPP) method for face recognition. The proposed method is designed to regulate LPP features corresponding to small and zero eigen values, i.e., the noise space and null space, and exploit the discriminant information from the whole space. In [20], a semi-supervised dimensionality reduction method called sparsity preserving discriminant analysis (SPDA) was developed by Lishan Qiao, Songcan Chen and Xiaoyang Tan. This algorithm models the ‘‘locality” and improves the performance of typical LDA. Sang-Ki Kim, Youn Jung Park, Kar-Ann Toh and Sangyoun Lee [21], proposed a feature extraction algorithm called SVM-based discriminant analysis (SVM-DA). Through his approach, the author aims at overcoming the limitations of LDA. Bidirectional principal component analysis (BDPCA) has been used for face recognition in [22] by Chuan-Xian

Ren and Dao-Qing Dai attempt to solve the small sample size problem of PCA.

In [23], Yong Wang and Yi Wu used Complete Neighborhood preserving embedding (CNPE) for the purpose of face recognition. CNPE aims at removing the singularity problem of eigen matrix suffered by Neighborhood preserving embedding (NPE).

III. DATABASE AND NORMALIZATION

In the presented work, standard ORL database is used. It consists of images of 40 subjects. There are 10 images of each subject in different orientations. This makes a total of 400 images. These images are in gray scale and consist of pixel values ranging from 0 to 255. The size of each image is 92 X 112 pixels. The subjects in the database are shown in Fig 1.

Figure 1: Subjects of the ORL database

The orientations of each subject are like:

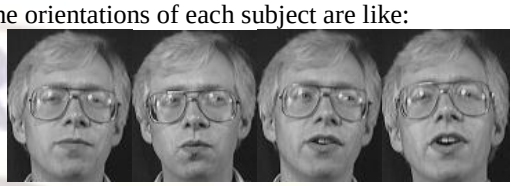

Figure 2: Different orientations of a particular subject in ORL database

Before proceeding with the method, image normalization is done. For normalizing an image, its pixel values are divided by the maximum pixel value contained in that image.

IV. FEATURE EXTRACTION

In image processing, feature extraction is a special form of dimensionality reduction. It involves simplifying the amount of resources required to describe a large set of data accurately. In the presented work, features are extracted from images using four methods: Hu moments, Zernike moments, Legendre moments and cumulants.

4.1 Hu moments

Hu moments have been derived from the geometric moments. Geometric moments are also known as regular or raw moments. These are nonnegative integers, which can be computed by equation (1):

$$m_{pq} = \int_{-\infty}^{+\infty}\int_{-\infty}^{+\infty} x^p y^q f(x,y)dxdy \quad (1)$$

where p,q = 0,1,2,3……

In equation (1), m_{pq} is the moment of order $(p+q)$ and $f(x,y)$ is a two dimensional, real and continuous density function of which the moment has to be calculated. For digital image we need a discrete version of the above equation represented as in equation (2):

$$m_{pq} = \sum_{x=1}^{M}\sum_{y=1}^{N} x^p y^q f(x,y) \quad (2)$$

Here, M×N is the size of the image. For the database used in the presented work, the values of M and N will be 92 and 112 respectively.

The central moment of order *(p+q)* of the image is defined by equation (3):

$$\mu_{pq} = \int_{-\infty}^{+\infty}\int_{-\infty}^{+\infty} (x-\bar{x})^p (y-\bar{y})^q f(x,y)dxdy \quad (3)$$

Here, $\bar{x}$ and $\bar{y}$ are the centroids of the image and are defined by:

$$\bar{x} = \frac{m_{1,0}}{m_{0,0}} \text{ and } \bar{y} = \frac{m_{0,1}}{m_{0,0}} \quad (4)$$

Now, if f(x, y) is the density function for a digital image, equation (3) in discrete format becomes:

$$\mu_{pq} = \sum_{x=1}^{M}\sum_{y=1}^{N} (x-\bar{x})^p (y-\bar{y})^q f(x,y) \quad (5)$$

The above defined central moments are origin independent and therefore they are translation invariant. But these moments are not invariant to scale or rotation in their original form.

Moments of order two or more can be constructed to be invariant to both translation and scale. Scale invariance can be achieved by dividing the corresponding central moment by the scaled energy of the original i.e. the 00^{th} moment as shown in equation (6):

$$\eta_{ij} = \frac{\mu_{ij}}{\mu_{oo}^{\left(1+\frac{i+j}{2}\right)}} \quad (6)$$

Hu, in 1962 introduced 'Hu moments' which are invariant to translation, scale as well as rotation. Hu moments are a set of seven moments which are nonlinear combinations of normalized central moments up to order three. The seven Hu moments are shown by equation (7):

$$\begin{aligned}
M_1 &= \eta_{20} + \eta_{02} \\
M_2 &= (\eta_{20} - \eta_{20})^2 + 4\eta_{11}^2 \\
M_3 &= (\eta_{30} - 3\eta_{12})^2 + (\eta_{03} - 3\eta_{21})^2 \\
M_4 &= (\eta_{30} - \eta_{12})^2 + (\eta_{03} + \eta_{21})^2 \\
M_5 &= (3\eta_{30} - 3\eta_{12})(\eta_{30} + \eta_{12})\left[(\eta_{30} + \eta_{12})^2 - 3(\eta_{21} + \eta_{03})^2\right] + \\
&\quad (3\eta_{21} - \eta_{03})(\eta_{21} + \eta_{03})\left[3(\eta_{30} + \eta_{12})^2 - (\eta_{21} + \eta_{03})^2\right] \\
M_6 &= (\eta_{20} - \eta_{02})\left[(\eta_{30} + \eta_{12})^2 - (\eta_{21} + \eta_{03})^2\right] + 4\eta_{11}(\eta_{30} + \eta_{12})(\eta_{21} + \eta_{03}) \\
M_7 &= (3\eta_{21} - \eta_{03})(\eta_{30} + \eta_{12})\left[(\eta_{30} + \eta_{12})^2 - 3(\eta_{21} + \eta_{03})^2\right] + \\
&\quad (3\eta_{12} - \eta_{03})(\eta_{21} + \eta_{03})\left[3(\eta_{30} + \eta_{12})^2 - (\eta_{21} + \eta_{30})^2\right]
\end{aligned} \quad (7)$$

The first moment, M_1, is analogous to the moment of inertia around the image's centroid, where the pixels' intensities are equivalent to physical density. The last one, M_7, is skew invariance. It enables it to distinguish mirror images of otherwise identical images. In our experiment conducted using Hu moments, all the seven Hu moments are calculated for each facial image.

Table 1 consists of 10 feature vectors for 10 orientations of subject 2 in the database.

Table 1: Hu moments of subject 2

Image no	M_1	M_2	M_3	M_4	M_5	M_6	M_7
2-1	0.0012	1.1145	1.7522	2.7004	1.0397	2.354	-2.9259
2-2	0.0012	0.9822	1.6067	1.7262	-0.6716	1.909	0.1064
2-3	0.0012	0.9967	2.451	3.2528	-2.0731	2.449	-0.4848
2-4	0.0012	1.0766	1.7206	1.4823	-1.1005	0.287	0.4849
2-5	0.0012	0.8636	0.2311	1.3562	-0.2185	-4.34	-0.0452
2-6	0.0012	0.9797	2.0262	1.8414	-2.2178	-1.646	1.6047
2-7	0.0012	1.1682	3.7579	4.4563	5.4096	13.215	1.0396
2-8	0.0012	1.0005	2.2362	2.5456	0.842	5.723	0.0691
2-9	0.0012	1.5421	2.3615	2.0594	-3.0265	-3.042	2.1438
2-10	0.0012	0.9115	2.5089	2.6352	-2.7682	1.922	0.2446

In the above table, we see that the first moment i.e. M_1 is same for all the orientations of the subject. Also, the variations in the lower order moments are less but in the higher order moments the variations are high. In M_5, M_6 and M_7, there are certain values which are negative also and hence the variation is too large. This affects the performance of the classifier and results in poor classification. The feature vector is formed using the calculated moment values which makes the length of the feature vector seven.

4.2 Zernike moments

Zernike in 1934 introduced a set of complex polynomials called the Zernike polynomials. These polynomials form a complete orthogonal basis set defined on the interior of the unit disc, i.e., $x^2 + y^2 = 1$. Let us denote the set of these polynomials by $V_{nm}(x,y)$. In polar coordinates, these are then represented as in equation (8):

$$V_{nm}(x,y) = V_{nm}(r,\theta) = R_{nm}(r)\exp(jm\theta) \quad (8)$$

Where:
'n' is positive integer or zero
'm' is positive and negative integer subject to constraint (n-|m|) is even and $|m| \le n$
'r' is length of vector from origin to (x , y) pixel
'θ' is angle between vector ρ and x axis in counter clockwise direction
In the above equation, R_{mn} is the Radial polynomial. It is orthogonal and is defined as in equation (9):

$$R_{nm}(r) = \sum_{s=0}^{(n-|m|)/2} \frac{(-1)^s (n-s)! r^{n-2s}}{s!\left[\frac{n+|m|}{2}-s\right]!\left[\frac{n-|m|}{2}-s\right]!} \quad (9)$$

It is to be noted that $R_{n-m}(r) = R_{nm}(r)$.

Complex Zernike moments are constructed using the set of Zernike polynomials. Zernike moments are the projection of the image density function on these orthogonal basis functions. The two dimensional Zernike moment for a continuous image function f (x, y) that disappears outside the unit circle is defined as in equation (10):

$$Z_{nm} = \frac{n+1}{\pi} \iint_{\text{unit disk}} f(x,y) V_{nm}^*(x,y)\, dxdy \quad (10)$$

Since in our case, the image is digital, so the integrals are replaced by summations as shown in equation (11):

$$A_{nm} = \frac{n+1}{\pi} \sum_x \sum_y f(x,y) V_{nm}^*(x,y) \quad (11)$$

Here, $x^2 + y^2 \le 1$

To calculate the Zernike moments of a particular image, we first take the centre of image as the origin and map the region of interest to the range of unit disc. Those image pixels which do not fall inside the unit disc are not used for computation. Thereafter, the image coordinates are described in terms of the length of the vector from the origin, the angle from the axis to the vector etc.

In the experiment conducted by us, Zernike moments of different orders (2 to 8) are calculated.
Table 2 consists of 10 feature vectors for 10 orientations of subject 2 in the database.

Table 2: Zernike moments of subject 2

Image no	Z_{20}	Z_{31}	Z_{42}	Z_{40}	Z_{51}	Z_{53}	Z_{62}
2-1	-1.102	-6.4727	-1.3869	-7.4029	-3.2025	3.3126	-0.4755
2-2	-1.099	-6.6799	-1.1644	-7.2521	-3.5483	2.2785	0.078
2-3	-1.0975	-6.825	-1.3694	-7.1614	-3.6634	2.586	-0.0683
2-4	-1.0854	-6.7228	-1.2138	-7.1546	-3.5915	2.2853	0.046
2-5	-1.1187	-6.7846	-0.9088	-7.494	-3.6191	2.7186	0.4117
2-6	-1.1037	-6.9002	-1.3914	-7.3231	-3.8162	2.0686	-0.2327
2-7	-1.1259	-7.0017	-2.4854	-7.3039	-3.4261	2.067	-1.2901
2-8	-1.1072	-7.0425	-1.7104	-7.2503	-3.7064	2.4051	-0.3873
2-9	-1.1033	-7.0592	-1.9559	-7.0575	-3.772	1.2888	-0.687
2-10	-1.142	-7.1451	-1.7801	-7.4172	-3.7097	2.1011	-0.3757

The results using Zernike moments are better than those using Hu moments. This is because we can see in the table above that the variations in the Zernike moments are less as compared to those in the Hu moments. Here again, the variations in lower order moments are less but those in higher order moments are large. We also calculated moments of order higher than 8 but they only degraded the performance of the classifier. The feature vector is formed using these calculated moments. The size of the feature vector is 7.

4.3 Legendre Moments

Legendre moments were derived from Legendre polynomials as kernel function. Legendre polynomials were first proposed by Teague. These are orthogonal moments which can represent an image with minimum information redundancy. Thus the moments represent the independent characteristics of an image.

The two-dimensional Legendre moments of order (p+q), are defined as in equation (12):

$$L_{pq} = \frac{(2p+1)(2q+1)}{4} \int_{-1}^{1}\int_{-1}^{1} P_p(x) P_q(y) f(x,y)\, dxdy \quad (12)$$

where p,q = 0,1,2,3…….∞ and x,y ∈ [-1,1].
P_p and P_q are Legendre polynomials and f(x, y) is the continuous image function. These Legendre polynomials define a complete orthogonal basis set over the interval [-1, 1]. In order to maintain orthogonality in the moments as well, the image

function is also defined over the same interval i.e. [-1, 1]. The Legendre polynomial of order 'n' is defined as in equation (13):

$$P_n(x)=\sum_{k=0}^{n}\left\{(-1)^{\frac{n-k}{2}}\frac{1}{2^n}\frac{(n+k)!x^k}{\left(\frac{n-k}{2}\right)!\left(\frac{n+k}{2}\right)!k!}\right\} \quad (13)$$

In the above definition, (n-k) should be even. Now, the Legendre moments for a discrete image consisting of pixels $M\times N$ with intensity function $f(i, j)$ are defined as in equation (14):

$$L_{pq}=\lambda_{pq}\sum_{i=0}^{M-1}\sum_{j=0}^{N-1}P_p(x_i)P_q(y_j)f(i,j) \quad (14)$$

where λ_{pq} is called the normalizing constant and is defined as in equation (15):

$$\lambda_{pq}=\frac{(2p+1)(2q+1)}{MN} \quad (15)$$

Where, $P_0(x)=1$ and $P_1(x)=x$.

The image is scaled in the region [-1, 1] since the definition of Legendre polynomials exists in this region only. So, x_i and y_j can be normalized as in equation (16):

$$x_i=\frac{2i}{(M-1)}-1 \quad \text{and} \quad y_j=\frac{2j}{(N-1)}-1 \quad (16)$$

Legendre moments are orthogonal moments and can be used to represent an image with minimum redundancy.

In the experiment conducted using Legendre moments, moments of different orders (2 to 4) are calculated. Table 3 shows the values of Legendre moments calculated for subject 2 in the database.

Table 3: Legendre moments subject 2

Image no	L_{02}	L_{20}	L_{11}	L_{21}	L_{12}	L_{30}	L_{03}	L_{22}	L_{40}	L_{04}	L_{31}	L_{13}
2-1	-233.06	-234.63	3.79	-0.42	5.59	12.5533	19.38	368.88	273.13	279.06	-4.08	2.32
2-2	-230.32	-239.42	-2.10	-13.65	4.43	10.4496	14.48	364.07	277.42	277.39	0.632	0.50
2-3	-236.67	-242.65	0.74	-1.77	5.21	12.2524	18.89	376.32	281.02	284.91	-2.59	0.96
2-4	-226.34	-236.17	-2.81	-13.22	1.64	11.1439	15.09	355.67	273.73	277.14	1.585	0.18
2-5	-234.10	-240.16	0.74	-9.22	5.77	12.5979	9.798	365.07	281.92	278.91	-2.87	1.59
2-6	-228.53	-235.15	-5.08	-23.25	3.69	9.8463	17.82	353.84	281.71	276.22	3.230	-0.11
2-7	-246.27	-250.07	1.91	8.76	5.21	14.7457	27.45	387.81	296.92	307.27	-1.36	3.082
2-8	-237.68	-242.04	0.33	0.23	3.06	13.5121	22.09	375.32	283.58	290.96	-0.79	2.924
2-9	-235.63	-251.38	-5.90	-13.74	9.56	8.7386	24.65	377.40	295.51	299.23	4.193	-0.67
2-10	-250.66	-252.53	1.08	2.03	8.07	14.0975	23.26	389.54	304.00	305.08	-1.71	2.035

The results using Legendre moments are better than those using Hu moments and comparable to those of Zernike moments. We can see in the table above that the variations are less. Here again, the variations in lower order moments are less but those in higher order moments are large. The variations in higher order moments were large which degraded the performance of the classifier. Hence, for the construction of feature vectors we have calculated only lower order moments (up to four). The feature vector is formed using these calculated moments. The size of the feature vector is 12.

4.4 Cumulants

Cumulants are quantities that are similar to moments and can be used to extract the inherent features of images. Cumulants can extract features which are otherwise very difficult to extract. Simple moments are used to derive cumulants. The r^{th} moment of a real valued continuous random variable X with probability density function $f(x)$ can be defined as shown in equation (17):

$$\mu_r=E(X^r)=\int_{-\infty}^{\infty}x^r f(x)dx \quad (17)$$

where r is a finite integer i.e. $r = 0,1, \ldots .$

All the moments can be represented with a single expression if the moment generating function has a Taylor expansion about the origin which is defined as in equation (18):

$$M(\xi)=E(e^{\xi X})=E\left(1+\xi X+.....+\xi^r X^r/r!+.....\right)=\sum_{r=0}^{\infty}\mu_r\xi^r/r! \quad (18)$$

The r^{th} derivative is the r^{th} moment of M at the origin.

Similarly, the cumulants represented as κ_r are the coefficients of the Taylor expansion of the

cumulants generating function about the origin defined as in equation (19):

$$K(\xi) = \log M(\xi) = \sum_r \kappa_r \xi^r / r! \quad (19)$$

The second and third order cumulants of a zero-mean stationary process *u* (n) are defined as in equation (20):

$$\kappa_2(\tau) = E\{u(n)u(n+\tau)\}$$

$$\kappa_3(\tau_1, \tau_2) = E\{u(n)u(n+\tau_1)u(n+\tau_2)\} \quad (20)$$

The first-order cumulant of a stationary process is the mean of the process and the second order cumulant is its variance. The higher-order cumulants are equivalent to the central moments; they are invariant to the mean shift and hence defined under the assumption of zero mean.

4.4.1 Polyspectra

The k[th] order polyspectrum or the k[th] order cumulants spectrum is the Fourier transform of the corresponding cumulants.

A polyspectrum exists when the corresponding k[th] order cumulants are absolutely summable. Special cases of the k[th] order polyspectrum are the power spectrum, bispectrum and the trispectrum [24].

For k = 2, we have the ordinary power spectrum defined by:

$$C_2(\omega_1) = \sum_{\tau_1=-\infty}^{\infty} \kappa_2(\tau_1)\exp(-j\omega_1\tau_1) \quad (21)$$

For k = 3, we have the bispectrum, defined by:

$$C_3(\omega_1, \omega_2) = \sum_{\tau_1=-\infty}^{\infty}\sum_{\tau_2=-\infty}^{\infty} \kappa_3(\tau_1, \tau_2)\exp\left[-j(\omega_1\tau_1 + \omega_2\tau_2)\right] \quad (22)$$

While the power spectrum is real-valued, bispectrum, and other higher order polyspectra are complex in nature.

For this experiment using cumulants, we first find the third order cumulant of the image and then take its Fourier transform to get the bispectrum. On calculating the bispectrum of the different facial images, we find that the patterns obtained are similar for the images of the same person (in different orientations) and different for the images of different persons. Few orientations of subject 1 are shown in Fig 3:

Figure 3: Four orientations of subject 1

Fig 4 shows the bispectrum patterns of the subject in Fig 3.

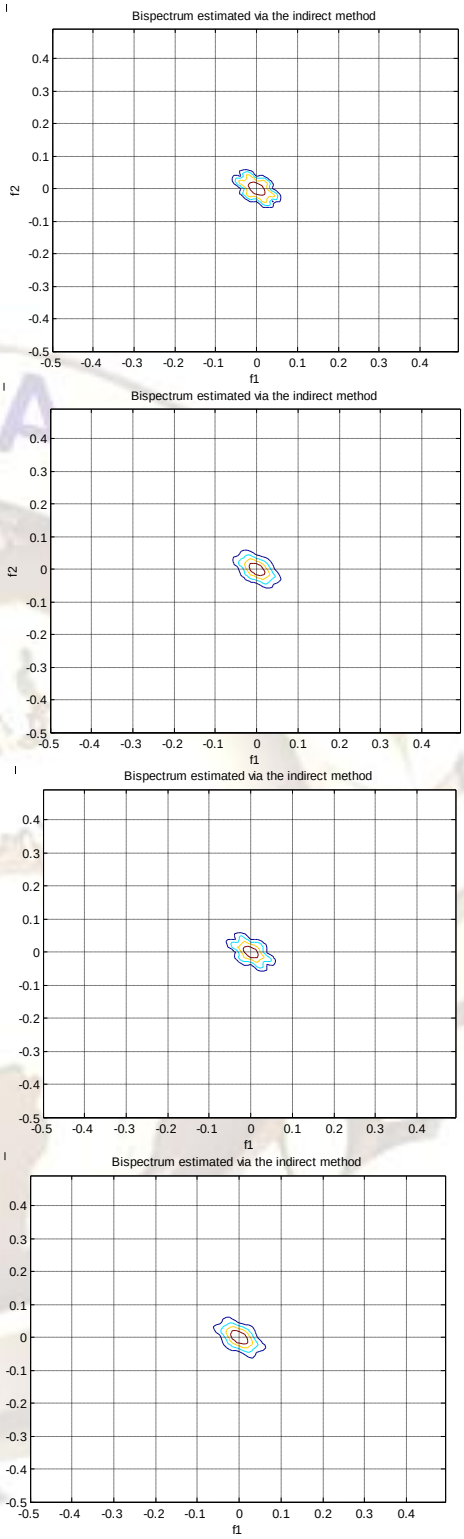

Figure 4: Bispectrum patterns of some orientations of subject 1

All the above patterns are similar to each other since they belong to the images of same person with different orientations. Fig 6 shows the bispectrum patterns of subject 4 in Fig 5.

Figure 5: Four orientations of subject 4

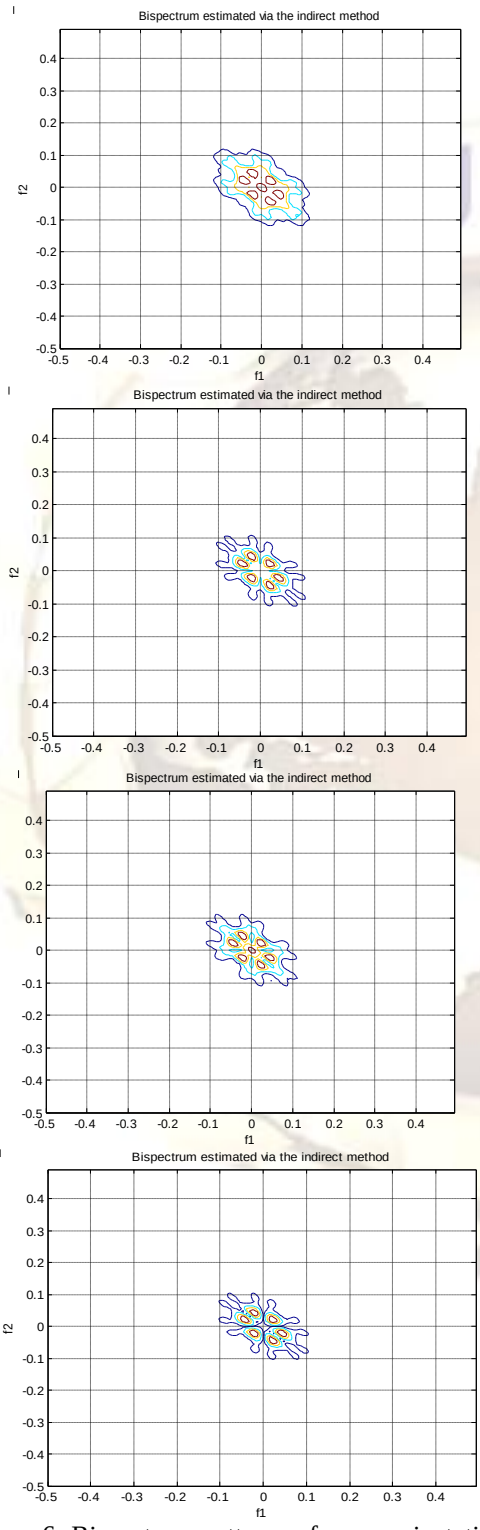

Figure 6: Bispectrum patterns of some orientations of subject 4

Again we notice that all the above patterns are similar to each other since they belong to the images of same person with different orientations. Also, the patterns of subject 1 are different from those of subject 4, which shows that they can be classified easily.

To ensure that the bispectrum patterns for all the subjects are different, we present below one more example.

Figure 7: Four orientations of subject 10

Fig 8 shows the bispectrum patterns of the orientations of subject shown in Fig 7.

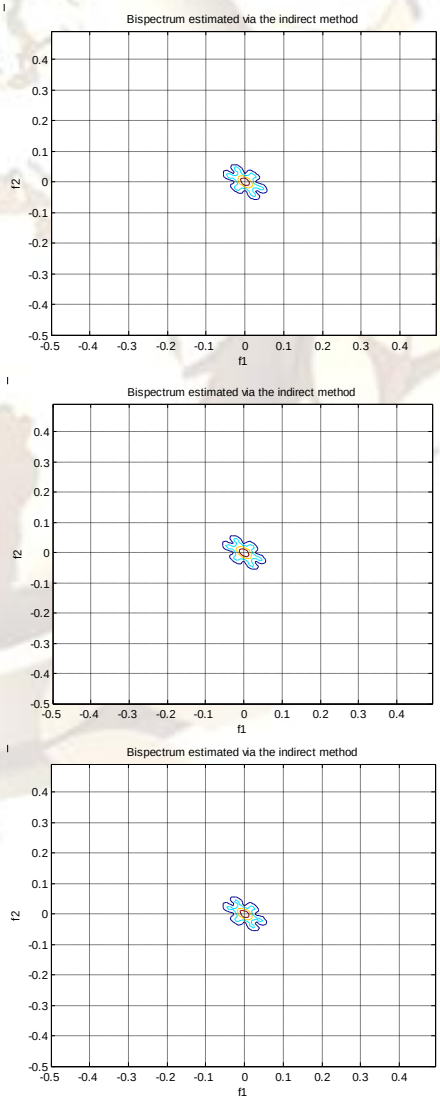

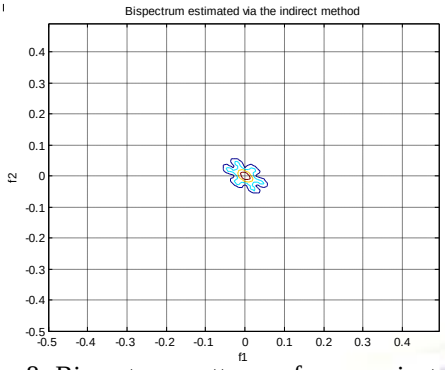

Figure 8: Bispectrum patterns of some orientations of subject 10

Again we see that the orientation patterns of subject 10 are different both from subject 1 and subject 4. Hence, we can conclude that these patterns of different orientations of same subjects are similar while those of different subjects are different. This fact can be used to classify the different subjects. For classification, we will form the biwavelant of the above patterns.

4.4.2 Biwavelant

For using bispectra for face recognition, the redundant information i.e. the high frequency components have to be removed and only the low pass information which corresponds to the significant features are retained. The two dimensional bispectrum matrix is converted into one dimensional matrix by concatenating the rows horizontally. The frequency response is given as:

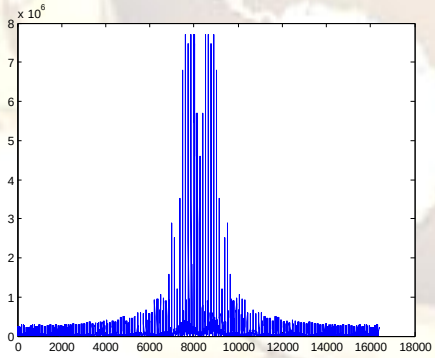

Figure 9: One dimensional frequency response of bispectrum

The frequency response above consists of very large number of values. To reduce the amount of computation, we try to find out its envelope (by removing the high frequency components). For this, we need to carry out low pass filtering which can be done using wavelets. Smoothing filters can also be used but they are not able to protect the precious details while removing the high pass information.

Wavelet transform was explained in [25] and [26]. It is the integral transform defined as in equation (23).

$$W_{\psi f}(a,b)=\frac{1}{\sqrt{|a|}}\int_{-\infty}^{\infty}\overline{\psi\left(\frac{x-b}{a}\right)}f(x)dx \tag{23}$$

where $f(x)$ is the signal being transformed and $\psi(x)$ is the 'analyzing wavelet' $\psi(x)$ satisfies the admissibility condition $\int|\psi(x)|^2\frac{d\omega}{\omega}<\infty$ which is equivalent to $\int\psi(t)dt=0$ i.e. a wavelet has zero mean.

The wavelet coefficients are given by equation (24):

$$c_{jk}=W_{\psi f}\left(2^{-j},k2^{-j}\right) \tag{24}$$

Here, $a=2^{-j}$ is called the binary dilation or dyadic dilation, and $b=k2^{-j}$ is the binary or dyadic position.

When we use the continuous wavelet transform, we can detect a signal buried in Gaussian noise. This fact has been used in the concept of wavelants. Before understanding wavelants, we need to know two properties of cumulants [27]:

1) The third order cumulant of a Gaussian (or any symmetrically distributed) random process is zero.
2) If a subset of random variables $\{x_i\}$ is independent of the rest, then the third-order cumulants is zero.

The above formulation exhibits properties closely related to those of cumulants [28]. The ideas from the two preceding topics have led to the motivation for the development of wavelants which is a combination of wavelet and cumulant theory. In the following section we shall consider only the third order wavelant which is defined as in equation (25):

$$W^3_{xxx}(b_1,a_1;b_2,a_2)=\frac{1}{\sqrt{a_1a_2}}\int\int x(t)x\left(\frac{t-b_1}{a_1}\right)x\left(\frac{t-b_2}{a_2}\right)dt \tag{25}$$

$$W^3_{xyz}(b_1,a_1;b_2,a_2)=\frac{1}{\sqrt{a_1a_2}}\int\int x(t)y\left(\frac{t-b_1}{a_1}\right)z\left(\frac{t-b_2}{a_2}\right)dt \tag{26}$$

Equation (25) represents the third order auto wavelant while equation (26) represents the third order cross wavelant. Now we apply the wavelet transform (db4) at different levels on the frequency response obtained earlier (example of which is shown in Fig 9). The result of applying the transform on an image of subject 1 is shown in Figure 10.

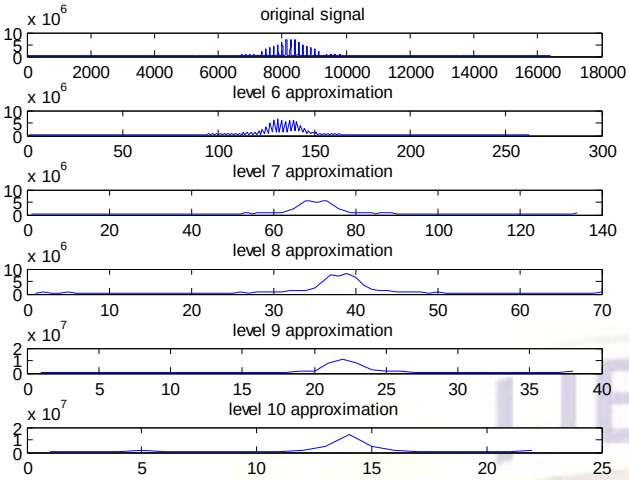

Figure 10: waveforms for subject 1 at various approximations]

We notice from the above figure, that we obtain a nice envelope at Level 7 approximation. This seems to be the most appropriate approximation level for classification because in further approximations, details are being lost. The similar waveforms for subjects 4 and 10 are shown below.

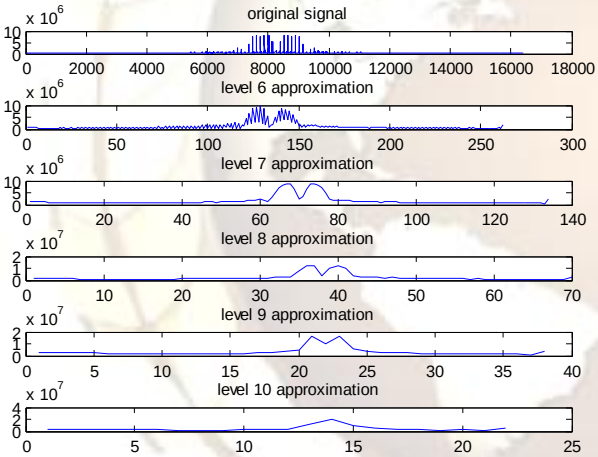

Figure 11: waveforms for subject 4 at various approximations

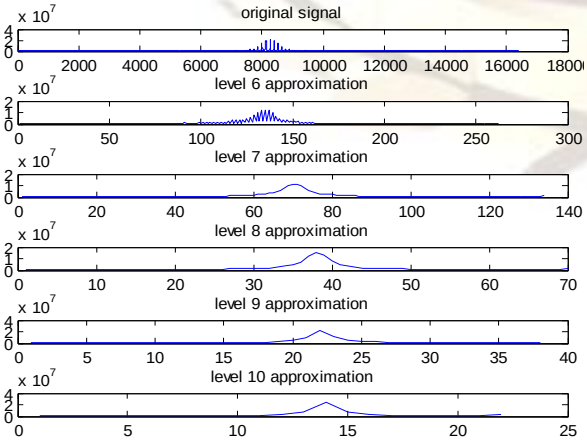

Figure 12: waveforms for subject 10 at various approximations

In all the above waveforms, level 7 approximation is most appropriate and also at this level all the three waveforms can easily be distinguished from one another. Let us now have a closer look at the level seven approximation of the frequency response for few orientations of all the three subjects.

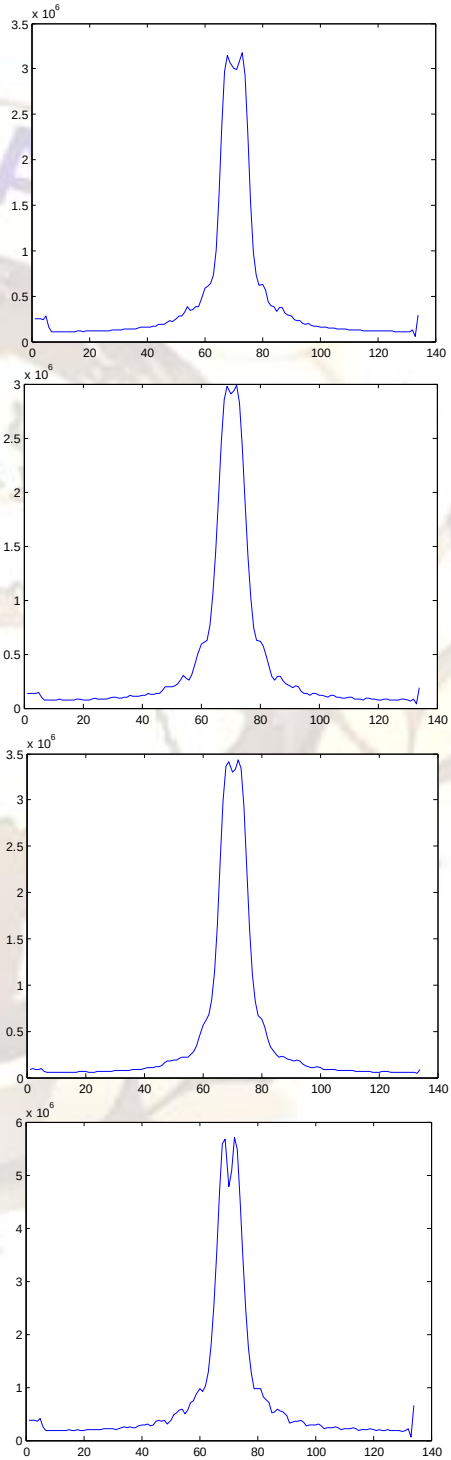

Figure 13: Level 7 approximations of subject 1

All the above waveforms belong to subject 1 and are similar to each other.

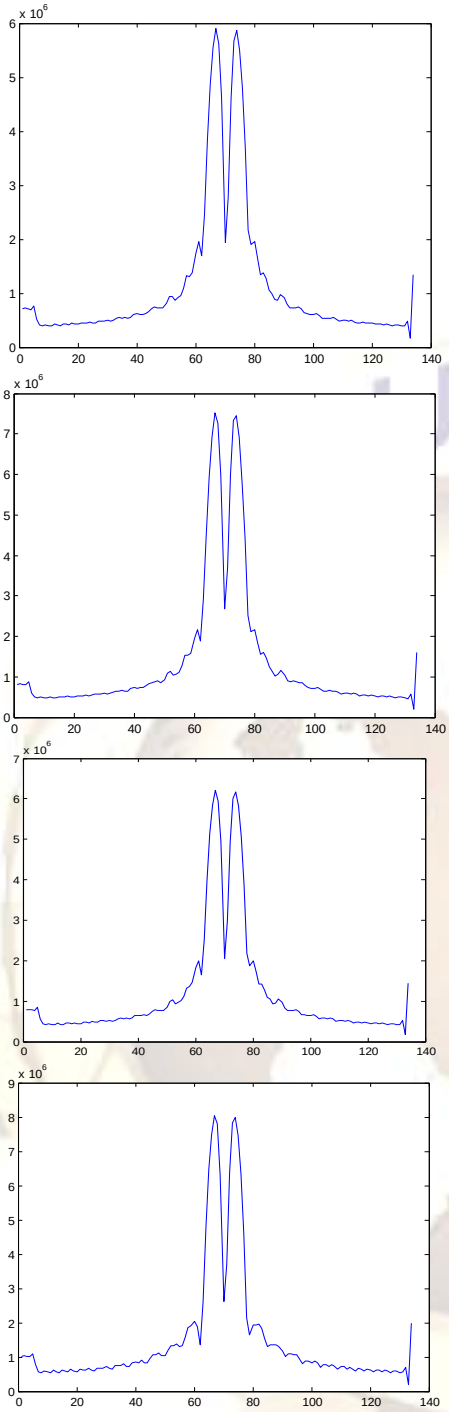

Figure 14: Level 7 approximation of subject 4

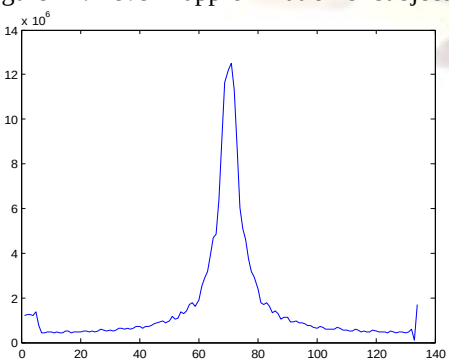

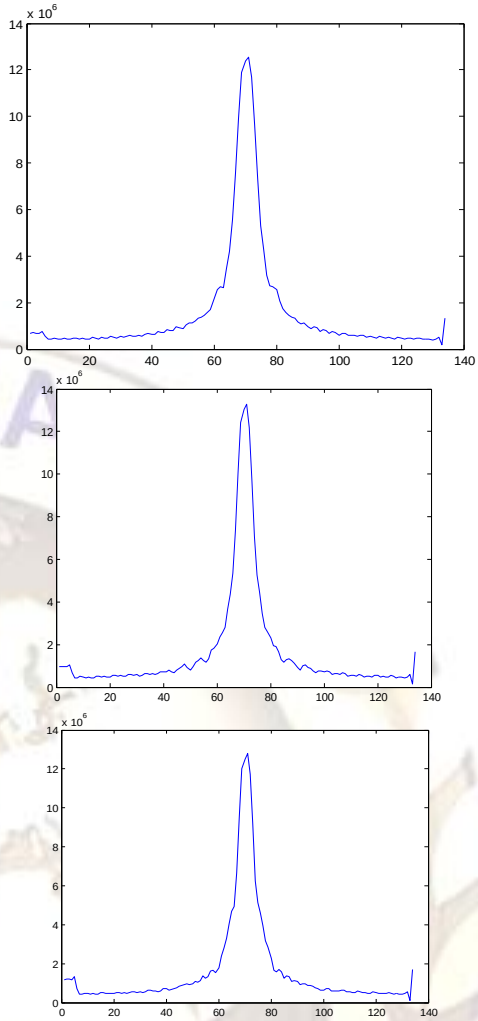

Figure 15: Level 7 approximations of subject 10

We notice from the above figures, that the waveforms for different orientations of one subject are similar while for different subjects they are different. Hence it is possible to classify them.

V. CLASSIFICATION

Image classification involves analyzing the numerical properties of various image features and organizing the data into categories. In this paper, we have used three classifiers for classifying the data: minimum distance classifier, support vector machine and k nearest neighbor. In all the three methods, out of the ten orientations of each subject, eight were used for training the classifier and two were used as test cases.

5.1 Minimum distance classifier

The classification was done using the minimum distance classifier. Euclidean distance has been used for calculating the distance. Since the total number of subjects is 40, there were 40 classes. After classification, following results were obtained:

Table 4: Classification accuracy using minimum distance classifier

Sr. No	Feature extraction method	Classification accuracy
1.	Hu moments	60%
2.	Zernike moments	90%
3.	Legendre moments	90%

The results of Hu moments are not as good as those of Zernike and Legendre moments as can be seen from the table.

5.2 Support Vector Machine

Classification using non linear SVM was done using the following parameters:

Table 5: Various parameters used to design the support vector machine

Sr. No.	Parameters	Parameter value
1.	Classifier Type	Nonlinear multi class SVM
2.	Kernel	Poly
3.	C	1000

The results of various feature extraction methods using SVM are shown below:

Table 6: Classification accuracy SVM

Sr. No	Feature extraction method	Classification accuracy
1.	Hu moments	60%
2.	Zernike moments	85%
3.	Legendre moments	95%

Here again, the results of Hu moments are the poorest. Also, the results of Legendre moments improved as compared to the ones from minimum distance classifier, while those of Zernike moments have degraded.

5.3 K Nearest Neighbor

When classified using the k nearest neighbor algorithm, most accurate results were obtained when the value of k = 3. The following figure shows the classification results obtained for face recognition using the nearest neighbor classifier for Hu moments:

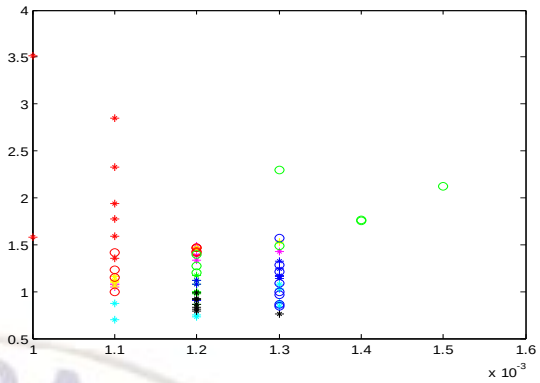

Figure 16: Classification results obtained using Hu moments

Each point in Fig 16 represents the feature vector corresponding to an image. Each sample is classified and associated to one of the ten clusters (subjects) i.e. to a particular subject. The clusters are shown with different colors and markers for easy understanding. In the above figure we see that the classes are not very distinct and kind of overlap. Hence the performance of Hu moments is not very good. Figure 17 shows the classification results obtained for face recognition using the nearest neighbor classifier for Zernike moments:

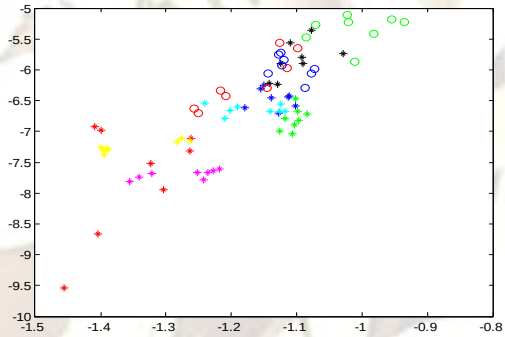

Figure 17: Classification results obtained using Zernike moments

In above figure, the cluster formation is better than that obtained from Hu moments. Hence the classification is better. Fig 18 shows the results obtained for face recognition using nearest neighbor classifier for Legendre moments:

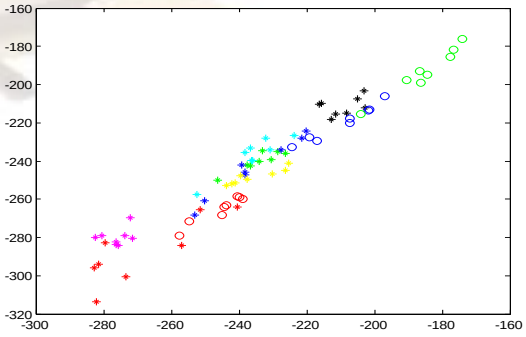

Figure 18: Classification results obtained using Legendre moments

Here also the cluster formation is good. The results of using k nearest neighbor classifier on the three feature extraction methods are shown in Table 7:

Table 7: Classification accuracy of the feature extraction methods using KNN

Sr. No	Feature extraction method	Classification accuracy
1.	Hu moments	44%
2.	Zernike moments	85%
3.	Legendre moments	95%

Once again the performance of Hu moments is the poorest. The results of Zernike and Legendre are same as those obtained from SVM.

VI. RESULTS

Four experiments were performed for extracting the features using four approaches: Hu moments, Legendre moments, Zernike moments and cumulants. The feature vectors obtained using these moments were classified using three methods: minimum distance classifier, SVM and k nearest neighbor. The average performance of the feature extraction methods can be tabulated as below:

Table 8: Average performance of the feature extraction methods

Sr. No	Feature extraction method	Classification accuracy
1.	Hu moments	53.33%
2.	Zernike moments	86.66%
3.	Legendre moments	93.33%

From the above table, we can infer that the performance of Hu moments was not satisfactory and hence they cannot be used for the purpose of face recognition using complex facial images. On the other hand, the results obtained using Zernike and Legendre moments are good.

For the experiment performed using cumulants, we have obtained waveforms which are similar for different orientations of same subject and different for different subjects. These waveforms can be classified using any suitable method.

Many techniques have been used for face recognition like LDA (Linear Discriminant Analysis), BLD (Bayesian logistic discriminant) etc. While the results of these techniques on ORL database are 87% and 91.9% respectively. The results of orthogonal moments like Zernike and Legendre are better than these (95%).

VII. CONCLUSION

In this paper a novel method for face recognition using moments and cumulants has been presented. Four experiments were conducted using Hu moments, Zernike moments, Legendre moments and cumulants. Features were extracted using the above mentioned moments and feature vectors were formed. The size of the feature vector for Hu moment was 7, for Zernike 7 and for Legendre moments it was 12. In all the experiments, three different classifiers were used for classification: minimum distance classifier, SVM and k nearest neighbor. From the experimental results it was observed that the feature representation using Hu moments provides a maximum recognition rate of 60%. Orthogonal moments like Zernike and Legendre which are also invariant in nature are capable of representing the image features with minimum number of coefficients and the percentage of accuracy is also superior. Hence these moments have been found very much suitable for feature representation of complex face images which are almost similar with respect to variations in size, pose, illumination and orientation within a smaller area. In this paper, we also worked with cumulants and used them for face recognition. The method can be used to successfully identify different faces. The proposed technique using cumulants is sensitive to the structural changes in the images and is able to distinguish them successfully. But, the same sensitivity makes the method vulnerable to noise in the samples, so the images have to be noise free for expected results.

REFERENCES

[1] R. Ksantini, B. Boufama, Djemelziou, Bernardcolin, A Novel Bayesian Logistic Discriminant Model: An Application to Face Recognition, *Pattern Recognition*, 43(4), 2010, 1421–1430.

[2] C.K. Hsieh, S.H. Lai, and Y.C. Chen, An Optical Flow-Based Approach to Robust Face Recognition Under Expression Variations, *IEEE Transactions on Image Processing*, 19(1), 2010, 233- 240.

[3] J. Yang, C. Liu, L. Zhang, Color Space Normalization, Enhancing the Discriminating Power of Color Spaces for Face Recognition, *Pattern Recognition*, 43(4), 2010, 1454–1466.

[4] H. Zhou, and A.H. Sadka, Combining Perceptual Features with Diffusion Distance for Face Recognition. *IEEE Transactions on Systems, Man, and Cybernetics Part C: Applications And Reviews*, 41(5), 2011, 577- 588.

[5] Z. Lei, M. Pietikäinen, S.Z. Li, S. Liao, Face Recognition by Exploring Information Jointly in Space, Scale and Orientation, *IEEE Transactions on Image Processing*, 20(1), 2011, 247- 256.

[6] Z. Liu, J. Yang, C. Liu, Extracting Multiple Features in the Cid Color Space for Face Recognition, *IEEE Transactions on Image Processing*, 19(9), 2010, 2502-2509.

[7] W. Zou, P.C. Yuen, Discriminability and Reliability Indexes: Two New Measures to Enhance Multi-Image Face Recognition, *Pattern Recognition*, 43(10), 2010, 3483–3493.

[8] X. Tan, B. Triggs, Enhanced Local Texture Feature Sets for Face Recognition Under Difficult Lighting Conditions, *IEEE Transactions On Image Processing*, 19(6), 2010, 168-182.

[9] R.M. Jiang, D. Crookes, N. Luo, Face Recognition in Global Harmonic Subspace, *IEEE Transactions on Information Forensics and Security*, 5(3), 2010, 416- 424.

[10] B. Zhang, Y. Gao, S. Zhao, J. Liu, Local Derivative Pattern Versus Local Binary Pattern: Face Recognition With High-Order Local Pattern Descriptor, *IEEE Transactions on Image Processing*, 19(2), 2010, 533-44.

[11] G.F. Lu, Z. Lin, Z. Jin, Face Recognition Using Discriminant Locality Preserving Projections Based on Maximum Margin Criterion, *Pattern Recognition*, 43(10), 2010, 3572–3579.

[12] S. Dabbaghchian, M. P. Ghaemmaghami, A. Aghagolzadeh, Feature Extraction Using Discrete Cosine Transform and Discrimination Power Analysis with a Face Recognition Technology, *Pattern Recognition* 43(4), 2010, 1431–1440.

[13] M. Cheng, B. Fang, Y.Y. Tang, T. Zhang, J. Wen, Incremental Embedding and Learning in the Local Discriminant Subspace with Application to Face Recognition, *IEEE Transactions on Systems, Man and Cybernetics Part C: Applications And Reviews*, 40(5), 2010, 580- 591.

[14] I. Naseem, R. Togneri, M. Bennamoun, Linear Regression for Face Recognition, *IEEE Transactions on Pattern Analysis and Machine Intelligence*, 32(11), 2010, 2106- 2112.

[15] W.C. Kao, M.C. Hsu, Y.Y. Yang, Local Contrast Enhancement and Adaptive Feature Extraction for Illumination-Invariant Face Recognition, *Pattern Recognition*, 43(5), 2010, 1736–1747.

[16] S. Yan, H. Wang, J. Liu, X. Tang, T. Huang, Misalignment-Robust Face Recognition, *IEEE Transactions on Image Processing*, 19(4), 2010,1- 6.

[17] R. Kumar, A. Barmpoutis, A. Banerjee, B.C. Vemuri, Non-Lambertian Reflectance Modeling and Shape Recovery of Faces Using Tensor Splines, *IEEE Transactions on Pattern Analysis and Machine Intelligence*,33(3), 2011, 553-567.

[18] T.K. Kim, J. Kittler, R. Cipolla, On-Line Learning of Mutually Orthogonal Subspaces for Face Recognition by Image Sets, *IEEE Transactions on Image Processing*, 19(4), 2010, 1067-74.

[19] J. Lu, Y.P. Tan, Regularized Locality Preserving Projections and its Extensions for Face Recognition. *IEEE Transactions on Systems, Man and Cybernetics—Part B: Cybernetics*, 40(3), 2010, 958- 963.

[20] L. Qiao, S. Chen, X. Tan, Sparsity Preserving Discriminant Analysis for Single Training Image Face Recognition, *Pattern Recognition Letters*, 31(5), 2010, 422–429.

[21] S.K. Kim, Y.J. Park, K.A. Toh, S. Lee, SVM Based Feature Extraction for Face Recognition, *Pattern Recognition*, 43(8), 2010, 2871–2881.

[22] C.X. Ren, D.Q. Dai, Incremental learning of bidirectional principal components for face recognition, *Pattern Recognition*, 43(1), 2010, 318 – 330.

[23] Y. Wang, Y. Wu, Complete neighborhood preserving embedding for face recognition, *Pattern Recognition*, 43(3), 2010, 1008 -1015.

[24] S. Haykin, *Adaptive Filter Theory*, (Prentice Hall, 2001)

[25] A. Grossman, R.K. Martinet, Time and scale representation obtained through continuous wavelet transform, *Signal Processing IV, Theories and Applications*, 1988, 475-482.

[26] S.G. Mallat, A theory for multiresolution signal decomposition, *IEEE Transactions on Pattern Analysis and Machine Intelligence*, 11(7), 1989, 674- 693.

[27] R. Kapoor, and A. Dhamija, A New Method for Identification of Partially Similar Indian Scripts, *International Journal of Image Processing, 6(2)*, 2012.

[28] M, Durrani TS. Wavelants - An Introduction to Higher Order Wavelets

From the Executive Editor

Dr. Ruchika Malhotra[1]

Published online April 2013

As always I take immense pleasure in presenting to you the fourth issue of SEIJ and hope that it shall inspire the researchers worldwide to utilize the knowledge and knowhow contained in this issue for newer applications and advancement of the frontiers of software engineering.

In this issue the first paper provides a framework for an adaptive service composer. The second research paper proposes a model for change predication using two open source software. The aim of the second paper is to propose use of few machine learning algorithms with an objective to predict change prone classes. The third paper reviews the existing literature on software testing techniques and provides guidelines for future research in this area. The last paper implements a transceiver system on hardware test-beds.

A practical framework of an adaptive service composer is introduced in the first paper. This paper is titled "A Practical Approach to Adaptive Service Composition" and is authored by Dimuthu U. Gamage, Ryan Rybarczyk, Rajeev R. Raje. In this paper, the authors propose a design of an adaptive service composer that will provide a focus on automatic adaptation of semantic and quality of service level contracts in compositions. This proposed implementation is empirically validated on the existing Enhanced Distributed Object Tracking System.

The second research paper titled "Inter Project Validation for Change Proneness Prediction using Object Oriented Metrics" authored by Ruchika Malhotra and Megha Khanna develops an prediction model one project and validate it on another project. For the results validation the authors have used two open source projects written in Java language. The performance of the predicted models are evaluated using Receiver Operating Characteristic analysis. The results of the study indicates that we can successfully apply the training sets for inter project validation. These results obtained from the study will help the researchers and software practitioners in optimizing time and effort required to generate training set of each project.

.

The need for efficient and effective software testing techniques is increasing so that the cost of testing can be reduced. The third paper titled "Empirical Evaluation of Software Testing Techniques – Need, Issues and Mitigation", authored by Sheikh Umar Farooq and SMK Quadri, explores the literature on software testing techniques evaluation and identifies the problems associated with them. The aim of this paper is to provide guidelines for evaluating software testing techniques that will help the researchers in carrying out the research on areas related to software testing.

"FPGA Implementation of MIMO System using Xilinx System Generator for Efficient Hardware/ Software co-design", authored by Sparsh Mittal and Saket Gupta implements a transceiver system on hardware test-beds, which can be useful in video streaming. They employed the 2*2 Alamouti MIMO technique to develop a transmission system and implemented the design on FPGA using Xilinx System Generator and AccelDSP. This paper will help to meet the rapid demands of multimedia services over wireless networks.

I also welcome your comments and reviews on this issue and welcome original research and new ideas in the areas of software engineering.

[1]Dr. Ruchika Malhotra
Department of Computer & Software Engineering
Delhi Technological University
Shahbad Daulatpur, Bawana Road, Delhi-110042, India
Email: ruchikamalhotra2004@yahoo.com

CONCRETE RESEARCH LETTERS www.crl.issres.net Vol. 4 (1) – March 2013

Influence of Aggressive Chemical Environment on High Volume Fly Ash Concrete

Verma, A.[1c], Shukla, M.[2], and Sahu, A. K.[1]
[1]Department of Civil Engineering,
Delhi Technological University, Delhi, INDIA
[2]Department of Civil Engineering,
Bundelkhand Institute of Engineering & Technology, Jhansi, INDIA

Abstract

The benefits of using fly ash in cement concrete construction are well recognized in terms of cost reduction and management of environmental pollution. The advantages offered by the use of fly ash in concrete have impelled engineers to further extend the use of this waste product in the form of 'High Volume Fly Ash Concrete' (HVFAC). In the present paper, results of a study concerning the effect of acidic environment on the compressive strength of HVFAC have been reported. On the basis of results obtained; it has been concluded that HVFAC may be a promising material under such types of aggressive environmental conditions.

Keywords: Fly ash, concrete, HVFAC, acidic environment, compressive strength.

1. Introduction

Recently there has been a growing trend towards the use of supplementary cementitious materials, whether natural, waste or by-products, in the production of concrete because of ecological, economical and diversified product quality reasons. Fly ash which is a by-product of combustion of pulverized coal in the thermal power plants, is used for these reasons. Fly ash is removed from the effluent gases of these power plants by electrostatic precipitators. Fly ash, along-with coal dust, is also collected from the furnaces of the thermal power plants. The intrusion of fly ash in concrete affects all aspects of concrete properties. The main objective in using the fly ash in concrete is to achieve a reduced cement content to reduce costs, reduced heat of hydration and attainment of required levels of ultimate strength of concrete with the help of pozzolanic reactions. In this study an attempt has been made to explore the possibility of maximum use of fly ash in concrete.

---

[c] Corresponding Author: Verma A.
Email: alokverma_dce@hotmail.com Telephone: +919968240071 Fax: +911127871328
© 20012-2013 All rights reserved. ISSR Journals

Shukla et al [1] have reported that use of waste materials such as fly ash and stone dust in concrete making is beneficial. It has been reported that the compressive strength of concrete increases up to about 40% replacement of sand by stone dust. Regourd [2] has carried out the strength tests on cubes subjected to sea water curing condition and found the loss in strength of cubes due to chemical environment. Building Research Establishment digest [3] discussed the factors responsible for sulphate attack on concrete below the ground level and recommended that suitable selection of cement type and concrete quality are important factors in resisting attack by naturally occurring sulphates.

Mehta [4] has studied the mechanism of sulphate attack on ordinary Portland cement. Wond and Poole [5] have studied the effect of pozzolana and slags on sulphate resistance of hydraulic cement mortar and found them to be beneficial for concrete. Lawrence [6] has observed the types of disruption during sulphate attack on mortars and concretes and explained the chemical processes involved. It was concluded that partial replacement of ordinary Portland by various latent hydraulic binders can lead to improved sulphate resistance.

Tikalsky and Carrasquillo [7] have carried out the experiments to observe the influence of fly ash on the sulphate resistance of concrete and explained the dilution effect and pozzolanic effect of fly ash in cement. The fly ashes with a low amount of calcium hydroxide and amorphous calcium aluminate decrease the susceptibility of concrete to sulphate attack. Several aspects related with the utilization of fly ash in concrete in sulfate aggressive environments have been examined by Torii and Kawamura [8]. Wang [9] has carried out the experiments on hardened cement paste specimens made with different cement types and varying water-cement ratios. These specimens were immersed in 5% sodium sulphate solution maintained at constant pH value of 6. The mechanism of sulphate attack is evaluated with the help of XRD analysis in regard to leaching of $Ca(OH)_2$ and formation of gypsum and Ettringite.

O.S.B. Al-Amoudi et al [10] have observed the effect of magnesium sulphate and sodium sulphate on durability performance of plain and blended cements. It was observed that the deterioration of blended cement exposed to sodium sulphate environment is less. This is attributed to reduced quantity of calcium hydroxide which significantly mitigates the sulphate attack in these cements. Naik et al [11] have carried out the experiments on fly ash blended cement concrete and reported the improvements in mechanical properties of concrete. Mosszza [12] has studied the chemistry of pozzolanic action of fly ash mixed cement and explained the mechanism of this action. Cohen and Bentur [13] have described the effect of sulfates on concrete as complex. In most of the practical situations the concentration of sulphates in ground waters and soils is upto the order of 1000 ppm while that of sea water and industrial effluents is more than this extent. Rasheeduzzafar et al [14] have reported the influence of cement composition on the corrosion of reinforcement and sulphate resistance of concrete.

The C_3S/C_2S ratio of cement has been shown to have a significant effect on sulphate resistance of the cement. Bureau of Indian standards [15] provides necessary guidelines for maintaining quality control on concrete materials to improve durability of concrete in aggressive conditions of exposure. Miyagawa [16] has observed the corrosion effect of chlorides on reinforcing steel and suggested a durable design and repair of concrete structures. Kumar and Rao [17,18,] have observed the effect of aggressive chemical environment on the setting time of cement and strength of concrete. They have reported that the setting times increase with the concentration of sulphate ions. This may be due to reduction in solubility of cement paste ions in presence of strong anions in solution (i.e., SO_4^{--}). The loss in compressive strength of concrete cubes cured under different types of sulphates was observed with the passage of time.

O.S.B. Al-Amoudi [19] has discussed the mechanism of sulphate attack in cement blended with fly ash. Concrete used for underground construction is generally subjected to aggressive soil and sub-soil conditions. Studies have reported replacement of 30% cement by fly ash in such cases.

In the case of road construction about 70% cement has been replaced by fly ash. Kumar and Rao [20,21,22] presented the results of experimental investigation showing the effect of sulphates on the strength of concrete under the conditions simulating cast in situ and precast situations. It was concluded that the use of precasting in place of cast in situ is preferable in situations exposed to sulphate environments. The compressive strength tests on cubes exposed to time varying sulphate environment have been reported by them and cumulative damage to concrete due to such aggressive environmental conditions was considered by them.

Garvin et al [23] have reported the effect of contaminated land on the performance of concrete. They observed the loss in strength of concrete due to the contaminated soil environment in which the concrete cubes were buried for a long duration of time. Aziz and Koe [24] have observed the durability of concrete sewers in aggressive sub-soil and ground water conditions. Berke et al [25] have considered several aspects of concrete protection in such conditions and pozzolanic materials have been recommended to be beneficial. Camps et al [26] have observed the influence of surface absorption on sulphate attack and reported the sorptivity of mortar to be sensitive to the condition of cure and type of mortar skin in contact with the fluid. The influence of cure has a dominant effect on the capillarity of mortar which was reflected in the variation of porosity and strength.

Nagele [27] has suggested new and powerful method for evaluation of multi-parameter corrosion test. Mehta [28] has carried out a laboratory investigation involving sixteen fly ash samples of varying calcium content with the objective of clarifying the relationship between fly ash composition and sulphate resistance. The results show that rather than the chemical composition it is the mineralogical composition of cement fly ash interaction product that controls the sulphate resistance.

On the basis of the literature survey it was proposed to study the strength and durability aspect of HVFAC with the following objectives.

1. To observe the development of compressive strength in concrete of M35 grade and HVFAC, of the similar grade (in which 50% cement is replaced by fly ash of fineness lower than that of cement), cured in ordinary water for different curing times.
2. To observe the loss in compressive strength of these mixes of concrete which were exposed to sulphuric acid of different concentrations for various time periods.

2. Experimental Program

The cement used for investigation was 43 grade ordinary Portland cement with specific gravity 3.15, fineness 3250 cm^2/gm (by Blaine's apparatus) and ignition loss 1.6%. Blaine's method was used to determine, as per ASTM C 204-92 [29], specific surface area of cement by passing a known volume of air through a bed of cement of known porosity and thickness under a prescribed average pressure. In this method the rate of flow of air through the cement bed diminishes continuously and time, taken for the flow of air, is measured. Considering these parameters, specific surface area of cement indicating fineness of cement was calculated. The initial and final setting times of cement were 45 and 300 minutes respectively. The 3, 7 and 28 days compressive strength of cement were 24.6, 36.2 and 49.1 N/mm^2 respectively. The sand used was confirming to grading zone-II as per IS:383-1970 [30]. The properties of sand were – specific gravity 2.63, water absorption 3.68 % and fineness modulus 3.05. Fineness modulus is a dimensionless index defining average size of a material which has various sizes mixed in different quantities. The coarse aggregate was crushed granite of maximum size 20 mm. The physical properties of coarse aggregate were – angular shape, rough texture, specific gravity 2.65, water absorption 0.5% and fineness modulus 7.4. Potable tap water, free from impurities, was used for making concrete.

Sodium Naphthalene Formaldehyde, a naphthalene based non-air-type superplasticizer, was used in the mix for imparting workability to the concrete mix. The fly ash used in the study had an average fineness 4270 cm^2/gm (by Blain's apparatus), loss of ignition 0.45% and conformed to IS: 3812-2003 (Part 1) [31]. The fly ash was collected from the thermal power plant, of an Indian public sector undertaking namely, National Thermal Power Corporation, located at Dadri. Dadri is located in Gautam Budh district of the state of Uttar Pradesh in India.

In order to observe the effect of sulphuric acid on concrete specimens, one tank with ordinary water and two tanks of sulphuric acid solutions having concentrations of 0.1 N and 0.2 N respectively were prepared. 60 samples of 150 mm size concrete cubes were cast for each type of concrete using table vibrator. The mix design was carried out for M 35 grade of concrete as per Indian standard guidelines and the compositions of these mixes were as given in Table 1. The water cementitious ratio of the mixes was maintained at 0.42. After one day of hardening, the moulds were stripped off and 20 samples of different types of mix were immersed in each type of curing tanks. After 7, 28, 90 and 180 days curing, 5 samples in each case were tested for compressive strength of cubes.

Table 1: Composition of Mixes

Type Of Concrete	**Quantities Of Mix Constituents (Kg/ m^3)**					
	Cement	CA 20 mm	CA 10 mm	FA	Fly Ash	Admixture (Liters/ m^3)
Plain Concrete	400	670	436	705	Zero	3.9
HVFAC	227	709	478	564	223	5.9

CA – Coarse aggregate, FA – Fine aggregate

3. Results

The results, obtained from the study, for the development of compressive strengths and losses in compressive strengths in both the types of mixes are summarized in Table 2.

Table 2: Variations of Compressive Strengths and Losses in Different Mixes

Time (Days)	**Concrete Mix Type**	**For Curing in Water**	**For Curing in 0.1 N Sulphuric Acid**		**For Curing in 0.2 N Sulphuric Acid**	
		Compressive Strength (N/mm^2)	Compressive Strength (N/mm^2)	Loss (%)	Compressive Strength (N/mm^2)	Loss (%)
7	PLAIN	28.60	28.50	0.35	26.90	5.94
	HVFAC	26.80	25.90	3.36	24.80	7.50
28	PLAIN	51.27	47.90	6.60	43.80	14.50
	HVFAC	49.28	46.60	5.40	44.20	10.31
90	PLAIN	63.30	55.70	12.00	50.40	20.40
	HVFAC	55.58	50.00	10.00	46.40	16.52
180	PLAIN	66.92	54.70	18.26	50.70	24.24
	HVFAC	63.42	54.40	14.22	51.00	19.58

4. Discussion of Results

Figure1 shows the development of compressive strength in plain concrete and HVFAC with time in the entire duration of 180 days. Since the mixes were designed for approximately the same strength levels, both the mixes attain strength in the same manner in the initial stage of hardening. But with time the rate of development of strength in HVFAC increases at a faster pace due to the pozzolanic reactions of fly ash.

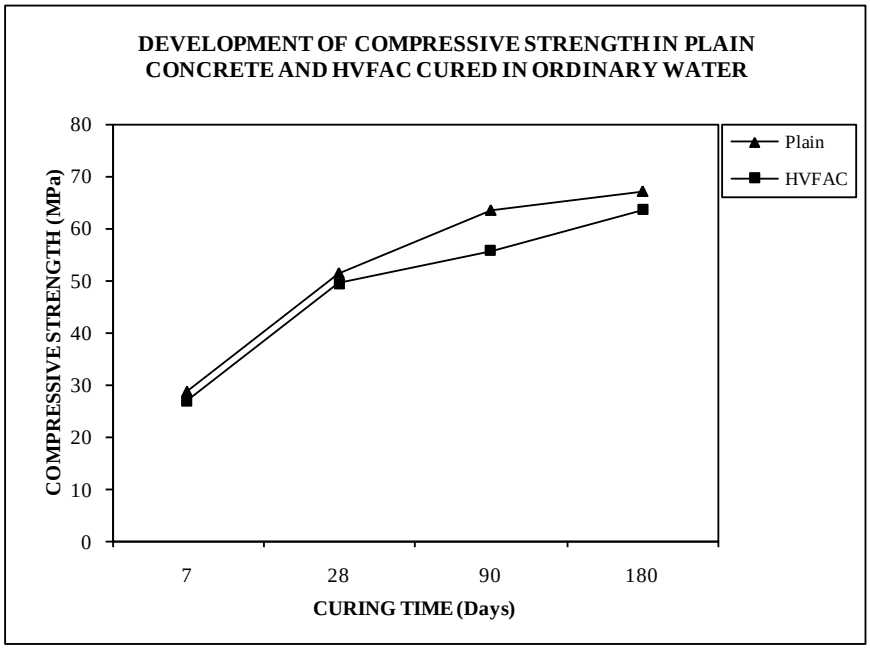

Figure 1: Development of compressive strength in plain concrete and HVFAC with time

Figure 2 shows the variations in loss of compressive strength in both of such mixes due to chemical aggressive environment of the order of 0.1 N and 0.2 N sulphuric acid.

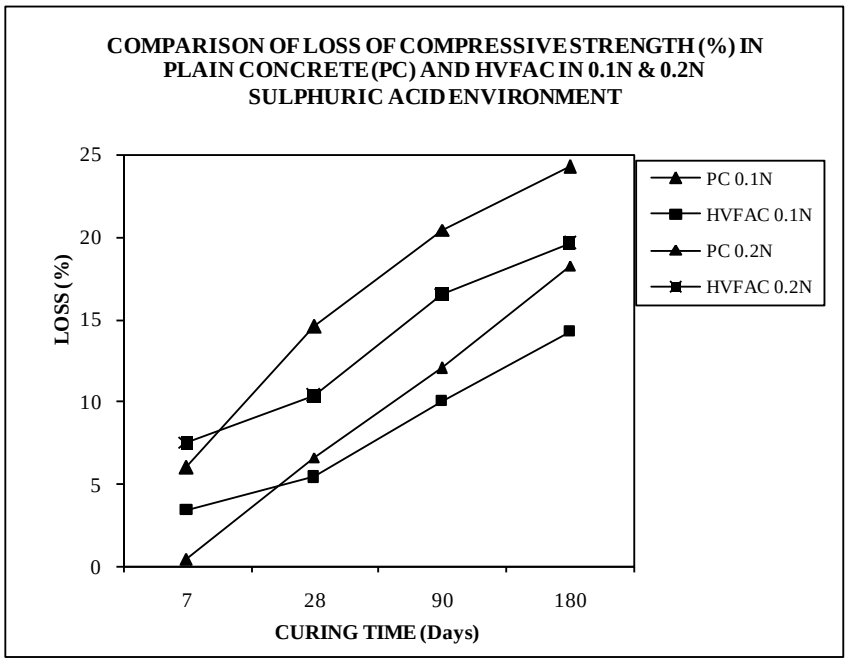

Figure 2: Variations in loss of compressive strength

In both the mixes the patterns of losses taking place show a similar trend. The losses in compressive strength increase with the time of exposure. But the percentage of losses in compressive strength in HVFAC in both the environments has been observed to be less than those in plain concrete except in the initial period of 7 day. The residual strength of HVFAC is found to be more than that of plain concrete at any stage of exposure. In the advanced stages of exposure time, the rate of increase in losses in the case of HVFAC is found to be less than that in the case of plain concrete. It gives indication of likely improved behaviour of HVFAC under aggressive environment conditions for a long time of exposure.

5. Conclusion

On the basis of the experimental results regarding the plain concrete and HVFAC subjected to aggressive acidic environment, it has been concluded that the utilization of fly ash reduces the loss in compressive strength in concrete. Therefore, fly ash has been proved as an effective material which can be used for making concrete in aggressive environmental conditions.

REFERENCES

[1] Shukla, M., Sahu, A.K. and Sachan, A.K., "Performance of Stone dust as fine aggregate replacing sand in concrete and mortar", National Seminar on Advances in Special concretes, Indian Concrete Institute, Bangalore, 1998, pp. 241-248.

[2] Regourd, M., "Resistance of Concrete to Chemical Attacks Sea Water Attack on Concrete and Precautionary Measures", Material & Structures, Vol. 18, 1985, pp. 223-226

[3] "Concrete in Sulphate-Bearing Soils and Ground Waters", Building Research Establishment Digest 250, H.M. Stationary office, London, 1986.

[4] Mehta, P.K., "Mechanism of Sulphate Attack on Portland cement concrete – another look", Cement and Concrete Research, Vol. 13, No. 3, May 1983, pp. 401-406.

[5] Wond, G. and Poole, T., "Effect of Pozzolans and Stags on the Sulfate Resistance of Hardraulic cement Mortars", Concrete Durability - Katharine and Bryant Mather International Conference, A.C.I. SP-100, 1987

[6] Lawrence, C.D., "Sulphate Attack on Concrete", Magazine of Concrete Research, Vol. No. 153, 1990, pp.249-264.

[7] Tikalsky, P.J. and Carras-quillo, R. L, "Influence of Fly Ash on the Sulfate Resistance of Concrete", A.C.I. Materials Journal, Vol. 89, No.1, 1992, pp. 69-75.

[8] Torii, M. and Kawamura, M., "Effects of Fly Ash on Silica Fume on the Resistance of Mortar to Sulfuric Acid and Sulfate Attack", Cement and Concrete Research, Vol. 24, No. 2, 1994, pp. 361-370.

[9] Wang, J.G., "Sulfate Attack on Hardened Cement Paste", Cement and Concrete Research, Vol. 24, No. 4, 1994, pp. 735–742.

[10] Al–Amoudi, O.S.B. et al, "Effects of Magnesium Sulfate and Sodium Sulfate on the Durability Performance of Plain and Blended Cements", A.C.I. Materials Journal, Vol. 92, No.1, 1995, pp. 15-24.

[11] Naik, T.R. et al, "Enhancement in Mechanical Properties of Concrete due to Blended Ash", Cement and Concrete Research, Vol. 26, No. 1, 1996, pp. 49-54.

[12] Mossazza, F., "Chemistry of Pozzolanic Addition and Mixed Cement", Principal paper, 6th International Congress on the Chemistry of Cement, Moscow, 1974, pp. 3–38.

[13] Cohen, M.D. and Bentur, A., "Durability of Portland Cement Silicon Fume Paste in Magnesium Sulfate and Sodium Sulfate Solutions", A.C.I. Materials Journal, Vol. 85, No. 3, 1988, pp. 148–157.
[14] Rasheeduzzafar et al, "Influence of Cement Composition on the Corrosion of Reinforcement and Sulfate Resistance of Concrete", A.C.I. Materials Journal, Vol. 87, No. 2, 1990, pp. 114-122.
[15] "Code of Practice for Plain and Reinforced Concrete", IS:456-2000, Bureau of Indian Standards, New Delhi.
[16] Miyagawa, T., "Durability Design and Repair of Concrete Structures: Chloride Corrosion of Reinforcing Steel and Alkali-Aggregate Reaction", Magazine of Concrete Research, Vol. 43, No. 156, 1991, pp. 155-170.
[17] Kumar, S. and Rao, C.V.S.K., "Sulfate Attack on Concrete in Simulated Cast–In Situ and Precast Situations", Cement and Concrete Research, Vol. 25, No. 01, 1995, pp. 1-8.
[18] Kumar, S., "Influence of Water Quality on the Strength of Plain and Blended Cement Concrete in Marine Environments", Cement and Concrete Research, Vol.30 (2000), pp. 345-350
[19] Al-Amoundi, O.S.B., "Mechanisms of Sulfate Attack in Plain and Blended Cements: A Review", "Extending Performance of Concrete Structures", Edited by Dhir, R.K. and Tittle, P.A.J., 1999, pp. 201-210.
[20] Kumar, S. and Rao, C.V.S.K., "Effect of Sulfates on the Setting Time of Cement and Strength of concrete", Cement and Concrete Research, Vol. 24, No. 7, 1994, pp. 1237–1244.
[21] Kumar, S. and Rao, C.V.S.K., "Durability of Materials under Random Exposure Conditions", Proceedings of International Seminar on "Civil Engineering Practices in the Twenty First Century", Roorkee, 1996, pp. 751–756.
[22] S. Kumar and C.V.S.K. Rao, "Strength Loss in Concrete due to varying Sulfate Exposure", Cement and concrete Research Vol. 25, No. 1, 1995, pp. 57-62
[23] Garvin, S.L., Ridal, J.P. and Halliwell, M., "Performance of Concrete in Contaminated Land", "Extending Performance of Concrete Structures", Edited by Dhir, R.K. and Tittle, P.A.J., 1999, pp. 201-210.
[24] Aziz, M.A. and Koe, L.C.C., "Durability of Concrete Sewers in Aggressive Subsoils and Ground Water Conditions", Geotechnical Aspects of Restoration Works, Edited by Balasubraman et al, Roterdam, 1990, pp 299-310.
[25] Berke, N.S., Pfeifer, D.W. and Weil, T.G., "Protection Against Chloride Induced Corrosion", Concrete International, Vol. 10, No. 12, 1988, pp.44-55
[26] Camps, J.P., Jauberthie, R. and Rendell, F., "The Influence of Surface Absorption on Sulphate Attack", "Concrete Durability and Repair Technology", Edited by Dhir, R.K. and McCarthy, M.J., pp 197-207.
[27] Nagele, E., "New and Powerful Method for the Evaluation of Multi Parameter Corrosion Tests", Cement and Concrete Research, Vol. 25, No. 6, 1995, pp.1209-1217.
[28] Mehta, P.K., "Effect of Fly Ash Composition on Sulfate Resistance of Cement", A .C.I. Materials Journal, Vol. 83, No. 6, 1986, pp. 994-1000.
[29] ASTM C 204-92, Test for fineness of Portland cement by Air Permeability Apparatus.
[30] IS:383-1970, "Specification for coarse and fine aggregates from natural sources for concrete", Bureau of Indian Standards, New Delhi.
[31] IS:3812-2003 (Part1), "Specification for Fly Ash for use as pozzolana and admixture", Bureau of Indian Standards, New Delhi.

NATURAL PIGMENTS-A MEDICINAL PERSPECTIVE

Anuja Agrawal*

Research scholar, Chemistry department, Delhi Technological University (Government of NCT of Delhi), Bawana Road, Delhi-110042, India

---

ABSTRACT: Pigments are present in all living matter and provide attractive colors and play basic roles in the development of organisms.. This review presents the basic information about pigments focusing attention on the natural ones; it emphasizes the principal plant pigments:flavonoids, carotenoids and betalains. Special considerations are given to their pharmacological activity .Several works are mentioned which have demonstrated the potent antioxidant activity of flavonoids and other pigments , which has been associated with protection against degenerative diseases.Our main focus is the pharmacological properties of some natural pigments,their sources and main hurdles in using them as medicines.

KEY WORDS: color, carotenoids, flavonoids, betalains, food, antioxidant.

INTRODUCTION

Pigments produce the colors that we observe at each step of our lives, because pigments are present in each one of the organisms in the world, and plants are the principal producers. They are in leaves, fruits, vegetables, and flowers. Also, they are present in skin, eyes, and other animal structures; and in bacteria and fungi. Natural and synthetic pigments are used in medicines, foods, clothes, furniture, cosmetics, and in other products. The melanins act as a protective screen in humans and other vertebrates, and in some fungi melanins are essential for their vital cycle. A lot of pigments have a well-known pharmacological activity in sickness such as cancer and

cardiovascular diseases, and this has stressed pigment importance for human beings. Some natural pigments has remarkable antioxidant activity, which is important in the development of their functions such as scavenging of radicals and disease treatment and prevention.

CLASSIFICATION

Pigments can be classified by their origin as natural, synthetic, or inorganic. Also, pigments can be classified by taking into account the chromophore chemical structure as: (a) Chromophores with conjugated systems: carotenoids, anthocyanins, betalains, caramel, synthetic pigments, and lakes.

(b) Metal-coordinated porphyrins: myoglobin, chlorophyll, and their derivatives.

PHARMACOLOGICAL EFFECTS OF NATURAL PIGMENTS

1.FLAVONOIDS: Flavonoids are phenolic compounds with two aromatic rings bonded by a C3 unit (central pyran ring) and divided in 13 classes based on the oxidation state of the pyran ring and on the characteristic color: anthocyanins, aurons, chalcones, yellow flavonols,flavones, uncolored flavonols, flavanones, dihydroflavonols, dihydrochalcones, leucoanthocyanidins, catechins, flavans, and isoflavonoids. Figure1 shows some flavonoid structures.

Several reports have shown the antioxidant activity of flavonoids. Rutin inhibited malonaldehyde formation from ethyl arachidonate by 70% at the level of 0.125 μmol. With ethyl linoleate, naringin, galangin, and rutin exhibited dose-related activities and showed inhibitions of 30% at 0.5μmol.

It has been pointed out that the major mode of flavonoids as antioxidants is in their ability to scavenge free radicals, and that hydroxylation of the B-ring is an important contributor to such activity.

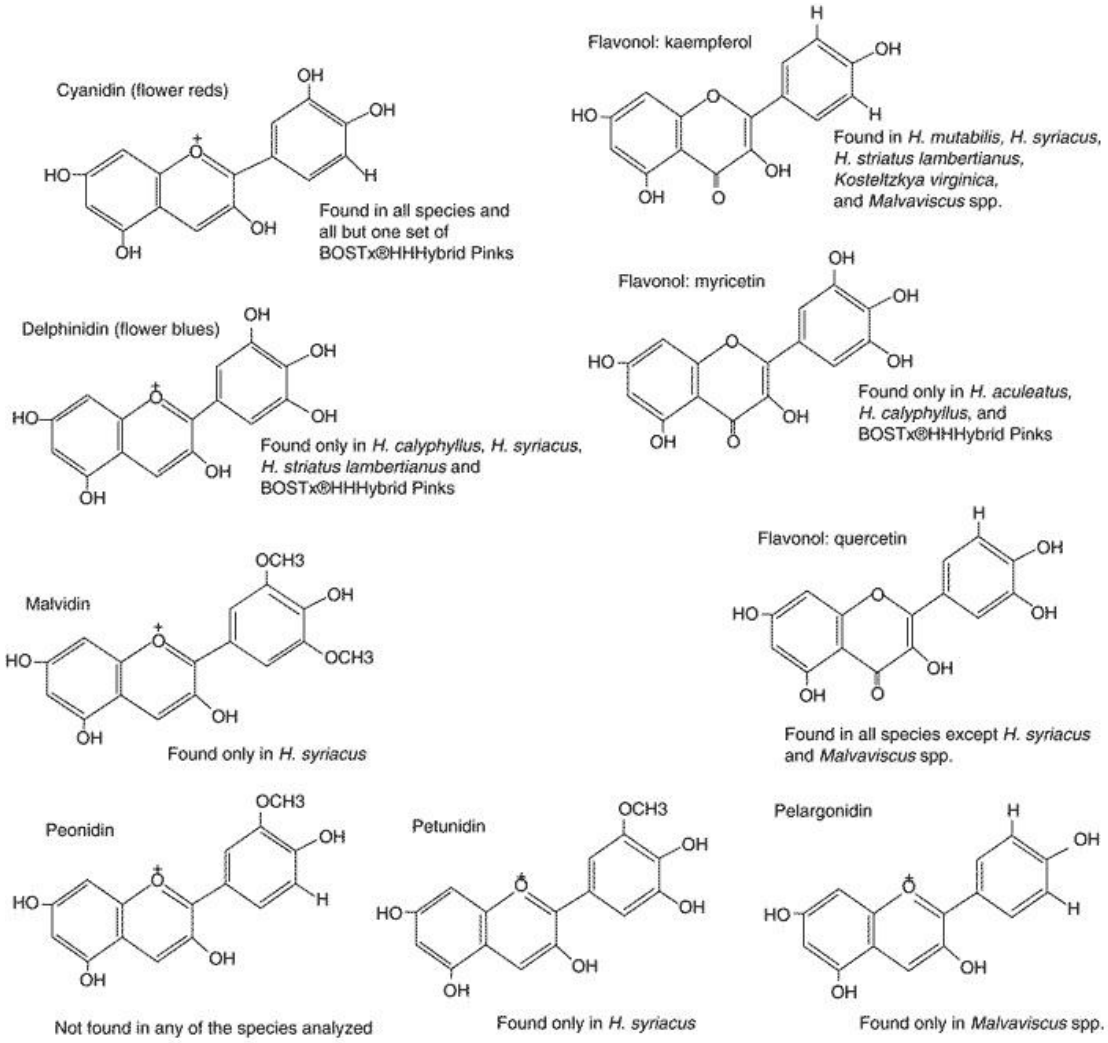

Fig.1 Structure of some flavonoids

In particular, hydroxyl groups at the 3′- and 4′- positions of the B-ring exhibited the highest antioxidant activity, but it was lower than the observed with BHT[24]. It was shown that luteolin has good antioxidant activity , and it was suggested that C2-C3 double bond and C4 keto group seem to be essential for high antioxidant activity (quercetin > (+)- catechin). Also, it was shown that aglycone flavonoids are more potent antioxidants. However, luteolin did not show quality antioxidant activity, and quercetin and other flavonoids were better.

TABLE 1: Pharmacological Activities of Some Flavonoids[1,11]

Flavonoid	**Activity**
(+)-Catechin, 3-O-Metil-(+)-Catechin , naringenin	Against ulcers
Naringenin	Antimicrobial and antifungic on skin
Proanthocyanidins	Astringent for digestive system, diuretic, cardiac tonic, in the treatment of high blood pressure
Rutin, silibin	Against disorders of the respiratory system
Butrin, isobutrin	Hepatic disorders and viral hepatitis
Chisin, floretin, apigenin, quercetin , kaempferol, baicaelin	Antiinflammatory
Epicatechin	Against diabetes
Genistein, kaempferol, sophoricoside	Antifertility
Galangin	Activity against Staphylococcus epidermis
Quercetin, morin, procyanidin, pelargonidin	Antiviral

The antioxidant activity of wines has also been evaluated, and it has been reported that almost 96% of the activity can be explained by the content of catechin, *m*-coumaric acid, epicatechin, *cis*-polydatin, and vanillic acid, showing higher correlations with several flavonoids (catechin, myricetin, quercetin, rutin, epicatechin, cyanidin, and

malvidin 3-glucoside). Wine flavonoids also show a good peroxynitrite scavenging activity.

It has been clearly established that flavonoids in natural products (e.g., grape, soybean, peanut, wine, tea) have a good antioxidant activity. In some instances a better activity than in the commercial antioxidants has been determined. Additionally, flavonoids contribute to the protection and/or regeneration of antioxidants. It has been suggested that the flavonoid action is by trapping free radicals. Flavonoids are antimutagenic that can reduce the atherogenesis and the risk for strokes, and that are modulators of arachidonic acid metabolism. This last point involves flavonoids in many metabolic processes[11].

Interestingly, flavonoids are ubiquitous of plants and a person can consume up to 1 g of them. This quantity implies that flavonoids can reach pharmacological concentrations in the organism. Thus, it is interesting to point out that many flavonoids have assigned pharmacological activities (Table 1), and that many medicinal plants are known and used by their flavonoid content. Moreover, it has been determined that flavonoid structure has the responsibility of a large part of the activity. Also, it has been shown that different substitutes give a molecule with an specific polarity that permits the presence of privileged bonds in the active sites[1]. This characteristic could have a relation with the antioxidant activity From an acetone extract of the root bark of *Ormosia monosperma* several flavonoids were isolated, and it was observed that 2,3-dihydroauriculatin showed a moderate activity against oral microbial organisms such as *Streptococcus mutants, Porphyromonas gingivalis,* and *Actinobacillus actinomycetemcomitans*, each at 6.3 µg /ml. From *Ononis spinosa* subsp. *Leeiosperma*,

two flavonoids with biological activity were isolated. Spinonin showed a moderate activity against *P. aeruginosa* and higher activity was obtained with ononin against β-hemolytic *Streptococcus* (minimal inhibitory concentration or MIC = 25 µg/ mL). It was shown that some flavonoids (isorhamnetin, rhamnetin, and quercetin) diminished the total serum cholesterol levels when rats were fed with these compounds. In view of the relatively low toxicity ofquercetin and related antitumor activity, its use as an anti-cancer drug seems feasible[2].

Flavonoids have been involved in the inhibition of several individual steps related to the thrombosis process, and one of the most active compounds was the biflavonoid hinokiflavone. Other biflavonoids (e.g., amentoflavone, agathisflavone, robusta-flavone) showed activity against the human immunodeficiency virus (HIV) reverse transcriptase (HIV- 1 RT). It was concluded that the presence of an unsaturated double bond at C-2, C- 3 and three hydroxyl groups at C-5, C-6, and C-7 positions were prerequisites for inhibition of RT[18].

The estrogenic activity of isoflavonoids has been reported, and 7-isopropoxyisoflavone is now sold on the market (‘Osten’ from Takeda Chemical Industries, Ltd.) as a therapeutic drug for osteoporosis. One of the main flavonoids in teas is scutellarein, which has been used as a diuretic, antiinflammatory, and antiasthmatic drug[14]. . Additionally, it has been suggested that a glucose moiety in the flavonoid structure plays an important role for its activity[14]. Flavonoids have also been proposed in the treatment of obesity.

2.CAROTINOIDS

carotenoids are compounds comprised of eight isoprenoid units (ip) whose order is inverted at the molecule center(FIG.2). Carotenoids are classified by their chemical structure as: (1) carotenes that are constituted by carbon and hydrogen; (2) oxycarotenoids or xanthophylls that have carbon, hydrogen, and, additionally, oxygen

Many diseases, such as cancer and strokes, involve oxidative processes mediated by free radicals. Carotenoids, by their antioxidant effect, can show benefits in such diseases. Carotenoids are an integral part of membranes. Carotenes are immersed in membranes, but xanthophylls showed a variable membranal position, polar groups in xanthophylls affect their position and mobility. Consequently, carotenes are able to react efficiently only with radicals generated inside the membrane.

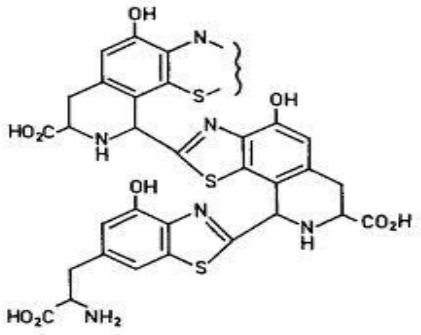

Fig.2 Structure of a carotenoid

While zeaxanthin, with their polar groups aqueous exposed, is able to react with radicals produced in that zone. Additionally, it has been suggested that carotenoids influence the strength and fluidity of membranes, thus affecting its permeability to oxygen and other molecules.

Also, it has been determined that carotenoids have a remarkable effect in the immune

response and in intercellular communication[3,8,13]. There exists evidence of the effectiveness of β-carotene in the treatment of certain kinds of cancer, for example, smoking related cervical intraepithelial neoplasia and cervical and stomach cancer[8]. More than 600 carotenoids are known, and 50 of them are consumed in meals to be transformed into the essential nutrient vitamin A. After their absorption, these carotenoids are metabolized by an oxidative rupture to retinal, retinoic acid, and small quantities of breakdown products. Carotenoids are transported by plasma lipoproteins. Vitamin A is required in the vision process, epithelial maintenance, mucose secretion, and reproduction[20,21]. It has been established that retinoids affect many biological process, such as cellular proliferation, differentiation, and morphogenesis. Additionally, retinoids have been used in treatments of certain kinds of cancers and some dermatological activities.Moreover, it is mentioned that a diet with deficiencies in vitamin A or supplemented with an excess of retinoic acid could induce teratogenesis. It was suggested that different combinations of retinoids produced different pharmacological responses in the specificity and potency in cancer therapy[9]. Retinoic acid induces the response of proteins associated with damage by ultraviolet light in F9 and NIH3T3 cells. However, this induction does not show a correlation with the repairer of DNA damage]. Currently, the effect of retinoic acid in arthritis treatment is controversial It was proposed that negative effects of alcohol consumption during fetus development could be caused by the inhibition in retinoic acid synthesis, catalyzed by alcohol dehydrogenase, which conduces to a failure in function of retinoic acid receptor (necessary for normal development).

Retinoic acid (RA) has also been related to the aging process.Prostaglandins are substances that have been involved in several physiological process, and in particular prostaglandin D2 has been involved in the endogenous sleep promotion, modulation of several central actions (regulation of body temperature, release of the luteinizing hormone), etc.

carpenter et al. observed that mixtures of canthaxanthin with low-density lipoproteins (LDL) inhibited macrophage formation from human monocytes. It was explained that all evaluated carotenoids show good antioxidant activity, and observed differences are caused due to their activity at different levels.It was concluded that antioxidant activity depends on the particular system: radical, carotenoid, microenvironment, etc. Thus,

diets with carotenoid mixtures are recommended instead of having just one particular carotenoid. Carotenoids have been considered that provide benefits in age-related diseases, against some forms of cancer (in especial lung cancer), strokes, macular degeneration, and cataracts. On the other hand, it is clear that carotenoids in association with other components of fruits and vegetables seem to have a protective effect against some chronic diseases and precancerous conditions. Additionally, in some studies β-carotene was supplied to smokers, and it was found that cancer mortality indexes were higher in smokers than those supplied with β-carotene[21]. It has been signaled that a combined supply of β-carotene, α-tocopherol, and selenium reduces stomach cancer mortality.

Carotenoids protect lab animals of UV-induced inflammation and certain type of cancers. Historically, carotenoid supplementation has been used in the treatment of diseases produced by light sensitivity, which are usually hereditary. Lutein and

zeaxanthin have been considered as protective agents against aging macular degeneration and senile cataracts[21]. Also, it has been suggested that β-carotene suppress the increment of hormones related to stress syndrome.

Nowadays it is thus premature to give final conclusions regarding the potential role of carotenoids in the therapeutics of degenerative diseases. However, the consumption of fruits, vegetables, and fortified foods with antioxidants is encouraged[8].

3.BETALAINS

Chemically, betalain definition embraces all compounds with structures based on the general formula shown in (Figure 3); therefore, they are immonium derivatives of betalamic acid. Betalains are water-soluble nitrogen-containing pigments, which are synthesised from the amino acid tyrosine into two structural groups: the red-violet betacyanins and the yellow-orange betaxanthins. Betalamic acid, is the chromophore common to all betalain pigments. The nature of the betalamic acid addition residue determines the pigment classification as betacyanin or betaxanthin .

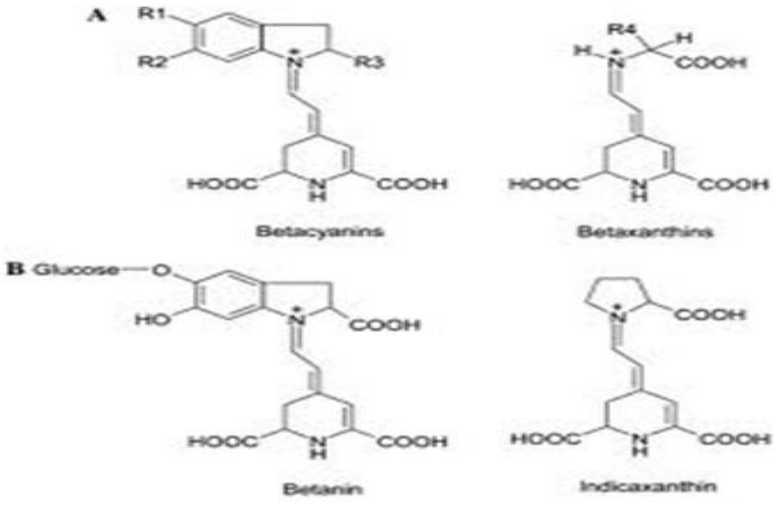

fig.3 structure of some betalains

Betanidin is the basic structural unit of most of the betacyanins, followed by its C15 epimer, the isobetanidin. In a strict sense, betalains do not belong to alkaloids because they are acidic in nature due to the presence of several carboxyl groups. Although structurally related to alkaloids, betalains have no toxic effects in the human body, as can be shown by the fact than they are present in considerably high amounts in certain foodstuffs, such as red-beet, prickly pear fruits and *Amaranthus* seeds. Therefore, betalains represent a safe natural alternative to some synthetic color additives that are currently in use. Interestingly, there is no upper limit to the recommended daily intake.

Several works have demonstrated the potent antiradical scavenging activity of betalains in vitro [10,15,4,25,5]. Kapadia et al. (1996) showed a significant inhibitory effect of beetroot towards skin and lung cancer in mice. Years later, Kapadia et al. (2003) demonstrated the efficacy of betanin for long-term local suppression of skin and liver tumours induced by different chemical carcinogens in mice. Kanner et al. (2001) reported the ability of both betanin and betanidin at very small concentrations to inhibit lipid peroxidation and heme decomposition. Tesoriere et al. (2005) showed that human red blood cells incorporate dietary betalains, which may protect the cells and avoid oxidative hemolysis. Tesoriere et al. (2004b) suggested that cactus pear fruit decreases oxidative damage to lipids, and improves antioxidant status in healthy humans. The structure–activity relationships of betalains with respect to free radical scavenging capacities were studied by Cai et al. (2003, 2005).

In a recent work, the importance of some natural pigments as nutraceutical ingredients was reviewed[19]. It was suggested that betalains like anthocyanins, β-carotene, and various vegetable and fruit extracts must be used for their potential health benefits. For

example, yellow betaxanthins, in addition to their potential role as natural food colorant, may be used as a means of introducing essential dietary amino acids into foodstuffs, giving rise to an “essential dietary colorant”.

CONCLUSION

The antioxidant properties of natural pigments make them a better option for curing and prevention of diseases. There is increasing evidence that oxidative stress leads to biochemical changes, which contribute to the development of several degenerative diseases, such as cancer and cardiac diseases. Antioxidant molecules, some of which are derived from the diet, protect against the potentially injurious effects of oxidative stress. They can be used on a wide scale as an alternative for synthetic drugs. Nowadays, people have shown a clear preference for natural products, including pigments, because more nutritious and healthy characteristics have been associated with them. Moreover, one of the main problems to be solved, that all the natural pigments are not approved by FDA and European Union for consumption. Thus, many research groups are looking for new sources of natural pigments.However, these efforts have vanished, because under the current legislation the FDA or the European Union approval of new natural sources of pigments is very difficult. The reason is, that they can have some side effects.The pigment research area is very wide. So a lot of research is required to establish all the properties of these pigments and find out natural pigments with improved characteristics.

REFERENCES

[1] Anton, R., Flavonoids and traditional medicine. In: Cody, V., Middleton Jr., E., Harborne, J.B., and Beretz, A.,(1988) Eds. *Progress in Chemical and Biological Research Vol. 280.* Alan R. Liss Inc., New York, 423–449

[2] Boege, F., Straub, T., Kehr, A., Boesenberg, C., Christiansen, K., Anderson, A., Jakob, F., and Köhrle, J.,(1996) Selected novel flavones inhibit the DNA binding or the DNA religation step of eukaryotic topoisomerase I, *J. Biol. Chem.,* 271(4): 2262–2270

[3] Britton, G.,(1995) Structure and properties of carotenoids in relation to function, *FASEB J.,* 9: 1551–1558.

[4] Butera, D., Tesoriere, L., Di Gaudio, F. et al. (2002). Antioxidant activities of Sicilian prickly pear (Opuntia ficus indica) fruit extracts and reducing properties of its betalains: betanin and indicaxanthin. Journal of Agricultural and Food Chemistry, 50, 6895–6901.

[5] Cai, Y., Sun, M. & Corke, H. (2003). Antioxidant activity of betalains from plants of the Amaranthaceae. Journal of Agricultural and Food Chemistry, 51, 2288–2294.

[6] Cai, Y.Z., Sun, M. & Corke, H. (2005). Characterization and application of betalain pigments from plants of the Amaranthaceae. Trends in Food Science & Technology, 16, 370–376

[7] Carpenter, K. L. H., vander Veen, C., Hird, R., Dennis, I. F., Ding, T., and Mitchinson, M .J., (1997) The carotenoid β-carotene, canthaxanthin and zeaxanthin inhibit macrophage-mediated LDL-oxidation, *FEBS Lett.,* 401: 262–266.

[8] Charleux, J. L.,(1996) Beta-carotene, vitamin C, and vitamin E: the protective micronutrients, *Nutr. Rev.,* 54(11): S109–S114.

[9] Eichele, G.,(1997) Retinoids: from hindbrain patterning to Parkinson disease, *Trends Genet.,* 13(9): 343– 345.

[10] Escribano, J., Pedren˜ o, M.A., Garcı´a-Carmona, F. & Mun˜ oz, R. (1998). Characterization of the antiradical activity of betalains from Beta vulgaris L. roots. Phytochemical Analysis, 9, 124–127.

[11] Haslam, E.,(1996) Natural polyphenols vegetable tannins) as drugs: possible modes of action, *J. Nat. Prod.,* 59(2): 205–215.

[12] Henriette M.C.Azeredo(2009) Betalains: properties, sources, applications, and stability – a review, International Journal of Food Science and Technology, 44, 2365–2376

[13] Hong, W. K. and Sporn, M. B.,(1997) Recent advances in chemoprevention of cancer. *Science,* 278: 1073– 1077.

[14] Hooijberg, J. H., Broxterman, H. J., Heijn, M., Fles, D.L. A., Lankelma, J., and Pinedo, H. M.,(1997) Modulation by (iso)flavonoids of the ATPase activity of the multi drug resistance protein, *FEBS Lett.,* 413: 344–348.

[15] Kanner, J., Harel, S. & Granit, R. (2001). Betalains - a new class of dietary cationized antioxidants. Journal of Agricultural and Food Chemistry, 49, 5178–5185.

[16] Kapadia, G.J., Tokuda, H., Konoshima, T. & Nishino, H. (1996). Chemoprevention of lung and skin cancer by Beta vulgaris (beet) root extract. Cancer Letters, 100, 211–214.

[17] Kapadia, G.J., Azuine, M.A., Sridhar, R. et al. (2003). Chemoprevention of DMBA-induced UV-B promoted, NOR-1-induced TPA promoted skin carcinogenesis, and DEN-

induced Phenobarbital promoted liver tumors in mice by extract of beetroot. Pharmacological Research, 47, 141–148.

[18] Lin, Y. M., Anderson, H., Flavin, M. T., Pai, Y. H. S., Mata-Greenwood, E., Pengsuparp, T., Pezzuto, J. M., Schinazi, R. F., Hughes, S. H., and Chen, F. C.,(1997) In vitro anti-HIV activity of biflavonoids isolated from *Rhus succedanea* and *Garcinia multiflora*, *J. Nat. Prod.,* 60(9): 884–888.

[19] Pszczola, D. E.,(1998) Natural colors: pigments of imagination, *Food Technol.,* 52(6): 70–76.

[20] Radlwimmer, F. B. and Yokoyama, S.,(1997) Cloning and expression of the red visual pigment of goat *(Capra hircus*), *Gene*, 198: 211–215

[21] Taylor-Mayne, S., (1996) Beta-carotene, carotenoids, and disease prevention in humans, *FASEB J.,* 10: 609– 701.

[22] Tesoriere, L., Butera, D., Pintaudi, A.M., Allegra, M. & Livrea, M.A. (2004b). Supplementation with cactus pear (Opuntia ficus-indica) fruit decreases oxidative stress in healthy humans: a comparative study with vitamin C. American Journal of Clinical Nutrition, 80, 391–395.

[23] Tesoriere, L., Butera, L., Allegra, M., Fazzari, M. & Livrea, M.A. (2005). Distribution of betalain pigments in red blood cells after consumption of cactus pear fruits and increased resistance of the cells to ex vivo induced oxidative hemolysis in humans. Journal of Agricultural and Food Chemistry, 53, 1266–1270.

[24] van Gadow, A., Joubert, E., and Hansmann, C. F.,(1997) Comparison of the antioxidant activity of aspalathin with that of other plant phenols of rooibos tea

Aspalathus linearis), α-tocopherol, BHT, and BHA, *J. Agric. Food Chem.,* 45(3): 632–638.

[25] Wettasinghe, M., Bolling, B., Plhak, L., Xiao, H. & Parkin, K. (2002). Phase II enzyme-inducing and antioxidant activities of beetroot (Beta vulgaris L.) extracts from phenotypes of different pigmentation. Journal of Agricultural and Food Chemistry, 50, 6704– 6707.

On The Application Of Artificial Life Based Test Data Generation

Harsh Bhasin
Delhi technological University
i_harsh_bhasin@yahoo.com

Shewani
M.Tech Scholar
A.I.T.M, Palwal

Deepika Goyal
Assistant Professor
A.I.T.M, Palwal

***Abstract*— Manual test data generation is not feasible in case of large Software. Moreover, the approach does not work for Component Based Modules. Automated Test Data Generation is the process of automatically generating the test cases on the basis of particular criteria. Automated Test Data Generators are intensely important owing to the fact that a good Test Case Generator would lead to better testing. The proposed work uses Artificial Life as the base of Test Data Generator. The technique produces test cases that can be used for Black Box Testing. It is a continuation of our earlier attempt to use Langton's loop to accomplish the task. The technique has been explained and exemplified in the work and is currently being applied on a larger enterprise resource planning system. The work uses module state diagrams to craft the test cases. The technique opens the door of Artificial Life to Test Case generation.**

Keywords: Automatic Test Case Generators, Artificial Life, Langton's Loop, Black Box Testing.

I. INTRODUCTION

The growth of software engineering can justifiably be attributed to the advancement in Software Testing. The quality of the test cases to be used in Software Testing determines the quality of software testing. However, generating test cases is an intense, complex and time consuming task. In order to save both time and resources, automated test data generators are used. During the Literature review it was found that the field has been explored by many researchers. However, the techniques proposed to accomplish the task are inefficient and inapt as far as coverage, execution time, and fault detecting capabilities are concerned. It may be noted that since, the importance of automated test data generators is growing day by day. Therefore, there is a need to develop a test data generator which is good in terms of the above parameter.

Test Data Generators have been developed using many mathematical and nature inspired techniques. The present work explores our earlier attempt of applying a Artificial Life (AL) based technique in order to generate test cases. It may be noted that AL has never been used in the Test Data generation. The work exemplifies the use of technique. The initial results obtained are encouraging and paves way for the use of technique in professional softwares. Currently an Enterprise Resource Planning (ERP) system is being verified. A set of 20 programs has also been chosen for the future verification. Rest of the paper has been organized as follows. The work is a part of our endeavor to examine testing techniques and apply the system being developed on the techniques [14-19].

II. LITERATURE REVIEW

An extensive Literature Review has been carried out in order to understand the work that has been done so far and to find the gaps in the existing work. The papers have been selected by a group of lecturers and Assistant Professors, keeping in mind the importance and applicability of the papers.

During the review it was found that, the period before 2006 saw publishing of very less number of articles in this domain. It has been observed by Shahid[] that owing to the fact that it is a specialized area, therefore very less number of people showed interest in that. It is also possible that the period mentioned did not require Automated Test Data Generation. In order to generate Automated Test, it was also essential to understand the crafting of Test Cases which was being done in that period. It was observed by many researchers that only 5% of the articles in the journals were related to Automated Test Data Generation. It may also be noted that papers were published each year after 1997 till 2013 which proves that the topic is continuously being explored. It was also noted that, both White Box Testing and Black Box Testing technique were used in Automated Test Data Generation.

The three main approaches of Automated Test Data Generation have got almost equal consideration. These approaches are Random, Path oriented and Goal oriented approaches. Many researchers have also tried numerical approaches for Automated Test Data Generator. These included simplex, branch and bound etc.

The stress on heuristic search method, an evolutionary technique, for example Genetic Algorithm and Simulated Annealing was not that much but some of the researchers did tried to explore the possibility of using such methods in test data generation.

The focus on the feasibility of the path selected by the technique has also been examined in various papers. The review has been summarized in Table 1.

Sr. No.	Author	Technique Used	Ref. No.
1	C. V. Ramamoorthy, Siu-Bun F. Ho, W. T. Chen	Symbolic Execution	1
2	Webb Miller, David L. Spooner	Numerical Maximization Method	2
3	Lori A. Clarke	Symbolic Execution	3
4	Praveen Ranjan Srivastava, Tai-hoon Kim	Variable length Genetic Algorithms, Critical Path Coverage	4
5	James Miller, Marek Reformat, Howard Zhang	Program Dependence Analysis Techniques and Genetic Algorithms.	5
6	Harmen and Hinrich Sthamer	Genetic Algorithms	6
7	Roy P. Pargas, Mary Jean Harrold, Robert R. Peck	Genetic Algorithms, Statement Coverage, Branch Coverage.	7
8	Joachim Wegener, Andre Baresel, Harmen Sthamer	Evolutionary Testing.	8

9	Moheb R. Girgis	Genetic Algorithms, Def-Use Association Coverage.	9
10	Dunwei Gong, Wanqui Zang, Xiangjuan Yao	Genetic Algorihtms, Many Paths Coverage based on Grouping	10
11	Anastasis A. Sofokleous, Andreas S. Andreou	Dynamic Test Data Generation, Genetic Algorithms,	11
12	Jin-Cherng Lin, Pu-Lin Yeh	Genetic Algorithms	12

Table 1: Test data Generation Techniques

III. BACKGROUND

In the previous task, Artificial Life method was used to produce test cases [13]. The technique uses modules as the basic unit. The technique is novel as it serves two purposes i.e. generation and minimization of the test cases. In the review it was found that, some of the works depict time as a major factor compared to the coverage of test cases but in the work coverage was given more importance. In the technique the stress was on the function coverage as testing is done to instill confidence in the software, therefore maximization of function coverage factor will lead to lesser time in the maintenance phase.

The technique generates the test cases for all the modules of the program. The technique presented a new state machine called the Function Flow Graph (FFG). The FFG will cover all the modules and help in generating the test suit.

In the technique, for all the modules, the calling sequence is identified, and it starts from the entry point. The input and the output values are identified for each node. Test data is generated for each module and they are fed to the Langton's Loop.

IV. Verification of the technique

So as to exemplify the technique a tool developed in C# has been taken. The purpose of the tool is to generate Genetic population and perform crossover and mutation. The various modules in the tools are given in Table 2.

S.NO.	NAME	INPUT	OUTPUT	TASK
1	generateButton_Click	Number of chromosomes and number of cells in a chromosome.	A 2D array which consists of 0's and 1's.	Produces a 2D array.
2	getValuesButton_Click	Population, 2D array.	A 1D array which consists of values corresponding to those chromosomes.	Produces a 1D array.
3	applyButton_Click	The 1D and 2D array generated above and also the threshold value.	Those chromosomes which have threshold greater than requisite value.	Produces chromosomes.
4	Button10_Click	Final population and mutation rate.	A mutated population which is a 2D array.	Produces an array containing mutated population.

5	Button_Click	A 2D array which depicts the population and crossover rate.	A 2D array which consists of original and crossover population.	Produces an array and crossover population.
6	ShowButton_Click	A 2D array which consists of original and crossover population.	A 2D array shown in text box.	Produces a 2D array.

Table 2: Modules in Genetic Tool, which is to be tested using the technique

Figure 1 shows the module state diagram of the tool.

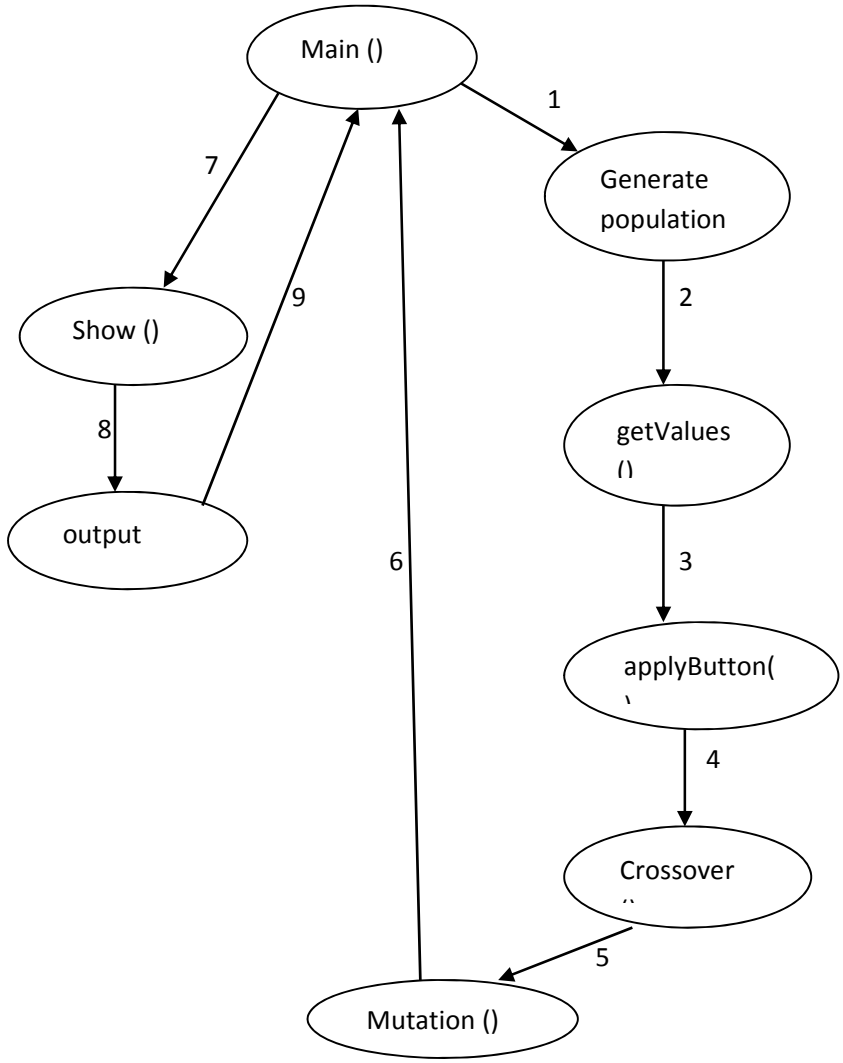

Figure 1: Module state diagram of the tool.

Langton's loops are a type of artificial life in a cellular automaton. They consist of a loop of cells having genetic information. The genes tutor it to make three left turns, finishing the loop, which then detaches from its parent. The intersection point of Lagtons loop generates 0 or 1, n number of times thus crafting the test cases. For example in the

above case let the population Size be 30 and the number of cells in chromosomes be 25, then 750 values are needed to craft the test population. Figure 2 depicts Langton's loop.

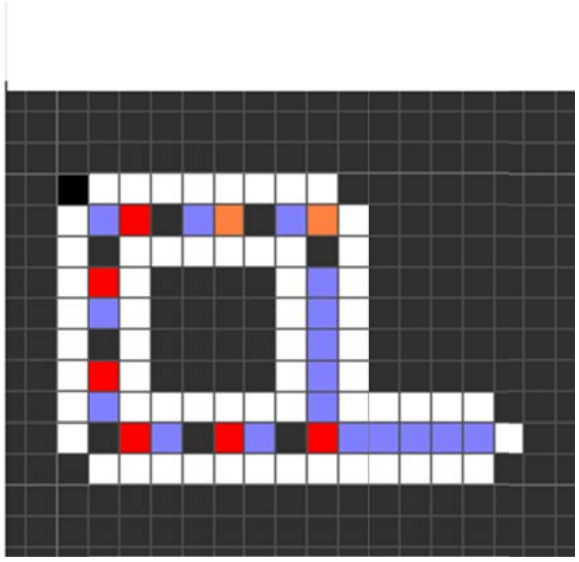

Figure 2: Langton's loop

V. CONCLUSION

The above work is a continuation of our effort to develop a framework of Automatic Test Case generation, which would be used both for Black Box and White Box Testing [13, 20]. The technique that can be used for Black Box Testing has been explained and exemplified in the work. The technique that would be used for White Box Testing has been designed and is been verified in parallel using cellular automata [20]. The above work successfully amalgamates the two disciplines. It also paves the way of application of Artificial Life to Software Testing.

VI. REFERENCES

1. C. V. Ramamoorthy, S. B. F. Ho, W. T. Chen, On the Automated Generation of Program Test Data, Trans. Softw. Eng., Vol. 2, pp. 293-300, 1976.
2. Webb Miller, David L. Spooner, Automatic Generation of Floating-Point Test Data, IEEE Trans. Software Eng 1976, Vol. 2,. pp.223-226, 1976
3. Lori A. Clarke, A System to Generate Test Data and Symbolically Execute Programs. IEEE Transactions on Software Engineering, Vol. 2, 1973.
4. Praveen Ranjan Srivastava, Tai-hoon Kim, Application of Genetic Algorithm in Software Testing, International Journal of Software Engineering and Its Applications, Vol. 3, No.4, October 2009
5. James Miller, Marek Reformat, Howard Zhang, Automatic test data generation using genetic algorithm and program dependence graphs, Information & Software Technology 01/2006; 48:586-605. pp.586-605.
6. Harmen and Hinrich Sthamer, The Automatic Generation of Software Test Data Using Genetic Algorithms, University of Glamorgan, 1995
7. Roy P. Pargas et. Al., Test Data Generation using Genetic Algorithms, Journal of Software Testing, Verification and Reliability. 1999.
8. Joachim Wegener et. Al., Evolutionary Test Environment for automatic Structural Testing, Information and Software Technology
9. Moheb R. Girgis, Automatic Test Data Generation for Data Flow Testing Using a Genetic Algorithm, Journal of Universal Computer Science, Vol. 11, No. 6, 2005.
10. Dunwei Gonga et. Al., Evolutionary generation of test data for many paths coverage based on grouping, The Journal of Systems and Software, Vol. 84, pp. 2222– 2233, 2011.
11. Anastasis A. Sofokleous, Andreas S. Andreou. Automatic, evolutionary test data generation for dynamic software testing. The Journal of Systems and Software, Vol. 81, pp. 1883–1898, 2008
12. J. C. Lin, P. L. Yeh, Automatic test data generation for path testing using GAs, Information Sciences, 131 (1-4), pp. 47-64, 2001.
13. Harsh Bhasin, Shewani and Deepika Goyal, Test Data Generation using Artificial Life, International Journal of Computer Applications, Vol. 67, No. 12, pp. 34-39, 2013.
14. Harsh Bhasin et. al., A Novel Approach to Cost Cognizant Regression Testing, International Journal of Computer Science and Management Research, Vol. 2, Issue 5, pp. 2595–2600, 2013.
15. Harsh Bhasin et.al, Software Architecture Based Regression Testing, International Journal on Computer Science and Engineering, Vol. 5, No. 04, pp. 226-229, 2013.

16. Harsh Bhasin et.al, Software Architecture Based Regression Testing Implementation, International Journal of Computer Science and Engineering, ISSN (Print):2278-9960, Vol. 2, issue 3, pp. 1-4, 2013.
17. Harsh Bhasin et. al., Regression testing using Fuzzy Logic, International journal of Computer Science and information technology, Vol. 4, issue 2, 2013.
18. Harsh Bhasin et. al., Implemenattion of Regression testing Using Fuzzy Logic, International Journal of Application or Innovation in Engineering and Management, Vol. 2, Issue 4, 2013.
19. Harsh Bhasin et. al., Orthogonal Testing Using genetic Algorithms, International Journal of Computer Science and Information Technology, Vol. 4, Issue 2, 2013,.
20. Harsh Bhasin and Neha singla, Cellular Automata Based Test Data Generation, ACM SIGSOFT Software Engineering Notes, Accepted.

Accepted Manuscript

Optical and electro-catalytic studies of nanostructured thulium oxide for vitamin C detection

Jay Singh, Manish Srivastava, Appan Roychoudhury, Dong Won Lee, Seung Hee Lee, B.D. Malhotra

PII: S0925-8388(13)01423-0
DOI: http://dx.doi.org/10.1016/j.jallcom.2013.06.026
Reference: JALCOM 28758

To appear in:

Received Date: 11 May 2013
Revised Date: 1 June 2013
Accepted Date: 4 June 2013

Please cite this article as: J. Singh, M. Srivastava, A. Roychoudhury, D.W. Lee, S.H. Lee, B.D. Malhotra, Optical and electro-catalytic studies of nanostructured thulium oxide for vitamin C detection, (2013), doi: http://dx.doi.org/10.1016/j.jallcom.2013.06.026

This is a PDF file of an unedited manuscript that has been accepted for publication. As a service to our customers we are providing this early version of the manuscript. The manuscript will undergo copyediting, typesetting, and review of the resulting proof before it is published in its final form. Please note that during the production process errors may be discovered which could affect the content, and all legal disclaimers that apply to the journal pertain.

ACCEPTED MANUSCRIPT

Optical and electro-catalytic studies of nanostructured thulium oxide for vitamin C detection

Jay Singh[1], Manish Srivastava[2], Appan Roychoudhury[3], Dong Won Lee[1], Seung Hee Lee*[1] and B. D. Malhotra*[3,4,5]

[1]*Department of BIN Fusion Technology and Department of Polymer-Nano Science and Technology, Chonbuk National University, Jeonju, Jeonbuk 561-756, Korea*

[2]*Department of Physics, Motilal Nehru National Institute of Technology, Allahabad, Allahabad 211004, India*

[3]*Department of Biotechnology, Delhi Technological University, Shahbad Daulatpur, Main Bawana Road, Delhi 110042, India*

[4]*Department of Science & Technology Centre on Biomolecular Electronics, Biomedical Instrumentation Section, Material Physics and Engineering Division, National Physical Laboratory, (CSIR), Dr. K. S. Krishnan Marg, New Delhi 110012, India*

[5]*Center for NanoBioengineering & Spintronics, Chungnam National University, 220 Gung-Dong, Yuseong-Gu, Daejeon 305-764, Korea*

ACCEPTED MANUSCRIPT

ACCEPTED MANUSCRIPT

Abstract

In this report, the nanostructured thulium oxide (Tm_2O_3) has been prepared using the hydrothermal process without using any template and without further heat treatment. The crystalline structure and morphology of prepared sample have been characterized by X-ray diffraction (XRD), field-emission scanning electron microscopy (FE-SEM), transmission electron microscopy (TEM), atomic force microscopy (AFM) and Fourier transform infrared (FTIR) spectroscopic techniques. The optical properties of prepared sample have been examined by ultra-violet (UV-Vis), photoluminescence (PL), Raman and X-ray photoelectron spectroscopy (XPS) studies. Furthermore, Tm_2O_3 nanoparticles have been electrophoretically deposited (EPD) onto indium-tin-oxide (ITO) glass substrate and utilize as electro-oxidation of ascorbic acid (AA). The electro-catalytic behaviour of Tm_2O_3/ITO and bare ITO electrodes for the AA electro-oxidation has been studied by cyclic voltammetry. Catalytic oxidation peak current shows a linear dependence on the AA concentration and a linear calibration curve is obtained in the concentration range of 0.2–8 mM of AA. The obtained results indicate that the nanostructured Tm_2O_3 based electrode offers an efficient strategy and a new promising platform for the application of rare earth metal oxide materials in electrochemistry and bioelectronics.

Key words: A. Rare earth; C. Electro-oxidation; C. Optical properties; D. X-ray diffraction

---

*Corresponding author. Email: *Corresponding author.

Prof. Seung Hee Lee (lsh1@jbnu.ac.kr) Tel.: +82-063-270-2343; Fax: +82-63-270-2341

Prof. B. D. Malhotra (bansi.malhotra@gmail.com) Tel.: +91-11-27294668; Fax: 91-11-27871023

ACCEPTED MANUSCRIPT

1. Introduction

Ascorbic acid (AA), commonly known as Vitamin C, acts as an antioxidant against a variety of diseases and is indispensable for life, health, and daily physical activities [1]. It has also been found to play an important role in the body as a free-radical scavenger, which may help to prevent free radical induced diseases such as cancer and Parkinsons disease. A recommended daily intake of AA is about 70–90 mg and the best way of getting the benefit of AA is to eat fresh fruits and vegetables or with a minimum process like cooking [2]. Due to its biological and technological importance, there is a continued interest to develop rapid and sensitive methods for routine determination of its concentration in the food industry. Many techniques such as electrophoresis [3], fluorescence [4], HPLC analysis with fluorimetric [5], liquid chromatography [6] and electrochemical methods [7,8] have been used for the quantitative determination of AA content in foods, drugs and plants. Due to their quick response, high sensitivity, low detection limit and simple use, electrochemical methods are considered to be one of the most potential approaches for AA determination by the electrocatalytic oxidation reaction on conventional electrodes. However, the oxidation of AA is difficult via direct oxidation using conventional electrodes because of its high over potential, low selectivity, poor sensitivity and poor reproducibility [9]. To solve these problems, numerous attempts to decrease the high working potentials and improve the reproducibility have been made by modifying the electrode surface with various nanostructured materials for the electrocatalytic oxidation of AA. Lin et al [10] reported L-cysteine self-assembled Au-Pt alloy modified electrode for AA determination by using cyclic voltammetry (CV), with a concentration range of 2 to 400 μM and detection limit of 1 μM. Hu et al [11] investigated the electrochemical behavior of AA at a mesopore-rich active carbon-modified pyrolytic graphite electrode and applied it for AA determination in urine and pharmaceutical dosage forms using differential pulse voltammetry (DPV) and obtained

ACCEPTED MANUSCRIPT

detection limit of about 0.3 µM. Hosseini et al [12] reported a titanium oxide nanotube films containing gold nanoparticles modified electrode for AA determination at 0.1 M phosphate buffer solution (PBS), with a concentration range of 1–5 mM. Recently, reported a bismuth sulfide nanorods modified glassy carbon electrode for determination of AA with linear range of 0.001–1 mM [13]. Therefore, it is challenging to develop new electrode materials with excellent electrocatalytic activity towards the oxidation of AA.

The electro-optical properties of rare-earth (RE) materials have recently aroused increased interest of researchers in various branches of materials science and bioscience because of their special properties and potential applications in the field of catalysis and solid oxide fuel cells [14-17]. RE metal oxides are known to display high surface basicity, fast oxygen ion mobility, efficient charge transfer ability and interesting catalytic properties [18]. The rare earth metal oxides with unique interesting surface morphologies represent an interesting class of materials because of their unique electronic, optical, magnetic and catalytic properties arising from the confinement of the 4*f* electrons [19]. These properties are useful for many applications such as optical display, optical communication, UV shielding, medical diagnostics and efficient catalysis for the oxidation of heavy oils, pollutants, jet fuels and automobile exhausts [20-25]. Among these, thulium oxide (Tm_2O_3) nanoparticles have currently been receiving much attention because of its potential in catalytic, electronic, optical and electrochemical application [26,27]. Thulium oxide films demonstrate efficient conductivity and are stable in usual acidic and alkaline solution. So, it has potential application as an electrode modification. For example, Ma et al [28], were investigated a catalytic effects of Tm_2O_3 and co-effects of Tm_2O_3 and porous SiO_2 on the de-hydrogenation and re-hydrogenation of $NaAlH_4$ for hydrogen storage because of because of its high dielectric constant of ~13, energy band gap of >5 eV. Li et al [29], was fabricated glucose oxidase immobilized on the nafion-Tm_2O_3 film achieves direct electron transfer with an

ACCEPTED MANUSCRIPT

apparent heterogeneous electron transfer rate constant (*ks*) of (3.27±0.43) s^{-1} and keeps its bioactivity and displays a potential application for the fabrication of glucose biosensors with a linear glucose response up to 7 $mmol \cdot L^{-1}$. Yan et al [30], was describe hemoglobin (Hb) immobilized on nafion-Tm_2O_3 nanoparticles which was synthesized by the hydrothermal homogeneous method indicate an excellent biocompatibility and provide a friendly microenvironment for the electron transfer between Hb and electrode surface. In addition, the investigated the catalytic properties of Tm_2O_3 in the dehydrogenation and dehydration of alcohols and the dehydrogenation of tetralin were investigated [31]. A variety of synthesis processes have been proposed for the deposition of thin films of nanomaterials and nanocomposites at the desired conductive electrode surfaces for the fabrication of electrochemical transducers. Among these, electrophoretic deposition (EPD) of the conducting nanostructured film at the surface of an electrode is a modern approach that can be used to electrochemically modify desired electrodes for determination of AA [32-34]. This technique is known to yield uniform, dense and porous films with the advantages of reduced processing time and simple experimental design. It can be accomplished via motion of the charged particles, dispersed in a suitable solvent, towards an electrode under the influence of an applied electric field [35]. In addition, as a wet process, EPD provides easy control of thickness and morphology of the deposited film by tailoring various parameters such as deposition time and applied potential etc [36-38].

In the present study, electro-optical properties of Tm_2O_3-modified indium-tin-oxide (ITO) glass electrode have been investigated, and AA has been chosen as a model compound to elucidate the electrocatalytic ability of the modified electrode. Based on the electrocatalytic ability of the modified electrode towards AA, amperometric method has been used for the determination of AA.

ACCEPTED MANUSCRIPT

2. Materials and Method

2.1. Reagents

Ascorbic acid (Purity 98.5%), thulium (III) nitrate pentahydrate were procured from Sigma-Aldrich, USA and sodium hydroxide (NaOH) pellets, purchased from MERCK (New Delhi, India). The AA solution (0.2–8 mM) prepared afresh in deionised (DI) water was stored at room temperature (25 °C). All the reagents were of analytical grade and used without any further purification. All electrochemical experiments were carried out at room temperature (25 °C). All solutions in these studies were prepared with DI water of resistivity not less than 18 MΩ cm obtained from a Milli-Q water purification system (Milli-Q, USA). Phosphate buffer solutions (PBS) of pH 7.0 were prepared using Na_2HPO_4 (0.05 mol L^{-1}) and NaH_2PO_4 (0.05 mol L^{-1}).

2.2. Preparation of nanostructured Tm_2O_3 nanoparticles

The Tm_2O_3 nano whiskers were prepared by the hydrothermal method: initially, we prepared 200 mM thulium nitrate [$Tm(NO_3)_3$, $5H_2O$] in 50 mL and 1M of sodium hydroxide (NaOH) in 100 mL of DI water separately. After that, NaOH solution was added drop-wise into the thulium nitrate solution with constant stirring to maintain the pH up to ~12 and obtained the turbid and white precipitate i.e. thulium hydroxide formed at room temperature. The resulting solution was transferred into 100 mL Teflon-lined stainless steel autoclave and the temperature was maintained at 180 °C for 15 h after which, the autoclave was allowed to cool to room temperature (25 °C). The resulting pale white precipitate was filtered and washed several times with DI water and absolute ethanol to eliminate the presence of ionic remnants and was then dried at 80 °C for 6 h. The proposed reaction mechanism for the formation of pure Tm_2O_3 nanoparticles is shown in Eq. i and ii.

$$Tm(NO_3)_3 + 3NaOH \longrightarrow Tm(OH)_3\downarrow + NaNO_3 \quad \text{.....Eq (i)}$$

$$2Tm(OH)_3 \xrightarrow[180\ ^oC\ for\ 15h]{\Delta} Tm_2O_3 + 3H_2O \quad \text{.....Eq (ii)}$$

ACCEPTED MANUSCRIPT

2.3. Electrophoretic deposition of Tm_2O_3/ITO electrode

Electrophoretic deposition (EPD) was carried out by using DC battery (BioRad, model 200/2.0). The 50 mg Tm_2O_3 nanorods were dispersed in 5 mL of double DI water followed by ultrasonication (30 min). A platinum foil (1 cm × 2 cm) was used as the cathode and a hydrolyzed ITO-coated glass plate as anode. The ITO electrode was washed with diluted ammonia, ethanol and water, respectively. The two electrodes, placed parallel to each other with separation of 1 cm, were dipped in the colloidal suspension of Tm_2O_3. The film deposition was carried out onto ITO plate (0.25cm^2) at 40 mV for about 60 s. The films were then removed from the suspension followed by washing with DI water to remove any unbound particles.

2.4. Characterization

Hydrothermally prepared nanostructured Tm_2O_3 nanoparticle were characterized by X-ray diffraction (XRD) from Rigaku D/Max 2200 diffractometer with CuKα radiation at λ=1.5406 Å. The FT-IR with FTIR spectrophotometer (PerkinElmer, Spectrum BX II), UV-Vis spectrum (PerkinElmer, Lamda 950) and photoluminescence (PL) were studied by using a Cd–He laser source with 325 nm excitation. Raman spectra of nanostructured Tm_2O_3 was obtained on a Nanofinder 30 (Tokyo Instruments Co., Osaka, Japan). X-ray photoelectron spectroscopy (XPS) was performed using Axis-Nova, Kratos Analytical Ltd., Manchester, UK. Transmission electron microscopy (TEM) was carried with a JEM-2200 FS (JEOL, Japan). The surface morphology studies were carried out by field emission scanning electron microscopy JSM-6701F (JEOL, Japan) and atomic force microscopy (AFM, VEECO 440) in non-contact mode. The cyclic voltammetry (CV), electrochemical impedance spectroscopy (EIS) and electro-oxidation of AA measurements were recorded on an Autolab Potentiostat/Galvanostat (Eco Chemie, The Netherlands). The electrochemical measurements were carried out in a three electrode setup: nanostructured Tm_2O_3/ITO electrode serving as

ACCEPTED MANUSCRIPT

the working electrode, a platinum foil electrode as the counter electrode, and a saturated Ag/AgCl, Cl^- electrode as the reference electrode.

3. Results and discussion

3.1. Structural and optical characterization of nanostructured Tm_2O_3 nanoparticles

The results of X-ray diffraction (XRD) studies shown in Fig. 1a that reveal nine diffraction lines at 2θ = 29.35, 34.00, 36.19, 40.12, 43.82, 48.94, 53.70, 58.14, and 61.07. These diffraction lines can be assigned to the (222), (400), (411), (322), (431), (440), (611), (622) and (211) reflections, respectively, corresponding to the cubic crystal structure (BCC) of Tm_2O_3 [JCPDS-760160] with cell constant a = b = c = 10.5249 Å. No impurity peak is observed in the XRD pattern, indicating high purity of the Tm_2O_3. The average crystalline size (D_{hkl}) has been estimated using the Debye–Scherrer equation:

$$d = \frac{o.9\lambda}{\beta \cos\theta} \quad \text{.....} \qquad \text{Eq (iii)}$$

where D is the grain size, λ is the wavelength of the target Cu-K_α (1.54060 Å) and β is the full width at half-maximum (FWHM), which corresponds to the most intense peak; this β value corresponds to the (222) plane and has been found to be ~35 nm.

The FTIR spectrum of nanostructured Tm_2O_3 powder (Fig. 1b) exhibits two strong absorption band of Tm_2O_3 nanoparticles at 578 and 513 cm^{-1} belonging to the stretching vibration mode of metal oxide (M–O) bond.

The UV-VIS spectra of Tm_2O_3 recorded in the spectral range of 200–800 nm by dispersing its powder in water solution (Fig. 1c). In order to calculate the energy band gap Tauc approaches have been utilized. The direct band gap is calculated by plotting the graph between the $[(\alpha h\nu)^2$ vs. $h\nu]$ as shown in inset of Fig. 1c. The extrapolation of linear part yields the band gap of 4.03 eV.

The PL spectrum of the as-prepared Tm_2O_3 nanoparticles recorded at room temperature is shown in Fig. 1d. The PL spectrum shows a well resolved broad peak in the

ACCEPTED MANUSCRIPT

range of 360-425 nm. In order to determine the peak position exactly, the spectrum is fitted by Gaussian functions. The peak position has found to be centered at 385 nm corresponds to the emission of 3.14 eV, is attributed to the inter band transition from the ground electronic sub-level to the ground heavy-hole sublevel of Tm_2O_3. However, the peak at 3.14 eV corresponds to luminescence in ultraviolet to near visible spectral range.

The Raman spectrum of the Tm_2O_3 is shown in Fig. 2a. It has been observed that at ambient pressure and temperature rare earth sesquioxides exist in three different phase designated as monoclinic (space group C2/m), hexagonal (space group P3m1) and cubic phase (space group Ia3). According to factor group theory analysis, there are 22 Raman vibrational modes for cubic type bixbyite structured rare earth sesquioxides have been assigned as 4Ag, 4Eg and 14Fg. The strong peak seen in the range of 325–390 cm^{-1} is assigned either to Ag [39]. The detailed assignment of the Raman peaks is not currently available in the literature. Dilawar et al. have studied Raman vibrational spectra of various types of rare earth sesquioxides. They have reported one dominant Raman peak corresponding to Ag and Ag/Fg symmetry vibrations for these body centered cubic structured sesquioxides [39]. In order to get the exact peak position, the spectrum is fitted with Lorentzian function. The fitted spectrum of Tm_2O_3, exhibits four vibrational peaks. One dominant peak ~ 380 cm^{-1} and the three vibrational ~ 336 cm^{-1}, 418 cm^{-1} and 482 cm^{-1} are consitent with the results reported earlier [39,40].

The compositional studies of the Tm_2O_3 synthesized sample have been done by XPS measurements. The wide range XPS spectrum exhibits the presence of Tm 4*d* and O1*s* band (Fig 2b-d). The deconvoluted spectrum for Tm 4*d* and O1*s* is shown in Fig. 2c and 2d respectively. The position of Tm 4*d* and O1*s* peak shows the binding energy as 176 eV and 530.4 eV suggesting the formation of Tm_2O_3. The O1*s* feature centered around 530 eV can be ascribed to the metal oxide bond [41,42]. As a rough estimation, the atomic sensitivity factor

ACCEPTED MANUSCRIPT

(ASF) method has been used to obtainthe semi-quantitative evaluation of the Tm_2O_3 composition. The Tm and O ratio determined from the measured peak intensities (area) of Tm 4*f* and O 1*s* and the ASFs is 1:1.6, indicating that Tm in the film is totally oxidized.

3.2. Morphological analysis of nanostructured Tm_2O_3 nanoparticles

The size, morphology and microstructure of the sample have been determined using FE-SEM, TEM and AFM techniques. The FE-SEM images of Tm_2O_3 particles are shown in Fig. 3a and b. The images clearly show that the sample is composed of both rods and sheet-like particles. The TEM image (Fig. 3c-d) reveals the formation of large number of nanorods along with a few rectangular nanosheets with diameters of 40–80 nm and lengths up to 600 nm agreement with results of the SEM observation. The aspect ratio is about 1:8. Some extents of nanorod are parallel with each other and the small ones are oriented along the bigger ones. With the higher magnification image of nanorods (inset 3c), it can be seen that the rods are well-shaped and are roughs with dense wrinkles. The overlap of rods forms orderly black spots with wrinkle like stripes. Fig. 3d, a sheet-like morphology with 300 x 500 nm size of the individual Tm_2O_3 can be in TEM images. The sheet-like and irregular rod-like morphologies perhaps arise due to the Ostwald ripening process during nucleation. At high reactant concentration, nucleation and crystal growth rate are higher and the produced crystals in the water cores tend to aggregate to form larger particles [43]. Under the influence of hydrothermal nucleation, the aggregation may perhaps leads to the formation of sheet-like and rod-like Tm_2O_3 nanocrystal.

The topology of electrophoretically deposited Tm_2O_3 thin film on ITO surface (image 3e-f) shows formation of the rough surface with uniformly distributed nanoporous granular morphology obtained using AFM technique. The AFM images of Tm_2O_3/ITO surface (Fig. 3e-f) indicate irregular globular morphology with root-mean squared surface roughness (R_a) of 40 nm and maximum average height of 200 nm.

ACCEPTED MANUSCRIPT

3.3. Electrochemical characterization of nanostructured Tm_2O_3 nanoparticles

3.3.1 Characterization of the Tm_2O_3/ITO electrode surface

To ensure good electrical contact between the ITO and the underlying nanostructured Tm_2O_3, the Tm_2O_3/ITO has been tested as an electrode using a one electron redox couple. Fig. 4a shows voltammetric curves indicating reduction of the Tm_2O_3/ITO electrode and bare ITO electrodes in presence of 0.1 M PBS as supporting electrolyte at 50 mV/s scan rate in the potential range of -0.5 V to 0.7 V. The voltammogram for the Tm_2O_3/ITO electrode shows the expected reversible behaviour for the reduction on a bare ITO electrode. It suggests that the adhesion and electrical contact behaviour of the electrodeposited Tm_2O_3 on to the surface of bare ITO is quite satisfactory and because of the high surface area of Tm_2O_3/ITO electrode, the observed oxidation current is higher than that of the bare ITO electrode.

3.3.2. Electro-oxidation of AA

In order to compare Tm_2O_3/ITO electrode with bare ITO electrode, the method of cyclic voltammetry has been used to follow the electrocatalytic behaviour of the electrodes. Fig. 4b shows the cyclic voltammograms of bare ITO and Tm_2O_3/ITO electrodes containing 2 mM AA in 0.1 M PBS, with a scan rate of 50 mV/s. The bare ITO electrode exhibits no oxidation peak for AA but the Tm_2O_3/ITO electrodes are illustrated with a distinguishable peak in the cyclic voltammetry. Therefore, the electrocatalytic activity of the Tm_2O_3/ITO electrodes is confirmed.

Electrochemical impedance spectroscopy has been done in order to further understand the electrocatalytic behaviour of Tm_2O_3/ITO electrode in 0.1 M phosphate buffer (PBS)–2 mM AA in the frequency range of 0.00–4.0 x 10^4 Hz, obtained from Nyquist plot. The Nyquist plot commonly includes a semicircle region lying on the axis followed by a straight line. The semicircular part seen at higher frequencies corresponds to the electron-transfer-

ACCEPTED MANUSCRIPT

limited process and its diameter is equal to the charge transfer resistance (*R*ct), which controls the electron transfer kinetics of the redox probe at the electrode interface. It can be seen from the Nyquist plot (Fig. 4c), the charge transfer resistance value of Tm_2O_3/ITO (R_{CT} = 10.43 KΩ) electrode is less than that of the bare ITO (R_{CT} = 17.35 KΩ) electrode. This decrease in R_{CT} value of Tm_2O_3/ITO is due to the the diffusion limiting step of the electrochemical process. These results suggest that Tm_2O_3/ITO electrode promotes electron transfer in between solution and the electrode during electro-oxidation of AA.

3.3.3. Effect of scan rate

The CV studies have been conducted on Tm_2O_3/ITO electrodes as a function of scan rate varying from 10 to 100 mV/s in presence of 2 mM AA with 0.1 M PBS (pH = 7) at 25 °C. Fig. 5a shows the effect of different scan rates on the electrocatalytic properties of Tm_2O_3/ITO electrode towards AA oxidation. The increase in scan rate leads to increased electro-catalytic peak current and results in a shift to more positive potential value for the catalytic oxidation of AA. It can be seen that magnitudes of anodic peak current increase linearly with the square root of scan rate ($\upsilon^{1/2}$) (Fig. 5b), suggesting that the reaction is mass transfer controlled. The similar results have been reported by Hosseini et al [12] concerning the AA oxidation onto modified Au/TiO_2/Ti electrode. It is observed that the peak height varies directly with the sweep rate (with linear regression coefficient 0.996), indicating improved electro-catalytic behaviour of Tm_2O_3 towards oxidation of AA. This result indicates the kinetic limitation in the reaction between the redox sites of Tm_2O_3/ITO electrode and AA.

The surface concentration of the Tm_2O_3/ITO electrode can be calculated using the Brown-Anson model [44] that is based on the following equation.

$$Ip = n^2F^2\gamma Av/4RT \qquad \ldots\ldots\ldots\ldots\ldots \text{ Eq (iv)}$$

ACCEPTED MANUSCRIPT

where n is the number of electrons transferred (1), F is the Faraday constant (96485 C/mol), γ is the surface concentration of the Tm_2O_3/ITO electrode (molcm^{-2}), A is the surface area of the electrode (0.25 cm^2), v is the scan rate (50 mV/s), R is the gas constant (8.314 J mol^{-1}k^{-1}) and T is the room temperature (25 °C). The surface concentration of Tm_2O_3/ITO electrode (3.61×10^{-12} molcm^{-2}) is higher than that of bare ITO (1.16×10^{-12} molcm^{-2}) electrodes.

The diffusion co-efficient value (D) for free diffusion of 0.1 M phosphate buffer (PBS, pH =7) from electrolyte solution to the Tm_2O_3/ITO electrode surface has been calculated using Randles-Sevcik equation [45].

$$Ip = (2.69 \times 10^5)\, n^{3/2} A D^{1/2} C v^{1/2} \quad \text{…….....} \quad \text{Eq (v)}$$

where Ip is peak current of the bioelectrode (Ipa anodic and Ipc cathodic), n is the number of electrons involved or electron stoichiometry (1), A is the surface area of the Tm_2O_3/ITO electrode (0.25 cm^2), D is diffusion co-efficient, C is surface concentration in mol (2 mM AA) and v is the scan rate (50 mV/s). The D value has been obtained as (3.15×10^{-7} cm^{2}s^{-1})

3.3.4. Electro-catalytic study of AA

The effect of AA concentration on the CV response of Tm_2O_3/ITO electrode has been investigated in 0.1 M phosphate buffer (PBS, pH =7). Fig. 5c shows the CV of the Tm_2O_3/ITO electrode as a function of AA concentration varying from 0.2- 8.0 mM. With increasing AA concentration in the solution, the anodic peak current increases. This catalytic peak current has a linear relationship with the concentration of AA in the range of 0.2 - 8.0 mM with a correlation coefficient of 0.99 (Fig. 5d). Linear calibration is obtained, with a coefficient of 0.997, demonstrating the good relationship between oxidation current and concentration. The limit of detection (LOD) has been estimated to be 0.42 mM based on the

ACCEPTED MANUSCRIPT

signal-to-noise ratio (S/N = 3). A proposed mechanism for the electrocatalytic oxidation of AA to dehydroascorbate at Tm_2O_3/ITO electrode is seen in Fig. 6. From these results, it can be concluded that the electro-oxidation of AA on these electrodes can be used for the quantitative determination of AA in given samples and it thus has a potential application as a chemical sensor for the determination of AA. Compared to modified carbon electrodes requiring tedious preparations and pre-treatment procedures, Tm_2O_3/ITO electrode can easily be prepared without any further need for modification and hence it can be used for the determination of AA.

4. Conclusion

In conclusion, we have analyzed the optical and electro-analytical behaviour of hydrothermally prepared nanostructured Tm_2O_3 towards AA. The rods as well as sheet-like morphology have been confirmed by FE-SEM, TEM and AFM analysis. The optical band gap (4.03 eV) and binding energy of prepared sample have also been examined. The electrochemical results of modified Tm_2O_3/ITO electrode show excellent electrocatalytic ability for the oxidation of AA with significant current enhancement. Moreover, the oxidation current of AA on Tm_2O_3/ITO electrode has been used for determination of AA in aqueous solution and a linear calibration has found in the range of 0.2–8 mM. The electrochemical oxidation of AA is irreversible and the current obtained is diffusion controlled. The present findings of these studies convey a new promising platform for the application of rare earth metal oxide materials for implications in rapid and accurate quantitative determination of AA in pharmaceutical and clinical samples.

Acknowledgements

This study was supported by World Class University (WCU) program (R31-20029) through the National Research Foundation (NRF) funded by the Ministry of Education, Science, and Technology (MEST) Republic of Korea. A.R sincerely acknowledges Indian

ACCEPTED MANUSCRIPT

Council of Medical Research (ICMR), New Delhi, for the award of Project Associateship. B.D.M thanks the Ministry of Education, Science and Technology (R32−20026) of Korea for the opportunity provided during his visit to the Chungnam National University as visiting professor under the World Class University project during 2013.

References

[1] O. Arrigoni, M.C. De Tullio, Biochim. Biophys. Acta 1569 (2002) 1–9.

[2] S. Gahler, K. Otto, J. Agric. Food Chem. 51 (2003) 7962-7968.

[3] T. Wu, Y. Guan, J. Ye, Food Chem. 100 (2007) 1573–1579.

[4] X. Wu, Y. Diao, C. Sun, J. Yang, Y. Wang, S. Sun, Talanta 59 (2003) 95–99.

[5] Z.H. Liu, Q.L. Wang, L.Y. Mao, R.X. Cai, Anal. Chim. Acta 413 (2000) 167–173.

[6] L. Nováková, D. Solichová, P. Solich, J. Chromatogr. A 1216 (2009) 4574–4581.

[7] G.H. Wu, Y.F. Wu, X.W. Liu, M.C. Rong, X.M. Chen, X. Chen, Anal. Chim. Acta 745 (2012) 33– 37.

[8] S. Qiu, S. Gao, Q. Liu, Z. Lin, B. Qiu, G. Chen, Biosens. Bioelectron. 26 (2011) 4326–4330.

[9] S.B. Khoo, F. Chen, Anal. Chem. 74 (2002) 5734-5741.

[10] Y. Lin, Y. Hu, Y. Long, J. Di, Microchim. Acta 175 (2011) 259–264.

[11] G. Hu, Y. Guo, Q. Xueb, S. Shao, Electrochimica Acta 55 (2010) 2799–2804.

[12] M.G. Hosseini, M. Faraji, M.M. Momeni, Thin Solid Films 519 (2011) 3457–3461.

[13] Y.P. Dong, L. Huang, J. Zhang, X.F. Chu, Q.F. Zhang, Electrochimica Acta 74 (2012) 189– 193.

[14] L. Yu, J. Xi, Int. J. Hydrogen Energy 37(21) (2012) 15938–15947.

[15] S. Singh, P. Srivastava, I.P.S. Kapoor, G. Singh, J. Therm. Anal. Calorim. 111 (2013) 1073–1082.

ACCEPTED MANUSCRIPT

[16] Chen H-F, Yu H-M, Zeng H-X, Shi W-L, Ji Y-J, J. Alloys Comp. 225 (1995) 626-628.

[17] Wang J, Xu Y, Hojamberdiev M, Cui Y, Liu H, Zhu G. J. Alloys Comp. 479 (2009) 772-776.

[18] L. Eyring, in: K.A. Gschneider Jr., L. Eyring (Eds.), The Handbook on the Physics and Chemistry of Rare Earths, North Holland, Amsterdam, 1979.

[19] B.A. Panda, G. Glaspell, S.M. El-Shall, J. Phys. Chem. C. 111 (2007) 1861-1864.

[20] K. Kompe, H. Borchert, J. Storz, A. Lobo, S. Adam, T. Moller, M. Angew. Chem. Int. Ed. 42 (2003) 5513-5516.

[21] M. Flytzani-Stephanopoulos, M. Sakbodin, Z. Wang, Science 312 (2006) 1508-1510.

[22] E. L. Muñoz, G.N. Darriba, A.G. Bibiloni, L.A. Errico, M. Rentería, J. Alloys Comp. 495 (2010) 532-536.

[23] K.A. Gschneider, Jr., L. Eyring, Eds.; Handbook on the Physics and Chemistry of Rare Earths; North-Holland: New York, (1983).

[24] Stouwdam, J. W.; van Veggel, F. C. J. M. Nano Lett. 2 (2002) 733-737.

[25] L. An, J. Zhang, M. Liu, S. Wang, J. Alloys Comp. 451 (2008) 538-541.

[26] M. Kouda, T. Kawanago, P. Ahmet, K. Natori, T. Hattori, H. Iwai, K. Kakushima, A. Nishiyama, N. Sugii, K. Tsutsui, J. Vac. Sci. Technol. B 29 (2011) 062202-062204.

[27] T.M. Pan, C.D. Lee, M.H. Wu, J. Phys. Chem. C 113 (2009) 21937-21940.

[28] J. Ma, J. Li, R. Tang, D. Li, W. Li, Q. Chen, Int. J. Hydrogen Energy 36 (2011) 9091-9097.

[29] Y. Li, Y. Gao, Y. Zhou, Y. Liu, J. Liu, J. Electroanal. Chem. 642 (2010) 1–5.

[30] L.Yan, G. Yanfang, L. Yuchen, Z. Yu, L. Jinrong, J. Inner Mongolia University of Technol. Natural Sci. Ed. 29 (2010) 254-259.

[31] A.A. Tolstopyatova, A.A. Balandin, Russ. Chem. Bull. 14 (1965) 1923-1928.

ACCEPTED MANUSCRIPT

[32] A. Malinauskas, R. Garjonyte, R. Mazeikiene, I. Jureviciute, Talanta 64 (2004) 121-129.

[33] A. Ambrosi, A. Morrin, M.R. Smyth, A.J. Killard, Anal. Chim. Acta 609 (2008) 37-43.

[34] A.S. Kumar, H.-W. Cheng, S.-M. Chen, React. Funct. Polym. 69 (2009) 364-370.

[35] S.S. Mahshid, S. Mahshid, A. Dolati, M. Ghorbani, L. Yang, S. Luo and Q. Cai, J. Alloys Comp. 554 (2013) 169-176.

[36] L. Besra, M. Liu, Progr. Mater. Sci. 52 (2007) 1–61.

[37] J. Singh, M. Srivastava, A. Roychoudhury, D.W. Lee, S.H. Lee, B.D. Malhotra, J. Physical. Chem. B. 117 (2013) 141-152.

[38] M. Srivastava, J. Singh, R. K. Mishra and A. K. Ojha, J. Alloys Comp. 555 (2013) 123-130.

[39] N. Dilawar, S. Mehrotra, D. Varandani, B.V. Kumaraswamy, S.K. Haldar, A.K. Bandyopadhyay, Mater. Characterizat. 59 (2008) 462– 467.

[40] L.A. Tucker, F.J. Karney Jr., P. McMillan, S.H. Lin, L. Lyring, Appl. Spectros. 38 (1984) 857-860.

[41] J.J. Wang, Z.B. Fang, T. Ji, W.Y. Ren, Y.Y. Zhu, G. He, Appl. Surface Sci. 258 (2012) 6107– 6110.

[42] J. Wang, T. Ji, Y. Zhu, Z. Fang and W. Ren, J. Rare Earths, 30 (2012) 233-235.

[43] M.P. Pileni, J. Experimental Nanosci. 1 (2006) 13–27.

[44] J. Singh, P. Kalita, M.K. Singh, B.D. Malhotra, Appl. Phy. Lett. 98 (2011) 123702.

[45] S.K. Yadav, J. Singh, V.V. Agrawal, B.D. Malhotra, Appl. Phy. Lett. 101 (2012) 023703.

ACCEPTED MANUSCRIPT

Figure caption

Figure 1 (a) X-ray diffraction, **(b)** FT-IR, **(c)** Plot of UV absorption as a function of wavelength λ (nm), Inset**:** Plot of $(\alpha h\upsilon)^2$ as a function of photon energy (eV) and **(d)** Photo luminance spectra of nanostructured Tm_2O_3 nanoparticles

Figure 2 (a) Raman Spectra of Tm_2O_3 nanorod **(b)** XPS spectrum of the Tm_2O_3 nanorods synthesized at 180 °C after calcination at 550 °C for 3 h. **(c)** The XPS valence-band of Tm 4*d* core level spectra and **(d)** O 1*s* energy-loss spectrum of annealed Tm_2O_3 sample.

Figure 3 (a & b) Scanning electron micrograph images, **(c & d)** Transmittance electron micrograph and **(e & f)** Atomic force microscopy images of prepared nanostructured Tm_2O_3 nanoparticles

Figure 4 (a) CV of a Tm_2O_3/ITO electrode and a bare ITO electrode, recorded at a scan rate of 50 mV/s in a 0.1 M PBS (pH =7) at 25 °C. **(b)** CV and **(c)** EIS of Tm_2O_3/ITO and a bare ITO electrode in 0.1 M PBS– 2 mM AA aqueous solution at 25 °C with a scan rate of 50 mV/s

Figure 5 (a) Effect of varying the scan rate (10 to 100 mV/s) on the CV of 2 mM ascorbic acid using Tm_2O_3/ITO electrode as a working electrode in 0.1 M PBS (pH = 7) at 25 °C. **(b)** The plot of ascorbic acid oxidation peak current on the Tm_2O_3/ITO electrode versus $\nu^{1/2}$. **(c)** The CV of Tm_2O_3/ITO electrode in 0.1 M PBS (pH = 7) with different concentrations of AA (0.2-8.0 mM). **(d)** The calibration plot of ascorbic acid oxidation peak current on the Tm_2O_3/ITO electrode versus concentration of AA.

Figure 6 Proposed mechanism shows for the electrocatalytic oxidation of AA to dehydroascorbate at the Tm_2O_3/ITO electrode

ACCEPTED MANUSCRIPT

Figure 1 (Singh et al.)

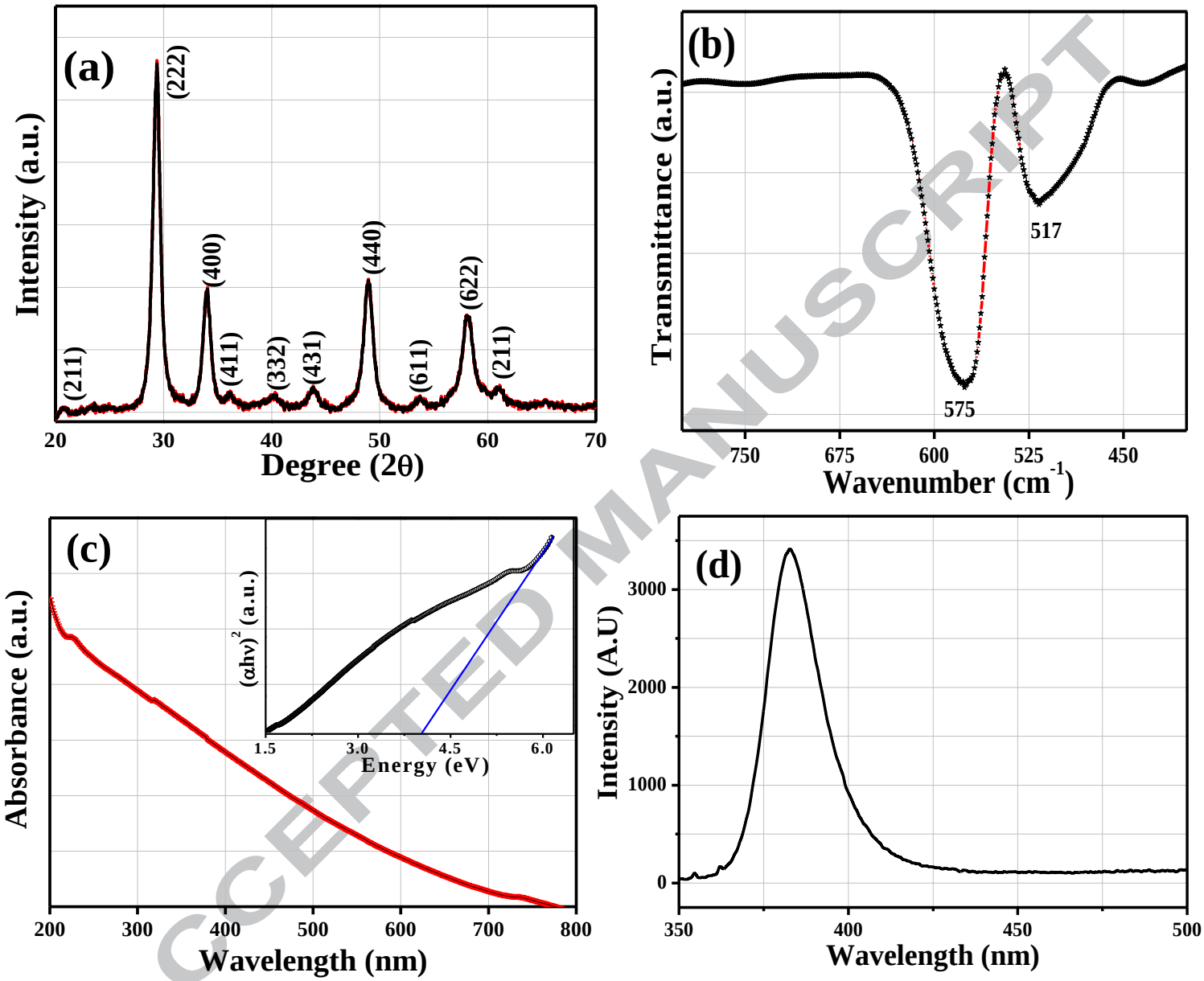

ACCEPTED MANUSCRIPT

ACCEPTED MANUSCRIPT

Figure 2 (Singh et al)

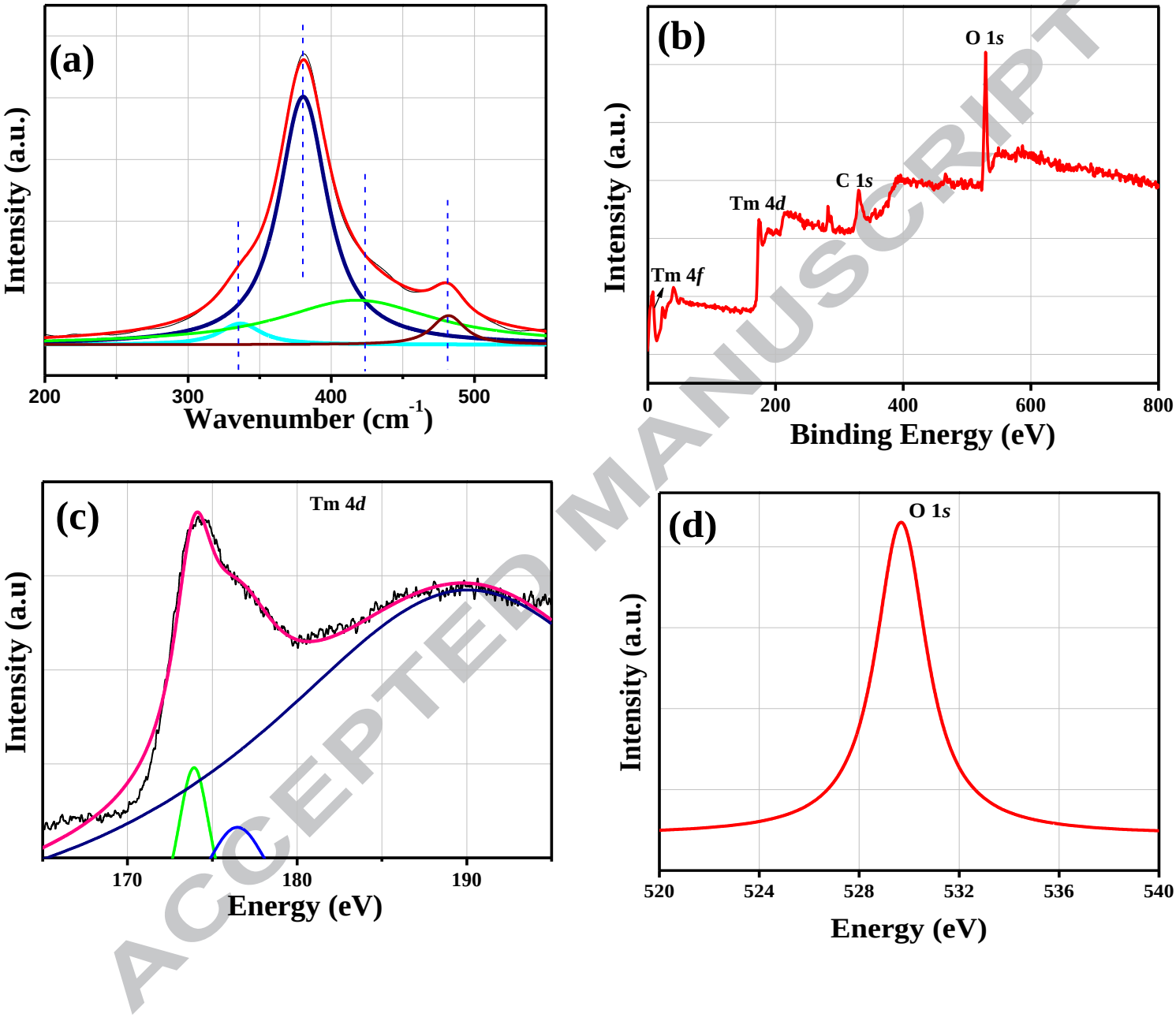

ACCEPTED MANUSCRIPT

ACCEPTED MANUSCRIPT

Figure 3 (Singh et al.)

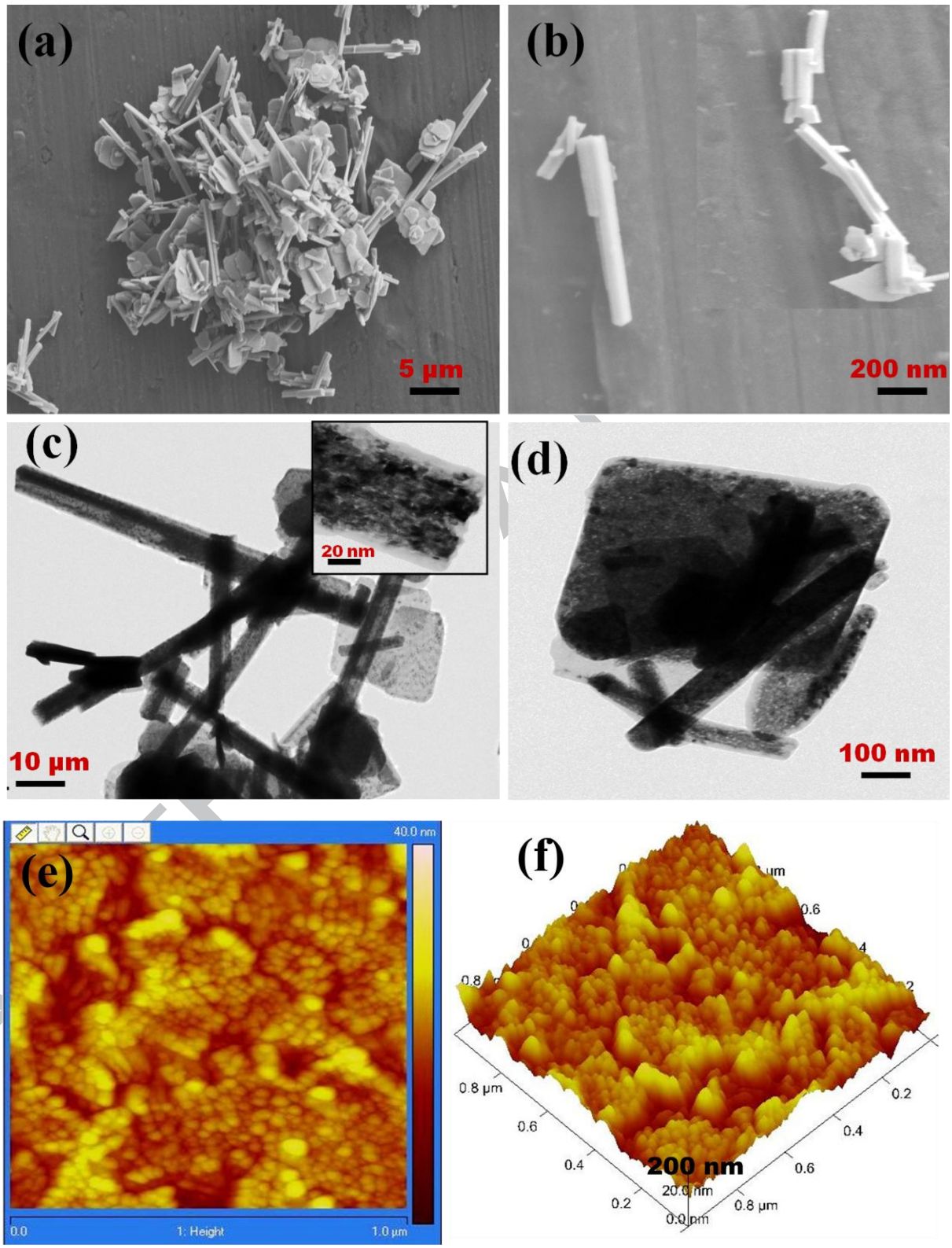

ACCEPTED MANUSCRIPT

Figure 4 (Singh et al.)

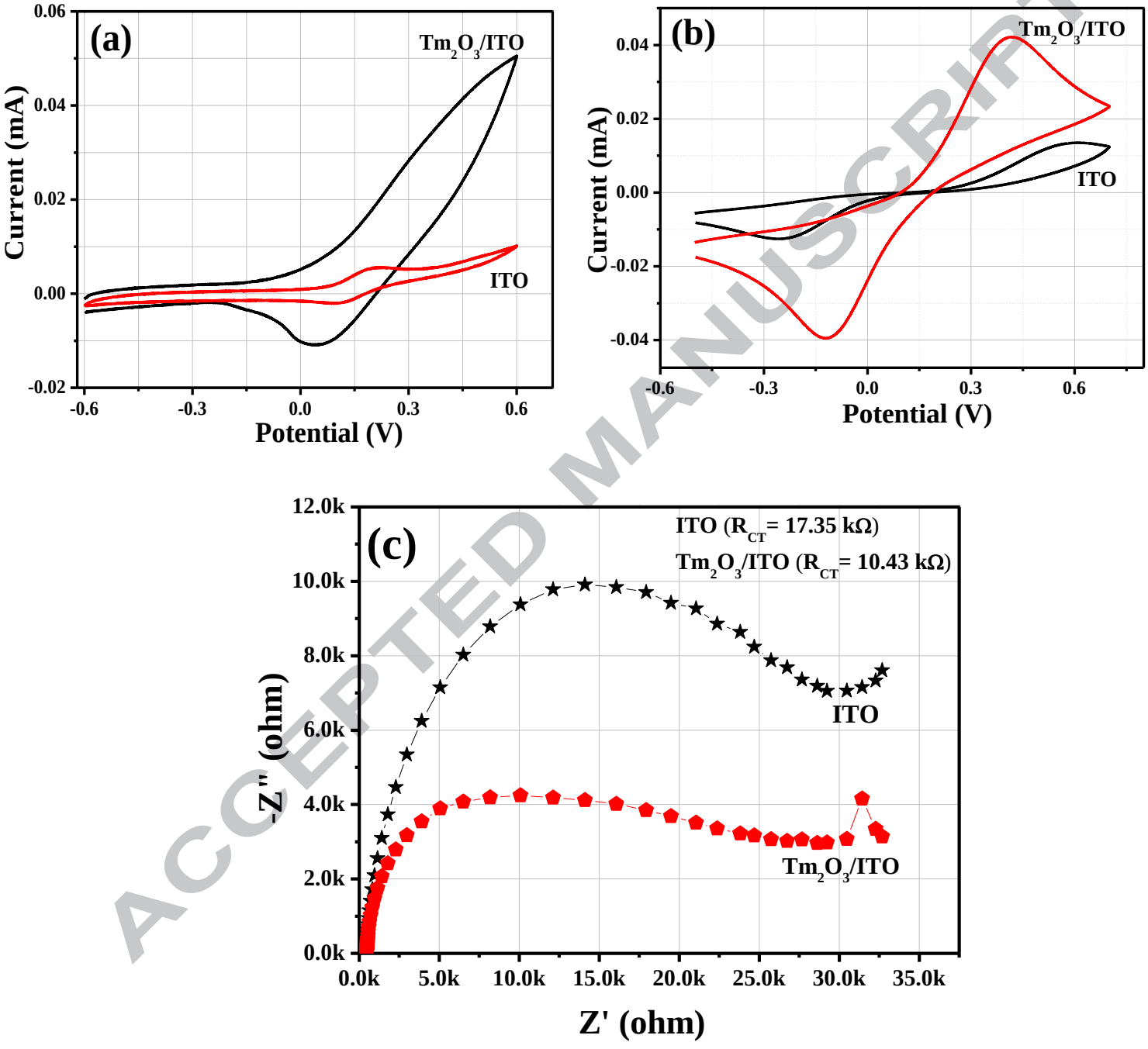

ACCEPTED MANUSCRIPT

ACCEPTED MANUSCRIPT

Figure 5 (Singh et al.)

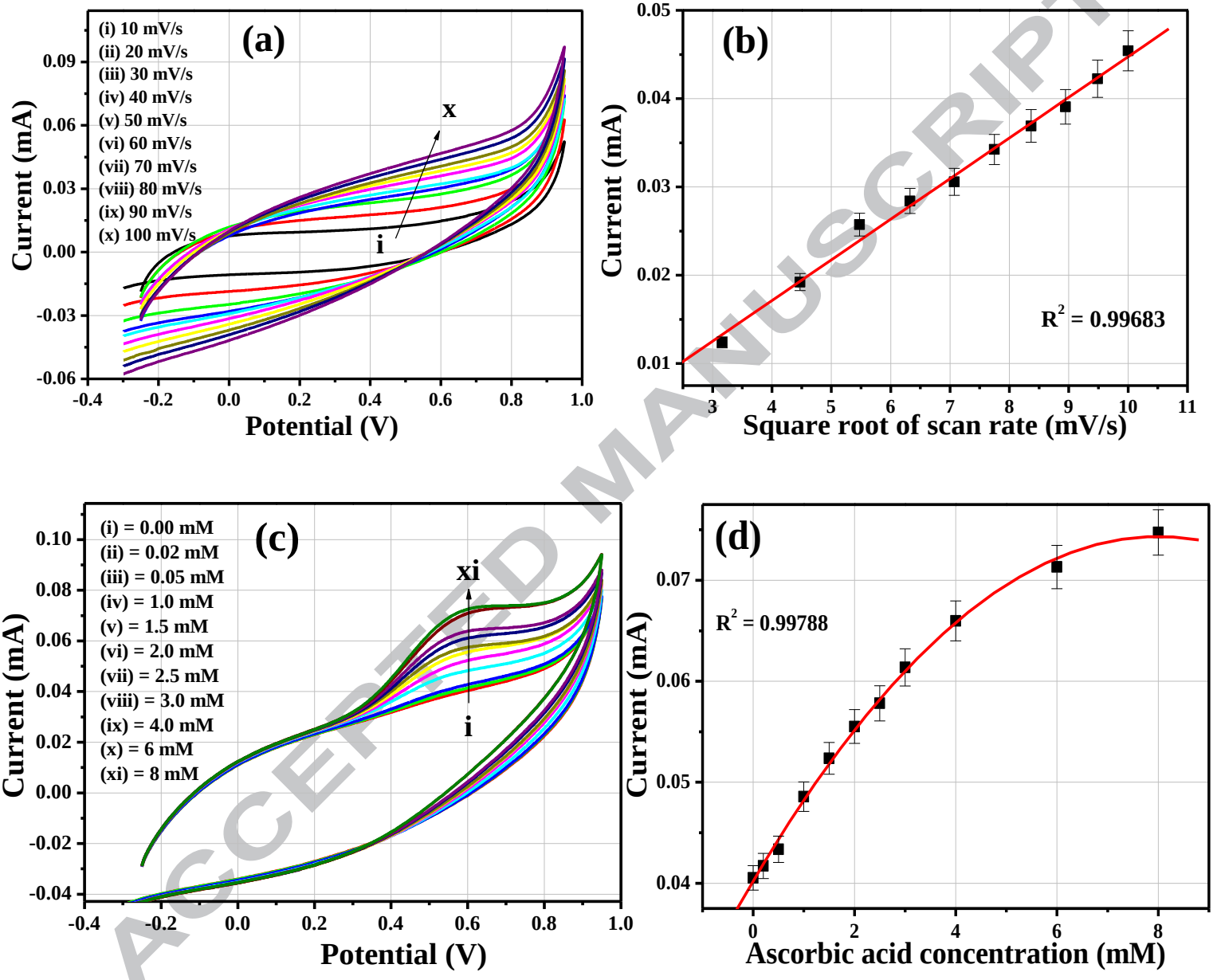

ACCEPTED MANUSCRIPT

ACCEPTED MANUSCRIPT

Figure 6 (Singh et al.)

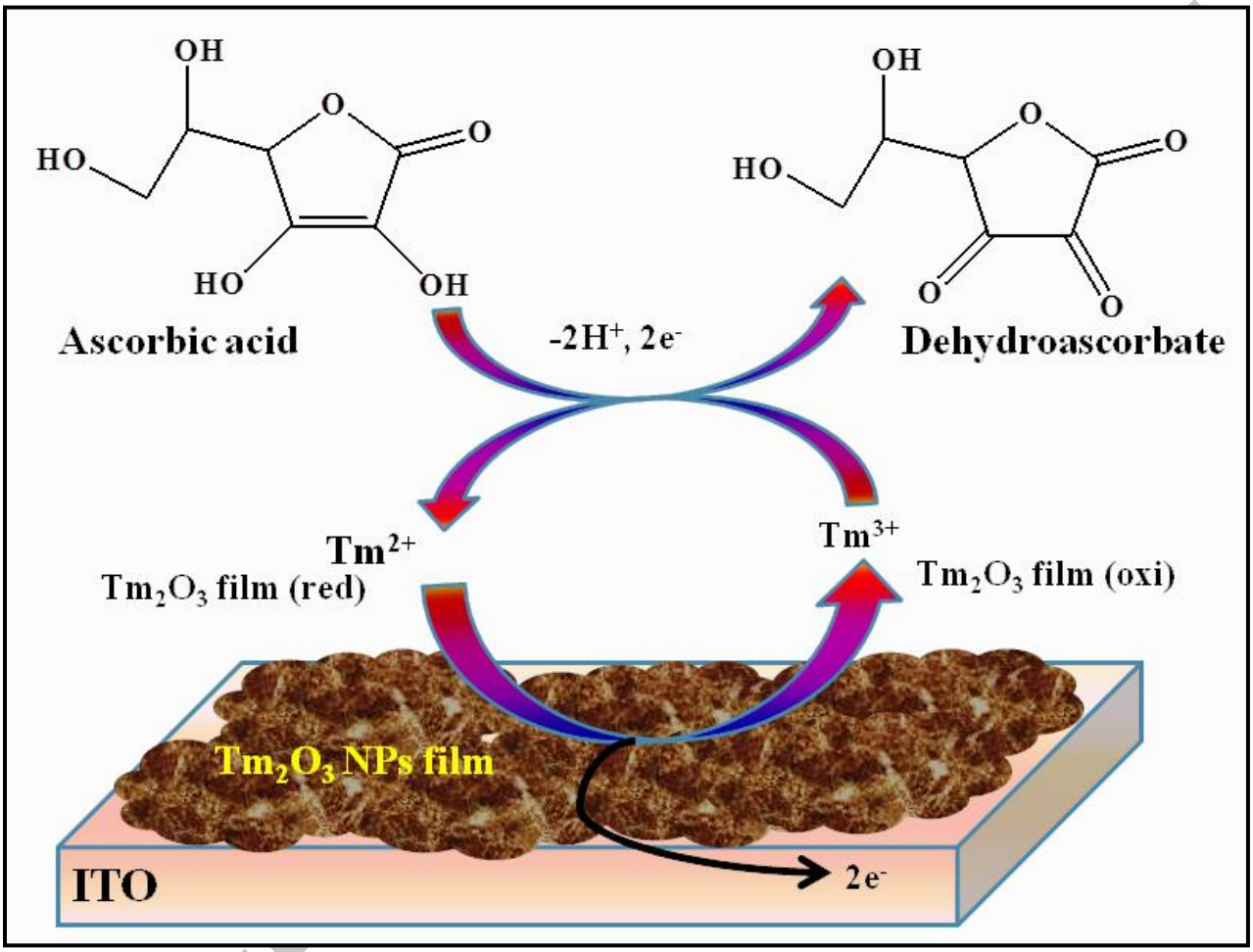

ACCEPTED MANUSCRIPT

Highlight

- Nanostructured thulium oxide has been prepared using the hydrothermal process
- Thulium oxide exhibit excellent electrochemical response towards ascorbic acid
- Thulium oxide are interesting electro-optical material
- Rare earth metal oxide offers potential application in biosensor & optoelectronics.

.

ACCEPTED MANUSCRIPT

Particle Swarm Optimization and Firefly Algorithm: Performance Analysis

Bharat Bhushan and Sarath S. Pillai
Department of Electrical Engineering
Delhi Technological University
Delhi, India
bharatdce@yahoo.co.in, sspillai305@gmail.com

***Abstract*—With the help of evolutionary concepts and behavior of biotic components of nature, many optimization algorithms were developed. Optimization techniques like Particle Swarm Optimization and Firefly Algorithms are among the latest research topics. Several advancements have also been made in these algorithms. This paper carves out a comparative analysis of Particle Swarm Optimization (PSO) and Firefly Algorithm (FFA) in detail along with simulation results carried out on some standard benchmark functions.**

Keywords— Particle Swarm Optimization; Firefly Algorithm; Optimization; Benchmark Functions.

I. INTRODUCTION

Learning from naturally abundant biological systems and structures to design and develop a number of different kinds of optimization algorithms have been widely used in both theoretical study and practical applications. The evolution is used to tune the algorithm parameters [4] while the study of bionics inspires and improves our modern technologies with the principles found in nature, biological structures and functions. Bionics study inspires us not only with its physical yields, but also with various computation methods that can be applied in different areas. In engineering, this ‘‘bioinspired’’ design approach has been used to exploit the evolved ‘‘tricks’’ of nature to design robust high performance technological solutions. Amongst them, one of the most popular bioinspired design approaches is what is called ‘‘Swarm Intelligence’’ [5]. Metaheuristic optimization algorithms can efficiently deal with non-linear optimization problems [14].

These techniques which are inspired by the collective behavior of animal societies as well as other social insect colonies that are naturally able to solve large-scale distributed problems are grouped in the Swarm Intelligence [28]. The swarm intelligence is defined as an algorithm or distributed problem-solving devices designed inspired by the collective behavior of many animal societies, particularly social insect colonies [10]. In current peer-to-peer systems swarm availability is proven to be a serious issue [13]. It has become a research interest among scientists of related fields in recent years [18].

Particle Swarm Optimization (PSO) technique was developed by Eberhart and Kennedy [6] and is an approach that mimics the behavior of social organisms where the behavior of different types of social interactions (e.g., flock of birds) is mimicked in order to create an optimization method that is able to solve continuous optimization problems [5]. PSO is a computational intelligence-based technique that is not largely affected by the size and nonlinearity of the problem thus converges to the optimal solution in many problems where most analytical methods fail to converge. Therefore, it can be effectively applied to different optimization problems in power systems [25] and [31]. Literature tells that it has been successfully applied to various problems viz. Economic Dispatch [26], Generation Expansion Problem (GEP), State Estimation etc. It has been again improved [16] upon to get, Modified PSO [19], Adaptive Particle Swarm Optimization (APSO) [3], Multi-dimensional Particle Swarm Optimization for Dynamic Environments [7] and [27], Self-Organizing Swarm (SOSwarm) for Financial Credit-Risk Assessment [8] and has been applied for PID control [32], Neural Network [34] and to train the PROAFTN [33], Multi-Criteria Decision Aid (MCDA) method etc. A valuable point of comparison can be made which can be used throughout the research areas to better test new advances while having a strictly-defined, well-known, standard algorithm [22].

Mechanisms of firefly communication have been implemented effectively in various areas of wireless networks design [9], dynamic market pricing [29] and mobile robotics [24] and [30] via luminescent flashes and their synchronization [11]. Many bio-inspired algorithm exist that use local information and simple rules to create a global agreement of a single parameter, such as clock time in the flashing firefly algorithm, or location in the slime algorithm. One of the most important techniques for performing image segmentation is Thresholding [15]. It is generally simple and computationally efficient. The segmentation results of the algorithm are promising which inspires and encourages further researches to apply this algorithm to real-time and complex image analysis problems [25] such as target recognition, complex document analysis and as biomedical image application. Other application includes synchronization of wireless network [20].

An application in pulse-coupled oscillator’s model addresses the problem of synchronization of the oscillators with different frequencies. Firefly algorithm has been applied in real time systems [23]-[24] and heartbeat synchronization techniques [12].

This paper is divided into several sections wherein Section II introduces the Particle Swarm Optimization, Firefly

978-1-4673-4529-3/12/$31.00 ©2012 IEEE

Algorithm (FFA) is introduced in section III, Section IV discusses the non-linear benchmark functions and section V shows the simulation results and discussion followed by section VI: conclusion and then references.

II. PARTICLE SWARM OPTIMIZATION (PSO)

PSO consists of a swarm of particles moving in a search space of possible solutions for a problem. Each particle has a position vector representing a candidate solution to the problem and a velocity vector and also contains a small memory that stores its own best position seen so far and a global best position obtained through communication with its neighbor particles. The advancement toward best location (xi*) and global best (g*) by the particle swarm optimizer is ideologically similar to the crossover operation utilized by genetic algorithms [2]. Similar to all evolutionary computation paradigms, it uses the concept of fitness. The swarm works through the interactions of members of the population, still the exact methods for moving the particles are quite flexible [35].

By assigning shortest path and by studying trajectories of particles [21] the optimization behavior of standard PSO can be made invariant to the rotations of the optimization function [17]. There are two major components in the movement of a swarming particle: a deterministic component and a stochastic component.

A. PSO Operation

Modification in the initial simulations was done to incorporate multidimensional search and acceleration by distance, nearest-neighbor velocity matching and eliminate ancillary variables [6]. Through a series of trial and error, a number of parameters extrinsic to optimization were eliminated from the algorithm, resulting in the very simple original implementation.

Consider flying through the parameter space swarm of particles searching for optimum. Each particle is attributed with position vector $x_i(t)$ and velocity vector $y_i(t)$.

The velocity vector is calculated by the following:

$$V_i^{t+1} = V_i^t + C_1 e_1 \Theta [g^* - x_i^t] + C_2 e_2 \Theta [x_i^* - x_i^t] \qquad (1)$$

where e_1 and e_2 are two random vectors taking the values between 0 and 1. C_1 and C_2 are the learning parameters or acceleration constants, which can typically be taken as $C_1 \approx C_2 \approx 2$ and g* is the fitness value. The initial velocity of a particle can be taken as zero, that is, $V_i^{t=0} = 0$. The new position can then be calculated by:

$$x_i(t+1) = x_i(t) + V_i^{t+1} \qquad (2)$$

Although V_i could be any value, usually it is bounded in some range $[0, V_{max}]$.

The Hadamard product of two matrices $u \Theta v$ is defined as the entry wise product, that is $[u \Theta v]_{ij} = u_{ij}v_{ij}$. Fig.1 gives the update of a particle in swarm at the next time instant where g(t) is the best value of the particle fitness.

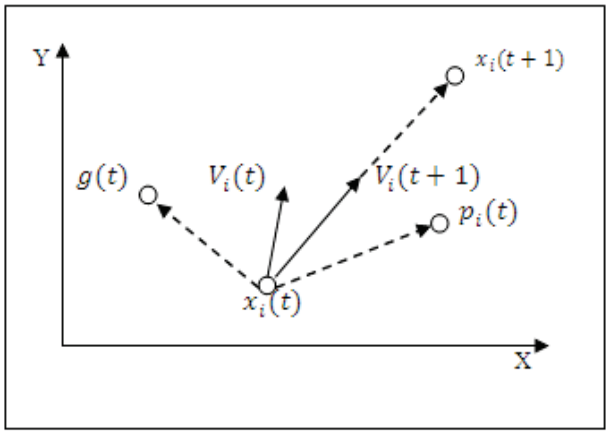

Fig. 1. Position (x) and Velocity (y) update of i^{th} particle in swarm

The velocity update equation in (1) has three major components:

- The first component is referred to as momentum, inertia or habit.
- The second component is a linear attractiveness towards the best position ever found by the given particle scaled by a random weight, referred to as self-knowledge, remembrance, memory or nostalgia.
- The third component of the equation is a linear attraction towards the best position found by any particle scaled by another random weight, referred to as group knowledge, cooperation, shared information, social knowledge.

B. Pseudocode for PSO

For implementation of PSO algorithm, following procedure can be used

1) Initialize the particles by assigning a random position in the problem hyperspace to each particle.
2) Evaluate the fitness function for every particle.
3) Compare the particle's fitness value with its x_i^* for each particle. If the current value is better than the x_i^* value, then set this value as the x_i^* and the current particle's position x_i.
4) The particle that has the best fitness value is identified. The value of its fitness function is identified as g* and its position as g.
5) Calculate the velocities and positions of all the particles using (1) and (2).
6) Repeat steps 2–5 until a stopping criterion is met (e.g., maximum number of iterations or a sufficiently good fitness value).

III. FIREFLY ALGORITHM (FFA)

Fireflies produce luminescent flashes as a signal system to communicate with other fireflies, especially to prey attractions. FFA is inspired by the firefly's biochemical and social aspects. The flashing light is produced by a process called Bioluminescence.

A. FFA Operation

The rhythmic flash, the rate of flashing and the amount of time constitutes the part of the signal system that bring both sexes together. Light intensity obeys inverse square law at a particular distance r from the light source.

$$Io \propto 1/r^2 \quad (3)$$

Thus, the light intensity I_o decreases with the distance r, which makes most fireflies visual to a limited distance.

Following are the assumptions made in the firefly algorithm:

- All fireflies will be attracted to every other fireflies regardless of their sex i.e to say that they are unisex.
- The attractiveness and brightness decrease as the distance increase and are also proportional to each other. The less bright will be moving towards the brighter one. It will move randomly if there is no brighter one.
- The brightness of a firefly is determined or affected by the shape of the objective function.

In the Firefly Algorithm, there are two important issues: formulation of the attractiveness and the variation of light intensity. In the simplest case particular location x can be I(x) $\propto$ f(x) however attractiveness β is relative. In order to avoid the singularity at r=0 in the expression $Io \propto 1/r^2$, combined effect of both the laws can be approximated as:

$$I(r) = I_0 e^{-\gamma r^2} \quad (4)$$

Attraction between them is proportional to the light intensity seen by the adjacent fireflies. The attractiveness β of the firefly can be defined as

$$\beta = \beta_0 e^{-\gamma r^2} \quad (5)$$

where β_0 is attractiveness at r=0.

B. Pseudocode for FFA

1) Define objective function. F(x),
   $X = (x_1, \dots, x_d)^T$
2) Generate initial population x_i (i = 1, 2, … , n)
3) Light intensity I_i at x_i is determined by $f(x_i)$.
   Also define light absorption coefficient γ.
4) Repeat until maximum generation is reached
   For i = 1 to n, n= no. of fireflies
   For j = 1 to n
   If ($I_i < I_j$), move firefly i towards j; end if
   Variation of attraction with distance r via $\exp(-\gamma r)$
   Evaluate new values and update light intensity.
   End for j
   End for i
5) Rank the fireflies, find the current global best g*
   Go to step 4
6) End

IV. NON-LINEAR BENCHMARK FUNCTIONS

This section describes the ten nonlinear benchmark functions. Table I shows the details of the Non-Linear Benchmark Functions used alongwith their Ranges and Optimum points.

TABLE I. NON-LINEAR BENCHMARK FUNCTIONS WITH THEIR RANGES AND OPTIMUM POINTS.

Function	Equation	Range	Optimum Point
De-jong's	$F(x,y) = x^2 + y^2$	-5.12<x, y<5.12	(0, 0)
Ackleys	$F(x,y) = -20\exp\left(-0.2\sqrt{\left(\frac{1}{2}\right)(x^2+y^2)}\right) - \exp\left((1/2)(\cos 2\Pi x + \cos 2\Pi y)\right) + 20 + e$	-30<x,y<30	(0,0)
Rastrigin	$F(x,y) = x^2 + y^2 - 10(\cos 2\Pi x + \cos 2\Pi y) + 20$	-5.12<x, y<5.12	(0,0)
Rosenbrock	$F(x,y) = (x-1)^2 + 100*(y-x^2)^2$	-5<x, y<5	(1, 1)
Easom's	$F(x,y) = -\cos x * \cos y * e^{(-(x-\pi)^2-(y-\pi)^2)}$	-100<x, y<100	(3.14, 3.14)
Matya's	$F(x,y) = 0.26*(x^2+y^2) - 0.48*x*y$	10<x, y<10	(0, 0)
Beale	$F(x,y) = (1.5 - x + xy)^2 + (2.25 - x + xy^2)^2 + (2.625 - x + xy^2)^2$	-4.5<x, y<4.5	(3, 0.5)
Booth	$F(x,y) = (x + 2y - 7)^2 + (2x + y - 5)^2$	-10<x, y<10	(1, 3)
Six Hump Camelback	$F(x,y) = (4 - 2.1*x^2 + \left(\frac{1}{3}\right)*x^4)*x^2 + x*y + 4*(y^2-1)*y^2$	-3<x<3 -2< y<2	(0.0898, -0.7126) (-0.0898, 0.7126)

V. SIMULATION RESULTS AND DISCUSSION

Table II and III below shows the Elapsed Time and Mean of both PSO and FFA on all the ten non-linear benchmark functions.

TABLE II. COMPARISON OF PSO WITH ELAPSED TIME AND MEAN

PSO		
Function	***Elapsed Time***	***Mean***
De-jong's	1.5355 secs	0.0221
Ackley's	10.1853 secs	2.2422
Rastrigin	6.2544 secs	1.0848
Rosenbrock	1.0603 secs	0.6210
Easom's	0.7701 secs	-0.6561
Matyas	1.5306 secs	0.0509
Beale	1.1900 secs	0.0435
Booth	0.9367 secs	0.3049
Six Hump Camelback	1.1599 secs	-1.0159
Four Peak	1.4604 secs	0.0747

TABLE III. COMPARISON OF FFA WITH ELAPSED TIME AND MEAN.

FFA		
Function	***Elapsed Time***	***Mean***
De-jong's	17.3444 secs	0.0268
Ackley's	32.6609 secs	19.1334
Rastrigin	115.627 secs	9.3281
Rosenbrock	14.7317 secs	5.4835
Easom's	9.3648 secs	-0.0000
Matyas	13.8999 secs	0.4417
Beale	16.6562 secs	1.2316
Booth	12.1996 secs	0.8295
Six Hump Camelback	16.0327 secs	-0.8885
Four Peak	22.4294 secs	0.4281

The convergence graph for each function between "Mean value of the function" and "Number of Iterations" is shown in the following figures 1 to 5.

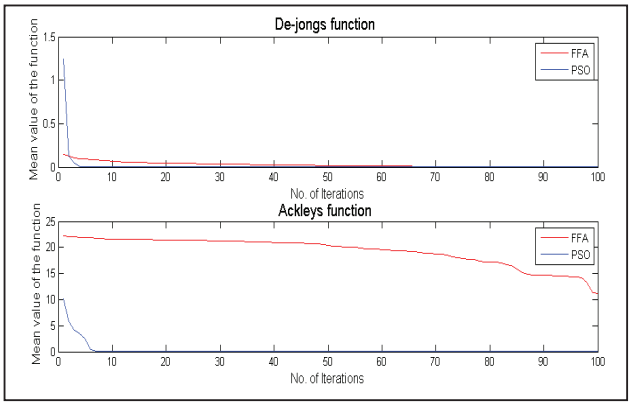

Fig. 2. Convergence graph for De-jong's and Ackleys functions

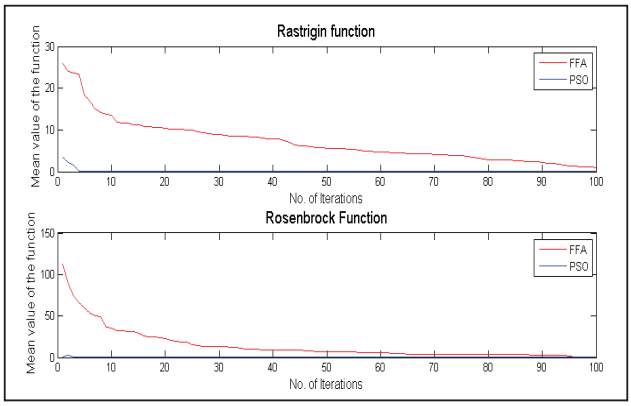

Fig. 3. Convergence graph for Rastrigin and Rosenbrock functions

Simulation have been performed in MATLAB 7.7 [20] and scratches have been developed using Intel(R) Core(TM) 2 Duo 2.80GHz , 3GB of RAM. All the algorithms have been conducted for same no. of population which is 100 and for 100 iterations.

It can be seen from Figure 2 that in the case of De-jongs function, PSO and FFA are both quick and reaches the optimum point, but in the case of Ackleys function, FFA does not reach the optimum point while PSO reaches the optimum point and also in a shorter time.

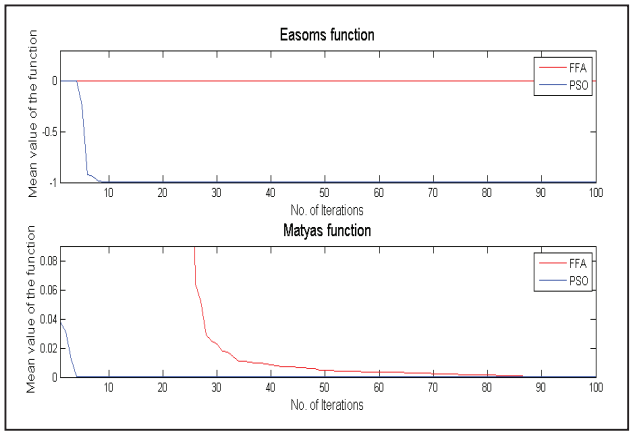

Fig. 4. Convergence graph for Easoms and Matyas functions

From Fig. 3, we see that for Rosenbrock function, PSO and FFA both reach the optimum point but PSO reaches much faster than FFA. But in the case of Rastrigin function, FFA does not reach the optimum point and takes much more time than PSO to even come close to the proximity of the optimum point. This shows that FFA has a tendency to converge less towards the optimum point when the function has a steep decline.

Fig. 4 shows the same fact that Easoms function, which is having a steep decline towards optimum point gives less convergent behavior with FFA and a better convergence with PSO. In the case of Matyas function, PSO converges much faster than the FFA and the mean value of PSO is much smaller than the mean value of FFA, if accounted closely.

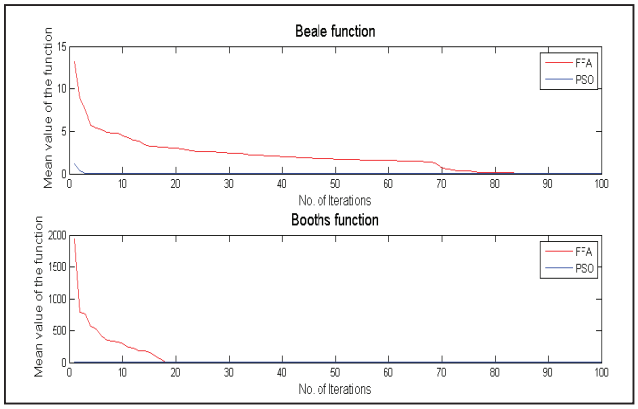

Fig. 5. Convergence graph for Beale and Booth functions

The convergence of Beale function is found to be much faster with PSO than with FFA which is shown in Figure 5. FFA is still outperformed by PSO in the case of Booths function.

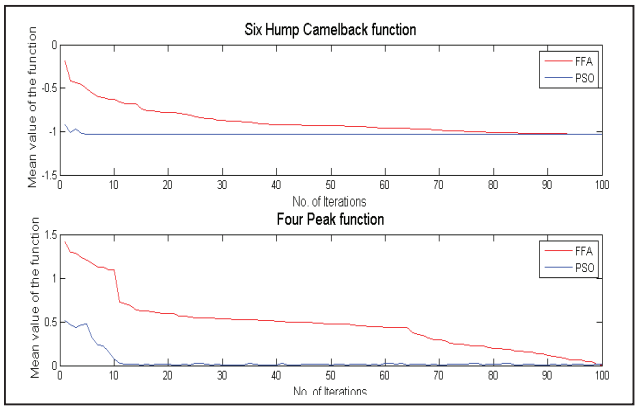

Fig. 6. Convergence graph for Six Hump Camelback and Four Peak functions

Fig. 6 shows convergence of Six Hump Camelback function where both PSO and FFA are converging with a significantly large time difference and in the case of Four Peak function, PSO converges after almost 10 iterations while FFA required 10 times more number of iterations than the PSO.

It can be seen with these results that PSO converges much faster in almost all the nonlinear benchmark functions with the least mean value and much less elapsed time than FFA. Sudden dip in the function is a matter of concern for FFA while PSO clearly converges to the optimum point with ease.

VI. CONCLUSIONS

PSO and FFA have been implemented on ten nonlinear benchmark functions. It is found that FFA is less stable in terms of Ackley, Rastrigin, Easoms and Beale functions. Elapsed time and mean value of simulations is minimum for PSO for most of the benchmark functions. In Matyas, Rosenbrock and De-jong's and Six Hump camelback function, PSO converges much faster than FFA. In the case of Four peak function, PSO converges to the optimum point within 10 iterations while FFA required 10 times more iterations to converge. Same is the case with the Booth function where PSO converges in just 0.9367 secs while FFA converged in 12.1996 secs. Also all the particles in PSO converge at global optimum point, while all the fireflies do not converge always at global operating point of nonlinear benchmark functions. Thus on analysis, it is found that PSO performs much better than FFA.

REFERENCES

[1] Xin-She Yang, "Engineering Optimization", 2010, Wiley.J and Sons.

[2] S.N. Sivanandam and S.N Deepa, "Introduction to Genetic Algorithms", 2008, Springer Publication.

[3] Z.Zhan, J.Zhang and H.S.Chung, "Adaptive Particle Swarm Optimization", IEEE Trans. on Systems, Man, and Cybernetics—Part B, Vol. 39, December 2009.

[4] H.Zang, S.Zhang, K.Hapeshi, "A Review of Nature-Inspired Algorithms", Journal of Bionic Engineering 7 Suppl. pp:232–S237, 2010.

[5] R. Eberhart and J. Kennedy, "A new optimizer using particle swarm theory." Proc.of 6th Int. Symp. Micro Machine and Human Science (MHS '95), pp. 39–43, 1995

[6] J. Kennedy and R. Eberhart, "PSO", Proc.of IEEE Int. Conf. Neural Networks, vol. 4, pp. 1942–1948, 1995.

[7] S. Kiranyaz, J. Pulkkinen and M. Gabbouj, "Multi-dimensional PSO for Dynamic Environments", International Conference on Innovations in Information Technology, 2008.

[8] M. O'Neill and A. Brabazon, "Self-Organizing Swarm (SOSwarm) for Financial Credit-Risk Assessment", IEEE Congress on Evolutionary Comp., pp:3087-3093, 2008.

[9] L.Cui and H.Wang, "Reach back Firefly synchronicity with Late Sensitivity Window in Wireless Sensor Networks," Proc. of IEEE Ninth International Conference on Hybrid Intelligent Systems, pp. 451-456, 2009.

[10] E. Bonabeau, M. Dorigo, G. Theraulaz, "Swarm Intelligence: From Natural to Artificial Intelligence", NY: Oxford University Press, NewYork, 1999.

[11] L. Coelho, D.Bernert and V.Mariani, "A Chaotic Firefly Algorithm Applied to Reliability-Redundancy Optimization", IEEE Congress on Evolutionary Computation (CEC),Pp: 517 - 521, 2011

[12] O. Babaoglu, T. Binci and M. Jelasity, "Firefly-inspired Heartbeat Synchronization in Overlay Networks", First International Conference on SASOs ,pp:77 - 86, 2007.

[13] Y. Zhao, Z. Zhang, Li Guo and B. Fang, "Revisiting the Swarm Evolution: A Long Term Perspective", IEEE Symposium on Computers and Communications (ISCC), pp: 1062 - 1067, 2011.

[14] Amir H. Gandomi, X.S.Yang and Amir H. Alavi, "Mixed variable structural optimization using Firefly Algorithm", IEEE, in press.

[15] M. H. Horng and T. W. Jiang, "Multilevel Image Thresholding Selection based on the Firefly Algorithm." Symposia and Workshops on Ubiquitous, Autonomic and Trusted Computing, pp: 58-63, 2010.

[16] T.Y.Chen and T.M.Chi, "On the improvements of the particle swarm optimization algorithm", Advances in Engineering Software 41 pp: 229–239, 2010.

[17] S. Janson and M. Middendorf, "On Trajectories of Particles in PSO", Proc. of the IEEE Swarm Intelligence Symposium (SIS), pp:150-155, 2007.

[18] B. Yang, Y. Chen and Z. Zhao, “A Hybrid Evolutionary Algorithm by Combination of PSO and GA for Unconstrained and Constrained Optimization Problems,” Proc of IEEE Int. Conf. on Control and Automation, pp. 166-170, 2007.

[19] S.F. Zheng et.al, "A Modified PSO Algorithm and Application", Proc. of the Sixth Intnl. Conf. on Machine Learning and Cybernetics, IEEE, pp: 945-951, 2007.

[20] S. Nakamura, “Numerical Analysis and Graphic Visualization with MATLAB,” Prentice Hall PTR,1996.

[21] A. W. Mohemmed, N. C. Sahoo and T. K. Geok, "Solving shortest path problem using PSO", Applied Soft Computing 8, Elsevier, pp:1643–1653, 2008.

[22] D. Bratton and J. Kennedy, "Defining a Standard for Particle Swarm Optimization", Proc. of the IEEE Swarm Intelligence Symposium (SIS), pp: 120 - 127, 2007.

[23] H. Someya, "Cautious particle swarm", IEEE Swarm Intelligence Symposium, pp: 1-6, 2008.

[24] X.S. Yang, “Firefly algorithms for multimodal optimization, Stochastic Algorithms Foundation and Applications,” SAGA 2009, Lecture Notes in Computer Sciences, 5792, pp.169-178, 2009.

[25] B. Y. Y. Chen and Z. Zhao, "Survey on Applications of Particle Swarm Optimization in Electric Power Systems", IEEE International Conference on Control and Automation, pp: 481-486, 2007.

[26] D.N.Jeyakumar, T.Jayabarathi and T.Raghunathan, "Particle swarm optimization for various types of economic dispatch problems", Electrical Power and Energy Systems 28, Elsevier,pp: 36–42,2006.

[27] Li Zhi-jie, Liu Xiang-dong, Duan Xiao-dong and Wang Cun-rui, "An Improved Particle Swarm Algorithm for Search Optimization", Global Congress on Intelligent Systems, IEEE, pp:154-158,2009.

[28] G.Theraulaz and J.L.Deneubourg, "On Formal Constraints in Swarm Dynamics", Proceedings of the 1992 IEEE International Symposium on Intelligent Control, pp: 225-233, 1992.

[29] J. Jumadinova and P. Dasgupta, “Firefly-inspired Synchronization for Improved Dynamic Pricing in Online Markets,” Proc of 2nd IEEE Intnl. Conf. on Self-Adaptive and Self-Organizing Systems, pp. 403-412, 2008.

[30] A. L.Christensen, R. O’Grady and M. Dorigo, “From Fireflies to Fault-Tolerant Swarms of Robots,” Trans. of IEEE on Evolutionary Computation, vol. 13, no. 4, pp. 754-766, 2009.

[31] Yamille del Valle, G.K. Venayagamoorthy et.al, "PSO: Basic Concepts, Variants and Applications in Power Systems", IEEE Transactions On Evolutionary Computation, VOL. 12, NO. 2, pp: 171-195, APRIL 2008.

[32] Rong-Jong Wai, Jeng-Dao Lee and Kun-Lun Chuang, "Real-Time PID Control Strategy for Maglev Transportation System via PSO", IEEE Transactions On Industrial Electronics, Vol. 58, No. 2,pp:629-646, FEBRUARY 2011

[33] Feras Al-Obeidat, Nabil Belacel, Juan A. Carretero and Prabhat Mahanti, "An evolutionary framework using PSO for classification method PROAFTN", Applied Soft Computing 11, Elsevier,pp:4971–4980, 2011.

[34] Qingnian Wang, Kun Yan, Xiaofeng Wan and Meiling Yuan, "Application of PSO in Fussy Neural Networks", Fifth International Conference on Information Assurance and Security, pp:158-161, 2009.

[35] James Kennedy, "Some Issues and Practices for Particle Swarms", Proc. of the IEEE Swarm Intelligence Symposium (SIS), pp:162-169, 2007.

[36] El-Gammal, El-Samahy, “A modified design of PID controller for DC motor drives using Particle Swarm Optimization PSO”, Power Engineering, Energy and Electrical Drives, International Conference on POWERENG’09, pp: 419-424,2009 .

CONCRETE RESEARCH LETTERS www.crl.issres.net Vol. 4 (1) – March 2013

Performance of Fly Ash and Stone Dust Blended Concrete in Acidic Environment

Verma, A.[1c], Shukla, M.[2], and Sahu, A. K.[1]
[1]Department of Civil Engineering,
Delhi Technological University, Delhi, INDIA
[2]Department of Civil Engineering,
Bundelkhand Institute of Engineering & Technology, Jhansi, INDIA

Received: 22/09/2012 – Revised 02/11/2012 – Accepted 26/2/2012

Abstract

Large scale housing construction activities require a huge amount of resources. Out of the total cost in a construction project the component of material cost has a major share. Therefore, the need of the hour is the replacement of costly and scarce conventional building materials by innovative, cost effective and environmental friendly alternatives. Fly ash and stone dust, generated as waste products in coal based thermal power plants and stone crusher industry respectively have been found appropriate for this purpose. The objective of this study was to investigate the performance of concrete mixes blended with fly ash and stone dust in chemically aggressive environmental conditions. The results indicate that a judicious selection of these waste products as ingredients in concrete shall further enhance benefits under aggressive environmental conditions of exposure.

Keywords: Fly Ash, Stone dust, Acidic Environment, Blended Concrete, Waste Products

1. Introduction

Concrete is many times exposed to aggressive chemical environments by coming in contact with acidic effluents in industry and sewage in underground pipes. Concrete is basically alkaline in nature and is also susceptible to acidic gases in the atmosphere, especially in and around urban industrial centers. The gaseous pollutant and particulates have a variety of damaging effects on concrete. Out of various gases present in atmosphere, the sulphurous ones have been found to be the most dangerous for calcareous materials such as cement mortar and concrete. Cohen and Bentur [1] have described the effect of sulfates on concrete as complex and Neville [2] has described the situation of the state of understanding in this respect as a confused one. Use of many environmentally polluting waste products such as fly ash and stone dust in construction industry has been gaining wide acceptance.

---

[c] Corresponding Author: Verma A.
Email: alokverma_dce@hotmail.com Telephone: +919968240071 Fax: +911127871328
© 20012-2013 All rights reserved. ISSR Journals

Mineral additives, which are pozzolanic in nature, densify the matrix and improve the interface of cement paste & aggregates and improve the performance of concrete in sulfate acidic environments. Kumar and Rao [3] have observed the effect of aggressive chemical environment on the setting time of cement and strength of concrete. They have reported that the setting times increase with the concentration of sulphate ions. This may be due to reduction in solubility of cement paste ions in presence of strong anions in solution (i.e., SO_4^{--}).

The loss in compressive strength of concrete cubes cured under different types of sulphates was observed with the passage of time. Tikalsky and Carrasquillo [4] have carried out the experiments to observe the influence of fly ash on the sulphate resistance of concrete and explained the dilution effect and pozzolanic effect of fly ash in cement. The fly ashes with a low amount of calcium hydroxide and amorphous calcium aluminate decrease the susceptibility of concrete to sulphate attack. Kumar and Rao [5] presented the results of experimental investigation showing the effect of sulphates on the strength of concrete under the conditions simulating cast in situ and precast situations. They concluded that the use of precasting in place of cast in situ is preferable in situations exposed to sulphate environments.

Wang [6] has carried out the experiments on hardened cement paste specimens made with different cement types and varying water-cement ratios. These specimens were immersed in 5% sodium sulphate solution maintained at constant pH value of 6. The mechanism of sulphate attack is evaluated with the help of XRD analysis in regard to leaching of $Ca(OH)_2$ and formation of gypsum and Ettringite. O.S.B. Al-Amoudi et al. [7] have observed the effect of magnesium sulphate and sodium sulphate on durability performance of plain and blended cements. It was observed that the deterioration of blended cement exposed to sodium sulphate environment is less. This is attributed to reduced quantity of calcium hydroxide which significantly mitigates the sulphate attack in these cements. Kumar and Rao [8] have carried out the compressive strength test on cubes exposed to time varying sulphate environment and measured cumulative damage to the material. Lawrence [9] has observed the types of disruption during sulphate attack on mortars and concretes and explained the chemical processes involved. It was concluded that partial replacement of ordinary Portland by various latent hydraulic binders can lead to improved sulphate resistance. Camps et al. [10] have observed the influence of surface absorption on sulphate attack and reported the sorptivity of mortar to be sensitive to the condition of cure and type of mortar skin in contact with the fluid. The influence of cure has a dominant effect on the capillarity of mortar which was reflected in the variation of porosity and strength. Rasheeduzzafar et al. [11] have reported the influence of cement composition on the corrosion of reinforcement and sulphate resistance of concrete. The C_3S/C_2S ratio of cement has been shown to have a significant effect on sulphate resistance of the cement. Building Research Establishment digest [12] discussed the factors responsible for sulphate attack on concrete below the ground level and recommended that suitable selection of cement type and concrete quality are important factors in resisting attack by naturally occurring sulphates.

Mehta [13] has carried out a laboratory investigation involving 16 fly ash samples of varying calcium content with the objective of clarifying the relationship between fly ash composition and sulphate resistance. The results show that rather than the chemical composition it is the mineralogical composition of cement fly ash interaction product that controls the sulphate resistance. Shukla et al. [14] have reported that the compressive strength of concrete increases with an increase in percentage replacement of sand by stone dust up to a percentage of about 40% and thereafter it reduces. Kumar [15] has studied the strength of fly ash blended cement concrete in marine environment. The blending of fly ash (10% and 20%) in both Type I and Type II cements has increased their resistance against seawater attack. Several aspects related with the utilization of fly ash in concrete in sulfate aggressive environments have been examined [16,17,18]. Research and field data on the effects of pozzolanas on durability and service life have been considered to be incomplete or at best inconclusive. Use of stone dust also has been found effective in improving the

strength of concrete. On the basis of literature review it may be suggested that the cement can be replaced upto 30% by fly ash and sand up to 40% by stone dust effectively. Use of super plasticizers also is required from the point of view of workability and strength of the blended concrete.

The objective of this study was to investigate the performance of concrete mixes blended with fly ash and stone dust in acidic sulphate environmental conditions. Normal concrete mix of strength grade 25 N/mm^2 and concrete mixes of the same grade blended with fly ash and / or stone dust and super plasticizers were tested under normal water curing and varying sulphuric acid concentration conditions up to 180 days. In this paper, performances of these mixes have been compared primarily on the basis of loss of compressive strength and residual compressive strength with time. The results indicate that a judicious selection of these waste products as ingredients in concrete is beneficial under aggressive environmental conditions of exposure.

2. Experimental Program

2.1 Materials

The cement used for investigation was ordinary Portland cement of Type I. The fly ash used for the investigation was procured from Indraprastha thermal power plant located in New Delhi, India. The physical and chemical properties of cement and fly ash are exhibited in Table 1. As a fine aggregate, sand obtained from the river Yamuna was used without any refinement. Stone dust of the Granite stone was procured from Goramachhia near the city of Jhansi in the state of Uttar Pradesh of India. The coarse aggregate was crushed granite of maximum size 20 mm. It was of angular shape and rough texture. Both the coarse and fine aggregates were thoroughly washed to remove dust as well as sulfates and chlorides, if any. The properties of stone dust and coarse & fine aggregates are shown in Table 2. The water used for mixing and curing was potable tap water free from organic and suspended impurities. The super plasticizer used was high molecular weight condensates of naphthalene formaldehyde polymer of brown colour and specific gravity 1.22. This has been found compatible with the cement used for the investigation. On the basis of chemical composition the potential composition of ordinary Portland cement was worked out using Bogue's equations and the percentages by weight of cement of C_3S, C_2S, C_3A and C_4AF were found to be 53.72, 22.58, 9.59 and 7.54 respectively.

2.2 Mix Proportions and Aggressive Environment

The concrete mix design was carried out for strength grade 25 N/mm^2 in which the cement, sand and coarse aggregates were proportioned in the ratio 1:1.3:2.5 with w/c 0.50. The details of mix designation are shown in Table 3. The dosage of superplasticizer was decided on the basis of Marsh cone test. In case of blended concretes, 1% superplasticizer by weight of cement was used to maintain the desired workability. In order to observe the effect of sulphuric acid on concrete specimens, one curing tank with ordinary water and two curing tanks of sulphuric acid having concentrations 0.1 N and 0.2 N respectively were prepared. Due precautions were taken while mixing sulphuric acid to water in the curing tanks and the concentration of the acid was maintained throughout the curing period.

The mixing of concrete was carried out in a power-driven mixer and 150 mm size concrete cubes were cast for each mix using a table vibrator. The moulds were stripped off after one day and cubes were immersed in each type of curing tank. After 28, 90 and 180 days curing, cubes from each tank were taken out and after air-drying they were tested for compressive strength. The

strength test was carried out in a universal testing machine maintaining the rate of loading as 1.25 mm/ minute.

Table 1: Properties of Cement and Fly Ash

S.N.	*Properties*	*Cement*	**Fly Ash**
	Physical Properties		
1.	Fineness – Blain's (m^2/Kg)	280	300
2.	Specific gravity	3.15	1.99
3.	Moisture content (%)	--	0.26
4.	Normal consistency (%)	36.00	--
5.	Setting times (minutes)		--
	Initial	85	
	Final	300	
6.	Compressive strength (N/mm^2)		
	3 days	24.60	--
	7 days	36.20	--
	28 days	49.10	--
7.	Soundness – Le Chatelier (mm)	0.70	--
	Chemical Properties (% by weight)		
8.	Silicon dioxide	19.87	40.2
9.	Calcium oxide	62.14	12.9
10.	Aluminum oxide	4.42	21.02
11.	Ferric oxide	3.01	11.7
12.	Magnesium oxide	2.91	2.43
13.	Sulphur trioxide	3.25	2.25
14.	Loss on ignition	2.4	2.29

Table 2: Properties of Aggregates

S.N.	*Properties*	*Stone Dust*	*Fine Aggregate*	**Coarse Aggregate**
1.	Specific gravity	2.74	2.63	2.65
2.	Water absorption (%)	2.14	1.68	0.54
3.	Fineness Modulus	2.55	3.05	7.4

Table 3: Mix Designations

S.N.	*Mix Designation*	**Proportions**
1.	A	M 25 concrete
2.	B	40% replacement of sand by stone dust in Mix A
3.	C	30% replacement of cement by fly ash in Mix A
4.	D	40% replacement of sand by stone dust and 30% replacement of cement by fly ash in Mix A

3. Results & Discussion

The cubes were taken out from various tanks after the completion of required curing time. The result of compressive strength of cubes of different mixes cured in ordinary water and sulphuric acid with concentration 0.1 N and 0.2 N for different curing periods are shown in Table 4.

Table 4: Compressive Strength of Cubes of Different Mixes

Age (Days)	*Mix Designations*	*Compressive Strength (N/mm^2)*			**Reduction in Compressive Strength (%)**	
		In Ordinary Water	In Sulphuric Acid With Concentration		In Sulphuric Acid With Concentration	
			0.1 N	0.2 N	0.1 N	0.2 N
28	A	36.0	35.28	33.90	2.0	3.9
	B	39.5	38.59	36.85	2.3	4.5
	C	33.0	32.50	31.46	1.5	3.2
	D	35.4	34.65	33.8	2.1	4.5
90	A	38.5	36.76	34.63	4.5	5.8
	B	41.4	39.33	36.85	5.0	6.3
	C	34.0	32.87	31.23	3.3	5.0
	D	37.6	35.98	34.48	4.3	8.3
180	A	42.0	38.47	34.62	8.4	10.0
	B	43.0	38.95	34.78	9.4	12.0
	C	35.5	33.01	30.37	7.0	8.0
	D	41.2	38.61	35.95	6.2	12.7

Before being tested for compressive strength the samples were visually examined. It was seen that visual effects in samples were the least in the case of water curing. These were the most obvious in the case of 0.2 N concentration of the acidic environment. Most of the samples showed efflorescence on their surfaces, with time, in the acidic environment. With the advancement of age, some of the samples were observed to have broken corners and edges. This effect was more prominent in the case of fly ash blended concrete mix samples. In acidic environments, some samples developed brown colour patches on their surfaces with time. This effect could be more clearly seen in the higher concentration of 0.2 N. In spite of these effects, samples could largely retain their structural integrity and shape throughout the duration of study.

Figure 1 shows variation of compressive strength of concrete cubes of different mixes cured in fresh water with age. The compressive strength of concrete cubes increases with age of concrete. The 90 days and 180 days compressive strengths are approximately 7.0% and 16.7% more than 28 days strength for the mix A, 4.8% and 8.86% for mix B, 3.0% and 7.58% for mix C and 6.2% and 16.38% for mix D. The percentage wise development of strength with time in ordinary water is similar for Mix A and Mix D and it is better for these compared to Mix B and Mix C.

The percentage increase of compressive strength remained positive for Mix A and Mix D for all curing environments in the duration of study. It is not so for Mixes B and C. Out of Mix A and Mix D, a larger rate of strength increase in all curing environments is reported by Mix D. The 90

days and 180 days compressive strengths are approximately 3.8% and 11.4% more than 28 days strength for 0.1N acidic environment and 2.9% and 6.4% more than the respective 28 days strength for 0.2N acidic environment for the Mix D. Respective values for the Mix A are 4.2% and 9% for 0.1N acidic environment and 2.2% and 2.1% for the 0.2N acidic environment.

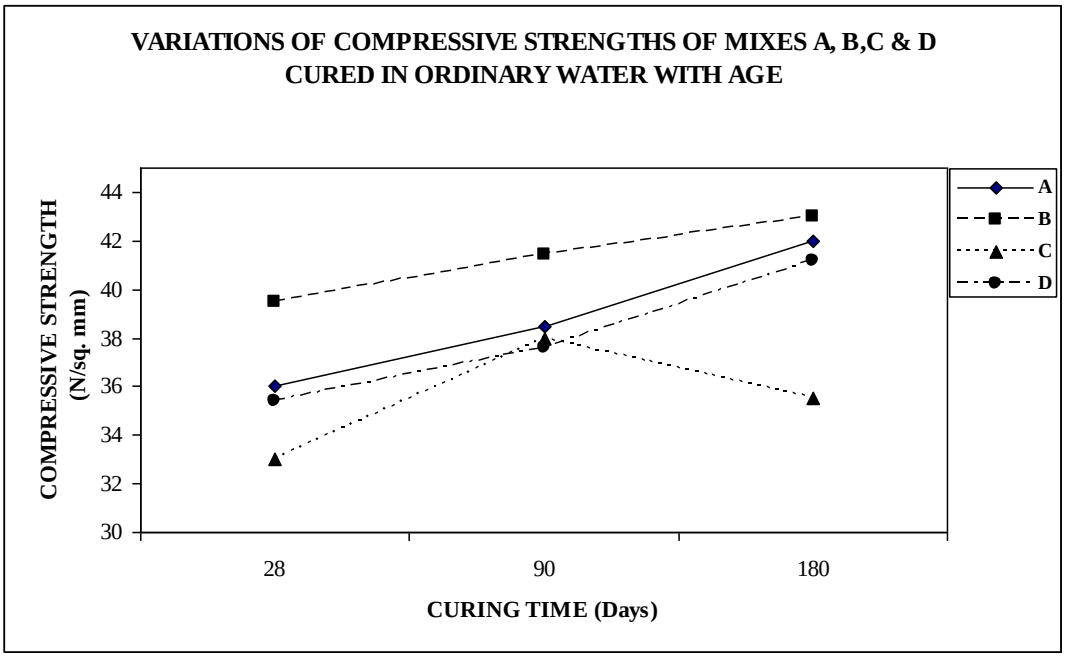

Figure 1: Variations of compressive strengths of different mixes with age

Figure 2 shows the loss in compressive strength of concrete cubes cured in acidic solution of various concentrations with age. The percentage loss in compressive strength at any age is estimated with reference to the strength of controlled concrete specimens in ordinary water at that age. It is seen that the loss in compressive strength of samples increases with sulphate ion concentration and age. This is due to the fact that acidic solution reacts with C_3A as well as C_3S compounds of cement. The more the concentration of the acidic solution, the formation of ettringite and gypsum is also more which results into the increased disintegration / deleterious effect.

In those mixes which were prepared by using stone dust, the loss of compressive strength increases with sulphate ion concentration and age. It is clear that the loss of strength in concrete with 40% replacement of sand is comparable to concrete made with only sand. But the addition of stone dust by replacing 40% sand increases the compressive strength of concrete. Hence the residual strength of the concrete after deducting the losses is still higher in concrete prepared with the stone dust.

The loss in compressive strength of concrete blended with fly ash is less compared to that of plain concrete at any age. It may indicate improved durability of fly ash blended concrete against the attack of sulphuric acid due to the dilution effect and pozzolanic effect. The dilution effect can be understood as the reduction in C_3A of the cement due to 30% replacement of cement by fly ash. The pozzolanic effect is due to the interaction between fly ash and calcium hydroxide, a byproduct of ordinary Portland cement. A refined calcium silicate hydrate binder matrix is formed. As a result, concrete becomes less permeable and the excess calcium present in fly ash is consumed and rendered unavailable to expansive formation of ettringite or gypsum compounds.

In case of the concrete blended with fly ash and stone dust the loss in compressive strength was observed which increases with curing time as well as the concentration of the sulphate ions. These losses in compressive strength at any particular age and concentration of sulphate ions are more than that of concrete blended with only the fly ash. This may be due to the conjoint effect of fly ash and stone dust. However, the residual strength in this case is comparable with that of plain concrete at the age of 180 days curing.

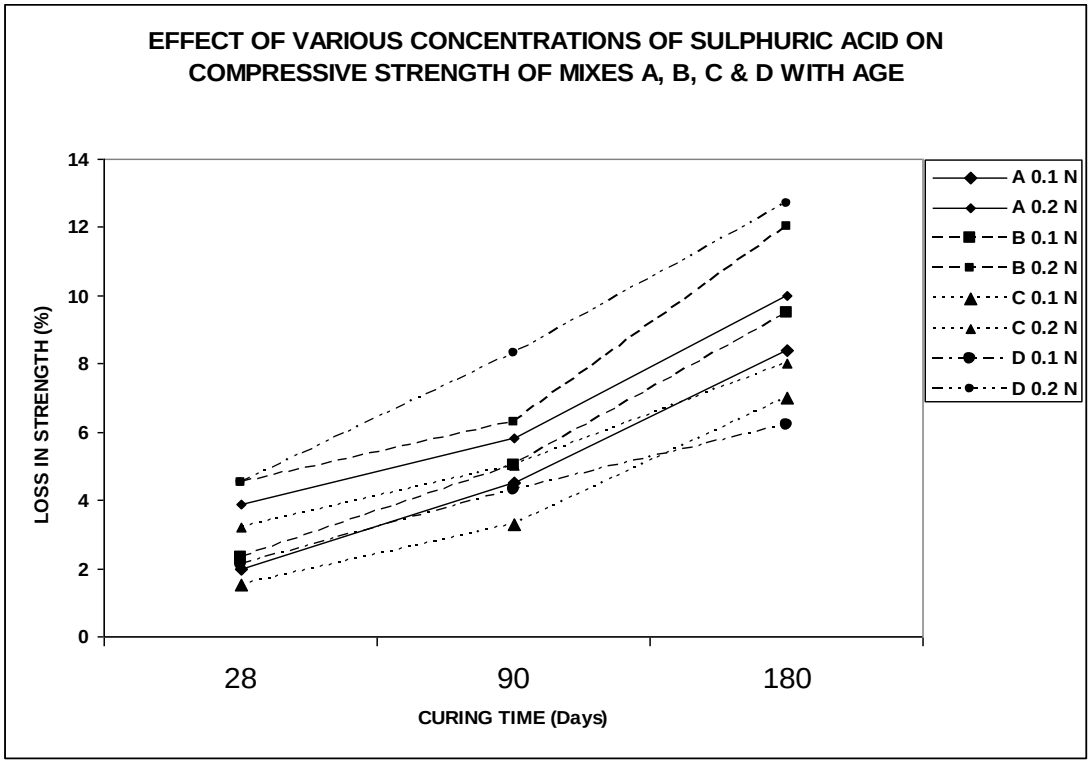

Figure 2: loss in compressive strengths of different mixes in acidic environments

To gain further insight into the trends of strength development of various types of plain and blended concrete mixes in acidic environments and to investigate into their respective performances, trend lines of strength developments of various mixes in different curing environments were drawn. These are shown in Figures 3, 4 and 5.

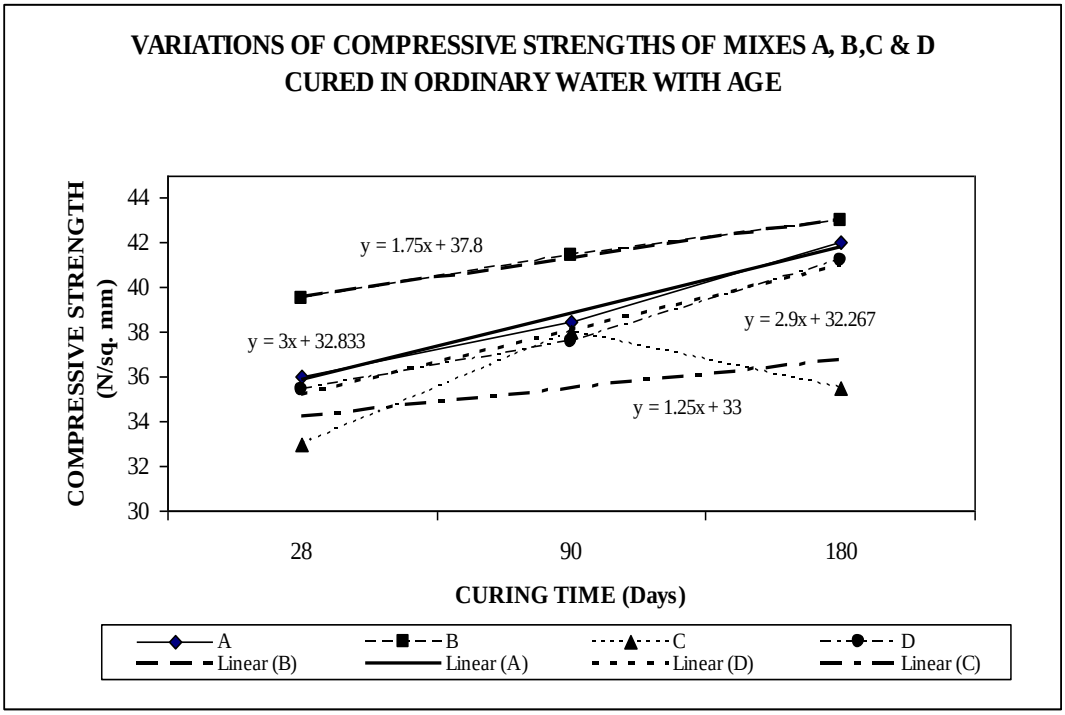

Figure 3: Trend lines for variations of compressive strength of mixes in ordinary water environment

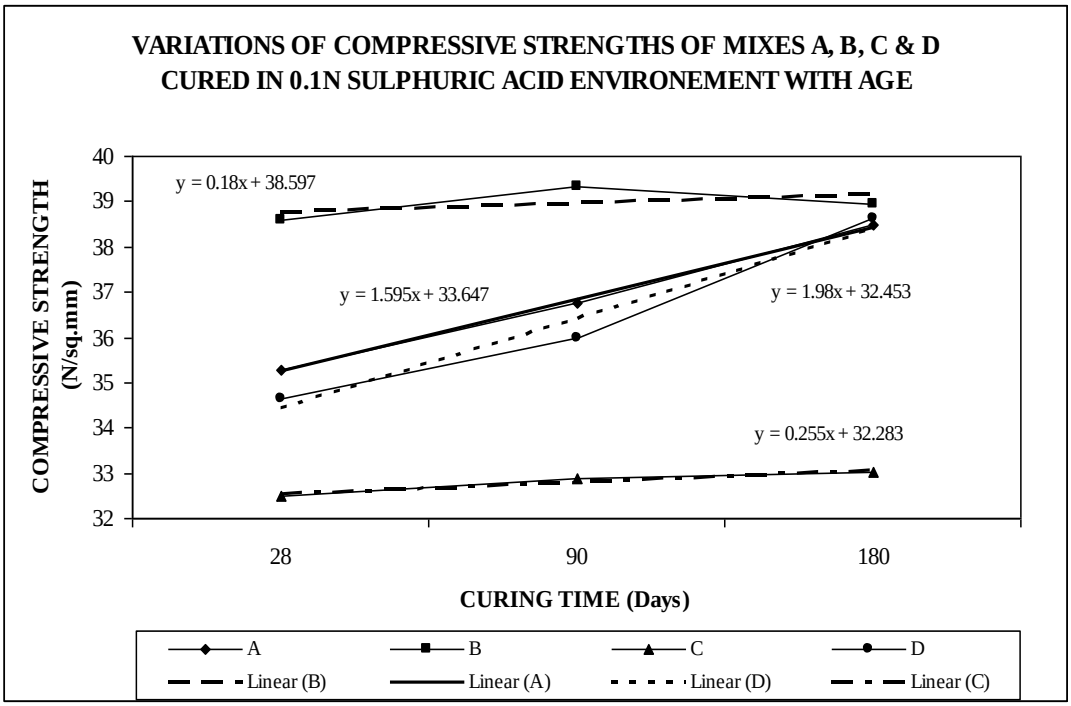

Figure 4: Trend lines for variations of compressive strength of mixes in 0.1N sulphuric acid environment

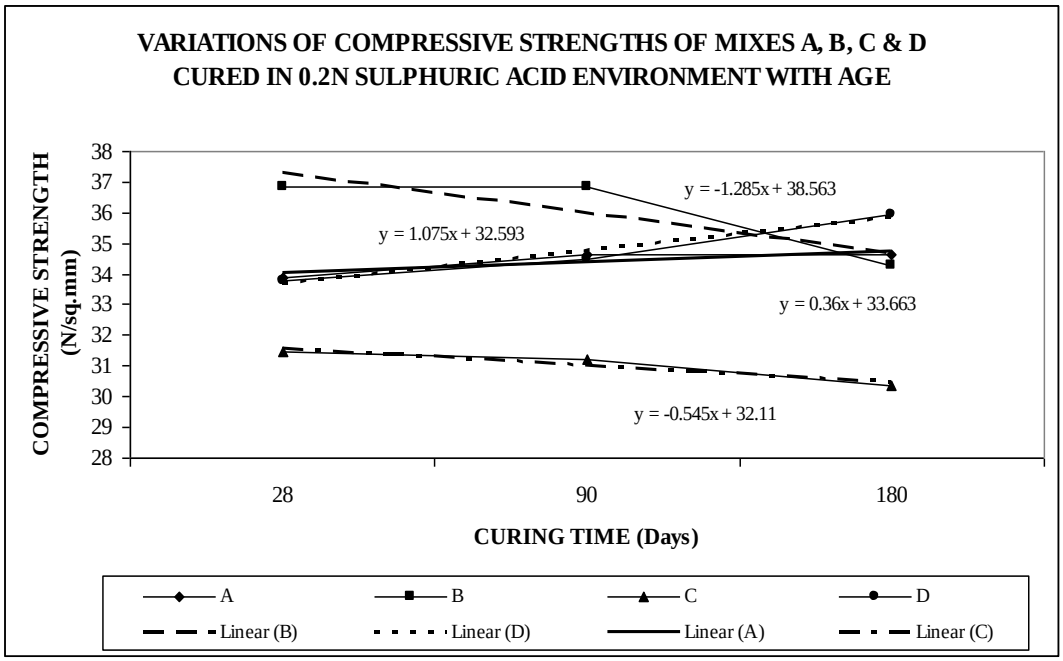

Figure 5: Trend lines for variations of compressive strength of mixes in 0.2N sulphuric acid environment

When slopes of these trend lines were considered, it was appreciated that slopes of these trend lines indicate the performance of these mixes in terms of strength development. A higher positive slope of a trend line of strength development with age in an environment would suggest a higher rate of strength development. Slopes of these trend lines are taken from their equations shown in Figures 3, 4 and 5. These equations are written in y=mx+c format where 'm' indicates the slope of the trend line. These values of slopes of trend lines are given in Table 5.

Table 5: Slopes of trend lines of strength development of different mixes

Name Of Mix	*In Ordinary Water (Case 1)*	*In 0.1 N Acidic Environment (Case 2)*	**In 0.2 N Acidic Environment (Case 3)**
A	3	1.595	0.36
B	1.75	0.18	-1.285
C	1.25	0.255	-0.545
D	2.9	1.98	1.075

It is seen that slopes of trend lines of strength development for all mixes in ordinary water (Case 1) and in 0.1 N acidic environment (Case 2) remain positive. When this is seen for 0.2 N acidic environment (Case 3), the slope is not positive for all the mixes. It remains positive for mixes A and D while becoming negative for mixes B and C. It indicates that type of environment (considering Case 1 and Case 3) and concentration of acidic environment (comparing Case 3 with Cases 1 and 2) is an important factor in the development of compressive strength of concrete. For Case 3 the slopes of trend lines of strength development are negative for Mixes B and C while these are positive for Mixes A and D. It shows better performance of Mixes A and D compared to Mixes B and C in terms of strength development for this case. For Cases 1 and 2 while the slopes of trend lines do not become negative, their slopes may still indicate relative performances of these mixes. It is clear that strength development is better for Mixes A and D for the case 1 while it is worst for the Mix C. It

may indicate a better strength increase for Mix B compared to Mix C due to a better filling of pore spaces by fine particles of stone dust and their shape and surface texture.

For the Case 2 the group of Mixes A and D still remain better than that of Mixes B and C. But relative positions of mixes giving a better performance are interchanged in both the groups. For this case, Mix D becomes the best one while Mix C becomes better than Mix B possibly because of benefits of pozzolanic reactions. It definitely indicates that nature of the concrete mix (e.g., containing fly ash) is an important factor in its performance in aggressive environment. The beneficial effect of the use of fly ash and stone dust is best seen in Case 3 where the slope of the trend line of strength development is the maximum for Mix D. Therefore, the utilization of stone dust as inert material and fly ash as a reactive material is beneficial especially when the concrete is exposed to the attack of aggressive environmental conditions such as acids containing sulphate ions.

4. Conclusion

On the basis of the experimental study the following conclusions are drawn.

1 The effect of the sulphuric acid environment on concrete is to decrease its compressive strength and this loss increases as a function of sulphate ion concentration and age of exposure.
2 The concrete blended with stone dust shows more loss of strength compared to plain concrete when exposed to acid environment. But the residual strength of concrete blended with stone dust is more than that of plain concrete.
3 The development of compressive strength of concrete blended with fly ash with age of curing is less compared to that in plain concrete. However, the concrete blended with fly ash shows less loss of strength compared to concrete blended with stone dust, when exposed to acid environment.
4 The residual strength of concrete blended with fly ash and stone dust is comparable with that of plain concrete at any age. Thus durable concrete can be made by replacing sand with stone dust up to 40% and cement with fly ash up to 30%. Hence stone dust and fly ash can be utilized effectively in making the durable concrete structures

REFERENCES

[1] Cohen, M.D. and Bentur, A., "Durability of Portland Cement Silicon Fume Paste in Magnesium Sulfate and Sodium Sulfate Solutions", A.C.I. Materials Journal, Vol. 85, No. 3, 1988, pp. 148 – 157.
[2] Neville, A., 'The confused world of sulfate attack on concrete', Cement and concrete research, 34(2004), pp. 1275-1296
[3] Kumar, S. and Rao, C.V.S.K., "Effect of Sulfates on the Setting Time of Cement and Strength of concrete", Cement and Concrete Research, Vol. 24, No. 7, 1994, pp. 1237 – 1244.
[4] Tikalsky, P.J. and Carras-quillo, R.L., "Influence of Fly Ash on the Sulfate Resistance of Concrete," A.C.I. Material Journal, Vol. 89, No.1, 1992, pp. 69-75.
[5] Kumar, S. and Rao, C.V.S.K., "Sulfate Attack on Concrete in Simulated Cast – In- Situ and Precast Situations", Cement and concrete Research, Vol. 25, No. 01, 1995, pp. 1-8.
[6] Wang, J. G., "Sulfate Attack on Hardened Cement Paste", Cement and Concrete Research, Vol. 24, No. 4 1994 pp. 735 – 742.

[7] Al – Amoudi, O.S.B. et al., "Effects of Magnesium Sulfate and Sodium Sulfate on the Durability Performance of Plain and Blended Cements" A.C.I. Material Journal, Vol. 92, No.1 1995. pp. 15-24.
[8] Kumar, S. and Rao, C.V.S.K., "Strength Loss in Concrete due to varying Sulfate Exposure", Cement and concrete Research, Vol. 25, No. 1, 1995, pp. 57-62
[9] Lawrence, C. D., "Sulphate Attack on Concrete", Magazine of Concrete Research, Vol, No. 153, 1990, pp.249-264.
[10] Camps, J. P., Jauberthie, R. and Rendell, F., "The Influence of Surface Absorption on Sulphate Attack, "Concrete Durability and Repair Technology", edited by R. K. Dhir and M. J. McCarthy, pp 197-207.
[11] Rasheeduzzafar et al. "Influence of Cement Composition on the Corrosion of Reinforcement and Sulfate Resistance of Concrete" A.C.I. Material Journal, Vol. 87, No. 2, 1990 pp. 114-122.
[12] Building Research Establishment Digest 250, "Concrete in Sulphate-Bearing Soils and Ground Waters", H.M. Stationary office, London, 1986.
[13] Mehta, P.K., "Effect of Fly Ash Composition on Sulfate 'Resistance of Cement", A .C.I. Material Journal, Vol. 83, No. 6, 1986, pp. 994-1000.
[14] Shukla, M., Sahu, A. K. and Sachan, A. K., "Performance of Stone dust as fine aggregate replacing sand in concrete and mortar", National Seminar on Advances in Special concretes Indian Concrete Institute,1998, Bangalore, pp. 241-248.
[15] Kumar, S., "Influence of Water Quality on the Strength of Plain and Blended Cement Concrete in Marine Environments", Cement and Concrete Research, Vol. 30(2000), pp. 345-350
[16] Torii, M. and Kawamura, M., "Effects of Fly Ash and Silica Fume on the Resistance of Mortar to Sulfuric Acid and Sulfate Attack," Cement and Concrete Research, Vol. 24 No. 2, 1994, pp. 361-370.
[17] Miyagawa, T., "Durability Design and Repair of Concrete Structures: Chloride Corrosion of Reinforcing Steel and Alkali-Aggregate Reaction", Magazine of Concrete Research, Vol. 43, No. 156, 1991, pp. 155-170.
[18] Almusallam, 'Effect of environmental conditions on the properties of fresh and hardened concrete', Cement and concrete research, 23-2001, pp. 353-361

Public Key Cryptography Using Genetic Algorithm

Swati Mishra, Siddharth Bali

Abstract*—Cryptography is an imperative tool for protecting and securing data. Security provides safety and reliability. Genetic Algorithm (GA) is typically used to obtain solution for optimization and search problems. This paper presents application of GA in the field of cryptography. Key Selection in public key cryptography is a selection process in which keys can be categorized on the basis of their fitness, making GA a good candidate for key generation. Primary goals of our algorithm was to provide fast and improved performance results having practical and feasible implementation. GA correlates nature to a great extent and produce population of keys such that keys with higher fitness value is replicated often. Good Fitness function helps in exploring search space more efficiently and effectively while bad fitness function traps GA operating in local optimum solution and losing its discovery power. Pearson's Coefficient of auto-correlation was used to calculate the fitness of keys. Ranking of keys was performed to find the best fit key. The private key generated cannot be derived from public key. The key samples satisfy gap and frequency test. Thus, purely random and non-repeating final keys were obtained by application of GA which increased the keys strength and security.

***Index Terms*— About four key words or phrases in alphabetical order, separated by commas.**

I. INTRODUCTION

GENETIC Algorithms (GAs) are adaptive heuristic search algorithms based on mechanics of natural selection and natural genetics. They belong to the class of Evolutionary Algorithms (EAs), which are used to find solutions to optimization problems using mechanisms based on biological evolution such as mutation, crossover, selection and inheritance. Cryptography is an imperative tool for protecting information. Public Key Cryptography (PKC) is an asymmetric outline that uses a pair of keys : a public key for encryption, and a private key for decryption. The fact that selecting key for the PKC is a selection process in which various keys can be categorized on the basis of their fitness, makes GAs a good candidate for the process to be followed for generating keys. The point which we intend to make in this paper is that if the quality of the random numbers produced to generate keys is good then the keys generated will always be purely random and non-repeating and hence increasing the strength of keys and security.

The main idea behind GAs is to replicate the randomness of the nature where population of individuals adapts to its surroundings through natural selection process and behavior of natural system. This means that survival and reproduction of an individual (i.e chromosome) is promoted by the elimination of unwanted traits.

GAs produce a population in such a way that the trait which is dominant, that is has higher fitness value is replicated more likewise rest is rejected based on threshold which is then evolved by the iterative application of a set of stochastic operators like mutation, crossover, and selection. This is also the fundamental concept behind evolution in nature. Highest rank of key fitness signifies the better fitness. The results obtained for generating keys should be good in terms of coefficient of autocorrelation. The samples satisfy the tests including gap test, and frequency test.

A simple GA makes use of following operators to transform a population into new population with better fitness :

A. Crossover

Crossover is a genetic operator that helps in joining two chromosomes to form a new chromosome. The newly generated chromosome is called child which takes one part of chromosome from each parent.

Number of crossovers depends on crossover-rate. Generally crossover rate is 2 to 5%.

$$\text{Number of Crossover} = \frac{(\text{No. of cells in a chromosome} * \text{No. of chromosomes} * \text{crossover rate})}{200} \quad (1)$$

Types of Crossover :

Crossover can be classified into following types :

1) Single point crossover

In this type of crossover, only one crossover point is chosen to generate new child.

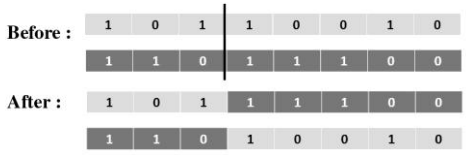

Fig. 1. Single Point Crossover

2) Two point crossover

This type of crossover involves selecting two crossover points to generate new child.

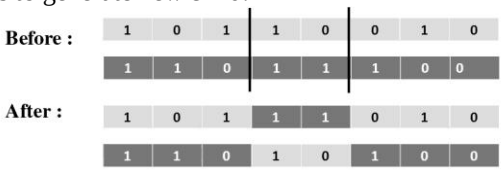

Fig. 2. Two Point Crossover

3) Uniform crossover : In this type of crossover bits of child are uniformly taken from both the parents.

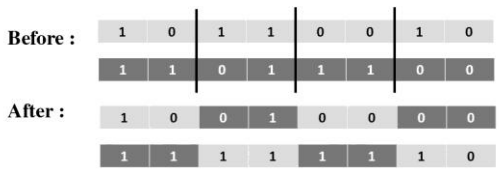

Fig. 3. Uniform Crossover

B. Mutation

Manuscript received on May 2013.

Swati Mishra, Department of Computer Engineering, Delhi Technological University, Delhi, India .

Siddharth Bali, Department of Computer Engineering, Delhi Technological University, Delhi, India.

Mutation is a genetic operator which changes one or more bit values in a chromosome. It is performed on a child after crossover which guarantees the entire state-space will be searched. Its performed infrequently (depending upon probability of altering a cell in a chromosome).
Number of Mutation =

$$\frac{(\text{No. of cells in a chromosome} * \text{No. of chromosomes} * \text{mutation rate})}{200} \quad (2)$$

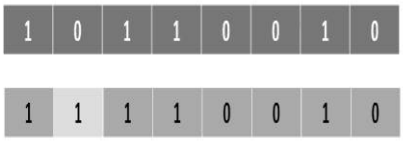

Fig. 4. Mutation

Types of Mutation :

1) Flipping of Bits : It involves selecting one or more bits of chromosome and inverting it.

2) Boundary Mutation : It involves randomly replacing chromosome with either lower or upper bound.

3) Non-Uniform Mutation : It is used to increase the probability that amount of mutation will go to 0 with the next generation.

4) Uniform Mutation : A chosen chromosome cell is replaced with a uniform random value whose range is selected by user.

5) Gaussian Mutation : It involves adding a unit gaussian random value to a chromosome cell.

C. Selection

Selection is the stage of a GAs in which individual chromosomes are chosen from a population for recombination (or crossover).The chromosome with higher fitness value will be considered better.

Classification of Selection :

1) Roulette-wheel Selection
If procedure is repeated until there are enough selected individuals.

2) Stochastic Universal Sampling
If instead of a single pointer spun multiple times, there are multiple, equally spaced pointers on a wheel that is spun once.

3) Tournament Selection
It refers to repeatedly selecting the best individual of a randomly chosen subset.

4) Truncation Selection
It involves taking the best half, third or another proportion of the individuals.

Population Size : The population size remains constant from generation to generation. Determining the size of the population is a crucial factor. Too small population size increases the risk of converging prematurely to a local minima. Initial Population can be determined by randomly or using some heuristic.

Fitness Function : The fitness function plays a very important role in guiding GA. Good fitness functions will help GA to explore the search space more effectively and efficiently. Bad fitness functions, can easily make GA get trapped in a local optimum solution and lose the discovery power. Fitness Function can be classified as Constant fitness function and Mutable fitness function.

II. LITERATURE REVIEW

This work proposes application of GA in the field of PKC which is an essential component of information security. The work makes an attempt to explore the key generating process for PKC to be unique and non-repeating by exploiting GA thus making PKC more secure as par to AES and DES.
To get an idea of the previous attempts made in this field, research papers have been studied and analyzed. In one of the work, GAs is used for searching the key space of encryption scheme [1]. In this work, cryptanalysis of vigenere cipher is done using GA. Another work proposes key generation using GA and deals with only vernam cipher [2].
Computer Scientist in the field of information security and privacy will be curious to investigate the role of GA in cryptography.
The concept of GAs has been highlighted in detail in one of the thesis, GAs in Cryptography by Bethany Delman [3]. In another work, key based bit level Cryptography is done using GA [4] consisting of two levels. In this Bitwise XOR operation is performed which is followed by Genetic Crossover and Mutation.
The primary goals of this work were to provide improved performance and to determine the validity of GA-based approach in the field of cryptography. Currently another work concerning PKC using neural network and GA is also been carried out. The present work is an essential part of bigger perspective work.

III. ALGORITHM FOR PUBLIC KEY CRYPTOGRAPHY USING GENETIC ALGORITHM

Step 1. Initial Population Generation : A GAs begins with a randomly generated set of individuals which is called initial population. Initial population array having values of 192 bit each respectively. Each bit is randomly assigned 0 or 1 bit value corresponding using a random generator function. If value obtained from generator is greater than 50 then bit value 1 is assigned otherwise 0 is assigned. Cell size of chromosomes depicts the key length. All 192 bits of chromosomes cell values are randomly assigned.
Size of initial 2D population array depends on value of MAX_POPULATION which is defined as macro.
Data Structure used : initPop[MAX_POPULATION][192], finalPop[MAX_POPULATION][192].
Step 2. Calculation of Chromosome Number and Threshold Check : Each chromosome should meet a threshold standard. This means that above average chromosomes should have more copies in the population, while below average chromosomes are subjected to extinction based on threshold. For each chromosome, a number is calculated, if its found to be greater than threshold then the corresponding chromosome is selected otherwise rejected. This threshold check is also performed in later stages.
Step 3. Now the GA enters a loop. At the end of each iteration, a new population is produced by applying a certain number of stochastic operators to the previous population. Each such iteration is known as a generation.

Step 4. Selection and Crossover : First a selection operator is applied, in which two parents are selected randomly from

initial Population. The selected parents are used to produce the individuals for next generation through the application of crossover operator.

For binary string individuals, one-point ring crossover, two-point, and uniform crossover are often used. To apply a crossover operator, parents are paired together using one-point Ring Crossover. The Two parents are combined in the form of ring and a random cut point is generated. With reference to this cutting point, one of the children (C1[ ] array) is created in the clockwise direction, while the other one (C2[ ] array) is created in anti-clockwise direction, as shown in Fig. 5. Every position of the child must retain a value found in the corresponding position of a parent, and the child must be a valid permutation. After Crossover, threshold check is performed.

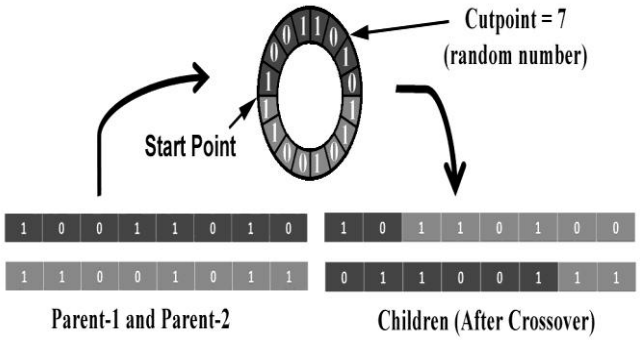

Fig. 5. Ring Crossover

Step 5. Mutation : Next, apply the mutation operator in which a child is randomly changed from what its parents produced in crossover. Number of Mutation is calculated using (2). Thus, Number of Mutation = (192 * 200 * 0.5) ÷ 200 = 96

Note : Sample space taken to be 200 and Mutation rate taken as 0.5%.
For each mutation, select bit number to be modified using random number function : rand()%192 (so one bit is only selected and flipped between 0 and 1).

Threshold check is performed after mutation.

Step 6. Fitness of key Calculation : Repeat the above mentioned steps until the final population array gets full. Chromosomes in final population are arranged according to their fitness values and the chromosome with the highest fitness value is selected.

Fitness value is calculated using following steps :

1) Calculate Shannon Entropy (H(X)) by comparing the percentage of randomness of bits in finalPop[][] against initialPop[][] array using the formula :

$$H(X) = -(p * (\log_2(p))) - ((1 - p) * (\log_2(1 - p))) \quad (3)$$

where p denotes percentage of randomness of finalpop[i][j] from initialpop[i][j] i.e. degree of movement from each bit.

2) Calculate Chi Square value against Shannon Entropy of each finalPop[][] array sample using the formula :

$$X^2 = (\text{observed_H} - \text{expected_H})^2/(\text{expected_H}) \quad (4)$$

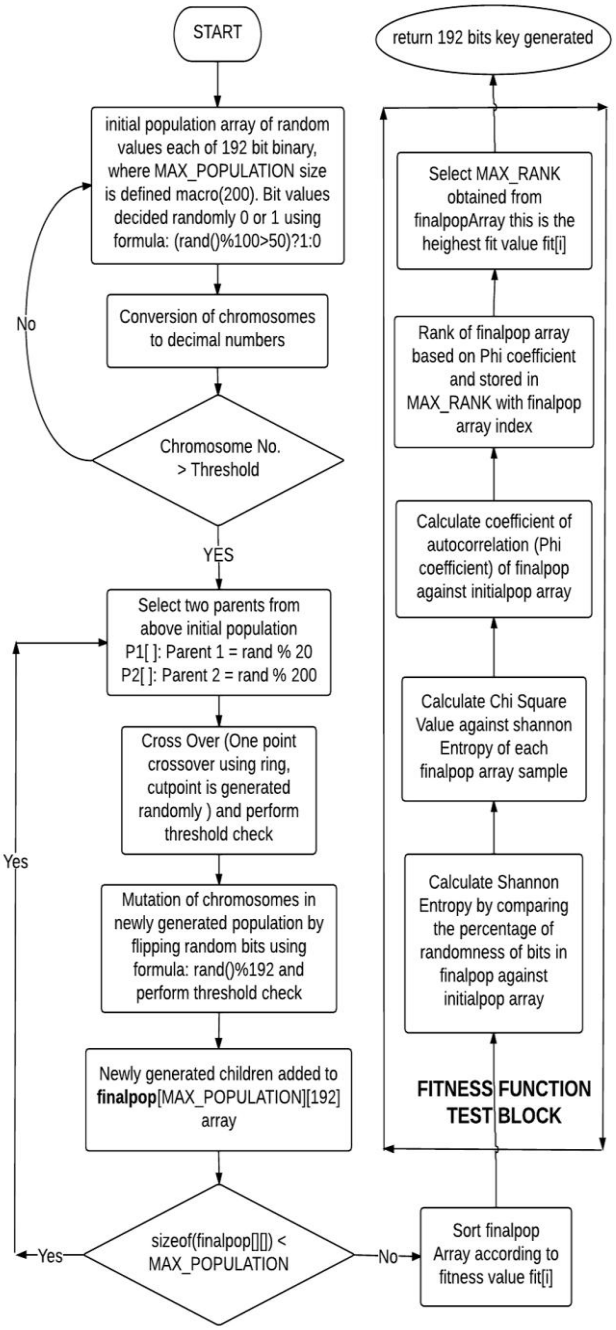

Fig. 6. Flowchart

3) Calculate the Coefficient of Auto-correlation (Phi-coefficient) of finalpop[][] against initialpop[][] array.

$$\varphi^2 = X^2 \div n, \text{ where n is sample space (n = 200).} \quad (5)$$

This coefficient of auto-correlation serves as fitness function and is used to find best fit random key.

Step 7. Ranking of Chromosomes based on Phi-coefficient : Calculate Ranks of chromosomes in finalpop[][] array based on Phi-coefficient and store the index of chromosome with maximum rank in MAX_RANK variable which serves as rank of maximum fit chromosome.

Step 8. Public and Private Key : Thus, chromosome with maximum fitness value serves as 192 bit key. This algorithm is run two times to get private and public keys respectively.

```
1  for(i=0; i<200; i++)
2  {       d1=0; d2=0;
3       for(j=0; j<192; j++)
4       {   int DM = abs(finalPop[i][j] - initPop[i][j]);
5           d1 += j * DM;
6           d2 += j * initPop[i][j];
7       }
8     // percentage of randomness observed
9       p = ((float) abs(d1-d2))/d2;
10  //H(X) calculation :
11  float observed_H=-(p*(log2(p)))-((1-p)*(log2(1-p)));
12  //X^2 Calculation
13   float X_2 = ((observed_H - expected_H) *
14          (observed_H - expected_H))/(expected_H);
15       summation_X_2 = summation_X_2 + X_2;
16      //PHI calculation
17   //PHI corresponding value against total 200 keys
18      float PHI=sqrt(X_2/200);
19          if( max_rank < PHI )
20         {   max_rank = PHI; //update max_rank to new
PHI
21              rank_index = i;
22          }
23  }
24  // find chi sqaure value avg of summation X_2
25  float chi_sqaure = summation_X_2/200;
```

Fig. 7. Pseudo-code

IV. RESULTS AND ANALYSIS

Degree Movement (DM) is calculated to depict the randomness of bit observed in final population against initial population. The implementation proposed generates good random sequences of keys and it is observed to have low running time . Index value is used to represent weights of equivalent position of bits. It is used for calculating expected value of chromosome whereas DM is used to calculate observed value. Percentage of Randomness is denoted by p.

Observed Shannon's Entropy (H(X)) is calculated by comparing the percentage of randomness of bits in final population with respect to initial population array using formula (3). Expected Shannon's Entropy is given by H(X) for p = 0.5 (when binary key consists of equal 0's and 1's).

Next, Chi-Square value is calculated against Shannon's Entropy of each chromosome in final population using formula (4). Statistically, coefficient of correlation gives a better idea of the relation between the items. Thus, coefficient of auto-correction (Phi-coefficient) is calculated using formula (4). The chromosome with maximum value of Phi-coefficient gets Maximum Rank and is taken to be as the best fit key. GAs co-relates the nature to large extent and produce a population in such a way that the trait which has higher fitness value is replicated more.

The chi-square test is used to determine whether there is a significant difference between the expected frequencies and the observed frequencies in one or more categories. Do the number of individuals or objects that fall in each category differ significantly from the number one would expect.

Steps for Chi-square Test :

1) Find observed frequencies
2) Find expected frequencies
3) Find the chi-square value using formula :
4) Find the degree of freedom.
5) Refer Chi Square Table for value.
6) If calculated chi-square value is equal to or greater than the value in table, reject the null hypothesis : differences in data are not due to chance alone.

Gap test counts the number of digits that appear between repetitions of a particular digit. It examines the length of gaps between occurrences of sample values and determines the length of consecutive subsequences with samples not in a specific range. Steps for Gap Test :

1) Specify the class df for the theoretical frequency distribution based on the selected class interval width.
2) Arrange the observed sample of gaps in a cumulative distribution.
3) Find D, the maximum deviation between F(x) and S(x).

Table I
Observed (d1) and Expected (d2) Values for 8-bit key sample

For ith iteration				Observed	Expected
index	initPop[i][j]	finalPop[i][j]	Degree Movement (DM)	index * DM	index * initPop[i][j]
0	1	0	1	0	0
1	1	1	0	0	1
2	1	0	1	2	2
3	1	1	0	0	3
4	0	1	1	4	0
5	1	0	0	0	5
6	0	1	1	6	0
7	0	0	0	0	0
Summation				12	11

The above table depicts calculation for 8-bit key length while in practice 192-bit key length was calculated and analyzed.

Table II
Chi-Square Test Results for 192-bit Key for 10 Sample space

sno	observed	expected	P	H(X) observed	H(X) expected	X^2	PHI=X^2/n
1	7170	7852	0.086856851757514	0.425890454495013	0.5	0.010984449469911	0.002196889893982
2	8618	8932	0.035154500671742	0.219616518939665	0.5	0.157229792903023	0.031445958580605
3	9305	8888	0.046917191719172	0.273154184892371	0.5	0.102918047663689	0.020583609532738
4	8240	7518	0.096036179835062	0.456303141288494	0.5	0.003818830922507	0.000763766184501
5	10114	7841	0.289886494069634	0.868574578083925	0.5	0.271694439219487	0.054338887843897
6	7256	7148	0.015109121432569	0.113018905968287	0.5	0.299508734275963	0.059901746855193
7	9003	8972	0.003455193936692	0.033229351125565	0.5	0.435749677301322	0.087149935460264
8	7580	7250	0.04551724137931	0.267040302883756	0.5	0.108540440960985	0.021708088192197
9	10222	15682	0.348169876291289	0.93242297114832	0.5	0.373979251953482	0.074795850390696
10	7980	8200	0.026829268292683	0.178232593754894	0.5	0.207068527443406	0.041413705488681

The above table is illustration for Chi-square test for 192-bit key. In practice the test was carried on 200 sample space.

4) Determine the critical value, D(α) for the specified value of α and the sample size N.
5) If the calculated value of D is greater, then null hypothesis of independence is rejected.

The frequency test results are shown in Table 1 and Table 2. Here chi-square test is applied on the random keys produced after running the program. Sample with maximum rank was found to have value 0.054 and Observed Chi-square was found to be 0.11 which was observed to be in acceptable range (i.e. below 6.63) according to chi-square table for $\alpha = 0.01$.

In Gap Test, all 200 sample were found to be unique and non-repeating possessing no relation of next random number with previous one. Security Services incorporated :

1) *Confidentiality :* It is used to protect identifiable information from forced disclosure to prevent its malicious use. Encipherment is done using the proposed algorithm.
2) *Data integrity :* No data modification confirmed that the information can only be accessed or modified by the authorised users. It is done using Digital Signatures.
3) *Authentication :* It gives the ability to know the identity of a user, without saying anything about the access rights of the individual.
4) *Non-repudiation :* Neither sender nor the recipient can deny later from sending or receiving the message respectively. It can be achieved using digital signatures.

V. CONCLUSION

The work has been implemented using C++. 192 bits random Public and Private key were generated. Public and Private Key Samples have been collected and analyzed in Microsoft Excel. In the analysis, population of 200 chromosomes were considered and were found to be randomly generated as proposed such that for each loop an entire new population is observed. Analysis was done for various sample values of keys generated which included frequency test (chi-square test) and gap test to check the nature of randomness and replication of chromosome, satisfactory results were obtained. In Gap Test, all 200 sample chromosomes were found to be unique and non-repeating possessing no relation of next random chromosome of keys with previous generated one.

Threshold check was also performed after crossover and mutation steps which was a deciding factor for the acceptance of chromosome generated throughout the process. This process is stopped when a given termination condition is met. Roulette Wheel Selection was applied which resulted in the replication of favorable data, thus making the population fitter. Ring crossover was applied and the rate of mutation was taken as 5%.

Fitness of keys was found using Pearson's coefficient of auto-correlation followed by ranking using phi-coefficient which decided the best fitness and has been verified from results. Results were analyzed even for large number of chromosomes > 200. The results have been compared with the standard results and were found to be in accepted and satisfactory range after verification. Coefficient of Correlation is found to be satisfactory, random chromosome is selected which is taken as key for PKC.

The primary goals of this work were to produce better and fast performance results and to determine the validity of typical GA-based methods in the field of cryptography. Thus from statistical analysis of results, final keys obtained from GA were observed to be purely random and hence increasing the strength of keys and security.

ACKNOWLEDGMENT

The authors thanks and gratefully acknowledges the support of Mr. H. Bhasin (DTU, Delhi) and Ms. S. Jhajharia (DTU, Delhi).

REFERENCES

[1] Omran, S.S.; Al-Khalid, A.S.; Al-Saady, D. M., "A cryptanalytic attack on Vigenère cipher using genetic algorithm," Open Systems (ICOS), 2011 IEEE Conference on, vol., no., pp.59,64, 25-28 Sept. 2011.
[2] Goyat, S., "Cryptography Using Genetic Algorithms (GAs). " IOSR Journal of Computer Engineering (IOSRJCE), Volume 1, Issue 5 , Volume 1, Issue 5 , June 2012.
[3] Delman, B., "Genetic Algorithms in Cryptography." Master of Science in Computer Engineering, Rochester Institute of Technology, Rochester, New York, July 2004.
[4] Som, S.; Chatergee, N.S.; Mandal, J.K., "Key based bit level genetic cryptographic technique (KBGCT)," Information Assurance and Security (IAS), 2011 7th International Conference on , vol., no., pp.240,245, 5-8 Dec. 2011.
[5] Goyat, S., "GENETIC KEY GENERATION FOR PUBLIC KEY CRYPTOGRAPHY." International Journal of Soft Computing and Engineering (IJSCE), Volume 2, Issue 3, July 2012.
[6] Sharma, L.; Pathak, B. K.; Sharma, R., "Breaking of Simplified Data Encryption Standard Using Genetic Algorithm ", Global Journal Of Computer Science And Technology, Volume 12, Issue 5, Version 1.0, March 2012.
[7] Khan F. U.; Bhatia, S., "A NOVEL APPROACH TO GENETIC ALGORITHM BASED CRYPTOGRAPHY ", International Journal of Research in Computer Science, Volume 2, Issue 3, pp. 7-10, 2012.
[8] Bhasin, H.; Bhatia, S., "Application of Genetic Algorithms in Machine learning", IJCSIT, Vol. 2 (5), 2011.
[9] Goldberg, D E., Genetic Algorithms in Search, Optimization, and Machine Learning. Reading, MA. : Addison-Wesley, 1989. Stallings, W., "Cryptography and Network Security : Principles and Practice", 3rd Edition. Prentice Hall. Boston Columbus Indianapolis.

Ms. Swati Mishra Currently a B.Tech. Student at Delhi Technological University. Her main area of research includes : Design and analysis of algorithms, intelligent system, cryptography and neural networks.

Mr. Siddharth Bali Currently a B.Tech. Student at Delhi Technological University. His main area of research includes : Design and analysis of algorithms, intelligent system, cryptography and neural networks.

SCOPE OF BETALAINS AS A FOOD COLORANT

Anuja Agrawal*

Research scholar, Chemistry department, Delhi Technological University (Government of NCT of Delhi), Bawana Road, Delhi-110042, India

---

Abstract: Consumers are avoiding foods containing synthetic colorants, which lead food industries to replace them by natural pigments. Food colorants may be classified into synthetic, nature-identical, inorganic and natural colorants. Natural colorants for food are made from renewable sources. Generally, the colorants are extracted from plant material, but other sources such as insects, algae, cyanobacteria and fungi are used also. Natural colorants are normally extracted and concentrated using either water or lower alcohols for water-soluble pigments and organic solvents for lipophilic pigments. But Legislation restricts which colorants are allowed, what sources may be used for that particular colorant, what solvents may be used to extract it and the purity of the pigment. Colorants are formulated to make them more suitable for a variety of foods and drinks and to increase their stability.

Key words: Food colorants, Natural colorants, Pigments, stability.

INTRODUCTION: Color is an important characteristic of food. First impressions are based on the color of the food. Human beings, like most animals, come in contact with their surroundings through color, and things can or cannot be acceptable based on their color characteristics Is the fruit immature, ripe, or overripe? Is the food fresh? Based on these first impressions, a judgment is made whether the food is safe to eat or not and whether it can be good in taste or not. Since color is closely associated with expectations, the addition of color to food is a way to fulfill these expectations. Color is

added to food for one or more of the following reasons: (1) to replace color lost during processing, (2) to enhance color already present, (3) to minimize batch-to batch variations, and (4) to color otherwise uncolored food. Food colors can be divided into four categories: (1) natural colors, (2) nature-identical colors, (3) synthetic colors, and (4) inorganic colors. Natural colors are pigments made by living organisms. Nature-identical colors are man-made pigments which are also found in nature. Examples are β-carotene, canthaxanthin, and riboflavin. Synthetic colors are man-made colors which are not found in nature—these are often azo-dyes. Examples of inorganic colors are titanium dioxide, gold, and silver.

The terms “pigment” and “dye” are often used interchangeably. Strictly speaking, a pigment is insoluble in the given medium, whereas a dye is soluble This distinction may be difficult to maintain if nothing is assumed about the medium, and in the following the term “pigment” will be used for colored substances in general.

NECESSITY OF FOOD COLORANTS:

The Natural and synthetic pigments are used in medicines, foods, clothes, furniture, cosmetics, and in other products. However, natural pigments have important functions other than the imparted beauty. Development of foods with an attractive colors appearance is an important goal in the food industry. . Increasingly, food producers are turning to natural food colors, since certain artificial color additives have demonstrated negative health issues following their consumption. Because of the deficiencies of existing natural food colorants, the demand for natural colorants is repeatedly raised by the food industry. This demand can be fuelled by research to offer a more natural-

healthy way of coloring foods and provide a clean label declaration. Therefore, part of plant pigment research is seeking new sources of pigments. This will not only directed in finding natural alternatives for synthetic dyes but also discover new procedures for the pigment production. The most common plant pigments are carotenoids, chlorophylls, anthocyanins and betalains. Most research has been focused on carotenoidsand and anthocyanins but betalains have recently gained interest in food science . Compared to anthocyanins, betalains are ideal for coloring low-acid foodstuff as they maintain their color over a wide array of pH, from 3 to 7.

Betalains as a pigment-Beet (*Beta vulgaris* subsp. *vulgaris*) has been bred to produce a number of varieties, some of which are used as fodder and some of which are used for human food consumption: chard (var. *cicla*), sugar beet (var. *altissima*), and beetroot (var. *rubra*). Beetroot is a variety with a strongly colored root. The purple root owes its color to the presence of betalains. Betalains are found in other plants than beetroot, but beetroot is the only allowed source of betalain colorant in the EU and the USA [2]. Betalains are actually comprised of two groups of pigments: the red–purple betacyanidins and the yellow betaxanthins (Fig. 1), both of which are water-soluble. Betacyanidins are conjugates of cyclo-DOPA and betalamic acid, and betaxanthins are conjugates of amino acids or amines and betalamic acid. Just as with anthocyanins, the betacyanidins (aglycones) are most often glycosylated, in which case they are called betacyanins, and the sugar residue may also be acylated. The red–purple betacyanins comprise the major part of pigments in beetroot, and of these a single one, betanin, comprises 75–95 % [2]. Compared to anthocyanins, beetroot color is more purple and brighter, and the color hue does not change with pH in the range 4–7. The major

disadvantage of beetroot color is its low heat stability.

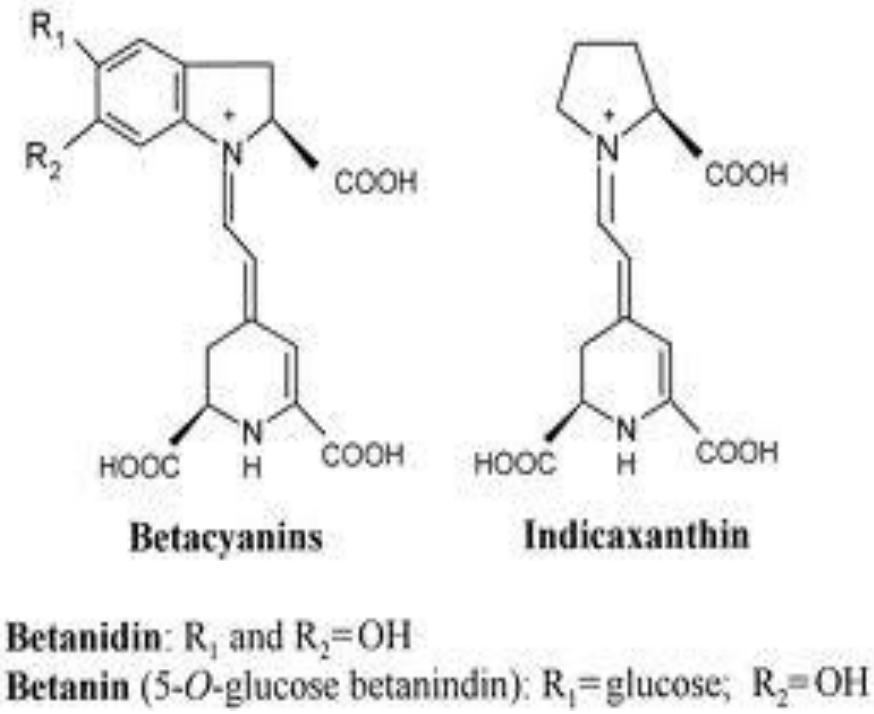

Fig.1 Structure of Betalains

PLANT SOURCES OF BETALAINS

Betalains can be found in roots, fruits and flowers [15]. They absorb visible radiation over the range of 476–600 nm with a maximum at 537 nm at pH 5.0. The few edible known sources of betalains are red and yellow beetroot (Beta vulgaris L. ssp. vulgaris), coloured Swiss chard (Beta vulgaris L. ssp. cicla), grain or leafy amaranth (Amaranthus sp.) and cactus fruits, such as those of Opuntia and Hylocereus genera [3,11,16.20].

The major commercially exploited betalain crop is red beetroot (Beta vulgaris), which contains two major soluble pigments, betanin (red) and vulgaxanthine I (yellow). According to Nilsson (1970), the betacyanin and betaxanthin contents of red beetroots vary within the ranges 0.04–0.21% and 0.02–0.14%, respectively, depending on the

cultivar[21], although some new varieties produce higher betalain contents[6,7,14] analysed five red beet varieties (‘Bonel’, ‘Nero’, ‘Favorit’, ‘Rubin’ and ‘Detroit’) in terms of their pigment composition. In all cases, the major red-violet pigments were betanin, isobetanin,betanidin and isobetanidin, and the major yellow components were vulgaxanthin I and vulgaxanthin II. ‘Bonel’, ‘Favorit’ and ‘Rubin’ exhibited the highest betacyanin contents (around 0.08%), while the ‘Nero’ variety showed the poorer betacyanin content (near 0.06%). The variety ‘Rubin’ showed the highest betacyanin ⁄ betaxanthin ratio (2.08), so was considered as the most suitable for food colourant production.

BIOTECHNOLOGICAL PRODUCTION OF BETALAINS

Some authors have investigated beet cell cultures for producing betalains [1,12]. With this technology, it would be easier to control quality and availability of pigments independently of environmental changes[4]. However, these cultures are unable to compete with the beetroot, which is an abundant and inexpensive crop which may produce up to 0.5 g of betanin per kg of roots [7]. The low productivity of the current bioreactor systems available and the high cost of the process impair its economic feasibility. Then, the selection of a bioreactor and cultivation techniques for optimal culture growth and betalain production is one of the most important issues to be solved [9].

CLASSIFICATION

They can be divided into two structural groups, the yellow betaxanthins (from Latin *beta*, red beet and Greek *xanthos*, yellow) and red-purple betacyanins (*kyanos*, blue color), depending on R1-*N*-R2 moieties(fig.1).

Table1 : Some Fully Identified Naturally Occurring Betalains[5]

Betalain[A]*1	**Residue[B]*2**
1.Aglycones	
Betanidin	**-**
2. Betanin group	
Betanin	5-O-Glc
Phyllocactin	5-O-Glc
Lampranthin-I	5-O-Glc
3. Amaranthin group	
Amaranthin	5-O-Glc-2-O-GlcU
Celosianin II	5-O-Glc-2-O-GlcU
4. Bougainvillein	
Bougainvillein	5-O-Glc-2-O-Glc
5. Gomphrenin group	
Gomphrenin-I	6-O-Glc
6. Betaxanthins	
DOPAxanthin	DOPA
Indicaxanthin	Proline

Portulaxanthin-II Vulgaxanthin-I	Glycine Glutamic acid

***1 A** Names were standardized by Strack et al.
***2 B** Abbreviations: **Glc** β-D-Glucose; **GlcU** β-D-Glucoronic acid; **DOPA** 3,4-dihidroxyphenylalanine.

More than 50 betalains are well known, and all of them have the same basic structure in which R1 and R2 may be hydrogen or an aromatic substituent. Their color is attributable to the resonating double bonds. Conjugation of a substituted aromatic nucleus to the 1,7-diazaheptamethinium chromophore shifts the absorption maximum from 480 nm in yellow betaxanthins to 540 nm in red-purple betacyanins.[19] . Betacyanin structures show variations in their sugar (e.g., 5-*O*–D-Glucose) and acyl groups (e.g., feruloyl), whereas betaxanthins show conjugation with a wide range of amines (e.g., glutamine) and amino acids (e.g., tyrosine) in their structures. Table 1 shows some well-studied betalains.

Up to date more than 50 structures of naturally occurring betalains have been identified.

IMPORTANCE OF BETALAINS AS FOOD COLORS

(a)Stability of betalains

When betalains are used as food colorants, color stability is a major concern. There are several factors that have been recognized to affect the stability of these pigments:

1. pH*.* The hue of betalains is unaffected at the pH between 3.5 to 7; the values of most foods are in this range. Betalain solutions in this pH range showed a similar visible for betacyanins and betaxanthins.

2. Temperature*.* Temperature also shows a clear effect on betalain stability. Thermal kinetic degradation of betanin has been evaluated by several authors. It has been reported that thermostability of betanin solutions is pH dependent and partially reversible. Heating of betanin solutions produces a gradual reduction of red color, and eventually the appearance of a light brown color.

3. Light. Von Elbe et al. found that rate of betanin degradation increased 15.6% after pigment daylight exposure at 15ºC. Degradation of light-exposed betalains followed a first-order kinetic. In addition, it was observed that degradation was higher at pH 3.0 (*k* = 0.35 days-1) than at pH 5.0 (*k* = 0.11 days-1), when betacyanins were exposed to fluorescent light.

4. Water activity*.* Recognizing the importance of water in many degradation reactions, it is not surprising that water activity (aw) is included among the primary factors affecting the betalain stability and/or color of a food product containing these pigments. Because the degradation reaction does involve water, the greatest stability of betalains has been reported in foods or model systems of low moisture and aw.

5. Oxygen*.* Oxygen causes a product darkening and loss of color. Von Elbe et al stored buffered betanin solutions at pH 7 under atmosphere of air and nitrogen for 6 days at 15ºC; it was observed that color degradation increases up to 15% due to air conditions. Betanin reacts withmolecular oxygen, producing pigment degradation in air-saturated solutions.

Several methods have been reported to prevent the destruction or to improve the stability of pigments, including degassing, addition of antioxidants and stabilizers, control of pH, minimal heat treatment and these efforts have been directed to their application in food products.

(b) Processing and Stability in Foods

The sensitivity of betalains to different factors suggests that their application as food colorants is limited. Based on these properties, betalains can be used in foods with a short shelf-life, produced by a minimum heat treatment, and packaged and marketed in a dry state under reduced levels of light, oxygen, and humidity . Betalains have several applications in foods, such as gelatins desserts, confectioneries, dry mixes, poultry, dairy, and meat products. Table 2 summarizes some applications of betalain pigments in food products. The amount of pure pigment required in these foods groups to obtain the desired color is relatively small and for most applications does not exceed 50 ppm of betalains, calculated as betanin. Problems associated with betalain degradation and pigment recovery during the processing operations are of economic importance and must be solved to betalains displace the application of synthetic dyes in some food products. .

Nowadays, beet roots represent the main commercial source of betalains (concentrates or powders). . The average pigment content of beets is approximately 130 mg/100 g fresh weight, but new red beet varieties produce around 450 to 500 mg/100 g fresh weight. Furthermore, this value is increasing as advanced selection is developed.

On a laboratory scale, betalains can be obtained by employing reverse osmosis, ultrafiltration solid -liquid extraction, and diffusion.

FUTURE TRENDS

Since the 1960s people have shown a clear preference for natural products, including pigments, because more nutritious and healthy characteristics have been associated with them. Moreover, one of the main problems to be solved, that natural colors approved by FDA and European Union do not cover all ranges of colors (e.g., blu

TABLE 2: Applications of Beet Root Powder as Natural Color in Food Products

Food products	**Shade**	**Level**
1. Dairy products:		
(a)· Strawberry yogurt	Rose–pink	0.08%
(b)· Ice creams	Pink	0.27%
	Rose–pink	0.25%
2. Meat products:		
·(a)Sausages	Pink	550 mg/100 g
·(b) Cooked ham	Pink–brown	0.15%
3. Dry powder beverages	Strawberry	1.1%
	Raspberry	1.5%
	Blackcurrant	1.0%
4. Water ices	Strawberry–red	0.8 to 1.0%
	Raspberry	0.5%
5. Marzipan	Pastel–red	0.45%
	Bluish–red	1.5 mg/cm2
6. Biscuit creams	Pink	0.27%
7. Baked goods	Pink–brown	2.5%

8.Hard candies	Pink	0.15%
9. Fruit cocktails	Raspberry–red	1.5%
10. Jellies	Raspberry–red	0.18%

Thus, many research groups are looking for new sources of natural pigments; however, these efforts have vanished, because under the current legislation the FDA or the European Union approval of new natural sources of pigments is very difficult. Consequently, it is expected that the world global market must contribute to the implementation of more realistic laws.

On the other hand, it has been clearly established that technology development has introduced new methodologies or processes to avoid the intrinsic instability and solubility problems of natural pigments, and today most of these problems can be solved through technological processes. Thus, a more adequate and updated legislation will provide a broad range of natural colors, and importantly with better stability characteristics.

Anthocyanins are the most widespread and most used natural pigments covering the red-purple colour range. However, the instability of anthocyanins at pH values above 3 [17] makes betacyanins the natural pigments of choice to provide red-purple colour shades to low acid foods. Moreover, betalains can effectively be stabilised by ascorbic acid, which on the other hand, impairs anthocyanin stability [15]. Hence, application of betalains instead of anthocyanins for colouring foods with high ascorbic acid contents may be interesting[9].

The demand for better natural- colored foods by an important sector of the society will be increased because it is highly likely that future studies will increase people's conscience about the positive health benefits of natural pigment consumption. Remarkably, the most impressive advances in these aspects have been reached using molecular biology techniques, and this will be so in the near future. Interestingly, model systems for pigment production under controlled conditions are now available, but production at the industrial level has not been feasible yet. Thus, carotenoid production by yeasts, bacteria and fungi, and anthocyanin and betalain production by plant tissue cultures require the development of better biotechnological approaches.Production of colors by fermentation has a number of advantages: cheaper production, possibly easier extraction, higher yields, no lack of raw materials, and no seasonal variations. Fermented colors are already used today: *D. salina*, *B. trispora*, spirulina, and monascus. It is not unlikely that new, fermented colors such as lycopene from *B. trispora* will become allowed in the near future. A giant leap forward in color production could be achieved by combining genetic manipulation and fermentation.

Finally, new colorants would have to be approved by the authorities, which is very costly because of the various toxicological studies needed to confirm the safety of a new food additive.

REFERENCES

[1] Akita, T., Hina, Y. & Nishi, T. (2000). Production of betacyanins by a cell suspension culture of table beet (Beta vulgaris L.). Bioscience, Biotechnology, and Biochemistry, 64, 1807–1812

[2] Alan Mortensen(2006) Carotenoids and other pigments as natural colorants *Pure Appl. Chem.*, Vol. 78, No. 8, pp. 1477–1491

[3] Cai, Y., Sun, M. & Corke, H. (1998). Colourant properties and stability of Amaranthus betacyanin pigments. Journal of Agricultural and Food Chemistry, 46, 4491–4495.

[4] Do rnenburg, H. & Knorr, D. (1997). Challenges and opportunities of metabolite production from plant cell and tissue culture. Food Technology, 51, 47–54.

[5] F. Delgado-Vargas,1 A. R. Jiménez,2 and O. Paredes-López3*(2000) Natural pigments:carotenoids,anthocyanins and betalains- characteristics, biosynthesis ,processing and stability *Critical Reviews in Food Science and Nutrition,* 40(3):173–289

[6] Gaertner, V. & Goldman, I.L. (2005). Pigment distribution and total dissolved solids of selected cycles of table beet from a recurrent selection program for increased pigment. Journal of the American Society for Horticultural Science, 130, 424–433

[7] Gasztonyi, M.N., Daood, H., Hajos, M.T. & Biacs, P. (2001). Comparison of red beet (Beta vulgaris var. conditiva) varieties on the basis of their pigment components. Journal of the Science of Food and Agriculture, 81, 932–933

[8] Han, D., Kim, S. J., and Kim, D. M.(1998) Repeated regeneration of degraded red beet juice pigments in the presence of antioxidants, *J. Food Sci.,* 63(1): 69–72

[9] Herbach, K.M., Stintzing, F.C. & Carle, R. (2006b). Betalain stability and degradation – structural and chromatic aspects. Journal of Food Science, 71, R41–R50.

[10] Jimenez-Aparicio, A. & Gutierrez-Lopez, G. (1999). Production of food related colourants by culture of plant cells. The case of betalains. Advances in Experimental Medicine and Biology, 464, 195– 210.

[11] Kugler, F., Stintzing, F.C. & Carle, R. (2004). Identification of betalains from petioles of differently coloured Swiss chard (Beta vulgaris L. ssp. cicla [L.] Alef. cv. Bright Lights) by highperformance liquid chromatography–electrospray ionization mass spectrometry. Journal of Agricultural and Food Chemistry, 52, 2975– 2981.

[12] Leathers, R.R., Davin, C. & Zryd, J.P. (1992). Betalain producing cell cultures of Beta vulgaris L. Var. Bikores Monogerm (red beet). In vitro Cellular & Developmental Biology, 28, 39–45.

[13] Nilsson, T. (1970). Studies into the pigments in beetroot (Beta vulgaris L. ssp. vulgaris var. rubra L.). Lantbrukhogskolans Annaler, 36, 179– 219

[14] Pszczola, D.E. (1998). Natural colours: pigments of imagination. Food Technology, 52, 70–76

[15] Shenoy, V.R. (1993). Anthocyanins - Prospective food colours. Current Science, 64, 575–579.

[16] Stintzing, F.C., Schieber, A. & Carle, R. (2002b). Identification of betalains from yellow beet (Beta vulgaris L.) and cactus pear [Opuntia ficus-indica (L.) Mill.]

by high-performance liquid chromatography– electrospray ionization mass spectroscopy. Journal of Agricultural and Food Chemistry, 50, 2302–2307.

[17] Stintzing, F.C., Conrad, J., Klaiber, I., Beifuss, U. & Carle, R. (2004). Structural investigations on betacyanin pigments by LC NMR and 2D NMR spectroscopy. Phytochemistry, 65, 415– 422.

[18] Strack, D., Vogt, T. & Schliemann, W. (2003). Recent advances in betalain research. Phytochemistry, 62, 247–269.

[19] Strack, D., Steglich, W., and Wray, V.(1993) Betalains. In: *Methods in Plant Biochemistry Vol. 8*, Academic Press, Orlando, 421–450.

[20] Vaillant, F., Perez, A., Davila, I., Dornier, M. & Reynes, M. (2005). Colourant and antioxidant properties of red-purple pitahaya (Hylocereus sp.) Fruits, 60, 1–10.

[21] von Elbe, J.H. (1975). Stability of betalaines as food colors. Food Technology, 5, 42–44.

ISSN (Print) : 2320 – 3765
ISSN (Online): 2278 – 8875

International Journal of Advanced Research in Electrical, Electronics and Instrumentation Engineering
Vol. 2, Issue 6, June 2013

Selection of Optimal Mother Wavelet for Fault Detection Using Discrete Wavelet Transform

Dr. Bhola Jha[1], R. B. Yadav[2], Dr. K. R. M Rao[3] and H. L. Yadav[4]

Asst. Prof., Dept. of Electrical Engg., G. B. Pant Engg. College, Pauri-Garhwal-246194, India[1]

Asst. Prof., Dept. of Electrical Engg., G. B. Pant Engg. College, Pauri-Garhwal-246194, India[2]

Professor, Dept. of Electrical Engg., M. J College of Engg.&Technology, Hyderabad-500034, India [3]

Asst. Prof., Dept. of Civil Engg., G. B. Pant Engg. College, Pauri-Garhwal-246194, India [4]

Abstract: This paper exploited the various mother wavelets for fault detection. A different value of fault resistances analyzed on different types of mother wavelets. Comparisons are made based on the sum of coefficients in multi resolution signal decomposition (MSD) using Discrete Wavelet Transform (DWT). Based on the extensive investigations on different value of fault resistance in Line-Ground (L-G) fault, optimal mother wavelet is proposed.

Keywords: Wavelet, wavelet coefficient, fault, multi resolution decomposition

I INTRODUCTION

Recently wavelet applications are extended to electrical engineering field especially in terms of faults detection and discrimination. An internationally recognized tool wavelet analyzed from theory point of view that it can be formulated via a family of basis functions such that the signals can be described in a localized time and frequency format. Hence, by employing the long windows at low frequency and short windows at high frequencies, the wavelet transform will be capable of comprehending the time and frequency information simultaneously. For those transients in time-varying signals, they would be supervised more effectively, thereby encouraging the application of such method to enhance the detection capabilities.

In the area of fault detection capability, still limited numbers of wavelet-based research papers are reported [1-5]. CWT-based approach is proposed in [1] for the enhancement of damage detection of wind turbine blades. Wavelet-based ARMA model is presented in [2] for the short-term wind speed forecasting. Comparative analysis of the approaches, MCSA, EPVA and DWT are made in [3] to detect the interturn fault in Doubly-Fed Induction Generator (DFIG). Based on Discrete Wavelet Transform (DWT), Fault Indicator and Fault Criteria, Detection of High Impedance Fault (HIF) is proposed in [4]. A solution to the problem of protecting aerial lines from high impedance fault in distribution systems is proposed in [5]. Transmission line faulty phase analysis is done in [6] by detailed coefficients. Based on the energy of differential-current signal, transformer fault's detection is proposed in [7]. Magnetizing in-rush current and fault current of transformer is discriminated in [8]. A new diagnostic method based on grid modulating signals is proposed in [9] to detect asymmetrical fault. Coefficients of wavelet used as a input for training back propagation neural network in high impedance fault detection is analyzed in [10]. Technique based on sensitive fault detection parameter from multi resolution decomposition of three phase currents is proposed in [11]. However, each of the paper improves fault detection capabilities to certain extent, but each has its drawbacks as well. In those papers authors have used different mother wavelets, but they did not predict the optimal mother wavelet which actually affects the accuracy of detection capabilities. In this paper, comparisons are made among different mother wavelet, based on the sum of coefficients in multi resolution signal decomposition (MSD) using Discrete Wavelet Transform (DWT). After the extensive investigations on different value of fault resistance, an optimal mother wavelet is proposed for the accurate fault detection.

II WAVELET TRANSFORM

Wavelet transform is of two types Discrete Wavelet Transform (DWT) and Continuous Wavelet Transform (CWT). Their brief explanations are as under.

ISSN (Print) : 2320 – 3765
ISSN (Online): 2278 – 8875

International Journal of Advanced Research in Electrical, Electronics and Instrumentation Engineering
Vol. 2, Issue 6, June 2013

A. Discrete Wavelet Transform (DWT)

The ability to provide variable time-frequency resolution is hallmarks of wavelet transform [12-14]. Wavelet transform is relatively new mathematical technique which is used to analyze signal in nature. It is becoming the focus point of much science, and is fondly delighted tool by scientists. It plays a very important role in signal and information processing.
The wavelet transformation is processes of determining how well a series of wavelet functions represent the signal being analyzed. The goodness of fitting of the function to the signal is described by the wavelet coefficients. The result is a bank of coefficients associated with two independent variables, dilation and translation. Translation typically represents time, while scale is a way of viewing the frequency content. Larger scale corresponds to lower frequency meaning thereby better resolution. The most efficient and compact form of the wavelet analysis is accomplished by the decomposing a signal into a subset of translated and dilated parent wavelets, where these various scales and shifts in the parent wavelet are related based on powers of two. Full representation of a signal can be achieved using a vector coefficients the same length as the original signal.
Considering a signal consisting of 2^M data points, where M is an integer. DWT requires 2M wavelet coefficients to fully describe the signal. DWT decomposes the signal into M+1 levels, where the level is denoted as j and the levels are numbered i = -1, 0, 1, 2, 3…M-1. Each level i consists of j = 2^i wavelet translated and equally spaced $2^M/j$ intervals apart. The $j = 2^i$ wavelets at level i are dilated such that an individual wavelet spans N-1 of that level interval, where N is the order of wavelet being applied. Each of the $j = 2^i$ wavelets at level i is scaled by a coefficient $a_{i,j}$ determined by the convolution of the signal with the wavelet. Notation is such that i corresponds to wavelet dilation and j is the wavelet translation in level i. The forward wavelet transform determines the wavelet coefficients $a_{i,j}$ of j wavelet at each level i.
For the signal f (n), the DWT is

$$a_{i,j} = a_{2^i + j} = \sum_n f(n)\psi_{i,j}(n)$$

Here, ψ is mother wavelet

B Continuous Wavelet Transform (CWT)

While the DWT is most efficient and compact, its power of two relationships the scale fixes its frequency resolution. Often it is desired to differentiate between smaller frequency bands than DWT allows. This is possible by using scales that are more closely spaced together than the 2^i relationship, and is the basis for the Continuous Wavelet Transform (CWT).

For a signal f (t), CWT determines the coefficients as

$$a(i,j) = \int_{-\infty}^{+\infty} f(t)\psi(i,j,t)dt$$

Here, ψ is mother wavelet

The number of coefficients necessary to describe the signal may be larger than the signal strength, as the CWT over samples the signal.

C Characteristics of Wavelets

The quality of various wavelet families vary according to the following criteria

- The speed of convergence to zero
- The number of vanishing moments
- The symmetry

ISSN (Print) : 2320 – 3765
ISSN (Online): 2278 – 8875

International Journal of Advanced Research in Electrical, Electronics and Instrumentation Engineering
Vol. 2, Issue 6, June 2013

- The regularity
- The othogonality/biorthogonality
- The existence of scaling function

The comparision of four mother wavelets are tabulated based on the qualities mentioned above. From this table it is found that the accuracy of Coiflets wavelet is better than remaining three.

SN	Characteristics	Haar (db1)	Daubechies(db4)	Symlets4	Coiflets4
1	Compact Support	Yes	Yes	Yes	Yes
2	Orthogonal/Biorthogonal	Yes	Yes	Yes	Yes
3	DWT/CWT	Possible	Possible	Possible	Possible
4	Symmetry	Yes	Far from	Near from	Near from
5	Regularity	No	0.8	No	No
6	No. of vanishing moments	1	4	4	4
7	Support width	1	7	7	23
8	Filter length	2	8	8	24

D Case Study

To validate the accuracy of Coiflets mother wavelet is better, a case study is done on the following test system which is shown in Fig.1.

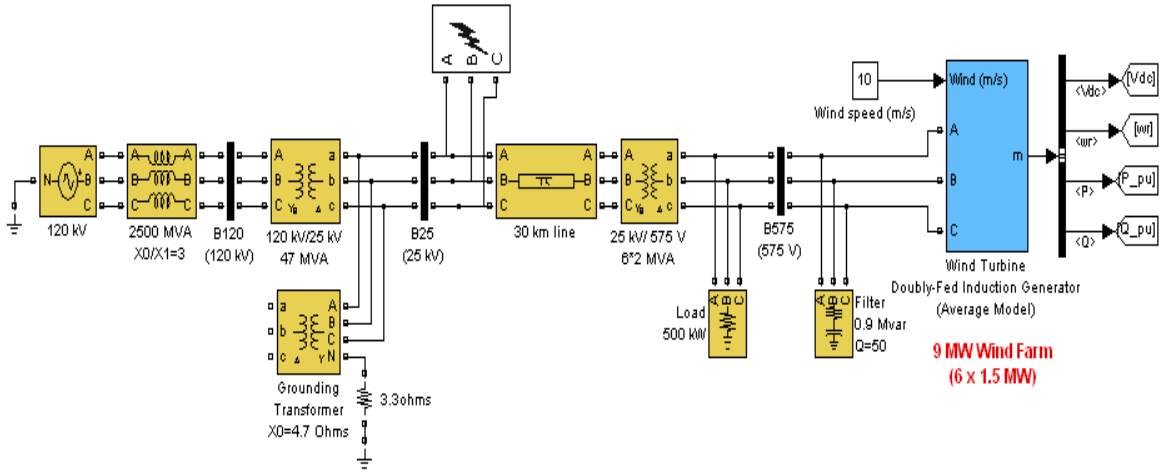

Fig.1: Test System

A 9MW Doubly Fed Induction Generator-Based Wind Turbine is connected to 120kV grid through transformers and transmission lines. Single Line-Ground (L-G) fault is created on 25kV bus transmission lines which is shown in test system of Fig.1.

III RESULTS ANALYSIS

The sum of coefficients of currents signals using different mother wavelet for different values of fault resistances are shown in Fig.2, Fig.3, Fig.4 and Fig.5. The coefficients are obtained through multi resolution decomposition using one dimensional discrete wavelet wavelet transform.

ISSN (Print) : 2320 – 3765
ISSN (Online): 2278 – 8875

International Journal of Advanced Research in Electrical, Electronics and Instrumentation Engineering
Vol. 2, Issue 6, June 2013

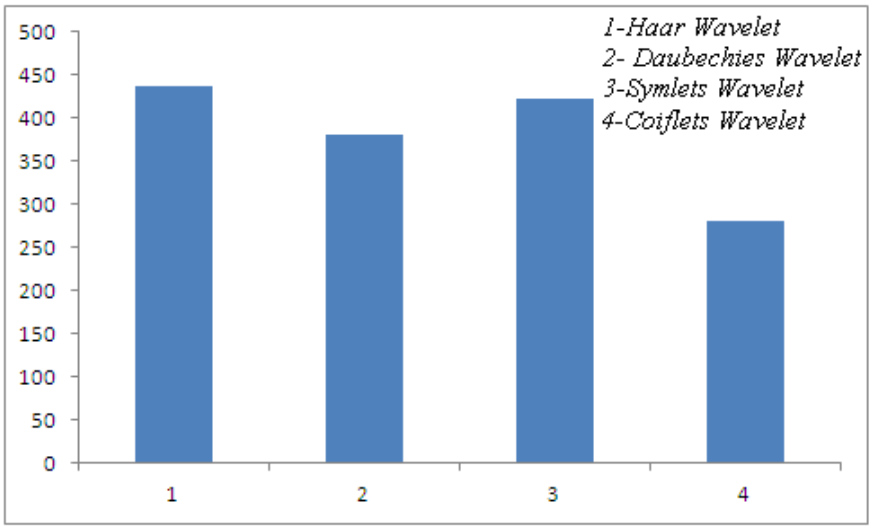

Fig.2: Wavelet Coefficients for fault resistance of 0.1 Ohm

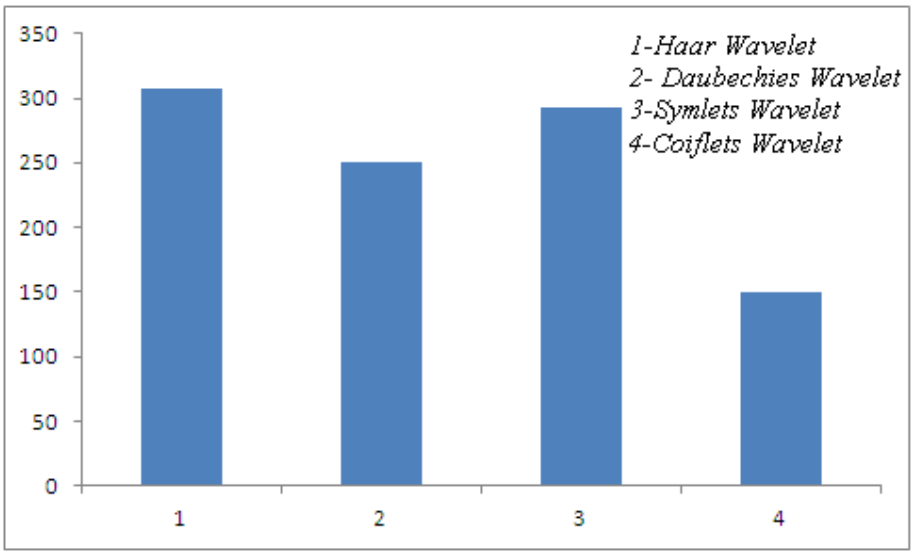

Fig.3: Wavelet Coefficients for fault resistance of 10 Ohm

ISSN (Print) : 2320 – 3765
ISSN (Online): 2278 – 8875

International Journal of Advanced Research in Electrical, Electronics and Instrumentation Engineering
Vol. 2, Issue 6, June 2013

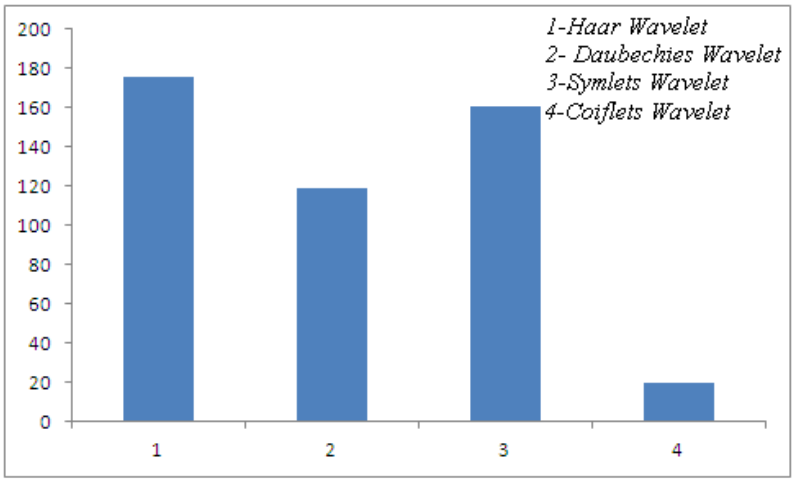

Fig.4: Wavelet Coefficients for fault resistance of 20 Ohm

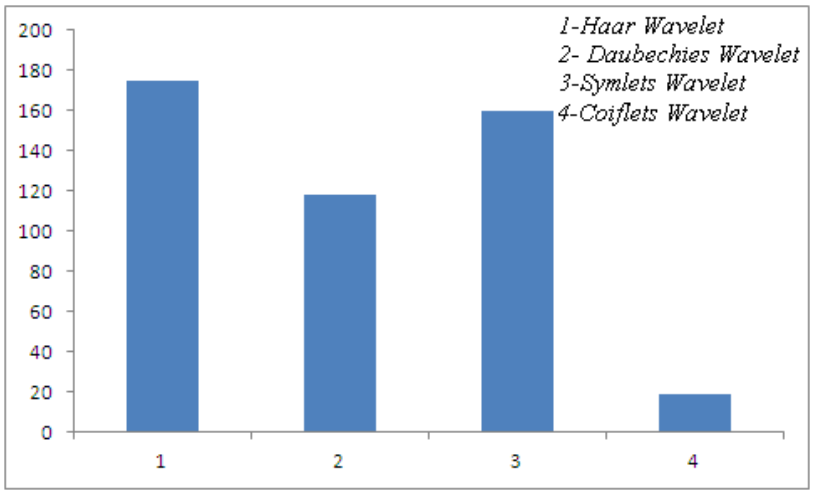

Fig.5: Wavelet Coefficients for fault resistance of 30 Ohm

This is found from the bar chart that the the sum of coefficients of Coiflets wavelet is less for all values of fault resistances. Hence, Coiflets is an optimal mother wavelet for fault detection.

IV CONCLUSION

Based on the extensive investigations on different value of fault resistance, Coiflets wavelet is proposed as an optimal mother wavelet.

REFERENCES

[1] Chin-Shun Tsai, Cheng-Tao Hsieh, and Shyh-Jier Huang " Enhancement of Damage-Detection of Wind Turbine Blades Via CWT-Based Approaches" IEEE transactions on Energy Con version, Vol. 21, No. 3, pp 776-781, Sept. 2006..

[2] CAO Lei and LI ran "Short-Term Wind Speed Forecasting Model for Wind Farm Based on Wavelet Decomposition" DRPT, 6-9 April, Nanjing China. pp 2525-2529, 2008.

[3] H. Douglas, P. Pillay and P. Barense " The Detection of Interturn Stator Faults in Doubly-Fed Induction Generators" IEEE, IAS, pp 1097-1102, 2005.

[4] Chul-Hwan Kim *et. al.* "A Novel Fault Detection Technique of High Impedance Arcing Faults in Transmission Lines Using the wavelet Transform" IEEE Transactions on Power Delivery, Vol.17, No.4, pp 921-929, Oct.2002.

ISSN (Print) : 2320 – 3765
ISSN (Online): 2278 – 8875

International Journal of Advanced Research in Electrical, Electronics and Instrumentation Engineering
Vol. 2, Issue 6, June 2013

[5] Miing-Ta Yang, Jin-Lung Guan and Jhy-Cherng Gu "High Impedance Faults Detection Technique Based on Wavelet Transform" World Academy of Science, Engg. and Technology, pp 308-312 , 2007.
[6] B. Ravindhraratnath Reddy et.al. "Detection and Localization of Fault in Transmission Line Using Wavelet Transform" Journal of Theoritical and Applied Information Technology, pp.99-104, 2009.
[7] Y. Ngafi Sarem, E. Hasemzadeh and M.A.Layegh "Transformer Fault Detection Using Wavelet Transform" International Journal on Technical and Physical Problems of Engg., Vo.4, No.1, Issue 10, pp17-26, March 2012.
[8] Okan Ozgonenel, Giiven Onbligein and Gagri Kocaman "Transformer Protection Using Wavelet Transform" Turk. J. Elect. Engin.,Vol13(1), 2005.
[9] R. K. Dubey "A Novel Technique for Asymmetrical Fault Detection in DFIG-Based Wind Farm" Bulletin of Electrical Engg. and Informatics, vo.1, No.4, pp.285-295, Dec.2012.
[10] Abdulhamid et.al. "Hybrid Algorithm for Detection of High Impedance Arcing Fault in Overhead Transmission Systems" International Journal of Electronic and Electrical Engg., Vol.2, Isuue4, May 2012.
[11] N. Zamanan, M. Gilany and W. Wahba "A Sensitive Wavelet-Based Algorithm for Fault Detection in Power Distribution Network" ACEEE Inernational Journal on Communication, Vol.2, No.1, pp.46-50, March 2011,.
[12] "Wavelet Transforms" by Rghuveer. M. Rao and Ajit. S. Bopardikar Pearson Education, Low Price Edition, 2005.
[13] Wavelet Tutorial Vol. I, II, III by Robi Polikar.
[14] www.mathworks.com

BIOGRAPHY

Dr. Bhola Jha received Bachelor of Science in Electrical Engineering from Muzaffarpur Institute of Technology (MIT), in 1998, M.Tech. Degree from Jawaharlal Institute of Engineering and Technology (JNTU), Hyderabad in 2004. Ph.D from Osmania University (O.U), Hyderabad in 2013. He is currently working as an Asst. Professor in G. B. Pant Engg. College, Pauri-Garhwal-246194. He is the life member of Solar Energy Society of India (SESI) and Indian Society for

R. B. Yadav received Bachelor of Technology in Electronics Engg. from U.P.T.U, Lucknow in 2005, M.Tech. Degree from G. B. Pant Govt. Engg. College, Pauri-Garhwal-246194.. He is currently working as an Asst. Professor in ECE, Dept., G. B. Pant Engg. College, Pauri-Garhwal-246194. He is the life member of Indian Society for Technical Education (ISTE). His research interests include application of DSP, Image Processing & Wavelet Transform.

Dr. K. Ram Mohan Rao received Bachelor of Science in Electrical Engineering from Andhra University in 1962, M.Sc Engg. From Banarus Hindu University (BHU) in 1964 and Ph.D from Wroclaw Technical University, Poland in 1968. He enriches the knowledge in different Institutions like H.B. Technical Institute, Kanpur from 1969 to 1974, Indian School of Mines, Dhanbad from 1974-1978, Osmania University College of Engg from 1978-1995. He served as a Dean in the Osmania University College of Engg. From 1995-2001. He enlightened the Dept. of Electrical and Electronics Engg of VNR Vignan Jyothi Institute of Engg. And Technology from 2001 to 2007. He is currently working as a Visiting Professor in M.J. College of Engg. And Technology, Hyderabad from 2007 to till date. He is the Fellow of Institution of Engineers (India) and member of various professional societies. His research interests include power electronics, drives and renewable energy.

H. L. Yadav received Bachelor of Engineering in Civil Engg. from Nagpur University in 1994, M.Tech. Degree from Aligarh Muslim University in 2008. He is currently pursuing Ph.D from Delhi Technological University. He is currently working as an Asst. Professor in G. B. Pant Engg. College, Pauri-Garhwal-246194. His research interests include environmental engineering.

Single Input Four Output Current mode filter using Operational Floating Current Conveyor

Neeta Pandey, Deva Nand, Zubair Khan

Dept. of Electronics and Communications, Delhi Technological University, Delhi, India

n66pandey@rediffmail.com, devkamboj07@gmail.com, zubair.k3@gmail.com

Abstract: This paper presents Operational Floating Current Conveyor (OFCC) based Single Input Four Output current mode filter. It employs only three OFCCs and two grounded capacitors and resistors each. The MOS based grounded resistors implementation is used which adds feature of electronic tunability to the filter parameters. The filter also enjoys low component spread and low sensitivity performance. The effect of finite transimpedance and parasites of OFCC on the proposed circuit is also analyzed. The functionality of the proposed circuit is demonstrated through SPICE simulations using 0.5 µm CMOS process model provided by MOSIS (AGILENT).

Keywords: Single Input Four Output, Operational Floating Current Conveyor, Filter.

1. Introduction

The development of current mode continuous time filters has received growing interest due to its applications in sampled data systems, communications and control systems [1, 2]. This is also in consonance with the trend of operating circuits at lower supply voltages where the current mode concept is more useful. The circuit operation in current mode circuits is decided by current which enables the system design having wider dynamic range [3]. These circuits are also simple and compact as current addition/subtraction does not require additional circuit elements. Owing to the advantages of current mode filters, considerable research has directed towards the realization of single input multiple output filters. A variety of current mode building blocks [4-10] namely current follower transconductance amplifier [4], current conveyor [5-7], operational transconductance amplifier [8], Z copy current follower transconductance amplifier [9] and Z-Copy Current Inverter Transconductance amplifier [10] have been used to implement these filters [1, 4 - 22]. The structures - use excessive number of elements [6, 7, 13, 15, some of the references cited in [17], do not present low input impedance [1, 8, 13-16, 19] which is necessary for a current mode filter, employ multiple inputs to provide output responses [15,16], put matching constraint [7, 10, 15, 16] to obtain all five responses of universal filter, has less than three simultaneous output responses

[4, 8, 15, 16 , 21],employ different type of active blocks [12, 19, 20].The operational floating current conveyor (OFCC) [23, 24] which was introduced as operational floating conveyor (OFC) [25], combines the features of current conveyor and the current feedback opamp along with additional current outputs that adds flexibility in the circuit design. Literature survey on OFCC based circuits [26 - 32] shows that voltage mode filter [26 - 28], variable gain amplifier [29], wheatsone bridge [30] and instrumentation amplifier [31] and read out circuit [32] are available. The study of current mode filters [1, 4 - 22] shows that no OFCC based current mode filter is available in literature. Therefore, this paper aims at presenting a single input four output OFCC based current mode filter The proposed filter uses three OFCCs, two grounded capacitors and two grounded resistors. The resistors are implemented using MOSFETs so as to achieve electronic tunability of filter parameters. The filter enjoys low component spread and low sensitivity performance. The proposed circuit is also analyzed to take finite transimpedance and parasites of OFCC into account. The functionality of the proposed circuit is demonstrated through SPICE simulations using 0.5 μm CMOS process model provided by MOSIS (AGILENT).

2. Circuit Description

2.1 OFCC

The circuit symbol of Operational Floating Current Conveyor (OFCC) [23, 24] is shown in Fig.1. It has a low impedance current input port X and a high impedance voltage input port Y. It also has a low impedance voltage output port W and high impedance current output ports Z1, Z2, Z3 and Z4. The output voltage at port W is multiplication of input current at port X and the open loop transimpedance gain Z_t. The port relationships of the OFCC is characterized by the following matrix

$$\begin{bmatrix} I_Y \\ V_X \\ V_W \\ I_{Z1} \\ I_{Z2} \\ I_{Z3} \\ I_{Z4} \end{bmatrix} = \begin{bmatrix} 0 & 0 & 0 & 0 & 0 & 0 & 0 \\ 1 & 0 & 0 & 0 & 0 & 0 & 0 \\ 0 & Z_t & 0 & 0 & 0 & 0 & 0 \\ 0 & 0 & 1 & 0 & 0 & 0 & 0 \\ 0 & 0 & 1 & 0 & 0 & 0 & 0 \\ 0 & 0 & -1 & 0 & 0 & 0 & 0 \\ 0 & 0 & -1 & 0 & 0 & 0 & 0 \end{bmatrix} \begin{bmatrix} V_Y \\ I_X \\ I_W \\ V_{Z1} \\ V_{Z2} \\ V_{Z3} \\ V_{Z4} \end{bmatrix} \quad (1)$$

It may be noted that the voltage at port X is the same as input voltage at port Y so voltage tracking action is available at input port. The output current flowing through port W is copied

to ports Z1, Z2 in phase and to ports Z3, Z4 out of phase, thereby offering current tracking at the output ports. Figure 2 shows the CMOS based schematic of OFCC which is based on topology proposed in [29].

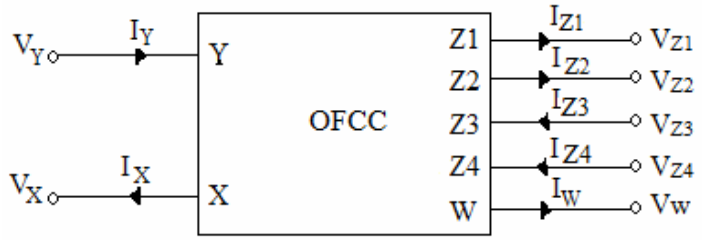

Fig. 1 Circuit symbol of OFCC.

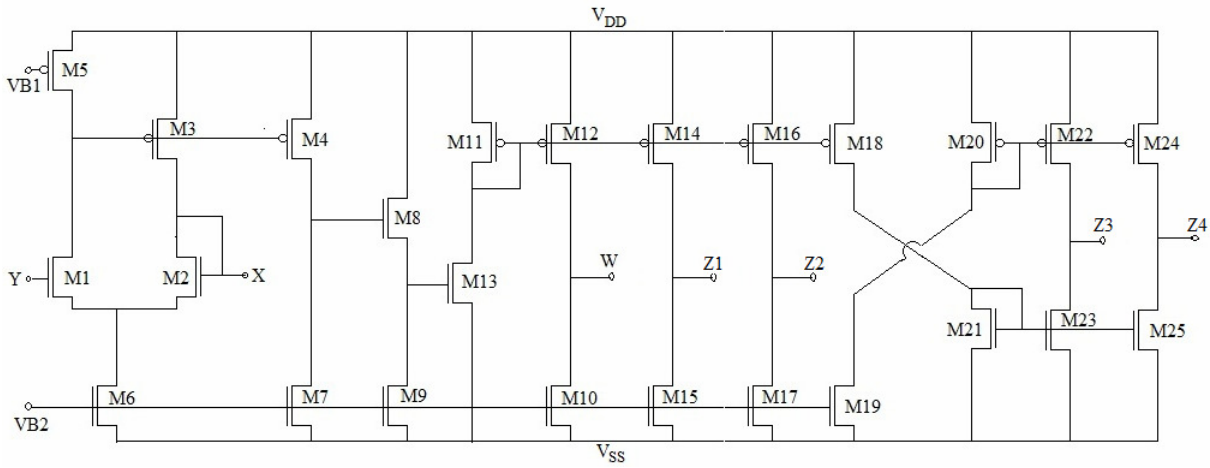

Fig. 2 CMOS schematic of OFCC [29].

2.2. Proposed Filter

In this section the implementation of OFCC based current mode single input four output filter, as shown in Fig. 3, is proposed. It employs three OFCCs, two grounded capacitors and resistors each. The analysis of the circuit gives the following transfer functions:

$$T_{LPF1} = T_{LPF2} = \frac{I_{LPF1}}{I_{in}} = \frac{I_{LPF2}}{I_{in}} = \frac{-1}{D(s)} \tag{2}$$

$$T_{BPF} = \frac{I_{BPF}}{I_{in}} = \frac{-sC_2R_2}{D(s)} \tag{3}$$

$$T_{HPF} = \frac{I_{HPF}}{I_{in}} = \frac{-s^2C_1C_2R_1R_2}{D(s)} \tag{4}$$

$$T_{NOTCH} = \frac{I_{NOTCH}}{I_{in}} = \frac{s^2 C_1 C_2 R_1 R_2 + 1}{D(s)} \tag{5}$$

where

$$D(s) = s^2 C_1 C_2 R_1 R_2 + s C_2 R_2 + 1 \tag{6}$$

Thus the proposed circuit provides low pass, band pass and notch (band stop) response simultaneously at high impedance. It may be noted that the current I_{HPF} is not explicitly available at high impedance and therefore can not be used directly. However, by connecting I_{NOTCH} and I_{LPF1}, the high pass response can be made available at high output impedance. This arrangement makes low pass, band pass and high pass responses available simultaneously. Similarly, the all pass function can easily be obtained by connecting band pass and notch output currents, i.e. $I_{AP} = I_{BP}+I_{NOTCH}$ and the corresponding transfer function is obtained as

$$T_{AP} = \frac{I_{AP}}{I_{in}} = \frac{s^2 C_1 C_2 R_1 R_2 - s C_2 R_2 + 1}{D(s)} \tag{7}$$

It may be noted that all the five filter responses can be made simultaneously available by adding Z stages in 2nd OFCC (Fig.3). Further, there is no matching constraint for realization of filter responses.

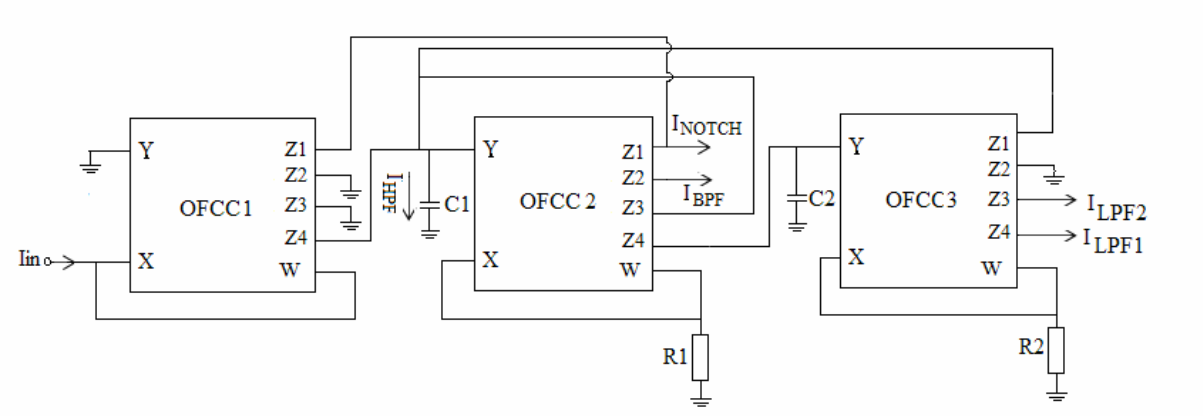

Fig. 3 Proposed OFCC based single input four output current mode filter.

All the responses are characterized by pole frequency (ω_0), bandwidth (ω_0/Q_0) and quality factor (Q_0) given as:

$$\omega_0 = \sqrt{\frac{1}{R_1 R_2 C_1 C_2}} \tag{8}$$

$$BW = \frac{\omega_0}{Q_0} = \frac{1}{R_1 C_1} \tag{9}$$

$$Q_0 = \sqrt{\frac{R_1 C_1}{R_2 C_2}} \tag{10}$$

Equations (8)-(10) reveals that the pole frequency (ω_0) and quality factor (Q_0) can be adjusted by R_2, without disturbing ω_0 / Q_0. The orthogonal adjustability of ω_0 and Q_0 can be achieved by simultaneous adjustment of R_1 and R_2 such that the product R_1R_2 remains constant and the quotient R_1/R_2 varies and vice versa. With moderate values of ratios of component values ($(R_1 / R_2) = (C_1 / C_2) = Q_0$) i.e. from low component spread [33], high values of Q-factor can be obtained. Hence the component spread is of the order of $\sqrt{Q_0}$.

The proposed filter uses grounded resistors which can easily be implemented using the MOS based structure given in Fig.4 [34]. It uses two diode connected matched transistors, operating in saturation region. Assuming $V_1 = - V_2$, the value of resistor is given by:

$$R = \frac{L}{2\mu C_{ox} W (V_1 - V_T)} \tag{11}$$

where μ is carrier mobility, Cox is gate capacitance per unit area, V_T is threshold voltage and W, L are the channel length and width respectively.

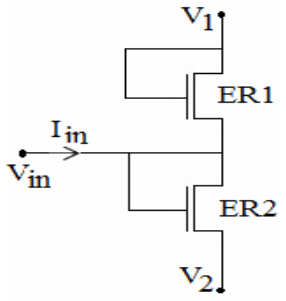

Fig. 4 MOS realization of a resistor [34]

The sensitivity analysis of the proposed circuit is as follows:

$$S_{R_1}^{\omega_0} = S_{R_2}^{\omega_0} = S_{C_1}^{\omega_0} = S_{C_2}^{\omega_0} = S_{R_2}^{Q} = S_{C_2}^{Q} = -\frac{1}{2}, \quad S_{R_1}^{Q} = S_{C_1}^{Q} = -S_{R_2}^{Q} = -S_{C_2}^{Q} = \frac{1}{2} \tag{12}$$

Thus the all passive sensitivities are not more than unity in magnitude. So the proposed filter circuit can be classified as insensitive.

2.3 Effect of finite transimpedance gain

In this section the effect of finite transimpedance gain of OFCC is considered and compensation is employed for high frequency applications. Ideally the transimpedance gain Z_t is assumed to approach infinity. However, in practice, Z_t is a frequency dependent finite value. Using single pole model for transimpedance gain, Z_t (s) is expressed as [29]

$$Z_t(s) = \frac{Z_{to}}{1 + s/\omega_{tc}} \tag{13}$$

The parameter Z_{to} is the dc open loop transimpedance gain and ω_{tc} is the transimpedance cut off frequency. For high frequency applications, the transimpedance gain, Z_t (s) is approximated as

$$Z_t(s) \cong \frac{1}{sC_p} \tag{14}$$

Where

$$C_p = \frac{1}{Z_{to}\omega_{tc}} \tag{15}$$

Taking single pole model of Z_t(s) into account, the low pass transfer function of (2) modifies to

$$T_{LPF\,1} = T_{LPF\,2} = \frac{I_{LPF\,1}}{I_{in}} = \frac{I_{LPF\,2}}{I_{in}} = \frac{-1}{D_n(s)} \tag{16}$$

Where

$$D_n(s) = s^2 R_1 \varepsilon_1(s) R_2 \varepsilon_2(s) C_1 C_2 + s R_2 \varepsilon_2(s) C_2 + 1, \tag{17}$$

and

$$\varepsilon_1(s) = \frac{1}{1 + sC_p R_1}, \varepsilon_2(s) = \frac{1}{1 + sC_p R_2} \tag{18}$$

The inclusion of a capacitor of value C_p connected between the terminal W and ground in 2nd and 3rd OFCC cancels the coefficient of 's' thereby making both $\varepsilon_1(s)$ and $\varepsilon_2(s)$ equal to unity. Thus the transfer function of low pass filter after compensation reduces to (2). Similar analysis is valid for other responses as well.

2.4 Effect of other non idealities

The second group of non-idealities comes from parasites of OFCC comprising of resistances and capacitances connected in parallel at terminals Y, Z1, Z2, Z3 and Z4 (i.e. R_Y, C_Y, R_z, C_Z). The effects of these parasites on filter response depend strongly on circuit topology. The proposed filter topology of Fig. 3 in the presence of these parasites modifies to Fig. 5 where $C_{1eq} = C_1 // C_{Y1} // C_{Z41} // C_{Z31} // C_{Z13}$, $C_{2eq} = C_2 // C_{Y3} // C_{Z42}$, $G_{1p} = 1/(R_{Z41} // R_{Z31} // R_{Z13})$ and $G_{2p} = 1/(R_{Y3} // R_{Z42})$; the subscript i (= 1, 2, 3) refers to parasites of i[th] OFCC and j denotes j[th] Z terminal. It may be noted that effect of parasitic capacitances can be accommodated by pre adjusting the value if external capacitor. The parasitics introduce poles at G_{1P}/ C_{1eq} and G_{2P}/ C_{2eq}. So by choosing operating frequencies sufficiently below these frequencies the effect of parasitic impedance can be practically eliminated and hence filter may approach towards ideal response.

3. Simulation results

To verify the functionality of the proposed OFCC based current mode filter, SPICE simulations have been carried out using 0.5 µm CMOS process model provided by MOSIS (AGILENT) and CMOS schematic of Fig. 2 with power supply voltage of $V_{DD} = -V_{SS} = 1.5$ V and $V_{B1} = -V_{B2} = 0.8$ V. The aspect ratios of the transistor are reported in Table 1 [29].

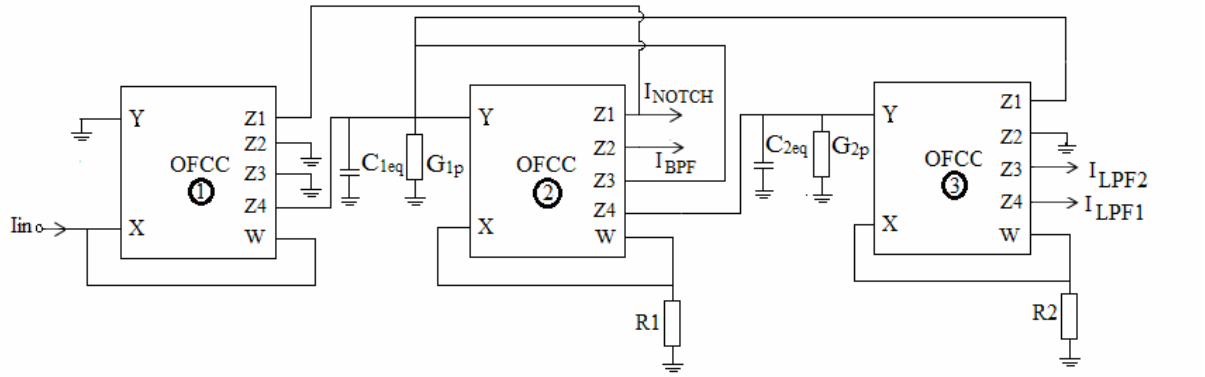

Fig. 5 Proposed OFCC based current mode filter with parasites.

Table 1: Transistors aspect ratios of the circuit shown in Fig. 2

Transistor	W (µm)/L (µm)
M1, M2	50/1
M3, M4, M11, M12, M14 M16, M18, M20, M22, M24	50/2.5
M5, M7, M10, M15, M17, M19 M21, M23, M25	20/2.5
M6, M8	40/2.5
M9, M13	100/2.5

The simulations have been performed for a pole frequency of 1.59 MHz with component values as $C_1 = C_2 = 100$ pF and MOS based resistors of value 1 kΩ by selecting bias voltages as ± 1.310V. Figure 6 shows the simulation results for low pass, band pass and high pass responses. The phase and magnitude plots for notch and all pass responses are depicted in Fig. 7 and 8 respectively. The responses confirm the theoretical predictions.

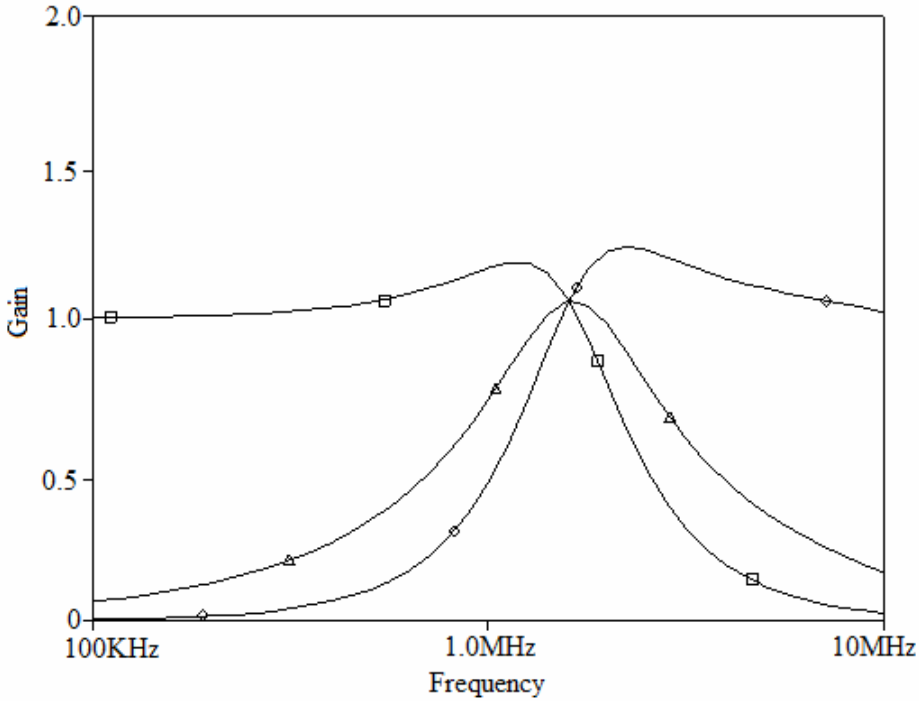

Fig. 6 Simulated low pass, band pass and high pass responses

The orthogonal adjustment of f_0 with Q_0 is depicted in Fig. 9 where the value of Q_0 = 1 is considered. The capacitors C_1 and C_2 are taken as 100 pF and the bias voltages along with the resistor values for different values of f_0 as given in Table 2. Figure 10 shows orthogonal adjustment of Q_0 with f_0 = 800 kHz. The values of Q_0 for constant value of f_0 as obtained with $C_1 = C_2$ = 100 pF and bias voltages and resulting resistor values are listed in Table 3.

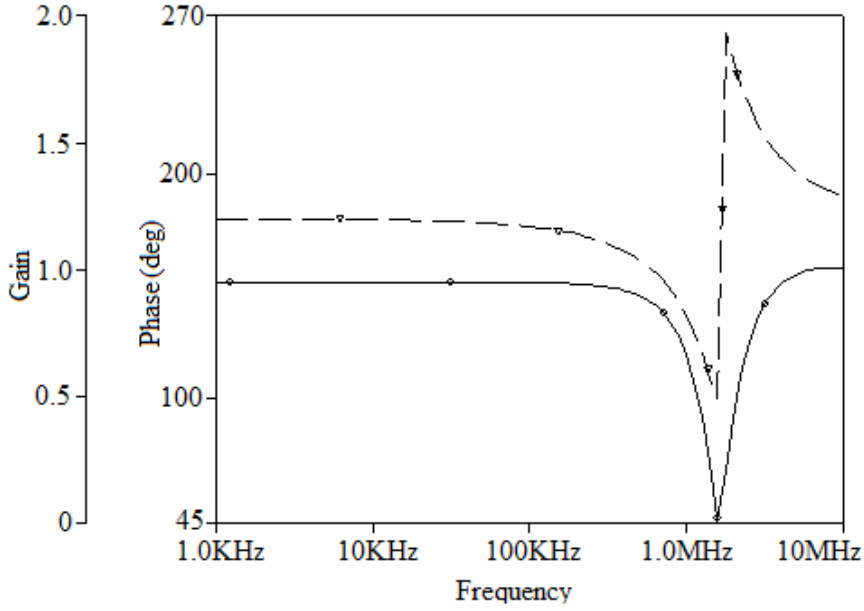

Fig. 7 Magnitude and phase plot for notch response

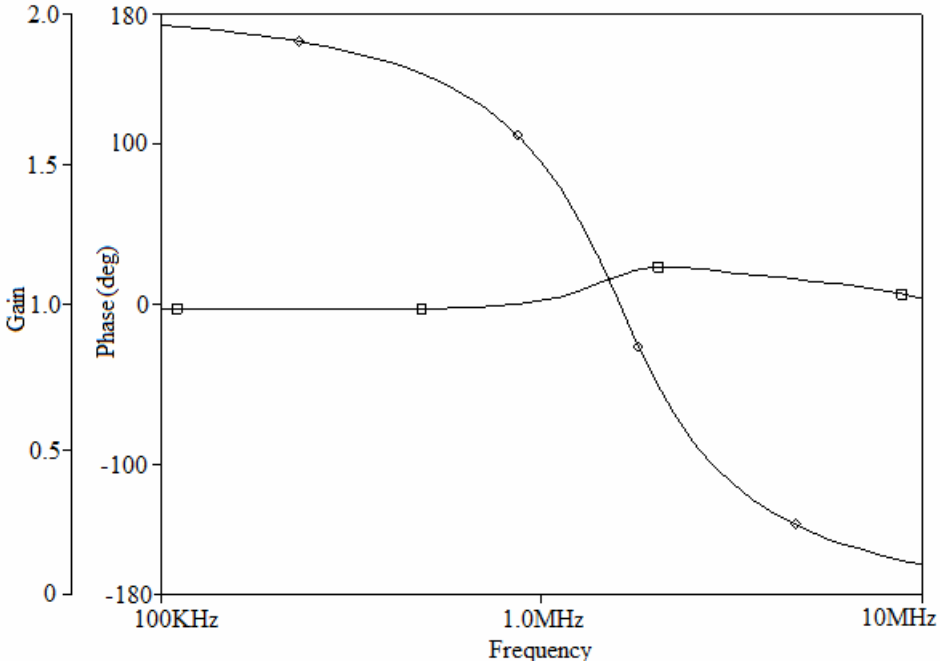

Fig. 8 Magnitude and phase plots for allpass response

Table 2: Bias voltages/ Resistor values for orthogonal adjustment of f_0 with Q_0

V_1(V)	R_1 (KΩ)	V_2(V)	R_2 (KΩ)	Q_0	f_0 (KHz)
1.310	1	- 1.310	1	1	1590
0.869	2	- 0.869	2	1	800
0.726	5	- 0.726	5	1	320
0.711	10	- 0.71	10	1	160

Table 3: Bias voltages/ Resistor and capacitor values for orthogonal adjustment of Q_0 with f_0

V_1 (V)	R_1 (KΩ)	V_2 (V)	R_2 (KΩ)	C_1 (nF)	C_2 (nF)	Q_0	f_0 (KHz)
1.310	1	- 0.729	2	0.1	0.2	0.5	800
0.870	2	- 0.870	2	0.1	0.1	1	800
0.729	2	-1.310	1	0.2	0.1	2	800

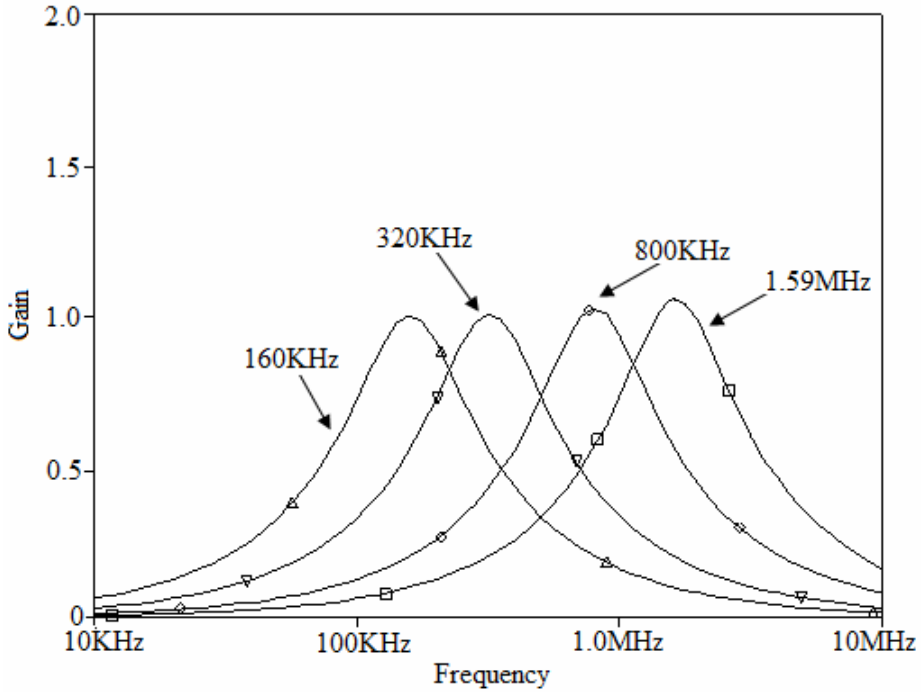

Fig. 9 Tuning of f_0

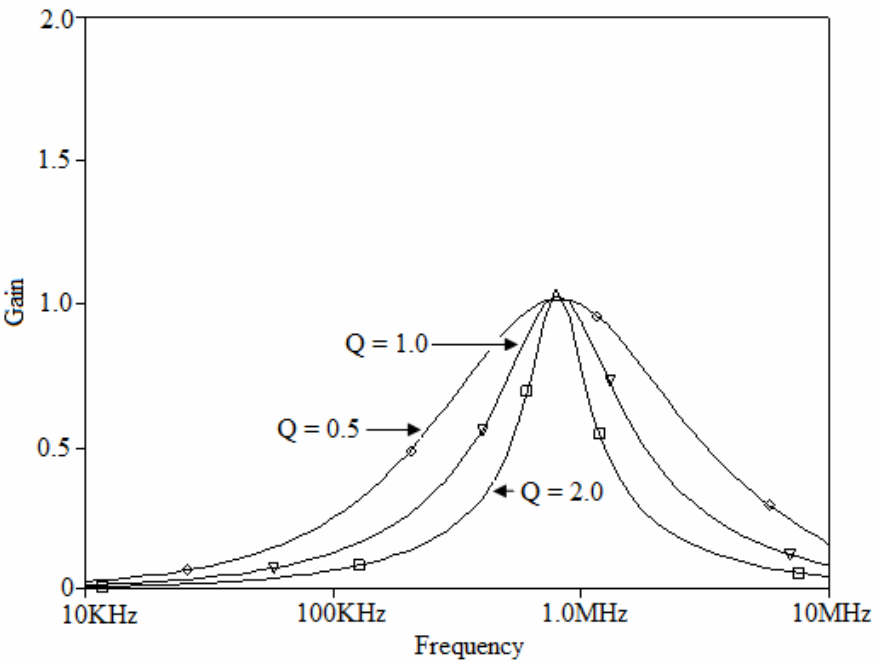

Fig. 10 Tuning of Q_0

To study the time domain behaviour of the proposed filter, an input sinusoidal signal of 500 KHz frequency and amplitude 2 µA is applied. The transient response for low pass output is shown in Fig. 11. To show the effectiveness of proposed filter a mixed sinusoidal signals of frequencies of 50 KHz, 500 KHz and 4 MHz having amplitude of 2 µA each is applied at the input of the filter. The transient response with its spectrum for input and output signals is shown in Fig. 12 (a) and (b). It is clear that the 50 KHz and 500 KHz signals are passed without attenuated and 4 MHz signal is significantly attenuated.

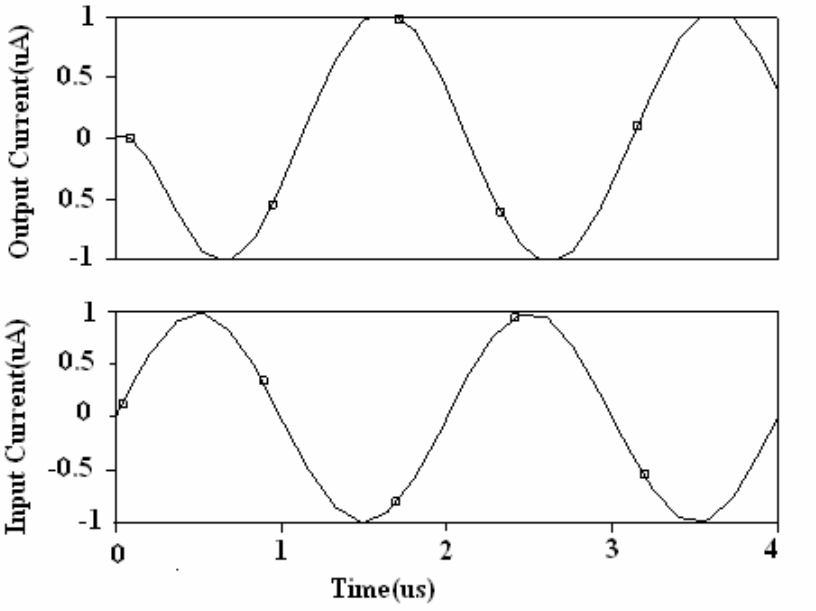

Fig. 11 Transient response for low pass output

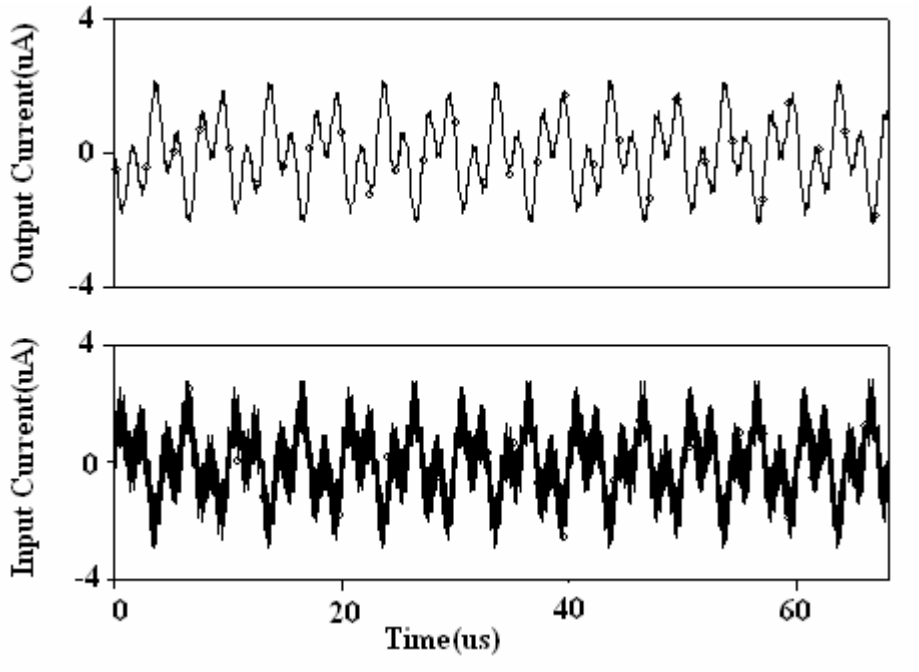

(a)

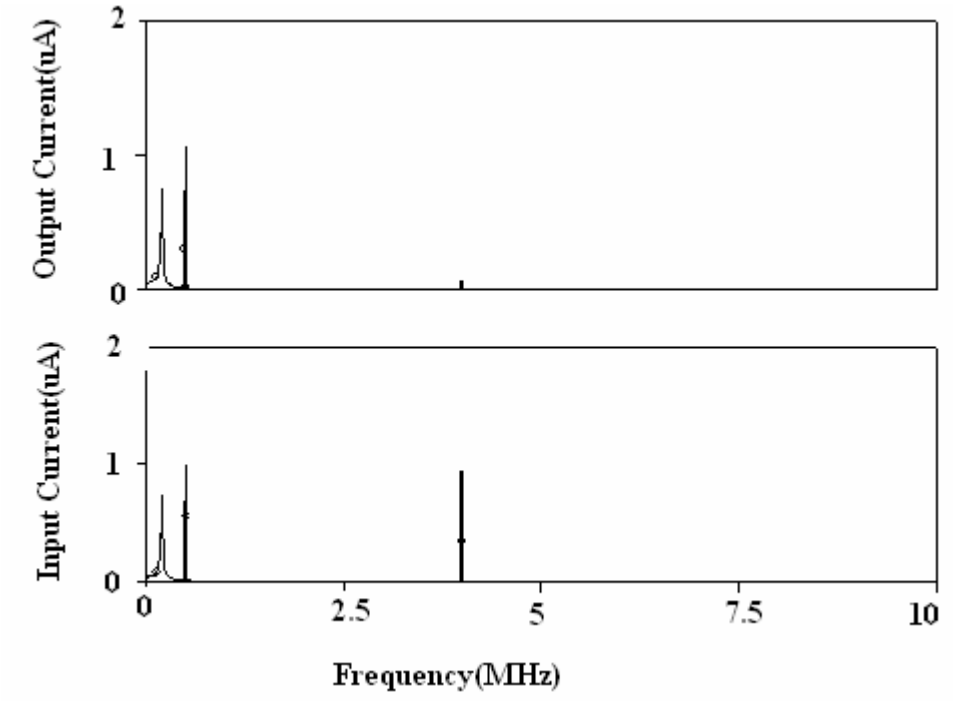

(b)

Fig. 12 (a) Transient response of input and output signals
(b) Spectrum of input and output signals

4. Conclusion

In this paper, a single input four output current mode filter based on OFCC is presented. The circuit uses only three OFCCs, two grounded resistors and two grounded capacitors. The low pass, band pass and notch responses are available at high impedance whereas high pass and all pass responses can be obtained by adding Z stages in 2nd OFCC. The filter parameters

are tuned electronically via MOS based grounded resistor. The effect of finite transimpedance and parasites on filter parameters is also included.

References

[1] M. A. Ibrahim, S. Minaei, H. A. Kuntman, "A 22.5 MHz current-mode KHN-biquad using differential voltage current conveyor and grounded passive elements", International Journal AEU of Electronics and Communications, vol. 59, pp. 311-318, (2005).

[2] A. S. Sedra, K. C. Smith, "Microelectronic Circuits", 3rd ed., Florida: Holt, Rinehart and Winston, (1991).

[3] S. S. Rajput, and S. S. Jamuar, "Advanced applications of current conveyors: A Tutorial", Journal of Active and Passive Electronic Devices, vol.2, pp.143-164, (2007).

[4] W. Tangsrirat, "Single-input three-output electronically tunable universal current-mode filter using current follower transconductance amplifiers", International Journal AEU of Electronics and Communications, vol. 65, pp.783– 787, (2011).

[5] C. Wang, J. Xu, A. U. Keskin, S. Du, Q. Zhang, " A new current-mode current-controlled SIMO-type universal filter", International Journal AEU of Electronics and Communications, vol. 65, pp. 231–234, (2011).

[6] J. W. Horng, "Current mode and transimpedance mode universal biquadratic filter using multiple outputs CCIIs", International Journal of Engineering and Materials Sciences, vol. 17, pp. 169-174, (2010).

[7] K. K. Abdalla, D. R. Bhaskar, R. Senani, "Configuration for realising a current-mode universal filter and dual-mode quadrature single resistor controlled oscillator", Institution of Engineering and Technology Circuits, Devices and Systems, vol. 6, issue 3, pp. 159-167, (2012).

[8] A. Qadir, T. Altaf, "Current Mode Canonic OTA-C Universal Filter with Single Input and Multiple Outputs", International Conference on Electronic Computer Technology, pp. 32-34, (2010)

[9] J. Satansup, W. Tangsrirat, "Single-Input Five-Output Electronically Tunable Current-Mode Biquad Consisting of Only ZC-CFTAs and Grounded Capacitors", Radio Engineering, vol. 20, no. 3, pp. 650-656, (2012).

[10] D. Biolek, V. Biolkova, Z. Kolka, J. Bajer, "Single-Input Multi-Output Resistorless Current-Mode Biquad", IEEE European Conference on Circuit Theory and Design, pp. 225-228, (2009).

[11] R. Senani, A. K. Singh, "A new Universal Current mode biquad filter", Frequenz: Journal of Telecommunications (Germany), 56, pp. 55-59, (2002).

[12] J. W Horng, "Current conveyors based current-mode universal biquadratic filter", J. of the Chinese Institute of Electrical Engg., 9, pp. 147-150, (2002)

[13] R. Senani, A. K. Singh, V. K. Singh, "New tunable SIMO-type current mode universal biquad using only three MOCCs and all grounded passive elements", Frequenz, 57, pp. 160-161, (2003)

[14] R. Senani, V. K. Singh, A. K. Singh, D. R. Bhaskar, "Novel electronically controllable current-mode universal biquad filter", IEICE Electronics Express (Japan), vol. 1, pp. 410-415, (2004)

[15] R. Senani, "New Universal Current-mode biquad employing all grounded passive components but only two DOCCs", Journal of Active and Passive Electronic Devices (USA), vol. 1, pp. 281-288, (2006).

[16] T. Tsukutani, Y. Sumi, N. Yabuki, "Novel current-mode biquadratic circuit using only plus type DO-DVCCs and grounded passive components", International Journal of Electronics, vol. 94, pp. 1137-1146, (2007)

[17] A. M. Soliman, "Current-mode universal filters using current conveyors: classification and review", Circuits Syst. Signal Process., vol. 27, pp. 405-427, (2008)

[18] M. Sagbas and M. Koksal, "Current-mode state-variable filter", Frequenz, 62, pp. 37- 42, (2008).

[19] C. Wang, Ali Umit Keskin, L. Yang, Z. Qiujing, Du Sichun, "Minimum configuration insensitive multifunctional current-mode biquad using current conveyors and all grounded passive components", Radioengineering, vol. 19, pp. 178-184, (2010)

[20] Kasim Karam Abdalla, "Universal current-mode biquad employing dual output current conveyors and MO-CCCA with grounded passive elements", Circuits and Systems, vol. 4, pp. 83-88, (2013)

[21] J. Jerabek, R. Sotner, K. Vrba, "Comparison of the SITO Current-Mode Universal Filters Using Multiple-Output Current Followers", 35th International Conference on Telecommunications and Signal Processing (TSP), 2012 , pp.406 – 410

[22] E. Yuce, "Current-mode electronically tunable biquadratic filters consisting of only CCCIIs and grounded capacitors", Microelectronics Journal, vol. 40, pp. 1719-1725, (2009).

[23] A. A. Khan, M. A. Al-Turaigi, M. A. El-Ela, "Operational floating current conveyor: Characteristics, Modeling and applications", IEEE Instrumentation and Measurement Technology Conference, Hamamtsu, Japan, pp. 788–790, (1994).

[24] Y. H. Ghallab, M. A. El-Ela and M. Elsaid, "Operational floating current conveyor: Characteristics, Modeling and Experimental results", Proceedings of International Conference on Microelectronics, Kuwait, pp. 59–62, (1999).
[25] C. Toumazou A. Payne, F. J. Lidgey, "Operational Floating Conveyor", Electronic Letters, vol. 27, no.8, pp. 651-652, (1991).
[26] Y. H. Ghallab, W. Badawy, K. V. I. S Kaler, M. A. El-Ela, M. H. El-Said, "A New Second-order Active Universal Filter with Single Input and Three Outputs Using Operational Floating Current Conveyor", IEEE International Conference on Microelectronics, pp. 42-45, (2002).
[27] Y. H. Ghallab, M. A. El-Ela and M. Elsaid, "A novel universal voltage mode filter with three inputs and single output using only operational floating current conveyor", Proceedings of International conference on Microelectronics, pp.95-98, (2000).
[28] Y. H. Ghallab, W. Badawy, " The Operational Floating Current Conveyor and its applications," Journal of Circuits, Systems, and Computers, vol. 15, no. 3, 351–372, (2006).
[29] H. M. Hassan, A. M. Soliman, "Novel CMOS realizations of Operational Floating Current Conveyor and applications," Journal of Circuits, Systems, and Computers, vol. 14, no. 6, pp. 1113–1143, (2005).
[30] Y. H. Ghallab, W. Badawy, "A New Design of a Current-mode Wheatstone Bridge Using Operational Floating Current Conveyor", International Conference on MEMS, NANO and Smart Systems, pp. 41-44, (2006).
[31] Y. H. Ghallab, W. Badawy, K. V. I. S. Kaler, B. J. Maundy, "A Novel Current-Mode Instrumentation Amplifier Based on Operational Floating Current Conveyor", IEEE Transactions on Instrumentation and Measurement, vol. 54, no.5, pp.1941-1949, (2005).
[32] Y. H. Ghallab, W. Badmy, "A New Differential PH Sensor Current Mode Readout circuit using only two Operational Floating Current Conveor", IEEE International workshop on Biomedical Circuits & Systems, pp. 13-16, (2004).
[33] S. I. Liu, "High input impedance filter with low component spread using current feedback amplifiers", Electronics Letters, 31, pp. 1042–1043, (1995).
[34] Z Wang, '2-MOSFET Trans-resistor with extremely low distortion for output reaching supply voltages' Electronics letters, vol. 26, no. 13, pp. 951-952, 1990.

ISSN 2278-7763

The Comparative Study of Software Maintenance Forecasting Analysis Based on Backpropogation (NFTOOL and NTSTOOL) and Adaptive nuero fuzzy interference system ANFIS.

Anuradha Chug[1] and Ankita Sawhney[2]

[1] *University School of Information and Communication Technology, GGSIP University, Dwarka, New Delhi 110077*

[2] *Computer Sc Department, University School of Information and Communication Technology, GGSIP University, Dwarka, New Delhi 110077*

a_chug@yahoo.co.in

ankitasawhney1@gmail.com

Abstract- Software could be called as heartbeat of today technology. In order to make our software pace with the modern day expansion, it must be inevitable to changes. Enhancements and defects can be stated as two major reasons for software change.Software maintainability refers to the degree to which software can be understood, corrected or enhanced. Maintainability of software accounts for more than any other Software engineering activity. The aim of the paper is to present a study based on the experimental analysis to show that ANFIS can more accurately predict maintainability as compared to other models. Predicting the maintainability accurately using ANFIS has got its benefits in now a day's risk sensitive business with economic environment where software holds the most valuable assets ,may it be transaction processing (governmental or banking service) ,manufacturing automation(chemicals ,automation) or any other industry.

Keywords-ANFIS (Adaptive nuero fuzzy interface system), ANN (Artificial nueral network), Software Maintainability, OO metrics, change, S.D (Standard Deviation), MSE (Mean square error)

.1. Introduction

Software systems after their release are subjected to continuous evolution and modification. Software includes many phases; maintenance is the last of all the phases .This phase is initiated after the product has been released. The maintenance phase of the software is the most expensive and time consuming of all the phases amongst its life cycle, and because of this it remains a major challenge in quality engineering studies [1]. This phase is required to keep the software up to date with the environment changes and changing user requirements. The maintenance phase can be defines as: Maintainability: The ease with which a software can be modified in order to isolate defect or its cause, correct defect or its cause, cope with a change environment or meet new requirements.

A good quality, maintainable software is always based on robust design. We can design a good design as one which allows easy plug in of new functionality in terms of new methods and new classes without reimplementing the previous iteration results. In order to calculate maintainability we first need to calculate the change effort, which deals with the average effort required to modify, add or delete a class. Maintenance could be regarded as the most important phase as it consumes as it consumes about 70% of the time of a softwares life and about 40-70% of the entire cost of software is spend on the maintenance of the software [1].

The maintenance process can be categorized in the following four areas of interest [2]:

a) Corrective maintenance: Modification of software which is performed after the delivery to correct the discovered problems. Examples of corrective maintenance include correcting a failure to test for all possible conditions or a failure to process the last record in a file.

Copyright © 2013 SciResPub.

ISSN 2278-7763

b) Adaptive maintenance: Modification of a software performed after the delivery so that the software product remains usable in a changing or changed environment. Examples of adaptive maintenance include implementation of a database management system for an existing application system and an adjustment of two programs to make them use the same record structures.

c) Perfective maintenance: Modification of a software performed after delivery so as to improve the performance or maintainability. Examples of perfective maintenance includes modifying the payroll program to incorporate a new union settlement, adding a new report in the sales analysis system, improving a terminal dialogue to make it more user-friendly, and adding an online help command.

d) Preventive maintenance: Modification of a software performed after the delivery such that the latent faults get detected and corrected before they become effective faults. Examples of preventive change include restructuring and optimizing code and updating documentation.

Many studies have been conducted in past which have found a strong link between the object oriented metrics and software maintainability and that maintainability prediction can be done using these metrics[3]. The Objective of our research is to apply ANFIS tool [4] along with the two other tools, all based on Nueral networks, compare them and ascertain their performance in terms of software maintainability.

For this we initially studied various metrics available and amongst them selected those which showed strong relationship to maintainability [5]. The metrics which were chosen by us for the analysis includes size, weighted methods per class, depth of inheritance tree, number of children, number of methods and coupling between objects. Then we divided the available data in three sets of ration 3:1:1 and used them for training, testing and validation.

2. RELATED WORK

There are several models which have been proposed to predict the software maintainability. These models varies from simple regression analysis models to complex machine learning algorithms .Some of the existing works are listed as below :

G. M. Berns used maintainability analysis tool which is a kind of lexical analyser to predict maintainability in the year 1984.D Kafura et al used static analyser as a count to predict maintainability in year 1987.They used seven different metrics to predict maintainability. For their study they took three different versions of the system and worked on it. Wake, S. et al used Multiple Linear Regression Model in year 1988 to predict maintainability. They used multiple metrics as parameter for their model and also showed that the effect of metrics also depends upon the development environment, programming language and the application. I W., Henry S. [3] used A Classic Ada Metric Analyzer in the year 1993 for predicting maintainability. In the year 1993 Rajiv D Banker et al [6] also predicted maintainability based on Statistical Models which assigned weights to each metric used.

In year 2002 K.K. Aggarwal et al [7] predicted software maintainability prediction based on fuzzy logic. They took into consideration three aspects of software to measure maintainability which was readability of source code, documentation quality and understandability of software. The advantages of using new rules base of fuzzy models were that they required less storage space and would be efficient when used to find the results in simulation. In year 2003 two predictibilty models were made one by Melis Dagpinar et al based on Correlation, Multivariate Analysis, Best subset Regression Model and the other by Stamelos et al based on Bayesian belief networks. In year 2005 Thwin et al [8] predicted the software development faults and software readiness using general regression nueral network and ward nueral network. In their research they performed two kinds of investigations- prediction of number of defects per class an prediction of number of lines changes per class.

In2008 N.Narayanan Prasanth et al based their analysis on Fuzzy repertory table and Regression analysis. They took into consideration sample of 4 products and calculated both absolute and relative complexities over it. Then using fuzzy repertory table technique they acquired the domain knowledge of testers and used it for software complexity analysis. Regression analysis was then used to predict maintainability from code complexity of product. In the year 2011 Marian Jureczkoused Stepwise logistic regression to predict maintainability.

3. METRICS STUDIED

Software metric is a measure of some property of a piece of software or its specifications [5]. To study the various features of object oriented languages which includes inheritance, encapsulation, data hiding, coupling, cohesion ,memory management we require careful selection of metrics. Object oriented metrics can be used throughout the software life cycle to quantify different aspects of an object oriented application. We studied various metrics and amongst those we have selected those which show strong relationship with software maintainability.

The following OO metrics described in table 1 have been taken as independent variables in our study:

TABLE 1

IJOART

Copyright © 2013 SciResPub.

ISSN 2278-7763

INDEPENDENT METRICS DEFINITION

Metrics	Definition
SIZE 1(Lines of code):	The number of total lines of code excluding the comments.
WMC (Weighted Methods per Class):	The sum of McCabe's cyclomatic complexities of all local methods in a class.
DIT (Depth of Inheritance Tree):	The depth of a class in the inheritance tree where the root class is zero.
NOC (Number of Children):	The number of child classes for a class. It counts number of immediate sub classes of a class in a hierarchy.
NOM (Number of Methods):	The number of methods in a class.
CBO (coupling between object):	CBO of a class is a count of the number of other classes to which that class is coupled.

Forecasting the maintenance of the software could help in better enhancements at a lower cost. In our study we propose to investigate relation between object oriented metrics and change effort, which indirectly reflects the maintainability of the software being developed. The dependant variable therefore used in our study is change. The dependant variable metric change has been described in TABLE 2:

TABLE 2

DEPENDENT METRICS DEFINITION

Metrics	Definition
CHANGE	The number of lines added and deleted in a class, change of the content is counted as change.

4. EMPERICAL DATA

In this section we will introduce our data sources and will provide description about the data collection method. Two different versions of C++ source codes varying in size and application domains were collected from different open source software progress. In our study we collected and analyzed 25 such classes. CCCC tool was used to analyse the codes and create a report on various metrics of the code. CCCC is a free software tool for measurement of source code related metrics by Tim Littlefair. Some of the advantages of using CCCC as a metric analyser are: It contains internal database recoded using STL which makes it faster, It has got persistent file format which allows analysis of outcomes to be saved across runs, reloaded, read by other tools, Using CCCC all the output files are generated into a single directory, (by default .cccc under the current working directory), Each class identified by CCCC has a detailed report attached with it. In report, low-level data are accompanied by HTML links to the location in the source file which gave rise to the data and configuration directory is no longer required.

Six different metrics calculated using CCCC for 25 sample classes are Size1, weighted methods per class, number of children, coupling between object, number of methods, and depth of inheritance tree.

The dependant variable change is calculated by keeping following rules in mind.

a. Any new comment in line in the new version of the software is not counted as an added line.
b. If any two consecutive lines of the previous version are merged as one single line in the recent version then it is regarded as one deleted line change and one modified line change.
c. Addition of any new lines to the source code and addition of curly braces which were not there in the previous version and have been added in the recent version of the software are counted as added lines change.
d. Deletion and addition of blank lines in not considered as a change.
e. Reordering the sequence of a line is not considered as a change.
f. Deletion of the statements, curly braces, lines of code which were present in the previous version and are no present in the recent version are regarded and counted as deleted lines.
g. Any change or variation in the lines of comment is not considered a change.

The data set was than divided in the ratio of 3:1:1 for the training data: testing data: validation data means 60% of the sample data is used for training that is using the specified algorithm machine learns from the data patterns. The next 20% of the data is used for testing to analyse how much the predicted and actual values are close to each other. The last 20% of the data is used for validating.

The samples were than trained according to the appropriate algorithm selected.

The table 3 shows the descriptive statistics of the various data metrics used.

IJOART

Copyright © 2013 SciResPub.

ISSN 2278-7763

TABLE 3

STATISTICS OF DATA SET

Metric	Minimum	Maximum	Mean	S.D
SIZE1	5	1040	281.16	293.9
WMC	1	24	6.64	5.51
DIT	0	1	0.12	0.33
NOC	0	1	0.16	0.37
CBO	0	2	0.32	0.56
NOM	1	24	5.88	5.80

After the collection of data we then used Nueral network toolbox to predict maintainability and validate the results. Following standard steps are followed while designing neural networks to solve problems application areas:

a. Collect data.
b. Create the network.
c. Configure the network.
d. Initialize the weights and biases.
e. Train the network.
f. Validate the network.
g. Use the network.

At the end the results obtained from all the three different techniques obtained based on the mean square error value obtained(MSE).The mean square error could be defined as the average square difference between the outputs obtained and the targets. Lower value of MSE implies better results and zero value of MSE depicts no error.

5. PREDICTION OF MAINTAINACE USING BACKPROPOGATION (NFTOOL)

Firstly maintenance effort prediction models are constructed and the predictive accuracies are compared with the actual values using NFTOOL available in the matlab nueral network toolbox.
Using the NFTOOL [10] we train the network to fit the inputs and targets. It solves the data fitting problem with a two layer feedforward network trained with Lerenberg-Marquardt.
Neural networks are good at fitting functions. In fact, there is proof that a fairly simple neural network can fit any practical function

Suppose, for instance, that we have data from a housing application and we want to design a network which can predict the value of a house given pieces of geographical and real estate information. We have a total number of homes for which we have items of data and their associated market values.
We can solve this problem in two ways:
a. Use a graphical user interface, NFTOOL, as described in “Using the Neural Network Fitting Tool”.
b. Use command-line functions, as described in “Using Command-Line

In our study we are working with the graphical user interface.
To work with the fitting problem we first arrange a set of input vectors as columns in a matrix than arrange another set of target vectors (that is the correct output vectors for each of the given input vectors) into a second matrix.

The number of hidden neurons selected for our sample data: 10

The structure of nueral network and the training algorithm selected in NFTOOL inside nueral network toolbox is as shown in figure 1

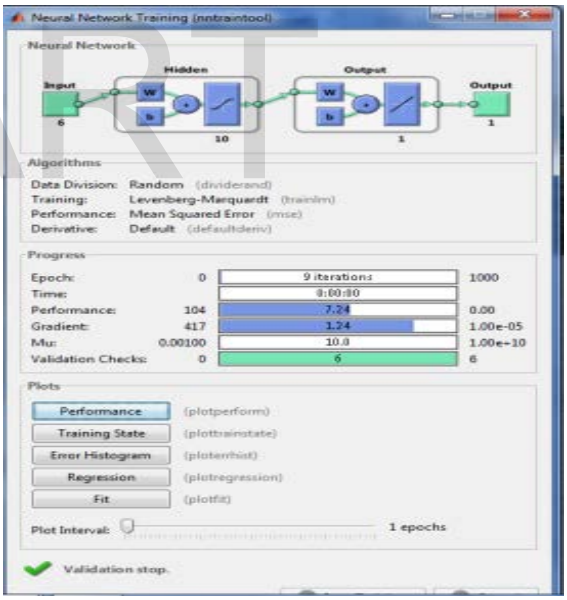

Fig 1 :(Snapshot of trained nueral network using NFTOOL)

The Mean Square Error values (MSE) values observed for the above system are listed as below in table 4.

TABLE 4

RESULTS OBTAINED FOR NFTOOL

IJOART

Copyright © 2013 SciResPub.

ISSN 2278-7763

Data	No of samples	MSE
Training	17	$8.98e^{-0}$
Testing	4	$28.26e^{-0}$
Validation	4	$33.53e^{-0}$

A plot of comparison between training, testing and validating data is shown in figure 2:

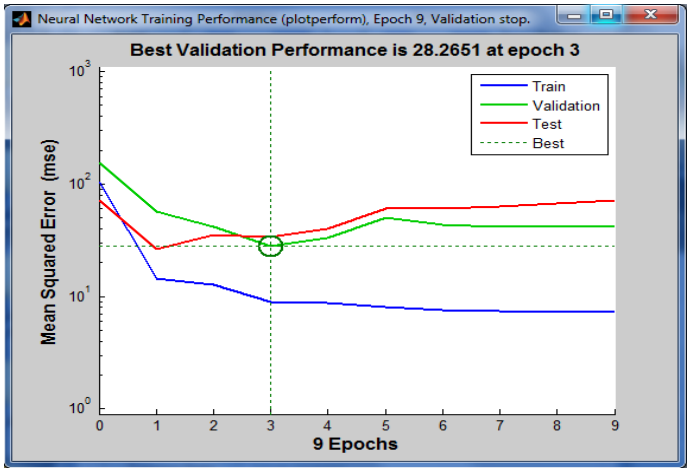

Fig2: comparison between trained, tested and validated values

6. PREDICTION OF MAINTAINACE USING BACKPROPOGATION (NTSTOOL)

The next investigation is to construct maintenance effort prediction models and compare the predictive accuracies with the actual values using NTSTOOL available in the matlab nueral network toolbox. NTSTOOL stands for neural network time series tool.
Time series can be defined as a series of data where the past values in the series may influence the future values. (The future value is a nonlinear function of its past m values)
NTSTOOL opens the nueral network time series wizard and leads you through solving a problem. This tool takes the past values and predicts the future values. NTSTOOL was introduced in Neural Network Toolbox version 7.0, which is associated with release R2010b.
In order to train the data using NTSTOOL, a set of input vectors are arranged as columns in a cell array then the target vectors (that is the correct output vector for each of the given input vectors) are arranged into a second cell matrix.
The number of hidden neurons selected for our sample data: 10
The structure of nueral network and the training algorithm selected in NFTOOL inside nueral network toolbox is as shown in figure 3

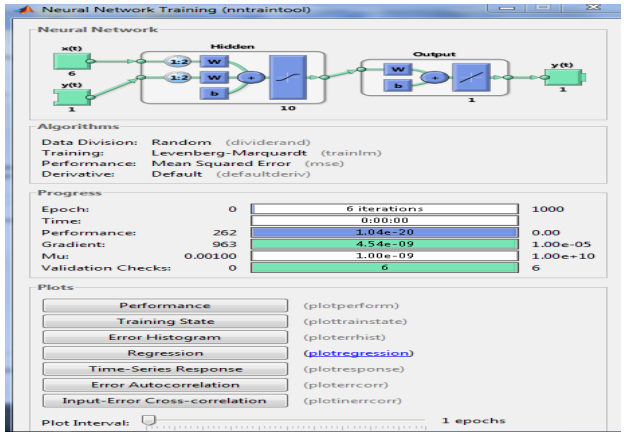

Fig 3: Snapshot of trained nueral network using NTSTOOL

The Mean Square Error values (MSE) values observed for the above system are listed as below in table 5.

TABLE 5

RESULTS OBTAINED FOR NTSOOL

Data	No of samples	MSE
Training	17	$262.13e^{-0}$
Testing	4	272.84^{-0}
Validation	4	$349.53e^{-0}$

A plot of comparison between actual and predicted maintenance effort on validation data is shown in fig 4:

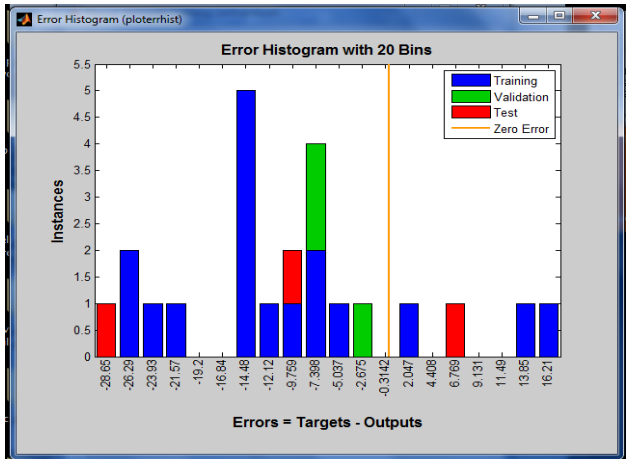

Fig4: Comparison between trained, tested and validated values

IJOART

Copyright © 2013 SciResPub.

ISSN 2278-7763

7. PREDICTION OF MAINTAINACE USING ADAPTIVE NUERO-FUZZY INTERFERENCE SYSTEM (ANFIS).

The next investigation is to calculate maintenance effort using nuero fuzzy technique .ANFIS are a class of adaptive network that are functionally equivalent to fuzzy interference systems, they use hybrid training algorithm. The ANFIS approach learns the rules and membership functions from data.

ANFIS is an adaptive network. An adaptive network is network of nodes and directional links. Associated with the network is a learning rule - for example back propagation. It's called adaptive because some, or all, of the nodes have parameters which affect the output of the node. These networks are learning a relationship between inputs and outputs

Using a given input/output data set, the toolbox function ANFIS constructs a fuzzy inference system (FIS) whose membership function parameters are tuned (adjusted) using either a backpropagation algorithm alone, or in combination with a least squares type of method. This allows your fuzzy systems to learn from the data they are modeling.

The Matlab Fuzzy Logic Toolbox function that accomplishes this membership function parameter adjustments called ANFIS. We can start ANFIS using either command line option or using graphical user interface. In our study we have worked on graphical user interface for ANFIS.As a initial step we load the data(training ,testing ,validation) using the appropriate radio buttons. The loaded data gets plotted on the plot region. We then either generate or load an initial FIS model and then we select the FIS model parameter optimization method-backpropagation or a mixture of backpropagation and least squares (hybrid method).after this the number of training epochs and the training error tolerance are chosen and the data is trained by clicking the train now radio button .We can view the FIS output versus the training, testing and checking data.

The Mean Square Error values (MSE) values observed for the above system are listed as below in table 6.

TABLE 6

RESULTS OBTAINED FOR NFTOOL

Data	No of samples	MSE
Training	17	$4.48e^{-0}$
Testing	4	$15.65e^{-0}$
Validation	4	$23.72e^{-0}$

A plot of actual and predicted maintenance effort on training data is shown in figure 5:

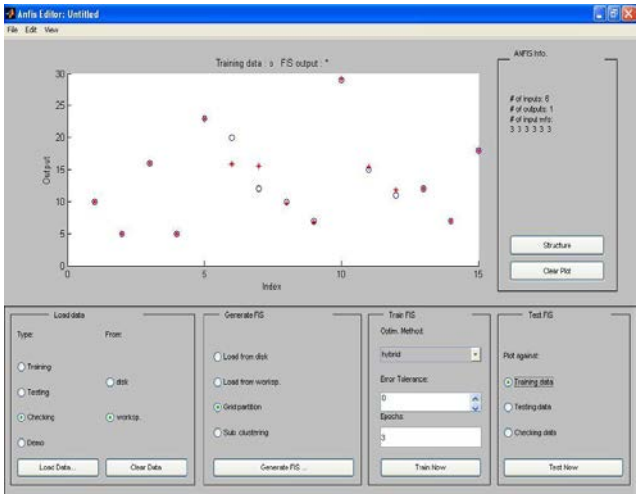

Fig 5 : Comparison between training and actual values

A plot of actual and predicted maintenance effort on testing data is shown in figure 6:

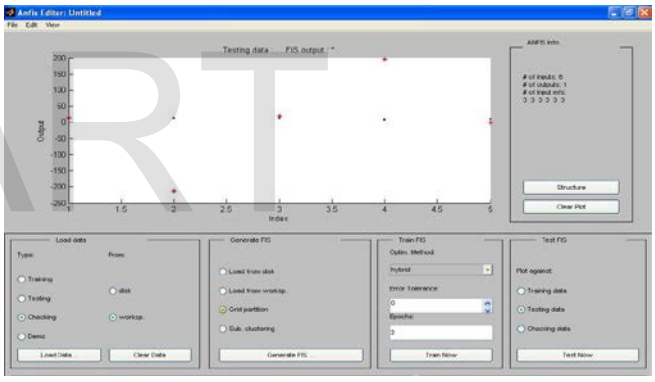

Fig 6: Comparison between testing and actual values

A plot of actual and predicted maintenance effort on validation data is shown in figure 7:

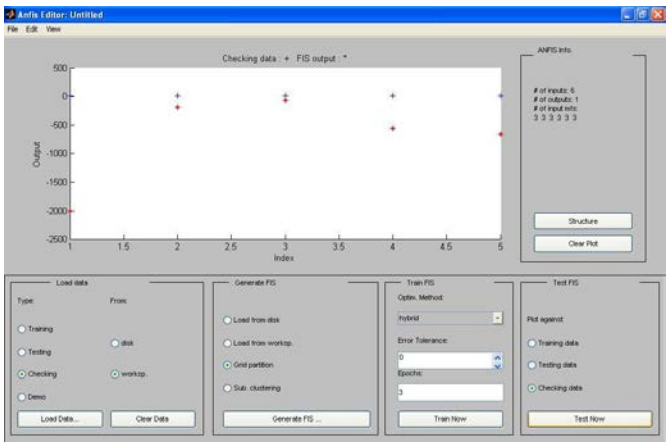

IJOART

Copyright © 2013 SciResPub.

ISSN 2278-7763

Fig 7 Comparison between checking and actual values]

8. THREATS TO VALIDITY

This section included some of the limitations related to the project. First, the object oriented classes are easier to analyze till their complexity is below the threshold level. The understandability difficulty increases as the complexity increase. Second, The project runs well for the small to medium scale projects but the matlab may show an out of memory exception for the v large scale projects for this we need to ensure sufficient memory free space memory is available in the drive where matlab has been installed.

9. CONCLUSIONS

In the work we have compared three different techniques (Fitting tool, Time series tool and Adaptive nuero fuzzy interference system) for predicting the software maintenance effort (change) of software system. Comparing the figures(figure2,figure4,figure5,figure6, figure7) showing the difference between actual and predicted values and the tables (table 4,table 5,table 6) showing mean square error obtained from for three techniques clearly shows that the mean square error value for validation data obtained for ANFIS ($23.7e^{-0}$)trained network is less compared to the networks trained using NFTOOL($33.53e^{-0}$) and NTSTOOL($349.53e^{-0}$) and therefore predicted values obtained using ANFIS are more closer to actual values in comparison to the values from the other two methods (NFTOOL and NTSTOOL).This concludes that results of ANFIS are better for the prediction purposes. However, this research has been done for a small system and therefore the results needs to be generalized by conducting similar analysis on data of other large real time systems. In future we are planning to take other paradigms apart from those taken in this study and perform validation on it.

REFERENCES

[1]Ruchika Malhotra and Anuradha Chug,„ Software Maintainability Prediction using Machine Learning Algorithms",Software Engineering: An International Journal (SEIJ) , Vol. XX, No. XX, 2012.

[2]Sandeep Sharawat "Software maintainability prediction using nueral networksInternational Journal of Engineering Research and Applications "(IJERA) ISSN: 2248-9622 www.ijera.com Vol. 2, Issue 2,Mar-Apr 2012, pp.750-755

[3]W. Li and S. Henry, "Object-Oriented Metrics that Predict Maintainability," Journal of Systems and Software, vol. 23, pp. 111-122, 1993.

[4]Jyh–Shing,Roger Jang ,"ANFIS-Adaptive network based fuzzy inference system",IEEE transactions on systems,man,cybernets VOL23,No 3 May/June 1993.

[5]S. Chidamber and C. Kemerer, "A Metrics Suite for Object Oriented Design," IEEE Transactions on Software Engineering, vol. 20, no. 6, pp. 476-493, 1994 .

[6] W. Li and S. Henry, "Object-Oriented Metrics that Predict Maintainability," Journal of Systems and Software, vol. 23, no 2, pp. 111-122, 1993.

[7]Chidamber, Shyam R. and Cris .F Kamerer, "Towards a metrics Suite for Object-Oriented Design Proceedings", OOPSLA'91, July 1991, pp.197-211 Conference 1991.

[8] K.K. Aggarwal, Yogesh Singh, Jitender Kumar Chhabra, "An Integrated Measure of Software Maintainability", proceedings reliability and maintainability symposium, 2002, 0-7803-7348-0/02/$10 2002 @IEEE .

.[9]M. Thwin and T. Quah, "Application of neural networks for software quality prediction using object oriented metrics", Journal of Systems and Software, vol. 76, no. 2, pp. 147-156, 2005.

[10]Dr. Arvinder Kaur, Kamaldeep Kaur, Dr. Ruchika Malhotra," Soft Computing Approaches for Prediction of Software Maintenance Effort", 2010 International Journal of Computer Applications (0975 - 8887) Volume 1 – No. 1680.

[11] Y. Zhou and H. Leung, "Predicting object-oriented software maintainability using multivariate adaptive regression splines," Journal of Systems and Software, vol. 80, no. 8, pp. 1349-1361, 2007.

[12] Mahmoud O. Elish and Karim O. Elish , " Application of TreeNet in Predicting Object-Oriented Software Maintainability: A Comparative Study", European Conference on Software Maintenance and Reengineering 1534-5351/09 $25.00 © 2009 IEEE DOI 10.1109/CSMR.2009.57.

[13]P. K. Suri1, Bharat Bhushan2. "Simulator for Software Maintainability" IJCSNS International Journal of Computer Science and Network Security, VOL.7 No.11, November 2007.

IJOART

ABOUT THE AUTHORS

Anuradha Chug is Assistant Professor in the Department of University School of Information and Communication Technology (USICT), Guru Gobind Singh Indraprastha University, New Delhi. Her areas of research interest are Software Engineering, Neural Networks, Analysis of Algorithms, Data Structures and Computer Networks. She is currently pursuing her Doctorate from Delhi Technological University in the field of Software Maintenance under the guidance of Ms Ruchika Malhotra. She has earlier achieved top rank in her M.Tech (IT) degree and conferred the University Gold Medal in 2006 from GGS IPU.

Copyright © 2013 SciResPub.

ISSN 2278-7763

Previously she has acquired her Master's degree in Computer Science from Banasthali Vidyapith, Rajasthan in the year 1993. She's additionally earned 'PG Diploma in Marketing Management' from IGNOU in 1995. She has long teaching experience of almost 19 years to her credit as faculty and in administration at various educational institutions in India. She has also presented number of research papers in national/international seminars, conferences and research journals. She can be contacted by E-mail at a_chug@yahoo.co.in

IJOART

Ankita Sawhney is perusing M.Tech(Computer Science) from University School of Information and Communication Technology(USCIT),Guru Gobind Singh Indraprastha University, New Delhi. Her areas of research interest are Software Engineering, nueral Networks, software Testing.Previously she has acquired her Bachelors degree(B.Tech) in Information Technology from Bharati Vidyapeeth's college of Engineering, Guru Gobind Singh Indraprastha University, New Delhi. She secured 1st position in IT department of Bharati Vidyapeeth's College of Engineering. Apart from this she has been adjudged as a scholar for both scholastic and non scholastic subjects in school days and has also achieved proficiency awards. She can be contacted by E-mail at ankitasawhney1@gmail.com

Copyright © 2013 SciResPub.

Journal of Scientific & Industrial Research
Vol. 72, June 2013, pp. 387-392

Waste cooking oil: a promising feedstock for biodiesel production through power ultrasound and hydrodynamic cavitation

Amit Pal and *Surendra S. Kachhwaha
Department of Mechanical Engineering, Delhi Technological University, Bawana Road, Delhi, India
*Department of Mechanical Engineering, School of Technology, Pandit Deendayal Petreoleum University, Gandhinagar, Gujarat, India

Received 24 July 2012; revised 03 December 2012; accepted 30 April 2013

The present research work deals with the details of development of laboratory test rigs for power ultrasound and hydrodynamic cavitation test rigs for conversion of WCO into biodiesel in comparison to conventional mechanical stirring. Results show that cavitation techniques can be successfully applied to transesterification reactions, to achieve more than 90% yield of the product for molar ratio 4.5:1 with minimum catalyst percentage of 0.5% and appears to be rapid and effective compared to the mechanical stirring method, for preparing alkyl esters from triglycerides.

Keywords: Cooking oil, Biodiesel

Introduction

Diesel fuel plays an important role in the industrial economy of developing countries, particularly in transport of industrial and agricultural goods, etc. Economic growth is always accompanied by commensurate increase in the transport activities[1]. Majority of the worldôs energy needs are supplied through non-renewable energy sources which are finite and at the current usage rates they will be depleted shortly[2]. Also, petroleum fuels are currently the dominant global source of CO_2 emissions and their combustion is causing damage to clean environment. This has stimulated the recent interest in alternative sources for petroleum-based fuels[3]. Bio-diesel is a promising alternative to petroleum-based fuels derived from vegetable oils or animal fats[4]. The glycerides present in vegetable oils can be separated in the transesterification reaction and may be used as a by-product[5]. Bio-diesel production is a very modern and challenging area for researchers because of its relevance due to increase in the petroleum price and the environmental advantages[6]. As vegetable oils are produced from plants, their burning is completely recyclable as it produces carbon dioxide (CO_2), which is consumed by the plants in photosynthesis[7]. Many vegetable oils like Soybean, Groundnut, Rapeseed, Palm, Olive etc. are wildly used for frying a number of food items. But once they are heated above a critical temperature for deep frying, they become unfit for further cooking, as their further use may lead to cholesterol formation in human beings. Presently, the waste cooking oil (WCOs) are still lower cost feedstock making biodiesel production more competitive to the production of petroleum based diesel fuel. Waste cooking oil can be used as a biodiesel feedstock, as it is available in vast quantities and in its present form if it is used in engines, it will be a big threat to the environment[8-10]. Some researchers[11] suggested to pre-heating the WCO before using it in diesel engines which reduces the viscosity of the WCO and lowers the exhaust emissions as compared to the diesel. Biodiesel can be produced by various conventional methods[12ï15], such as: alkali catalysis, acid catalysis, lipase catalysis etc. Due to the fact that the transesterification is an equilibrium reaction, an excess of alcohol is used to displace the reaction towards ester formation. Non-edible oil and alcohols are immiscible, so that their reaction takes place at the interface in a very slow process. Acid catalyzed process is useful when a high amount of free fatty acids are present in the vegetable oil, but the reaction time is very long (48ï 96 h), and a high molar ratio of alcohol is needed (20:1 wt/wt to the oil). Base catalyzed process is strongly affected by the mixing of the reactants and/or by efficient heating

*Author for correspondence
E-mail: sskachhawaha@rediffmail.com

that produces tiny droplets, thus increasing the reaction contact area.

Considering these limitations, there is a strong quest to develop an efficient, time-saving, economically functional and environmental friendly biodiesel production process at industrial scale having superiority over the classical procedure. Saka and Kusdian[16] and Dembribas[17] have proposed that biodiesel fuels may be prepared from vegetables oil via non-catalytic transesterification supercritical methanol process which works at very high pressure of the order of 120 atmospheric or more. Han et al.[18] succeeded in preparing biodiesel from soybean oil using supercritical methanol and CO_2 as co-solvent at relatively lower temperature and pressure. Hydrodynamic cavitation is one of the potential methods for biodiesel production at industrial scale due to its easy scale-up property. Pal *et al*[19] presented the details of thumba biodiesel production test rig based on hydrodynamic cavitation. The transesterification reaction of vegetable oils using base catalyst and short-chain alcohols using the method of hydrodynamic cavitation was studied by Gogate *et al*[20-21] This is a rapid technique for preparing alkyl esters from triglycerides at pilot plant scale operation. As reported by Ji *et al*[22], cavitating conditions identical to acoustic cavitation could be generated in hydrodynamic cavitation (HC), which even had a better effect on mixing immiscible liquids. In the last decade, ultrasound cavitation[22] has seen diverse applications in a number of fields, such as synthesis of nanostructure material, processing of biomass, sonofusion, sonodynamic therapy, and sonochemical degradation of pollutants and hazardous chemicals. Low frequency ultrasound irradiation is widely used in industry for emulsification of immiscible liquids. Stavarache *et al*[23-24] showed the low frequency ultrasound (28 and 40 kHz) transesterification of vegetable oil with short-chain alcohols in the presence of base-catalyst, in order to obtain biodiesel fuel. Hoang *et al*[25- 26] investigated the transesterification of triolin ethanol to make biodiesel fuel under ultrasound irradiation to evaluate the effect of the amount of base catalyst, molar ratio, and temperature and concluded that alcoholysis of triolin by ultrasound irradiation has the potential for producing cheap Biofuels, which could reduce pollution and protect the environment. Biodiesel production from canola oil methanol was performed by Thanh *et al*.[27] in the presence of a base-catalyst by an ultrasound assisted circulation process at room temperature. Teixeira *et al*[28] investigated the conventional and ultrasound irradiation transesterification of beef tallow by methanol. In the open literature very few studies are available regarding production of biodiesel from WCO using recently developed ultrasound and hydrodynamic cavitation techniques in comparison to mechanical stirring methods. Therefore, in the present study these methods are compared with conventional mechanical stirring method, in terms of reaction time, molar ratio, catalyst % and yield obtained at different time intervals followed by engine performance analysis. For this purpose a laboratory scale test rig for hydrodynamic cavitation and power ultrasound are indigenously designed and fabricated.

Biodiesel production through cavitation technology

The chemical reactions requiring stringent conditions can be effectively carried out using cavitation at ambient conditions. Moreover, free radicals are generated in the process due to the dissociation of vapours trapped in the cavitating bubbles, which results in either intensification of the chemical reactions or in the propagation of certain unexpected reactions. Cavitation also results in the generation of local turbulence and liquid micro- circulation (acoustic streaming) in the reactor, enhancing the rates of transport processes. The generation, subsequent growth and collapse of cavities results in very high energy densities of the order of 1- 10^{18} kW/m^3. Cavitation can occur at millions of locations in a reactor simultaneously and generate conditions of very high temperatures and pressures locally, overall environment being that of ambient conditions. The two principle types of cavitations and their application for transesterification process are described below:

Power Ultrasound

Ultrasonic Cavitation is a useful tool for strengthening mass transfer of liquid-liquid heterogeneous system. In this process cavities are created by the irradiation of power ultrasonic having sufficient energy in the immiscible liquids. As a result micro fine bubbles are formed. The asymmetric collapse of the cavitation bubbles disrupt the phase boundary and impinging of the liquids create micro jets, leading to intensive emulsification of the system. By using ultrasounds the reaction time observed was much shorter (30-45 min) as compared to mechanical stirring. The quantity of required catalyst was also lower.

Hydrodynamic Cavitation

Hydrodynamic cavitation is another technology developed recently, allows the generation of cavity

Table 1—Oil, alcohol and catalyst used for mechanical stirring and cavitation techniques

Molar ratio (alcohol/oil)	Quantity of WCO(g)	Quantity of methanol (g)	Catalyst (KOH) 0.5%	0.75%	1.0%
6:1	300.00 g	66.00 g	1.50 g	2.25 g	3.00 g
4.5:1	300.00 g	49.18 g	1.50 g	2.25 g	3.00 g

collapse conditions similar to acoustic cavitation, thereby enabling different applications requiring different cavitational intensities, which have been successfully carried out using acoustic cavitation phenomenon but at much lower energy inputs. It is reported that hydrodynamic cavitation can be successfully applied to transesterification reaction producing more than 90% yield of the product according to stoichiometry within 15 min of the reaction time.

Experimental work on biodiesel production

Chemistry of Biodiesel

Biodiesel is made using the process of transesterification. In the transesterification of different type of oils, triglycerides react with an alcohol, generally methanol or ethanol, to produce esters and glycerin in the presence of a catalyst[3].

$$\begin{array}{lcl} CH_2\text{-}OOC\text{-}R_1 & & R_1\text{-}COO\text{-}R\hat{o} \quad CH_2\text{-}OH \\ | & \text{Catalyst} & | \\ CH\text{-}OOC\text{-}R_2 + 3R\hat{o}OH & \rightleftharpoons & R_2\text{-}COO\text{-}R\hat{o} + CH\text{-}OH \\ | & & | \\ CH_2\text{-}OOC\text{-}R_3 & & R_3\text{-}COO\text{-}R\hat{o} \quad CH_2\text{-}OH \\ \text{Glycerides} \quad \text{Alcohol} & & \text{Esters} \quad \text{Glycerin} \end{array}$$

Where, term R represents to different alkyl groups.

The overall process is normally a sequence of three consecutive steps, which are reversible reactions. In the first step from triglycerides, diglycerides are obtained. From diglyceride, monoglyceride is produced and in the last step from monoglycerides, glycerin is obtained. In all these reactions esters are produced. The stoichiometric ratio between alcohol and the oil is 3:1. However, an excess of alcohol is usually more appropriate to improve the reaction towards the desired product. Thus molar ratios of 4.5:1 and 6:1 are generally preferred.

Triglycerides (TG) + $R\hat{o}OH \rightleftharpoons$ Diglycerides (DG) + $R\hat{o}COOR_1$

Diglycerides (DG) + $R\hat{o}OH \rightleftharpoons$ Monoglycerides (MG) + $R\hat{o}COOR_2$

Monoglycerides (MG) + $R\hat{o}OH \rightleftharpoons$ Glycerin (GL) + $R\hat{o}COOR_3$

The catalyst used for the reaction is mainly of three types which are listed below.

Alkali Catalyst

This catalyst can be used with methanol or ethanol as well as any kind of oils, refine, crude or frying. The main alkali catalysts are sodium hydroxide (NaOH) and potassium hydroxide (KOH).

Acidic Catalyst

Acid transesterification is the most convenient way to make biodiesel if the sample has relatively high free fatty acid content. The main acidic catalysts are Sulfuric acid (H_2SO_4) and Sulfonic acid.

Enzymes-catalyzed

Enzymes-catalyzed procedures, using lipase as catalyst, are very expensive for industrial scale production and involve three-step process to achieve a 95% conversion. Due to this three step process the reaction time is too large.

Material and Methods

In this work the WCO is collected from five star hotels of Delhi. It was first properly filtered to separate any kind of suspended impurities present. Then WCO sample (300g for mechanical stirring and ultrasonic cavitation and 3 kg for hydrodynamic cavitation) is taken in a beaker and the oil is heated up to 120^0C for about 10 minutes in order to remove water content in the oil to avoid soap formation. This oil is then allowed to cool up to 65^0C temperature so that after mixing with KOH and methanol the mixture temperature is limited to 55^0C. Simultaneously methyl alcohol (CH_3OH) is taken in molar ratio of (1:4.5 & 1:6) and Catalyst (KOH) is taken as (0.5%, 0.75% and 1% by weight of oil). The details of the Oil, alcohol and catalyst used for mechanical stirring are given in Table 1. The mixer of methyl alcohol and KOH is stirred until whole KOH dissolves in methyl alcohol. For conventional mechanical stirring method this

Table 2—Properties of WCO Biodiesel and Diesel

Property	Unit	Acceptable Limit	Diesel ASTM D 975	WCO Biodiesel
Appearance	ð ð	ð ð	clear	clear
Colour	ð ð	ð ð	ð ð	Yellowish
Density at 15 ^{0}C	kg/m^3	860-900	830	886
Kinematic viscosity at 40 ^{0}C	m^2/s	(3.5 - 5) x 10^{-6}	(2.5 - 6)x 10^{-6}	4.3 x 10^{-6}
Flash point	^{0}C	Min 100	51	>210
Sulphur contents	ppm	Max 350	500	<120
Water content	w/w%	0.02-0.05	0.005	>0.04
Calorific Value	MJ/kg	ð	42.0	36.34

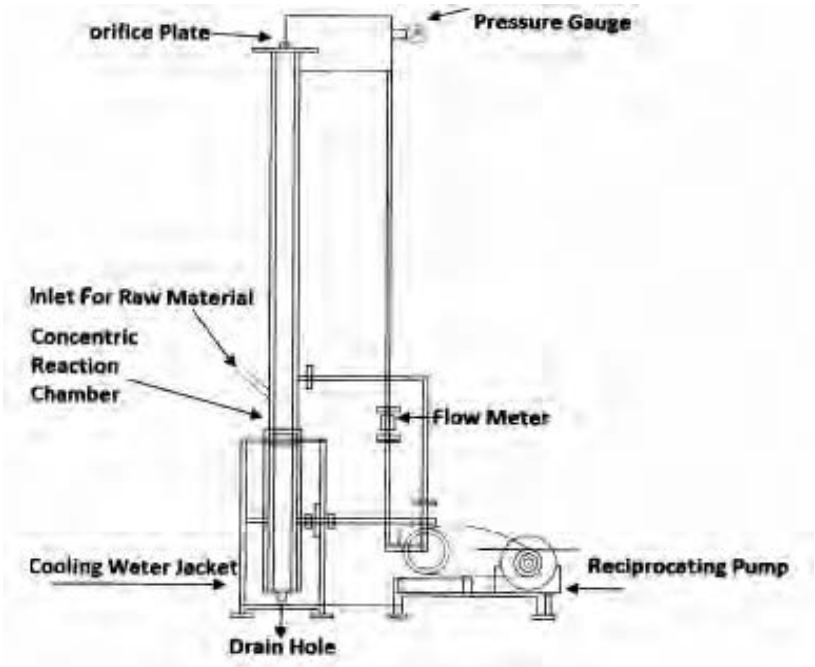

Fig. 1—Schematic diagram of hydrodynamic cavitation system setup

mixture is continuously rotated to mix on a magnetic stirrer. During the whole process temperature is controlled between 50^{0}C to 60^{0}C. After the time intervals of 30, 45 and 60 minutes samples were allowed for gravity settlement in separating funnel for 4-6 hours. The heavier glycerin settled at the bottom was removed and then remaining sample was washed in warm water by stirring with 30-40% warm water for one minute and then again this water is allowed to settle in a separating funnel for 4-6 hours to remove the catalyst and other impurities which are dissolved in water. Finally, the remaining sample is heated up to 110^{0}C ~120^{0}C for 8-10 minutes for removing any water content. The final biodiesel sample so produced was tested for the important chemical and physical properties of WCO biodiesel and these were compared with diesel in Table 2. Density of WCO biodiesel is 6.7% higher than diesel. The experimental observations for both density and viscosity are within the acceptable limits. Flash point of WCO biodiesel is double as compared to permissible limits. Therefore, based on the property data, the present varieties of WCO biodiesel fuels are considered to be suitable for blending and can be used in CI engines.

The schematic diagram of the hydrodynamic cavitation test rig developed is shown in Figure 1. The setup consists of a closed loop circuit comprising a feed tank of about 12 liter capacity, a reciprocating pump (7.36 kW), a control valve and the orifice plate (1mm diameter). The suction side of the pump is connected to the bottom of the feed tank. Discharge from the pump divides into

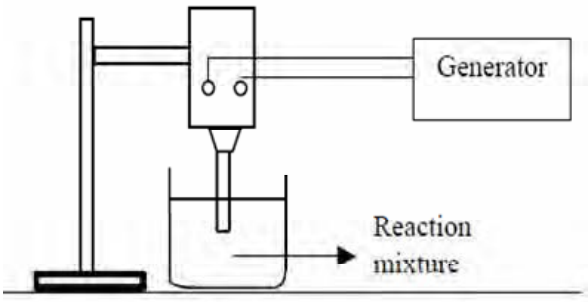

Fig. 2—Schematic diagram of ultrasonic horn type reactor

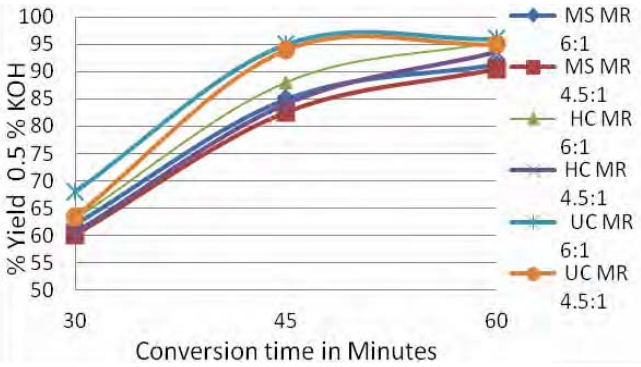

Fig. 3—WCO Biodiesel production yield vs. time [KOH= 0.5%]

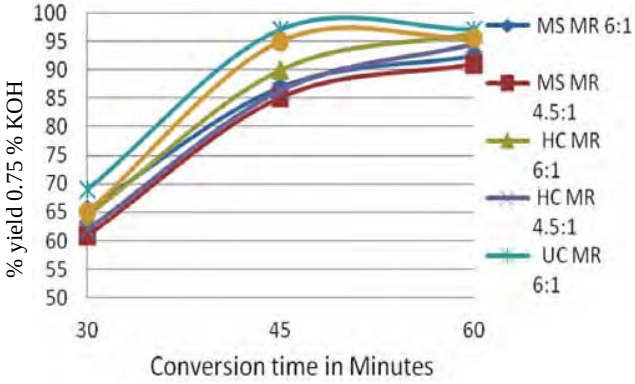

Fig. 4—WCO Biodiesel production yield vs. time [KOH=0.75%]

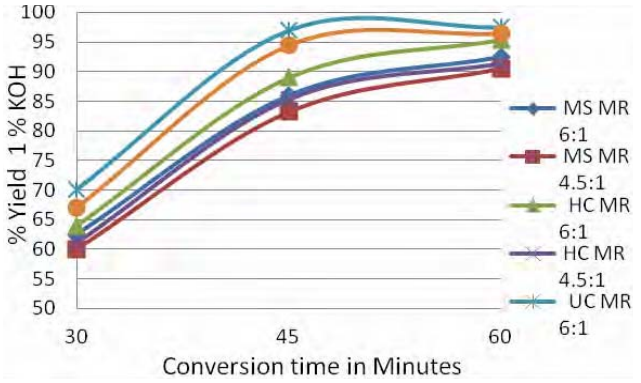

Fig. 5—WCO Biodiesel production yield vs. time [KOH= 1%]

main and bypass lines. The bypass line helps to control the pressure and inlet flow rate into the main line housing and the orifice. The main line consists of a coupling to accommodate the orifice plate. When the liquid passes through the orifice plate (10 bar upstream pressure), it comes out in the form of spray and the velocities at the orifice increase due to the sudden reduction in the area offered for the flow, resulting in the decrease of the pressure. Cavitating conditions are generated just after the orifice plate in the spray chamber. The intensity of the cavitating conditions are strongly depends on the spray. At the far downstream of the orifice, however, due to an increase in the area of cross-section, the velocity decreases giving rise to increasing pressure and pressure fluctuations, which control the different states of cavitation, mainly formation, growth & collapse. The feed tank is provided with a cooling jacket to control the temperature of the circulating liquid. Setup is capable of processing vegetable oil in the range of 2.5 to 10 kg.

Figure 2 shows an ultrasonic horn type biodiesel processor which consumes about 150 W and produces ultrasonic frequencies between 32 to 40 kHz and is suitable for preparing the biodiesel samples of 50 to 300 grams. In the present experiment the processor has been utilized for 300 gram samples. The ultrasonic horn is dipped into the WCO and reactants mixture. The mixture is taken initially at 45^0C and is monitored not to exceed beyond 55^0C limit during the reaction process. Experiments have been performed to convert WCO into biodiesel by both ultrasound and hydrodynamic cavitation techniques and to compare the same with conventional magnetic stirring method in terms of biodiesel production time and yield (%). Experiments were carried out with molar ratio of 4.5:1 and 6:1. A comparison of results for biodiesel production yield and time for these processes for different KOH % are shown in Fig. 3 to Fig. 5 respectively. From the experimental results it is clear that there is a significant increase in yield (%) by using cavitation techniques as compared to mechanical stirring method has been observed. The yield obtained in UC technique is more than 95% after 45 minutes which is higher by 10% as compared to MS for similar experimental conditions. The yield data of HC lies between the data obtained for UC and MS for the entire time range. Thus cavitation techniques can be successfully applied to transesterification reactions, to

achieve more than 90% yield of the product for molar ratio 4.5:1 with minimum catalyst percentage of 0.5%. Therefore, cavitation techniques with molar ratio of 4.5:1 appears to be a rapid and effective technique compared to the mechanical stirring method, for preparing alkyl esters from triglycerides at laboratory scale of operation.

Conclusion

Results show that hydraudynamic and ultrasound cavitation techniques can be successfully applied to transesterification reactions, to achieve more than 90% yield of the biodiesel for molar ratio 4.5:1 with minimum catalyst percentage of 0.5% and appears to be rapid and effective compared to the mechanical stirring method, for preparing alkyl esters from triglycerides at laboratory scale of operation using WCO. The relatively mild reaction conditions and high yield of methyl esters using these environmentally friendly techniques makes them viable for industry.

References

1 Hebbal O D, Reddy V K & Rajagopal K, Performance characteristics of a diesel engine deccan hemp oil, *Fuel*, **85** (2006) 2187ï 2194.

2 Srivastava A, Prasad R & Triglycerides based diesel fuels, *Renew Sustain Energy Rev*, **4** (2000) 111ï 133.

3 Agarwal A K, Biofuels (alcohols and biodiesel) applications as fuels for internal combustion engines, *Progress in Energy and Combustion Science* **33** (2007) 233-271.

4 Murugesan A, Umarani C, Chinnusamy T R, Krishnan M, Subramanian R & Neduzchezhain N, Production and analysis of bio-diesel from non-edible oilsð A Review, *Renew Sustain Energy Rev* **13**(4) (2008) 825-834.

5 Wang, Y D, Al-Shemmeri T, Eames P, McMullan J, Hewit T N & Huang Y, An experimental investigation of the performance and gaseous exhaust emissions of a diesel engine using blends of a vegetable oil, *Appl Thermal Eng*, **26** (2006) 1684ï 1691.

6 Dmytryshyn S L, Dalai A K, Chaudhari S T, Mishra H K & Reaney M J, Synthesis and characterization of vegetable oil derived esters: evaluation for their diesel additive properties. *Bioresour Technol*, **92** (2004) 55ï 64.

7 Marchetti J M, Miguel V U & Errazu A F, Possible methods for biodiesel production, *Renew Sustain Energy Rev*, **11** (2005) 1300ï 1311.

8 Achanai B, Nattawut C & Kowit P, Production of Biodiesel from Waste Cooking Oil Using Mixed Alcohol System. *KMITL Science Journal*, **8**(2) (Sec B) (2008) 59-63.

9 Cigizoglu K B, Ozaktas T & Karaosmanoglu F, Used sunflower oil as an alternative fuel for diesel engines. *Energy Sources*, **19** (6) (1997) 559ï 566.

10 Kerschbaum S & Rinke G, Measurement of the temperature dependent viscosity of biodiesel fuels, *Fuel*, **83** (2004) 287ï 291.

11 Pugazhvadivu M & Jeyachandran K, Investigations on the performance and exhaust emissions of a diesel engine using preheated waste frying oil as fuel. *Renew Energ*, **30**(14) (2005) 2189-2202.

12 Ma F R & Hanna M A, Biodiesel Production: A Review, *Bioresour Technol*, **70** (1999) 1-15.

13 Gerpen J V, Biodiesel processing and production. *Fuel Processing Technology*, **86** (2005) 1097ï 107.

14 Meher L C, Sagar D V & Naik S N, Technical aspects of biodiesel production by transesterification ï a review. *Renew Sustain Energy Rev*, **10** (2006) 248-68.

15 Bouaid A, Diaz Y, Martinez M & Aracil J, Pilot plant studies of biodiesel production using Brassica carinata as raw material, *Catalysis Today* **106** (2005) 193ï 196.

16 Saka S & Kusdiana D, Biodiesel fuel from rapseed oil as prepared in supercritical methanol, *Fuel*, **80** (2001) 225-231.

17 Demirbas A, Biodiesel from vegetable oils via transesterification in supercritical methanol, *Energy Conv Mgmt*, **43** (2000) 2349ï 2356.

18 Han H, Cao W & Zhang J, Preparation of biodiesel from soybean using supercritical methanol and CO_2 as co-solvent, *Process Biochemistry*, **40** (2005) 3148-3151.

19 Pal A, Verma A, Kachhwaha S S & Maji S, Biodiesel production through hydrodynamic cavitation and performance testing, *Renew Energ*, **35**(3) (2010) 619ï 624.

20 Gogate P R & Pandit A B, A review and assessment of hydrodynamic cavitation as a technology for the future, *Ultrasonics Sonochemistry*, **12**(1) 2005 21ï 27.

21 Gogate P R, Tayal R K & Pandit A B, Cavitation: a technology on the horizon. *Current Science*, **91** (2006) 35ï 46.

22 Jianbing J, Jianli W, Yongchao L, Yunliang Y & Zhichao X, Preparation of biodiesel with the help of ultrasound and hydrodynamic cavitations. ñ*Ultrasonics*, 44(1) (2006) 411ï e414.

23 Stavarache C, Vinatoru M, Nishimura R & Maeda Y, Fatty acids methyl esters from vegetable oil by means of ultrasound energy. *Ultrasonics sonochemistry*, 12 (2005) 367ï 372.

24 Stavarache C, Vinatoru M & Maeda Y, Aspects of ultrasonically assisted transesterification of various vegetable oils with methanol, *Ultrasonics Sonochemistry*, **14**(3) (2006) 380-386.

25 Hoang D H, Nguyen T D, Kenji O, Yasuaki M & Rokuro N, Effect of Molar Ratio, Catalyst Concentration and temperature on transesterification of Triolein Ethanol under Ultrasound Irradiation, *J of the Japan Petro Inst*, **50**(4) (2007) 195-199.

26 Hoang D H, Nguyen T D, Kenji O, Rokuro N & Yasuaki M, Biodiesel production by esterification of oleic acid short-chain alcohols under ultrasound irradiation condition, *Renew Energ*, **34** (2009) 780ï 783.

27 Thanh L T, Okitsu K, Sadanaga Y, Takenaka N, Maeda Y & Bandow H, Ultasound assisted production of biodiesel fuel from vegetable oils in a small scale circulation process. *Bioresour Technol*, **101** (2010) 639-645.

28 Teixeira L S G, Assis J C R, Mendonca D R, Santaos I T V, Guimaraes P R B, Pontes L A M & Teixeira J S R, Comparison between conventional and ultrasound preparation of beef tallow biodiesel. *Fuel Processing Technology*, **90** (2009)1164-1166.